Isotope Fractionation during Volatile Loss from Planets and Asteroids



Aart R.W. van der Waal

Department of Earth Sciences
St. Cross College
University of Oxford

Thesis submitted for the degree of *Doctor of Philosophy*

Trinity Term 2023

Abstract

Volatile element depletion trends of the terrestrial mantle and extra-terrestrial bodies relative to CI carbonaceous chondrites indicate that evaporative loss from silicate melts had a considerable effect on the trace element budget and isotopic composition of these bodies. This large scale volatile loss occurred during the early stages of planetary evolution where bodies were partially or wholly molten due to the heat generated by impactors and the decay of short-lived radionuclides. The 50% condensation temperature is often used to describe volatility in planetary sciences, but the restriction to solar nebula conditions hinders its applicability beyond the first ~3 Myr of the solar system.

This study assessed evaporative loss of Li, P, V, Cu, Zn, Ga, Ge, As, Rb, Ag, Cd, In, Sn, Sb, Cs, Tl and Pb from silicate melts. Evaporation experiments were performed in a one atmosphere gas mixing furnace at 1300 – 1400°C and fO_2 between air and the iron-wüstite oxygen buffer reaction in three different melt compositions. Evaporative loss was quantified using the volatility factor which showed that evaporative loss for all elements increased with decreasing fO_2 and that trace element volatility decreased in more felsic melts. Volatility factors showed reasonable correlations with CI carbonaceous chondrite normalized bulk silicate Earth abundances and experimentally determined 1% evaporation temperatures, but poor correlations with the equilibrium partial pressures and the 50% condensation temperature. The modified Hertz-Knudsen-Langmuir equation (HKL) was used to infer the apparent equilibrium constant, enthalpy and entropy of the evaporation reactions with mixed results.

The Zn isotopic composition showed that evaporative loss of Zn from silicate melts was a diffusion-limited process with a Zn depleted boundary layer in the silicate melt. Liquid – vapour fractionation factors ($\alpha_{66/64}$) closer to unity than expected further confirmed that evaporation was diffusion-limited. The experimental $\alpha_{66/64}$ were used to model isotope fractionation on various solar system bodies and terrestrial materials assuming a closed-batch system. These showed that $\alpha_{66/64}$ were able to reproduce the Zn isotopic fractionation observed in lunar basalts. For the other (extra-)terrestrial environments the observed fractionation was not reproduced using experimental $\alpha_{66/64}$.

The contents of this thesis are my own work, unless otherwise stated.

A MASSIVE THANK YOU TO

My Supervisors
dr. Jane Barling
prof. Bernard J. Wood

The Examiners
prof. Jon Wade
prof. Helen M. Williams

The Experimental Petrology Group
Ed Baker
Julien Boulliung
Laura Garcia-Ramos
Andrew Matzen
Elena Melekhova
Bei Bei Morrison Evans
Daniella Reis
Richard Thomas
Jon Wade
…and many more

For their contributions to the project
Nicholas Belshaw
Lewis Collins
Chris Day
George Green
Owen Green
Phil Holdship
Jamie Long †
Richard Reid
Duane Smythe
Steve Wyatt

For the good times
Hamish Couper
James King
Zoltan Taracsák
Annika Voigt
David Wang
Iris van Zelst

The Wolfson – St. Cross Football Team

Family and friends back home

And anyone else I may have forgotten

FOR THEIR SUPPORT

Table of Contents

Chapter 1 – Introduction **1**
1.1 – Formation of Planets 1
1.1.1 – Introduction 1
1.1.2 – Formation of the Solar System 1
1.1.3 – Accretion of Rocky Bodies 2
1.1.4 – Core-Mantle Segregation 4
1.1.5 – The Composition of the Earth 5
1.2 – Volatility 8
1.2.1 – Background 8
1.2.2 – Describing Volatility 8
1.2.3 – Metal-Silicate Partitioning 10
1.2.4 – Volatile Loss 11
1.3 – Isotope Fractionation 12
1.3.1 – Introduction 12
1.3.2 – Zinc 13
1.3.2.1 – Background 13
1.3.2.2 – Mass-Dependent Fractionation 15
1.3.2.3 – Mass-Independent Fractionation 16
1.3.2.4 – Previous Work 16
1.3.2.4.1 – Isotope Fractionation in (extra-)Terrestrial Materials 16
1.3.2.4.2 – Experimental Studies into Evaporation 18
1.4 – Aim of This Work 20

Chapter 2 – Methodology: Evaporation Experiments **23**
2.1 – Introduction 23
2.2 – Preparation of Starting Materials 25
2.2.1 – Preparation of Major Element Mixes 25
2.2.1.1 – Decarbonation and Fe Reduction 25
2.2.2 – Trace Element Doping 26
2.2.2.1 – Halogen Bearing Trace Element Mix 26
2.2.2.2 – Halogen-Free Trace Element Doping 26
2.2.2.3 – “Glassed” Starting Composition 27
2.3 – Experimental Set-up 28
2.3.1 – The One Atmosphere Furnace 28
2.3.2 – Description of an Experiment 29
2.3.2.1 – Sample Holders and Fe Presaturation 30
2.4 – Major and Trace Element Analysis 32
2.4.1 – Electron Microprobe 32
2.4.2 – Laser Ablation ICP-MS 33
2.4.3 – Composition of the Starting Materials 35
2.5 – Thermodynamic Predictions of Evaporation Reactions 37
2.5.1 – General Description and Assumptions 37
2.5.2 – Oxidation Reactions in the Melt 39
2.5.3 – Evaporation Reactions 39
2.5.4 – Gas Species Interactions 41
2.5.4.1 – Presence of Chloride Species 41

2.6 – Quantifying Volatility 43
2.6.1 – Defining C_i^0 43
2.6.2 – The Volatility Factor 44
2.6.3 – The Modified Hertz-Knudsen-Langmuir Equation 44
2.6.3.1 – Introduction 44
2.6.3.2 – Derivation of the Modified HKL Equation 45
2.6.3.2.1 – One Species in Melt and Gas Phase 45
2.6.3.2.2 – One Species in the Melt, Two Species in the Gas Phase 47
2.6.3.3 – Solving the Modified HKL Equation 47
2.6.3.3.1 – Parameters used in the Modified HKL Equation 47
2.6.3.3.2 – Non-Linear Least Squares 48

Chapter 3 – Methodology: Isotope Analysis 51
3.1 – Introduction 51

3.2 – Sample Preparation 53
3.2.1 – Description of Samples and Starting Material 53
3.2.2 – Isolating Sample Material 53
3.2.3 – Processing Sample Material 54
3.2.3.1 – Clean Lab Environment and Acid Preparation 54
3.2.3.2 – Beaker Cleaning 54
3.2.3.3 – Sample Weighing 54
3.2.3.4 – Sample Digestion 55
3.2.3.5 – Double Spiking the Sample 55

3.3 – Analytical Methodology 57
3.3.1 – The Double Spike 57
3.3.2 – Isotope Dilution 60
3.3.3 – Delta Notation 61
3.3.4 – Three Isotope Plots 62

3.4 – Ion Exchange Chromatography 63
3.4.1 – Purification of Zn 63

3.5 – Mass Spectrometry 65
3.5.1 – Quadrupole ICP-MS 65
3.5.2 – Multiple Collector ICP-MS 66
3.5.2.1 – Principles of MC-ICP-MS 66
3.5.2.2 – MC-ICP-MS Analysis of Zn 68

3.6 – Blank Exercise 74
3.6.1 – Background 74
3.6.2 – Methodology 74
3.6.3 – Results 75
3.6.4 – Established Cleaning Regimen 77

3.7 – Interference Corrections 79
3.7.1 – Potential Interferences on Zn 79
3.7.2 – Interference Corrections 81
3.7.2.1 – The Ba Correction 81
3.7.2.1.1 – The Ba Interference 81
3.7.2.1.2 – Parameterizing the Effect of Ba on Zn 83
3.7.2.1.3 – Applying the Ba Correction 84
3.7.2.1.4 – Problems with the Ba Corrections 86

3.7.2.1.4.1 – Erroneous Ba Corrections 86
3.7.2.1.4.2 – Using $^{137}Ba^{2+}$ for Interference Corrections 87
3.7.2.1.4.3 – Modelling the Ba Correction 89
3.7.2.2 – The Ni Correction 92
3.7.2.2.1 – The Ni Interference 92
3.7.2.2.2 – Parameterizing the Effect of Ni on Zn 92
3.7.2.2.3 – Applying the Ni Correction 94

Chapter 4 – Trace Element Volatility 96
4.1 – Introduction 96

4.2 – Thermodynamic Predictions of Trace Element Behaviour 98
4.2.1 – Evaporation Reactions 98
4.2.2 – Total Partial Pressure of Trace Element Gas Species 100
4.2.3 – Chlorine 100
4.2.3.1 – Chlorine Volatility 100
4.2.3.2 – Chloride Gas Speciation 101

4.3 – Results 103
4.3.1 – Table of Trace Element Abundances 103
4.3.2 – Compositional Gradients 106
4.3.2.1 – Evaporation Induced Compositional Gradients 106
4.3.2.2 – Interaction with the Sample Holder 108
4.3.3 – Metal Blobs 109
4.3.4 – Refractory Elements 110
4.3.5 – Highly Volatile Elements 110
4.3.6 – Moderately Volatile Elements 110

4.4 – Volatility Factors 112
4.4.1 – Temporal Evolution 112
4.4.2 – Effect of Oxygen Fugacity 113
4.4.3 – Effect of Melt Composition 116

4.5 – Modified Hertz-Knudsen-Langmuir Equation 119
4.5.1 – Copper 120
4.5.2 – Zinc 121
4.5.3 – Gallium 121
4.5.4 – Germanium 122
4.5.5 – Arsenic 123
4.5.6 – Rubidium 123
4.5.7 – Indium 124
4.5.8 – Tin 125
4.5.9 – Antimony 125
4.5.10 – Caesium 126
4.5.11 – Lead 127

4.6 – Discussion 128
4.6.1 – Volatility Factor 128
4.6.1.1 – Previous Work 128
4.6.1.2 – CI Chondrite Normalized Bulk Silicate Earth Abundances 130
4.6.1.3 – Partial Pressure of Gas Species 132
4.6.1.4 – 50% Condensation Temperature 137
4.6.1.5 – 1% Evaporation Temperature 139
4.6.2 – Modified Hertz-Knudsen-Langmuir Equation 141

4.6.2.1 – The Apparent Equilibrium Constant 141
4.6.2.2 – Comparing log(K*) and log(K) 142
4.6.2.3 – Apparent Enthalpy and Entropy of the Evaporation Reactions 144
4.6.2.4 – Potential Issues with the Modified HKL Equation 146
4.6.2.4.1 – Validity in Multicomponent Systems 146
4.6.2.4.2 – Fixed and Adjustable Parameters 146
4.6.2.4.3 – Non-Linear Least Squares Minimization 148

Chapter 5 – Zinc Isotope Measurements 152
5.1 – Introduction 152

5.2 – Results 155
5.2.1 – Processing of Samples and Starting Materials 155
5.2.1.1 – Zn Abundances and Double Spiking 155
5.2.1.2 – Isotopic Composition of the Starting Materials 157
5.2.2 – Isotopic Composition of Samples 159
5.2.2.1 – Measured δ^{66}Zn values 159
5.2.2.2 – Zn Abundance Dependence of δ^{66}Zn 160
5.2.2.3 – Time Dependence of δ^{66}Zn 163
5.2.2.4 – Oxygen Fugacity Dependence of δ^{66}Zn 164
5.2.3 – Fractionation Factors 165
5.2.3.1 – Rayleigh Equation 165
5.2.3.2 – Calculating Fractionation Factors 165
5.2.3.3 – Samples 167
5.2.3.4 – Comparing Samples and Modelled Fractionation 169

5.3 – Discussion 172
5.3.1 – Comparison with Previous Work 172
5.3.2 – The Zn Isotopic Composition of Solar System Bodies 173
5.3.2.1 – Experimental Conditions vs. Magma Ocean Conditions 173
5.3.2.2 – The Earth – Moon System 174
5.3.2.3 – Mars 177
5.3.2.4 – Meteorites 179
5.3.2.4.1 – Chondrites 179
5.3.2.4.2 – Achondrites 180
5.3.2.4.2.1 – HEDs and Asteroid 4 Vesta 181
5.3.2.4.2.2 – Ureilites and the Ureilite Parent Body 183
5.3.2.4.2.3 – Aubrites and the Aubrite Parent Body 185
5.3.3 – The Zn Isotopic Composition of Terrestrial Environments 187
5.3.3.1 – Volcanism 187
5.3.3.2 – Tektites and Trinitites 188

Chapter 6 – Summary and Future Recommendations 193
6.1 – Summary 193

6.2 – Future Recommendations 200
6.2.1 – Preparation of the Starting Materials 200
6.2.2 – Experimental Set-up 201
6.2.3 – Starting Compositions and Experimental Conditions 201
6.2.4 – Analysis of Gas Species 202
6.2.5 – Thermodynamic Properties 203
6.2.6 – Trace Element Activity and Evaporation Coefficient Data 204
6.2.7 – Applications to the Volcanic Environment 204

6.2.8 – Integration into Planetary Formation and Evolution Models 205
6.2.9 – Expansion of Isotope Systems 205

References 208

Appendix 1 – Description of Cleaning and Preparation of Lab Plastics I

Appendix 2 – Thermodynamic Predictions: Gas Speciation during Evaporation III
A2.1 – Monometallic Gas Species III
A2.1.1 – Lithium IV
A2.1.2 – Phosphorus V
A2.1.3 – Vanadium V
A2.1.4 – Copper VI
A2.1.5 – Gallium VII
A2.1.6 – Germanium VII
A2.1.7 – Arsenic VIII
A2.1.8 – Cadmium IX
A2.1.9 – Tin IX
A2.1.10 – Antimony X
A2.1.11 – Caesium XI
A2.1.12 – Lead XI

A2.2 – Mono- and Polymetallic Gas Species XIII
A2.2.1 – Lithium XIV
A2.2.2 – Gallium XIV
A2.2.3 – Arsenic XV
A2.2.4 – Rubidium XV
A2.2.5 – Indium XVI
A2.2.6 – Antimony XVI
A2.2.7 – Caesium XVII
A2.2.8 – Thallium XVIII
A2.2.9 – Lead XVIII

A2.3 – Total Partial Pressures XX
A2.3.1 – Volatility Factor Plots – Ideal Trace Element Behaviour XXI
A2.3.2 – Volatility Factor Plots – Non-Ideal Trace Element Behaviour XXII

A2.4 – References XXIII

Appendix 3 – Thermodynamic Predictions: Formation of Chloride Gas Species XXIV
A3.1 – Chloride Gas Speciation XXIV

A3.2 – Element-Specific Plots XXVI
A3.2.1 – Copper XXVI
A3.2.2 – Zinc XXVI
A3.2.3 – Gallium XXVII
A3.2.4 – Germanium XXVII
A3.2.5 – Arsenic XXVIII
A3.2.6 – Rubidium XXVIII
A3.2.7 – Silver XXIX
A3.2.8 – Cadmium XXIX
A3.2.9 – Indium XXX
A3.2.10 – Tin XXX
A3.2.11 – Antimony XXXI

A3.2.12 – Caesium XXXI
A3.2.13 – Thallium XXXII
A3.2.14 – Lead XXXII

A3.3 – References XXXIII

Appendix 4 – Standard Deviations on Trace Element Abundances and Volatility Factors XXXIV

Appendix 5 – Element-Specific Time Series Plots of Volatility Factors XLIX
A5.1 – Lithium XLIX
A5.2 – Phosphorus L
A5.3 – Vanadium LI
A5.4 – Copper LII
A5.5 – Zinc LIV
A5.6 – Gallium LVI
A5.7 – Germanium LVII
A5.8 – Arsenic LIX
A5.9 – Rubidium LX
A5.10 – Silver LXI
A5.11 – Cadmium LXIII
A5.12 – Indium LXV
A5.13 – Tin LXVI
A5.14 – Antimony LXVIII
A5.15 – Caesium LXIX
A5.16 – Thallium LXX
A5.17 – Lead LXXII

Appendix 6 – The Effect of Sample Geometry LXXIII
A6.1 – General Equations LXXIV

A6.2 – Evaporative Surface Area LXXIV

List of Figures

Chapter 1

Figure 1.1: The abundance of elements in the BSE relative that of CI carbonaceous chondrites, normalized to Mg = 1.0, plotted against condensation temperature. The shaded area shows the expected depletion trend based purely on volatile loss. Adapted from Wood et al. (2019).

Figure 1.2: Overview of the Zn isotopic composition of various (extra-)terrestrial materials. The dashed line represents the average δ66ZnLyon of the BSE (Chen et al., 2013a). [1]Luck et al. (2005); [2]Moynier et al. (2006); [3]Moynier et al. (2007); [4]Herzog et al. (2009); [5]Moynier et al. (2009a); [6]Moynier et al. (2010); [7]Ghidan and Loss (2011); [8]Lindsay et al. (2011); [9]Moynier et al. (2011); [10]Barrat et al. (2012); [11]Paniello et al. (2012a); [12]Paniello et al. (2012b); [13]Chen et al. (2013b); [14]Bridgestock et al. (2014); [15]Kato et al. (2015); [16]Pringle et al. (2017); [17]Sossi et al. (2018b); [18]Brugier et al. (2019).

Chapter 2

Figure 2.1: The temporal evolution of the fraction of FeO_T in the silicate glass (FeO_t) relative to the shortest experiment (FeO_0) at different fO_2 for the SM composition, illustrating the effect of fO_2 and capsule material. "(Fe sat)" indicates the Fe-presaturated Pt sample holders.

Figure 2.2: Temporal evolution of the measured Zn abundance of GSE-1G. The solid black line is the GeoReM preferred abundance and the dotted red lines its associated error. The error bar in the bottom left illustrates the average error on each measured Zn data point.

Chapter 3

Figure 3.1: Schematic depiction of the double spike taken from Rudge et al. (2009).

Figure 3.2: The effect of the double spike:sample ratio on the error of the double spike inversion. The red cross is the target double spike:sample ratio and the black crosses are the double spike:sample ratio of the samples.

Figure 3.3: An example of a magnet scan of the Ba-doped unspiked Zn standard tuning solution for all collectors. Vertical scale was adjusted such that peaks of individual elements were clustered together. Interference-free isotopes of other potentially interfering elements Ni (^{64}Ni) and Xe ($^{128}Xe^{2+}$, $^{132}Xe^{2+}$, $^{134}Xe^{2+}$, $^{136}Xe^{2+}$) are shown near the top of the figure with colour-coded labels to match the lines.

Figure 3.4: The temporal evolution of $\delta^{66}Zn_{Lyon}$ (‰) of ETH-AA within a single run. Diamonds represents the average value of the individual measurements (circles) for with 2 s.d. on the average error bars.

Figure 3.5: The temporal evolution of $\delta^{66}Zn_{Lyon}$ (‰) of BCR-2 and IRMM-3702 between runs. Each colour corresponds to a different run. Diamonds represent averages values of the individual measurements (circles) for each run. Error bars represent 2 s.d. on the average within the run. The dashed black line is the average $\delta^{66}Zn_{Lyon}$ and the solid lines represent 2 s.d. on the average of all measurements.

Figure 3.6: Comparison of the BCR-2 and IRMM-3702 values with previous values reported in the literature. All errors are reported as 2 s.d. on the average, but most values from literature were converted to 2 s.d. from two standard errors or 95% confidence intervals.

Figure 3.7: The shift in $\delta^{66}Zn$ for the IRMM-3702 secondary standard as a function of increasing blank size. The measured blanks were included to illustrate that the measured blanks do not impact the measured $\delta^{66}Zn$ beyond the analytical error. The dashed red line represents the ~0.05‰ per amu analytical error.

Figure 3.8: The evolution of the Zn blank with time and illustration of how an increasingly rigorous cleaning procedure decreased the Zn blank.

Figure 3.9: An integrated (22 passes) mass scan over the mass range between 120 amu and 142 amu. Numbers and elements indicate the (expected) peak positions for each mass. The intensity of the highest peak, ^{127}I, is $\sim 8 \cdot 10^{-5}$ V.

Figure 3.10: Comparison of the effectivity of the Ba correction using different isotopes by plotting the Ba-corrected $\delta^{66}Zn_{IRMM}$ (‰) plotted against the $^{x}Ba^{2+}/^{64}Zn$ intensity ratio, a measure of the amount of Ba.

Figure 3.11: (a) The linear growth of $\delta^{66}Zn$ (‰) as a function of increasing $I^{138}Ba^{2+}$ without a Ba correction and **(b)** the evolution of Ba-corrected $\delta^{66}Zn$ (‰), both as a function of increasing Ba concentration in a solution of constant composition. The red circle indicates a Ba-free measurement with an erroneous Ba correction.

Figure 3.12: Comparison of the calculated and modelled $\Delta^{66}Zn$. The dashed line represents the one-to-one line. Erroneous corrections are indicated with a red outline. The inlay on the bottom-right shows the full range of samples and $\Delta^{66}Zn$. Information regarding individual samples can be found in Chapter **4**, Table **4.1** and Chapter **5**, Table **5.1.**

Figure 3.13: The measured $^{137}Ba^{2+}$ and $^{138}Ba^{2+}$ intensities plotted against each other. The dashed line represents the IUPAC reference isotope abundance ratio for $^{137}Ba/^{138}Ba$. Red circles show the three separate sets of repeat analyses of sample Q52.

Figure 3.14: (a) Plot showing how the slope of the $\Delta^{66}Zn$ – $I^{138}Ba/I^{64}Zn$ changes as a function of the double spike:sample ratio. **(b)** Plot of $\Delta^{66}Zn$ against $I^{138}Ba/I^{64}Zn$. Lines show the modelled $\Delta^{66}Zn$ for different double spike:sample ratios.

Figure 3.15: Plot of the $^{61}Ni/^{64}Zn$ intensity ratio as a function of the ^{61}Ni intensity.

Figure 3.16: Comparison of the calculated (data points) and modelled (dashed line) $\Delta^{66}Zn$. The inlay shows the two samples (Q20 and Q49) that require significant Ni corrections and their deviation from the modelled values.

Chapter 4

Figure 4.1: Evolution of the total equilibrium partial pressures of monometallic trace element gas species as a function of fO_2 at fixed temperature. Vertical lines indicate the experimental fO_2 conditions.

Figure 4.2: Compositional gradients for a refractory (V), low valence (Rb) and high valence moderately volatile (In) element in the three major element compositions at $\log(fO_2) = -6$ after 60 minutes.

Concentrations were normalized to the data point furthest away from the evaporating surface. The error on an individual measurement was ~±15%.

Figure 4.3: Plot of compositional gradients from the sample – sample holder interface into the sample for a Pt sample holder. Measured concentrations were normalized to data point furthest away from sample holder. Error bar in bottom left indicates the average one standard deviation on the measurements.

Figure 4.4: Temporal evolution of trace element abundances in the silicate melt normalized to the starting abundance in Table **2.2**. **(a)** Germanium in the SM-2 experiments. Deviations from linearity in the $\log(fO_2) = -8$ time series is caused by the detection limit in LA-ICP-MS analysis. **(b)** Silver in the AN composition.

Figure 4.5: The fO_2 dependence of the volatility factor for the **(a)** SM, **(b)** IB, **(c)** AN, **(d)** SM-2 and **(e)** IB-G compositions.

Figure 4.6: The compositional dependence of the volatility factor at **(a)** $\log(fO_2) = -0.68$, **(b)** $\log(fO_2) = -3.05$, **(c)** $\log(fO_2) = -6$ and **(d)** $\log(fO_2) = -8$.

Figure 4.7: Example comparison of the fit, calculated using the modified HKL equation, to the measured trace element abundance.

Figure 4.8: The volatility factor plotted against the CI chondrite normalized trace element abundance of the bulk silicate Earth, normalized to Mg for the **(a)** SM and **(b)** IB experiments at $\log(fO_2) = -8$ and **(c)** IB-G at $\log(fO_2) = -9$. Trace element abundance of the BSE and CI chondrites taken from Palme and O'Neill (2014).

Figure 4.9: The volatility factor plotted against the total equilibrium partial pressure of the oxide gas species for the **(a)** SM and **(b)** IB experiments at $\log(fO_2) = -8$ and **(c)** IB-G at $\log(fO_2) = -9$ assuming ideal trace element behaviour in the silicate melt.

Figure 4.10: The volatility factor plotted against the total equilibrium partial pressure of the oxide gas species for the **(a)** SM and **(b)** IB experiments at $\log(fO_2) = -8$ and **(c)** IB-G at $\log(fO_2) = -9$ considering non-ideal trace element behaviour in the silicate melt.

Figure 4.11: Log of the volatility factor plotted against the 50% condensation temperature for **(a)** SM and **(b)** IB at log(fO_2) = -8 and **(c)** IB-G at log(fO_2) = -9. The 50% condensation temperatures were taken from Wood et al. (2019).

Figure 4.12: The calculated 1% evaporation temperatures as a function of fO_2.

Figure 4.13: The 1% evaporation temperatures plotted against the log of volatility factor for the SM composition at log(fO_2) = -8.

Figure 4.14: Summary of the log(K*) calculated in Section **4.5** and log(K*) from literature.

Figure 4.15: Plots of the equilibrium constant of the evaporation reaction of the pure species plotted against **(a)** log(K*) and **(b)** an experimental log(K) calculated by correcting log(K*) for non-ideal trace element behaviour in the melt. The dashed line is the one-to-one fit.

Figure 4.16: Plot of RTln(K) against RTln(K*) to illustrate correlation between the two parameters.

Figure 4.17: Three potential fits to the 60 minute fO_2 series of In in the SM composition with **(a)** a linear y-axis and **(b)** logarithmic y-axis. LSQ is the sum of the non-linear least squares misfit between the data points and the model.

Figure 4.18: Three potential fits to the 60 minute fO_2 series of Sn in the SM composition. LSQ is the sum of the non-linear least squares misfit between the four data points and the model.

Chapter 5

Figure 5.1: Overview of the Zn isotopic composition of various (extra-)terrestrial materials. The dashed line represents the average $\delta^{66}Zn_{Lyon}$ of the BSE (Chen et al., 2013a). [1]Luck et al. (2005); [2]Moynier et al. (2006); [3]Moynier et al. (2007); [4]Herzog et al. (2009); [5]Moynier et al. (2009a); [6]Moynier et al. (2010); [7]Ghidan and Loss (2011); [8]Lindsay et al. (2011); [9]Moynier et al. (2011); [10]Barrat et al. (2012); [11]Paniello et al. (2012a); [12]Paniello et al. (2012b); [13]Chen et al. (2013b); [14]Bridgestock et al. (2014); [15]Kato et al. (2015); [16]Pringle et al. (2017); [17]Sossi et al. (2018b); [18]Brugier et al. (2019).

Figure 5.2: Comparison of Zn abundances obtained via isotope dilution and LA-ICP-MS measurements. The dashed line shows the one-to-one line. Error bars are 1 s.d. on the average.

Figure 5.3: The effect of the Zn abundance on the accuracy of sample spiking. The dashed line indicates a one-to-one line. The dashed line is the one-to-one line and the red cross shows the expected spike:sample ratio of 1.4:1 ± 15% and compositional match of 1:1 ± 15%.

Figure 5.4: The effect of the double spike:sample ratio on the error of the double spike inversion. The red cross is the target double spike:sample ratio and the black crosses are the double spike:sample ratio of the samples.

Figure 5.5: The fraction of Zn in the doped starting material [X_{Zn}] added as reagent-grade ZnO plotted against $\delta^{66}Zn_{Lyon}$ (‰) of the (un)doped starting materials and ZnO. Dashed lines represent the mixing lines between undoped starting material and ZnO. Main plot shows $X_{Zn} > 0.8$ with $0 < X_{Zn} < 1$ shown in the top right.

Figure 5.6: Plot of $\delta^{66}Zn_{Lyon}$ (‰) and the ln of the volatility factor for the **(a)** SM and **(b)** IB composition.

Figure 5.7: Plot of the time dependence of $\delta^{66}Zn_{Lyon}$ (‰) at fixed fO_2 for the **(a)** SM and **(b)** IB composition.

Figure 5.8: Plot of the oxygen fugacity dependence of $\delta^{66}Zn_{Lyon}$ (‰) at fixed runtimes for the **(a)** SM and **(b)** IB composition.

Figure 5.9: A plot of volatile loss plotted as a function of the difference in isotopic composition of sample and starting material. Solid lines represent different fractionation factors.

Figure 5.10: Comparison of the measured $\delta^{66}Zn_{Lyon}$ (‰) as a function of the volatility factor for the SM composition (**a)** in air, **(b)** at $\log(fO_2) = -3$, **(c)** at $\log(fO_2) = -6$ and **(d)** at $\log(fO_2) = -8$. Coloured lines represent the different evaporation scenarios of Young et al. (2019) and Sossi et al. (2020) described in the main text.

Figure 5.11: Comparison of the measured $\delta^{66}Zn_{Lyon}$ (‰) as a function of the volatility factor for the IB composition (**a)** in air, **(b)** at $\log(fO_2) = -3$, **(c)** at $\log(fO_2) = -6$ and **(d)** at $\log(fO_2) = -8$. Coloured lines represent the different evaporation scenarios of Young et al. (2019) and Sossi et al. (2020) described in the main text.

Figure 5.12: The Zn isotopic composition of the Earth – Moon system compared to different model fits. Trace element and isotopic data for terrestrial and lunar mantles and individual lunar basalts from Moynier et al. (2006), Herzog et al. (2009), Paniello et al. (2012a), Chen et al. (2013a), Palme and O'Neill (2014), Kato et al. (2015) and Day et al. (2020a). Coloured lines represent different model fits using $\alpha_{66/64}$ for **SM**, **IB** and the three theoretical approaches discussed in Section **5.2.3.2**.

Figure 5.13: The Zn isotopic composition of the Martian mantle and meteorites (Paniello et al., 2012a; Paquet et al., 2023a), modelled using two separate chondrite starting compositions; **(a)** 95% EH enstatite chondrite + 5% carbonaceous chondrite and **(b)** 95% ordinary chondrite + 5% carbonaceous chondrite. Dashed lines represent best fit between average compositions. Coloured lines represent different model fits using $\alpha_{66/64}$ for **SM**, **IB** and the three theoretical approaches discussed in Section **5.2.3.2**.

Figure 5.14: The Zn isotopic composition of unbrecciated eucrite and diogenite meteorites and asteroid 4 Vesta (Paniello et al., 2012b), modelled using two separate chondrite starting compositions; **(a)** 85% EH enstatite chondrite + 15% CI carbonaceous chondrite and **(b)** 85% ordinary chondrite + 15% CI carbonaceous chondrite. Dashed lines represent best fit between average compositions. Coloured lines represent different model fits using $\alpha_{66/64}$ for **SM**, **IB** and the three theoretical approaches discussed in Section **5.2.3.2**.

Figure 5.15: The Zn isotopic composition of ureilites (Moynier et al., 2010; Brugier et al., 2019) modelled using a UPB with an enstatite chondrite starting composition. Coloured lines represent different model fits using $\alpha_{66/64}$ for **SM**, **IB** and the three theoretical approaches discussed in Section **5.2.3.2**.

Figure 5.16: The Zn isotopic composition of the Shallowater aubrite (Moynier et al., 2011) modelled using an APB with an enstatite chondrite starting composition. The [Zn] of individual samples was not reported, so average [Zn] of Shallowater aubrite was used. Coloured lines represent different model fits using $\alpha_{66/64}$ for **SM**, **IB** and the three theoretical approaches discussed in Section **5.2.3.2**.

Figure 5.17: The Zn isotopic composition of tektites (Moynier et al., 2009b; Rodovská et al., 2017; Jiang et al., 2019; Wimpenny et al., 2019) modelled using an average upper crust (Hu and Gao, 2008; Chen et al., 2013a) as the starting composition. Dashed lines represent best fits for each data set. Solid lines represent different model fits using $\alpha_{66/64}$ for **SM**, **IB** and the three theoretical approaches discussed in Section **5.2.3.2**.

Figure 5.18: The Zn isotopic composition of trinitites (Day et al., 2017; Wimpenny et al., 2019) modelled using an arkosic soil starting composition (Wimpenny et al., 2019). Dashed line represents best fit for the data set. Solid lines represent different model fits using $\alpha_{66/64}$ for **SM**, **IB** and the three theoretical approaches discussed in Section **5.2.3.2**.

List of Appendix Figures

Appendix 2

Figure A2.1: The relative partial pressures of Li (g), LiO (g) and LiO_2 (g) plotted as a function of fO_2.

Figure A2.2: The relative partial pressures of P (g), PO (g) and PO_2 (g) plotted as a function of fO_2.

Figure A2.3: The relative partial pressures of V (g), VO (g) and VO_2 (g) plotted as a function of fO_2.

Figure A2.4: The relative partial pressures of Cu (g) and CuO (g) plotted as a function of fO_2.

Figure A2.5: The relative partial pressures of Ga (g) and GaO (g) plotted as a function of fO_2.

Figure A2.6: The relative partial pressures of Ge (g) and GeO (g) plotted as a function of fO_2.

Figure A2.7: The relative partial pressures of As (g) and AsO (g) plotted as a function of fO_2.

Figure A2.8: The relative partial pressures of Cd (g) and CdO (g) plotted as a function of fO_2.

Figure A2.9: The relative partial pressures of Sn (g) and SnO (g) plotted as a function of fO_2.

Figure A2.10: The relative partial pressures of Sb (g) and SbO (g) plotted as a function of fO_2.

Figure A2.11: The relative partial pressures of Cs (g) and CsO (g) plotted as a function of fO_2.

Figure A2.12: The relative partial pressures of Pb (g) and PbO (g) plotted as a function of fO_2.

Figure A2.13: The partial pressure of potential Li gas species as a function of oxygen fugacity.

Figure A2.14: The partial pressure of potential Ga gas species as a function of oxygen fugacity.

Figure A2.15: The partial pressure of potential As gas species as a function of oxygen fugacity.

Figure A2.16: The partial pressure of potential Rb gas species as a function of oxygen fugacity.

Figure A2.17: The partial pressure of potential In gas species as a function of oxygen fugacity.

Figure A2.18: The partial pressure of potential Sb gas species as a function of oxygen fugacity.

Figure A2.19: The partial pressure of potential Cs gas species as a function of oxygen fugacity.

Figure A2.20: The partial pressure of potential Tl gas species as a function of oxygen fugacity.

Figure A2.21: The partial pressure of potential Pb gas species as a function of oxygen fugacity.

Figure A2.22: The total partial pressure of trace elements considering all potential gas species.

Figure A2.23: The volatility factor plotted against the total equilibrium partial pressure of the oxide gas species for the **(a)** SM and **(b)** IB experiments at log(fO_2) = -8 and **(c)** IB-G at log(fO_2) = -9 assuming ideal trace element behaviour in the silicate melt.

Figure A2.24: The volatility factor plotted against the total equilibrium partial pressure of the oxide gas species for the **(a)** SM and **(b)** IB experiments at log(fO_2) = -8 and **(c)** IB-G at log(fO_2) = -9 considering non-ideal trace element behaviour in the silicate melt.

Appendix 3

Figure A3.1: The ratio of the total partial pressure of the Cu chloride and oxide gas species as a function of fCl_2 and fO_2.

Figure A3.2: The ratio of the total partial pressure of the Zn chloride and oxide gas species as a function of fCl_2 and fO_2.

Figure A3.3: The ratio of the total partial pressure of the Ga chloride and oxide gas species as a function of fCl_2 and fO_2.

Figure A3.4: The ratio of the total partial pressure of the Ge chloride and oxide gas species as a function of fCl_2 and fO_2.

Figure A3.5: The ratio of the total partial pressure of the As chloride and oxide gas species as a function of fCl_2 and fO_2.

Figure A3.6: The ratio of the total partial pressure of the Rb chloride and oxide gas species as a function of fCl_2 and fO_2.

Figure A3.7: The ratio of the total partial pressure of the Ag chloride and oxide gas species as a function of fCl_2 and fO_2.

Figure A3.8: The ratio of the total partial pressure of the Cd chloride and oxide gas species as a function of fCl_2 and fO_2.

Figure A3.9: The ratio of the total partial pressure of the In chloride and oxide gas species as a function of fCl_2 and fO_2.

Figure A3.10: The ratio of the total partial pressure of the Sn chloride and oxide gas species as a function of fCl_2 and fO_2.

Figure A3.11: The ratio of the total partial pressure of the Sb chloride and oxide gas species as a function of fCl_2 and fO_2.

Figure A3.12: The ratio of the total partial pressure of the Cs chloride and oxide gas species as a function of fCl_2 and fO_2.

Figure A3.13: The ratio of the total partial pressure of the Tl chloride and oxide gas species as a function of fCl_2 and fO_2.

Figure A3.14: The ratio of the total partial pressure of the Tl chloride and oxide gas species as a function of fCl_2 and fO_2.

Appendix 5

Figure A5.1: Temporal evolution of the volatility factor for Li in all compositions.

Figure A5.2: Temporal evolution of the volatility factor for P in all compositions.

Figure A5.3: Temporal evolution of the volatility factor for V in all compositions.

Figure A5.4: Temporal evolution of the volatility factor for Cu in all compositions.

Figure A5.5: Temporal evolution of the volatility factor for Zn in all compositions.

Figure A5.6: Temporal evolution of the volatility factor for Ga in all compositions.

Figure A5.7: Temporal evolution of the volatility factor for Ge in all compositions.

Figure A5.8: Temporal evolution of the volatility factor for As in all compositions.

Figure A5.9: Temporal evolution of the volatility factor for Rb in all compositions.

Figure A5.10: Temporal evolution of the volatility factor for Ag in all compositions.

Figure A5.11: Temporal evolution of the volatility factor for Cd in all compositions.

Figure A5.12: Temporal evolution of the volatility factor for In in all compositions.

Figure A5.13: Temporal evolution of the volatility factor for Sn in all compositions.

Figure A5.14: Temporal evolution of the volatility factor for Sb in all compositions.

Figure A5.15: Temporal evolution of the volatility factor for Cs in all compositions.

Figure A5.16: Temporal evolution of the volatility factor for Tl in all compositions.

Figure A5.17: Temporal evolution of the volatility factor for Pb in all compositions.

List of Tables

Chapter 2

Table 2.1: The temperature and oxygen fugacity conditions used in experiments.

Table 2.2: Overview of the measured isotopes for the GSE-1G secondary standard. The measured average abundance and its standard deviation (s.d.) with GeoReM preferred values (Jochum et al., 2005b), the detection limits and errors on individual measurements. The number of times an element was measured is indicated with n.

Table 2.3: Major (wt. %) and trace element (ppm) composition of the doped starting materials. The number of individual measurements is indicated with **n**. The reported errors are standard deviations on the average of all measurements.

Table 2.4: An explanation of the different parameters involved in the modified Hertz-Knudsen-Langmuir equation.

Chapter 3

Table 3.1: A schematic overview of the Zn ion exchange chromatography, adapted from the Zn and Cd chemistry used by Sweere et al. (2018). Each eluent added to the columns is allowed to pass through the resin before the next is added. The procedures for the preparation of resin and cleaning of plastics are outlined in Appendix **3A**.

Table 3.2: Typical operating conditions for the MC-ICP-MS set-up for Zn analyses.

Table 3.3: An overview of the collector array for Zn isotope analysis.

Table 3.4: The blanks of Zn and potential interferences for the elements relevant to the Zn isotope measurements. Two blanks were prepared independently for all components considered. Acid blanks are reported in ng per mL of reagent and work environment and consumable blanks are reported in ng. A '-' indicates that the measured concentration was below the detection limit (3 standard deviations of the average of the washes).

Table 3.5: The full range of (half-)masses in the collectors and the potential isobaric, doubly-charged and polyatomic interferences. For polyatomic interferences only nitride (^{14}N), oxide (^{16}O) and argide (^{40}Ar) species of major element and gas complexes were considered. Percentages next to isotopes indicate their IUPAC representative isotopic abundances (Melja et al., 2016).

Chapter 4

Table 4.1: Summary of the evaporation reactions for the relevant trace elements, considering only monometallic gas species, and the constants (A and B) used to calculate the equilibrium constant of the evaporation reaction at a given temperature [$\log(K) = A/T\ (in\ K) + B$]. n is the change in valence state of the trace element in the reaction. Thermodynamic data taken from Barin et al. (1989).

Table 4.2: Chlorine abundances of IB experiments. Details of Cl measurements were discussed in Chapter **2**. The **n** represents the number of measurements, out of 50, above detection limit. [1]Volatility factors were calculated using an initial Cl abundance of 507 ppm. [2]Chlorine fugacity calculated using Thomas and Wood (2021).

Table 4.3: The experimental conditions and LA-ICP-MS trace element abundances (ppm) for the volatility experiments. A "-" indicates the abundance was either below the detection limit or not measured. The "(Fe s)" indicates that the sample holders were pre-saturated before the experiment. For "comp" SM, IB and AN were doped with the halogen-bearing trace element mix, IB-G was the glassed starting material and SM-2 was doped with a halogen-free trace element mix (see Chapter **2**). Masses represent the mass of sample material loaded into the furnace. For oxygen fugacity a log(fO_2) of -0.68 represents air. At 1400°C: log(fO_2) values of -3, -6 and -8 correspond to ΔIW+6.7, ΔIW+3.7 and ΔIW+1.7 respectively. At 1300°C: log(fO_2) values of -7, -9 and -11 correspond to ΔIW+3.8, ΔIW+1.8 and ΔIW-0.2. Instrument operating conditions and analytical precision on individual measurements were discussed in detail in Chapter **2**. The standard deviations on the average trace element abundances are available in Appendix **4**.

Table 4.4: The n and log(K*) values obtained via non-linear least squares regression using a [1]variable and [2]fixed n for the evaporation reaction Cu_2O (l) = 2 Cu (g) + 0.5 O_2 (g).

Table 4.5: The n and log(K*) values obtained via non-linear least squares regression using a [1]variable and [2]fixed n for the evaporation reaction ZnO (l) = Zn (g) + 0.5 O_2 (g).

Table 4.6: The n and log(K*) values obtained via non-linear least squares regression using a [1]variable and [2]fixed n for the evaporation reaction Ga_2O_3 (l) = 2 Ga (g) + 1.5 O_2 (g). [3]Value was based on a single fO_2 series. [4] Value was based on two fO_2 series.

Table 4.7: The n and log(K*) values obtained via non-linear least squares regression using a [1]variable and [2]fixed n for the evaporation reaction GeO_2 (l) = GeO (g) + 0.5 O_2 (g).

Table 4.8: The n and log(K*) values obtained via non-linear least squares regression using a [1]variable and [2]fixed n for the evaporation reaction As_2O_3 (l) = 2 AsO (g) + 0.5 O_2 (g).

Table 4.9: The n and log(K*) values obtained via non-linear least squares regression using a [1]variable and [2]fixed n for the evaporation reaction Rb_2O (l) = 2 Rb (g) + 0.5 O_2 (g).

Table 4.10: The n and log(K*) values obtained via non-linear least squares regression using a [1]variable and [2]fixed n for the evaporation reaction In_2O_3 (l) = 2 In (g) + 1.5 O_2 (g). [3]Value was based on two fO_2 series.

Table 4.11: The n and log(K*) values obtained via non-linear least squares regression using a [1]variable and [2]fixed n for the evaporation reaction SnO_2 (l) = SnO (g) + 0.5 O_2 (g).

Table 4.12: The n and log(K*) values obtained via non-linear least squares regression using a [1]variable and [2]fixed n for the evaporation reaction Sb_2O_3 (l) = 2 SbO (g) + 0.5 O_2 (g).

Table 4.13: The n and log(K*) values obtained via non-linear least squares regression using a [1]variable and [2]fixed n for the evaporation reactions (1): Cs_2O (l) = 2 Cs (g) + 0.5 O_2 (g) and (2): Cs_2O (l) + 0.5 O_2 (g) = 2 CsO (g).

Table 4.14: The n and log(K*) values obtained via non-linear least squares regression using a [1]variable and [2]fixed for the evaporation reactions (1): PbO (l) = PbO (g) and (2): PbO (l) = Pb (g) + 0.5 O_2 (g).

Table 4.15: Range of activity coefficients compiled from literature. [1]Reyes and Gaskell (1983), [2]Holzheid and Lodders (2001), [3]Wood and Wade (2013), [4]Norris (2016), [5]Sossi et al. (2019). *Extrapolated, see main text.

Table 4.16: The apparent enthalpy [kJ] and entropy [$kJmol^{-1}K^{-1}$] for the evaporation reactions from silicate melt compared to data for pure species (Barin et al., 1989) and previous work.

Chapter 5

Table 5.1: The Zn concentration [ppm; Isotope Dilution] and $\delta^{66}Zn_{Lyon}$ (‰) of samples, starting materials and secondary standards. Errors on the Zn abundance and $\delta^{66}Zn_{Lyon}$ are 2 standard deviations on the average. [1]Ba correction was applied using $^{137}Ba^{2+}$ intensity instead of $^{138}Ba^{2+}$ intensity. [2]Ba correction was applied using the modelled approach and $^{137}Ba^{2+}$ intensities. The starting major and trace element composition of "SM" and "IB" can be found in Chapter **2** Table **2.2.**

Table 5.2: The expected liquid–vapour fractionation factor for $^{66}Zn/^{64}Zn$ at different fO_2 calculated using Equation **5.6**.

List of Appendix Tables

Appendix 1

Table A1.1: The cleaning procedures for the different plastics

Table A1.2: The cleaning and preparation of the AG1-X8 200-400 mesh resin

Appendix 2

Table A2.1: Summary of the potential evaporation reactions for the trace elements with multiple evaporation reactions, considering only monometallic gas species. Thermodynamic data taken from Barin et al. (1989). *Indicates thermodynamic data was extrapolated to cover the experimental temperature range.

Table A2.2: Summary of all evaporation reactions for the trace elements considering all potential gas species. Thermodynamic data taken from Barin et al. (1989). *Indicates thermodynamic data was extrapolated to cover the experimental temperature range.

Appendix 3

Table A3.1: The evaporation potential evaporation reactions involving monometallic chloride gas species, n_{Cl} is the change in oxidation state for chloride evaporation. El/Ox are the stable and abundant monometallic elemental and oxide gas species, n_{Ox} is the change in oxidation state for these gas species.

Appendix 4

Table A4.1: The standard deviations (1 s.d.; ppm) for the trace element abundances in Table **4.3**. Calculated as the standard deviation on the average of individual points. The error on individual LA-ICP-MS measurements was discussed in Chapter **2**.

Table A4.2: The volatility factors normalized to the shortest experiment in each time series for SM, SM-2, IB and AN. For IB-G it was normalized against the trace element abundance of the starting

material. These volatility factors were used to quantify volatility using the modified Hertz-Knudsen-Langmuir equation. For "comp" SM, IB and AN were doped with the halogen-bearing trace element mix, IB-G is the glassed starting material and SM-2 was doped with a halogen-free trace element mix. For oxygen fugacity a log(fO_2) of -0.68 represents air at 1400°C: log(fO_2) values of -3, -6 and -8 correspond to ΔIW+6.7, ΔIW+3.7 and ΔIW+1.7 respectively. At 1300°C: log(fO_2) values of -7, -9 and -11 correspond to ΔIW+3.8, ΔIW+1.8 and ΔIW-0.2. The standard deviation on the volatility factors can be found in Table **A4.3**.

Table A4.3: The standard deviations (1 s.d.; ppm) for the volatility factors in Table **A4.2**.

Table A4.4: The volatility factors as normalized to the starting trace element abundances in Table **2.2**. These volatility factors were used to construct the time, fO_2 and compositional dependence figures in Sections **4.2.2** – **4.2.4**.

Table A4.5: The standard deviations (1 s.d.; ppm) for the volatility factors in Table **A4.4**.

Chapter 1 – Introduction

1.1 – Formation of Planets

1.1.1 – Introduction

The present-day bulk elemental and isotopic composition of bodies in the solar system reflects the environment and the processes that took place during their formation and early evolution. The main processes that controlled its composition were the composition of the accreting material, the accretionary process (Fischer et al., 2017; Braukmüller et al., 2019), the evolution of a potential magma ocean through core-mantle segregation (Siebert et al., 2011; Righter, 2016; Steenstra et al., 2016) and degassing (Norris and Wood, 2017; Pringle and Moynier, 2017; Dhaliwal et al., 2018). These processes have been quantified and modelled for a variety of solar system bodies including Mercury (Brown and Elkins-Tanton, 2009; Riner et al., 2009), Venus (Jacobson et al., 2017), Earth (Monteux et al., 2016), the Moon (Elkins-Tanton et al., 2011), Mars (Debaille et al., 2007) and Vesta (Righter and Drake, 1997; McSween Jr. et al., 2019).

1.1.2 – Formation of the Solar System

The solar system formed following the gravitational collapse of an interstellar molecular could. This resulted in the genesis of a central star, the Sun, surrounded by a rapidly rotating molecular cloud of gas and dust particles which orbited the Sun, the protoplanetary disk. The timing of solar system formation was constrained using the Pb-Pb age of calcium-aluminium rich inclusions, micrometre-scale grains found in meteorites that are the oldest preserved solids in the solar system (4567.3 ± 0.16 Ma; Connelly et al., 2017). These are thought to have started condensing from the solar nebula within the first 10 ky of solar system formation. Their age is considered the best estimate of the age of the solar system (Halliday and Canup, 2023).

In the early protoplanetary disk elements condensed to form micrometre-scale grains in an order that was dependent on their volatility and solubility in major element phases. The order in which condensation occurred was dependent on the 50% condensation temperature (T^{50}). This parameter

describes the temperature at which 50% of an element will have condensed from the gas phase under solar nebula conditions, $P \approx 10^{-4}$ bar and a highly reducing, H_2-rich, atmosphere (Lodders, 2003). The T^{50} parameter can be determined from thermodynamic data, but may vary significantly depending on activity coefficients of trace elements in the solid phase and the chosen composition of the solar nebula (e.g. Wood et al., 2019). Conditions in the protoplanetary disk were not homogeneous and changed with distance from the centre. As a result, the elemental and isotopic composition of the bodies that formed varied based on their location in the solar system. Bodies that formed in the inner solar system were more depleted in volatiles compared to those that formed further out (Dullemond and Monnier, 2010; Armitage, 2011).

1.1.3 – Accretion of Rocky Bodies

The grains of condensed material collided and accreted into increasingly large bodies that eventually formed the planets and moons observed today. The mechanisms controlling the accretionary growth of smaller bodies are not yet fully understood. For the evolution of μm-scale grains to km-sized planetesimals, streaming instability is thought to have played a major role. This process concentrated grains and pebbles in specific areas of the protoplanetary disk through aerodynamic effects and drag to increase the number of collisions and potentially cause gravitational collapse (Johansen et al., 2015; Chambers, 2016; Vollstaedt et al., 2020). As planetesimals grew to a sufficient size to facilitate gravitational interactions between bodies this became the controlling factor on accretion in a period of "oligarchic growth" where the number of collisions decreased but their intensity increased (Kokubo and Ida, 1998). After ~1 My the number of planetesimals had decreased significantly to bodies of 1 – 10 % the size of the Earth. Collisions became less frequent and the larger bodies affected each other's orbits through gravitational interactions. This resulted in the clearing of interplanetary dust and gas from the inner solar system (Weidenschilling et al., 1997) and the change of planetary orbits (Tsiganis et al., 2005). This final accretionary period was marked by giant impacts and lasted ~100 My.

The composition of a planetary body is directly dependent on the duration of accretion and the heliocentric distance of the orbit in which the body is accreting. These two factors have a significant impact on the temperature, pressure, oxygen fugacity and the density and composition of the accreted material which all affect the reaction kinetics and therefore both the elemental and isotopic composition of the accreting body. The timescale of the gradual accretionary growth of micrometre scale grains and dust to planetesimals accretion and core-mantle segregation has been inferred using radiometric dating of iron meteorites. These suggest that accretion of meteorites occurred within 0.1 – 0.3 My of solar system formation (Kruijer et al., 2014). The accretion of Venus (11 My; Jacobson et al., 2017), Mars (≤10 My; Kruijer et al., 2017a) and Vesta (4.5 My; Roszjar et al., 2016) is thought to have finished relatively early with large scale surface volcanism and internal evolution persisting beyond this period. Terrestrial accretion lasted longer and ended with the Moon-forming Giant Impact 70-120 My after solar system formation which is often considered as the end of the accretionary stages of planet formation (Halliday and Canup, 2023 and references therein).

During the earliest stages of accretion the inner solar system bodies accreted mostly from predominantly volatile depleted bodies as these were abundant in the inner solar system as evidenced by nucleosynthetic isotope anomalies (e.g. Kruijer et al., 2017). The conditions during accretion facilitated (partial) melting due to the heat generated by impacts and the decay of short-lived radionuclides. After ~2.5 – 3 Myr conditions were more favourable for accreting material to retain its volatiles (Spitzer et al., 2021). Zinc isotope anomalies suggest that the volatile budget of the Earth is derived predominantly from the inner solar system (Steller et al., 2022). The addition of volatile-rich material from the outer solar system also contributed to the volatile budget of the terrestrial planets, but the eventual growth of Jupiter to tens of Earth masses is expected to have limited material exchange between the inner- and outer solar system (Kruijer et al., 2017b).

1.1.4 – Core-Mantle Segregation

The accreting bodies experienced phases of partial and/or whole-scale melting and vaporization induced volatile loss as a result of the conversion of kinetic energy to heat during collisions and the decay of short-lived radionuclides, e.g. ^{26}Al and ^{60}Fe (Kleine et al., 2009). These heat sources caused melting and resulted in the formation of magma oceans in which metal and silicate fractions in the melt differentiated through density differences, resulting in the formation of a Fe-metallic core and a silicate mantle and crust for (proto-)planetary objects ≥∼10km. This fractionated elements between the core and mantle based on their preferential partitioning into Fe-metal (siderophile), sulphur (chalcophile) or silicate (lithophile) phases. Simultaneously volatile loss occurred at the surface of the magma ocean affected the abundance of the moderately and highly volatile elements. As accretion and differentiation were contemporaneous, the latter stages of accretion involved impacts of partially or fully differentiated bodies where the remelting of colliding bodies meant that the resulting body experienced multiple differentiation events.

Conditions inside the terrestrial magma ocean were initially highly reducing and gradually became more oxidizing through either the late addition of oxidized, volatile-rich meteorites (Schönbächler et al., 2010), or internal oxidation mechanisms, e.g. the disproportionation of $Fe^{2+}O$ to Fe^{3+}-perovskite (bridgmanite) and metallic Fe^0 which would both oxidize the mantle and produce Fe^0 for core formation (Williams et al., 2012). The change in oxygen fugacity as well as changes in pressure and temperature directly affected the partitioning behaviour of an element. Metal-silicate partitioning experiments were performed over a range of conditions to understand how elements partitioned between the core and mantle. This also enabled the comparison of bulk silicate Earth (BSE) and inferred bulk Earth trace element abundances to estimate the conditions in the terrestrial magma ocean (e.g. Wood et al., 2009). The addition of chondritic material after core-mantle segregation had ceased, a “late veneer”, has been argued to be required to explain the highly siderophile element

abundances. However, Rubie et al. (2016) argue that it was not required and that core formation alone was sufficient to explain the observed abundances.

1.1.5 – The Composition of the Earth

The bulk composition of planetary bodies is generally compared to the average composition of the solar system. As the Sun comprises >99% of the mass of the solar system, its composition is considered the average of the solar System. The composition of the Sun was determined by spectroscopic analysis of the solar photosphere. The ever-growing catalogue of meteorites provides a means of directly sampling conditions in the early solar system. The undifferentiated, chondritic, meteorites are thought to represent the most primitive meteorites as these have not experienced large-scale melting and differentiation. Chondrites are further divided into carbonaceous, ordinary and enstatite chondrites and further divided into subgroups based on their mineralogy, volatile and organic content, and trace element and isotopic composition. Among the meteorite collection, the CI carbonaceous chondrites

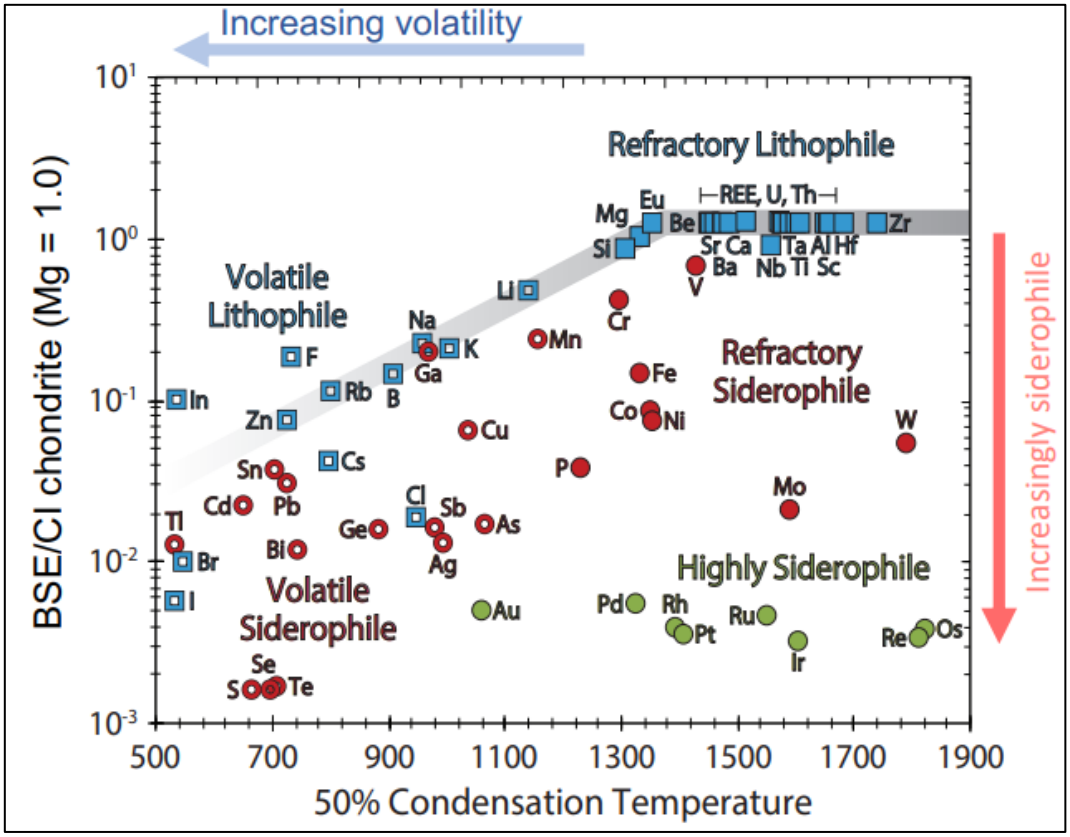


Figure 1.1: The abundance of elements in the BSE relative that of CI carbonaceous chondrites, normalized to Mg = 1.0, plotted against condensation temperature. The shaded area shows the expected depletion trend based purely on volatile loss. Adapted from Wood et al. (2019).

were found to most closely match the solar abundances and their composition is considered representative of the average composition of the solar system (Palme et al., 2014).

The trace element and isotopic composition of the Earth can be compared to that of the different chondritic meteorites to identify the predominant meteorites that contributed to the accretion of the Earth. A comparison of the BSE composition with different types of chondrites indicated that the refractory lithophile element abundances are present in the Earth at chondritic levels whereas more volatile and/or siderophile elements are depleted (Fig. **1.1**). A comparison of the volatile depletion patterns of the BSE with that of different meteorite types was shown to best match that of CI chondrites (Mezger et al., 2020). Plotting the CI chondrite normalized element abundance of the BSE against T^{50} illustrates the different processes that occurred during the early stages of terrestrial evolution (Fig. **1.1**; Wood et al., 2019). The refractory lithophile elements are present at solar system abundances whereas the more volatile lithophile elements generally fall on a depletion trend that is a function of T^{50}. Siderophile elements are depleted compared to lithophile elements with similar T^{50} because these elements have been incorporated into the core. For highly and moderately volatile siderophile elements it is expected that the present-day BSE abundances also include a component of volatile loss. Similar depletion patterns are observed for other meteorites, but the BSE is seen to have a larger depletion compared to other meteorites (Braukmüller et al., 2019). This suggests that the volatile patterns of the Earth are inherited from its building blocks, but the magnitude of depletion reflects more the longer evolutionary process and potentially more extreme conditions during its evolution compared to chondrites.

The isotopic composition of the Earth showed that there the Earth is made up of different type of meteorites. Isotopically the Earth is closest to enstatite chondrites (Javoy et al., 2010; Kruijer et al., 2020), but a contribution of ordinary chondrites is required during the later stages of accretion (Dauphas, 2017). Considering trace element depletions, Braukmüller et al. (2019) argued that ~10-15% carbonaceous chondrites are required to explain volatile element abundances. Others have

argued that the Earth is not chondritic at all (Campbell and O'Neill, 2012). Moreover, nucleosynthetic Mo isotope anomalies were shown to not match any of the currently known meteorite reservoirs, suggesting that there was potentially another, unknown, source contributing to the Earth (Burkhardt et al., 2011; Render et al., 2017).

1.2 – Volatility

1.2.1 - Background

The volatility of an element refers to its tendency to be present in gaseous form instead of a condensed form. If an element is considered volatile it is likely to evaporate with non-volatile elements being referred to as refractory. The chemical process of evaporation is commonly associated with volatility as it describes the transition from a condensed phase to a gaseous phase. In a thermodynamic framework, the volatility of an element at equilibrium is controlled mainly by temperature and the partial pressure of the different gas species in the system. An understanding of trace element evaporation from silicate melts is important as it is applicable to a variety of topics such as the degassing of magmas during ascent or eruption (Mather et al., 2012; Zelenski et al., 2014; Edmonds, 2015), meteorites and Ca-Al rich inclusions (Richter et al., 2007; Kato and Moynier, 2017; Braukmüller et al., 2018) and the formation and early evolution of planetary bodies (Hauri et al., 2015; Sossi et al., 2016; Wang et al., 2016; Norris and Wood, 2017; Dhaliwal et al., 2018).

1.2.2 – Describing Volatility

Goldschmidt (1930) grouped elements based on their preferred host phase; atmophile elements prefer the gas phase, lithophile elements prefer silicate phases, siderophile elements prefer iron phases and chalcophile elements prefer sulphide phases. To study volatile loss from silicate melts this study focuses on moderately volatile lithophile, siderophile and chalcophile elements (MVE). Palme et al. (2014) defined MVE as elements with "condensation temperatures below Mg-silicates and FeNi, but above the condensation temperature of the highly volatile elements that are incompletely condensed" which corresponds to T^{50} values between 252 K and 1250 K. Elements with high or low T^{50} were unsuitable to study evaporative loss as these would be concentrated in either the silicate melt or the gas phase. Instead, elements that partition between the silicate melt and gas phase in a more balanced manner, the moderately volatile elements (MVE), are best used to study volatile loss.

The use of T^{50} to quantify volatility outside of early solar nebula conditions has been challenged under the notion that the volatility of elements rapidly shifted away from the T^{50}, because the composition of and conditions in the solar nebula changed rapidly in the early stages of its evolution. This can be illustrated by considering Figure **1.1** which shows that volatile element abundances do not always correlate well with T^{50} or the lithophile element volatility trend. This is because the oxygen fugacity (fO_2) provides a strong control on volatility as evaporation reactions typically change the oxidation state of the evaporating element. Since the environment in a magma ocean is different from early solar system conditions and grew more oxidizing as it evolved the behaviour of the trace elements changed. This implies that T^{50} is not an adequate description of element volatility outside of the early solar system environment (e.g. Blanchard et al., 2015; Wang et al., 2016; Norris and Wood, 2017). Alternative means of quantifying volatility are required to describe volatile loss in environments outside the solar nebula, such as planetary evolution or magmatic ascent and/or degassing. Norris and Wood (2017) qualitatively quantified volatility experimentally by considering the fraction of material that was lost using the volatility factor (F_M; Eq. **1.1**).

$$(Eq.\,1.1):\quad F_M = \frac{X_{M,measured}}{X_{M,initial}}$$

This parameter describes the difference in abundance of trace element *M* before and after an experiment. This approach enables the determination of the relative volatility of a set of elements. The experiments by Norris and Wood (2017) showed that volatility factors obtained in conditions comparable to a magma ocean correlate well with the CI chondrite normalized trace element abundances of the Earth. This showed that conditions in the solar System during early stage planetary evolution did not correspond to those in the early solar nebula and therefore T^{50} was inadequate to describe volatility in this environment.

The Hertz-Knudsen-Langmuir (HKL) equation (Eq. **1.2**; Knudsen, 1909; Langmuir, 1916; Hirth and Pound, 1963) is a quantitative method of describing volatility, rooted in thermodynamics and quantum mechanics. It describes the evaporative flux of gas atoms from a condensed phase. It is only valid in

an isothermal ideal gas, because the kinetic theory of gases dictates that in this case the velocity distribution of the gas particles will follow a Maxwell-Boltzmann distribution, an assumption made in the derivation of this equation.

$$(Eq.\,1.2):\ J_i = -\frac{n_i \alpha_e \left(P_{i,sat} - P_i\right)}{\sqrt{2\pi m_i RT}}$$

In Equation **1.2**, J_i is the flux of species *i* in $molm^{-2}s^{-1}$, n_i is the amount of atoms of *i* in the dominant gas phase species, α_e is the evaporation coefficient, m_i is the mass of the evaporating species and $(P_{i,sat} - P_i)$ describes the difference between the equilibrium vapour pressure ($P_{i,sat}$) and the pressure at the evaporating surface (P_i). The evaporation coefficient is an empirical parameter describing the non-ideality of evaporation as some of the evaporating molecules will immediately recondense and remain in the melt. The HKL equation was modified by Sossi et al. (2019) to describe the temporal evolution of trace element abundances in an experiment as a function of various experimental parameters and the properties of the evaporation reaction. In this study slight adjustments were to their approach to suit the experimental set-up in this study. The derivation of this modified HKL equation is discussed in Chapter **2**.

1.2.3 – Metal-Silicate Partitioning

Trace element loss from the BSE through core-mantle differentiation has been studied extensively via high-pressure and temperature experiments looking at the partitioning behaviour of elements between metal and silicate phases (e.g. Siebert et al., 2011; Righter, 2016). This experimental data provides constraints on trace element abundances in the mantle, the conditions in a planetary magma ocean in terms of P, T and fO_2 and, for refractory elements, allows for estimates of trace element abundances in the core. Stable isotope analyses of metal-silicate partitioning experiments showed that isotopic compositions of siderophile elements may be fractionated between the metal and silicate phases (e.g. Young et al., 2015; Bourdon et al., 2018; Hopp et al., 2018; Xia et al., 2019; Guignard et al., 2020). The magnitude of Si, Cr, Fe, Ni, Cu and Mo isotope fractionation observed in these

experiments was small but identifiable and would result in an isotopically heavy core and light mantle. Similar experiments for Zn showed that isotope fractionation of Zn during metal-silicate partitioning is negligible (Bridgestock et al., 2014; Wang et al., 2017; Seegers et al., 2020). The presence of sulphur further complicates the observed isotope fractionation as metal-sulphide-silicate partitioning experiments showed that sulphide-bearing melts were isotopically lighter than silicate melts (Savage et al., 2015; Xia et al., 2019). Bourdon et al. (2018) showed that isotope fractionation during metal-silicate partitioning was an equilibrium isotope fractionation process that followed the predicted T^{-2} dependence (Urey, 1947). Therefore they argued that isotope fractionation for refractory elements in natural samples that are not isotopically fractionated during melting could be used to infer the temperature in the planetary interior during core-mantle segregation.

1.2.4 – Volatile Loss

Volatile loss played a significant role in the compositional evolution of the terrestrial mantle. The present-day abundances of moderately volatile lithophile elements in the BSE requires evaporative loss as partitioning of these elements into the core is insufficient to explain the observed depletions (Witt-Eickschen et al., 2009; Wang et al., 2016). Evaporation induced isotope fractionation resulted in an isotopically heavy residual silicate melt, the terrestrial mantle, and an isotopically light vapour phase that is removed from the system. Trace element depletions and heavy isotope enrichments relative to CI chondrite abundances have been observed in the Earth-Moon system and meteorites for a range of, both lithophile and siderophile, elements covering a range of volatilities including H (Boyce et al., 2015), Li (Day et al., 2016), Mg (Hin et al., 2017), Si (Pringle et al., 2014), Cl (Sharp et al., 2010; Boyce et al., 2015), K (Wang and Jacobsen, 2016), Ti (Greber et al., 2017), Cr (Sossi et al., 2018b), Fe (Sossi et al., 2016), Cu and Zn (Herzog et al., 2009), Ga (Kato and Moynier, 2017), Rb (Pringle and Moynier, 2017), Sn (Wang et al., 2019) and Te (Fehr et al., 2018). The consistent heavy isotope enrichment is a strong indicator that volatile loss provided a strong control on the early compositional evolution of the Earth and other rocky bodies in the solar system.

1.3 – Isotope Fractionation

1.3.1 – Introduction

Isotopes are atoms of the same element with different masses caused by a differing number of neutrons in the nucleus. Different isotopes of an element are chemically identical, but the slight mass differences between isotopes affect the bond strength. This, in turn, affects the amount of energy required to break a bond and therefore rate at which this occurs, facilitating isotopic fractionation. The physical and chemical principles underlying isotope fractionation were first described by Bigeleisen and Mayer (1947) and Urey (1947). Using the equilibrium constants of isotope exchange reactions they showed how isotope fractionation was caused by differences in the vibrational energy of atomic bonds as a result of the mass difference between the isotopes with bonds involving the light isotope being preferentially broken over the heavy isotope. This "mass-dependent" fractionation describes most natural fractionation processes and the fractionation trends for these processes can be predicted based on the mass differences between the isotopes (Young et al., 2002). Considering all properties are equal, the expected range of isotope fractionation is directly dependent on the relative mass difference between isotopes. Therefore lighter elements tend to exhibit a wider range of isotopic values than heavier elements. However, different elemental properties, such as oxidation state or electron configuration, bonding environments or interactions with different anions can result in different elements of similar mass exhibiting significantly different ranges of natural fractionation, e.g. Cu and Zn (Schauble, 2004).

Isotope fractionation is expressed using the delta (δ) notation which calculates the per mille (‰) deviation of the isotope ratio of the measured sample relative to that of a recognized standard reference material. By convention the isotope ratios used for calculating delta values have the light isotope in the denominator such that the delta value becomes larger as the isotopic composition gets heavier. For Zn isotope ratios are expressed relative to ^{64}Zn and the reference standard is the JMC 3-0749 Lyon Zn (Maréchal et al., 1999; Eq. **1.3**).

$$(Eq.\,1.3):\ \ \delta^{x}Zn\ (‰) = 10^{3}\left(\frac{(\,^{x}Zn/^{64}Zn)_{measured}}{(\,^{x}Zn/^{64}Zn)_{JMC\ Lyon}} - 1\right)$$

1.3.2 – Zinc

1.3.2.1 – Background

Zinc is a moderately volatile (T^{50} = 704K; Wood et al., 2019) and lithophile element with five naturally occurring stable isotopes, with the IUPAC reference isotope abundances (Melja et al., 2016) listed in brackets, ^{64}Zn (49.17%), ^{66}Zn (27.73%), ^{67}Zn (4.04%), ^{68}Zn (18.45%) and ^{70}Zn (0.61%). It is not a transition metal by definition, as its electron subshells are fully occupied. However, because its properties are closer to the transition metals than the post-transition metals it is often considered alongside the transition metals.

The Zn abundance of the BSE (53.5 ± 5 ppm) is depleted relative to CI carbonaceous chondrites (361 ± 40 ppm; Fig. **1.1**; Palme and O'Neill, 2014; Paquet et al., 2023b). The average Zn isotopic composition of the BSE, obtained through the analysis of a range of peridotites, mid-ocean ridge basalts and ocean island basalts, is $\delta^{66}Zn_{Lyon}$ = 0.28 ± 0.05‰ (Chen et al., 2013a) and is fractionated <0.1 ‰ during partial melting and fractional crystallization (Huang et al., 2018; Sun et al., 2023). This is identical within error to the Zn isotopic composition of enstatite and carbonaceous chondrite meteorites, the terrestrial building blocks. This suggested that isotope fractionation occurred in the solar nebula and that the Zn isotopic composition of the bulk Earth remained constant throughout its subsequent evolutionary steps. The BSE Zn depletion compared to carbonaceous chondrites was attributed to the volatility of Zn. The lithophile behaviour of Zn suggests that the majority of terrestrial Zn will be concentrated in the mantle. Recent experiments have shown that Zn can be slightly siderophile, but only for experiments containing sulphur-bearing species (Mahan et al., 2018) or in highly reducing conditions (Steenstra et al., 2020). In the absence of sulphur species Zn will always be present as $Zn^{2+}O$ in the silicate melt and as Zn^{0} in the gas phase which makes Zn a perfect element to study volatility as it has a simple evaporation chemistry that is insensitive to changes in redox conditions.

The earliest isotopic measurements were performed on the traditional stable isotopes (H, C, N, O and S) and were generally measured using gas source mass spectrometry. The analysis of the non-radiogenic isotopes of other elements, including Zn, is considered “non-traditional” stable isotope analysis. The earliest studies regarding the isotopic variability of Zn were conducted using neutron activation analysis (NAA; Filby, 1964) or thermal ionization mass spectrometry (TIMS; Rosman, 1972). However, the electron configuration of Zn results in it having a comparatively high ionization potential of Zn (9.39 eV). This meant that Zn has a low ionization efficiency, a measure of the fraction of an element that is ionized during TIMS analysis and is difficult to ionize thermally (e.g. Ghidan and Loss, 2012). Therefore it was difficult to precisely measure Zn isotope fractionation using TIMS. Moreover, the precision of data obtained in the early TIMS Zn measurements was generally low with 1-2 ‰ per amu errors. This exceeded most of the range of natural Zn isotope fractionation which meant that these studies found no discernible Zn isotopic variability in terrestrial samples.

The increased accuracy and precision of isotope measurements provided by the development of multi-collector inductively coupled plasma mass spectrometry (MC-ICP-MS) techniques (Halliday et al., 1995) led to a rapid expansion of non-traditional stable isotope measurements, including Zn. Because the MC-ICP-MS operates using an ionized Ar plasma it has a higher ionization efficiency than TIMS. As a result the MC-ICP-MS yielded a significant increase of precision with present-day measurements being able to measure ≤0.05 ‰ per amu fractionation for Zn. This enabled the quantification of the small scale isotopic variability of Zn observed in terrestrial materials. The first analytical methods and high-precision isotope fractionation data for Zn using MC-ICP-MS were reported by Maréchal et al. (1999). This study laid the groundwork and has since been followed by a wealth of data regarding Zn isotope fractionation in experimental, magmatic, aqueous, anthropogenic, soil, microbial and biological systems (e.g. Shiel et al., 2010; Moynier et al., 2017; Sossi et al., 2020; Hoefs, 2021 and references therein).

1.3.2.2 – Mass-Dependent Fractionation

For the vast majority of processes isotope fractionation can be described using mass-dependent isotope fractionation laws. The magnitude of the fractionation is directly dependent on the relative mass difference between the isotopes of one element. Isotope fractionation during volatile loss is known to be a mass-dependent process and therefore it is expected that all observed fractionation in this study will be mass-dependent (e.g. Hoefs, 2021). This is also the case for the experiments in this study as Sossi et al. (2020) showed that Zn isotope fractionation in volatile loss experiments was mass dependent. For elements consisting of at least three stable isotopes mass dependent fractionation is often visualized in so-called three isotope plots, where two isotope ratios with a common denominator isotope are plotted against each other. For mass-dependent fractionation processes all data should plot on a line where the slope is given by the fractionation factor (β). This slope then shows whether the fractionation process is an equilibrium or a kinetic fractionation process.

In equilibrium mass-dependent fractionation processes the partitioning of isotopes depends on zero-point energy differences that describe the different vibrational modes within molecules (Young et al. (2002). In evaporative processes this occurs when the vapour pressure of the evaporating species is equal to its equilibrium partial pressure, allowing the system to reach equilibrium. For kinetic mass-dependent isotope fractionation processes the partitioning of isotopes is based on the interchange of kinetic energies between the isotopes (Young et al., 2002). In evaporative processes this occurs when the evaporating species is transported away instantaneously from the evaporation interface and the actual partial pressure of the evaporating species is significantly smaller than its equilibrium partial pressure. For the experiments performed in this study isotope fractionation is expected to be a kinetic process as a consistent gas flow inside the furnace removed evaporating species from the reaction interface.

1.3.2.3 – Mass-Independent Isotope Fractionation

For the majority of processes, including evaporation induced volatile loss, isotope fractionation is mass-dependent. However, not all observed isotope fractionation is mass dependent as mass-independent fractionation (MIF) has been observed for a variety of elements including Zn. For some elements, e.g. O, S and Hg, MIF has mostly been linked to atmospheric photochemical effects (Pavlov and Kasting, 2002; Epov et al., 2011; Ivanov and Babikov, 2013; Zerkle et al., 2021). For Zn MIF has been observed in extra-terrestrial material (Loss and Lugmair, 1990; Völkening and Papanastassiou, 1990; Savage et al., 2022; Steller et al., 2022) and for redox state changes during Zn-Cl complexation experiments (Fujii et al., 2009). The Zn MIF signatures in extra-terrestrial materials are consistent with those observed for other "iron peak" elements (Ca, Ti, Cr, Fe and Ni) and are attributed to nuclear field effects and/or nucleosynthetic processes that occurred in the solar nebula and protoplanetary disk. This is reflected in the distinctly different MIF isotopic compositions of various meteorite subgroups thought to have originated in the inner- and outer solar system which may aid in constraining sources of volatile elements on Earth and Mars (Fujii et al., 2006; Bermingham et al., 2020; Kleine et al., 2023; Martins et al., 2023; Paquet et al., 2023a).

1.3.2.4 – Previous Work

1.3.2.4.1 – Isotope Fractionation in (extra-)Terrestrial Materials

The isotopic composition of (extra-)terrestrial materials exhibits a large range of isotopic compositions. For example, meteorites cover a range between $\delta^{66}Zn_{Lyon}$ = –7‰ in aubrites and $\delta^{66}Zn_{Lyon}$ = +7.5‰ in EL enstatite chondrites and lunar samples vary between $\delta^{66}Zn_{Lyon}$ = –5.5 ‰ in specific high-Ti lunar basalt samples and $\delta^{66}Zn_{Lyon}$ = –4 ‰ in lunar pyroclastic glasses to $\delta^{66}Zn_{Lyon}$ = +6‰ in lunar regolith (Fig **1.2**). On the other hand, the isotopic composition of terrestrial igneous rocks is generally homogeneous and does not exhibit a wide range of $\delta^{66}Zn_{Lyon}$ with an average composition of the BSE of $\delta^{66}Zn_{Lyon}$ = 0.28 ± 0.06 ‰ (Chen et al., 2013a). Heavier Zn isotopic signatures ($\delta^{66}Zn_{Lyon} \leq$ 0.69 ‰) have been observed for rocks derived from mantle sources containing carbonate-bearing

subducted material (Liu et al., 2016; Yao et al., 2022). Martian meteorites show similar isotopic signatures to the BSE, suggesting the Zn isotopic composition of Mars is similar to that of the Earth and both are indistinguishable from CI chondrites ($\delta^{66}Zn_{Lyon}$ = 0.25 ± 0.03 ‰; Day and Moynier, 2014). Lunar basalts mostly exhibit a consistent heavier Zn isotopic composition with average $\delta^{66}Zn_{Lyon}$ ≈ +1.4 ± 0.2 ‰ reflecting significant volatile loss during the Moon-forming Giant Impact (Day et al., 2020a). The origin of the isotopically light lunar basalts is not yet fully understood, but thought to be the result of the recondensation of isotopically light Zn gas species (Paniello et al., 2012a; Hopkins, 2019; Ma and Liu, 2019; Gargano et al., 2022). The howardite-eucrite-diogenite (HED) meteorites, thought to have originated from asteroid 4-Vesta, exhibit a range of $\delta^{66}Zn_{Lyon}$ that is attributed to brecciation and

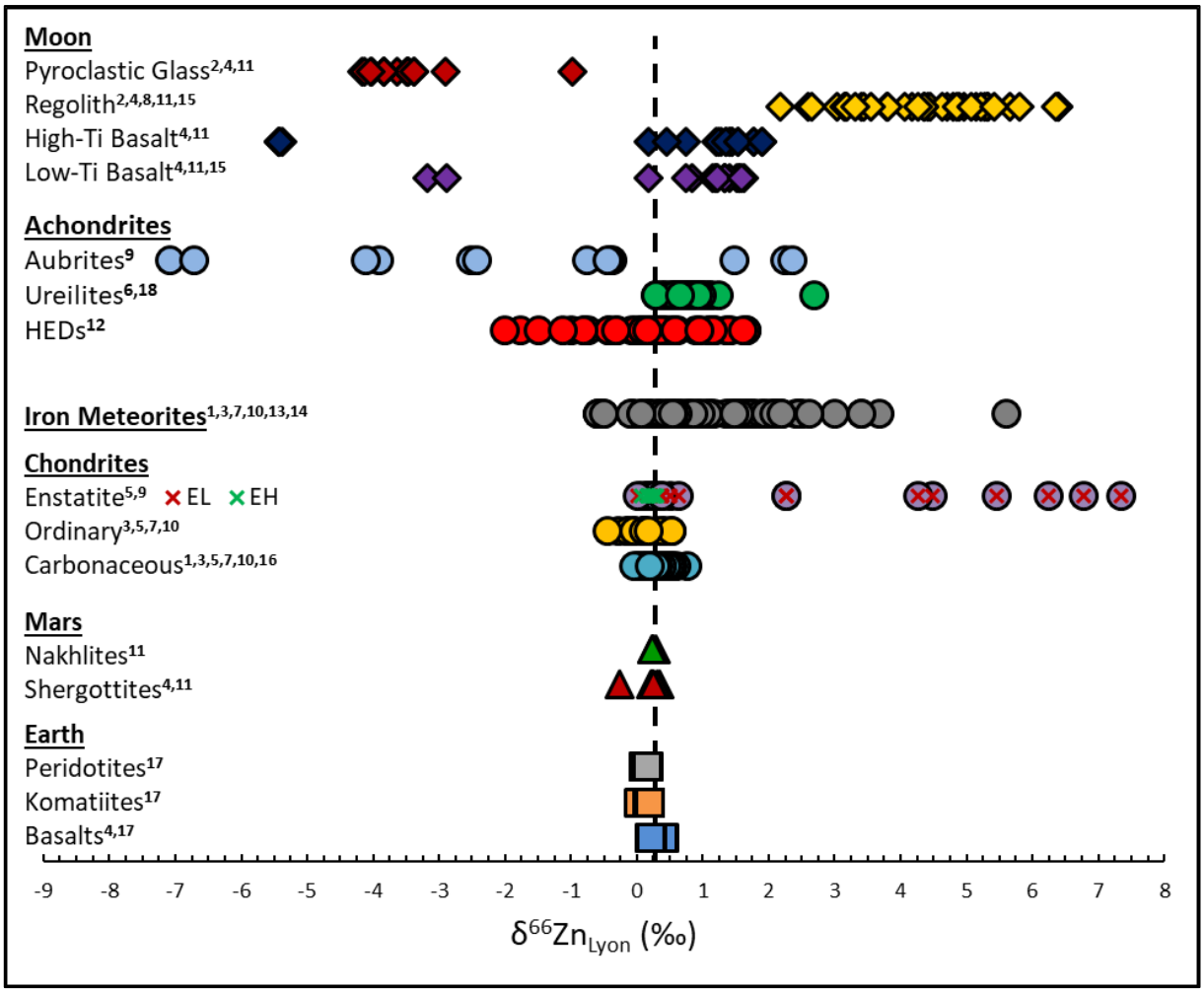


Figure 1.2: Overview of the Zn isotopic composition of various (extra-)terrestrial materials. The dashed line represents the average $\delta^{66}Zn_{Lyon}$ of the BSE (Chen et al., 2013a).
[1]Luck et al. (2005); [2]Moynier et al. (2006); [3]Moynier et al. (2007); [4]Herzog et al. (2009); [5]Moynier et al. (2009a); [6]Moynier et al. (2010); [7]Ghidan and Loss (2011); [8]Lindsay et al. (2011); [9]Moynier et al. (2011); [10]Barrat et al. (2012); [11]Paniello et al. (2012a); [12]Paniello et al. (2012b); [13]Chen et al. (2013b); [14]Bridgestock et al. (2014); [15]Kato et al. (2015); [16]Pringle et al. (2017); [17]Sossi et al. (2018b); [18]Brugier et al. (2019).

volatile loss (Paniello et al., 2012b). For the other meteorites the range of $\delta^{66}Zn_{Lyon}$ varies between (sub-)groups; carbonaceous, ordinary and low-metamorphic grade (EH) enstatite chondrites exhibit a small range of $\delta^{66}Zn_{Lyon}$ and are mostly comparable to terrestrial values whereas thermally metamorphosed (EL) enstatite chondrite, achondrite and iron meteorites all exhibit large ranges of $\delta^{66}Zn_{Lyon}$. This variability has been attributed to a variety of processes including thermal metamorphism, sulphide sequestration, volatile loss and/or recapturing of isotopically light materials from parent bodies with bulk $\delta^{66}Zn_{Lyon}$ comparable to terrestrial values (Moynier et al., 2011; Paniello et al., 2012b; Bridgestock et al., 2014; Pringle et al., 2017; Creech and Moynier, 2019). A more detailed review of Zn isotope fractionation in (extra-)terrestrial materials is available in Moynier et al. (2017).

1.3.2.4.2 – Experimental Studies into Evaporation

Experimental evaluation of evaporation induced isotope fractionation from silicate melts is imperative in understanding the observations made for natural samples and the application to models of planetary formation and evolution. Recent interest in this problem has resulted in rapid developments of the theoretical frameworks surrounding experimental evaporative loss (e.g. Sossi et al., 2019; 2020; Young et al., 2022) and an increase in the number of elements that have been studied; Na, Mg, K, Ca, Ti, Fe, Cr, Cu, Zn, Ge, Rb, In, Te and Tl (Zhang et al., 2014; Luais et al., 2018; Rogaski et al., 2018; Gellissen et al., 2019; Wimpenny et al., 2019; Sossi et al., 2020; Ni et al., 2021; Nielsen et al., 2021; Zhang et al., 2021; Heck, 2022; Klemme et al., 2022; Liu et al., 2022; Neuman et al., 2022; Renggli et al., 2022; Young et al., 2022).

The first experimental assessment of Zn isotope fractionation in silicate melts was performed by Xue et al. (1996) who found that it was a diffusion controlled process where the evaporation rates of Zn exceeded its diffusion rate in the silicate melt. More recently Zn isotope fractionation during volatile loss at high temperature was studied by Wimpenny et al. (2019) who melted arkosic and rhyolitic soils as well as tektites at 1600-2200°C in air or Ar and Sossi et al. (2020) who used a synthetic primitive basaltic composition at a range of T and fO_2 conditions. The presence of compositional gradients in

the experiments of Sossi et al. (2020) reaffirmed observations by Xue et al. (1996) that evaporation of Zn from a silicate melt can be a diffusion-limited process depending on the melt composition. Sossi et al. (2020) covered a range of experimental conditions and found significant heavy isotopic composition with $\delta^{66}Zn \leq 12.83$ ‰ relative to the starting material in the samples with the highest Zn depletion. This range $\delta^{66}Zn$ of covers the full range of positive $\delta^{66}Zn_{Lyon}$ values observed for natural (extra-)terrestrial samples.

1.4 – Aim of This Work

The elemental and isotopic composition of the terrestrial bodies in the solar system is controlled by processes that took place during the early stages of their formation and evolution. In a planetary scale magma ocean evaporative loss at the surface provided a strong control on the moderately volatile trace element budget of these bodies. The aim of this work is to provide additional constraints and insight into the evolution of the volatile budget of the bodies in the inner solar system. This is achieved by combining two separate fields within earth sciences; experimental petrology and stable isotope geochemistry by considering the trace element abundance and Zn isotopic composition of experimentally acquired silicate glasses.

Multiple sets of evaporation experiments were performed in a one atmosphere gas mixing furnace at varying conditions to assess how oxygen fugacity and melt composition affected trace element volatility. The samples obtained from these experiments were then analysed using electron probe microanalysis and laser ablation inductively coupled plasma mass spectrometry. The specifics of the sample preparation and the experimental- and analytical methodology for this are outlined in Chapter **2**.

Chapter **3** is dedicated to the methodology relating to the measurements of the Zn isotope composition of the samples. It discusses the preparation and analysis of the starting materials and a subsection of samples obtained from the experiments described in Chapter **2**. This includes the purification of Zn from the sample, multi-collector ICP-MS analysis and a detailed discussion on blank suppression and interference corrections required for Zn isotope analysis.

Chapter **4** discusses the results of the volatility experiments and explores how trace element volatility changes as a function of time, melt composition and oxygen fugacity. It quantifies the observed volatility trends as a function of time, fO_2 and silicate melt composition using the volatility factor and modified HKL equation. The volatility factors are subsequently linked to the CI chondrite normalized

BSE abundances and various parameters that aim to describe volatility to assess their accuracy for conditions in this study. The modified HKL equation will be used to infer the thermodynamic properties of the evaporation reaction(s) for the moderately volatile trace elements.

Chapter **5** focuses on the results of the Zn isotope analyses and explores how the isotopic composition of the samples changes as a function of time, oxygen fugacity and Zn abundance in the residual silicate melt and what this means for the evaporative enviroment. Furthermore, liquid – vapour fractionation factors will be computed and compared theoretical values and those fractionation factors obtained in previous studies. These liquid – vapour fractionation factors will then be used to model isotope fractionation trends and compared with the isotopic composition of various bodies in the solar system to understand the impact of volatile loss on their Zn abundance and isotopic composition.

Findings from Chapters **2 – 5** are summarized in Chapter **6** which also includes suggestions for potential improvements of the experimental and/or analytical set-up, discusses the potential integration of the results of this study in a wider scientific context and explores potential avenues for future studies.

Chapter 2 – Methodology: Evaporation Experiments

2.1 – Introduction

The bulk trace element budget of bodies in the solar system reflects the environment and the processes that took place during their formation and early evolution. It is directly dependent on the composition of its accreted meteorite "building blocks". The main processes that control the composition are the accretion (Fischer et al., 2017; Braukmüller et al., 2019) and the evolution of a planetary magma ocean through core-mantle segregation (Siebert et al., 2011; Righter, 2016; Steenstra et al., 2016) and degassing (Norris and Wood, 2017; Pringle and Moynier, 2017; Dhaliwal et al., 2018). Trace element loss from the bulk silicate Earth (BSE) through core-mantle differentiation has been studied extensively through high-pressure and temperature experiments which constrain the partitioning behaviour of, mostly, siderophile and chalcophile elements, between metal and silicate phases (e.g. Siebert et al., 2011; Righter, 2016). The observed depletions of moderately volatile lithophile elements in the BSE (e.g. Wood et al., 2019) requires evaporative loss or incomplete condensation to have played a major role during the early stages of planetary evolution as the partitioning of these elements into the core is insufficient to explain the observed depletions (Witt-Eickschen et al., 2009; Wang et al., 2016). Previous work on trace element volatility suggested that the observed moderately volatile lithophile and siderophile element depletions in the BSE correlate better with evaporation from a silicate melt than from condensation in the solar nebula (Norris and Wood, 2017).

This chapter focuses on the experimental and analytical methodology of a set of experiments that was performed with the aim to increase the understanding of volatile loss from silicate melt and further quantify the volatility of a range of trace elements. These experiments were performed in a one atmosphere gas mixing furnace with three silicate melt compositions and variable runtime and oxygen fugacity (fO_2) to constrain how trace element volatility changes as a function of these parameters. The samples were analysed for their major-, minor- and trace element compositions using electron probe

micro analysis (EPMA) and laser ablation inductively-coupled plasma mass spectrometry (LA-ICP-MS) respectively. It will also outline the methods used to predict of gas phase stability using thermodynamic properties of pure species and discuss previously derived methods of quantifying both absolute (Sossi et al., 2019) and relative (Norris and Wood, 2017) volatility and the potential problems that lie at the base of these experiments.

2.2 – Preparation of Starting Materials

2.2.1 – Preparation of Major Element Mixes

Three starting compositions were prepared for volatility experiments, covering a range of major element compositions. Two of these were synthetic silicate rocks, prepared from >99% pure reagent-grade oxides (SiO_2, Al_2O_3, MgO, Fe_2O_3 and TiO_2) and carbonates ($CaCO_3$, Na_2CO_3 and K_2CO_3); a primitive ferrobasalt (SM; Sossi et al., 2019) and an andesite (AN; Carmichael et al., 1974). Reagent-grade oxides and carbonates were supplied by Alfa-Aesar (SiO_2 and Fe_2O_3) and Sigma-Aldrich (Al_2O_3, MgO, $CaCO_3$, Na_2CO_3, K_2CO_3 and TiO_2). These were weighed, ground and mixed to homogeneity under reagent-grade ethanol in a porcelain (SM) or agate (AN) pestle and mortar. The third starting composition was a natural basalt, dredged from the Reykjanes Ridge, Iceland (IB; Norris, 2016).

2.2.1.1 – Decarbonation and Fe-Reduction

After mixing the major element powders, the carbonate species, $CaCO_3$, Na_2CO_3 and K_2CO_3, were decarbonated to oxides, CaO, Na_2O and K_2O, and Fe_2O_3 was reduced to FeO to accurately reflect the speciation of these elements in a silicate melt. As the oxidation state of Fe is fO_2 dependent and that of Na, Ca and K is fO_2 independent within the FeO stability field, and both have the reaction rate increased with increasing temperature, decarbonation and Fe reduction were performed simultaneously in a one atmosphere furnace. To reduce Fe_2O_3 to FeO the oxygen fugacity (fO_2) was controlled to be between the iron-wüstite (IW) and fayalite-magnetite-quartz (FMQ) oxygen buffer reactions. The maximum temperature was chosen to be 1050°C, well below the solidus of the melt, as calculated with MELTS for Excel (Gualda and Ghiorso, 2015) to ensure there was no partial melting. To prevent an instant release of large amounts of CO_2 through the decomposition of the carbonates the temperature was gradually increased to the target temperature and the sample was stepwise lowered into the hot zone of the furnace.

First, the starting material was pressed into pellets, placed in an alumina crucible and slowly lowered into the hot zone of the furnace in 3-5 minute increments. Once the crucible had reached the hot zone

it was left overnight at a temperature range between 600 – 1050°C with a 2°C·min^{-1} ramp rate to facilitate gradual decarbonation of the sample. The fO_2 inside the furnace was controlled with a 80:20 CO_2:CO gas mix, which was between IW and FMQ over the full temperature range. After the pellets were removed from the furnace, they were ground and rehomogenized in a pestle and mortar. This was repeated twice for all starting materials to ensure full decarbonation and Fe reduction. For the AN composition, which contained both FeO and Fe_2O_3, the Fe_2O_3 fraction was added after the decarbonation and Fe reduction had finished. The addition of Fe_2O_3 was followed by rehomogenization of the starting material powder.

2.2.2 – Trace Element Doping

2.2.2.1 – Halogen Bearing Trace Element Mix

Trace elements were added via a Na_2CO_3-K_2CO_3 matrix trace element mixture containing 22 trace elements (Li, F, P, Cl, V, Cu, Zn, Ga, Ge, As, Br, Rb, Ag, Cd, In, Sn, Sb, I, Cs, Hg, Tl and Pb) which were added to the trace element mix using reagent-grade oxide (V_2O_5, ZnO, Ga_2O_3, GeO_2, As_2O_3, Ag_2O, CdO, In_2O_3, SnO_2, Sb_2O_3, HgO, Tl_2O_3 and PbO), carbonate (Li_2CO_3, Rb_2CO_3 and Cs_2CO_3), phosphate ($Ca_3P_2O_8$) and halide (CaF_2, CuCl, CuI and KBr) species. This trace element mix was added to the undoped starting materials such that the final mixture of the powders contained ~500 ppm of all trace elements except for Cu (~1200 ppm) which had a higher abundance because it was present in two halide compounds. This resulted in a total of ~1.5 wt. % trace elements in the starting materials. The trace element mixture was not heated before use to decompose the carbonate, phosphate and halogen species to prevent evaporative loss of the most volatile elements. As this trace element mix had a K_2CO_3 and Na_2CO_3 matrix and contained multiple Ca-bearing trace element species, the addition of 500 ppm trace elements also affected the major element composition of the starting materials.

2.2.2.2 – Halogen-Free Trace Element Doping

The presence of halogen species in the main trace element mix might affect the volatility of the other trace elements as it enabled additional evaporation reactions by the potential formation of halide gas

species in addition to the oxide and elemental gas species. To assess the effects of halogens, a second 5 g batch of SM starting material was doped with seven trace elements (Cu, Zn, Ge, Ag, Cd, Sn and Tl). These elements were added directly to the undoped starting material using reagent-grade oxide species: Cu_2O, ZnO, GeO_2, Ag_2O, CdO, SnO_2 and Tl_2O_3 at concentrations of 2500 – 3500 ppm. Elements and species were chosen to include the most volatile elements and to cover elements with differing affinities for forming halide gas species.

2.2.2.3 "Glassed" Starting Composition

The halogen bearing trace element mix contained trace elements that were not speciated the same way they would be in a silicate melt, particularly the phosphate, carbonate and halogen species. These trace element species have different physical and chemical properties than the representative silicate melt species. As a result, the volatile loss during these initial stages of melting and decomposition may not accurately reflect the actual volatility of these elements in a silicate melt. To investigate this stage of melting, a batch of trace element doped IB composition starting material was melted at 1300°C in air for 15 minutes and quenched to a glass. This glass was then ground to a powder and used as starting material.

2.3 – Experimental Set-up

2.3.1 – The One Atmosphere Furnace

Experiments were performed in a GERO alumina tube one atmosphere gas mixing furnace. The temperature inside the furnace was controlled by an external Eurotherm 3200 PID temperature controller. The fO_2 inside the furnace was controlled using a CO-CO_2 gas mixture where the composition of the gas is controlled by Omega FMA5400/5500 mass-flow controllers. The total gas flow for all experiments was 200 mL·min^{-1} and the composition of the CO-CO_2 gas mix corresponded to oxygen fugacities, calculated using Deines et al. (1974). The fO_2 and T were monitored and calibrated in situ prior to an experiment using an yttria-stabilised zirconia oxygen sensor (O'Neill and Pownceby, 1993). The sensor was placed inside the furnace and left to equilibrate at the target temperature and fO_2 for at least 20 minutes before the sample was introduced. The total volume of CO and CO_2 that was flushed through the furnace in 20 minutes exceeded thrice the volume of the furnace tube and was assumed to be sufficient to equilibrate the fO_2 conditions inside the furnace. The in-situ measured temperatures were ± 3°C of the target temperature after 20 minutes. The fO_2 sensor quantifies the oxygen fugacity inside the furnace by measuring the difference in electrochemical potential of oxygen between the CO-CO_2 gas mix and air in accordance with the Nernst equation. Based on previous calibrations the measured electrochemical potential (E in mV) can be converted to an oxygen fugacity as a function of temperature (T in K) using Equation **2.1**.

$$(Eq.2.1): \quad \log(fO_2) = -\left[\frac{20.159\,E}{T} + 0.68\right]$$

The fO_2 of an experiment is expressed either in its logarithmic form, log(fO_2), as calculated using Equation **2.1**, or relative to a common mineral buffer reaction, such as iron-wüstite (IW) or fayalite-magnetite-quartz (FMQ) where deviations are then expressed as ΔIW ± X where X is the $\log_{10}$ deviation of the fO_2 relative to the mineral buffer reaction. Table **2.1** lists the T-fO_2 conditions used in this study and how they compare to the mineral buffer reactions (Table **2.1**).

	1300°C				1400°C			
log(fO_2)	-0.68	-7	-9	-11	-0.68	-3.05	-6	-8
Air	200	0	0	0	200	0	0	0
CO [ml·min^{-1}]	0	10	68	163	0	0	10	67
CO_2 [ml·min^{-1}]	0	190	132	37	0	200	190	133
ΔIW	+10.08	+3.76	+1.76	-0.24	+9.03	+6.66	+3.71	+1.71
ΔFMQ	+6.89	+0.57	-1.43	-3.43	+5.86	+3.49	+0.54	-1.46

Table 2.1: The temperature and oxygen fugacity conditions used in experiments.

2.3.2 – Description of an Experiment

To perform an experiment, 0.8 – 1 g of starting material was wetted with ethanol and pressed into a pellet and placed in a furnace at 110°C for 10 minutes to dry the pellet. Next, the pellet was cut into smaller chunks using an ethanol-cleaned razorblade to produce chips of 70 ± 5 mg which were placed in a box-shaped sample holder. These were made from 0.25 mm thickness Pt or Re foil with approximate dimensions 4.5x4.5x1.5 mm. These were preferred over wire loops because of difficulties in keeping SM composition experiments suspended in more reducing conditions. This was not observed for the other starting materials, but the approach was maintained for consistency. The sample holders were then placed on a wire loop, made from 0.25 mm diameter Pt or Re wire, to suspend the sample in the furnace. This wire loop was attached to a piece of 0.25 mm Pt wire that was wrapped around a silica glass rod that was used to suspend the sample in the furnace. The silica glass rod was threaded through a furnace cap using an O-ring which allowed the rod to be moved up and down inside the furnace. This set-up enabled quick and accurate movement of the sample inside the furnace for introduction to the hot zone and quenching on a sub-5 second time scale. Samples were quenched by pulling the silica glass rod up to the top of the furnace. The assembly was subsequently removed from the furnace and the sample recovered.

The air quench was preferred over a drop quench in water, because early experiments showed that the thermal shock during the water quenches frequently caused the sample to shatter. It was important for the sample to remain intact to assess the homogeneity of the glasses to identify potential compositional gradients in the sample. Air quenches ensured the sample remained intact at the cost of a slightly longer quench time. However, the time difference between air and water

quenches is expected to be minimal as the melt will cool and solidify within seconds of leaving the hot zone while still in the furnace. Moreover, the absence of quench crystals and the observed major element homogeneity of each sample suggested quenching occurred rapidly.

The quenched sample was removed from the wire loop and mounted in an epoxy resin inside its sample holder. The epoxy mounts were polished first using increasingly fine grades of silicon carbide sandpaper and finally using 3 and 1 micron diamond paste on polishing pads to expose a polished surface for analysis. After polishing the sample was cleaned using isopropanol and dried using Kimwipes.

2.3.2.1 – Sample Holders and Fe Presaturation

Samples were suspended inside the furnace on a noble metal loop and/or sample holder. The composition of the noble metal wire changed with fO_2 to minimize interactions between the sample holder and the sample during the experiment. Platinum was used for the experiments in more oxidizing conditions, but as Pt readily alloys with metallic Fe (Kushida et al., 2003), and the equilibrium concentration increases with decreasing fO_2, Re was used for the experiments in more reducing conditions as it does not alloy with Fe (Borisov and Jones, 1999). Rhenium was not used in more oxidizing conditions as it oxidizes to form ReO_2.

For the experiments at ΔIW+3.7 the Pt capsule material was presaturated with Fe, as the conditions were close to the conditions of the $Re\ (s) + O_2\ (g) = ReO_2\ (s)$ reaction. Therefore, any slight increase in fO_2, e.g. during sample introduction, would result in the oxidation and decomposition of the Re sample holder. The presaturation of Pt sample holder material with Fe was required as conditions were sufficiently reducing such that using Pt would result in significant Fe loss, even over the short duration of the experiments (Fig. **2.1**).

The presaturation of Pt capsules with Fe was done to minimize Fe loss during an experiment. It was achieved by performing multiple “dummy runs” where some undoped starting material was loaded

on the sample holder and placed in the furnace at conditions identical to those of the experiment for approximately 3 hours. This allowed the Fe- Pt alloy forming reactions to proceed before the sample was loaded on the sample holder. The sample material from the dummy runs was separated from the Pt sample holder by dissolving the quenched glass using concentrated HF. Next, the sample holders were rinsed with deionized water and recovered to be used for the experiment. A comparison of three time series for the SM composition run at 1400°C and fO_2 of ΔIW+3.7 showed that ~15% of the FeO_T in the sample was lost to the Pt after an hour whereas Fe-presaturated Pt and Re retained >98% of the Fe (Fig. **2.1**).

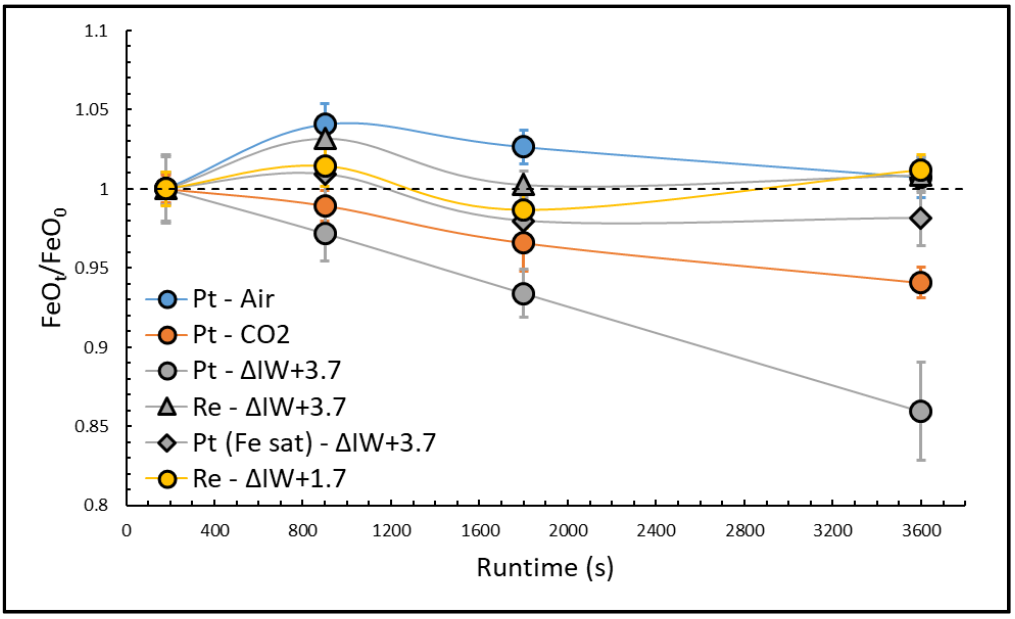


Figure 2.1: The temporal evolution of the fraction of FeO_T in the silicate glass (FeO_t) relative to the shortest experiment (FeO_0) at different fO_2 for the SM composition, illustrating the effect of fO_2 and capsule material. "(Fe sat)" indicates the Fe-presaturated Pt sample holders.

2.4 – Major- and Trace Element Analysis

2.4.1 – Electron Microprobe

Electron probe micro analysis (EPMA) of the quenched silicate glasses and the sample holders was used to assess their major and trace element composition. This was done using a CAMECA SX5-FE EPMA situated in the Department of Earth Sciences, University of Oxford. The different analyses described here served to assess (1) the major element abundances of the starting materials, (2) the Cu, Fe and Pt content of both sample and sample holder and/or (3) the Cl abundance of the IB experiments.

A 15 keV accelerating voltage and 20 nA beam current were used for all analyses with a spot size of 5 µm for the IB major element and Cl abundance measurements and 10 µm for the AN and SM major element and sample holder Cu and Pt content analyses. The counting times on the peak were 30 seconds for the Na, Mg, Al, Si, K, Ca, Ti, Mn, Cu and Pt and 80 seconds for Cl. Points were placed randomly across the sample, taking care to avoid the edges of the sample, the sample holder or any visible surface features that were potentially not representative of the sample material. For the initial undoped starting material measurements 10 points were used for all three starting abundances. The Cl abundance in the IB experiments was determined using 50 measurements per sample. For the SM and AN sample and sample holder measurements 10 – 25 points were placed on both the silicate glass and the Pt sample holders.

The mineral standards used to calibrate the instrument for analysis were albite ($NaAlSi_3O_8$) for Na, Al and Si, sanidine ($KAlSi_3O_8$) for K, MgO for Mg, wollastonite ($CaSiO_3$) or andradite ($Ca_3Fe_2Si_3O_{12}$) for Ca, Fe or fayalite (Fe_2SiO_4) for Fe, TiO_2 for Ti, synthetic NaCl for Cl, Cu for Cu and Pt for Pt. Secondary standards were measured, 3 – 5 times each, at the start and end of a run to check the calibration. The secondary standard measurements included at least three of: albite, andradite, labradorite ($(Ca,Na)_{1-2}(Al,Si)_{2-3}O_8$), sanidine, wollastonite, St. John's Island olivine and Durango apatite. Measured compositions of the secondary standard replicates corresponded within 3% relative to the expected

values. Detection limits in silicate glasses were 200 – 500 ppm for major elements, ~100 ppm for Cl, ~600 ppm for Cu and ~1000 ppm for Pt. For the Pt capsule material detection limits were ~650 ppm for Fe, ~1200 ppm for Cu and ~1600 ppm for Pt.

2.4.2 – Laser Ablation ICP-MS

The trace element compositions of the silicate glasses were determined using laser ablation inductively coupled plasma mass spectrometry (LA-ICP-MS). Analysis was conducted using a 213 nm New Wave Research UP213 laser unit in conjunction with a Perkin Elmer NexION 400Q ICP-MS at the Earth Sciences department, University of Oxford. The bulk trace element composition was assessed by measuring 5 – 15 spots, randomly spread across the sample, using a spot size of 50 or 100 µm. Compositional variability in the sample was assessed through compositional profiles that were made from 20 – 25 evenly spread 10 µm spots placed perpendicular to the evaporation surface of the sample or the sample holder inwards. Each measurement lasted 60 seconds and started with a 20 second laser warm-up time which provided background readings of the carrier gas. This was followed by a 40 second ablation time, using a 10 Hz laser repetition rate with a total fluence of ~15 Jcm^{-2} and a He flow of 650 $mL \cdot min^{-1}$, during which the sample was analysed. After data acquisition a 30 – 60 second wash-out time was used between each measurement to reduce the signal down to background levels.

The isotopes measured in all runs were ^{7}Li, ^{29}Si, ^{31}P, ^{42}Ca, ^{43}Ca, ^{51}V, ^{62}Ni, ^{65}Cu, ^{66}Zn, ^{71}Ga, ^{72}Ge, ^{75}As, ^{85}Rb, ^{95}Mo, ^{107}Ag, ^{111}Cd, ^{113}In, ^{115}In, ^{118}Sn, ^{121}Sb, ^{133}Cs, ^{203}Tl and ^{208}Pb. Other isotopes that were measured in a subset of runs were ^{19}F, ^{35}Cl, ^{57}Fe, ^{79}Br, ^{127}I, ^{135}Ba, ^{187}Re and ^{195}Pt. Specific isotopes were chosen to minimize the risk of interferences (May and Wiedmeyer, 1998) and maximize the signal. The dwell time on each isotope was 50 ms, resulting in ~45 repeat measurements for a 60 second analysis of a sample. The halogens were measured initially, but later omitted due to high detection limits, large errors on the measurements for F, Cl and Br and the lack of available standards for I (Table **2.2**). The inclusion of ^{57}Fe, ^{135}Ba, ^{187}Re and ^{195}Pt was to assess the Ba abundance and infer interactions between the sample and capsule material (Fe, Re and Pt). Ni and Mo were not added to the trace

element mix, but were measured to assess stability and were potentially required for interference corrections. Hg was not measured despite its presence in the trace element mixture due to it not readily ionizing during LA-ICP-MS analyses.

Samples were measured using a sample-standard bracketing approach where a set of 5 primary and/or secondary standard measurements were taken every 5-15 spots for bulk trace element analysis and every 20-25 points for compositional profiles. This was done to allow for the correction of potential instrumental drift. The primary standard was the reference material NIST-610, a glass doped with 400 – 500 ppm of most elements in the periodic table (Jochum et al., 2011). The secondary standard was USGS standard material GSE-1G, a synthetic basalt doped with ~500 ppm of a wide array of trace elements (Jochum et al., 2005a). The measured counts were processed and reduced to concentrations using the Glitter (GEMOC) software package where ^{43}Ca was used as the internal standard isotope. The Ca abundances required to process the sample data were obtained by EPMA. The Glitter software corrects for instrumental drift with time via linear interpolation between two sets of standard measurements that bracket unknowns.

	n	GeoREM [ppm]	Measured [ppm]	D.L. [ppm]	σ [%]		n	GeoREM [ppm]	Measured [ppm]	D.L. [ppm]	σ [%]
^{7}Li	376	430 ± 60	439 ± 15.4	0.10	8.99	**^{95}Mo**	410	390 ± 30	390 ± 16.2	0.02	8.86
^{31}P	376	70 ± 20	53.3 ± 19.5	3.80	40.2	**^{107}Ag**	410	200 ± 20	215 ± 12.0	0.05	9.38
^{35}Cl	180	-	921 ± 169	112	190	**^{111}Cd**	410	160 ± 50	281 ± 26.7	0.05	13.1
^{51}V	376	440 ± 20	434 ± 13.0	0.03	5.89	**^{115}In**	376	370 ± 60	418 ± 19.6	0.03	10.3
^{62}Ni	410	440 ± 30	447 ± 19.6	0.32	8.47	**^{118}Sn**	410	280 ± 50	359 ± 16.0	0.03	9.32
^{65}Cu	410	380 ± 40	385 ± 15.7	0.08	7.28	**^{121}Sb**	376	450 ± 110	398 ± 19.4	0.03	10.5
^{66}Zn	410	460 ± 10	510 ± 27.0	0.13	10.5	**^{133}Cs**	376	310 ± 20	316 ± 15.3	0.01	10.5
^{71}Ga	376	490 ± 70	533 ± 18.2	0.02	7.55	**^{135}Ba**	20	427 ± 5	443 ± 17.0	0.04	6.48
^{72}Ge	410	320 ± 80	426 ± 16.0	0.39	7.84	**^{187}Re**	296	78.9 ± 7.7	77.0 ± 5.30	0.01	13.9
^{75}As	376	260 ± 90	370 ± 16.7	0.13	10.7	**^{195}Pt**	296	30	31.5 ± 12.0	0.02	23.1
^{79}Br	204	-	1289 ± 354	23.2	61.0	**^{203}Tl**	410	2.00 ± 0.2	1.97 ± 0.28	0.01	15.9
^{85}Rb	376	356 ± 4	386 ± 15.4	0.01	8.06	**^{208}Pb**	376	378 ± 12	399 ± 25.4	0.01	12.9

Table 2.2: Overview of the measured isotopes for the GSE-1G secondary standard. The measured average abundance and its standard deviation (s.d.) with GeoReM preferred values (Jochum et al., 2005b), the detection limits and errors on individual measurements. The number of times an element was measured is indicated with n.

Measurements of GSE-1G were used to infer the detection limits and expected percent errors for the individual elements using 50 µm spots (Table **2.2**). This showed that detection limits were <1 ppm and errors on individual measurements (σ) were on average 5.89 – 15.9 % for the doped trace elements,

excluding P and halogens. A comparison of the trace element abundances of GSE-1G measured in this study with the GeoReM preferred values (Jochum et al., 2005b) showed that there were differences between the two for Zn, Ge, As, Rb, Cd, Sn, Ba and Pb which were all measured at a concentration higher than the reference value. The GSE-1G measurements were performed over a 2.5 year time period and the instrument was tuned periodically during this time, but the measured trace element abundances were consistent over this entire duration (Fig **2.2**). This suggests the instrument was operating stably during the period of time.

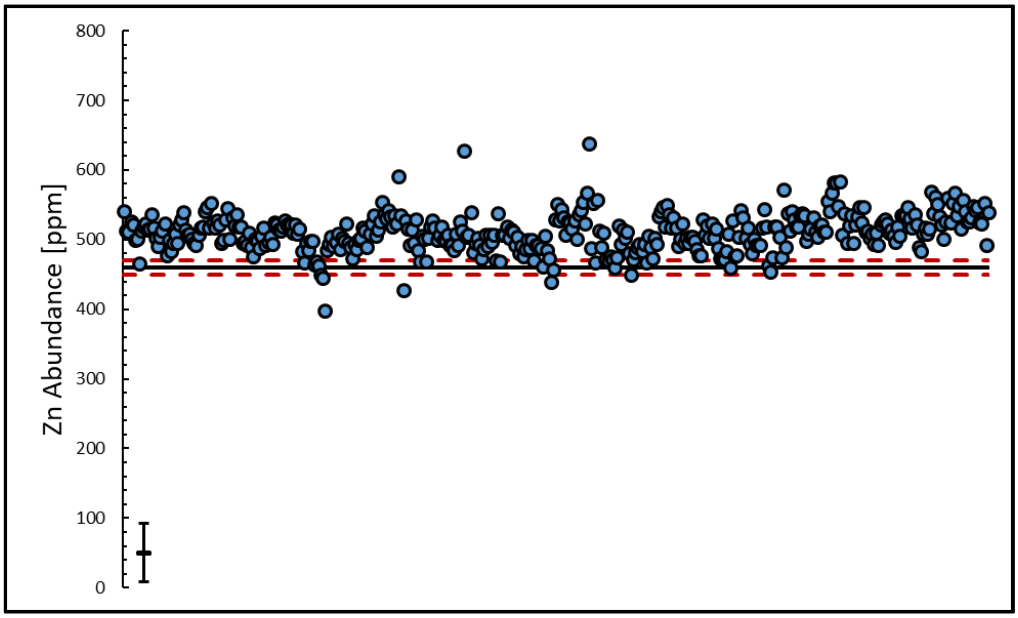


Figure 2.2: Temporal evolution of the measured Zn abundance of GSE-1G. The solid black line is the GeoReM preferred abundance and the dotted red lines its associated error. The error bar in the bottom left illustrates the average error on each measured Zn data point.

2.4.3 – Composition of the Starting Materials

The major and trace element compositions of the undoped starting materials were determined by melting approximately 50 mg of each for 10 minutes in air. This was done to assess the major element composition prior to trace element doping to assess the accuracy of the preparation of the mixes. The major element abundances obtained from these analyses were combined with those obtained from later EPMA analyses of samples to find the average major element composition of the starting materials (Table **2.3**). The trace element abundances reported in Table **2.3** for SM, SM-2, IB and AN were calculated by addition of the measured trace element abundance of the undoped starting material to the calculated abundance of a trace element added by trace element doping, using the

amount of trace element mix used. The exception to this is the IB Glass where the starting material was a glass, which enabled direct measurement of the starting trace element abundances.

	SM n = 192	IB n = 740	AN n = 305
SiO_2	38.91 ± 0.63	48.96 ± 0.32	60.78 ± 1.38
Al_2O_3	10.57 ± 0.20	14.55 ± 0.12	16.82 ± 0.63
MgO	15.09 ± 0.20	8.31 ± 0.09	3.18 ± 0.13
FeO_T	15.05 ± 0.36	9.37 ± 0.11	3.70 ± 0.13
CaO	16.57 ± 0.23	12.16 ± 0.10	6.37 ± 0.34
Na_2O	0.73 ± 0.05	2.39 ± 0.06	4.43 ± 0.44
K_2O	1.53 ± 0.13	1.62 ± 0.05	2.85 ± 0.11
TiO_2	-	0.93 ± 0.03	0.58 ± 0.02
MnO	-	0.17 ± 0.02	-
SUM	98.45 ± 1.17	98.49 ± 0.49	98.72 ± 0.97
nbo/t	1.88	0.85	0.27

	SM n = 5	SM-2 n = 5	IB n = 5	IB-G n = 5	AN n = 5
Li	588 ± 9.11	-	591 ± 9.15	572 ± 8.86	594 ± 9.20
F	492	-	492	-	492
P	614 ± 32.9	-	837 ± 44.8	777 ± 41.6	683 ± 36.6
Cl	507	-	507	-	507
V	517 ± 2.88	-	807 ± 4.50	767 ± 4.28	516 ± 2.88
Cu	1182 ± 70.7	3438 ± 206	1268 ± 75.9	1098 ± 65.7	1225 ± 73.3
Zn	574 ± 16.1	3297 ± 92.6	598 ± 16.8	659 ± 18.5	538 ± 15.1
Ga	516 ± 13.5	-	525 ± 13.7	483 ± 12.6	521 ± 13.6
Ge	510 ± 11.5	2700 ± 60.8	547 ± 12.3	497 ± 11.2	509 ± 11.5
As	511 ± 7.97	-	526 ± 8.21	441 ± 6.88	511 ± 7.97
Br	529	-	529	-	529
Rb	509 ± 17.1	-	512 ± 17.2	469 ± 15.8	513 ± 17.3
Ag	506 ± 47.2	3911 ± 364	507 ± 47.2	396 ± 36.9	512 ± 47.7
Cd	508 ± 54.8	3610 ± 389	508 ± 54.8	308 ± 33.2	508 ± 54.8
In	511 ± 8.30	-	545 ± 8.85	458 ± 7.44	508 ± 8.25
Sn	520 ± 19.0	3080 ± 112	588 ± 21.4	447 ± 16.3	511 ± 18.6
Sb	516 ± 12.7	-	552 ± 13.6	452 ± 11.1	509 ± 12.5
I	507	-	507	-	507
Cs	533 ± 14.9	-	547 ± 15.3	461 ± 12.9	533 ± 14.9
Tl	508 ± 105	3742 ± 771	508 ± 105	46.4 ± 9.56	508 ± 105
Pb	544 ± 10.7	-	543 ± 10.7	460 ± 9.07	547 ± 10.8

Table 2.3: Major (wt. %) and trace element (ppm) composition of the doped starting materials. The number of individual measurements is indicated with **n**. The polymerization of the melt is indicated by nbo/t (See Section **4.4.3**).
The reported errors on IB-G are standard deviations on the average of all measurements. The errors on SM, SM-2, IB and AN were estimated from the errors on IB-G as the starting trace element abundances of these starting materials were not directly measured and abundances were calculated by adding a measured undoped starting material trace element abundance and a weighed amount of trace element doping for which errors were not considered. Errors on halogen starting abundances could not be accurately quantified using LA-ICP-MS due to analytical difficulties. This has likely led to an over-estimate of the error on the most volatile elements as they were partially volatilized during sample preparation of IB-G.

2.5 – Thermodynamic Predictions of Evaporation Reactions

2.5.1 – General Description and Assumptions

The stable species of an element at a given temperature and oxygen fugacity can be derived from its thermodynamic properties. The stable and/or dominant species in both the melt and the gas phase can be determined by investigating how the stability of the different trace element species varies in T-fO_2 space. The relative stability of oxidized and reduced melt and/or gas phase trace element species is governed by the equilibrium constant of the oxidation reaction between the two species. Temperature and fO_2 are the main variables that affect the equilibrium constant. It can be determined how these parameters affect the relative abundances of the trace element species by considering a generic oxidation reaction involving element M where the oxidation state of M changes from x to x+n is described by Equation **2.2**.

$$(Eq.\,2.2):\quad M^xO_{\frac{x}{2}}\,(g/l) + \frac{n}{4}O_2\,(g) = M^{x+n}O_{\frac{x+n}{2}}\,(g/l)$$

The equilibrium constant (K) of this reaction is given by Equation **2.3**

$$(Eq.\,2.3):\quad K = \frac{[M^{x+n}O_{\frac{x+n}{2}}]\gamma_{M^{x+n}O_{\frac{x+n}{2}}}}{[M^xO_{\frac{x}{2}}]\gamma_{M^xO_{\frac{x}{2}}}[O_2]^{n/4}\gamma_{O_2}^{n/4}}$$

The square brackets indicate the concentration of the species and the n/4 exponent is the stoichiometric coefficient of O_2 in the reaction. The following derivation and use of the equilibrium constant relies on two assumptions for the different phases involved in the reaction:

(1) All species in the melt behave as pure solids which defines the concentration and activity coefficient as one.

(2) All vapour species behave as an ideal gas. This means that the concentration is equal to the partial pressure and fugacity: $[A] = P_A = fA$.

Equation **2.3** illustrates the fO_2 dependence of the equilibrium constant of the oxidation reaction. The temperature dependence is taken from another definition of the equilibrium constant (Eq. **2.4**).

$$(Eq.\,2.4): \quad K = \exp\left(-\frac{\Delta G_f^0}{RT}\right)$$

Here ΔG_f^0 is the standard state Gibbs free energy change of the reaction at the temperature of interest, T in K, and R is the gas constant (8.3145 $Jmol^{-1}K^{-1}$). The above equations and assumptions show that the equilibrium coefficient of any reaction can be used to find a temperature-fO_2 dependence of the species involved.

For any given reaction, the equilibrium constant of the reaction (K_f) can be calculated using the properties of the product and reactant species involved in the reaction (Eq. **2.5**).

$$(Eq.\,2.5): \quad \log\left(K_{f,reaction}\right) = \sum \log\left(K_{f,products}\right) - \sum \log\left(K_{f,reactants}\right)$$

Here K_f are the equilibrium constants of formation of the products and reactants. The thermodynamic properties of pure species as a function of temperature can be found in thermodynamic databases of pure species, e.g. Pedley and Marshall (1983) or Barin et al. (1989). The $\log(K_f)$ of any reaction at a given temperature can be inferred from the temperature dependence of $\log(K_f)$ by plotting it against $1/T$ which will yield a straight line (Eq. **2.6**).

$$(Eq.\,2.6): \quad \log\left(K_f\right) = -\frac{\Delta G_f^0}{RTln(10)}$$

The $\log(K_f)$ at the target temperature can then be determined by interpolating the value at the target temperature. For some of the highly volatile elements and species thermodynamic data was available at the temperature of the experiments. In this case the data at lower temperature was extrapolated linearly to infer $\log(K_f)$ of a given species at the target temperature. The following sections contain a brief description of how the three different type of reactions, (1) oxidation reactions in the melt, (2) evaporation reactions and (3) gas species interactions affect the abundance of different trace element species in the melt and gas phase.

2.5.2 – Oxidation Reactions in the Melt

Oxidation reactions within the melt are described by Equation **2.7**.

$$(Eq.\,2.7):\;\; M^{x}O_{\frac{x}{2}}\,(l) + \frac{n}{4}O_2\,(g) = M^{x+n}O_{\frac{x+n}{2}}\,(l)$$

Here x is the valence state of the reduced trace element species and n is the change in valence state of the trace element during the reaction. Considering the earlier assumptions regarding melt and gas phase species behaviour, $[M^{x}O_{x/2}]$ and $[M^{x+n}O_{(x+n)/2}] = 1$ and $[O_2] = fO_2$, a direct relation between the equilibrium constant and fO_2 was derived (Eq. **2.8**).

$$(Eq.\,2.8):\;\; \log(K) = -\frac{n}{4}\log(fO_2)$$

This equation describes the line in T-fO_2 space at which the oxidized and reduced trace element species are equally abundant. Combining Equations **2.6** and **2.8** gives an equation that describes how the stability of the different melt species changes with temperature and fO_2 (Eq. **2.9**).

$$(Eq.\,2.9):\;\; \log(fO_2) = -\frac{4\Delta G_f^0}{nRTln(10)}$$

This shows that there is an inverse relation between log(fO_2) and T where the slope is defined by the thermodynamic properties of the oxidation reaction. The T-fO_2 stability field of various trace element species can then be constructed using Equations **2.8** and **2.9**.

2.5.3 – Evaporation Reactions

The reaction describing the evaporation of trace element species (Eq. **2.10**) resembles that of the oxidation reaction in the melt. The difference is that the product species is now present in the gas phase instead of the melt which means that it can no longer be considered unity and remains a factor in describing the equilibrium constant. In this study only monometallic trace element gas species, i.e. those with a single M atom, were considered because it is assumed that the transport of the reaction products away from the reaction interface by the CO-CO_2 gas mix, the low melt concentration and low

gas phase partial pressure of the trace element inhibits the formation of polymetallic gas species, both through evaporation and reactions between monometallic gas species.

$$(Eq.\,2.10):\;\; M_{\alpha}^{x+n}O_{\frac{\alpha(x+n)}{2}}\,(l) = \alpha M^{x}O_{\frac{x}{2}}\,(g) + \frac{n}{4}O_{2}\,(g)$$

Because it is possible for a polymetallic trace element species in the melt to evaporate as multiple monometallic gas species (e.g. Ga_2O_3 (l) → 2 GaO (g)) there is an additional parameter, α, which represents the number of M atoms in the melt species. For these reactions the main aim was to determine the partial pressure of the different trace element gas species and, for elements with multiple stable species, to determine which gas species are most abundant as a function of fO_2 (Eq. **2.11**).

$$(Eq.\,2.11):\;\; \log\left(P_{M^{x}O_{\frac{x}{2}}}\right) = \frac{1}{\alpha}\left[\log(K) + \frac{n}{4}\log(fO_2)\right]$$

Equation **2.11** was applied to all potential stable monometallic gas species for a given element to determine the abundant gas species for an element (see Appendix **2**).

This approach is applicable to a silicate melt system as the elements are assumed to follow pure species behaviour during the evaporation reactions. However, interactions between different elements and a more complex bonding environment in the silicate melt will cause trace element behaviour in the melt to deviate from the pure species behaviour as activity in the silicate melt for certain elements deviates significantly from unity (e.g. Sossi et al., 2019). The oxidation state of most trace elements in the experiments is expected to be consistent between compositions and comparable to those found in natural samples. Using data from natural samples only V (V^{2+}, V^{3+}, V^{4+} and V^{5+}; Righter et al., 2006) is expected to see changes in its oxidation state within the range of fO_2 considered in the experiments. The oxidation state of the other elements in the silicate melt is expected to remain unchanged over the full range of experimental conditions: Li^{+}, P^{5+}, Cu^{+}, Zn^{2+}, Ga^{3+}, Ge^{4+}, As^{3+}, Rb^{+}, Ag^{+}, Cd^{2+}, In^{3+}, Sn^{4+}, Sb^{3+}, Cs^{+}, Tl^{+} and Pb^{2+} (Capobianco et al., 1999; Lanzirotti et al., 2019; Lee et al., 2010; Norris, 2016; Maciag and Brenan, 2020; Steenstra et al., 2020).

2.5.4 – Gas Species Interactions

It is assumed that there will be no interactions between gas species inside the furnace, because the CO-CO_2 gas mix will sufficiently remove any forming gas species from the reaction interface and dilute them sufficiently to minimize the likelihood of gas species reactions. However, the presence of halogens in one of the trace element mixes means that trace element evaporation may occur via interactions with halogens instead of with oxygen. The reactions between gas species were used to calculate the relative partial pressures of the different gas species. The generalized reaction between gas species is shown in Equation **2.12**.

$$(Eq.\,2.12):\;\; M^{x}O_{\frac{x}{2}}\,(g) + \frac{n}{4}O_2\,(g) = M^{x+n}O_{\frac{x+n}{2}}\,(g)$$

The presence of two gas species changes the definition of the equilibrium constant calculations compared to the oxidation and evaporation reactions (Eq. **2.13**).

$$(Eq.\,2.13):\;\; \log(K) = \log\left(P_{M^{x+n}O_{\frac{x+n}{2}}}\right) - \log\left(P_{M^{x}O_{\frac{x}{2}}}\right) - \frac{n}{4}\log(fO_2)$$

As this equation contains two unknowns, it cannot be solved to calculate the partial pressure of a single gas species. However, it is possible to assess the relative partial pressures of both gas species (Eq. **2.14**).

$$(Eq.\,2.14):\;\; \log\left(\frac{P_{M^{n+}O_{\frac{x+n}{2}}}}{P_{M^{m+}O_{\frac{x}{2}}}}\right) = \log(K) + \frac{n}{4}\log(fO_2)$$

2.5.4.1 – Presence of Chloride Species

The addition of halogens (F, Cl, Br and I) to the melt alters the bonding environment in the melt and may facilitate the formation of halide gas species. These species can affect the evaporation reactions that occur if an element preferentially forms halide gas species over oxides or elemental species. The presence of halogen gas species was investigated by considering the partial pressure of chloride species relative to that of elemental or oxide gas species by considering the reaction between gas species to infer the relative partial pressures (Eq. **2.15**). The focus here is solely on Cl as it is the halogen

considered most likely to bond with trace elements and thus expected to have the largest partial pressure. Moreover, the behaviour of Cl in the silicate melt is better understood than that of other halogens.

$$(Eq.\,2.15):\ \ MO_a\ (g) + \frac{x}{2}\ Cl_2\ (g) = MCl_x\ (g) + \frac{a}{2} O_2(g)$$

The relative abundance of the two gas species for trace element *M* then becomes directly dependent on the equilibrium constant and the oxygen and chlorine fugacities (Eq. **2.16**).

$$(Eq.\,2.16):\ \log\left(\frac{MCl_x}{MO_a}\right) = \log(K) + \frac{x}{2}\log(fCl_2) - \frac{a}{2}\log(fO_2)$$

The fO_2 is constrained by the experiments and fCl_2 can be calculated from the chlorine abundance in the melt and the experimental conditions (fO_2, T and P) based on the equation of Thomas and Wood (2021; Eq. **2.17**).

$$(Eq.\,2.17):\ \log(fCl_2) = 2\left(\log(Cl_{melt}) - 0.984 + \frac{930P}{T} + 0.25\log(fO_2)\right)$$

Here Cl_{melt} is the Cl abundance in the melt in wt. %, P is the pressure in GPa and T the temperature in Kelvin. Because the experiments are performed at 1 atmosphere ($P \approx 10^{-4}$ GPa), the PT term becomes negligible.

2.6 – Quantifying Volatility

2.6.1 – Defining C_i^0

Constraining the initial abundance (C_i^0) of each trace element is the first step in quantifying volatility. The trace element doping introduced a range of elements, some of which as species that did not accurately represent their speciation in a silicate melt. For the starting materials that consisted of a powder, the decomposition of the Cu-halide (CuCl, CuI), alkali-carbonate (Li_2CO_3, Na_2CO_3, K_2CO_3, Rb_2CO_3, Cs_2CO_3) and phosphate ($Ca_3P_2O_8$) compounds to their respective melt species during the initial stages of melting does not reflect their behaviour in a silicate melt as they were not dissolved in the melt before the experiment. As these compounds generally have lower evaporation temperatures any volatile loss during this stage did not reflect the volatility of these elements in a silicate melt. Therefore it was necessary that the value of C_i^0 represented the trace element abundance after the sample had fully melted. As volatility is known to be fO_2 dependent, the degree of volatile loss during the initial melting stage is also expected to be fO_2 dependent. Taking all of this into account it was decided to use the concentration of the trace element in the shortest experiment for each time series at fixed fO_2 as C_i^0 for the modified Hertz-Knudsen-Langmuir equation. This increased the volatility factors of the elements introduced as halide or carbonate as the losses during decomposition were not included. However, it also resulted in enhanced volatility factors for the highly volatile elements where the volatility factor may not accurately reflect their volatility, because the majority was lost during the initial three minutes. For visualizing the volatility factors as a function of time, fO_2 and melt composition it was therefore chosen to normalize to the starting trace element abundances in Table **2.2**.

The experiments performed using the “glassed” IB starting composition were already dissolved in their appropriate melt species at the start of the experiment. Therefore, the trace element abundance of the initially quenched glass was used as C_i^0 for this set of experiments.

2.6.2 – The Volatility Factor

The volatility factor (F_M; Norris and Wood, 2017) is the ratio of the concentration of a given trace element after a certain amount of time relative to its starting abundance (Eq. **2.18**).

$$(Eq.\,2.18):\ \ F_M = \frac{C_i^t}{C_i^0}$$

This parameter describes the degree of volatile loss at the most basic level, but does not link it to any experimental parameters, evaporation reaction kinetics or potential evaporation mechanics. Therefore its main purpose is to evaluate and make qualitative estimates of volatility, such as an order of trace element volatility based purely on the degree of depletion as a function of time, fO_2 or melt composition.

2.6.3 – The Modified Hertz-Knudsen-Langmuir Equation

2.6.3.1 – Introduction

The number of particles in a monoatomic gas that strike a surface over a given time can be described by the Hertz-Knudsen-Langmuir equation (HKL; Eq. **2.19**; Knudsen, 1909; Langmuir, 1916; Hirth and Pound, 1963). This equation, rooted in the kinetic theory of gases, describes the collision frequency of atoms of an ideal monoatomic gas hitting a surface at equilibrium within a container. It was derived from the velocity distribution of particles in a monoatomic isothermal gas that follows Maxwell-Boltzmann behaviour.

$$(Eq.\,2.19):\ \ J_i = \frac{N_i}{A} = -\frac{n_i \alpha_e \left(P_{i,sat} - P_i\right)}{\sqrt{2\pi m_i RT}}$$

This equation describes how the evaporative flux of gas species *i* per surface area, J_i (mol·m^{-2}), changes as a function of the number of atoms of *i* in the dominant gas phase species (n_i), mass of the evaporating species (m_i), the difference between the saturated vapour pressure ($P_{i,sat}$) and the pressure of *i* at the evaporating surface (P_i), the temperature (*T*), the gas constant (*R*) and the Langmuir

evaporation coefficient (α_e), an empirical parameter that describes the non-ideal nature of evaporation. The evaporation coefficient is discussed in greater detail in Ackermann et al. (1962).

2.6.3.2 – Derivation of the Modified HKL Equation

Sossi et al. (2019) performed a time integration of the HKL equation to derive an equation that was applied to describe the evaporative loss from a silicate melt in terms of experimental parameters and the properties of the evaporation reaction(s) for a given element. This derivation relied on four assumptions;

(1) The sample is spherical.

(2) Any evaporating gas is transported away from the reaction interface ($P_i << P_{i,sat}$).

(3) Ideal gas behaviour of the evaporating gases ($P_{i,sat} = f(i)$) and can therefore be described using the equilibrium constant of any evaporation reaction.

(4) The low trace element abundance in the melt and low density in the gas phase inhibits the formation of polymetallic gas species ($n_i = 1$).

2.6.3.2.1 – One Species in the Melt and Gas Phase

The step-by-step modification of the HKL equation following the Sossi et al. (2019) approach will be discussed here using the simplest example where there is a single stable species in both the melt and the gas phase. This derivation will differ from Sossi et al. (2019) by considering a generalized sample geometry, using a basic surface area term that must be determined separately, to find an equation to describe evaporative loss.

First, Equation **2.19** is adjusted by applying assumptions (2) and (4) while retaining a generalized geometry term and considering the temporal evolution of N_i (Eq. **2.20**).

$$(Eq.\,2.20):\ \frac{dN_i}{dt} = -A\frac{\alpha_e P_{i,sat}}{\sqrt{2\pi m_i RT}}$$

The saturated vapour pressure can be defined through equilibrium thermodynamics where an expression is found by considering the equilibrium constant (K) of the evaporation reaction (Eq. **2.21**).

$$(Eq.\,2.21):\ K = \frac{P_{M^xO_{\frac{x}{2}}} fO_2^{n/4}}{X_{M^{x+n}O_{\frac{x+n}{2}}} \gamma_{M^{x+n}O_{\frac{x+n}{2}}}}$$

In Equation **2.21** *X* and γ are the mole fraction and activity coefficient of the condensed trace element species and P is the partial pressure of the gas species where assumption (3) means P_{O_2} can be substituted with fO_2. By adjusting Equation **2.21** and substituting the subscripts with *i* the saturation partial pressure is defined by Equation **2.22.**

$$(Eq.\,2.22):\ P_{i,sat} = K\frac{X_i\gamma_i}{fO_2^{n/4}}$$

Equation **2.22** is then implemented into Equation **2.20** and an "apparent equilibrium constant" (K*) is defined as $K^* = K\alpha_e\gamma_i^\infty$. This is the equilibrium constant of the reaction multiplied with the evaporation coefficient and the activity of the trace element species in the melt at infinite dilution (γ_i^∞). Next, both sides of the equation were divided by the total number moles of *i* in the starting material ($N_{i,0}$), converting to mole fractions (Eq. **2.23**).

$$(Eq.\,2.23):\ \frac{dX_i}{dt} = -A\frac{K^*X_i}{fO_2^{n/4}{N_0}^T\sqrt{2\pi m_i RT}}$$

Next, the initial number of moles of *i* is defined as the ratio of the mass of the sample (m_s) and the average molecular mass of the silicate melt (M_{avg}), ${N_0}^T = m_s/M_{avg}$ (Eq. **2.24**).

$$(Eq.\,2.24):\ \frac{dX_i}{X_i} = -A\frac{K^*M_{avg}}{fO_2^{n/4}m_s\sqrt{2\pi m_{i,e}RT}}dt$$

Equation **2.24** differs slightly from Sossi et al. (2019) as they considered m_s and M_{avg} to be the same parameter. Next, Equation **2.24** is integrated over the runtime of an experiment to find the final equation describing the volatile loss from the silicate melt (Eq. **2.25**). The different parameters involved in the equation are described in Table **2.4**.

$$(Eq.\,2.25):\quad \ln\left(\frac{X_i^t}{X_i^0}\right) = -A\frac{K^* M_{avg}}{fO_2^{n/4} m_s \sqrt{2\pi m_{i,e} RT}}(t - t_0)$$

2.6.3.2.2 – One Species in the Melt, Two Species in the Gas Phase

Equation **2.25** applies to the scenario where there is a single stable species in both the condensed and gas phase which is sufficient for the majority of the studied elements. However, four elements, Li, P, Cs and Pb, were predicted to have one stable species in the melt, but two stable gas species. As there are two concurrent evaporation reactions for these elements, Equation **2.25** does not accurately describe their evaporation environment. Equation **2.25** had to be expanded to consider both evaporation reactions. This was achieved by adding a $\left(K^*/\left[fO_2^{n/4}\sqrt{m_{i,e}}\right]\right)$ term for each additional evaporation reaction which, for two gas species, results in Equation **2.26**.

$$(Eq.\,2.26):\quad \ln\left(\frac{X_i^t}{X_i^0}\right) = -A\left(\frac{K_1^*}{fO_2^{n_1/4}\sqrt{m_{i,e,1}}} + \frac{K_2^*}{fO_2^{n_2/4}\sqrt{m_{i,e,2}}}\right)\frac{M_{avg}}{m_s\sqrt{2\pi RT}}(t - t_0)$$

The other scenarios where there are (1) multiple species in melt and one species in the gas phase or (2) multiple species in both the melt and gas phase can also be shown to have their own unique solutions. However, because these are not required for the elements in this study the derivations were not included. The interested reader is referred to Sossi et al. (2019).

2.6.3.3 – Solving the Modified HKL Equation

2.6.3.3.1 – Parameters used in the Modified HKL Equation

Despite the large number of parameters involved the modified HKL equation, only two are definitive unknowns: K* and t_0. Furthermore, n can be treated as either known or unknown. By treating n as known it is predefined that evaporation occurs through certain evaporation reaction while treating it as unknown means that it is calculated without an assumptions regarding the evaporation mechanics and the obtained *n* can then be compared to the expected value. Previous studies by Sossi et al. (2019; 2020), Heck (2022) and Liu et al. (2022) have all treated n as known based on thermodynamic

predictions. Other parameters are experimental conditions (T, t and fO_2) or sample properties (m_s, A), measured with LA-ICP-MS (X_i^t and X_i^0), predicted based on the thermodynamic properties of the evaporation reaction(s) of the pure species ($m_{i,e}$) or calculated based on the melt composition (M_{avg}).

Parameter	Definition
X_i^t	The concentration of element *i* in the sample [ppm].
X_i^0	The initial concentration of element *i* in the sample [ppm]. See section **2.6.1**
A	The surface area of the evaporating surface [m^2]. Based on average sample dimensions A = $2.06 \cdot 10^{-5}$ m^2.
K^*	The apparent equilibrium coefficient which is calculated by $K^*=K \cdot \alpha_e \cdot \gamma_i$.
α_e	The evaporation coefficient.
γ_i^∞	The activity of trace element species *i* in the melt at infinite dilution.
M_{avg}	The average molar mass of the silicate melt [$kg \cdot mol^{-1}$]. $M_{avg,SM}$ = $6.14 \cdot 10^{-2}$ $kgmol^{-1}$, $M_{avg,IB}$ = $5.92 \cdot 10^{-2}$ $kgmol^{-1}$ and $M_{avg,AN}$ = $6.83 \cdot 10^{-2}$ $kgmol^{-1}$
fO_2	The oxygen fugacity during the experiment.
n	The change in oxidation state of trace element *i* as a result of evaporation.
m_s	The mass of the sample, $7 \cdot 10^{-5}$ kg.
$m_{i,e}$	The molar mass of the evaporating species of trace element *i* [$kg \cdot mol^{-1}$].
R	The gas constant [8.3145 $J \cdot K^{-1} \cdot mol^{-1}$].
T	The temperature of the experiment [K].
t	The runtime of the experiment [s].
t_0	The "lag time" which depends on the experimental set-up and varies per element $0 \leq t_0 \leq t$ [s] (Sossi et al., 2019).

Table 2.4: An explanation of the different parameters involved in the modified Hertz-Knudsen-Langmuir equation.

The apparent equilibrium coefficient is dependent on the activity coefficient of the trace element in the melt at infinite dilution and the evaporation coefficient. The scarcely available data for α_e is mostly focused on major element or alkali evaporation (Alexander, 2001; Fedkin et al., 2006; Richter et al., 2011; Tachibana et al., 2011). Sossi et al. (2019) determined that evaporation coefficients for trace elements in the silicate melt tend to be close to unity, but can vary within an order of magnitude. Trace element activity in silicate melts is more widely studied (e.g. O'Neill and Eggins, 2002; Wood and Wade, 2013; Norris, 2016) but the absence of available data for all elements and/or at compositions and/or temperatures relevant to the experimental conditions inhibits their use. The activity coefficient may deviate from unity, because silicate melts are non-ideal solutions.

2.6.3.3.2 – Non-Linear Least Squares

The modified HKL equations was solved analytically, employing the method of Sossi et al. (2019), by fitting the measured data to Equation **2.25** or **2.26** to find K^*, n and t_0. This approach used the

Microsoft Excel add-in "SOLVER" to minimize the misfit between the measured and calculated concentration ratios by non-linear least squares minimization of the misfit between the measured and modelled concentration ratios (Eq. **2.27**). This was done by considering a set of experiments at constant temperature and runtime, but variable fO_2.

$$(Eq.\,2.27):\ \chi^2(K^*, n, t_0) = \sum_N \left(\frac{\frac{X_i^t}{X_i^0}_{meas} - \frac{X_i^t}{X_i^0}_{calc}}{\sigma\left(\frac{X_i^t}{X_i^0}\right)_{meas}} \right)^2$$

Here σ is the standard deviation on the measured data, X_i^t/X_i^0 is the concentration ratio where $_{meas}$ and $_{calc}$ indicate measured and calculated ratios respectively, N is the amount of experiments and χ is the misfit as function of the unknowns. Solutions of Equations **2.25** and **2.26** are best visualized by plotting X_i^t/X_i^0 as a function of $\log(fO_2)$ at constant runtime.

Chapter 3 – Methodology: Zinc Isotope Analysis

3.1 – Introduction

The earliest studies regarding the isotopic variability of Zn isotopic were conducted using neutron activation analysis (NAA; Filby, 1964) or thermal ionization mass spectrometry (TIMS; Rosman, 1972). However, the comparatively high ionization potential of Zn (9.39 eV) affected its ionization efficiency, a measure of the fraction of an element that is ionized during TIMS analysis, which is generally low as it is difficult to ionize thermally (e.g. Ghidan and Loss, 2012). This meant that it was difficult to accurately determine the isotope fractionation of Zn using TIMS. Moreover, the precision of data obtained in the early TIMS Zn measurements was generally low with 1–2 ‰ per amu errors meant that there was no discernible variability observed in terrestrial samples.

The advent of the multiple collector inductively coupled plasma mass spectrometry (MC-ICP-MS) techniques for stable metal isotope measurements rapidly resulted in it being the dominant method for measuring Zn isotope fractionation. The MC-ICP-MS has a higher ionization efficiency than TIMS for Zn because it operates using an ionized Ar plasma and has the capacity of ionizing most elements in the periodic table. As a result the MC-ICP-MS yielded a significant increase of accuracy and precision to ≤0.05 ‰ per amu which enabled the quantification of the small scale natural isotopic variability of Zn observed in terrestrial materials (Maréchal et al., 1999). One of the problems with MC-ICP-MS measurements is the instrumental mass fractionation that occurs during analyses. The double spike method (Dodson, 1963) was used to correct for Zn isotope fractionation of the sample during the processing and analysis.

Zn isotope analysis was performed on a subsection of the silicate glasses obtained from the high-temperature evaporation experiments described in Chapter **2**. This chapter will discuss the methods employed to prepare these samples for isotope analysis. It outlines the methods used for sample preparation, acid digestion and purification of Zn through ion exchange chromatography. Purification of the element of interest from the sample matrix is crucial as it removes potential interferences and

minimizes the chances of matrix effects occurring during mass spectrometric analysis. For Zn purification a shortened version of the Sweere et al. (2018) Zn-Cd manual ion exchange chromatography column chemistry was used.

3.2 – Sample Preparation

3.2.1 – Description of the Samples and Starting Material

A total of 32 of the high temperature, one atmosphere experiments described in Chapter **2** were processed for Zn isotope analysis. The samples that were chosen were time and oxygen fugacity series of trace element doped experiments for the synthetic ferrobasaltic (SM) and natural Icelandic basalt (IB) starting compositions discussed in Chapter **2**, Section **2**. These samples were silicate glasses in noble metal (Pt or Re) capsule materials and mounted in epoxy resin as they were analysed with both the electron microprobe (EPMA) and laser ablation ICP-MS.

The starting material and dopant (ZnO) powders were analysed to assess the isotopic composition of the pure trace element compounds and to provide a benchmark isotopic composition of the starting materials to compare with the samples. Moreover, this enabled the treatment of the starting materials as a secondary standard alongside the samples as the consistent inclusion of one or two in for each separate ion exchange chromatography allowed for the comparison between runs as a measure of consistency.

3.2.2 – Isolating Sample Material

For isotope analysis the silicate glass was separated from the sample holder and epoxy resin. The excess epoxy was cut off and the remaining material was submerged in reagent-grade acetone in a glass vial to facilitate the breakdown of the remaining epoxy resin and subsequent extraction of the sample from the epoxy resin. The remaining pieces of epoxy resin were separated using heavy-liquid separation to exploit the density difference between the epoxy resin and silicate glass and the noble metal sample holder.

The remaining sample and sample holder were crushed in an agate pestle and mortar inside a laminar flow hood with the sample submerged in reagent-grade acetone. After crushing, the acetone was removed from the pestle and mortar and the sample material was poured onto a piece of weighing

paper and collected in a glass vial. Between samples the pestle and mortar was cleaned using a high-purity (>99.7% SiO_2) quartz sand, Lochaline quartz silica sand (LQS-85; Lochaline Quartz Sand Ltd.), and rinsed with acetone. Next, the silicate glass sample fragments were hand-picked from the sample holder material under an optical microscope and collected in an acetone-rinsed glass vial.

3.2.3 – Processing Sample Material

3.2.3.1 – Clean Lab Environment and Acid Preparation

The preparation for and execution of the ion exchange chromatography was performed in a class 100 laminar flow hood in a class 10000 metal-free laboratory (MFL) at the Department of Earth Sciences, University of Oxford. All reagents were ultra-pure concentrated acids obtained from in-house sub-boiled distillation of acids using quartz glass (HCl, HNO_3) or PTFE (HF) stills or commercial sources (HBr; Romil-UPA™). Batches of fresh sub-boiled distilled acid were titrated to determine their molarity for accurate reagent preparation. All dilutions of concentrated acids were done in a laminar flow hood using ultrapure 18.2 $M\Omega \cdot cm^{-1}$ water (Milli-Q®). A blank test was performed to assess the blanks of the concentrated acids and Milli-Q H_2O which is discussed in a later section of this chapter (Table **3.4**).

3.2.3.2 – Beaker Cleaning

Savillex® beakers and Teflon vials used to process sample materials or store acids were cleaned through acid leaching at 120°C in detergent, 50:50 mixtures of reagent grade HCl and Milli-Q H_2O and HNO_3 and Milli-Q H_2O followed by an overnight clean in Milli-Q H_2O at 120°C. The acid leached beakers were then left to dry on Kimwipes in a laminar flow hood. All beakers, vials and bottles were refluxed with conc. sub-boiled HNO_3 at 120°C overnight before use. A more detailed explanation of the cleaning procedure for the different laboratory plastics is available in Appendix **1**.

3.2.3.3 – Sample Weighing

Samples were weighed in acid-leached Savillex beakers using a five-figure Sartorius balance. The mass of the sample was determined from an average of 5-10 individual weighings where the mass of

individual samples was ≤40 mg. Samples were processed in their entirety while starting materials and secondary standard powders (BCR-2) were weighed to have 10 µg Zn in solution. After weighing samples were wetted with 200 µL 2% v/v HNO_3 to prevent sample loss on transfer to the laminar flow hood. One procedural blank was weighed per batch of twelve samples and standards.

3.2.3.4 – Sample Digestion

Samples were digested using a two-step approach. First, 1 mL of a 1:3 mixture of conc. HF and conc. HNO_3 was added to the samples which caused the breakdown of SiO_2 bonds to form hexafluorosilicic acid (H_2SiF_6). The beakers were closed and placed in an ultrasonic bath for 10 minutes and then left in a laminar flow hood overnight to allow the reaction to proceed. Each sample was checked for a visible residue before being placed on a hotplate at 90°C and evaporated to dryness. The increase in temperature resulted in the decomposition of H_2SiF_6 to the volatile Si-tetrafluoride (SiF_4) species which evaporated and removed Si from the sample. The second step was the addition of 2 mL 6 M HCl to the beaker, beakers were closed and placed in the ultrasonic bath for 15 minutes. Next, the beakers were refluxed overnight on a hotplate at 120°C. Beakers were checked for any residue to assess the complete digestion and stored in 6 M HCl until use.

3.2.3.5 – Double Spiking the Sample

Prior to the purification of the sample material to isolate the Zn through ion exchange chromatography individual aliquots were taken of the total sample solution. The volume of these aliquots was determined using the Zn abundance of each sample as determined with LA-ICP-MS (see Chapter **4** for Zn abundances) to achieve a solution containing 1000 ng Zn. For samples where the total Zn abundance was <1000 ng all of the sample solution was used. It is imperative to have accurate knowledge of the Zn abundances of the samples as this affects the sample preparation process to avoid over- or underspiking the sample. The under- and overspiking of samples is discussed in detail in Chapter **5**.

Zn aliquots were spiked by addition of a pre-prepared ^{67}Zn-^{64}Zn double spike solution to the sample aliquot with the aim of a 1.4:1 double spike:sample ratio (Sweere et al., 2018). The closed beakers were then placed on the hotplate overnight at 90°C to reflux and homogenize the double spike-sample mixture. Two "chemistry blanks" were prepared in addition to the main blank to assess contamination during the ion exchange chromatography. All Zn blanks were prepared by pipetting the equivalent of 100 ng of double spike Zn into a Savillex beaker and otherwise treated identically to the samples.

3.3 – Analytical Methodology

3.3.1 – The Double Spike

The double spike method is a well-established technique where a sample of unknown composition is mixed with a "double spike" solution of known composition (Dodson, 1963). It is a proven robust and accurate approach for correcting any fractionation experienced by the sample during processing, ion exchange chromatography and instrumental analysis and has been applied to a wide range of both stable and radiogenic isotope systems comprised of four or more naturally occurring isotopes (e.g. Galer, 1999; Johnson and Beard, 1999; Rudge et al., 2009; Klaver and Coath, 2019). Four isotopes was long considered the minimum as three isotope ratios are required for the data reduction, but a solution has been derived for three isotope systems (Coath et al., 2017). Double spike solutions are designed to be enriched in two isotopes with minor amounts of the other isotopes. Their preparation, optimization and error minimization requires careful consideration of the isotopes used in the double spike, their relative abundances and the double spike:sample ratio (Galer, 1999; Rudge et al., 2009). Because this technique only requires a single element it has an advantage over external normalization methods as it does not have to rely on the assumption that two different elements behave the same in the mass spectrometer.

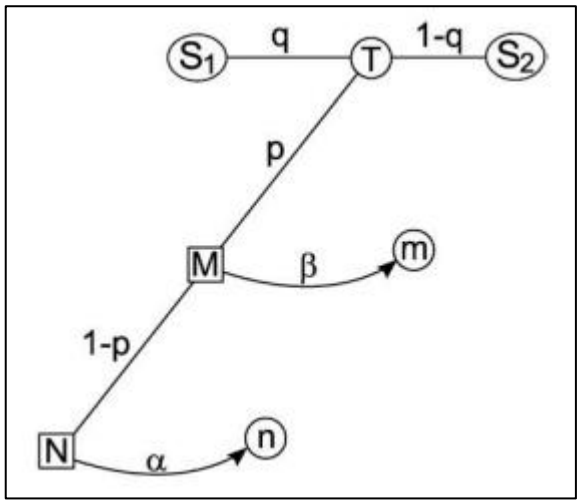


Figure 3.1: Schematic depiction of the double spike taken from Rudge et al. (2009).

The true isotopic composition of the sample material can be deconvolved from the measured raw isotope ratios of the double spike-sample mixture through an inversion. This is done for a single measurement as the isotopic composition of the double spike, mixture and sample are assumed to be on a mixing line and the composition of the double spike is known (Fig. **3.1**; Rudge et al., 2009). Figure **3.1** depicts schematically how two single spike solutions, S_1 and S_2, are combined in proportions q and

(1-q) to form double spike solution T. The double spike solution T is added to a sample solution N in proportions p and (1-p) to get mixed solution M where the mixed solution (M) is different from the measured isotope ratio (m) because it is fractionated during analysis by an instrumental mass fractionation (IMF) factor (β). Similarly, the sample solution (N) is fractionated from the natural composition through the natural fractionation factor (α). Any natural or instrumental mass fractionation is assumed to follow the exponential generalized fractionation law (Maréchal et al., 1999).

For Zn the generalized equations for measured and natural isotope ratios are given by Equations **3.1** and **3.2**.

$$(Eq.3.1):\ \ m_i = M_i\left(\frac{mass_i}{mass_{66_{Zn}}}\right)^{\beta} \qquad (Eq.3.2):\ \ n_i = N_i\left(\frac{mass_i}{mass_{66_{Zn}}}\right)^{\alpha}$$

Here the isotope ratios of the sample and double spike solutions are given by Equation **3.3**.

$$(Eq.3.3):\ \ N_i = \frac{^{i}Zn}{^{66}Zn_{sam}};\ \ T_i = \frac{^{i}Zn}{^{66}Zn_{DS}}$$

To find an expression for the mixed isotope ratio a second parameter, λ, is introduced which is related to the proportion of double spike in the double spike-sample mixture (Eq. **3.4** and **3.5**).

$$(Eq.3.4):\ \ M_i = \frac{^{i}Zn}{^{66}Zn_{mix}} = \lambda T_i + (1-\lambda)N_i$$

$$(Eq.3.5):\ \ \lambda = \left[1 + \frac{1-p}{p}\left(\frac{1+\sum_k N_k}{1+\sum_k T_k}\right)\right]^{-1}$$

Here $\sum_k N_k$ and $\sum_k T_k$ represent the sum of moles of Zn over all isotope ratios of both the double spike and sample solution. Combining the six above equations results in Equation **3.6** which has to be solved for the three unknowns; α, β and λ.

$$(Eq.3.6):\ \ F_i(\alpha,\beta,\lambda) = \lambda T_i + (1-\lambda)n_i\left(\frac{mass_i}{mass_{66_{Zn}}}\right)^{-\alpha} - m_i\left(\frac{mass_i}{mass_{66_{Zn}}}\right)^{-\beta} = 0$$

Equation **3.6** is solved through Newton-Raphson iteration on the derivatives of the F_i with respect to each unknown for all three isotope ratios relative to ^{66}Zn (Albarède and Beard, 2004). The ^{x}Zn/^{66}Zn ratios were used over ^{x}Zn/^{64}Zn ratios to prevent potential issues arising during the deconvolution of the ^{67}Zn/^{64}Zn ratio which contains both isotopes that make up the double spike. The unmixed sample Zn isotope ratios were converted to be relative to ^{64}Zn after the double spike deconvolution as this is the common way of showing Zn isotope ratios. The main drawback of this inversion technique is that it is not capable of recording any potential mass independent fractionation as any fractionation is inherently assumed to be mass dependent. However, as evaporation-induced isotope fractionation is known to be mass dependent (Sossi et al., 2018a; 2020; Wimpenny et al., 2019), this limitation should not be an issue in this study.

The double spike solution used was a pre-prepared ^{67}Zn-^{64}Zn solution, therefore any detailed information regarding its preparation and calibration can be found in the original work by Sweere (2018). As the double spike used was pre-prepared the only factor that will be discussed is the error

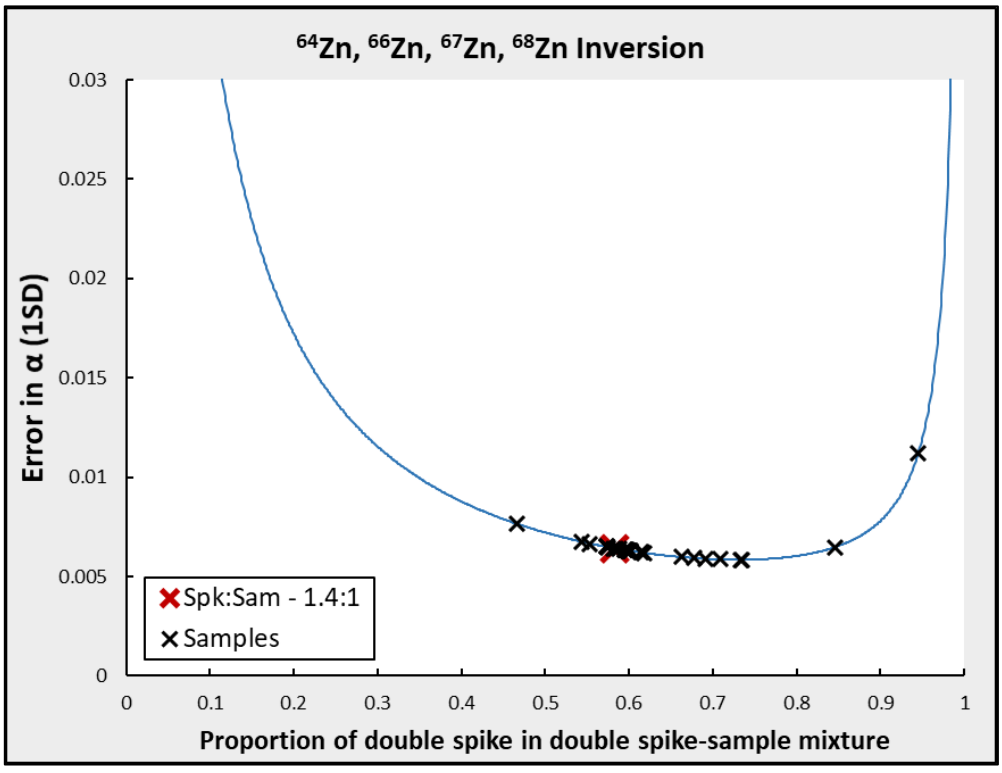


Figure 3.2: The effect of the double spike:sample ratio on the error of the double spike inversion. The red cross is the target double spike:sample ratio and the black crosses are the double spike:sample ratio of the samples.

introduced by variations in the double spike:sample ratios. Using the "Double Spike Toolbox" (Rudge et al., 2009) an error curve was calculated for the ^{64}Zn-^{67}Zn double spike used which showed the errors the double spike:sample ratio introduced during the inversion (Fig. **3.2**). Based on the considerations of minimizing both the introduced error and the volume of double spike solution used a double spike:sample ratio of 1.4:1 was chosen, identical to that of Sweere et al. (2018). The cause of the variability in double spike:sample ratio observed for the samples in Figure **3.2** is discussed in Chapter **5**.

3.3.2 – Isotope Dilution

The isotope dilution equations can be used to determine the double spike:sample ratio and/or trace element concentration and abundance for samples of known isotopic composition and mass (Boelrijk, 1968). By adjusting the general equation to be applicable to Zn (Eq. **3.7**) it is shown that the Zn abundance of the sample (Zn_{sam}) can be calculated using the Zn abundance of the double spike (Zn_{DS}), the isotope abundance ($\%^{X}Zn$) of both sample and double spike, measured Zn isotope ratio of the sample and the average atomic mass of Zn ($\sum_x m_x(\%^x Zn)$) in both sample and double spike. The isotope abundance of the sample was chosen to be the IUPAC reference isotope abundance (Melja et al., 2016) and that of the double spike was determined during its calibration (Sweere et al., 2018).

$$(Eq.\,3.7):\quad Zn_{sam} = Zn_{DS}\left(\frac{(\%^{66}Zn)_{DS} - \left(^{66}Zn/^{64}Zn\right)_{sam}(\%^{64}Zn)_{DS}}{\left(^{66}Zn/^{64}Zn\right)_{sam}(\%^{64}Zn)_{sam} - (\%^{66}Zn)_{sam}}\right)\frac{\sum_x m_x(\%^x Zn)_{sam}}{\sum_x m_x(\%^x Zn)_{DS}}$$

The sample concentration is subsequently calculated by dividing the Zn abundance with the sample mass and the double spike:sample ratio ($\varphi_{DS/sam}$) is found by dividing the Zn abundances of the double spike and sample (Eq. **3.8**).

$$(Eq.\,3.8):\quad \varphi_{spk/sam} = \frac{Zn_{DS}}{Zn_{sam}}$$

3.3.3 – Delta Notation

The isotopic composition of a sample is expressed using the delta (δ) notation which calculates the per mille (‰) deviation of the isotope ratio of the sample relative to that of a recognized standard reference material (Eq. **3.9**).

$$(Eq.3.9):\ \ \delta^{i}X\ (‰) = 10^{3}\left(\frac{(\ ^{j}X/\ ^{i}X)_{sam}}{(\ ^{j}X/\ ^{i}X)_{ref}} - 1\right)$$

Here $\left(\ ^{j}X/\ ^{i}X\right)$ is the isotope ratio of isotopes *i* and *j* of element *X*. For elements with more than two isotope it is standard to keep the isotope in the denominator constant and vary that of the nominator. The standard practice for reporting delta values is to have the lightest isotope in the denominator so delta values increase as the abundance of the heavy isotope increases. Considering multiple isotope ratios of the same element helps identify the fractionation process if they are normalized. This normalization is achieved by comparing the fractionation of the different isotope combinations in ‰·amu^{-1}, which is calculated by dividing the delta by the difference in atomic mass of the two isotopes. For mass-dependent fractionation the delta values per amu for different isotope combinations of the same element will have similar values. If there are significant differences between the values it suggests that there is either an interference or a mass-independent fractionation process.

For Zn the delta value was calculated relative to the ETH-AA Zn reference standard (Eq. **3.10**; Ponzevera et al., 2006; Moeller et al., 2012).

$$(Eq.3.10):\ \ \delta^{66}Zn\ (‰) = 10^{3}\left(\frac{\left(^{66}Zn/^{64}Zn\right)_{sam}}{\left(^{66}Zn/^{64}Zn\right)_{ETH-AA}} - 1\right)$$

To allow the obtained delta values to be placed in a wider framework and compared with other studies, δ^{66}Zn has to be expressed in terms of the international Zn isotope reference standard JMC 3-0749 Lyon Zn. Archer et al. (2017) showed that the δ^{66}Zn of ETH-AA is indistinguishable from the IRMM3702 Zn reference standard and can be converted to a value relative to the JMC 3-0749 Lyon Zn reference standard, henceforth referred to simply as “Lyon” (Eq. **3.11**; Maréchal et al., 1999).

$$(Eq.3.11):\ \ \delta^{66}Zn_{Lyon}(‰) = \delta^{66}Zn_{ETH-AA} + 0.28\ ‰$$

3.3.4 – Three Isotope Plots

Three-isotope plots, where two delta values with a common denominator isotope are plotted against each other, are widely used to visualize isotope fractionation for elements with more than two stable isotopes. For mass-dependent fractionation all data will plot on a line where the fractionation factor (β), which is the slope of the line, is governed by the masses of the three isotopes involved. How the slope of this line is defined by the isotopic masses depends on the type of mass-dependent fractionation process, equilibrium or kinetic. In the case of evaporation from the silicate melt it is expected that isotope fractionation is a kinetic process.

For equilibrium mass-dependent fractionation processes the partitioning of isotopes depends on zero-point energy differences that describe the different vibrational modes within molecules (Young et al., 2002). For equilibrium fractionation the equilibrium fractionation factor (β_{eq}) of a three isotope plot involving isotopes *i*, *j* and *k* is described by Equation **3.12**.

$$(Eq.\,3.12):\quad \beta_{eq} = \frac{m_k(m_j - m_i)}{m_j(m_k - m_i)}$$

For kinetic mass-dependent isotope fractionation processes the partitioning of isotopes is based on the interchange of kinetic energies between the isotopes (Young et al., 2002). The kinetic fractionation factor (β_{kin}) of a three isotope plot involving isotopes *i*, *j* and *k* is described by Equation **3.13**.

$$(Eq.\,3.13):\quad \beta_{kin} = \frac{\ln(m_i/m_j)}{\ln(m_i/m_k)}$$

The evaporative loss in the experiments of this study are expected to produce mostly kinetic fractionation as the magnitude of equilibrium fractionation is inversely proportional to temperature (Urey, 1947). However, the data presented in this study cannot be used to verify this as the use of the double spike method used to correct for fractionation during sample processing and purification inherently assumes that all fractionation follows an equilibrium fractionation law.

3.4 – Ion Exchange Chromatography

3.4.1 – Purification of Zn

The double spiked sample aliquots were processed using a two-stage ion exchange chromatography column chemistry to separate the Zn from the matrix. The method used was a shortened version of the Zn-Cd ion exchange chromatography used by Sweere et al. (2018) where the ion exchange chromatography was ended after Zn elution. The ion exchange chromatography was performed in a laminar flow hood that was used solely for Zn purification and was cleaned before use. Up to 18 solutions were processed simultaneously during a single run. These were usually divided into three blanks, one full preparation blank and two chemistry blanks, a secondary standard (BCR-2), 12 samples and two starting material repeats that matched the major element composition of the samples. The ion exchange chromatography was done using a single, adjustable 1 mL, pipette with one box of acid-cleaned pipette tips.

In preparation for the ion exchange chromatography the elements in the samples were converted to chloride species by twice adding 250 µL conc. HCl and evaporating to dryness at 100°C. Next, 0.6 mL 1M HF/0.5M HCl was added as the loading solution and placed in the ultrasonic bath for five minutes. At the same time, the ion exchange columns were loaded with batch pre-cleaned AG1-X8 (200-400 dry mesh size) anion exchange resin. The resin was loaded onto the column in a dilute HCl solution and 1 mL 7.5M HNO_3, 0.2 mL MQ H_2O, 1 mL 6M HCl and 3 mL 1M HCl were added consecutively to pre-clean and prepare the resin, allowing each solution to pass through the column before the next was added. If the column pre-clean was completed before the sample were fully prepared the columns were wetted with MQ H_2O.

Following sample and column preparation the sample was loaded on the ion exchange column in the 0.6 mL 1M HF/0.5M HCl loading solution. An additional 1.6 mL 1M HF/0.5M HCl was added after the loading solution passed through the resin. These steps eluted the major elements as well as potential interferences Ni and Ba. Next, 1 mL 4M HCl was added to the column to further elute Ba. After this

eluent had fully passed through the resin, the waste beakers were replaced by beakers to collect the Zn cut. For the first pass this was the original sample beaker and for the second pass this was a clean Savillex beaker. Next, 2.2 mL 0.5M HF/0.1M HBr was added to elute the Zn. The Zn eluates were collected and evaporated to dryness overnight on a hotplate at 90°C. This procedure was repeated for the second pass.

After the second Zn eluate was collected and dried down overnight. Next, it was converted to nitrate form by twice adding 250 µL conc. HNO_3 and evaporating to dryness at 90°C. The residue was then dissolved in 2 mL 2% v/v HNO_3, placed in the ultrasonic bath for five minutes and refluxed overnight at 90°C. The ion exchange chromatography and its preparation are summarized in Table **3.1**.

Zinc Chemistry Overview	
Preparation	
Column Prep	**Sample Prep**
Add resin to column	250 µL conc. HCl
1 mL 7.5M HNO_3	Evaporate to dryness at 100°C
200 µL 18 MΩ H_2O	250 µL conc. HCl
1 mL 6M HCl	Evaporate to dryness at 100°C
3 mL 1M HCl	0.6 mL 1M HF/0.5M HCl
Ion Exchange Chromatography	
Step	**Purpose**
Load Sample	Elute matrix (majors, Ni, Ba, Cu)
1.6 mL 1M HF/0.5M HCl	Elute matrix (Ni, Ba, Cu)
1 mL 4M HCl	Elute matrix (Ti, Zr, Ba)
Place Zn cut beaker	
2.2 mL 0.5 M HF/0.1M HBr (**Zn Cut**)	Elute Zn
Evaporate Zn cut to dryness at 90°C	
For the second pass, the preparation and ion exchange chromatography steps are repeated.	
On the first pass the Zn cut is collected in the original sample beaker. On the second pass the Zn cut is collected in a clean Savillex beaker.	
Post-Ion Exchange Chromatography	
250 µL conc. HNO_3	
Evaporate to dryness at 90°C	
250 µL conc. HNO_3	
Evaporate to dryness at 90°C	
2 mL 2% v/v HNO_3 and reflux overnight at 90°C	
Samples stored in 2 mL 2% v/v HNO_3 until analysis	

Table 3.1: A schematic overview of the Zn ion exchange chromatography, adapted from the Zn and Cd chemistry used by Sweere et al. (2018). Each eluent added to the columns is allowed to pass through the resin before the next is added. The procedures for the preparation of resin and cleaning of plastics are outlined in Appendix **1**.

3.5 – Mass Spectrometry

3.5.1 – Quadrupole ICP-MS

The trace element abundance of the solutions for the blank tests was assessed using a PerkinElmer NexION 350D quadrupole inductively coupled plasma mass spectrometer (ICP-MS), in conjunction with an automated flow injection sample introduction system (Elemental Scientific Inc. PrepFAST FIAS) at the Department of Earth Sciences, University of Oxford. The instrument was calibrated with a series of major and trace element standard solutions that were robotically diluted to a range of concentrations from stock standard solutions using the PrepFAST system. Stock standard solutions were prepared on the day of analysis by mixing and diluting single element and mixed synthetic ICP elemental standard solutions (Merck Certipur) using 2% v/v HNO_3. The instrument was tuned to minimize the presence of oxides by adjusting the conditions to minimize the CeO^+/Ce^+ ratio. All elements were measured together in a single method prepared in the PerkinElmer Syngistix ICP-MS software. This method also incorporated the suppression of polyatomic interferences and the improvement of the signal-to-background ratio for a range of elements through the use of dynamic reaction (^{39}K, ^{40}Ca and ^{56}Fe) and collision cell (^{23}Na, ^{24}Mg, ^{27}Al, ^{31}P, ^{45}Sc, ^{47}Ti, ^{51}V, ^{52}Cr, ^{55}Mn, ^{59}Co, ^{60}Ni, ^{63}Cu, ^{66}Zn, ^{69}Ga, ^{85}Rb, ^{88}Sr, ^{89}Y, ^{90}Zr, ^{93}Nb, ^{98}Mo, ^{107}Ag, ^{118}Sn, ^{121}Sb, ^{128}Te, ^{133}Cs and ^{138}Ba) technologies.

The instrument was set-up to measure the following isotopes of different elements: ^{7}Li, ^{23}Na, ^{24}Mg, ^{27}Al, ^{31}P, ^{39}K, ^{40}Ca, ^{45}Sc, ^{47}Ti, ^{51}V, ^{52}Cr, ^{55}Mn, ^{56}Fe, ^{59}Co, ^{60}Ni, ^{63}Cu, ^{66}Zn, ^{69}Ga, ^{85}Rb, ^{88}Sr, ^{89}Y, ^{90}Zr, ^{93}Nb, ^{98}Mo, ^{107}Ag, ^{118}Sn, ^{121}Sb, ^{128}Te, ^{133}Cs, ^{138}Ba, ^{139}La, ^{140}Ce, ^{141}Pr, ^{143}Nd, ^{147}Sm, ^{153}Eu, ^{157}Gd, ^{159}Gd, ^{163}Dy, ^{165}Ho, ^{166}Er, ^{169}Tm, ^{173}Yb, ^{175}Lu, ^{178}Hf, ^{181}Ta, ^{182}W, ^{185}Re, ^{205}Tl, ^{208}Pb and ^{238}U. Following system calibration, samples were measured in groups of ten where each group was bracketed with instrument blanks. Between every twenty samples a clean 2% v/v HNO_3 and two different dilutions (10x and 500x) of a certified reference material, the SPS-SW2 surface water standard (Specpure Solutions), solution were analysed to assess memory effects and act as a quality- and consistency check respectively. Every

blank, standard and sample solution was doped with indium, using the PrepFAST, to act as an internal standard to assess plasma conditions.

3.5.2 – Multi Collector (MC-)ICP-MS

3.5.2.1 – Principles of MC-ICP-MS

The isotopic composition of the samples was measured at Oxford University using a Nu Plasma II HR multi collector inductively coupled plasma mass spectrometer (MC-ICP-MS) in low resolution mode. Samples were dissolved in 2% v/v HNO_3 and placed in an ASX-112 FR auto sampler from which they were drawn into a CETAC Aridus II desolvation nebulizer ("Aridus") at a rate of ~60 $\mu L min^{-1}$. The sample is introduced to the Aridus through a self-aspirating PFA nebulizer which produces an aerosol that is sprayed into the spray chamber. Next, the sample vapour enters the desolvator where vapour rich sample aerosols are dried by passing the solvent vapours through a membrane after which the sample material continues to the MC-ICP-MS. This sample introduction method minimizes the formation of hydride, nitride and oxide species and increases the sensitivity of measurements.

The MC-ICP-MS operates by sending sample material through an ionized Ar plasma in a quartz torch where collisional interactions between the ionized Ar and sample material ionizes the sample material. The plasma is initially lit using a high-voltage spark and sustained by a constant supply of energy and flow of Ar gas where ionization is maintained through a chain reaction of collisions between Ar atoms. This results in the plasma reaching temperatures in excess of 5000 K, sufficient to ionize most elements in the periodic table. The resulting beam of Ar and sample ions then passes through the Ni sample- and skimmer cones and the source and transfer chambers where the ion beam is accelerated, shaped and guided into the mass spectrometer. From sample introduction to the sample passing into the mass spectrometer the pressure is stepwise decreased from 1 bar at sample introduction to 10^{-10} bar inside the mass spectrometer by differential pumping.

As the ion beam passes through the slit at the end of the lens stack it enters the mass spectrometer. Inside the ion beam is first filtered based on the kinetic energy of individual ions using an electrostatic analyser (ESA) which only allows ions of a fixed amount of kinetic energy to pass through and reach the magnet. The ion beam then passes through the magnet where it is separated into multiple ion beams based on the mass-to-charge (m/z) ratio of the ions. A set of quad lenses are then used to alter the trajectory of the ion beams to ensure they reach the Faraday collectors. These Faraday collectors contain resistors which are used to convert the measured current of the ion beam to voltages that are used to determine the concentrations of the isotopes of interest.

Sample data was recorded using the Nu Plasma II Control software in conjunction with the Nu Instruments Calculation Editor (NICE) software to write separate method files that were set-up to subtract baselines from measured intensities, perform fractionation and interference corrections, calculate isotope ratios and report these measured intensities. The average values and standard deviations of multiple individual measurements of each sample were compiled in an Excel Spreadsheet which stored the specified parameters for all samples that were analysed using the same method. Furthermore, each individual measurement for each sample was recorded in a separate, sample-specific, file. While determining the average sample intensities the Nu Plasma Control software eliminated individual measurements which exceed 3 standard deviations on the average. Any further data reduction was performed offline.

3.5.2.2 – MC-ICP-MS Analysis of Zn

The Zn isotopic composition of the samples was analysed using a standard-sample bracketing approach where the standard (AA-ETH (Archer et al., 2017)) was used to normalize the data, assess the reproducibility and trace and correct for instrumental drift during a run. The mass range of the collector array was set around an axial mass of ~65.5 and covered the mass range between 61 – 70.5 amu (Table **3.3**). This set-up was used because it enabled the measuring of ^{61}Ni, required to correct for ^{64}Ni on the ^{64}Zn peak, and a range of (half-)masses up to 69 to correct for potential doubly-charged Ba on ^{66}Zn, ^{67}Zn and ^{68}Zn. This meant that it was impossible to measure all Zn isotopes as ^{70}Zn overlapped with a gap in the collector array. However, using ^{64}Zn, ^{66}Zn, ^{67}Zn and ^{68}Zn was deemed sufficient to assess Zn isotope fractionation as all fractionation is assumed to be mass dependent and ^{70}Zn is the lowest abundance (0.6 %) Zn isotope. The operating conditions of the instrument for Zn isotope analysis are outlined in Table **3.2**.

Instrument Parameters	
MC-ICP-MS	
RF Power [W]	1300
Coolant gas flow [L·min^{-1}]	13
Auxillary gas flow [L·min^{-1}]	1.2
Nebuliser gas flow [L·min^{-1}]	25.8
Sample and Skimmer Cone	Ni
Mass Resolution	Low
Number of cycles and blocks	20, 3
30 second baseline before each block	
Signal integration time [s]	10
Axial mass [amu]	~65.5
Mass spacing [amu]	0.5
Sensitivity [V·ppm^{-1}]	90-110
Zero by ESA Deflection	
Count for zero [s]	30
Aridus	
Spray chamber temperature [°C]	110
Desolvator temperature [°C]	160
Ar sweep gas flow [L·min^{-1}]	3.9 – 4.1
Sample uptake rate [µL·min^{-1}]	~55-60

Table 3.2: Typical operating conditions for the MC-ICP-MS set-up for Zn analyses.

	H8	-	-	H7	H6	H5	H4	H3	H2	H1
mass	**70.5**	**70**	**69.5**	**69**	**68.5**	**68**	**67.5**	**67**	**66.5**	**66**
Zn	-	-	-	-	-	^{68}Zn	-	^{67}Zn	-	^{66}Zn
Ba	-	-	-	^{138}Ba^{2+}	^{137}Ba^{2+}	^{136}Ba^{2+}	^{135}Ba^{2+}	^{134}Ba^{2+}	-	^{132}Ba^{2+}
Xe	-	-	-	-	-	^{136}Xe^{2+}	-	^{134}Xe^{2+}	-	^{132}Xe^{2+}
Ga	-	-	-	^{69}Ga	-	-	-	-	-	-
	Ax	**L1**	**L2**	**L3**	**L4**	**L5**	**-**	**-**	**-**	**L6**
mass	**65.5**	**65**	**64.5**	**64**	**63.5**	**63**	**62.5**	**62**	**61.5**	**61**
Zn	-	-	-	^{64}Zn	-	-	-	-	-	-
Ba	-	^{130}Ba^{2+}	-	-	-	-	-	-	-	-
Ni	-	-	-	^{64}Ni	-	-	-	-	-	^{61}Ni
Te	-	^{130}Te^{2+}	-	^{128}Te^{2+}	-	^{126}Te^{2+}	-	-	-	^{122}Te^{2+}
Xe	^{131}Xe^{2+}	^{130}Xe^{2+}	^{129}Xe^{2+}	^{128}Xe^{2+}	-	^{126}Xe^{2+}	-	-	-	-
Cu	-	^{65}Cu	-	-	-	^{63}Cu	-	-	-	-

Table 3.3: An overview of the collector array for Zn isotope analysis.

The ion beam intensities were recorded for ^{61}Ni, ^{63}Cu, ^{64}Zn, ^{65}Cu, ^{66}Zn, ^{67}Zn, ^{68}Zn, $^{135}Ba^{2+}$, $^{137}Ba^{2+}$ and $^{138}Ba^{2+}$. The zero intensities were subtracted from the measured intensities and the resulting Zn intensities were used to calculate and report the $^{66}Zn/^{64}Zn$, $^{67}Zn/^{64}Zn$, $^{68}Zn/^{64}Zn$, $^{64}Zn/^{66}Zn$, $^{67}Zn/^{66}Zn$ and $^{68}Zn/^{66}Zn$ isotope ratios. The observed total Zn intensity for an analysis was on average 5.5 V. The instrument was tuned by adjusting the Ar flow rate through the nebulizer, the torch position and occasionally HV2. After tuning the peak alignment was checked and adjusted by changing the Q15 and Q16 corrections as necessary. Peak positions were determined using a Ba-doped unspiked Zn standard solution to ensure that all elements were measured on their peak flats (Figure **3.3**). The axial mass was set manually through the peak flats of Zn and Ba isotopes and no automatic peak centring was used between samples, maintaining a constant axial mass for each sample. Figure **3.3** shows that Zn and Ba peaks overlap and that Ba intensities could be measured accurately to identify Ba interferences. The absence of peaks for all other potential interferences on Zn suggests that there were no measurable amounts of ^{61}Ni or doubly-charged ions of I, Xe, Cs or Pr on the half-masses.

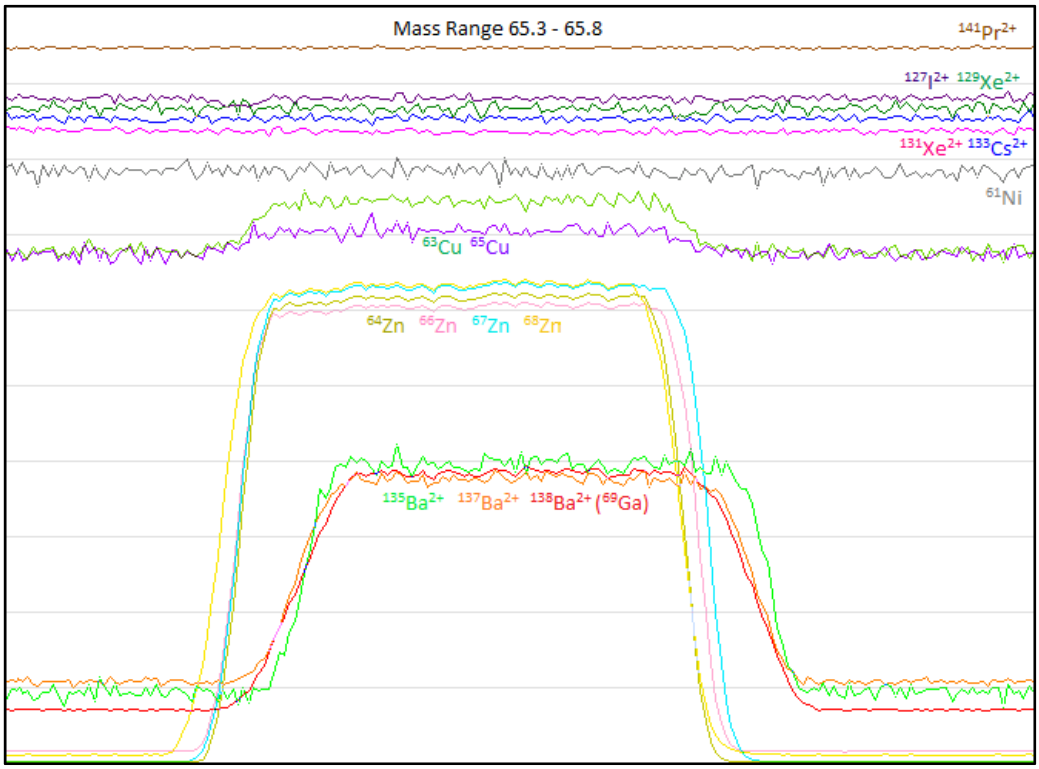


Figure 3.3: An example of a magnet scan of the Ba-doped unspiked Zn standard tuning solution for all collectors. Vertical scale was adjusted such that peaks of individual elements were clustered together. Interference-free isotopes of other potentially interfering elements Ni (^{64}Ni) and Xe ($^{128}Xe^{2+}$, $^{132}Xe^{2+}$, $^{134}Xe2+$, $^{136}Xe^{2+}$) are shown near the top of the figure with colour-coded labels to match the lines.

To achieve the best accuracy on data a match of signal intensity (±10%) and double spike:sample ratio (±3%) between sample and bracketing standard is required (Moore, 2017). To achieve this each analysis was preceded by a, so called, "dummy run" where dilute sample solutions and the 50 ppb bracketing standard solutions were analysed. These were prepared in 2 and 20 mL Teflon vials respectively. For the dummy runs a dilute sample aliquot of known volume was prepared, diluted to 2 mL with 2% v/v HNO_3 and analysed for 10x 10 second measurements to determine the total Zn intensity and double spike:sample ratio. The bracketing standard solutions were prepared at 50 ppb with double spike:standard ratios that matched the double spike:sample ratios of the samples. They were also analysed over 10x 10 second measurements to assess the accuracy of the double spike:standard ratio and the total Zn intensity. The volume of the sample aliquot required to prepare a sample with proper signal intensity and double spike:standard matching was then calculated using the volume of the dilute sample aliquot and the total Zn intensity of the sample and bracketing standard solutions.

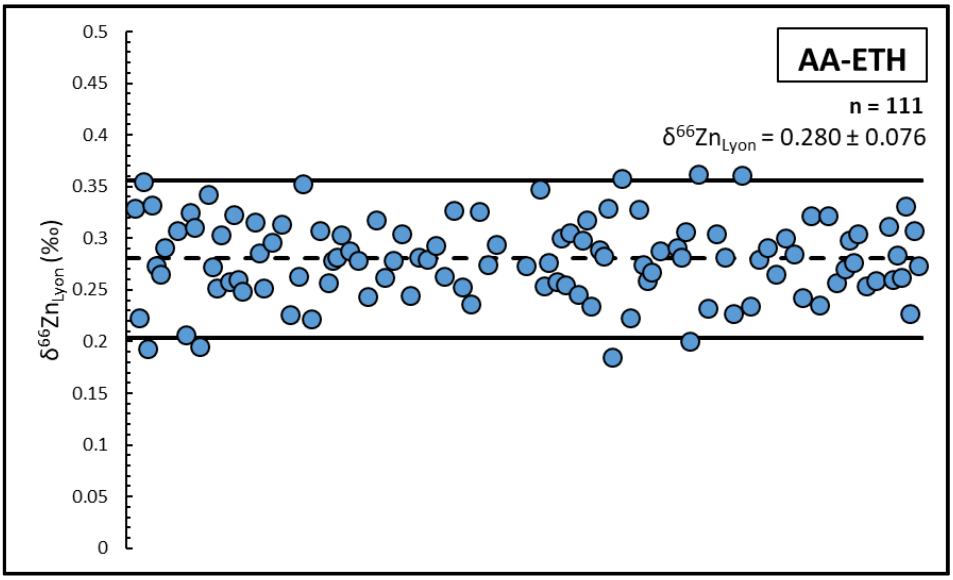


Figure 3.4: The temporal evolution of $\delta^{66}Zn_{Lyon}$ (‰) of ETH-AA within a single run. Diamonds represents the average value of the individual measurements (circles) for with 2 s.d. on the average error bars.

Following the dummy run, all measurements were at normal operating conditions and the stability of the instrument was assessed by running 10 replicates of a standard solution to determine the reproducibility of the measured delta values. The instrument was considered stable if the 2 s.d. of the

standard $\delta^{66}Zn < 0.05$ ‰ per amu. This was followed by running sample-standard bracketed secondary standards to assess the accuracy of the measured isotopic composition of the secondary standards relative to literature values. Samples were only run after both checks were completed. Instrument stability during sample analysis was monitored by evaluating the isotopic variability of the bracketing standards where the run was considered stable when 2 s.d. on $\delta^{66}Zn < 0.05$ ‰ per amu. Due to the variability in the double spike:sample ratio (Fig. **3.2**) of the samples there was only a single run for which the same double spike:sample ratio bracketing standard was used throughout most of the run.

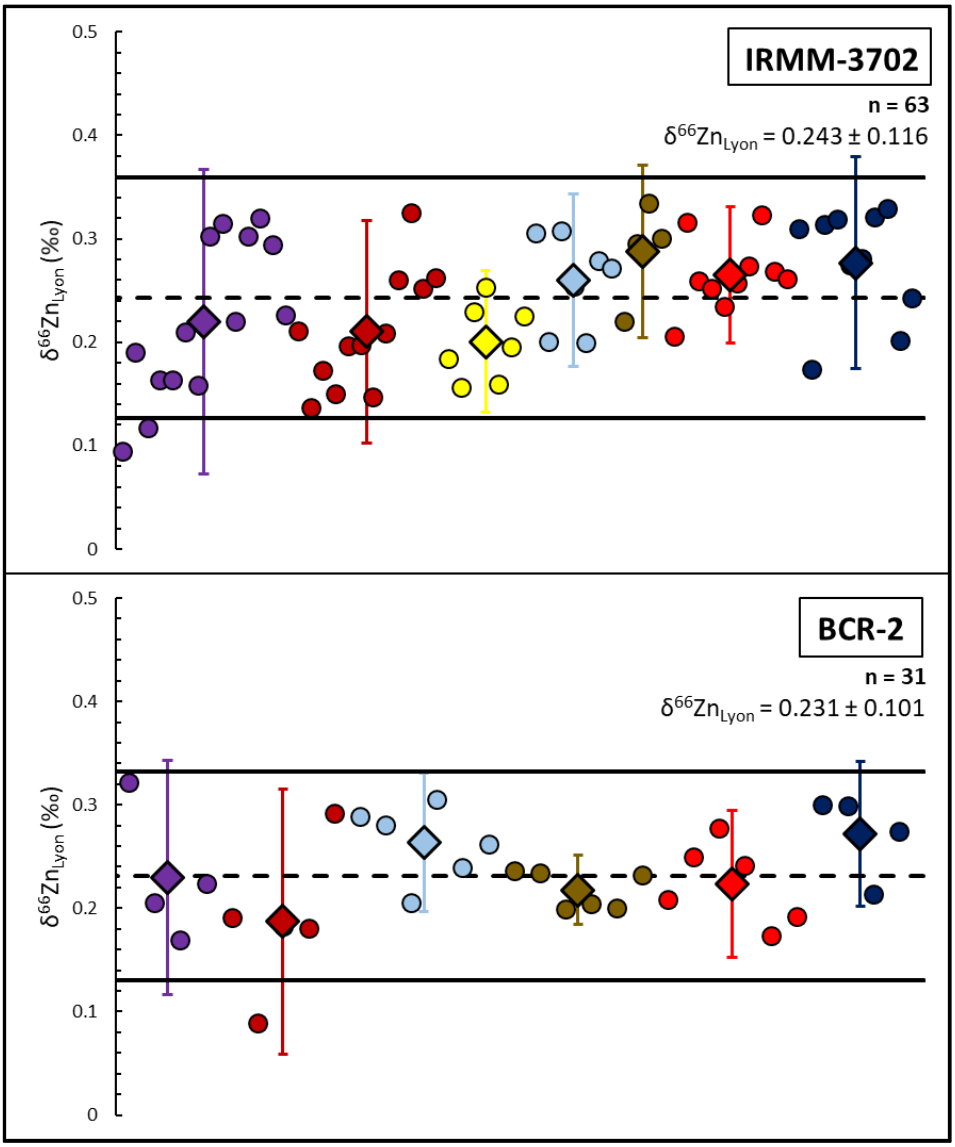


Figure 3.5: The temporal evolution of $\delta^{66}Zn_{Lyon}$ (‰) of BCR-2 and IRMM-3702 between runs. Each colour corresponds to a different run. Diamonds represent averages values of the individual measurements (circles) for each run. Error bars represent 2 s.d. on the average within the run. The dashed black line is the average $\delta^{66}Zn_{Lyon}$ and the solid lines represent 2 s.d. on the average of all measurements.

The temporal evolution of ETH-AA within this run is shown in Figure **3.4**. The obtained average value was $\delta^{66}Zn_{Lyon}$ = 0.280 ± 0.076‰.

The short- and long term stability and reproducibility of the results was assessed by monitoring the evolution of the Zn isotopic composition of the bracketing standard within a run and secondary standards between runs. The USGS rock standard BCR-2 and synthetic Zn reference material IRMM-3702 were used to serve as secondary standards. The temporal evolution of BCR-2 and IRMM-3702

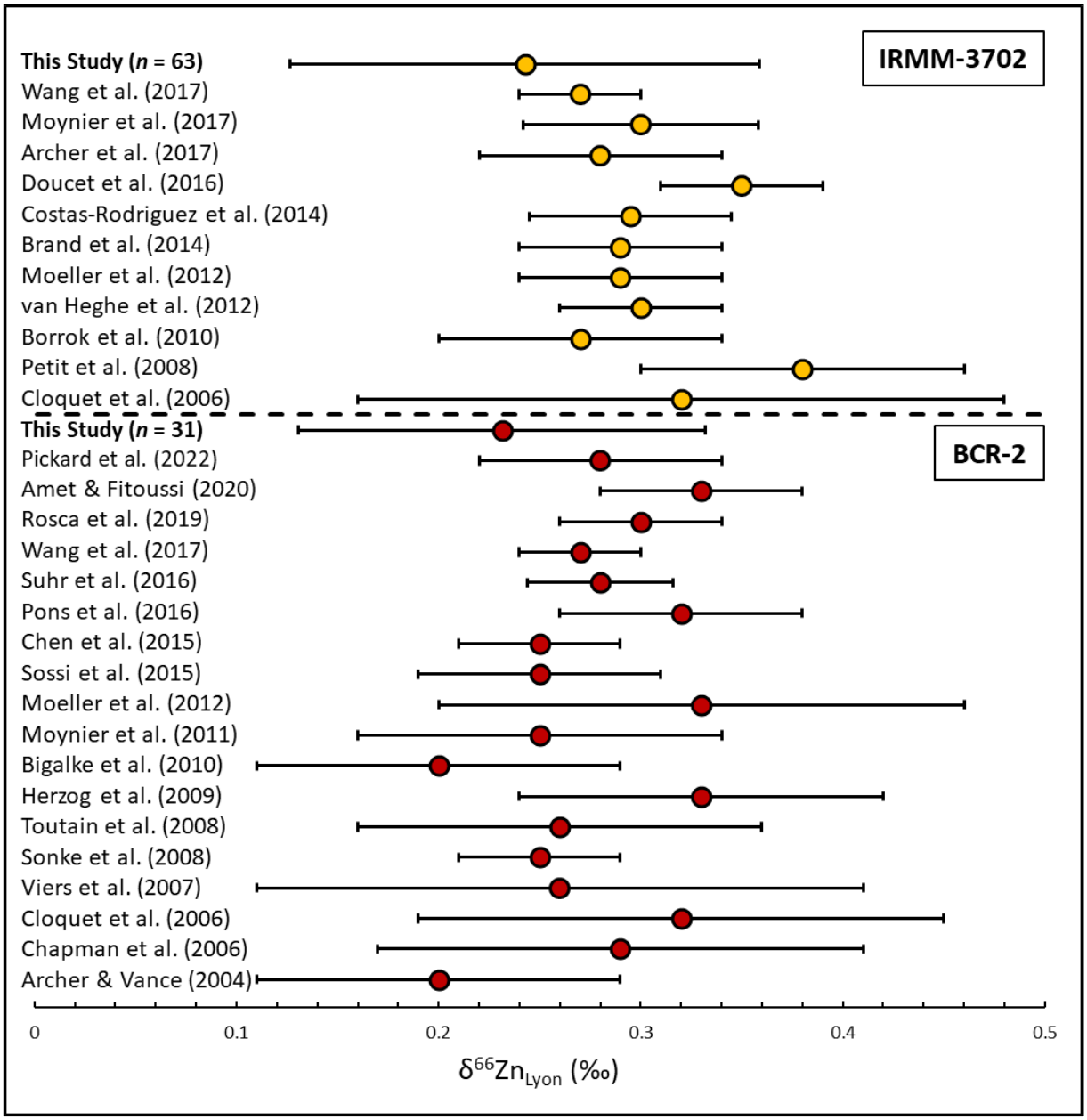


Figure 3.6: Comparison of the BCR-2 and IRMM-3702 values with previous values reported in the literature. All errors are reported as 2 s.d. on the average, but most values from literature were converted to 2 s.d. from two standard errors or 95% confidence intervals.

covered a 13 month period and is shown in Figure **3.5**. The obtained average values for BCR-2 and IRMM-3702 are $\delta^{66}Zn_{Lyon}$ = 0.231 ± 0.101‰ and $\delta^{66}Zn_{Lyon}$ = 0.243 ± 0.116‰ respectively. These values are comparable to, but on the lower end of, those found in the literature (Fig. **3.6**) for both BCR-2 and IRMM-3702. However, the error bars on the average are larger than those in more recent work. One potential explanation for these errors compared to other studies is that the samples were run at comparatively low total Zn intensities (~5.5 V) compared to other studies which ran at upwards of 34 V (Suhr et al., 2016). Running at low intensities translated to poorer counting statistics on individual measurements which increased the errors.

3.6 – Blank Exercise

3.6.1 – Background

Initial ion exchange chromatography and mass spectrometry measurements indicated that there were significant Zn blanks and non-Zn interferences on Zn isotope measurements. A blank exercise was carried out to identify key sources of Zn blanks and identify non-Zn interferences on the measured Zn signal. This resulted in the development of a rigorous cleaning regimen to ensure cleanliness in the working environment for the ion exchange chromatography and mass spectrometry analyses.

3.6.2 – Methodology

Previous work suggested that the Zn chemistry is highly susceptible to blanks (e.g. Sweere et al., 2018), because lab plastics can have substantial Zn blanks as Zn is used as part of the mould-release compound during the production of these materials. Previous work showed that the most significant source of Zn in lab plastics and consumables was the gloves (Garçon et al., 2017). A blank exercise was performed to identify all potential sources of Zn and potential interferences with the aim to minimize blanks during any stage of sample preparation and ion exchange chromatography. Blanks were measured for all acids and reagents (HF, HBr, HCl, HNO_3 and Milli-Q H_2O), work environments (balance room, MC-ICP-MS sampling chamber, laminar flow and fume hoods and the lab bench), consumables (zip-lock storage bags, Kimwipes, nitrile and (washed) vinyl gloves) and acids taken directly from the preparation stills. All blanks were sampled in duplicate in acid leached and conc. HNO_3 refluxed 12 mL Savillex beakers. Two beakers were not refluxed to assess cleanliness of the cleaning procedure and the effect of the conc. HNO_3 refluxing.

For the hood- and surface blanks, beakers were filled with ~5 mL Milli-Q H_2O using an acid-cleaned measuring cylinder and left for a week. Laminar flow and fume hood blank beakers were positioned with one near the front and one at the back. Bench and balance room blanks were positioned evenly throughout the room and the MC-ICP-MS hood blanks were placed in the working hood and auto-sampler chamber. These blanks were checked daily and topped up with an additional 5 mL Milli-Q H_2O

if most of the liquid had evaporated. Acid and Milli-Q H_2O blanks were sampled by adding 5 mL concentrated acid to the beaker, using a measuring cylinder rinsed 3-5x with Milli-Q H_2O between acids, and evaporated to dryness overnight at 120°C. Consumable blanks were prepared on the day; for glove blanks the fingertips of each glove type were submerged in 5 mL 2% v/v HNO_3 for 10 seconds, sufficient to mobilize trace elements (Garçon et al., 2017). For the Kimwipe blanks a small piece was submerged in ~7 mL 2% v/v HNO_3 and 5 mL of this solution was pipetted into a test tube.

Blanks were prepared for Quadrupole ICP-MS analysis by addition of 5 mL 2% v/v HNO_3 to each beaker and heating them to 40°C overnight to ensure all material was in solution. A visible residue in the HF blank beakers required the ultrasonic bath to get digested.

3.6.3 – Results

Table **3.4** shows that the work environment in the Zn laminar flow hood and adjacent "hotplate hood 1" have small Zn blanks and that trace amounts of Zn were present in the concentrated HF, HNO_3 and HBr as well as the Milli-Q H_2O. Potentially interfering elements are found exclusively in the conc. HF (Ni and Ba) and HBr (Ni). The MFL and MC-ICP-MS environments are also shown to have a small Zn blank. However, the consumables are by far the biggest source of Zn blanks as the gloves in particular have significant abundances of both Zn and interfering elements. The trace element presence was expected in the consumables (Garcon et al., 2017), but the magnitude was higher than expected and illustrated that steps had to be taken to minimize the use of consumables during sample preparation and ion exchange chromatography.

The minimal expected procedural Zn and Ba blanks were calculated from the acid blanks and volumes of concentrated acid and MQ H_2O used during sample preparation and Zn purification to provide a benchmark value. These values, 1.02 ng for Zn and 5 pg for Ba, are likely underestimates as they do not consider the contribution of the work environment and consumables. The procedural Zn blanks of the ion exchange chromatographies containing samples were 21.0 ng, 7.58 ng and 2.27 ng. Average

chemistry blanks (n = 2) were 16.0 ± 1.65 ng, 5.03 ± 1.18 ng and 2.35 ± 1.08 ng. This was a substantial decrease compared to the initial trial Zn purifications which had blanks ≤67.8 ng. The decreased blank is directly attributed to the establishment of an incrementally more rigorous cleaning regimen and more restricted consumable usage in the ion exchange chromatography hood before and during Zn purification.

Blank	Ni	Cu	Zn	Ga	Te	Ba	La	Ce
HCl still 1	-	0.060	0.048	-	-	-	-	-
HCl still 2	-	-	-	-	-	-	-	-
HNO_3 still 1	-	0.015	0.021	-	-	-	-	-
HNO_3 still 2	-	0.031	0.091	-	-	-	-	-
HF still	-	0.034	0.060	0.015	-	0.079	-	-
conc. HF	0.014	0.009	0.088	0.020	-	0.119	0.005	0.010
conc. HNO_3	-	-	0.014	-	-	-	-	-
conc. HCl	-	-	-	-	-	-	-	-
conc. HBr	0.008	0.009	0.054	-	-	-	-	-
Milli-Q H_2O	-	-	0.042	-	-	-	-	-
Not HNO_3 refluxed acid leached beaker	-	-	-	-	-	-	-	-
Det. Limit [ng·mL^{-1}]	0.007	0.007	0.012	0.009	0.085	0.014	0.0003	0.0004
Zn Hood	-	0.998	0.153	-	-	-	-	-
Hotplate Hood 1	-	0.737	0.258	-	-	-	-	-
Hotplate Hood 2	-	0.075	0.261	0.156	-	1.078	-	-
Fume Hood	-	0.468	0.907	-	-	-	-	0.003
MFL Bench	-	0.056	0.215	-	-	-	-	-
Balance Room	-	-	0.337	-	-	-	-	-
MC-ICP-MS Hood	-	0.432	0.081	-	-	-	-	-
Nitrile Glove	0.475	0.169	8046	31.91	-	183.0	0.128	0.123
Vinyl Glove	-	0.064	82.23	-	-	0.132	0.003	0.002
Washed Vinyl Glove	-	0.047	28.17	0.079	-	0.321	0.003	0.002
Ziplock Bag	-	-	11.55	-	-	-	-	-
Kimwipe	0.262	1.623	10.28	2.661	-	15.04	0.071	0.053
Det. Limit [ng]	0.033	0.033	0.059	0.043	0.426	0.068	0.001	0.002
Sample [ng]	-	500	1000	-	-	-	-	-

Table 3.4: The blanks of Zn and potential interferences for the elements relevant to the Zn isotope measurements. Two blanks were prepared independently for all components considered. Acid blanks are reported in ng per mL of reagent and work environment and consumable blanks are reported in ng. A '-' indicates that the measured concentration was below the detection limit (3 standard deviations of the average of the washes).

The absence of Ba in the acids is an indication that the Ba interference was introduced to the sample via the consumables or inadequate cleaning of the plastics. It is unlikely to be a remnant of the ion exchange chromatography as Sweere (2018) showed that it effectively eluted Ba from the sample before Zn elution. Moreover, the measured Ba intensity of the same sample solution can vary significantly between analyses. This suggests that the Ba originates from the consumables as the blank

exercise showed that the cleaning procedure removes all Ba and that the chemistry does effectively remove Ba.

The isotopic composition of two procedural blanks of test-runs with high Zn blanks (45.2 ng and 69.3 ng) were analysed to determine the isotopic composition of the blank to determine the effect of the blank on the isotopic composition of the samples. A mass balance calculation was performed to establish the maximum acceptable size of the blank. This showed that the change in isotopic composition of a 1000 ng Zn sample due to a blank of this isotopic composition was within the analytical error of ±0.05‰ per amu for all ion exchange chromatographies involving samples (Fig. **3.7**).

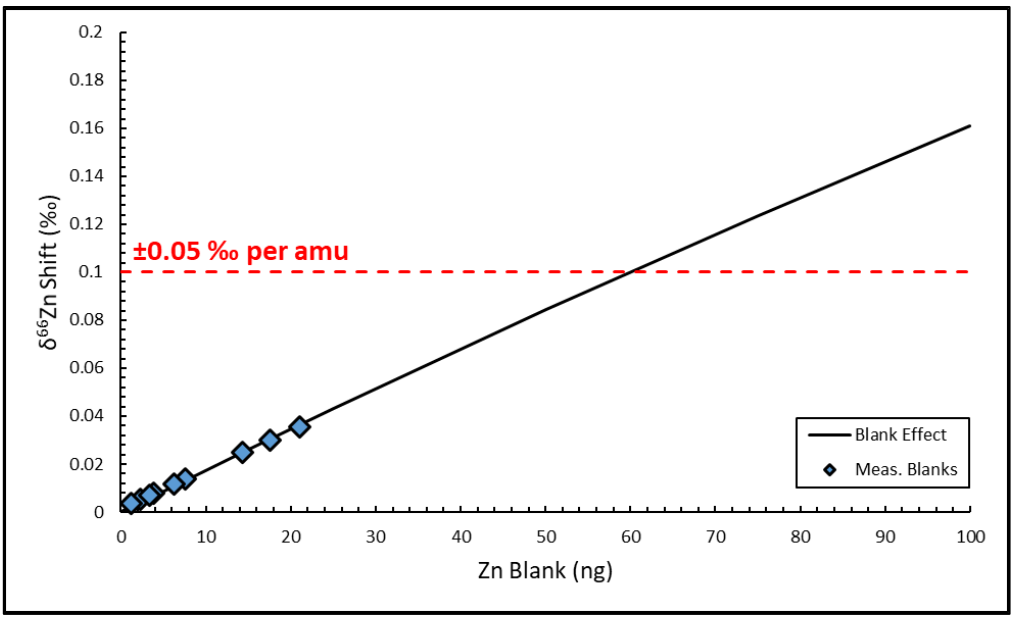


Figure 3.7: The shift in $\delta^{66}Zn$ for the IRMM-3702 secondary standard as a function of increasing blank size. The measured blanks were included to illustrate that the measured blanks do not impact the measured $\delta^{66}Zn$ beyond the analytical error. The dashed red line represents the ~0.05‰ per amu analytical error.

3.6.4 – Established Cleaning Regimen

The blank exercise showed that there were blank and interference problems for Zn related to the working environment and consumables. A thorough cleaning regimen was established on top of the regular cleaning regimen for plastics to minimize the contamination sources and suppress blanks. The day before the ion exchange chromatography all exposed surfaces, including the ceiling, walls and floor, of the MFL were cleaned with Milli-Q water and Kimwipes. Reagents were prepared on the day before in the cleaned laminar flow hood. On the first day of the Zn purification process the laminar

flow hoods and bench were again cleaned. Idle time during column preparation and between elution steps was spent cleaning the bench and other surfaces on which dust may gather.

Sample beakers were only handled wearing two sets of vinyl gloves and the outer vinyl glove was washed with Milli-Q water and dried with Kimwipes. Gloves were washed and/or replaced whenever time was spent outside of the laminar flow hood. No Kimwipes were used inside the hood. Potential sources of contamination were minimized during the ion exchange chromatography by cleaning everything, i.e. waste beaker, column rack, acid beaker, tip box or pipette, placed in the laminar flow hood with a Kimwipe wetted with Milli-Q water before introduction to the hood. Lastly, sample beakers did not leave the laminar flow hood environment until the ion exchange chromatography had finished unless the ultrasonic bath was required to digest a sample. The effects of the progressive implementation of more cleaning steps resulted in a significant decrease in the Zn blank with time (Fig. **3.8**).

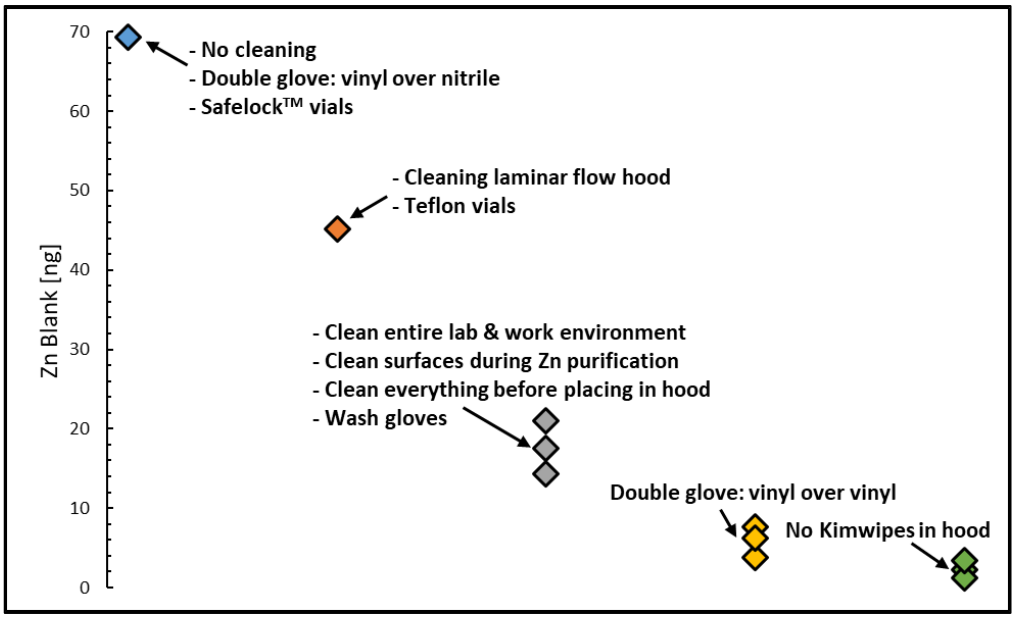


Figure 3.8: The evolution of the Zn blank with time and illustration of how an increasingly rigorous cleaning procedure decreased the Zn blank.

3.7 – Interference Corrections

3.7.1 – Potential Interferences on Zn

Initial mass spectrometry measurements showed an unnaturally fractionated isotopic composition. These big shifts could only be explained by non-Zn interferences on the measured Zn isotope intensities. The only isobaric interference for Zn isotopes is ^{64}Ni on ^{64}Zn which would decrease δ^{66}Zn. Therefore doubly-charged or polyatomic interferences or matrix effects were considered. It is unlikely that these interferences were caused by polyatomic species involving matrix elements, because the ion exchange chromatography was proven to be effective at removing matrix elements, but the presence of plasma-derived polyatomic species could not be ruled out. The use of a 0.5 amu mass spacing for the collector array enabled the identification of potential doubly-charged Te, Xe and Ba interferences on Zn isotope masses by looking at the half-mass collectors (Table **3.5**).

Mass	Isotope of interest	Isobaric and doubly charged interferences	Polyatomic interferences
61	^{61}Ni (1.14%)	$^{122}Sn^{2+}$ (4.63%), $^{122}Te^{2+}$ (2.60%)	$^{21}Ne^{40}Ar$
63	^{63}Cu (69.17%)	$^{126}Te^{2+}$ (18.95%), $^{126}Xe^{2+}$ (0.09%)	$^{23}Na^{40}Ar$, $^{47}Ti^{16}O$
63.5	-	$^{127}I^{2+}$ (100%)	-
64	**^{64}Zn (49.17%)**	^{64}Ni (0.93%), $^{128}Te^{2+}$ (31.69%), $^{128}Xe^{2+}$ (1.91%)	$^{24}Mg^{40}Ar$, $^{48}Ti^{16}O$, $^{48}Ca^{16}O$
64.5	-	$^{129}Xe^{2+}$ (26.40%)	-
65	^{65}Cu (30.83%)	$^{130}Te^{2+}$ (33.80%), $^{130}Xe^{2+}$ (4.07%), $^{130}Ba^{2+}$ (0.11%)	$^{25}Mg^{40}Ar$, $^{49}Ti^{16}O$
65.5	-	$^{131}Xe^{2+}$ (21.23%)	-
66	**^{66}Zn (27.73%)**	$^{132}Xe^{2+}$ (26.91%), $^{132}Ba^{2+}$ (0.10%)	$^{26}Mg^{40}Ar$,$^{50}Ti^{16}O$
66.5	-	$^{133}Cs^{2+}$ (100%)	-
67	**^{67}Zn (4.04%)**	$^{134}Xe^{2+}$ (10.44%), $^{134}Ba^{2+}$ (2.42%)	$^{27}Al^{40}Ar$
67.5	-	$^{135}Ba^{2+}$ (6.59%)	-
68	**^{68}Zn (18.45%)**	$^{136}Xe^{2+}$ (8.86%), $^{136}Ba^{2+}$ (7.85%)	$^{28}Si^{40}Ar$, $^{54}Fe^{14}N$
68.5	-	$^{137}Ba^{2+}$ (11.23%)	-
69	$^{138}Ba^{2+}$ (71.70%)	^{69}Ga (60.11%), $^{138}La^{2+}$ (0.09%), $^{138}Ce^{2+}$ (0.25%)	$^{29}Si^{40}Ar$
70.5	-	^{141}Pr (100%)	-

Table 3.5: The full range of (half-)masses in the collectors and the potential isobaric, doubly-charged and polyatomic interferences. For polyatomic interferences only nitride (^{14}N), oxide (^{16}O) and argide (^{40}Ar) species of major element and gas complexes were considered. Percentages next to isotopes indicate their IUPAC representative isotopic abundances (Melja et al., 2016).

An integrated intensity scan was performed over a mass range of 120 – 142 amu using a dirty standard solution to cover the full range of potential sources for doubly charged interferences (Figure **3.9**). This figure confirmed the blank test results that there was no Te in the samples. Figure **3.9** shows that both Ba was present in solutions that were analysed in vials that were not cleaned following the extensive

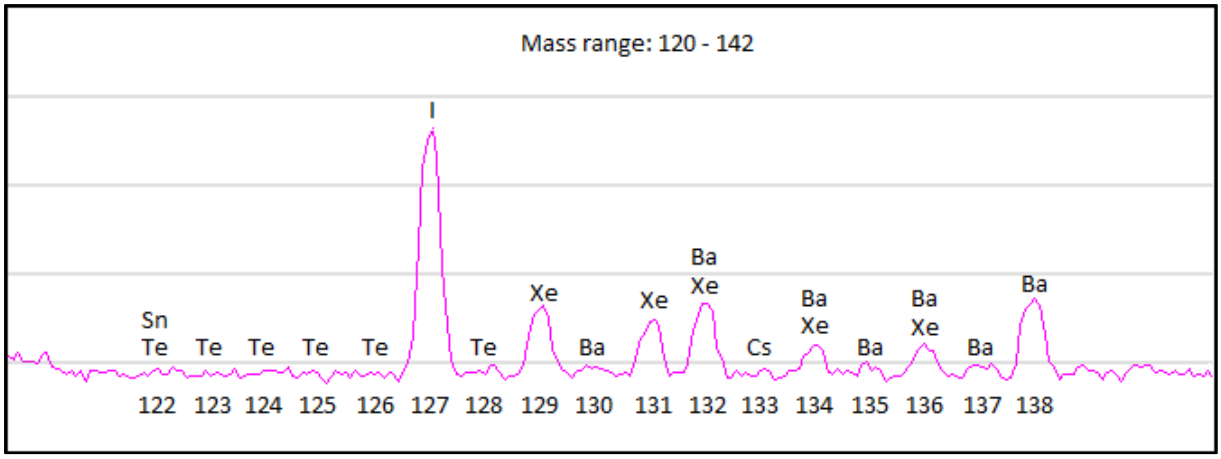


Figure 3.9: An integrated (22 passes) mass scan over the mass range between 120 amu and 142 amu. Numbers and elements indicate the (expected) peak positions for each mass. The intensity of the highest peak, ^{127}I, is $\sim 8 \cdot 10^{-5}$ V.

cleaning protocol for lab plastics and that Xe was present in the plasma. The observed relative peak intensities are broadly consistent with the expected IUPAC reference isotope abundances (Melja et al., 2016) and interferences from these elements would affect the Zn isotopic composition by artificially enhancing $\delta^{66}Zn$.

Xenon would be introduced to the plasma because of its trace abundances in both air and as a contaminant in the Ar source tank. However, as a noble gas, the second ionization potential of Xe (20.98 eV) is high relative to the first ionization potential of Ar (15.76 eV) which suggests that the presence of Xe^{2+} is unlikely. On the other hand, Ba, as an earth-alkali element, has a relatively low second ionization potential (10.00 eV) which is comparable to the first ionization potential of Zn (9.39 eV) and well below that of Ar. Therefore it is likely that some of the Ba that may be present will be doubly ionized. This was confirmed by the relative measured intensities on the mass 67.5, 68.5 and 69 collectors which are consistent with the IUPAC reference isotope abundance ratios for Ba.

The ion exchange chromatography was shown to effectively remove Ba before Zn elution (Sweere, 2018). Moreover, the blank exercise showed that the ion exchange chromatography and sample preparation only contribute negligible Ba. Therefore it is most likely that the Ba originated from the consumables and the implementation of a more rigorous cleaning protocol reduced the Ba intensities. However, as the following section will show, mV-level Ba intensities are capable of shift $\delta^{66}Zn$ in excess

of 10 ‰ per amu it is imperative to correct for the presence of Ba in the samples to get accurate values for $\delta^{66}Zn$.

3.7.2 – Interference Corrections

3.7.2.1 – The Ba Correction

3.7.2.1.1 – The Ba Interference

It was not possible to eliminate the Ba interference through instrument tuning. Instead, a correction was applied that subtracted the expected intensity of the interfering Ba isotope from the respective Zn isotope intensity. This correction was applied by calculating the intensities of the interfering Ba isotopes, $^{132}Ba^{2+}$, $^{134}Ba^{2+}$ and $^{136}Ba^{2+}$, using the intensity of an interference free Ba isotope. The obtained Ba isotope intensities were then subtracted from the total raw intensities to obtain the ^{66}Zn, ^{67}Zn and ^{68}Zn intensities. The Ba-corrected Zn isotope ratios were then used to calculate the Ba-corrected delta values.

There are three doubly-charged Ba isotopes, $^{135}Ba^{2+}$, $^{137}Ba^{2+}$ and $^{138}Ba^{2+}$, that can be considered to be interference free based on the blank tests, column calibration (Sweere, 2018) and integrated intensity scan (Fig. **3.9**). The IMF factor (*f*) from raw data was used to correct, what was assumed to initially be, the natural abundance of Ba isotopes in the sample for IMF using the exponential form of the generalized fractionation law (Maréchal et al., 1999). The double spike deconvolution of the non-Ba corrected Zn isotope ratios yields f_{Zn} and for the Ba correction it is then assumed that $f_{Ba} = f_{Zn}$ (Eq. **3.14**). Due to the different chemical properties of Zn and Ba it is likely that $f_{Ba} \neq f_{Zn}$, but because it was impossible to directly determine f_{Ba} the assumption that it is equal to f_{Zn} is the best possible approximation.

$$(Eq.3.14):\ f_{Ba} \cong f_{Zn} = \frac{\ln\left(\frac{\left(^{67}Zn/^{66}Zn\right)_{corr}}{\left(^{67}Zn/^{66}Zn\right)_{raw}}\right)}{\ln\left(m_{^{67}Zn}/m_{^{66}Zn}\right)}$$

The generalized expressions of the Ba correction of the three Zn isotopes (^{66}Zn, ^{67}Zn and ^{68}Zn) is expressed relative to $^{138}Ba^{2+}$ in Equations **3.15** and **3.16**.

$$(Eq.3.15):\ \left[\frac{Ab^{2x}Ba}{Ab^{138}Ba}\right] = \left({}^{2x}Ba/{}^{138}Ba\right)_{corr} = \left({}^{2x}Ba/{}^{138}Ba\right)_{nat}\left(\frac{m_{^{2x}Ba}}{m_{^{138}Ba}}\right)^{-f_{Zn}}$$

$$(Eq.3.16):\ I\,{}^{x}Zn_{corr} = I\,{}^{x}Zn_{raw} - \left[\frac{Ab^{2x}Ba}{Ab^{138}Ba}\right] I^{138}Ba_{raw}$$

Here $\left[Ab^{2x}Ba/Ab^{138}Ba\right]$ is the IMF corrected isotope abundance ratio of Ba isotopes where ^{2x}Ba is the Ba isotope corresponding to ^{x}Zn, I is the intensity and m the mass of the different isotopes. The $_{raw}$ and $_{corr}$ indicators show the measured raw and Ba-corrected intensities and $\left({}^{2x}Ba/{}^{138}Ba\right)_{nat}$ is the ratio of IUPAC reference isotope abundance values. These equations are expressed relative to $^{138}Ba^{2+}$ because the application of the Ba correction to a series of Zn standard solution doped with different amounts of Ba, between 1 ppt and 1 ppb, showed that the Ba correction using $^{138}Ba^{2+}$ was able to cover the largest range of Ba intensities as it is the most abundant Ba isotope and there was no evidence for the presence of $^{69}Ga^{+}$, $^{138}La^{2+}$ or $^{138}Ce^{2+}$ interfering on mass 69 (Fig. **3.10**).

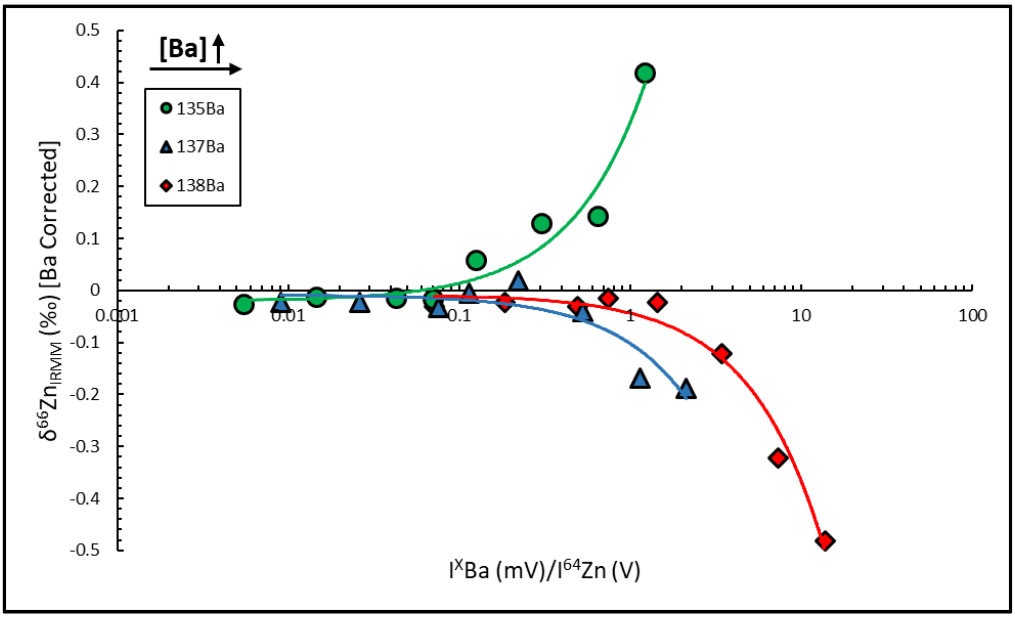


Figure 3.10: Comparison of the effectivity of the Ba correction using different isotopes by plotting the Ba-corrected $\delta^{66}Zn_{IRMM}$ (‰) plotted against the $^{x}Ba^{2+}/^{64}Zn$ intensity ratio, a measure of the amount of Ba.

3.7.2.1.2 – Parameterizing the Effect of Ba on Zn

The effects of the Ba interference on the Zn intensities were quantified using Equations **3.15** and **3.16**. The measured Zn intensities ($I\ ^{x}Zn_{raw}$) are defined as a combination of the actual sample Zn intensity ($I\ ^{x}Zn_{corr}$) and a Ba interference which is a function of the IMF corrected $^{2x/138}$Ba isotope abundance ratio and the measured ^{138}Ba intensity.

$$I^{64}Zn_{corr} = I^{64}Zn_{raw}$$

$$I^{66}Zn_{corr} = I^{66}Zn_{raw} - \left[\frac{Ab^{132}Ba}{Ab^{138}Ba}\right] I^{138}Ba_{raw}$$

$$I^{67}Zn_{corr} = I^{67}Zn_{raw} - \left[\frac{Ab^{134}Ba}{Ab^{138}Ba}\right] I^{138}Ba_{raw}$$

$$I^{68}Zn_{corr} = I^{68}Zn_{raw} - \left[\frac{Ab^{136}Ba}{Ab^{138}Ba}\right] I^{138}Ba_{raw}$$

All isotope ratios were determined relative to ^{64}Zn as it is the most abundant Zn isotope, the denominator for δ-values and the only measured Zn isotope without a Ba interference. This was preferred because it retains the linear dependence of the Zn isotope ratio on $I^{138}Ba_{raw}/I^{64}Zn_{raw}$ through the entire derivation. The equations below were generalized where x = 66, 67 or 68 and 2x the corresponding Ba^{2+} isotope as the derivation is the same for all three Zn isotopes. The effect of Ba on isotope ratios is shown in Equation **3.17**.

$$(Eq.\,3.17):\ \left(^{x}Zn/^{64}Zn\right)_{corr} = \left(^{x}Zn/^{64}Zn\right)_{raw} - \left[\frac{Ab^{2x}Ba}{Ab^{138}Ba}\right]\frac{I^{138}Ba_{raw}}{I^{64}Zn_{raw}}$$

Equation **3.17** illustrates the linear dependence of $\left(^{x}Zn/^{64}Zn\right)_{corr}$ on $I^{138}Ba_{raw}/I^{64}Zn_{raw}$, because $^{2x/138}$Ba abundance ratio was near-constant because f_{Zn} varied minimally during a run, but may vary between runs. Therefore, (1) it was possible to use the measured isotope ratio to quantify the effect of changing Ba intensities on the Zn isotope ratio and (2) the isotope ratio of the sample could be calculated from the measured isotope ratio using $I^{138}Ba_{raw}/I^{64}Zn_{raw}$.

The effect of Ba on δ^{x}Zn was quantified by inserting Equation **3.17** in the definition of the delta value (Eq. **3.9**). Rewriting the equation and expressing $I^{138}Ba_{raw}$ in mV instead of V gives Equation **3.18**.

$$(Eq.\,3.18):\ \ \delta\,^{x}Zn_{corr} = \delta\,^{x}Zn_{raw} - \left[\frac{Ab^{2x}Ba}{Ab^{138}Ba}\right]\left(^{64}Zn/\,^{x}Zn\right)_{std}\frac{I^{138}Ba_{raw}\ (in\ mV)}{I^{64}Zn_{raw}\ (in\ V)}$$

This shows that the shift in delta induced by the Ba interference is linearly dependent on $I^{138}Ba_{raw}/I^{64}Zn_{raw}$, because the isotope ratio of the standard is a constant. The magnitude of the Ba correction on δ^{x}Zn (Δ^{x}Zn) is defined as difference between the true and measured sample δ^{66}Zn (Eq. **3.19**). This parameter was used to evaluate the effectiveness of and assess potential over- or under-corrections of δ^{x}Zn induced by the Ba correction.

$$(Eq.\,3.19):\ \ \Delta^{x}Zn = -\left[\frac{Ab^{2x}Ba}{Ab^{138}Ba}\right]\left(^{64}Zn/\,^{x}Zn\right)_{std}\frac{I^{138}Ba_{raw}\ (in\ mV)}{I^{64}Zn_{raw}\ (in\ V)}$$

Equations **3.18** and **3.19** can be used to calculate the expected shifts of δ^{x}Zn as a function of Ba intensity. Therefore it can also be used to confirm the accuracy of the applied correction and assess if the proper interference correction is being applied.

3.7.2.1.3 – Applying the Ba Correction

The parameterization of the Ba interference showed that there was a direct dependence on $I^{138}Ba_{raw}/I^{64}Zn_{raw}$. However, as the measured Ba intensity increases, there will be a point where the Ba intensity becomes too high to accurately correct. The limits of the correction were assessed using a single 50 ppb Zn ICP-MS standard solution doped with a Ba ICP-MS standard solution (Alfa Aesar) to cover a range of Ba concentrations between 1 ppt – 1 ppb. Plotting δ^{66}Zn against $I^{138}Ba/I^{64}Zn$ showed that the deviation from the expected δ^{66}Zn increased linearly with the Ba abundance (Fig. **3.11a**). This was an expected shift, because the Ba interference artificially enhances the heavy isotope abundances relative to ^{64}Zn, generating a shift towards more positive δ^{66}Zn. Application of the Ba correction to this data showed that the Ba correction was able correct some of the Ba-doped solutions back to δ^{66}Zn = 0, but for those with ≥250 ppt Ba there was an overcorrection

and indicated the upper limit of the Ba correction (Fig. **3.11b**). The shift away from $\delta^{66}Zn = 0$ increases systematically with $I^{138}Ba/I^{64}Zn$ and by fitting a line through the high Ba concentration data points, the upper limit of the Ba correction was found to correspond to approximately 150 ppt Ba. There are no indications of a lower limit of the Ba correction in the ppt concentration range as the 1 ppt Ba solution is corrected accurately.

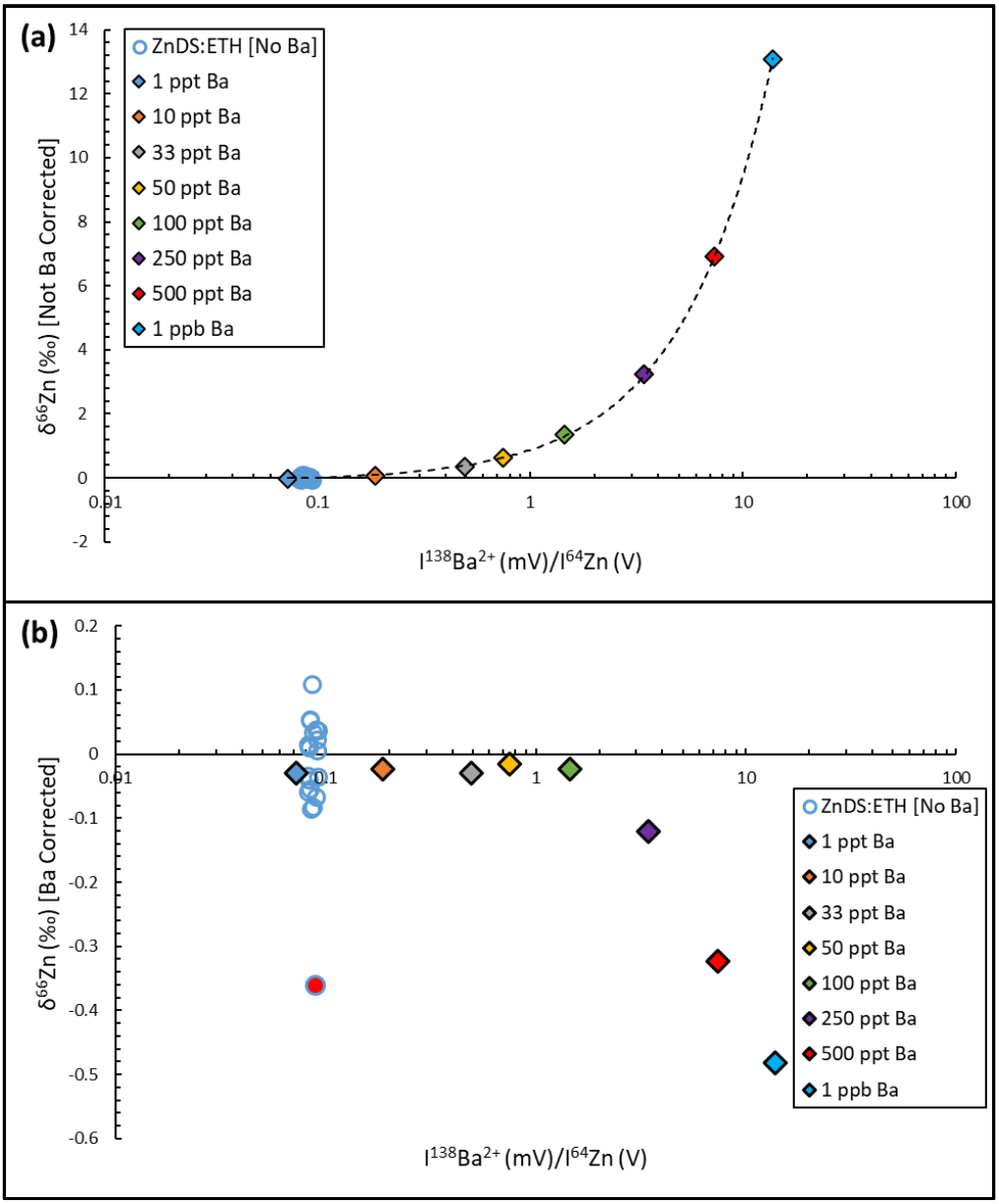


Figure 3.11: (a) The linear growth of $\delta^{66}Zn$ (‰) as a function of increasing $I^{138}Ba^{2+}$ without a Ba correction and **(b)** the evolution of Ba-corrected $\delta^{66}Zn$ (‰), both as a function of increasing Ba concentration in a solution of constant composition. The red circle indicates a Ba-free measurement with an erroneous Ba correction.

3.7.2.1.4 – Problems with the Ba Corrections

3.7.2.1.4.1 – Erroneous Ba Corrections

Figure **3.11b** shows one outlier Ba-corrected $\delta^{66}Zn$ value for a Ba-free measurement, indicated by the red circle. This offset was introduced by the Ba correction as there were no outliers before the Ba correction was applied. For the bracketing standards the Ba-corrected $\Delta^{66}Zn$ = -0.090 ± 0.02 ‰ for the well-corrected measurements with the outlier at $\Delta^{66}Zn$ = -0.434‰. A correction of this magnitude does not match the $I^{138}Ba/I^{64}Zn$ ratio of the sample, which suggests the correction should be of a similar magnitude to the other bracketing standard measurements. The Ni, Zn and Ba intensities provided no explanation as these were consistent with the intensities of the other bracketing standard measurements.

These erroneous corrections were observed on individual measurements across most MC-ICP-MS runs with a total of 3.98% (72 out of 1808) of sample and bracketing standard measurements being affected. These erroneous corrections shifted $\delta^{66}Zn$ in both positive and negative directions with a roughly equal distribution. Moreover, the distribution of affected measurements between sample and bracketing standards, approximately 15% samples and 85% standards, reflects the relative number of

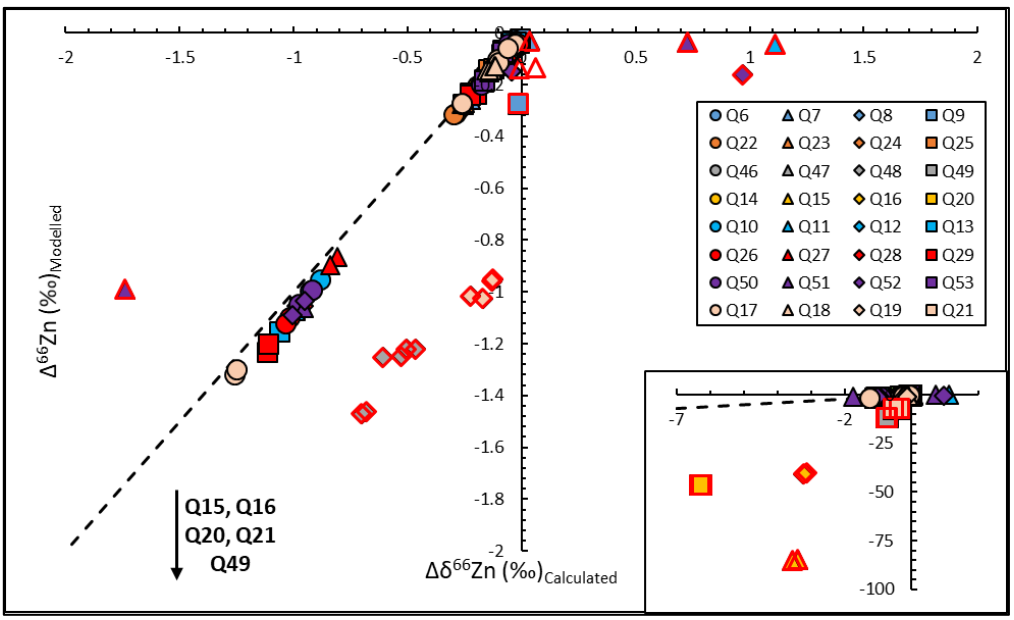


Figure 3.12: Comparison of the calculated and modelled $\Delta^{66}Zn$. The dashed line represents the one-to-one line. Erroneous corrections are indicated with a red outline. The inlay on the bottom-right shows the full range of samples and $\Delta^{66}Zn$.
Information regarding individual samples can be found in Chapter **4** and **5**.

secondary standards and samples relative to bracketing standards during a run and does not preferentially affect any specific sample or standard solution.

At present there is no viable explanation regarding the source of the erroneous Ba corrections, but it could be caused by the presence of a polyatomic species. However, the Ba correction of individual samples was assessed for erroneous Ba corrections by comparing the $\Delta^{66}Zn$ obtained through the Ba correction and double spike deconvolution spreadsheet to $\Delta^{66}Zn$ calculated using Equation **3.19** (Fig. **3.12**). For an accurate Ba correction, the measurement must fit on the one-to-one line. The majority of samples show a good fit between the two values with some outliers causing shifts in either direction. For some of the samples (Q15, Q16, Q19, Q20, Q48 and Q49) none of the individual measurements fall on the one-to-one line. These are all low Zn samples for which an additional interference was identified on the mass-69 collector which affected the $^{138}Ba^{2+}$ intensity and $\Delta^{66}Zn$.

3.7.2.1.4.2 – Using $^{137}Ba^{2+}$ for Interference Corrections

The downside of using $^{138}Ba^{2+}$ for the Ba correction is the dependence on interference-free data acquisition on mass 69. However, it is preferred over the interference-free $^{135}Ba^{2+}$ and $^{137}Ba^{2+}$ due to its higher abundance and therefore intensity. Because the ion exchange chromatography was shown to efficiently elute the main interfering isotope on the mass, ^{69}Ga, before Zn elution there should be no interference on this mass (Sweere, 2018). However, an interference that enhances $I^{138}Ba^{2+}$ relative to $I^{137}Ba^{2+}$ to cause it to deviate from the IUPAC reference isotope abundance ratio was observed for some samples (Fig. **3.13**). These deviations suggested an interference on $^{138}Ba^{2+}$ which inhibited its use for the Ba correction. The increased scatter in Figure **3.13** at the lower end of Ba intensities were related to detection limits where $I^{138}Ba^{2+}$ decreases while $^{137}Ba^{2+}$ remains roughly constant as it is close to the detection limits.

Figure **3.13** illustrates that there was an interference on the mass 69 collector as some samples (Q15, Q16, Q19, Q20, Q21, Q48 and Q49) plot below the IUPAC reference isotope abundance ratio.

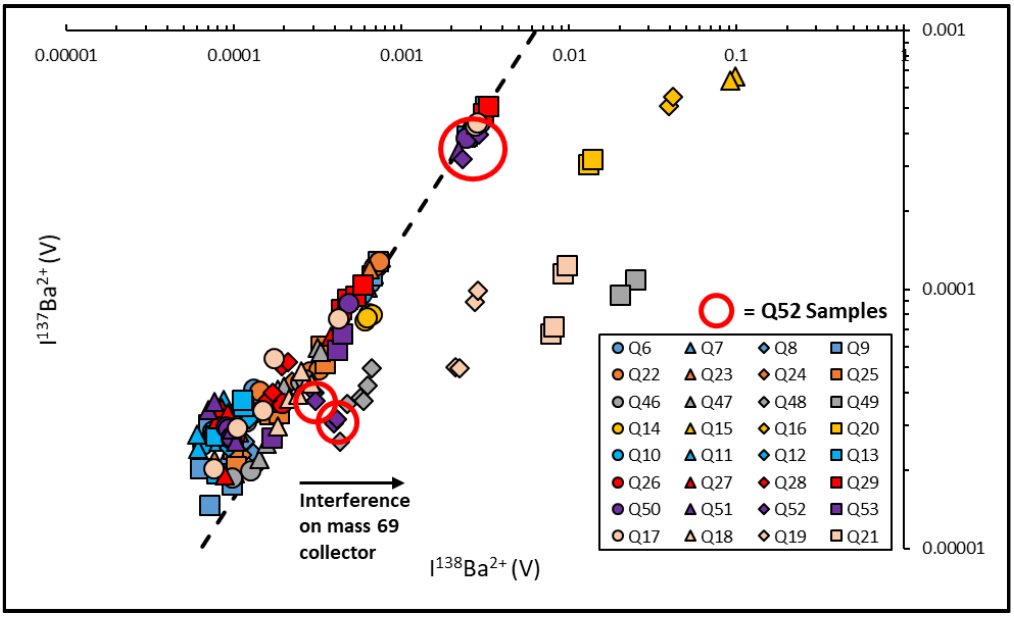


Figure 3.13: The measured $^{137}Ba^{2+}$ and $^{138}Ba^{2+}$ intensities plotted against each other. The dashed line represents the IUPAC reference isotope abundance ratio for $^{137}Ba/^{138}Ba$. Red circles show the three separate sets of repeat analyses of sample Q52.

Moreover, the two outlying data points for Q52, part of the same analysis, indicated that the Teflon vial used for the measurement of this sample was likely contaminated. This is consistent with the clustering of sets of two repeat measurements of the same sample solution. Similar clustering is also observed for other samples, most clearly observable for the outlier samples. The source of this contamination was not investigated further but could be caused by the presence of $^{69}Ga^{+}$, $^{138}La^{2+}$ or $^{138}Ce^{2+}$. All three would be potential sources to be introduced as contamination through either consumables or by incomplete removal during ion exchange chromatography as La and Ce were not considered by Sweere (2018) in their column calibration. The relatively low second ionization potential of La (11.06 eV) and Ce (10.85 eV) also suggests that these elements will doubly ionize readily in the Ar plasma if they are present.

To obtain a Ba corrected delta value for Q15, Q16, Q19, Q20, Q21, Q48 and Q49 the Ba correction was applied using $^{137}Ba^{2+}$ as it is the second-most abundant interference-free Ba isotope. Applying the $I^{137}Ba^{2+}$ correction accurately resolves the Ba correction for Q19, Q21, Q48, Q49 and Q52. However, for samples Q15, Q16 and Q20 using $^{137}Ba^{2+}$ or $^{135}Ba^{2+}$ for the Ba correction does not yield an accurate

δ^{66}Zn. These samples were all depleted in Zn (< 1 ppm) which resulted in Ba/Zn ratios outside the range of corrigible values.

3.7.2.1.4.3 – Modelling the Ba Correction

For samples Q15, Q16 and Q20 the magnitude of the Ba correction was modelled. The Ba correction is essentially solely dependent on $I^{x}Ba/I^{64}Zn$, as the other parameters are (near-)constant between samples within an analytical run. Therefore the slope of a line plotting Δ^{66}Zn against $I^{x}Ba/I^{64}Zn$ should be independent of any other parameters. However, when measurements within an analytical run were grouped using the double spike:sample ratio and plotted it showed that the slope of this line is linearly dependent on the double spike:sample ratio (Fig. **3.14a**). As this effect is not a function of the Ba correction, it is likely related to the deconvolution of the double spike. However, identifying the source of this linear dependence within the underlying mathematics of the double spike methodology is beyond the scope of this work. Regardless, this allowed for the calculation of the magnitude of the Ba correction based on the double spike:sample ratio and the intensity of ^{64}Zn and the various Ba isotopes. As the double spike:sample dependence is linear, Δ^{66}Zn could be predicted using the double spike:sample ratio, I^{64}Zn (in V) and $I^{138}Ba^{2+}$ (in mV). Figure **3.14b** shows the results of these calculations for a range of double spike:sample ratios and illustrates the effects of the double spike:sample ratio on the magnitude of the Ba correction.

Figure **3.14** was determined using data from the Ba correction using $^{138}Ba^{2+}$, but the shift to $^{137}Ba^{2+}$ is straightforward. If the isotopic composition of Ba is assumed to be the IUPAC reference isotope abundance ratio and only fractionated due to IMF, it is possible to predict where a $^{137}Ba^{2+}$ correction would fit on a $\Delta\delta^{66}$Zn – $I^{138}Ba/I^{64}Zn$ plot because the change in slope is defined by the change from $I^{137}Ba^{2+}$ to $I^{138}Ba^{2+}$. This was then quantified using the abundance ratio of the different Ba isotopes (Eq. **3.20**).

$$(Eq.3.20):\ \Delta^{66}Zn = (dy/dx)_{138_{Ba}} \frac{I^{137}Ba^{2+}_{raw}\left[\left[\frac{Ab^{138}Ba}{Ab^{137}Ba}\right]\left(\frac{m_{138_{Ba}}}{m_{137_{Ba}}}\right)^{-f_{Zn}}\right]}{I^{64}Zn_{raw}}$$

Here $(dy/dx)_{138_{Ba}}$ is the slope of the Ba correction as predicted from Figure **3.14a**, $Ab^{2x}Ba/Ab^{138}Ba$ and $m_{x_{Ba}}$ are the abundance (in %) and mass of the Ba isotopes, f_{Zn} is the IMF for Zn of the sample and $I^{137}Ba^{2+}$ and $I^{64}Zn$ are the Ba and Zn intensities in mV and V respectively.

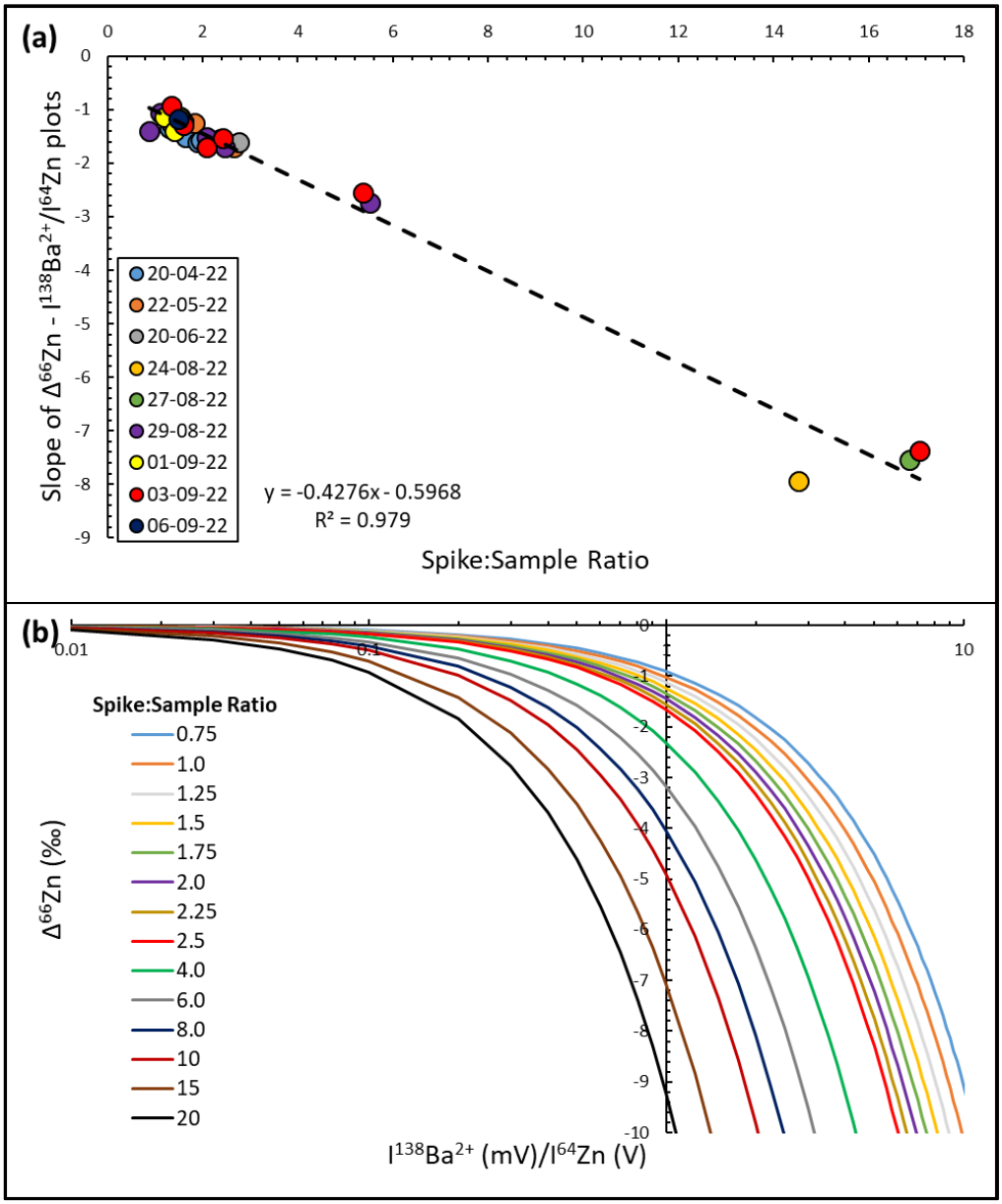


Figure 3.14: (a) Plot showing how the slope of the $\Delta^{66}Zn - I^{138}Ba/I^{64}Zn$ changes as a function of the double spike:sample ratio. **(b)** Plot of $\Delta^{66}Zn$ against $I^{138}Ba/I^{64}Zn$. Lines show the modelled $\Delta^{66}Zn$ for different double spike:sample ratios.

As $I^{137}Ba^{2+}$ is free of any interference, this approach was used to best approximate the Ba correction for measurements of the three samples, Q15, Q16 and Q20, where an unknown interference on the mass-69 collector and erroneous corrections for the $^{135}Ba^{2+}$ and $^{137}Ba^{2+}$ hindered the accurate determination of $\delta^{66}Zn$. Equation **3.20** was used to apply the Ba correction for these samples to find Ba corrected $\delta^{66}Zn$.

3.7.2.2 – Ni Correction

3.7.2.2.1 – The Ni Interference

Separate from the Ba interference, there was also the potential isobaric interference of ^{64}Ni on ^{64}Zn to consider. This interference was monitored using ^{61}Ni intensities which was considered an interference-free Ni isotope because Sn ($^{122}Sn^{2+}$) was not eluted until after Zn elution (Sweere, 2018) and Te ($^{122}Te^{2+}$) was not found in the blank exercise. The data showed that the ^{64}Ni interference in the samples was smaller than Ba with generally low $^{61}Ni^{+}$ intensities. This showed Ni was effectively removed during the ion exchange chromatography. Potential Ni sources would be either consumables or the instrument cones. However, as elevated Ni intensities were only observed in a single sample, it suggested something went wrong during the processing of this sample. It was not possible to reprocess or reanalyse this sample due to limited availability of sample material.

3.7.2.2.2 – Parameterizing the Effect of Ni on Zn

The Ni correction was parameterized in the same way as the Ba correction to correct ^{64}Zn intensities (Eq. **3.21**; **3.22**). The IMF factor (*f*) was used to correct, what was assumed to initially be, the natural abundance of Ni isotopes in the sample for IMF using the exponential form of the generalized fractionation law (Maréchal et al., 1999). The double spike deconvolution of the uncorrected Zn isotope ratios yields f_{Zn} and for the Ni correction it is assumed that $f_{Ni} = f_{Zn}$. It is likely that $f_{Ni} \neq f_{Zn}$, but as it is impossible to directly determine f_{Ni} this was the best possible approximation.

$$(Eq.\,3.21): \quad \left[\frac{\mathrm{Ab}^{64}Ni}{\mathrm{Ab}^{61}Ni}\right] = \left({}^{64}Ni/{}^{61}Ni\right)_{corr} = \left({}^{64}Ni/{}^{61}Ni\right)_{nat}\left(\frac{m_{{}^{64}Ni}}{m_{{}^{61}Ni}}\right)^{-f_{Zn}}$$

$$(Eq.\,3.22): \quad I^{64}Zn_{corr} = I^{64}Zn_{raw} - \left[\frac{\mathrm{Ab}^{64}Ni}{\mathrm{Ab}^{61}Ni}\right] I^{61}Ni_{raw}$$

Here $[\mathrm{Ab}^{64}Ni/\mathrm{Ab}^{61}Ni]$ is the fractionation corrected isotope abundance ratio, I is the intensity (in V) and m is the mass of the isotopes. The ^{x}Zn/^{64}Zn isotope ratios were then calculated using the Ni-corrected $^{64}Zn^{+}$ intensities and δ^{x}Zn were then determined through Zn double spike deconvolution.

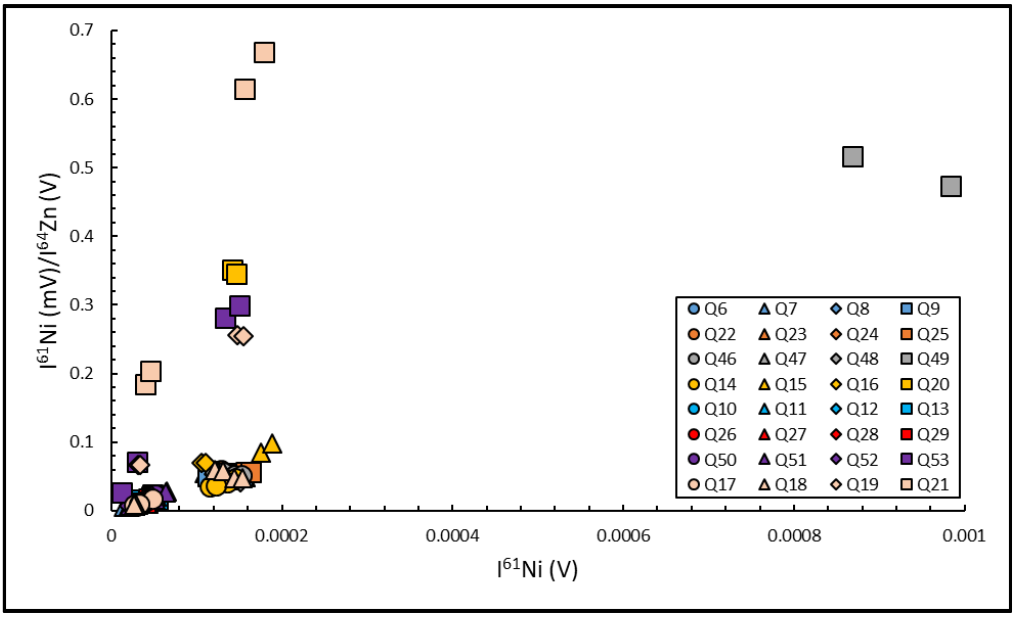


Figure 3.15: Plot of the $^{61}Ni/^{64}Zn$ intensity ratio ^{64}Ni as a function of the ^{61}Ni intensity.

Equation **3.22** shows that the ^{64}Zn correction is linearly dependent on $I^{61}Ni$. As the other Zn isotopes are unaffected by the Ni interference and variability in $\delta^{x}Zn$ due to Ni was caused by changes in $I^{64}Zn$. The measured $I^{61}Ni$ were ≤ $2 \cdot 10^{-4}$ V for all samples except Q49 (Fig. **3.15**).

To quantify the effect of the Ni interference on $\delta^{66}Zn$ it was easier to work with $\delta^{64/66}Zn$ as this results in an equation with the interfered isotope in the nominator and an isotope free of Ni interference in the denominator (Eq. **3.23**). In this equation the $I^{66}Zn$ is the intensity after Ba correction.

$$(Eq.3.23):\ \left(^{64}Zn/^{66}Zn\right)_{corr} = \left(^{64}Zn/^{66}Zn\right)_{raw} - \left[\frac{Ab^{64}Ni}{Ab^{61}Ni}\right]\frac{I^{61}Ni_{raw}}{I^{66}Zn_{corr}}$$

Equation **3.23** is substituted into the equation describing delta values (Eq. **3.9**) to find the equation describing the Ni corrected $\delta^{64/66}Zn$.

$$(Eq.3.24):\ \delta^{64/66}Zn_{corr} = \delta^{64/66}Zn_{raw} - \left[\frac{Ab^{64}Ni}{Ab^{61}Ni}\right]\left(^{66}Zn/^{64}Zn\right)_{std}\frac{I^{61}Ni_{raw}\ (in\ mV)}{I^{66}Zn_{corr}(in\ V)}$$

Next, Equation 3.24 is converted to $\delta^{66}Zn$ using to quantify the magnitude of the Ni correction (Eq. **3.25**).

$$(Eq.3.25):\ \Delta^{66}Zn = \left[\frac{Ab^{64}Ni}{Ab^{61}Ni}\right]\left(^{66}Zn/^{64}Zn\right)_{std}\frac{I^{61}Ni_{raw}\ (in\ mV)}{I^{66}Zn_{corr}(in\ V)}$$

3.7.2.2.3 – Applying the Ni Correction

The magnitude of the Ni correction was determined for all samples and compared to the modelled Δ^{66}Zn (Fig. **3.16**). However, the samples that exhibited elevated $I^{61}Ni/I^{66}Zn$, due to either low Zn abundances or a Ni inference, tend to deviate slightly from the modelled trend. The bulk of measurements were concentrated at lower $I^{61}Ni/I^{66}Zn$ ratios where the magnitude of the Ni correction, ≤0.025 ‰ per amu, was within the analytical error of the measurements. For these samples the Ni correction was applied with the calculated values. Two samples yield Ni corrections that exceed the analytical error on the measurements. Sample Q49 has a ~1 mV I^{61}Ni interference and sample Q20 has a low Zn intensity (I^{66}Zn ≅ 60 mV). In both cases it is likely that the $I^{61}Ni/I^{66}Zn$ ratios exceed limitations of the correction and therefore the correction was applied using the modelled values.

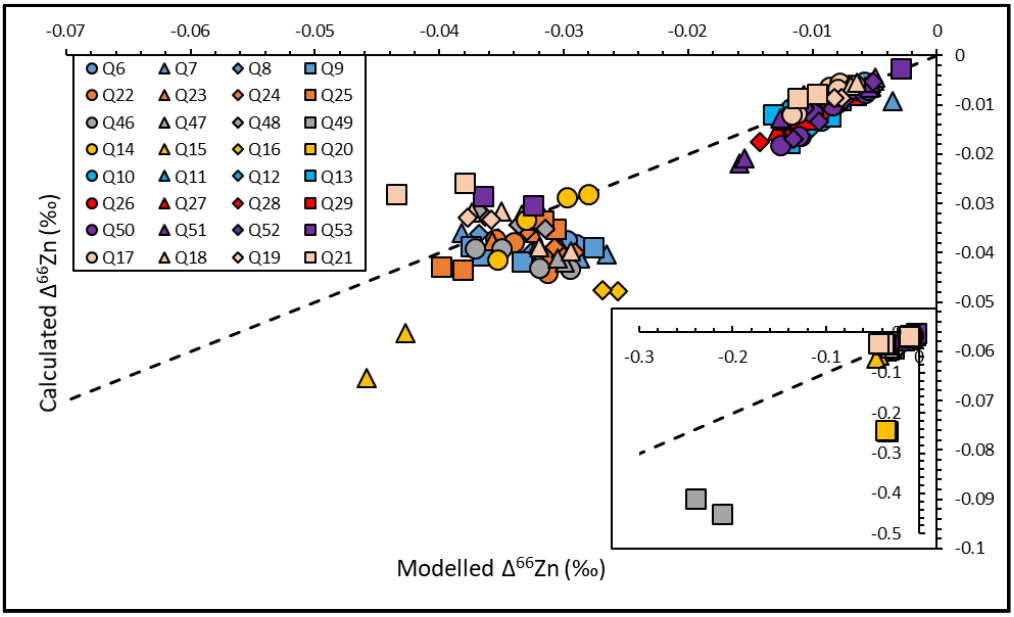


Figure 3.16: Comparison of the calculated (data points) and modelled (dashed line) Δ^{66}Zn. The inlay shows the two samples (Q20 and Q49) that require significant Ni corrections and their deviation from the modelled values.

Chapter 4 – Trace Element Volatility

4.1 – Introduction

The measured abundance of moderately volatile lithophile and siderophile elements in the bulk silicate Earth (BSE) cannot be explained solely through core-mantle segregation as they are lower than expected based on their metal-silicate partitioning coefficients. Norris and Wood (2017) showed that the observed trace element depletions of moderately volatile lithophile elements in the BSE correlated well with their evaporation experiments, suggesting volatile loss had an impact on the trace element budget of the Earth. Volatile loss occurred in a large-scale surface magma ocean where conditions were vastly different from those in the solar nebula. Initially the oxygen fugacity (fO_2) in the magma ocean was expected to be 1 – 2.5 log units below the iron-wüstite oxygen buffer reaction (ΔIW-2.5 – ΔIW-1), facilitating the formation of a metallic core (Wood et al., 2006). The mantle gradually became more oxidized through internal processes, e.g. bridgmanite dissociation (Williams et al., 2012), the potential addition of oxidized, volatile-rich meteoritic material (Schönbächler et al., 2010) and evaporative loss at the surface, where the evaporating species were generally more reduced than the condensed species. Through these processes the mantle became more oxidizing and eventually reached oxygen fugacities comparable to the fayalite-magnetite-quartz oxygen buffer reaction (ΔFMQ+0) as recorded in terrestrial igneous rocks (Armstrong et al., 2019; Hirschmann, 2022).

Norris and Wood (2017) used the volatility factor, the ratio of the trace element abundance in the silicate melt before and after an experiment, as a qualitative tool of measuring volatility. They showed that this matched the CI chondrite normalized BSE abundances better than T^{50}, but it does not quantify volatility in terms of any thermodynamic or physicochemical parameters. Sossi et al. (2019) performed a time integration of the Hertz-Knudsen-Langmuir (HKL; Knudsen, 1909; Langmuir, 1916) equation to describe experimental volatile loss and quantify it in terms of the experimental conditions and thermodynamic properties of the evaporation reaction.

This chapter will discuss the results of the high-temperature one atmosphere volatility experiments described in Chapter **2**. The volatility of 17 elements Li, P, V, Cu, Zn, Ga, Ge, As, Rb, Ag, Cd, In, Sn, Sb, Cs, Tl and Pb will be considered. It will explore the volatility of the individual elements as well as their order of relative volatility and assess how this changed as a function of time, oxygen fugacity and melt composition. Additionally there will be a brief discussion regarding the volatility of chlorine to show how the volatility of halogens is expected to change with time and oxygen fugacity and how the presence of halogens in the melt may impact the potential evaporation reactions. For the moderately volatile elements there is a more detailed discussion where the modified HKL equation (Sossi et al., 2019) was applied to the trace element data to quantify volatility in terms of thermodynamic principles and properties of the evaporation reaction. There will also be a brief discussion about some of the pitfalls when using the modified HKL equation and why using it to quantify volatility in a silicate melt is contentious. Finally the observed trace element volatilities will be compared to the observed trace element abundances in the terrestrial mantle and the 1% evaporation (Sossi et al., 2019) and 50% condensation (Lodders, 2003; Wood et al., 2019) temperatures which have been used as a measure of trace element volatility.

4.2 – Thermodynamic Predictions of Trace Element Behaviour

4.2.1 – Evaporation Reactions

To quantify volatility it is important to constrain the potential evaporation reactions that may occur (Table **4.1**). The oxidation state of the trace elements in the silicate melt was constrained based on observations in natural samples; Li^{+}, P^{5+}, Cu^{+}, Zn^{2+}, Ga^{3+}, Ge^{4+}, As^{3+}, Rb^{+}, Ag^{+}, Cd^{2+}, In^{3+}, Sn^{4+}, Sb^{3+}, Cs^{+}, Tl^{+} and Pb^{2+} (Capobianco et al., 1999; Lanzirotti et al., 2019; Lee et al., 2010; Norris, 2016; Maciag and Brenan, 2020). The oxidation state of V (V^{2+}, V^{3+}, V^{4+} or V^{5+}) was variable across the experimental T-fO_2 range and was calculated from thermodynamic data. The potential gas species were determined using a thermodynamic dataset of pure species (Barin et al., 1989). The evaporation reactions were used to calculate the equilibrium partial pressures of each individual gas species, their relative abundance compared to other gas species of the same element and the total equilibrium partial pressure of all gas species of an element in the system (see Chapter **2**, Section **5**). For most trace elements only a single evaporation reaction was considered, because the others were deemed to have no significant contribution to the total equilibrium partial pressure of a trace element gas species (Appendix **2**). Only for two elements, Cs and Pb, multiple evaporation reactions were considered.

	Evaporation Reactions	n	A	B
Cu	Cu_2O (l) = 2 Cu (g) + 0.5 O_2 (g)	1	-43045	17.78
Zn	ZnO (l) = Zn (g) + 0.5 O_2 (g)	2	-24918	10.94
Ga	Ga_2O_3 (l) = 2 Ga (g) + 1.5 O_2 (g)	3	-85059	28.67
Ge	GeO_2 (l) = GeO (g) + 0.5 O_2 (g)	2	-27496	14.00
As	As_2O_3 (l) = 2 AsO (g) + 0.5 O_2 (g)	1	-27946	22.46
Rb	Rb_2O (l) = 2 Rb (g) + 0.5 O_2 (g)	1	-25795	15.50
Ag	Ag_2O (l) = 2 Ag (g) + 0.5 O_2 (g)	1	-16428	10.18
Cd	CdO (l) = Cd (g) + 0.5 O_2 (g)	2	-19191	10.75
In	In_2O_3 (l) = 2 In (g) + 1.5 O_2 (g)	3	-73331	27.70
Sn	SnO_2 (l) = SnO (g) + 0.5 O_2 (g)	2	-31122	13.95
Sb	Sb_2O_3 (l) = 2 SbO (g) + 0.5 O_2 (g)	1	-26453	23.21
Cs	Cs_2O (l) = 2 Cs (g) + 0.5 O_2 (g)	1	-22095	11.41
	Cs_2O (l) + 0.5 O_2 (g) = 2 CsO (g)	-1	-10407	8.995
Tl	Tl_2O (l) = 2 Tl (g) + 0.5 O_2 (g)	1	-27410	15.71
Pb	PbO (l) = Pb (g) + 0.5 O_2 (g)	2	-21175	9.849
	PbO (l) = PbO (g)	0	-14622	7.788

Table 4.1: Summary of the evaporation reactions for the relevant trace elements, considering only monometallic gas species, and the constants (A and B) used to calculate the equilibrium constant of the evaporation reaction at a given temperature [$\log(K) = A/T\ (in\ K) + B$]. n is the change in valence state of the trace element in the reaction. Thermodynamic data taken from Barin et al. (1989).

The equilibrium partial pressure is strongly dependent on the activity of the trace element in the silicate melt. However, the paucity of data and absence of a comprehensive model on trace element activity in silicate melts at relevant conditions for most elements inhibited the use of accurate activity coefficients. Instead it was assumed that all trace elements behaved ideally in the melt despite previous work suggesting the trace element activity in silicate melts may significantly deviate from ideal behaviour (O'Neill and Eggins, 2002; Borisov, 2009; Wood and Wade, 2013; Norris, 2016; Sossi et al., 2019).

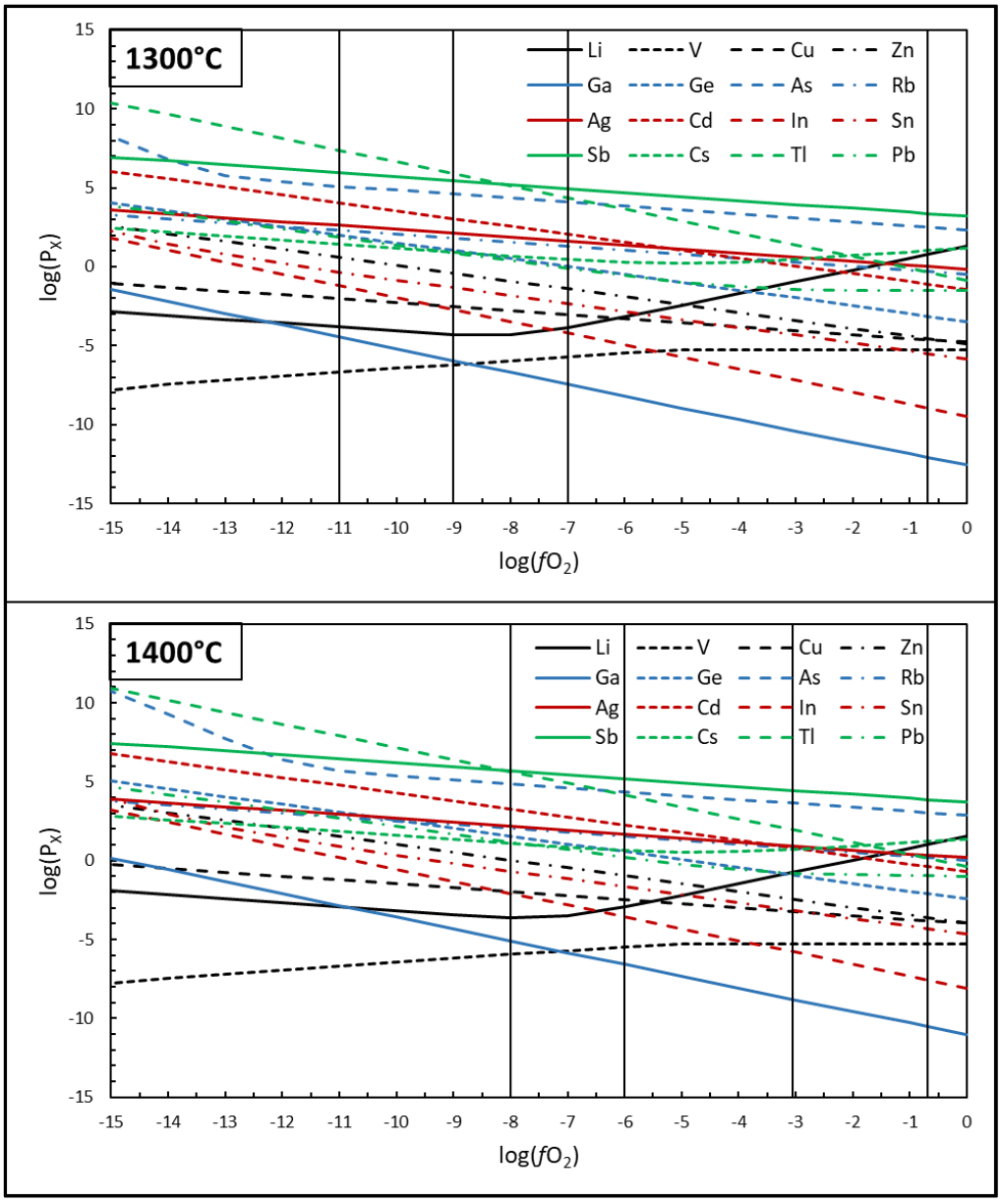


Figure 4.1: Evolution of the total equilibrium partial pressures of monometallic trace element gas species as a function of fO_2 at fixed temperature. Vertical lines indicate the experimental fO_2 conditions.

4.2.2 – Total Partial Pressure of Trace Element Gas Species

The reactions described in Table **4.1** and Appendix **2** were used to calculate the total partial pressure of all stable gas species for each element across a range of fO_2 at constant temperature (Fig. **4.1**). Changes in slope of the total equilibrium partial pressure trends were observed for multiple elements in this figure and reflect a change of the most abundant gas species. For elements with multiple species in the gas phase the oxide species are more abundant in oxidizing conditions whereas elemental species are more abundant in more reducing conditions. Differences between Fig. **4.1** and similar figures in Norris (2016) are the result of the assumption in this work that only monometallic gas species were formed while Norris (2016) considered all potential gas species. The reasoning behind only considering monometallic gas species was outlined in Chapter **2**. This assumption had an effect on the total equilibrium partial pressure of the elements with stable polymetallic gas species; Ga, As, Rb, In, Sb, Cs, Tl and Pb. A figure identical to Fig **4.1** which considers all mono- and polymetallic gas species to calculate the total equilibrium partial pressure is available in Appendix **2**.

4.2.3 – Chlorine

4.2.3.1 – Chlorine Volatility

The initial abundance of ~500 ppm of halogens (F, Cl, Br and I) in the SM, IB and AN experiments enabled halogen complexation and trace element evaporation via halide species. To assess halogen retention in the silicate melt the Cl content of the IB experiments was measured with EPMA (Table **4.2**). Chlorine was chosen as it is the halogen whose behaviour in silicate melts is best understood (e.g. Thomas and Wood, 2021). The measurements showed that Cl abundances were mostly below the ~100 ppm detection limits for experiments performed at $\log(fO_2)$ = -0.68; -3 and -6. For experiments at $\log(fO_2)$ = -8 Cl was measured in all experiments, decreasing with runtime, suggesting that Cl volatility decreases with fO_2. This is in agreement with the observations by Thomas and Wood (2021) that fCl_2 decreases with decreasing fO_2.

4.2.3.2 – Chloride Gas Speciation

The presence of halogens in the SM, IB and AN experiments opened up the possibility for trace element evaporation through halide gas species over oxide or elemental gas species. This could not be assessed directly, because the experimental set-up did not involve trapping the evaporating species for analysis (e.g. Renggli and Klemme, 2020). The modified HKL equation may provide an indication that additional evaporation reactions, other than those in Table **4.1**, are taking place in the system if fits are poor and n deviates from its expected value. However, it does not reveal which reaction may be taking place, hence it is only a potential indicator of evaporation via halide speciation.

	n	[Cl] (ppm)	F_{Cl}[1]	log(fCl_2)[2]
Q10	9	119 ± 18.8	0.234 ± 0.037	-6.16 ± 0.14
Q11	0	-	-	-
Q12	7	163 ± 31.6	0.322 ± 0.062	-5.70 ± 0.49
Q13	0	-	-	-
Q26	0	-	-	-
Q27	0	-	-	-
Q28	1	127	0.250	-7.29
Q29	0	-	-	-
Q50	12	124 ± 14.2	0.245 ± 0.028	-8.78 ± 0.10
Q51	1	101	0.199	-8.96
Q52	0	-	-	-
Q53	0	-	-	-
Q17	50	295 ± 69.8	0.583 ± 0.138	-9.03 ± 0.21
Q18	44	183 ± 35.8	0.362 ± 0.071	-9.44 ± 0.17
Q19	16	124 ± 19.2	0.244 ± 0.038	-9.78 ± 0.14
Q21	2	104 ± 4.50	0.204 ± 0.009	-9.93 ± 0.04

Table 4.2: Chlorine abundances of IB experiments. Details of Cl measurements were discussed in Chapter **2**. The **n** represents the number of measurements, out of 50, above detection limit. [1]Volatility factors were calculated using an initial Cl abundance of 507 ppm. [2]Chlorine fugacity calculated using Thomas and Wood (2021).

The equilibrium partial pressure of a chloride gas species relative to that of an oxide or elemental gas species for a given trace element was calculated using the method outlined in Chapter **2**, Section **5.4**. These calculations showed that there were some elements; Cu (CuCl), Ga ($GaCl_{1-3}$), Rb (RbCl), In ($InCl_{1-3}$), Cs (CsCl) and Tl (TlCl) for which the total equilibrium partial pressure of the chloride species exceeds the total equilibrium partial pressure of the monometallic elemental/oxide gas species listed in Table **4.1**. For Zn ($ZnCl_2$), Ag (AgCl) and Pb ($PbCl_{1-2}$) the total equilibrium partial pressure of the chloride species exceeds the total equilibrium partial pressure of the monometallic elemental/oxide gas

species in more oxidizing conditions. For Ge ($GeCl_{1-4}$), As ($AsCl_3$), Cd ($CdCl_2$), Sn ($SnCl_{1-2,4}$) and Sb ($SbCl_{1,3}$) the total equilibrium partial pressure of the chloride species is significantly smaller than the total equilibrium partial pressure of the monometallic oxide/elemental gas species in all experiments. More detailed information in the form of fO_2-fCl_2 dependence plots of the equilibrium partial pressure ratios of the chloride and elemental or oxide gas species as a function of fO_2 and fCl_2 can be found in Appendix **3**.

4.3 – Results

A total of 76 experiments were performed at 1300°C and 1400°C with runtimes between 3 and 60 minutes and oxygen fugacities between air and the iron-wüstite mineral buffer. The preparation of the starting trace element doped major element compositions was discussed in detail in Chapter **2**. The experiments were air quenched to silicate glasses and no quenching structures were observed in any of the samples. The trace element abundances of these glasses, measured with laser ablation inductively coupled plasma mass spectrometry (LA-ICP-MS) are listed in Table **4.3**.

4.3.1 – Table of Trace Element Abundances

	t (min)	comp	m (mg)	log(fO_2)	T (°C)	capsule	type	Li	P	V	Cu	Zn	Ga	Ge	As	Rb	Ag	Cd	In	Sn	Sb	Cs	Tl	Pb
Q6	3	SM	71.7	-0.68	1400	Pt	Loop	566	594	492	1078	664	499	513	372	424	227	183	530	488	504	324	4.22	424
Q7	15	SM	73.6	-0.68	1400	Pt	Loop	562	587	491	1046	641	512	514	164	405	61.3	18.8	538	492	467	259	0.52	196
Q8	30	SM	69.7	-0.68	1400	Pt	Loop	544	572	485	1026	631	496	494	44.6	389	11.8	0.91	514	460	403	219	0.07	57.9
Q9	60	SM	72.0	-0.68	1400	Pt	Loop	535	580	483	974	610	495	500	24.2	370	11.4	1.53	505	470	380	175	0.09	37.4
Q22	3	SM	71.0	-3.05	1400	Pt	Box	563	563	478	839	617	489	484	489	450	259	3.86	501	475	486	395	0.32	537
Q23	15	SM	68.5	-3.05	1400	Pt	Box	555	577	472	565	604	486	486	217	431	52.9	30.2	484	443	448	336	0.13	315
Q24	30	SM	73.1	-3.05	1400	Pt	Box	543	574	471	399	627	477	440	67.7	413	2.77	0.56	465	395	405	289	0.04	127
Q25	60	SM	69.0	-3.05	1400	Pt	Box	548	586	477	373	512	502	412	12.0	367	1.21	0.06	498	383	398	186	0.03	30.0
Q46	3	SM	69.3	-5.98	1400	Pt(Fe s)	Box	566	552	475	884	559	483	479	361	431	254	268	457	442	442	366	1.02	444
Q47	15	SM	70.7	-5.98	1400	Pt(Fe s)	Box	564	558	482	532	356	496	335	147	429	27.7	54.0	361	151	278	329	0.58	196
Q48	30	SM	70.0	-5.98	1400	Pt(Fe s)	Box	564	558	473	227	42.6	484	68.9	10.3	385	3.90	1.44	136	30.9	80.6	247	0.10	13.0
Q49	60	SM	70.1	-5.98	1400	Pt(Fe s)	Box	567	555	484	200	1.68	479	4.58	0.81	349	0.45	0.18	56.3	15.9	38.2	195	-	0.40
Q14	3	SM	69.3	-8.01	1400	Re	Box	550	575	480	913	46.2	443	113	52.4	355	6.87	1.14	62.4	57.4	71.5	217	0.08	9.76
Q15	15	SM	72.7	-8.01	1400	Re	Box	552	555	482	558	1.45	436	8.23	2.30	268	0.30	0.06	2.73	1.18	3.58	85.5	0.01	0.07
Q16	30	SM	67.6	-8.02	1400	Re	Box	545	558	478	311	1.00	421	0.86	0.47	176	0.14	0.12	0.38	0.29	0.32	29.8	0.01	0.12
Q20	60	SM	66.5	-7.99	1400	Re	Box	541	552	484	90.8	1.07	391	-	0.28	71.7	0.04	0.04	0.20	0.26	0.10	2.39	0.004	0.01
Q10	3	IB	74.8	-0.68	1400	Pt	Loop	575	800	782	1229	642	487	521	284	477	256	206	542	483	477	408	9.32	444
Q11	15	IB	64.1	-0.68	1400	Pt	Loop	561	785	782	1136	609	495	502	238	439	119	129	499	455	447	309	1.42	355
Q12	30	IB	71.5	-0.68	1400	Pt	Loop	571	745	795	1087	636	518	480	83.7	465	50.6	20.0	527	448	423	388	0.76	234
Q13	60	IB	72.9	-0.68	1400	Pt	Loop	575	744	790	1056	614	509	473	57.4	456	27.4	6.84	530	432	391	352	0.56	139
Q26	3	IB	67.9	-3.05	1400	Pt	Box	573	760	792	908	633	498	504	303	436	226	137	396	446	475	370	0.79	500

	t (min)	comp	m (mg)	log(fO_2)	T (°C)	capsule	type	Li	P	V	Cu	Zn	Ga	Ge	As	Rb	Ag	Cd	In	Sn	Sb	Cs	Tl	Pb
Q27	15	IB	68.5	-3.05	1400	Pt	Box	604	770	775	677	623	528	504	349	449	79.3	93.9	462	434	461	377	0.70	516
Q28	30	IB	67.2	-3.05	1400	Pt	Box	593	783	788	486	602	500	462	188	447	31.2	27.1	455	361	414	383	0.53	388
Q29	60	IB	66.7	-3.05	1400	Pt	Box	582	776	777	368	566	509	376	92.1	441	6.69	6.00	452	281	384	372	0.30	234
Q50	3	IB	71.4	-6.01	1400	Pt(Fe s)	Box	586	762	768	967	601	500	438	155	449	123	30.0	492	350	447	387	1.58	440
Q51	15	IB	70.5	-5.94	1400	Pt(Fe s)	Box	580	756	780	540	240	494	224	54.1	442	3.64	0.68	296	92.7	292	377	0.29	126
Q52	30	IB	70.7	-5.94	1400	Pt(Fe s)	Box	577	791	771	324	170	479	200	36.7	443	3.41	1.51	206	42.2	173	385	0.21	73.0
Q53	60	IB	68.2	-6.01	1400	Pt(Fe s)	Box	571	769	757	253	101	456	137	20.7	432	0.84	0.63	155	30.6	124	356	0.12	61.3
Q17	3	IB	64.7	-8.02	1400	Re	Box	578	647	758	1196	554	454	494	399	446	271	17.7	280	434	454	359	1.16	423
Q18	15	IB	69.2	-8.02	1400	Re	Box	552	732	772	864	208	448	284	207	391	40.4	5.48	119	215	257	274	0.49	161
Q19	30	IB	70.5	-8.02	1400	Re	Box	580	743	791	617	29.2	477	171	115	422	0.71	0.44	31.0	93.4	128	310	0.07	23.5
Q21	60	IB	70.2	-7.98	1400	Re	Box	571	708	780	379	27.7	421	71.4	38.4	377	0.59	0.44	18.6	55.1	65.3	247	0.08	22.6
Q30	3	AN	66.7	-0.68	1400	Pt	Box	605	681	528	998	579	442	527	532	479	442	615	452	503	503	440	9.62	564
Q31	15	AN	69.8	-0.68	1400	Pt	Box	601	656	494	903	558	491	506	516	484	361	558	491	501	500	466	15.2	579
Q32	30	AN	69.2	-0.68	1400	Pt	Box	582	679	502	823	565	475	474	519	464	213	543	469	486	491	452	9.55	563
Q33	60	AN	67.9	-0.68	1400	Pt	Box	575	639	498	655	564	482	494	513	454	104	523	488	492	476	431	8.45	569
Q34	3	AN	67.4	-3.05	1400	Pt	Box	590	667	483	950	559	475	574	508	467	390	574	512	489	497	453	78.8	565
Q35	15	AN	68.0	-3.05	1400	Pt	Box	579	651	511	845	559	458	535	521	446	241	558	464	471	469	421	37.3	563
Q36	30	AN	69.9	-3.05	1400	Pt	Box	598	649	495	752	562	498	441	539	451	132	559	474	473	478	411	10.6	562
Q37	60	AN	71.2	-3.05	1400	Pt	Box	587	647	505	678	563	508	498	533	458	57.0	554	500	484	483	426	3.79	572
Q38	3	AN	69.9	-6.05	1400	Pt(Fe s)	Box	579	607	465	784	523	435	475	499	422	318	539	543	426	439	400	46.1	546
Q39	15	AN	70.0	-6.05	1400	Pt(Fe s)	Box	576	597	470	514	529	450	459	479	432	106	579	458	479	454	417	68.9	553
Q40	30	AN	69.5	-5.98	1400	Pt(Fe s)	Box	586	639	492	318	521	454	490	511	442	16.5	478	445	423	436	417	41.1	514
Q41	60	AN	67.5	-5.98	1400	Pt(Fe s)	Box	601	682	489	246	516	450	479	485	450	6.30	458	440	423	425	419	44.3	504
Q42	3	AN	67.6	-8.02	1400	Re	Box	597	727	504	1083	534	428	403	499	458	187	535	492	482	461	432	11.7	537
Q43	15	AN	68.3	-8.02	1400	Re	Box	587	603	483	919	545	490	566	514	462	43.0	533	489	499	479	436	11.6	545
Q44	30	AN	70.0	-8.02	1400	Re	Box	562	629	471	655	492	424	466	454	416	11.1	391	467	432	419	381	26.8	458
Q45	60	AN	69.6	-8.02	1400	Re	Box	586	600	498	396	469	480	546	452	442	1.77	376	443	438	450	390	3.49	442
Q54	15	IB-G	68.7	-0.68	1300	Pt	Loop	575	779	760	1149	646	490	492	381	458	302	213	449	460	444	432	14.7	409
Q55	30	IB-G	68.9	-0.68	1300	Pt	Loop	566	771	750	1069	607	478	482	280	448	126	44.1	441	448	427	410	2.27	259
Q56	60	IB-G	72.7	-0.68	1300	Pt	Loop	576	767	757	1070	626	473	466	222	434	65.0	23.8	431	439	410	384	1.46	198
Q63	15	IB-G	69.1	-6.99	1300	Pt(Fe s)	Loop	576	788	758	950	506	464	346	162	442	19.6	6.41	375	267	371	405	1.64	259
Q64	30	IB-G	71.6	-6.99	1300	Pt(Fe s)	Loop	564	768	754	928	398	475	317	130	449	2.41	3.98	348	207	352	406	1.15	187
Q65	60	IB-G	67.8	-6.99	1300	Pt(Fe s)	Loop	569	814	756	700	70.3	497	119	21.2	454	0.10	0.10	155	41.5	190	403	0.04	18.7

	t (min)	comp	m (mg)	log(fO_2)	T (°C)	capsule	type	Li	P	V	Cu	Zn	Ga	Ge	As	Rb	Ag	Cd	In	Sn	Sb	Cs	Tl	Pb
Q57	15	IB-G	70.3	-8.94	1300	Re	Loop	556	780	753	1033	144	484	274	161	422	2.13	7.10	158	240	291	363	1.86	83.6
Q58	30	IB-G	72.7	-8.94	1300	Re	Loop	560	788	735	780	86.2	460	223	132	434	0.29	2.69	77.8	164	224	386	1.18	51.0
Q59	60	IB-G	71.6	-8.94	1300	Re	Loop	562	753	742	519	19.3	423	111	69.8	417	-	1.32	27.6	79.8	101	346	0.57	13.6
Q60	15	IB-G	69.3	-11.00	1300	Re	Loop	579	794	777	760	314	471	408	348	455	26.1	117	232	314	356	426	17.1	247
Q61	30	IB-G	70.1	-11.00	1300	Re	Loop	592	802	778	383	169	430	261	99.1	472	5.38	64.4	132	211	189	437	9.11	151
Q62	60	IB-G	69.4	-11.00	1300	Re	Loop	581	751	770	161	39.8	334	142	17.6	449	0.18	10.7	30.3	84.8	69.4	394	2.14	41.7
Q66	3	SM-2	67.8	-0.68	1400	Pt	Box	-	-	-	2354	3542	-	2169	-	-	2302	2560	-	2408	-	-	1336	-
Q67	15	SM-2	69.4	-0.68	1400	Pt	Box	-	-	-	2110	3471	-	2150	-	-	1281	1081	-	2362	-	-	405	-
Q68	30	SM-2	68.7	-0.68	1400	Pt	Box	-	-	-	1827	3447	-	2121	-	-	694	481	-	2348	-	-	153	-
Q69	60	SM-2	70.5	-0.68	1400	Pt	Box	-	-	-	1451	3154	-	2024	-	-	138	34.8	-	2138	-	-	8.22	-
Q70	3	SM-2	68.8	-3.05	1400	Pt	Box	-	-	-	2111	3417	-	2107	-	-	1989	1459	-	2314	-	-	1027	-
Q71	15	SM-2	70.0	-3.05	1400	Pt	Box	-	-	-	1190	3051	-	1975	-	-	348	92.1	-	1873	-	-	254	-
Q72	30	SM-2	71.4	-3.05	1400	Pt	Box	-	-	-	972	2880	-	1797	-	-	115	9.52	-	1702	-	-	51.1	-
Q73	60	SM-2	72.4	-3.05	1400	Pt	Box	-	-	-	623	2597	-	1413	-	-	25.0	1.80	-	1130	-	-	16.2	-
Q74	3	SM-2	69.7	-6.10	1400	Re	Box	-	-	-	2298	2296	-	1331	-	-	114	16.7	-	1534	-	-	34.2	-
Q75	15	SM-2	70.4	-6.10	1400	Re	Box	-	-	-	2065	379	-	147	-	-	0.07	0.03	-	391	-	-	0.01	-
Q76	30	SM-2	70.9	-6.10	1400	Re	Box	-	-	-	1661	41.9	-	19.0	-	-	0.05	0.02	-	102	-	-	0.004	-
Q77	60	SM-2	73.5	-6.10	1400	Re	Box	-	-	-	957	0.86	-	0.56	-	-	0.06	0.14	-	2.48	-	-	0.01	-
Q78	3	SM-2	67.4	-8.01	1400	Re	Box	-	-	-	2255	279	-	426	-	-	78.3	0.05	-	1100	-	-	85.4	-
Q79	15	SM-2	69.8	-8.01	1400	Re	Box	-	-	-	1413	1.43	-	9.50	-	-	2.96	0.03	-	137	-	-	0.10	-
Q80	30	SM-2	70.5	-8.01	1400	Re	Box	-	-	-	993	0.78	-	4.97	-	-	0.07	0.02	-	55.7	-	-	0.07	-
Q81	60	SM-2	69.6	-8.01	1400	Re	Box	-	-	-	385	0.66	-	-	-	-	-	0.03	-	1.62	-	-	0.01	-

Table 4.3: The experimental conditions and LA-ICP-MS trace element abundances (ppm) for the volatility experiments. A "-" indicates the abundance was either below the detection limit or not measured. The "(Fe s)" indicates that the sample holders were pre-saturated before the experiment.

For "comp" SM, IB and AN were doped with the halogen-bearing trace element mix, IB-G was the glassed starting material and SM-2 was doped with a halogen-free trace element mix (see Chapter **2**). Masses represent the mass of sample material loaded into the furnace. For oxygen fugacity a log(fO_2) of -0.68 represents air. At 1400°C: log(fO_2) values of -3, -6 and -8 correspond to ΔIW+6.7, ΔIW+3.7 and ΔIW+1.7 respectively. At 1300°C: log(fO_2) values of -7, -9 and -11 correspond to ΔIW+3.8, ΔIW+1.8 and ΔIW-0.2.

Instrument operating conditions and analytical precision on individual measurements were discussed in detail in Chapter **2**.

The standard deviations on the average trace element abundances are available in Appendix **4**.

4.3.2 – Compositional Gradients

Electron microprobe analysis of samples Q6–Q53 showed that major element compositional variability within a sample was negligible. Minor variability in FeO_T between samples at different fO_2 was attributed to Pt-Fe alloy formation with the steps taken to minimize these interactions discussed in Chapter **2**. Trace element zoning was assessed by measuring 20 points placed along transects perpendicular to both the evaporation interface and sample-sample holder interface into the sample. This yielded two perpendicularly orientated compositional profiles. The remainder of this section will show examples of compositional gradients, but for all transects the reader is referred to the Supplementary Information **Zoning Profiles**.

4.3.2.1 – Evaporation Induced Compositional Gradients

Transects from the evaporative surface into the sample showed that trace element abundances were not homogeneous in all samples and that compositional gradients were common. The ubiquity and magnitude of these gradients correlated well with the composition of the silicate melt, the fO_2 and the element of interest. Compositional gradients were not observed for elements that were either refractory (Li, P, V, Ga) or monovalent (Cu^+, Ag^+, Rb^+ and Cs^+) in the silicate melt but were observed for the higher valence elements (Zn^{2+}, Ge^{4+}, As^{3+}, In^{3+}, Sn^{4+}, Sb^{3+} and Pb^{2+}). For the highly volatile elements (Ag, Cd and Tl) it was not possible to measure compositional gradients in most samples as the higher detection limits inhibited accurate concentration measurements across the full transect (Fig. **4.2**).

The absence of compositional gradients in the SM composition for all but the most volatile elements in the shortest experiments in reducing conditions suggested that diffusion rates exceed evaporation rates for all elements. For the IB composition only the monovalent elements did not exhibit compositional gradients. The higher valence elements developed compositional gradients for the experiments in more reducing conditions at $\log(fO_2) = -6$ and $\log(fO_2) = -8$. This suggested that the increased evaporation rate, as a result of decreasing fO_2, exceeded the diffusion rate. For the AN

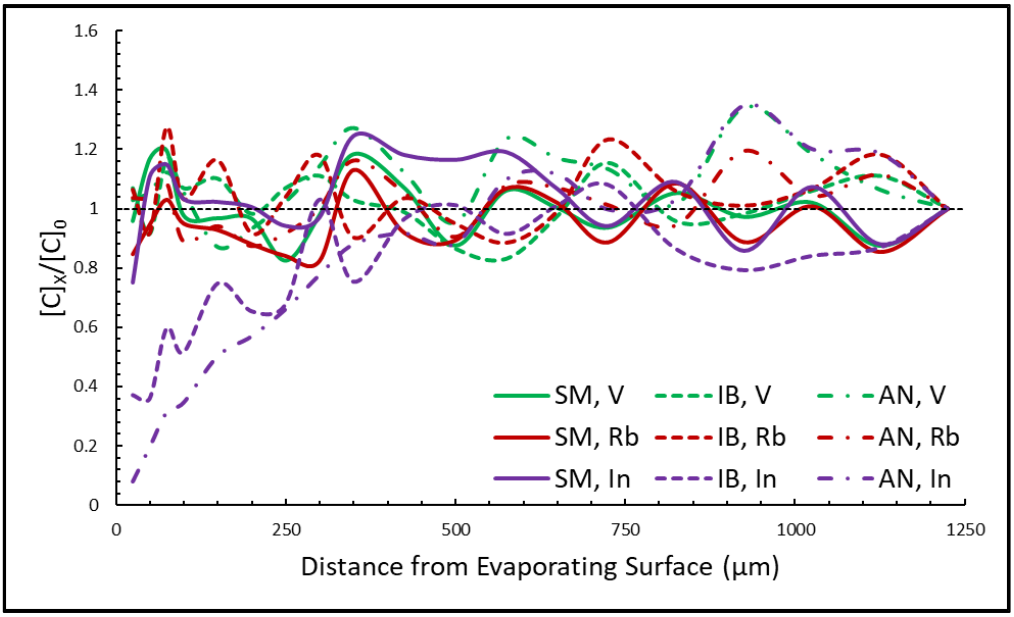


Figure 4.2: Compositional gradients for a refractory (V), low valence (Rb) and high valence moderately volatile (In) element in the three major element compositions at log(fO_2) = -6 after 60 minutes. Concentrations were normalized to the data point furthest away from the evaporating surface. The error on an individual measurement was ~±15%.

composition the only elements that did not exhibit compositional gradients were the monovalent elements (Cu, Rb, Ag and Cs). However, the compositional gradients were not reflected in the bulk trace element composition, which remained approximately constant, as diffusion coefficients were orders of magnitude lower than in the SM and IB compositions and volatile losses were only observed in the melt close to the evaporation interface.

Compositional gradients became more abundant with decreasing oxygen fugacity. This was consistent with the properties of the evaporation reactions. For all but one of the evaporation reactions considered in this study the silicate melt species is more oxidized than the gas species. For these reactions it can be shown that the equilibrium shifts further towards the gas phase with decreasing fO_2. Diffusion coefficient are expected to be independent of fO_2 unless changing fO_2 affects the oxidation state of the trace element or indirectly affects melt properties. Therefore a decrease in fO_2 may result in the evaporation rate exceeding the diffusion rate.

Mungall (2002) showed that diffusion was related to the ionic charge to ionic radius ratio of the trace element and the properties of the silicate melt, particularly viscosity. Diffusion coefficients (D) were

calculated for all trace elements using the Mungall (2002) model with viscosities calculated using Shaw (1972). Resulting D values were between $5.3 \cdot 10^{-10}$ – $1.1 \cdot 10^{-9}$ m^2s^{-1} for SM, $1.9 \cdot 10^{-12}$ – $1.1 \cdot 10^{-9}$ m^2s^{-1} for IB and $1.2 \cdot 10^{-15}$ – $1.1 \cdot 10^{-9}$ m^2s^{-1} for AN. This showed that D for the SM composition had a much smaller range than D for the IB and AN compositions. The D of the monovalent elements was almost independent of composition, e.g. $D_{Cu,SM} = 1.12 \cdot 10^{-9}$ m^2s^{-1}, $D_{Cu,IB} = 1.06 \cdot 10^{-9}$ m^2s^{-1} and $D_{Cu,AN} = 1.09 \cdot 10^{-9}$ m^2s^{-1}, whereas the D of higher valence elements decreased from SM > IB > AN, e.g. $D_{Sn,SM} = 1.72 \cdot 10^{-9}$ m^2s^{-1}, $D_{Sn,IB} = 5.11 \cdot 10^{-12}$ m^2s^{-1} and $D_{Sn,AN} = 1.31 \cdot 10^{-14}$ m^2s^{-1}. This was most egregious for high valence elements (Ge^{4+} and Sn^{4+}) where D varied up to six orders of magnitude between the SM and AN compositions.

These observations illustrate that the presence of compositional gradients in some samples and their absence in others is a result of the differences between the rate of diffusion of the trace element in the silicate melt and the rate of evaporation at the surface. There will be no compositional gradients for experiments where the diffusion rate exceeds the evaporation rate. For experiments where the evaporation rate exceeds the diffusion rate compositional gradients will form. This fits observations by Xue et al. (1996), Sossi et al. (2020) and Zhang et al. (2021) that evaporation from silicate melts can be a diffusion-limited process.

4.3.2.2 – Interaction with the Sample Holder

In Chapter **2** the use of different noble metal sample holders was discussed to minimize Fe loss during experiments in more reducing conditions. Certain trace elements may also interact with the Pt sample holders. Sossi et al. (2019) found that Cu, Ga, Ag and Pb potentially dissolve into Pt metal, but they concluded that the effect trace element diffusion into the Pt on the total trace element budget was negligible. Their use of a wire loop set-up over the box-shaped sample holders used in this study meant a significantly smaller contact area between the melt and Pt. However, depending on the size of the sample the ratio of sample to sample holder material may be higher.

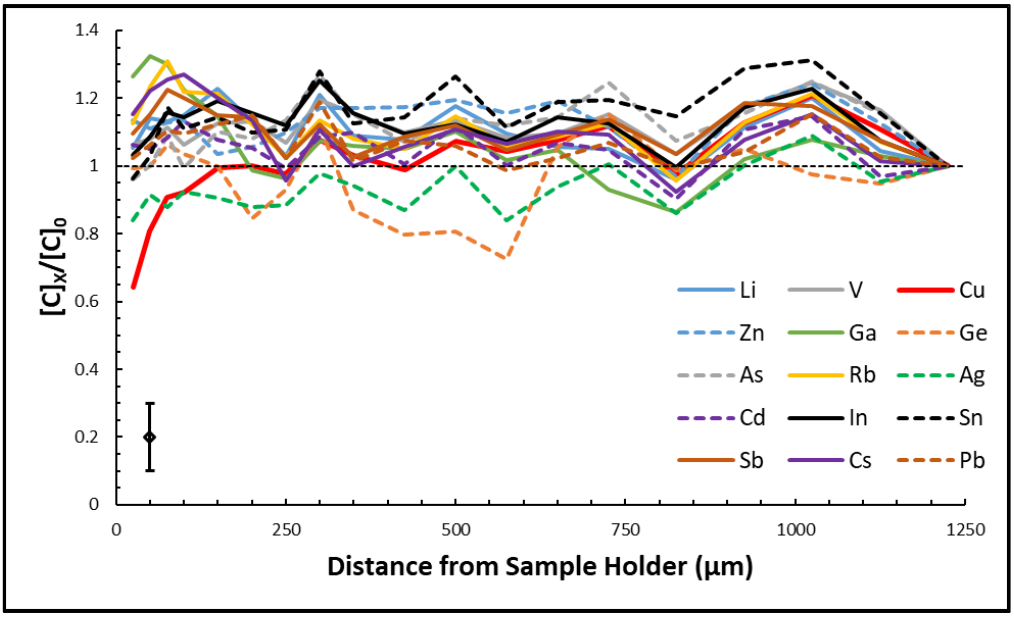


Figure 4.3: Plot of compositional gradients from the sample – sample holder interface into the sample for a Pt sample holder. Measured concentrations were normalized to data point furthest away from sample holder. Error bar in bottom left indicates the average one standard deviation on the measurements.

The transects from the sample holder into the sample showed that there were no observed depletions for experiments in air or for those with Fe-presaturated or Re sample holders. However, for experiments with Pt in a CO_2 atmosphere ($\log(fO_2) \approx -3.05$) there was a gradient observed for Cu close to the Pt sample holder which disappeared after ~150 µm and for Ag a potentially shallower gradient with Ag concentrations gradually climbing with distance from the sample holder (Fig. **4.3**). Further analysis of Pt and Re sample holders for either all trace elements (LA-ICP-MS) or just Cu (EPMA) did not provide evidence of significant trace element loss from the sample to the sample holder.

4.3.3 – Metal Blobs

The time series at 1300°C and $\log(fO_2) = -11$ contained small metal blobs that were observable with an optical microscope. This time series was the most reducing of all experiments with the T-fO_2 conditions just below the iron-wüstite oxygen buffer reaction (ΔIW-0.25). The metal blobs were too small to accurately quantify their trace element abundance without also ablating the surrounding silicate melt. However, the measurements where metal blobs were purposefully ablated had elevated Ni, Ga, Ge, Mo, As, Sn and Sb contents and decreased Zn, Cd and In contents compared to measurements of the same sample that avoided metal blobs. This was in agreement with the expected

general lithophile and siderophile behaviour of these elements (Goldschmidt, 1930). However, the presence of this additional metallic phase potentially affected volatility and therefore these experiments were omitted from quantifying volatility with the modified HKL equation.

4.3.4 – Refractory Elements

Lithium, phosphorus and vanadium exhibited no quantifiable volatile loss or compositional gradients in any experiment. These elements were considered refractory within the conditions of this study and could not be used to quantify volatility. They will not be discussed in detail in subsequent sections.

4.3.5 – Highly Volatile Elements

Silver, cadmium and thallium were elements where >95% of the starting abundance was lost rapidly at all fO_2 except in air. Because the volatility factor for the HKL equation was calculated by normalizing to the three minute experiment in each time series, these elements had artificially enhanced volatility factors that were not representative of their actual volatility. Moreover, the fO_2 dependence of the volatility factor at constant runtime only yielded a scatter or had between two and four of the data points approaching $C_i^t / C_i^0 \rightarrow 0$, depending on the choice of C_i^0. The exception to this was Cd in the AN composition where the diffusion-limited evaporation environment meant most Cd was retained in the melt. For these elements it was not possible to accurately quantify volatility using the modified HKL equation.

4.3.6 – Moderately Volatile Elements

Eleven elements (Cu, Zn, Ga, Ge, As, Rb, In, Sn, Sb, Cs and Pb) were considered to be moderately volatile in that they exhibited varying degrees of volatile loss in most experiments. These elements covered a range of volatile behaviour with the more refractory (Ga, Rb and Cs) elements only experiencing volatile loss in the low viscosity compositions and/or in more reducing conditions whereas the other moderately volatile elements exhibited losses in all SM and IB experiments. For the AN composition evaporative loss was strongly diffusion-limited as localized compositional gradients

were ubiquitous for polyvalent elements. These compositional gradients were only present near the evaporative surface and this volatile loss was not reflected in the bulk trace element measurements, inhibiting assessment of volatility in AN. The only moderately volatile element for which volatility was quantifiable across all conditions in the AN composition was Cu.

4.4 – Volatility Factors

The volatility factor (Norris and Wood, 2017) enabled a qualitative assessment of relative volatility for different elements. Tables of volatility factors normalized to the shortest experiment in each time series and normalized to the starting trace element abundances from Table **2.2** can be found Appendix **4**. The volatility factor of an element is affected by runtime, oxygen fugacity and silicate melt composition. A more quantitative approach that incorporates these parameters, in the form of the modified HKL equation, is covered later in this chapter.

The figures describing the time, fO_2 and compositional dependence of the volatility factor were plotted using C_0 from Table **2.2** instead of the shortest experiment at the same fO_2. This did not adhere to the C_0 defined in Chapter **2** for the application of the modified HKL equation. This was done to demonstrate the importance of properly defining C_0 as these figures showed clearly that the degree of volatile loss during melting changed depending on the experimental conditions. The speciation of a trace element during melting may not accurately reflect its volatility in the silicate melt. This is most clear for Rb and Cs, added as carbonates, which are lost during melting and retained in the melt afterwards. Since the modified HKL equation considers an evaporation reaction it was necessary to normalize to the shortest experiment in each time series to ensure the trace element was present in the appropriate species in the silicate melt.

4.4.1 – Temporal Evolution

The temporal evolution of volatile loss for time series at constant T, fO_2 and composition followed the $\ln\left(C_i^t/C_i^0\right) \propto t$ correlation predicted by the modified HKL equation. This was observed for most of the time series, independent of composition and experimental conditions, where the trace element concentrations did not approach the detection limit (Fig. **4.4**). Time series plots for all elements can be found in Appendix **5**.

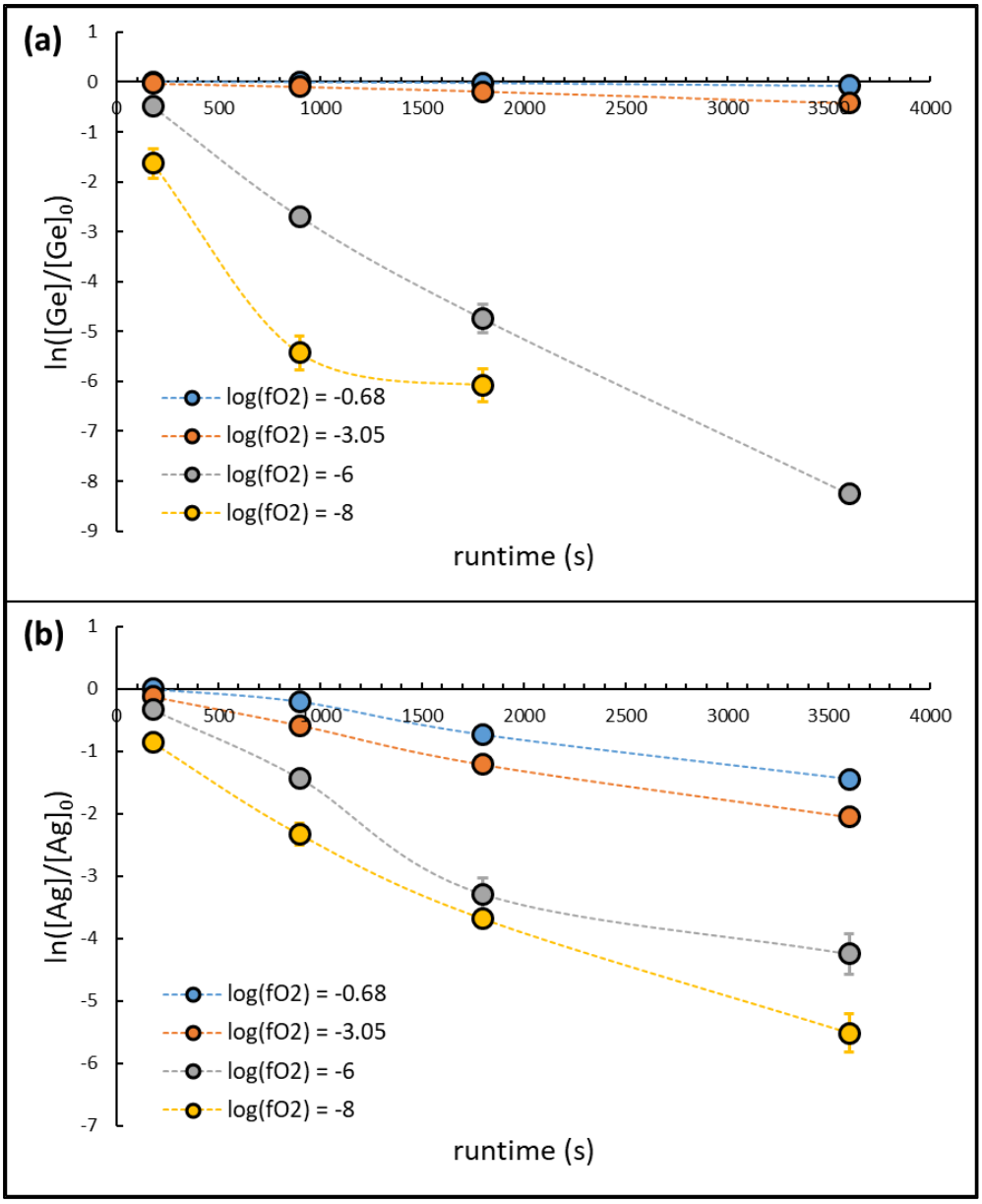


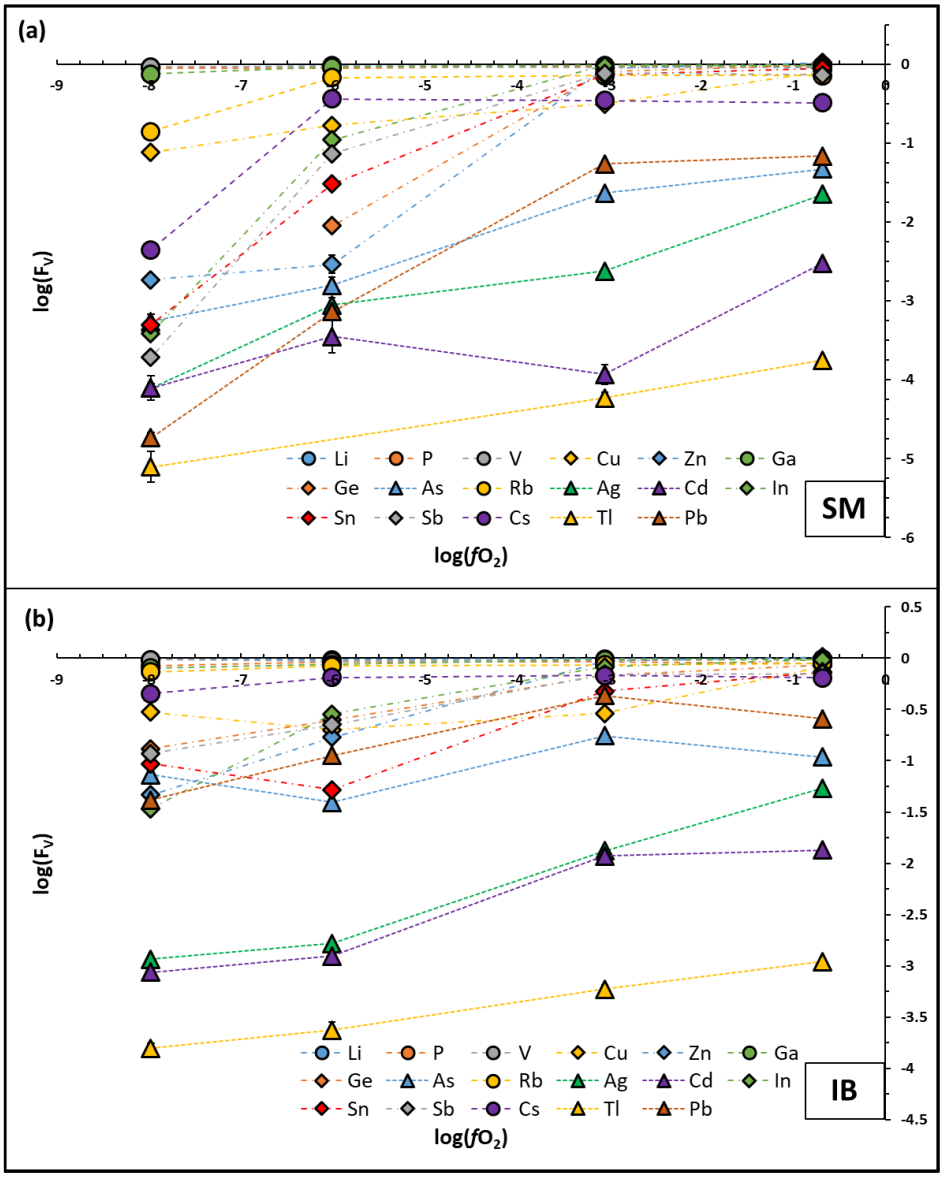
Figure 4.4: Temporal evolution of trace element abundances in the silicate melt normalized to the starting abundance in Table **2.2**. **(a)** Germanium in the SM-2 experiments. Deviations from linearity in the log(fO_2) = -8 time series is caused by the detection limit in LA-ICP-MS analysis. **(b)** Silver in the AN composition.

4.4.2 – Effect of Oxygen Fugacity

Figure **4.4** confirmed that trace element evaporation is oxygen fugacity dependent as the slope of the time dependence increased with decreasing fO_2. This observation was consistent for most elements considered in this study. For Cu some time series in Pt sample holders exhibited more loss than those in Re capsules, likely in part due to Cu loss to the Pt. Also, for the most volatile elements small variations close to detection limits may cause deviations from this trend. To illustrate this fO_2 dependence and enable comparison of trace element volatility across a range of fO_2 the logarithm of

the volatility factor of the 60 minute experiments was plotted against log(fO_2) for all compositions (Fig. **4.5**). This figure showed that both the number of elements exhibiting volatile loss and the magnitude of the volatile loss increased with decreasing fO_2. Furthermore, a comparison of the moderately volatile elements suggested that there was a compositional control on volatility as the observed magnitude of volatile loss was not consistent between compositions.

Another observation was that the rate of volatile loss was not necessarily constant as a function of fO_2. Figure **4.5a** showed that Rb and Cs only exhibited volatile loss at log(fO_2) = -8, but were retained in the silicate melt in more oxidizing conditions. Moreover, Figures **4.5a** and **4.5b** showed that F_{Pb} is similar for the experiments at log(fO_2) = -0.68 and -3.05, but decreases rapidly in more reducing



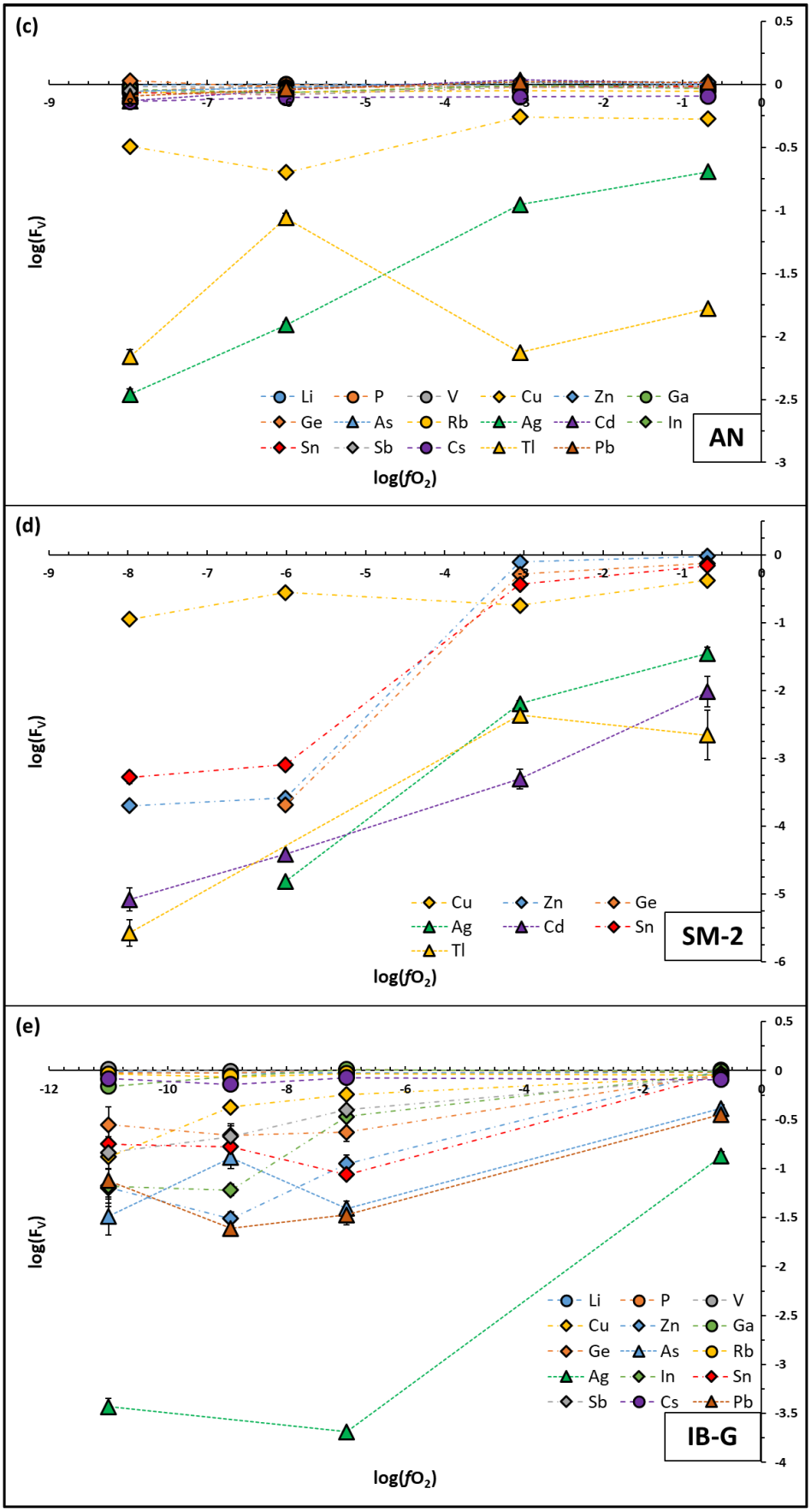


Figure 4.5: The fO_2 dependence of the volatility factor for the **(a)** SM, **(b)** IB, **(c)** AN, **(d)** SM-2 and **(e)** IB-G compositions.

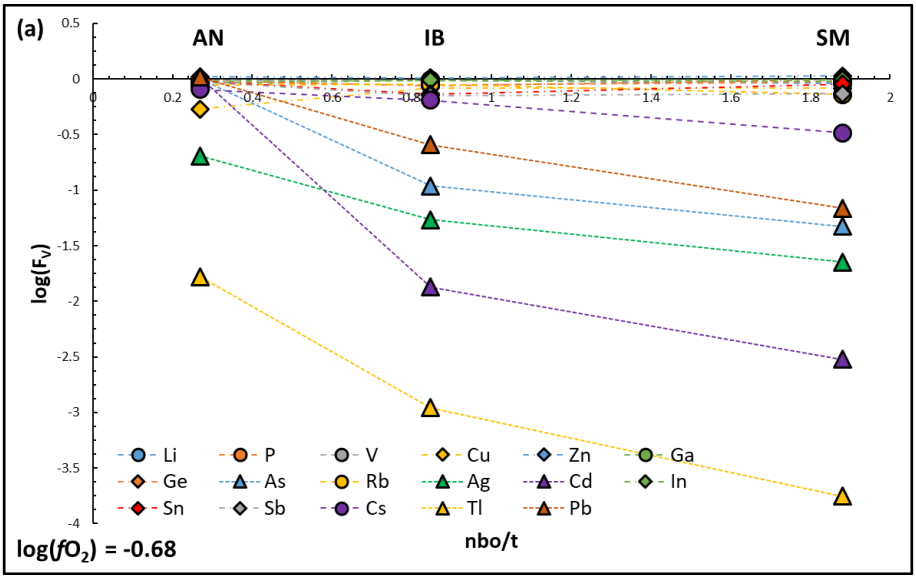
conditions. This may be explained by changes in the predominant evaporation reactions. While the limited number of data points inhibit accurate determination of the exact fO_2 where the slope changes it does roughly match the fO_2 for the changes in dominant gas species from CsO (g) to Cs (g) and from PbO (g) to Pb (g). For Rb only one gas species was considered and therefore it may indicate that there was an additional evaporation to consider at higher fO_2.

4.4.3 – Effect of Melt Composition

The compositional gradients observed in most samples indicated that diffusion rates, and therefore melt composition, acted as a control on evaporative loss. Nbo/t was used to describe differences between melt compositions (Mills, 1993). This parameter describes melt polymerization in terms of the ratio of non-bridging oxygens to tetrahedrally coordinated cations and can be calculated from the major element composition of the melt (Eq. **4.1**). In this equation $O = X_O$ and $T = X_{Si} + X_{Al} + X_{Ti}$ of the silicate melt. Normally T should also include the Fe^{3+} mole fraction, but since Fe was measured as FeO_T its speciation was not considered.

$$(Eq.4.1):\ nbo/t = \frac{2O - 4T}{T}$$

Equation **4.1** yields $(nbo/t)_{SM}$ = 1.88, $(nbo/t)_{IB}$ = 0.85 and $(nbo/t)_{AN}$ = 0.27. To assess the effects of silicate melt composition, nbo/t was plotted against the log of the volatility factor for the 60 minute experiments for SM, IB and AN (Fig **4.6**).



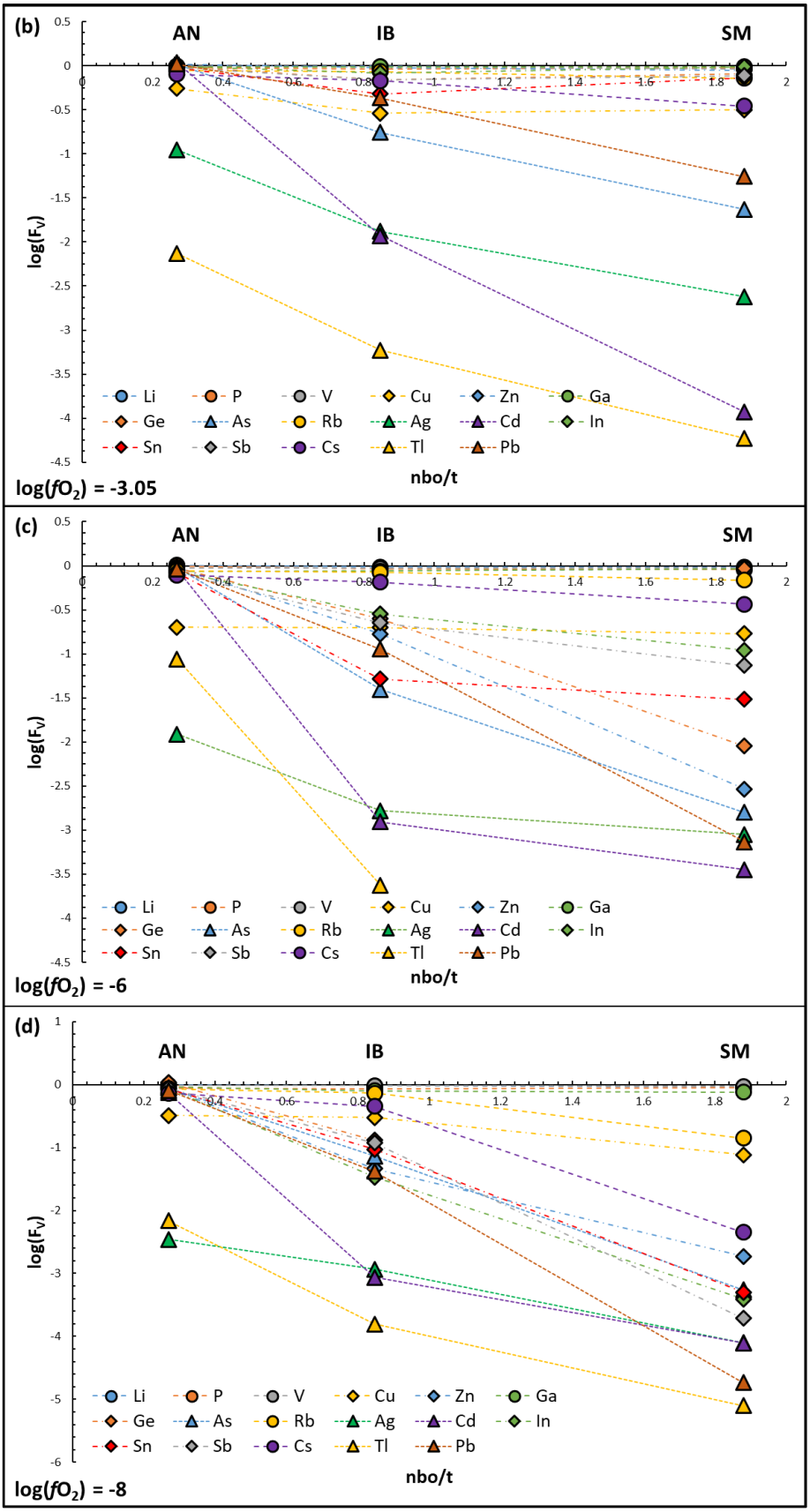


Figure 4.6: The compositional dependence of the volatility factor at **(a)** log(fO_2) = -0.68, **(b)** log(fO_2) = -3.05, **(c)** log(fO_2) = -6 and **(d)** log(fO_2) = -8.

These figures showed that the both the magnitude of volatile loss and the number of elements experiencing volatile loss decreased as the melt became more polymerized. The volatile loss of polyvalent trace elements decreased significantly as the degree of melt polymerization increased. This is best illustrated by considering the highly volatile Cd which was lost near-completely in the SM and IB compositions, but only exhibited limited volatile loss in the most reducing experiments in the AN composition.

The monovalent elements, Rb, Cu, Ag, Cs and Tl, appear to be least affected by changing melt composition. Silver and thallium are lost (near-)completely in all compositions whereas the flat slope of Cu in Figure **4.6** compared to other elements suggests its volatility was unaffected by changing silicate melt composition. The volatility of Rb and Cs in the SM experiments compared to IB and AN does suggest their volatility is affected by melt composition, despite no compositional gradients being observed. The observed decreased volatility for more polymerized melts, with the decrease more pronounced for higher valence elements, is an indicator that diffusion acted as a strong control on trace element volatility. A further discussion on diffusion-limited evaporation is available in Chapter **5**.

4.5 – The Modified Hertz-Knudsen-Langmuir Equation

The volatility of the moderately and highly volatile elements was quantified using the modified HKL equation. This was done in two separate ways; firstly by leaving both n and K* free, where it was checked if n matched the expected integer value based on the thermodynamic predictions (Table **4.1**). Next, log(K*) was calculated with n fixed at its predicted integer value. To assess the modelled fits using the modified HKL equation concentrations to the measured data and identify potential outliers the volatility factor was plotted against fO_2 at three runtimes, 15, 30 and 60 minutes (Fig. **4.7**). The log(K*) and variable n were calculated as an average of the values obtained for the three regressions. Overall, the regressions show that, for some elements, composition had an impact on the obtained log(K*). This was likely due to the effect of melt composition on the activity coefficient of the trace element species being reflected in K*.

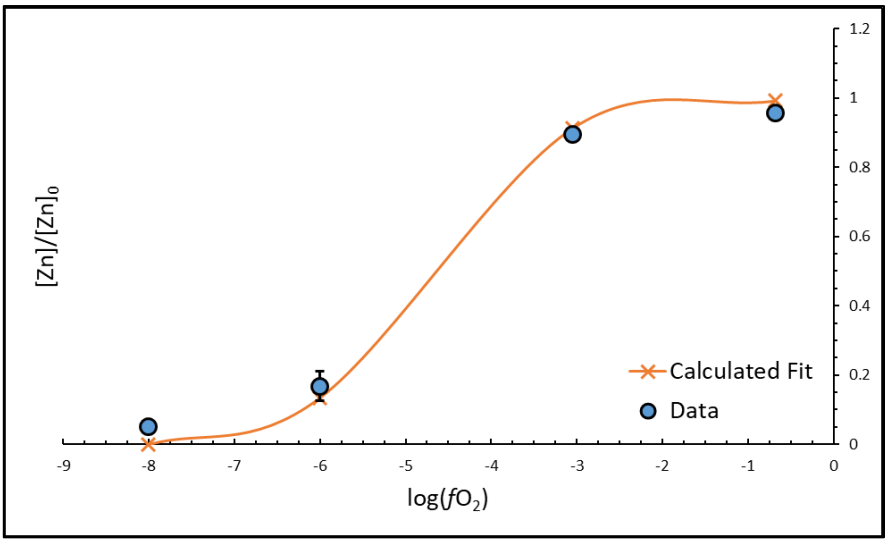


Figure 4.7: Example comparison of the fit, calculated using the modified HKL equation, to the measured trace element abundance.

Comparing with values in other studies is challenging due to the observed compositional effect on trace element volatility. However, the SM major element composition was mimicked from that of Sossi et al. (2019) and was close to the major element compositions of Liu et al. (2022; "FCMAS") and Heck (2022; "MVE-02"). Moreover, the MORB composition (Liu et al., 2022) compared reasonably well to the IB composition used in this work. The diffusion-limited evaporation environment in the AN composition suppressed volatile loss which inhibited accurate determination of the properties of the evaporation reactions for all elements except Cu.

4.5.1 – Copper

Copper was lost in all experiments, enabling quantification of the properties of the evaporation reaction for all starting materials. Solving for variable n and K* yielded consistent n and log(K*) values for all compositions at 1400°C with n ≈ 0.5 whereas for IB-G n is closer to one. The $\log(K^*)_{IB\text{-}G}$ was expectedly lower than $\log(K^*)_{SM}$, $\log(K^*)_{SM\text{-}2}$ and $\log(K^*)_{IB}$ (Table **4.4**).

	T (K)	n^1	$\log(K^*)^1$	n^2	$\log(K^*)^2$
SM	1673	0.53 ± 0.14	-2.37 ± 0.08	1	-3.14 ± 0.38
SM-2	1673	0.50 ± 0.16	-2.47 ± 0.11	1	-3.15 ± 0.09
IB	1673	0.55 ± 0.02	-2.44 ± 0.06	1	-3.00 ± 0.34
AN	1673	0.56 ± 0.05	-2.74 ± 0.07	1	-3.28 ± 0.07
IB-G	1573	0.74 ± 0.08	-3.83 ± 0.23	1	-4.51 ± 0.23
Sossi et al. (2019)	1573	-	-	1	-4.09 ± 0.12
	1673	-	-	1	-3.70 ± 0.10
Heck (2022)	1673	-	-	1	-4.05 ± 0.07

Table 4.4: The n and log(K*) values obtained via non-linear least squares regression using a [1]variable and [2]fixed n for the evaporation reaction Cu_2O (l) = 2 Cu (g) + 0.5 O_2 (g).

The consistently observed n ≈ 0.5 for variable n regressions may be explained by the presence of a second, concurrent, evaporation reaction with n < 1 which would reduce the average n below one. Two reactions that could have occurred and had n < 1 were $Cu_2O\ (l) + 0.5\ O_2\ (g) = 2\ CuO\ (g)$ and $Cu_2O\ (l) + Cl_2\ (g) = 2\ CuCl + 0.5\ O_2(g)$. Thermodynamic predictions suggested that the equilibrium partial pressure of CuO (g) was orders of magnitude below that of Cu (g) (Appendix **2**). CuCl (g) was expected to be more abundant in the gas phase than Cu (g) at relevant fO_2 and fCl_2 and may provide an explanation (Appendix **3**). However the strong similarity of n and log(K*) for the halogen-bearing (SM) and halogen-free (SM-2) experiments suggested that halogen speciation did not significantly affect n and log(K*). An alternative explanation would be that the formation of Cu-Pt alloys may have acted as a Cu sink in experiments with Pt sample holders as these elements are known to alloy (Liu et al., 2009). However, since the CuPt alloy would have Cu^0 it would also involve a reaction where n = 1.

At fixed n the $\log(K^*)_{SM}$, $\log(K^*)_{SM\text{-}2}$, $\log(K^*)_{IB}$, $\log(K^*)_{AN}$ were identical within error an all are higher than the log(K*) obtained by Sossi et al. (2019) and Heck (2022). The $\log(K^*)_{IB\text{-}G}$ is slightly lower than the log(K*) obtained by Sossi et al. (2019).

4.5.2 – Zinc

Zinc exhibited volatile loss in the most experiments which enabled quantification of the properties of the Zn evaporation reaction in all starting materials. Solving for variable n and K* consistently yielded n ≈ 2 for SM, SM-2 and IB. The $\log(K^*)_{SM}$ was identical to $\log(K^*)_{IB}$, and both were ~0.5 log units above $\log(K^*)_{SM\text{-}2}$. For IB-G n < 2 and $\log(K^*)_{IB\text{-}G}$ was smaller than $\log(K^*)_{SM}$, $\log(K^*)_{SM\text{-}2}$ and $\log(K^*)_{IB}$ (Table **4.5**).

	T (K)	n^1	$\log(K^*)^1$	n^2	$\log(K^*)^2$
SM	1673	1.94 ± 0.12	-4.34 ± 0.10	2	-4.43 ± 0.28
SM-2	1673	1.90 ± 0.06	-3.91 ± 0.09	2	-4.07 ± 0.02
IB	1673	1.85 ± 0.02	-4.34 ± 0.08	2	-4.56 ± 0.08
AN	1673	-	-	-	-
IB-G	1573	1.70 ± 0.09	-4.86 ± 0.14	2	-5.57 ± 0.29
Sossi et al. (2019)	1573	-	-	2	-5.06 ± 0.09
	1673	-	-	2	-3.96 ± 0.09
Liu et al. (2022)	1573	-	-	2	-6.01 ± 0.12
	1673	-	-	2	-4.34 ± 0.10
Heck (2022)	1573	-	-	2	-5.69 ± 0.10

Table 4.5: The n and log(K*) values obtained via non-linear least squares regression using a [1]variable and [2]fixed n for the evaporation reaction ZnO (l) = Zn (g) + 0.5 O_2 (g).

At fixed n $\log(K^*)_{SM}$, $\log(K^*)_{SM\text{-}2}$ and $\log(K^*)_{IB}$ compositions were similar and comparable to the log(K*) reported by Sossi et al. (2019) and Liu et al. (2022). The $\log(K^*)_{IB\text{-}G}$ was within error of the log(K*) of Heck (2022) and compared reasonably well with the values of Sossi et al. (2019) and Liu et al. (2022).

4.5.3 - Gallium

Gallium was among the least volatile of the elements considered in this study. Losses were only observed for the experiments at $\log(fO_2) = -8$ at 1400°C in SM and for those at $\log(fO_2) = -7$ and below in IB-G. Therefore data to quantify of the properties of the evaporation reaction was limited and it was not possible to have a compositional comparison. For SM only the 60 minute and for IB-G the 30

and 60 minute fO_2 series had sufficient volatile loss to solve for n and log(K*). Solving for variable n yielded values that are close, but slightly below the expected n = 3 (Table **4.6**).

The $\log(K^*)_{SM}$ at fixed n was an order of magnitude above the value obtained by Sossi et al. (2019). No values were found in literature for Ga volatility at 1300°C to compare with $\log(K^*)_{IB\text{-}G}$.

	T (K)	n^1	$\log(K^*)^1$	n^2	$\log(K^*)^2$
SM	1673	2.73[3]	-8.30[3]	3	-8.85[3]
SM-2	1673	-	-	-	-
IB	1673	-	-	-	-
AN	1673	-	-	-	-
IB-G	1573	2.71 ± 0.16[4]	-9.96 ± 0.50[4]	3	-10.25 ± 0.58[4]
Sossi et al. (2019)	1673	-	-	3	-9.92 ± 0.32

Table 4.6: The n and log(K*) values obtained via non-linear least squares regression using a [1]variable and [2]fixed n for the evaporation reaction Ga_2O_3 (l) = 2 Ga (g) + 1.5 O_2 (g). [3]Value was based on a single fO_2 series. [4] Value was based on two fO_2 series.

4.5.4 – Germanium

Germanium exhibited volatile loss in the SM and IB compositions, but not for AN. Solving for variable n and K* yielded consistent n ≈ 2, but $\log(K^*)_{SM}$, $\log(K^*)_{SM\text{-}2}$ and $\log(K^*)_{IB}$ were more variable (Table **4.7**). For the IB-G experiments n ≠ 2 and $\log(K^*)_{IB\text{-}G}$ was above the values obtained at higher temperature where the opposite would be expected considering the temperature dependence of the equilibrium constant of an evaporation reaction.

	T (K)	n^1	$\log(K^*)^1$	n^2	$\log(K^*)^2$
SM	1673	1.92 ± 0.04	-4.33 ± 0.22	2	-4.47 ± 0.29
SM-2	1673	1.98 ± 0.07	-3.94 ± 0.09	2	-3.97 ± 0.02
IB	1673	1.94 ± 0.01	-4.52 ± 0.06	2	-4.71 ± 0.14
AN	1673	-	-	-	-
IB-G	1573	0.69 ± 0.03	-3.18 ± 0.06	2	-5.86 ± 0.41
Sossi et al. (2019)	1573	-	-	2	-5.04 ± 0.13
	1673	-	-	2	-3.70 ± 0.06
Heck (2022)	1673	-	-	2	-4.12 ± 0.07

Table 4.7: The n and log(K*) values obtained via non-linear least squares regression using a [1]variable and [2]fixed n for the evaporation reaction GeO_2 (l) = GeO (g) + 0.5 O_2 (g).

The $\log(K^*)_{SM\text{-}2}$ at fixed n compared well with log(K*) obtained by Sossi et al. (2019) and Heck (2022) while $\log(K^*)_{SM}$ and $\log(K^*)_{IB}$ were lower. The difference of 0.5 log units between $\log(K^*)_{SM}$ and $\log(K^*)_{SM\text{-}2}$ was unexpected as Ge was not expected to form abundant chloride gas species (Appendix **3**). The $\log(K^*)_{IB\text{-}G}$ was ~0.8 log units below the value of Sossi et al. (2019).

4.5.5 – Arsenic

Arsenic was among the most volatile elements and was lost in the reducing experiments in the SM, IB and IB-G experiments, but was retained in AN. For the SM and IB compositions the large extent of volatile depletion resulted in a scatter and large misfits in some of the fO_2-F_V plots which inhibited accurate quantification of the properties of the As evaporation reaction. Solving for variable n and log(K*) showed that consistently n ≈ 0.3, independent of composition. This may suggest that an alternate reaction was taking place with n < 1. It is unlikely to be caused by the presence of $AsCl_3$ (g) as thermodynamic calculations showed that $\log(P_{AsCl3(g)}/P_{AsO\ (g)}) < 10^{-10}$ in all experiments. Alternate species cannot explain this decrease in n and it was more likely attributable to the scatter in the data resulting in poor fits. The log(K*) showed more variability between compositions and between fO_2 series within a single starting composition, resulting in larger errors on the average (Table **4.8**).

	T (K)	n^1	$\log(K^*)^1$	n^2	$\log(K^*)^2$
SM	1673	0.26 ± 0.05	-1.41 ± 0.08	1	-1.54 ± 0.08
SM-2	1673	-	-	-	-
IB	1673	0.28 ± 0.26	-2.00 ± 0.41	1	-2.28 ± 0.63
AN	1673	-	-	-	-
IB-G	1573	0.32 ± 0.09	-2.09 ± 0.08	1	-2.65 ± 0.62
Heck (2022)	1573	-	-	1	-4.09 ± 0.13
	1673	-	-	1	-2.44 ± 0.06

Table 4.8: The n and log(K*) values obtained via non-linear least squares regression using a [1]variable and [2]fixed n for the evaporation reaction As_2O_3 (l) = 2 AsO (g) + 0.5 O_2 (g).

At fixed n the log(K*) the fit between the modelled modified HKL equation solution and the measured data was poor. The $\log(K^*)_{IB}$ compared well with the value obtained by Heck (2022) whereas $\log(K^*)_{SM}$ was 0.7 – 0.8 log units above. The $\log(K^*)_{IB\text{-}G}$ was also an order of magnitude higher than the value obtained by Heck (2022).

4.5.6 – Rubidium

Rubidium was among the least volatility elements with volatility observed solely in experiments at 1400°C and $\log(fO_2) = -8$, volatile loss was not observed at 1300°C. Rb was lost relative to the expected starting abundance in the 3 minute experiments in all compositions attributed to volatile loss during

the decomposition of Rb_2CO_3. This did not impact the quantification of the properties of the evaporation reaction because of the normalization to the three minute experiments. Volatile losses in the IB composition were quantified, but the magnitude of volatile loss was substantially smaller than in SM and only for a few data points in a fO_2 series. Solving for variable n and log(K*) yielded consistent n values, slightly below the expected n = 1 and $\log(K^*)_{SM}$ and $\log(K^*)_{IB}$ were not similar (Table **4.9**).

	T (K)	n^1	$\log(K^*)^1$	n^2	$\log(K^*)^2$
SM	1673	0.84 ± 0.09	-3.46 ± 0.22	1	-3.77 ± 0.07
SM-2	1673	-	-	-	-
IB	1673	0.88 ± 0.02	-4.27 ± 0.19	1	-4.70 ± 0.23
AN	1673	-	-	-	-
IB-G	1573	-	-	-	-
Sossi et al. (2019)	1573	-	-	1	-4.15
	1673	-	-	1	-3.12 ± 0.10

Table 4.9: The n and log(K*) values obtained via non-linear least squares regression using a [1]variable and [2]fixed n for the evaporation reaction Rb_2O (l) = 2 Rb (g) + 0.5 O_2 (g).

At fixed n the $\log(K^*)_{SM}$ and $\log(K^*)_{IB}$ were lower than the value obtained by Sossi et al. (2019). Moreover, there was an order of magnitude difference between $\log(K^*)_{SM}$ and $\log(K^*)_{IB}$. The only other element for which a discrepancy of this magnitude is observed between SM and IB was Cs.

4.5.7 – Indium

Indium was among the moderately volatile elements and was partially retained in the SM and IB composition experiments and fully retained in AN. Solving for variable n and log(K*) yielded n ≈ 3 for SM and IB with $\log(K^*)_{SM}$ and $\log(K^*)_{IB}$ being. For IB-G, n < 3 and $\log(K^*)_{IB\text{-}G}$ was higher than for $\log(K^*)_{SM}$ and $\log(K^*)_{IB}$ (Table **4.10**). This was the opposite of what would be expected considering the temperature dependence of the equilibrium constant of the evaporation reaction, but may be caused by the poor fits and outlying n values as the log(K*) for fixed n do follow the expected temperature dependence.

For fixed n the observed $\log(K^*)_{SM}$ and $\log(K^*)_{IB}$ were identical within error, but are ∼2 log units below the value reported by Liu et al. (2022). The $\log(K^*)_{IB\text{-}G}$ compared well with that of Heck (2022), but was ∼2 log units below that of Liu et al. (2022).

	T (K)	n^1	$\log(K^*)^1$	n^2	$\log(K^*)^2$
SM	1673	2.84 ± 0.11	-5.85 ± 0.28	3	-6.11 ± 0.18
SM-2	1673	-	-	-	-
IB	1673	2.95 ± 0.10[3]	-6.15 ± 0.06[3]	3	-6.18 ± 0.10[3]
AN	1673	-	-	-	-
IB-G	1573	1.29 ± 0.34	-4.26 ± 0.71	3	-7.72 ± 0.44
Liu et al. (2022)	1573	-	-	3	-9.63
	1673	-	-	3	-8.01
Heck (2022)	1573	-	-	3	-8.00 (+0.67/-0.35)

Table 4.10: The n and log(K*) values obtained via non-linear least squares regression using a [1]variable and [2]fixed n for the evaporation reaction In_2O_3 (l) = 2 In (g) + 1.5 O_2 (g). [3]Value was based on two fO_2 series.

4.5.8 – Tin

Tin was among the moderately volatile elements and was partially retained in the SM and IB composition experiments and fully retained in AN. Solving for variable n and log(K*) yielded n < 2 for all compositions. Individual fO_2 series fits for IB and IB-G at different runtimes displayed a variety of n and log(K*) with n ≈ 2 for some fits, but n < 2 for others whereas fits for SM at different runtimes were consistently smaller than 2 (Table **4.11**).

	T (K)	n^1	$\log(K^*)^1$	n^2	$\log(K^*)^2$
SM	1673	1.60 ± 0.10	-3.58 ± 0.20	2	-4.09 ± 0.05
SM-2	1673	1.25 ± 0.10	-2.92 ± 0.14	2	-3.86 ± 0.28
IB	1673	1.76 ± 0.34	-3.80 ± 0.47	2	-4.26 ± 0.14
AN	1673	-	-	-	-
IB-G	1573	1.09 ± 0.61	-3.14 ± 0.27	2	-4.30 ± 1.15

Table 4.11: The n and log(K*) values obtained via non-linear least squares regression using a [1]variable and [2]fixed n for the evaporation reaction SnO_2 (l) = SnO (g) + 0.5 O_2 (g).

The log(K*) at fixed n were consistent between compositions for the SM, SM-2 and IB compositions. Poor fits for the IB-G composition resulted in $\log(K^*)_{IB\text{-}G}$ comparable to the $\log(K^*)_{IB}$ despite the 100°C temperature difference between the experiments, but with a large error. Considering the three IB-G fO_2 series fits separately two yield log(K*) ≈ -3.5 and one log(K*) ≈ -5.9.

4.5.9 – Antimony

Antimony wass among the moderately volatile elements and was partially retained in all SM and IB experiments, except for SM at $\log(fO_2)$ = -8, and fully retained in AN. Solving for variable n and log(K*)

yielded n ≈ 1 for SM, but n < 1 for IB and IB-G with comparable log(K*) for all compositions (Table **4.12**).

	T (K)	n^1	$log(K^*)^1$	n^2	$log(K^*)^2$
SM	1673	1.11 ± 0.25	-3.04 ± 0.45	1	-2.82 ± 0.11
SM-2	1673	-	-	-	-
IB	1673	0.75 ± 0.05	-2.88 ± 0.06	1	-3.25 ± 0.13
AN	1673	-	-	-	-
IB-G	1573	0.62 ± 0.05	-3.06 ± 0.10	1	-3.83 ± 0.09

Table 4.12: The n and log(K*) values obtained via non-linear least squares regression using a [1]variable and [2]fixed n for the evaporation reaction Sb_2O_3 (l) = 2 SbO (g) + 0.5 O_2 (g).

The log(K*) at fixed n were different between the SM and IB compositions and $log(K^*)_{IB\text{-}G}$ was smaller than that of IB. No values for Sb were found in literature.

4.5.10 – Caesium

Caesium was among the least volatile moderately volatile elements. It was partially retained in all SM and IB experiments with no observed volatile loss in AN. Cs was lost relative to the expected starting abundance in the 3 minute experiments in all compositions due to volatile loss attributed to the decomposition of Cs_2CO_3. This did not impact the quantification of the properties of the evaporation reaction because concentrations were normalized to the three minute experiments. Fitting for variable n and log(K*) yielded $n_1 \approx 1$ and $n_2 \approx -1$ for SM and IB whereas for IB-G $n_1 \neq 1$ and $n_2 \approx 1$. The obtained $log(K^*)_{SM}$ and $log(K^*)_{IB}$ for the n = 1 evaporation reaction were lower than those for the n = -1 evaporation. This was reversed for the $log(K^*)_{IB\text{-}G}$ of both reactions, likely caused by fits where $n_1 <$ 1 (Table **4.13**).

	T (K)	n^1	$log(K^*)^1$	n^2	$log(K^*)^2$
SM	1673	1.13 ± 0.27	-3.27 ± 0.58	1	-3.22 ± 0.05
		-0.92 ± 0.09	-1.81 ± 0.09	-1	-1.67 ± 0.12
SM-2	1673	-	-	-	-
IB	1673	1.08 ± 0.14	-4.40 ± 0.51	1	-4.25 ± 0.30
		-1.00 ± 0.09	-2.34 ± 0.40	-1	-2.63 ± 0.09
AN	1673	-	-	-	-
IB-G	1573	0.38 ± 0.19	-2.77 ± 0.39	1	-3.68 ± 0.23
		-0.96 ± 0.07	-3.48 ± 0.83	-1	-2.27 ± 0.11

Table 4.13: The n and log(K*) values obtained via non-linear least squares regression using a [1]variable and [2]fixed n for the evaporation reactions (1): Cs_2O (l) = 2 Cs (g) + 0.5 O_2 (g) and (2): Cs_2O (l) + 0.5 O_2 (g) = 2 CsO (g).

The log(K*) values at fixed n have $\log(K_1^*) < \log(K_2^*)$ for all compositions. The difference between $\log(K^*)_{SM}$ and $\log(K^*)_{IB}$ was ~1 log unit, comparable to the difference observed for Rb and not observed for any other element. No values for Cs were found in literature

4.5.11 - Lead

Lead was among the most volatile elements considered in this study. It was (partially) retained in most experiments, with only the most reducing experiments in the SM composition having Pb abundances at the detection limit. Solving for variable n yielded $n_1 \approx 0$ for SM, IB and IB-G and $n_2 \approx 2$ for IB and IB-G with $n < 2$ for SM. The $\log(K^*)_{SM}$ and $\log(K^*)_{IB}$ differed by ~0.5 log units for both evaporation reactions. The $\log(K_1^*)_{IB\text{-}G}$ was comparable to $\log(K_1^*)_{IB}$ whereas $\log(K_2^*)_{IB\text{-}G}$ was lower than $\log(K_2^*)_{IB}$ as expected (Table **4.14**).

	T (K)	n^1	$\log(K^*)^1$	n^2	$\log(K^*)^2$
SM	1673	0.05 ± 0.04	-1.33 ± 0.16	0	-1.30 ± 0.14
		1.52 ± 0.15	-3.70 ± 0.32	2	-4.07 ± 0.39
SM-2	1673	-	-	-	-
IB	1673	0.01 ± 0.01	-1.97 ± 0.15	0	-1.82 ± 0.12
		1.92 ± 0.05	-4.21 ± 0.31	2	-4.35 ± 0.24
AN	1673	-	-	-	-
IB-G	1573	0.09 ± 0.05	-1.92 ± 0.07	0	-1.87 ± 0.08
		1.86 ± 0.06	-5.06 ± 0.19	2	-5.38 ± 0.36
Sossi et al. (2019)	1573	-	-	0	-2.90 ± 0.12
		-	-	2	-4.47 ± 0.19
	1673	-	-	0	-2.00
		-	-	2	-3.49
Heck (2022)	1573	-	-	0	-2.83(+0.46/-0.16)
		-	-	2	-5.65(+1.09/-0.23)

Table 4.14: The n and log(K*) values obtained via non-linear least squares regression using a [1]variable and [2]fixed for the evaporation reactions (1): PbO (l) = PbO (g) and (2): PbO (l) = Pb (g) + 0.5 O_2 (g).

At fixed n the $\log(K_1^*) > \log(K_2^*)$ for all compositions. The $\log(K_2^*)_{SM}$ and $\log(K_2^*)_{IB}$ were within error of each other and ~0.7 log units below the value of Sossi et al. (2019). For $\log(K_1^*)_{SM}$ and $\log(K_1^*)_{IB}$ there was a ~0.5 log unit difference between the compositions and $\log(K_1^*)_{IB}$ compared reasonably well to the value of Sossi et al. (2019). The $\log(K^*)_{IB\text{-}G}$ of both reactions were a log unit below the values of Sossi et al. (2019). The $\log(K_1^*)_{IB\text{-}G}$ was higher than the value reported by Heck (2022), but $\log(K_2^*)$ was within error.

4.6 – Discussion

4.6.1 – Volatility Factor

4.6.1.1 – Previous Work

Overall volatility trends with time and fO_2 matched those found in other studies (Norris, 2016; A.K. Matzen, pers. comm.; Sossi et al., 2019; Zhang et al., 2021; Heck; 2022; Liu et al., 2022). However, a direct comparison of volatility factors with previous work is not possible, because major element compositions and experimental set-ups and conditions varied between studies. The volatility factor does not consider these parameters which were shown to affect trace element volatility.

Firstly, this study used Pt and Re box-shaped containers whereas Norris (2016) used Ni crucibles, Zhang et al. (2021) used Ir wire loops and A.K. Matzen (pers. comm.), Sossi et al. (2019), Heck (2022) and Liu et al. (2022) used Pt and Re wire loops. Sample geometry affects evaporative loss as it changes the effective evaporative surface area of the sample relative to its volume (Appendix **6**) and trace element diffusion through the sample (Crank, 1975). Considering two samples of identical mass and melt density, one as a sphere and one as a beam with dimensions 4.5x4.5x1.5 mm with only the top surface exposed, the sphere would have an evaporative surface 2.325 times larger than that of the slab. Assuming an evaporation reaction with a constant reaction rate, the evaporative loss should be in the sphere should be larger than the beam for experiments of identical runtime.

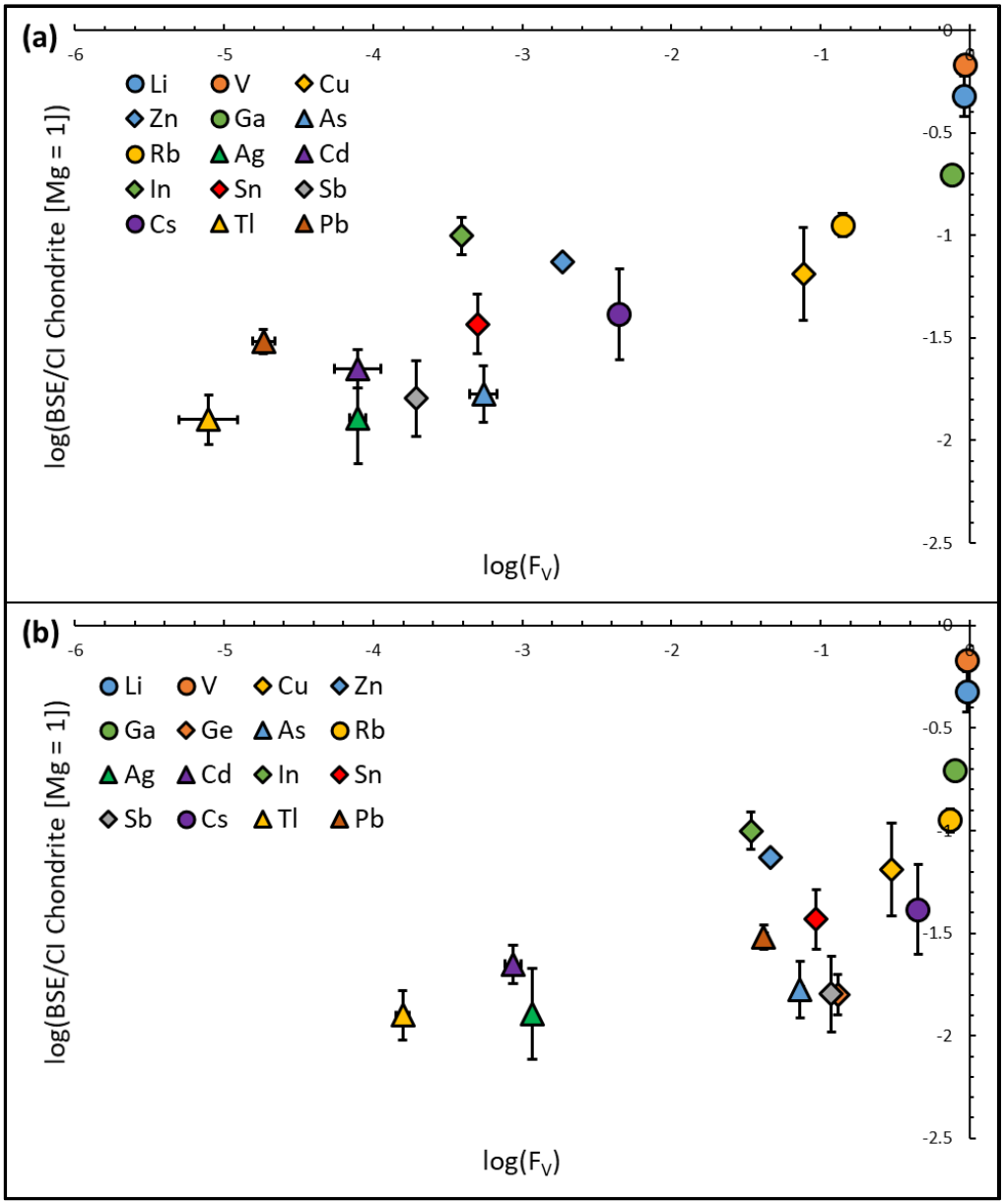
Secondly, most studies used a similar one atmosphere gas mixing furnace to the one used in this study, but Norris (2016) modified his to stir the experiments in situ with a Ni rod, Zhang et al. (2021) used a vacuum furnace, which fixed the fO_2 of the gas phase at ~FMQ ($\log(fO_2) \approx -6.5$ at 1400°C; Visscher and Fegley Jr, 2013). Thirdly, the amount of sample material used varied between ~25 mg (Sossi et al., 2019) and ~1 g (Norris, 2016). Lastly, the starting trace element abundance has an impact on the magnitude of the volatility factor. This was also apparent in this study when comparing F_V for SM and SM-2 where the difference in initial trace element abundances was reflected in the range of F_V. Since

the starting trace element abundances varied up to two orders of magnitude between studies it inhibited direct comparison using F_V.

Instead, the following sections compare the volatility factors obtained in this study with the composition of the terrestrial mantle and different parameters related to trace element volatility. It will be assessed how well these parameters match the experimentally observed volatility to see which are best used for quantifying trace element volatility in silicate melts. Focus will be on the SM, IB and IB-G experiments as AN experiments had minimal volatile loss and SM-2 experiments only contained a small number of trace elements.

4.6.1.2 – CI Chondrite Normalized Bulk Silicate Earth Abundances

Trace element abundances in the bulk silicate Earth cannot be explained solely by core formation. Evaporative loss from a magma ocean and vaporization during large impacts has had a strong control on the abundance, particularly of volatile lithophile elements. To assess if evaporation was a major factor, the CI chondrite normalized bulk silicate Earth trace element abundances, normalized to Mg = 1, were plotted against the volatility factors (Fig **4.8**). This showed that there was a good correlation between the experimentally observed volatility and trace element abundances. Considering elements with similar volatility factors in all three experiments, In, Sn and As plot in a consistent order that can be attributed to core formation as the metal-silicate partition coefficients (D) of these elements are,



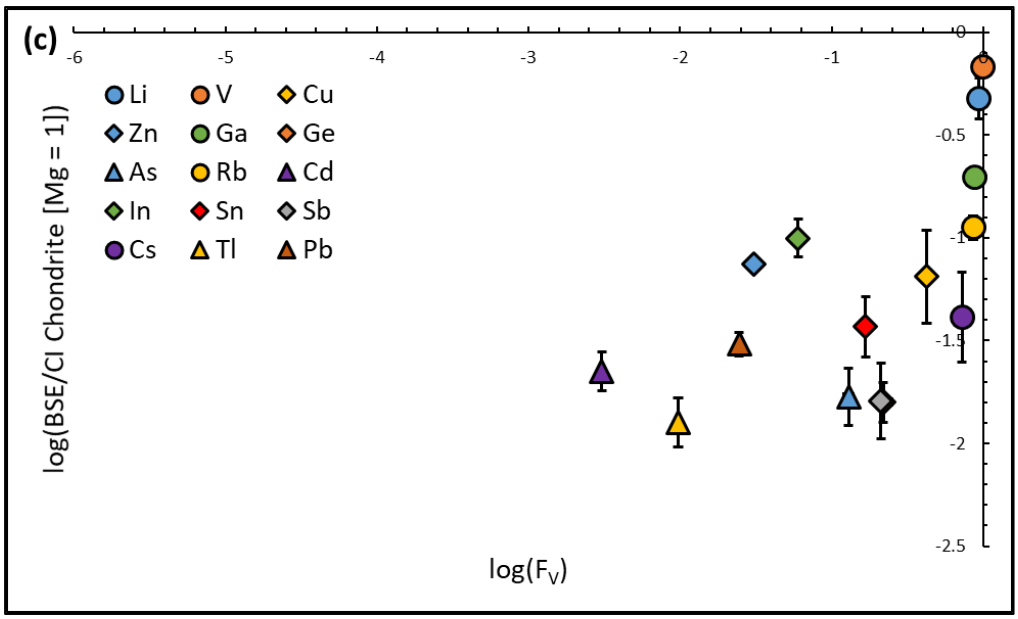
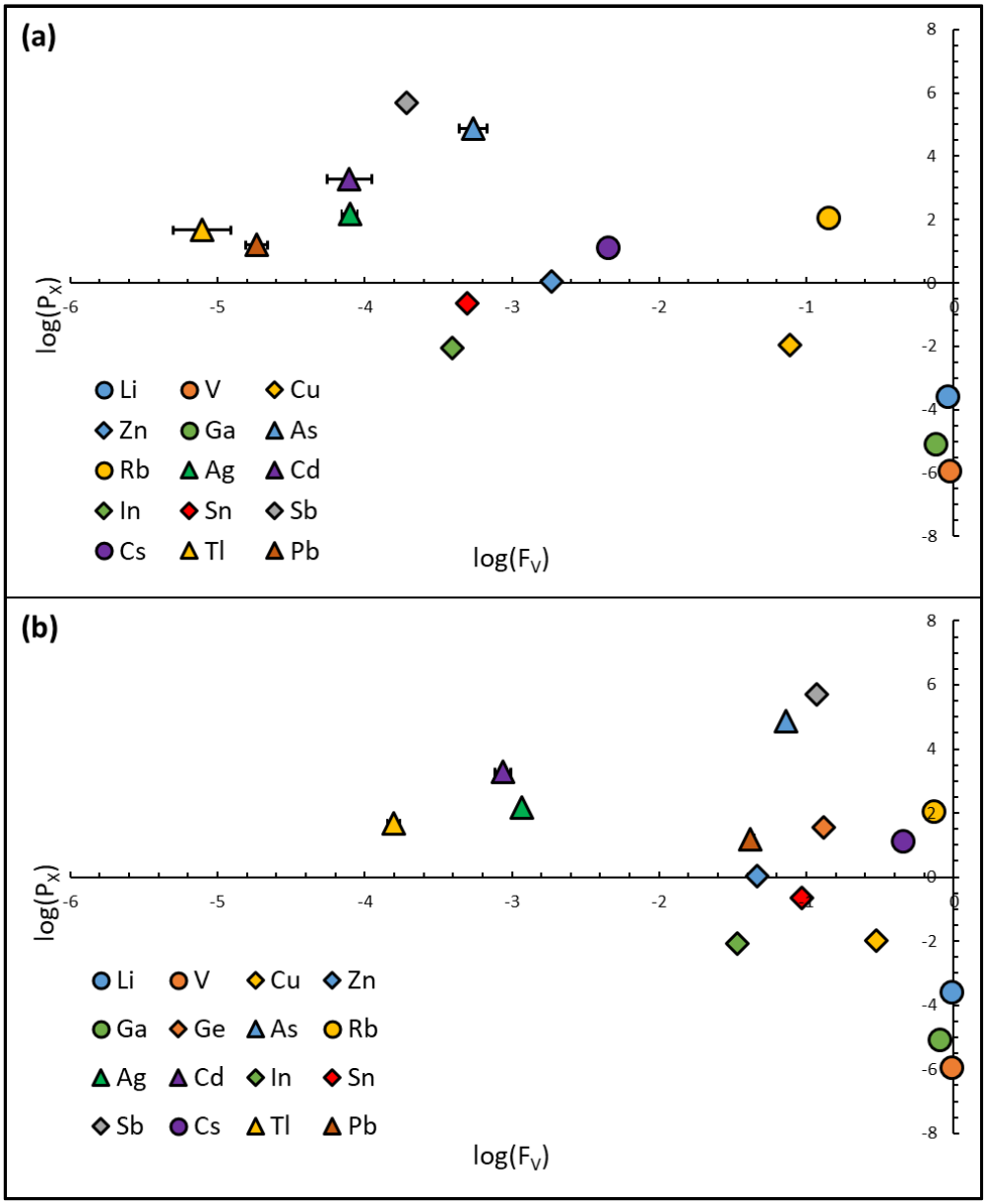


Figure 4.8: The volatility factor plotted against the CI chondrite normalized trace element abundance of the bulk silicate Earth, normalized to Mg for the **(a)** SM and **(b)** IB experiments at log(fO_2) = -8 and **(c)** IB-G at log(fO_2) = -9. Trace element abundance of the BSE and CI chondrites taken from Palme and O'Neill (2014).

from least to most siderophile, $D_{In} < D_{Sn} < D_{As}$ (Righter, 2002; Wood et al., 2014). Similar observations can be made for Ag and Cd where Ag is consistently depleted in the BSE compared to Cd, because of its siderophile behaviour whereas Cd is lithophile. However, both of these elements are close to or at detection limits and therefore may not reflect their relative volatility accurately. The different BSE abundances of elements of similar volatility suggests that ratios of lithophile and siderophile elements of similar volatility may be used as an indicator of whether or not a system has experienced segregation of metal and silicate phases.

4.6.1.3 – Partial Pressure of Gas Species

Following the assumption that P_i << $P_{i,sat}$ in the derivation of the modified HKL equation, the partial pressure of the gas species was not considered in quantifying volatility. Intuitively it would be expected that more volatile elements would have higher equilibrium partial pressures and therefore should correlate with the volatility factor. However, equilibrium thermodynamics do not provide a reason why volatile loss should correlate with the equilibrium partial pressure as it does not consider the reaction rate of the evaporation reaction and it is not the only parameter that affects volatility. It should also be noted that the equilibrium partial pressure was used where it is unlikely that equilibrium was reached between the silicate melt and the gas phase as the fO_2 buffering CO-CO_2 gas



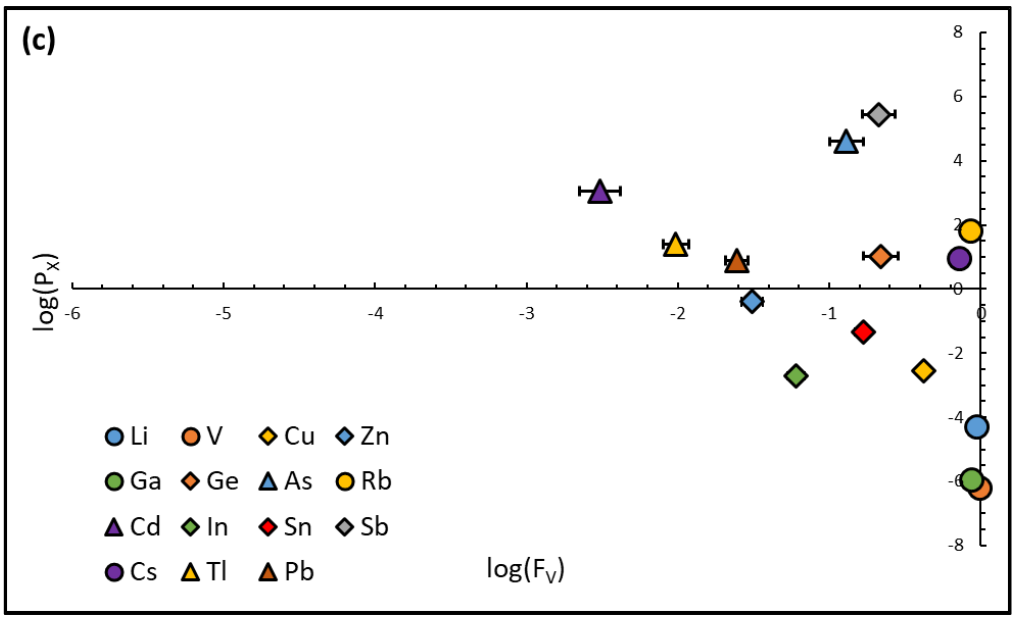


Figure 4.9: The volatility factor plotted against the total equilibrium partial pressure of the oxide gas species for the **(a)** SM and **(b)** IB experiments at log(fO_2) = -8 and **(c)** IB-G at log(fO_2) = -9 assuming ideal trace element behaviour in the silicate melt.

mix provided a consistent gas flow that transported the evaporating species away from the reaction interface.

Figure **4.9** shows how the volatility factor relates to the total equilibrium partial pressure for the SM and IB compositions at log(fO_2) = -8. This figure showed that, generally, the magnitude of volatile loss was larger for trace elements with higher equilibrium partial pressures. Equilibrium partial pressures were calculated assuming ideal trace element behaviour in the silicate melt which could explain some of the scatter in the data. Borisov (2009) and Sossi et al. (2019) showed that the activity of Rb and Cs in silicate melts is on the order of 10^{-4} – 10^{-5}. Other elements that have activity coefficients (γ_x) that may deviate significantly from unity are Zn, Ge, Cd, In, Sn, and Tl (Table **4.15**). The activity coefficients in Table **4.15** were determined in a range of silicate melt compositions and over a temperature range of 1300°C – 1650°C. Activity coefficients from Sossi et al. (2019) may be representative for this study as they were determined for the same major element composition (SM) and temperature (1673 K) as this study. The Norris (2016) activity coefficients were determined for the IB composition at higher temperature (1923 K). There was no available data for γ_{As} and γ_{Cs} in a silicate melt. The activity coefficient of As was considered unity whereas the latter was determined by extrapolation of the

activity coefficients of Na, K and Rb from Sossi et al. (2019) at 1673 K as the activity coefficients of the alkali elements change with ionic radius (Borisov, 2009).

Element	γ	Sources
Li	1.8 ± 0.2 – 15.4 ± 3.1	[5]
V	4.8 ± 0.32	[4]
Cu	3.5 – 11.8 ± 1.7	[2, 3, 4, 5]
Zn	$1.9 \cdot 10^{-2} \pm 1 \cdot 10^{-2}$ – 0.51 ± 0.13	[1, 4, 5]
Ga	1.82 ± 0.53	[4]
Ge	$3.7 \cdot 10^{-3} \pm 1 \cdot 10^{-3}$ – 0.11 ± 0.01	[4, 5]
As	-	-
Rb	$1.3 \cdot 10^{-4} \pm 1.5 \cdot 10^{-5}$	[5]
Ag	0.11 ± 0.023 – 0.67	[4, 5]
Cd	0.15 – 1561 ± 206	[4, 5]
In	0.02 – $0.039 \pm 8.5 \cdot 10^{-3}$	[3, 4]
Sn	$1.6 \cdot 10^{-4} \pm 3.6 \cdot 10^{-4}$	[4]
Sb	1.90 ± 0.43	[4]
Cs	$3.4 \cdot 10^{-5}$	*
Tl	2535 ± 146	[4]
Pb	0.17 – 0.50 ± 0.11	[3, 4, 5]

Table 4.15: Range of activity coefficients compiled from literature. [1]Reyes and Gaskell (1983), [2]Holzheid and Lodders (2001), [3]Wood and Wade (2013), [4]Norris (2016), [5]Sossi et al. (2019). *Extrapolated, see main text.

Correcting the equilibrium partial pressures for non-ideal behaviour in the silicate melt does not significantly improve the correlation (Fig **4.10**). The equilibrium partial pressures of Rb and Cs still plot above elements of similar volatility (Li, V and Ga), but accounting for non-ideal activity has decreased the gap. The total equilibrium partial pressure of In and Sn decreased by considering non-ideal trace element activity. This resulted in Sn dropping below elements with similar volatility. This could be related to the assumptions of gas speciation for these elements (Table **4.1**). For Sn consideration of Sn (g), the only other stable gas species, was not able to sufficiently increase the equilibrium partial pressure and it remained below the trend observed for other elements. Instead, if equilibrium partial pressure does correlate to volatile loss, it may suggest that γ_{Sn} is incorrect, as it was determined from a melt of IB composition. Two elements, As and Sb, have higher partial pressures than expected from their volatility factor in IB and IB-G experiments. This is observed for both ideal and non-ideal trace element behaviour in the silicate melt for Sb as $\gamma_{Sb} \approx 1$, the activity of As in the silicate melt is not known. Moreover, considering all potential gas species only increases the misfit as

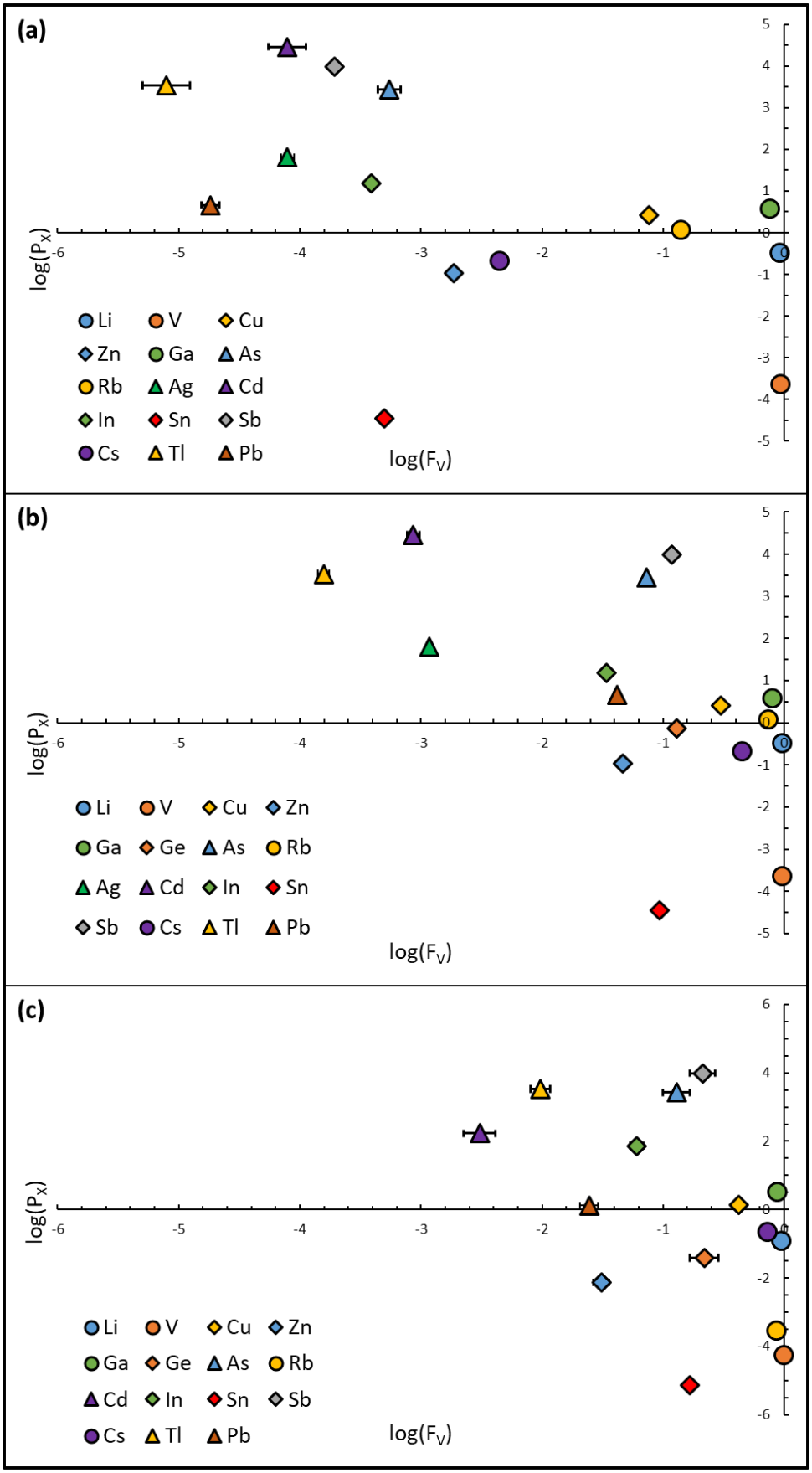
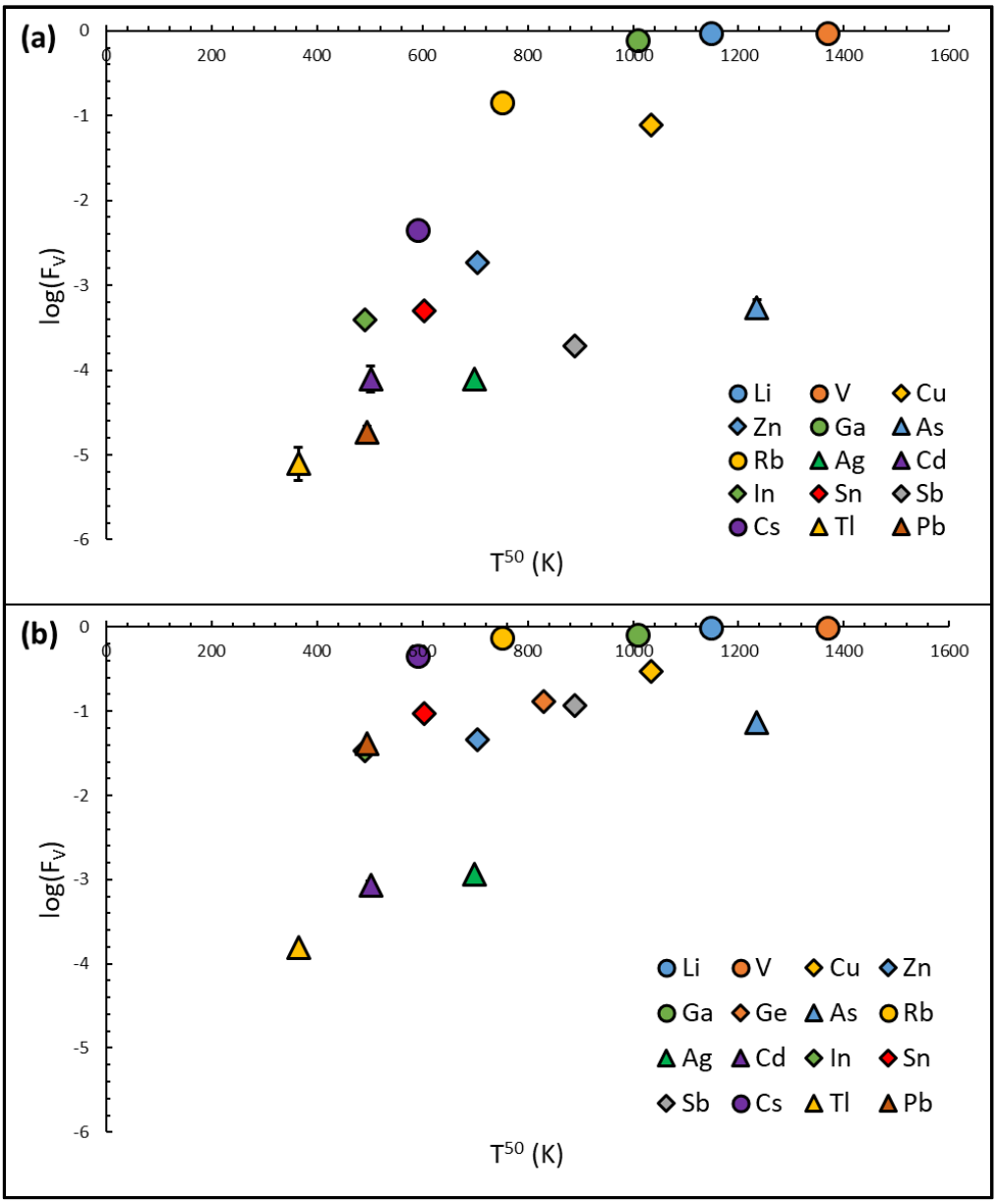


Figure 4.10: The volatility factor plotted against the total equilibrium partial pressure of the oxide gas species for the **(a)** SM and **(b)** IB experiments at log(fO_2) = -8 and **(c)** IB-G at log(fO_2) = -9 considering non-ideal trace element behaviour in the silicate melt.

the polymetallic elemental gas species not considered in this study have high partial pressures in these conditions. Plots of the volatility factor plotted against the total equilibrium partial pressure of mono- and polymetallic gas species can be found in Appendix **2**.

4.6.1.4 – 50% Condensation Temperature

The 50% condensation temperature (T^{50}) is known to not accurately describe conditions in a magma ocean as the solar nebula gas is expected to have evolved over the first few million years after solar system formation (Haisch et al., 2001) whereas large-scale surface magma oceans were present >100 My after solar system formation (Halliday, 2008). A comparison of T^{50} with volatility factors for the most reducing experiments for SM, IB and IB-G showed that generally the elements with a lower T^{50} were more volatile than those with higher T^{50} (Fig. **4.11**). However, there were some elements that did not match well, e.g. Cu, As, Rb and Cs, and comparisons between elements with similar T^{50}, e.g. Zn and Rb, Sn and Cs or In and Cd, showed that there may be in excess of an order of magnitude difference



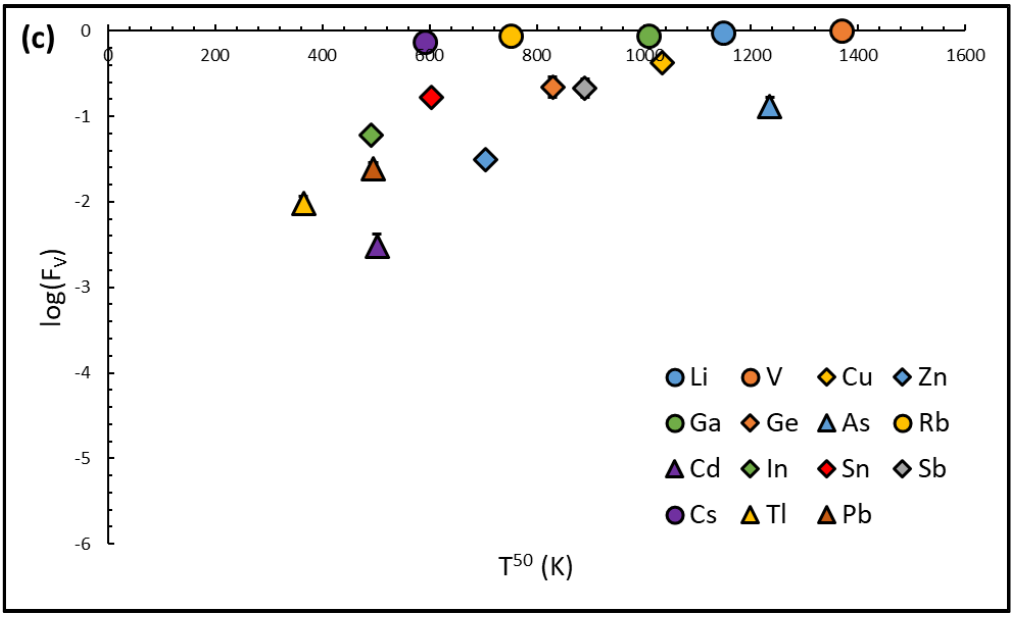


Figure 4.11: Log of the volatility factor plotted against the 50% condensation temperature for **(a)** SM and **(b)** IB at log(fO_2) = -8 and **(c)** IB-G at log(fO_2) = -9. The 50% condensation temperatures were taken from Wood et al. (2019).

in the amount of volatile loss. If T^{50} were the main control on trace element volatility a better correlation would be expected and differences in volatility between elements with similar T^{50} should be smaller. Moreover, elements with higher T^{50}, Cu and As, were more volatile in the experiments than elements with lower T^{50}, e.g. Rb and Cs.

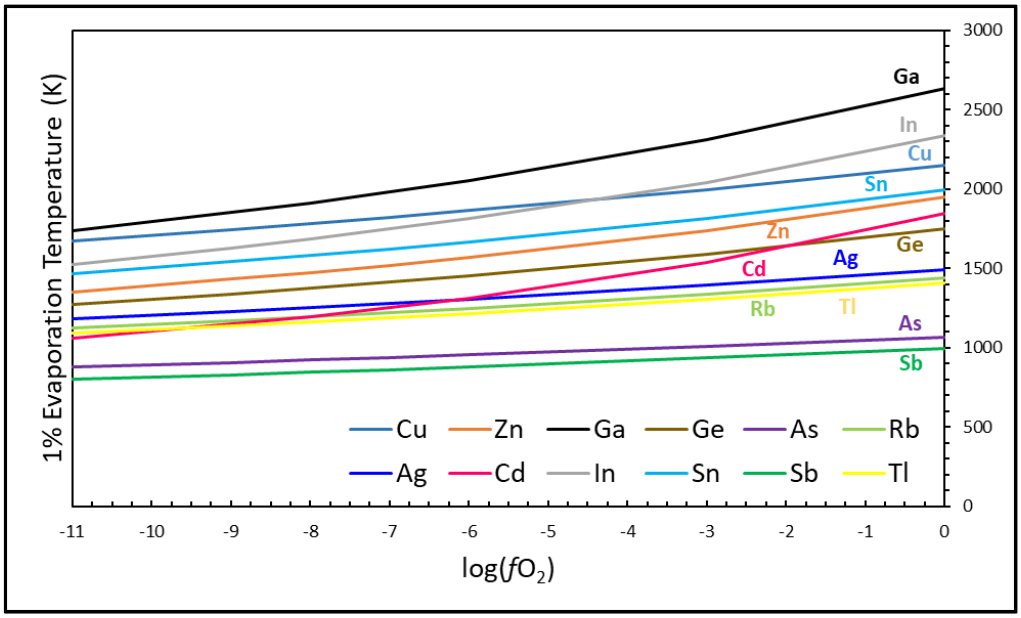
These differences likely originate from differences in speciation of these elements in a silicate melt and in the solar nebula. The H_2-rich atmosphere in the solar nebula was highly reducing (~ΔIW-7), well below the fO_2 in a magma ocean (ΔIW-2.5 – ΔIW-1; Wood et al., 2019). The reducing conditions would stabilise metallic Fe and the presence of sulphur would facilitate the formation of sulphide species. Both Cu and As are known to exhibit both chalcophile and siderophile behaviour, alloying with S and Fe to decrease their volatility. Both Lodders (2003) and Wood et al. (2019) consider the main phase of both Cu and As in their model to be alloyed with Fe.

4.6.1.5 – 1% Evaporation Temperature

The 1% evaporation temperature (T^1) is a parameter that was proposed by Sossi et al. (2019) to describe volatility based on their experimental data. The T^1 parameter was defined to have a volatility parameter that was accurate outside of solar nebula conditions. They showed that there was a strong correlation between T^{50} and the 1% evaporation temperature for lithophile elements. For chalcophile and siderophile elements this correlation was not as clear due to their incorporation into metal phases in reducing conditions. While the fraction of evaporated material was chosen arbitrarily, the parameter itself is not limited to solar nebula conditions. Instead, it is calculated independently for a given silicate melt composition and fO_2. Because trace element volatility exhibits a compositional dependence it cannot be used widely at present.

$$(Eq.\,4.2):\quad T_i^1 = \frac{-\Delta H_i^*}{\left(R\left(\frac{n}{4}\ln(fO_2) + \ln(P_T) + \ln\left(\frac{f_i^{vap}}{1-f_i^{vap}}\right)\right) - \Delta S_i^*\right)}$$

For trace elements with only a single evaporation reaction T^1 can be calculated from the properties of the evaporation and experimental conditions (Eq. **4.2**; Sossi et al., 2019). Here ΔH_i^* and ΔS_i^* are the apparent enthalpy and entropy of the evaporation reaction of element i – obtained from K^*, f_i^{vap} is the fraction of i in the gas phase, 0.01 for T^1, n is the change in oxidation state of i in the evaporation reaction and P_T is the total pressure in the system in atm. The ΔH_i and ΔS_i used to calculate T^1 were



determined from the thermodynamic properties of the pure species (Barin et al., 1989) by interpolation of $\Delta G = \Delta H - T\Delta S$ across a range of temperatures and assuming ideal trace element behaviour in the melt (Fig. **4.12**). In the next section ΔH_i^* and ΔS_i^* will be determined for various evaporation reaction from data obtained in this study. However, the unrealistic values obtained for some elements using this method led to doubts about its validity and inhibited their use.

Plotting the 1% evaporation temperature against the volatility factors showed that there was a broadly linear trend with three outliers; As, Rb and Sb (Fig. **4.13**). For Rb this is potentially because ideal behaviour is assumed in the melt, but γ_{Rb} ≈ 1.3·10^{-4} (Sossi et al., 2019). For most elements the ΔH and ΔS of the pure species compare well with ΔH* and ΔS* obtained for evaporation from a silicate melt by Sossi et al. (2019) and Heck (2022). Only for As Heck (2022) found that ΔH* (857 ± 45 kJmol^{-1}) and ΔS* (0.472 ± 0.028 kJmol^{-1}K^{-1}) of the evaporation reaction deviated strongly from ΔH (266 kJmol^{-1}) and ΔS (0.212 kJmol^{-1}K^{-1}) determined for pure species. Calculating T^1 using the Heck (2022) data increases T^1 by approximately 600 K, resulting in a volatility comparable to Zn, In and Sn. Similar data was not available for Sb, but it is known to behave similar to As (Maciag and Brenan, 2020). Therefore it would not be surprising if ΔH* and ΔS* of the Sb evaporation reaction in a silicate melt differ strongly from those of the pure species.

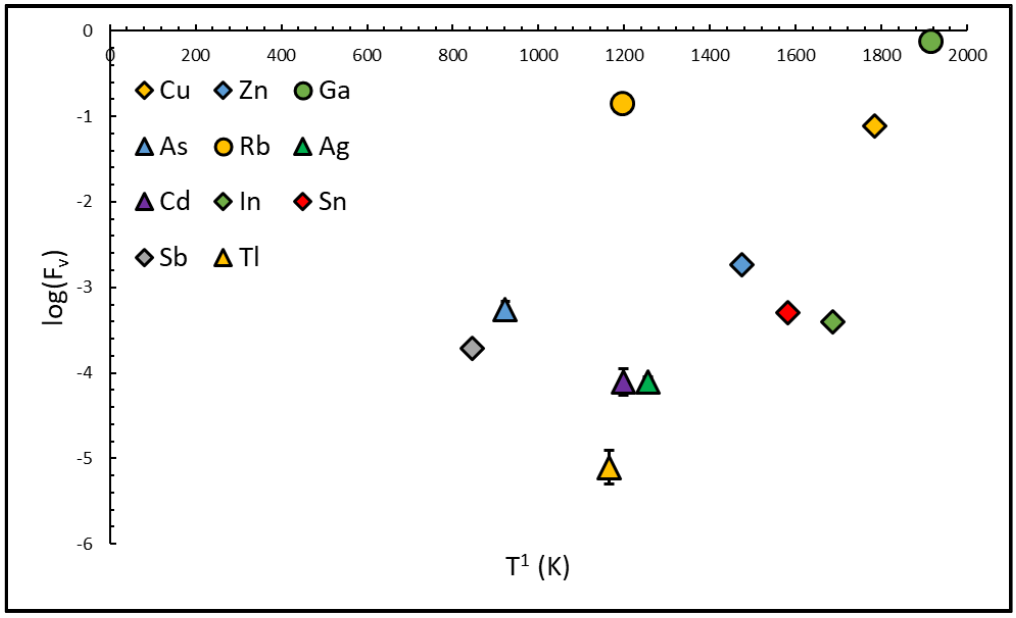


Figure 4.13: The 1% evaporation temperatures plotted against the log of volatility factor for the SM composition at log(fO_2) = -8.

4.6.2 – Modified Hertz-Knudsen-Langmuir Equation

4.6.2.1 – The Apparent Equilibrium Constant

The apparent equilibrium constants obtained from the modified HKL equation, with fixed n, in Section **4.5** generally compare well with values obtained in literature (Fig. **4.14**). The elements for which the biggest differences were observed were Ga and In. Moreover, the log(K*) of Ge, As and Pb matched well between studies at 1400°C, but did not at 1300°C. Both Heck (2022) and Liu et al. (2022) consider two evaporation reactions, one including In_2O (g), when they determine $log(K^*)_{In}$ which could be an explanation for the difference. However, the $log(K^*)_{In}$ of Heck (2022) matches the $log(K^*)_{In}$ at 1300°C

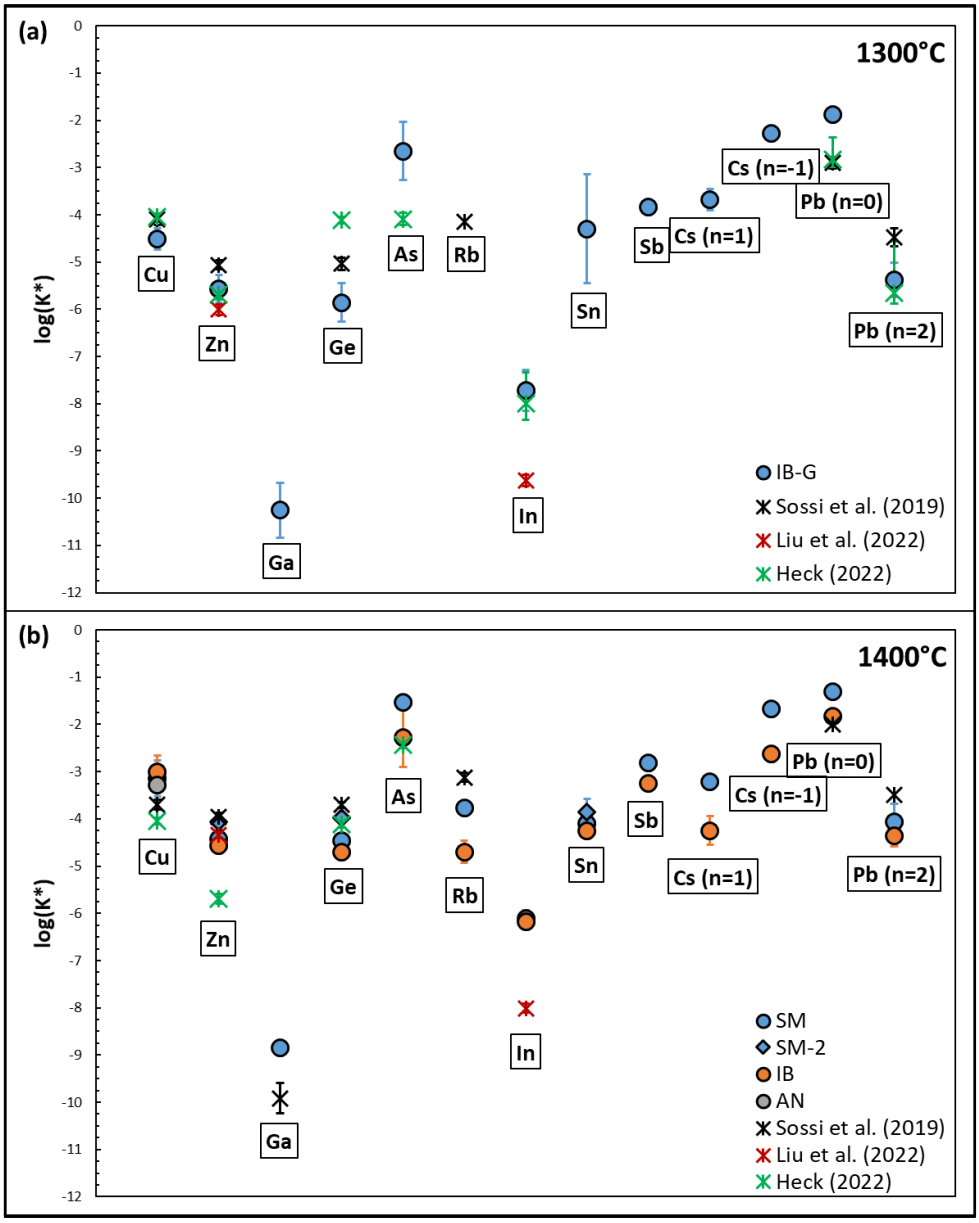


Figure 4.14: Summary of the log(K*) calculated in Section **4.5** and log(K*) from literature.

whereas Liu et al. (2022) is ~2.5 log units lower. For Ga the lack of volatility across a range of fO_2 may have inhibited accurate quantification of log(K*) in this study. Sossi et al. (2019) had experiments with a longer runtime which allowed for more evaporative loss and therefore their $\log(K^*)_{Ga}$ is likely more accurate.

A second observation is that, at 1400°C, the $\log(K^*)_{IB}$ is either comparable to or smaller than $\log(K^*)_{SM}$. This could be caused by the effect of the compositional differences on trace element activity. Considering the activity coefficients of Norris (2016) for the IB composition and Sossi et al. (2019) for the SM composition this does not appear to fully explain the differences. They report similar values for Cu ($\gamma_{Cu,SM}$ = 11.8 ± 1.7 and $\gamma_{Cu,IB}$ = 6.33 ± 0.86) and Pb ($\gamma_{Pb,SM}$ = 0.38 and $\gamma_{Pb,IB}$ = 0.50 ± 0.11), but different values for Zn ($\gamma_{Zn,SM}$ = 0.51 ± 0.19 and $\gamma_{Zn,IB}$ = 0.019 ± 0.19) and Ge ($\gamma_{Ge,SM}$ = 0.11 ± 0.01 and $\gamma_{Ge,IB}$ = 0.001 ± 0.001) yet the differences between $\log(K^*)_{SM}$ and $\log(K^*)_{IB}$ are similar for all four elements. The biggest difference between compositions was observed for Rb and Cs which exhibited limited volatility in the IB composition. Experiments with an increased runtime or in more reducing conditions may provide more insight into this compositional difference as the magnitude of volatile loss will be larger for the less volatile elements.

4.6.2.2 – Comparing log(K*) and log(K)

Apparent equilibrium constants were not necessarily expected to match the equilibrium constant of the evaporation reaction as $K^* = K\gamma_i\alpha_e$. Sossi et al. (2019) showed that α_e was not expected to deviate significantly from unity and therefore differences between K* and K were the result of non-ideal behaviour of the trace element in the silicate melt. Using the activity coefficients in Table **4.15** the $\log(K^*)_{SM}$, $\log(K^*)_{IB}$ and $\log(K^*)_{IB\text{-}G}$ of Cu, Zn, Ga, Ge, Rb, In, Sn, Sb, Cs and Pb were converted to log(K), assuming $\alpha_e \approx 1$ (Fig. **4.15**). This showed that correcting log(K*) for non-ideal trace element activity in the silicate melt had a detrimental effect on the fit between log(K) and log(K*). This is most clear for elements which have activity coefficient that strongly deviate from unity; Rb, Sn and Cs. This suggests that the $\gamma_i\alpha_e$ product is not correct. A poor fit for Sb is observed in both cases. Both γ_i and α_e are known

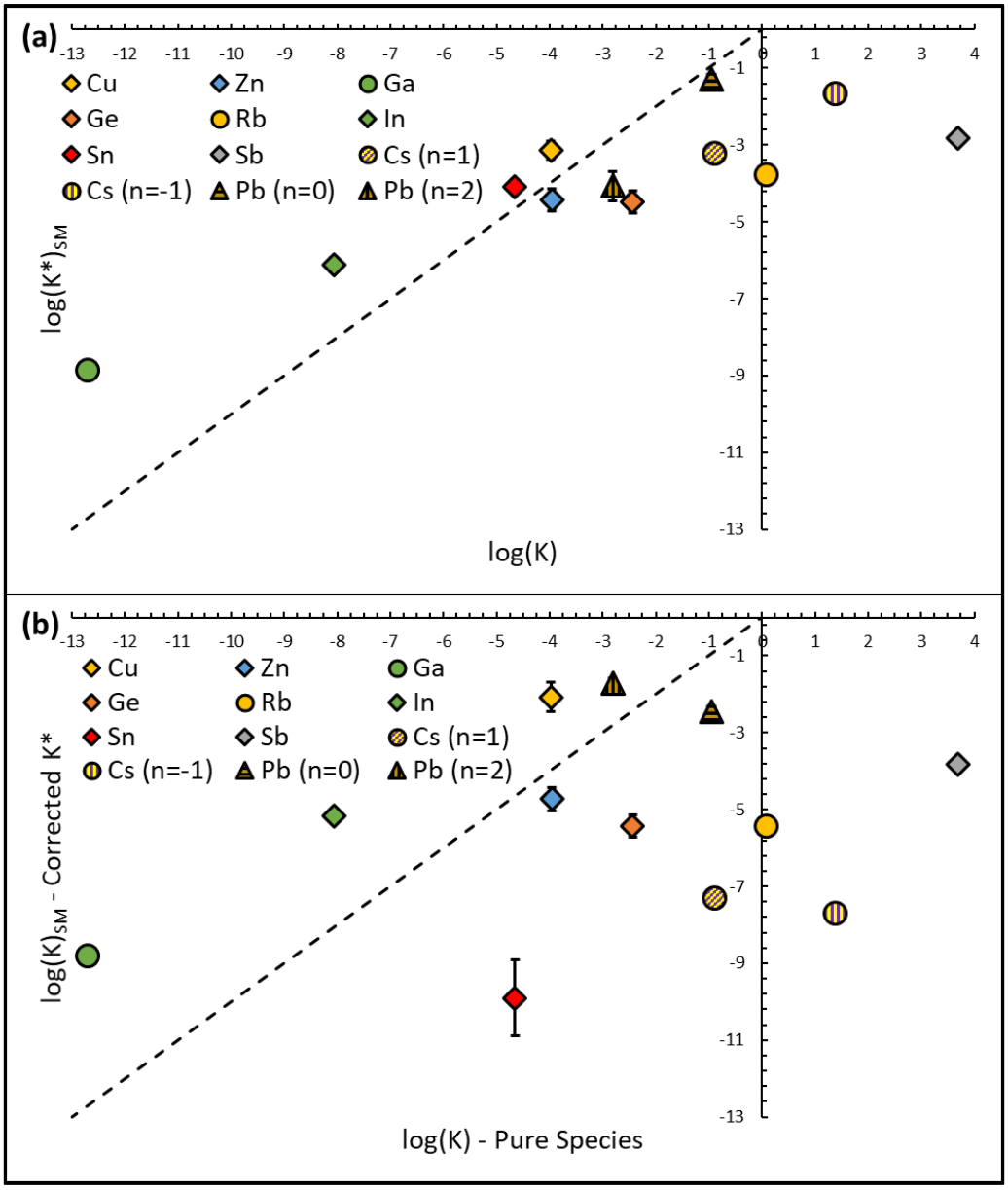


Figure 4.15: Plots of the equilibrium constant of the evaporation reaction of the pure species plotted against **(a)** log(K*) and **(b)** an experimental log(K) calculated by correcting log(K*) for non-ideal trace element behaviour in the melt. The dashed line is the one-to-one fit.

to vary with melt composition and temperature (Alexander, 2001; Fedkin et al., 2006; Wood and Wade, 2013). Therefore Figure **4.15** may indicate that either the activity coefficients were not applicable to this melt, despite being obtained by Sossi et al. (2019) for a melt of identical composition, or that the evaporation coefficient varied significantly from unity. Beyond the Sossi et al. (2019) study an evaporation coefficient could only be found for Rb where Zhang et al. (2021) found that in a basaltic melt in a vacuum $\propto_e \approx 0.07 - 0.18$. Ackermann et al. (1962) showed that $0 \leq \alpha_e \leq 1$ and therefore it

alone cannot get a one-to-one fit for log(K) and log(K*) for elements that plot above and below the one-to-one line.

4.6.2.3 – Apparent Enthalpy and Entropy of the Evaporation Reactions

It was possible to determine the apparent enthalpy (ΔH*) and entropy (ΔS*) of the evaporation reaction from log(K*) for experiments performed using the same starting material at different temperatures. This was possible because of the relationship between the equilibrium constant and Gibbs' free energy of the evaporation reaction (Eq. **4.3**).

$$(Eq. 4.3): \quad \Delta G^* = \Delta H^* - T\Delta S^* = -RTln(K^*)$$

This equation shows that RTln(K*) changes linearly with temperature with ΔH^* as intercept and ΔS^* as slope of this line. It was used to determine ΔH^* and ΔS^* for the IB composition for which log(K*) were available at 1300°C and 1400°C, assuming ideal trace element activity in the silicate melt (Table **4.16**).

	This study		Pure Species		Sossi et al. (2019)	
Element	ΔH^*	ΔS^*	ΔH^*	ΔS^*	ΔH^*	ΔS^*
Cu	761 ± 94.5	0.397 ± 0.036	412	0.170	264.0 ± 15.7	0.089 ± 0.009
Zn	509 ± 28.0	0.217 ± 0.030	477	0.209	548.6 ± 19.6	0.253 ± 0.011
Ge	579 ± 44.0	0.256 ± 0.036	526	0.268	612.7 ± 23.9	0.294 ± 0.014
As	186 ± 67.5	0.068 ± 0.052	268	0.215	-	-
In	776 ± 46.0	0.345 ± 0.037	702	0.265	-	-
Sn	20.2 ± 5.43	-0.070 ± 0.059	596	0.267	-	-
Sb	292 ± 13.6	0.112 ± 0.022	253	0.222	-	-
Cs (n = 1)	-287 ± 27.1	-0.253 ± 0.034	212	0.109	-	-
Cs (n = -1)	-181 ± 10.8	-0.159 ± 0.021	100	0.086	-	-
Pb (n = 0)	25.2 ± 1.98	-0.020 ± 0.021	280	0.149	452.1 ± 70.6	0.232 ± 0.043
Pb (n = 2)	519 ± 45.0	0.227 ± 0.036	405	0.189	490.9 ± 112	0.227 ± 0.070

	Heck (2022)		Liu et al. (2022)	
Element	ΔH^*	ΔS^*	ΔH^*	ΔS^*
Cu	376 ± 20	0.154 ± 0.01	-	-
Zn	424 (+53/-34)	0.166 ± 0.04	-	-
Ge	643 (+31/-18)	0.310 ± 0.02	-	-
As	857 (+47/-43)	0.472 ± 0.03	-	-
In	389 (+167/-0)	0.096 ± 0.11	791 ± 87	0.319 ± 0.05
Sn	-	-	-	-
Sb	-	-	-	-
Cs (n = 1)	-	-	-	-
Cs (n = -1)	-	-	-	-
Pb (n = 0)	521 (+321/-89)	0.279 ± 0.21	-	-
Pb (n = 2)	-	-	-	-

Table 4.16: The apparent enthalpy [kJ] and entropy [$kJmol^{-1}K^{-1}$] for the evaporation reactions from silicate melt compared to data for pure species (Barin et al., 1989) and previous work.

This table shows that some elements, e.g. Zn, Ge, In, Sb and Pb (for Pb (g)), correlate well with pure species data and previous work whereas other elements, e.g. Cu, As, Sn, Cs and Pb (for PbO (g)), correlate poorly. For Ga and Rb it was not possible to determine ΔH* and ΔS* as log(K*) was only available at one temperature. These differences were visualized in Figure **4.16** where elements with a better fit plotted close to or parallel to the one-to-one line comparison between RTln(K) and RTln(K*). Elements that plot above the one-to-one line have a $\gamma_i \alpha_e > 1$ and those that plot below have $\gamma_i \alpha_e < 1$. Deviations from pure species behaviour were indicative of non-ideal behaviour of the trace element in the silicate melt, evaporation coefficients deviating significantly from unity or poor data quality. The former two may explain the differences between studies as both trace element activity and the evaporation coefficient dependent on temperature and silicate melt composition. Poor data quality was expected to pose a potential problem for Cu and As at both temperatures and Sn at 1300°C as these elements had poor fits between the data and modelled solution of the modified HKL equation. Since this temperature series only contained two data points, data may improve significantly by performing additional experiments at different temperatures as fits through two data points are generally associated with larger misfits.

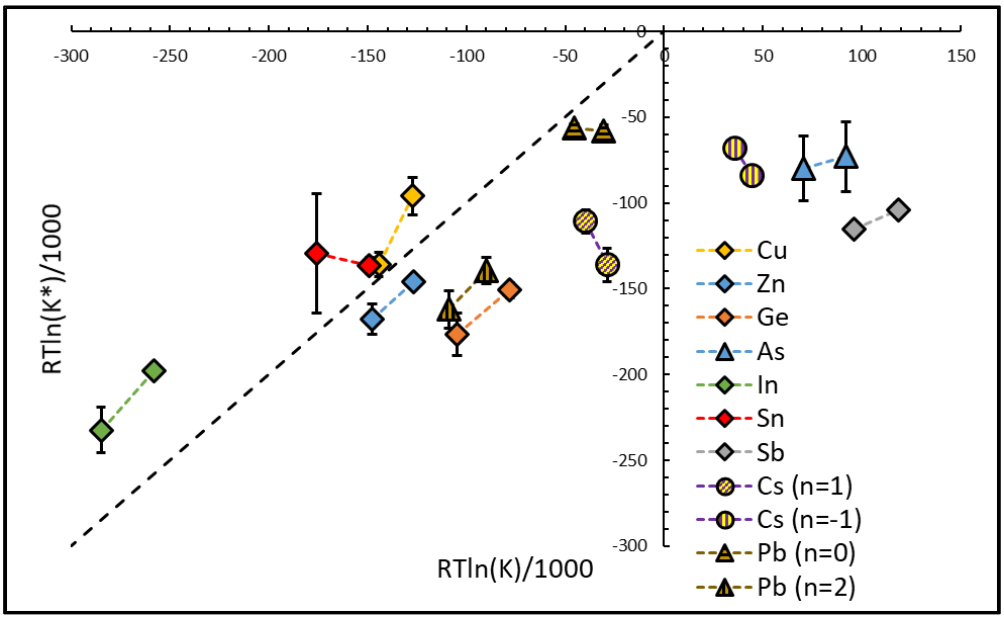


Figure 4.16: Plot of RTln(K) against RTln(K*) to illustrate correlation between the two parameters.

4.6.2.4 – Potential Issues with the Modified HKL Equation

4.6.2.4.1 – Validity in Multicomponent Systems

The applicability of the HKL equation to experimental and/or natural processes is still under scrutiny, because it is poorly understood how deviations from ideal gas behaviour or thermal equilibrium conditions affect the assumptions made in its derivation (Sossi and Fegley Jr, 2018) and how it behaves in multicomponent systems (Hołyst et al., 2015). This is in part related to the ambiguity surrounding the evaporation coefficient, both in terms of a non-empirical method of quantifying it and overall paucity of data in the literature. Another, unlikely, issue is that it is assumed that the temperature in the condensed and evaporated phases is equal, which may not necessarily be the case. However, the effects of small temperature differences between phases in a high temperature system for small samples close to the evaporative surface is likely negligible. Moreover, Hołyst et al. (2015) compared the results from the HKL equation to molecular dynamics simulations of evaporation reactions and found that there was a significant difference between the two approaches. They argued that this is because the HKL equation, which was established in a single component system, does not accurately describe the physical mechanisms of evaporation in a multicomponent system. Sossi et al. (2019) have attempted to correct for this by correcting for the activity of the trace element in the silicate melt. However, again a lack of data inhibits a coherent assessment of the validity of the HKL in multicomponent systems.

4.6.2.4.2 – Fixed and Adjustable Parameters

The original derivation of the modified HKL equation by Sossi et al. (2019) described their fitting procedure to include three adjustable parameters, n, K* and t_0. Having more adjustable parameters will decrease the overall misfit between the model and the data as fits will generally be better with and increasing number of variables. Out of these parameters K* and t_0 must be obtained from data fitting as they cannot be predicted in any way as trace element activity in the melt and the evaporation coefficient are unknown parameters required to find K* and t_0 is a remnant of the time integration of

the HKL equation and is treated solely as a fitting parameter. This section discusses the importance of adjustable n and t_0 parameters in determining K* of the evaporation reactions.

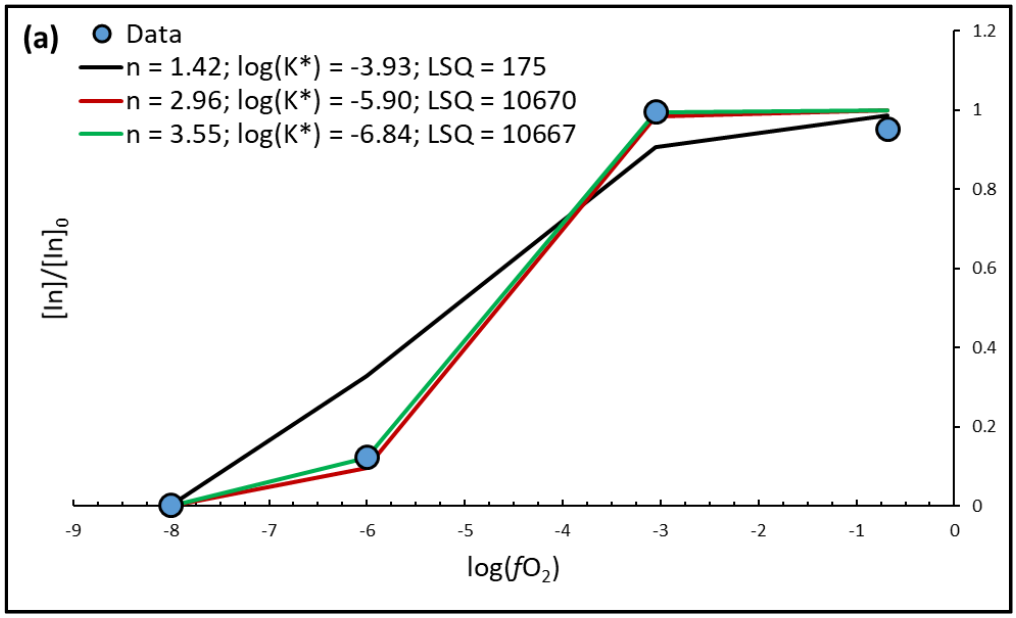
In their own data reduction Sossi et al. (2019) assume that n is a fixed parameter and use n obtained from thermodynamic predictions of evaporation reactions from pure species. Other studies by Heck (2022) and Liu et al. (2022) follow a similar approach where n is fixed to find K*. In this study it was shown that fitting for both K* and n simultaneously may yield n close to the expected value for some elements, but will result in vastly different values for others, e.g. $n_{Cu} \approx 0.5$, $n_{As} \approx 0.3$, $n_{Sn} = 1.2 – 1.6$ and $n_{Sb} = 0.62 – 1.1$. Deviations from the expected values could be explained by an inaccurate description of the evaporative environment of these elements. However, thermodynamic predictions suggested that these reaction were adequate for these elements in the experimental environment (Appendix **2**). Moreover, since n is the change in oxidation state of an element in the evaporation reaction it must be an integer value. It is suggested that it should either be predefined to be an integer in the fitting approach, or be considered a fixed parameter based on thermodynamic predictions.

The "lag time" (t_0) describes the time between sample introduction and evaporative loss (Sossi et al. (2019) and was considered in this study initially. However, the fitting approach adjusted it to zero in every single reduction for the SM and IB compositions. Fitting by predefining t_0 as a non-zero value increased the sum of non-linear least squares misfit of the obtained fits, as such $t - t_0$ was defined to be equal to the runtime of the experiment, or $t_0 = 0$. Sossi et al. (2019) also found that $t_0 = 0$ for most elements, only Zn (540 s), Ge (624 s) and Rb (863 s) had non-zero values in their work. The purpose of the lag time in their study was to remove a systematic increase of log(K*) with increasing runtime. Liu et al. (2022) did not discuss the values they used for t_0 but consider $(t - t_0)$ as a constant value of either 30 or 60 minutes for all experiments, suggesting that it was constant for all experiments and likely $t_0 = 0$. Heck (2022) did not discuss t_0 at all in their work. Combining these observationos with results from this work it is suggested that further application of the modified HKL should assume that $t_0 = 0$.

4.6.2.4.3 – Non-Linear Least Squares Minimization

The non-linear least squares minimization of the misfit between the data and the modelled solution of the modified HKL equation using the Excel SOLVER function resulted in trace elements generally conforming to their thermodynamically predicted behaviour for n, with values differing only slightly between compositions. However, two considerations were made when fitting the data to ensure the best fit was found; (1) the impact of the misfit on each individual data point and (2) how well does the obtained fit for n correspond to its expectation based on thermodynamic predictions.

Regarding the first point it was observed that data points for experiments that had experienced near-complete volatile depletion had a disproportionate impact on the fitting of data. This is best illustrated by comparing multiple fits. Figure **4.17** shows multiple modelled fits for In where the black line was fitted considering all four data points and the red and green only considered three data points at log(fO_2) = -0.68, -3.05 and -6. The additional data point to fit through resulted in a smaller relative misfit between all four points, but a visually poor fit and the obtained n was substantially lower than the expected n_{In} = 3. By fitting through only three data points n is closer to 3 and the visual fit through all considered data points improved. However, the sum of least squares misfit increased drastically due to misfit on the omitted data point at log(fO_2) = -8. In Figure **4.17a** all three fits appear to pass through the data point at log(fO_2) = -8, but sum of least squares misfit increased significantly, due to



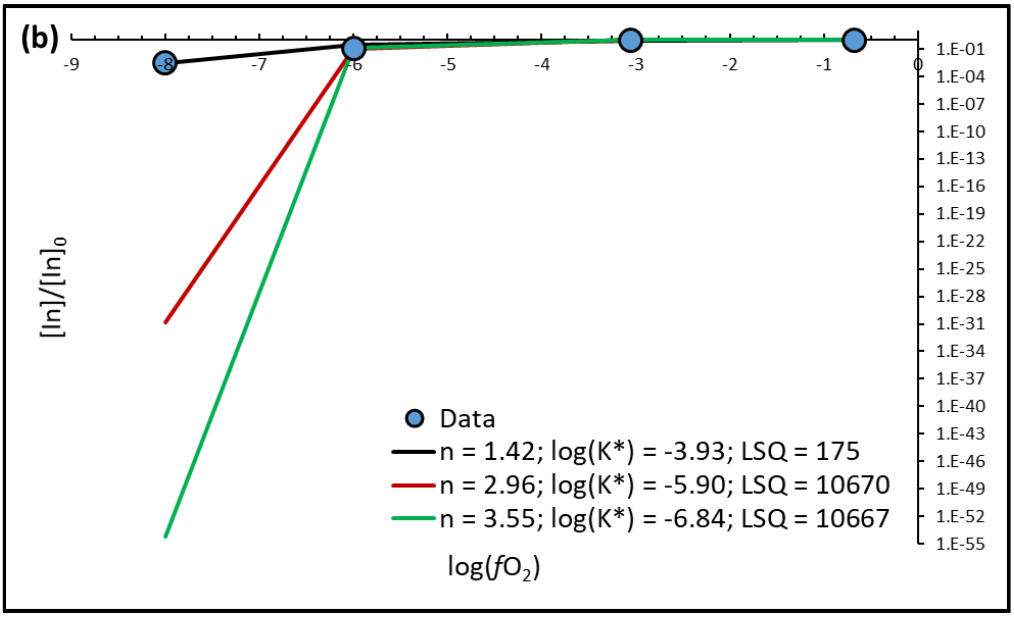


Figure 4.17: Three potential fits to the 60 minute fO_2 series of In in the SM composition with **(a)** a linear y-axis and **(b)** logarithmic y-axis. LSQ is the sum of the non-linear least squares misfit between the data points and the model.

the rate at which these fits approach zero as a result of the curvature of the fit by providing an accurate fit through the other three data points. Figure **4.17b** is the same as Figure **4.17a**, but with a logarithmic y-axis and it shows that the sum of least squares misfit is mainly controlled by the relative misfit on the data point at log(fO_2) = -8. The absolute misfit on the data points at log(fO_2) = -3 and -6 for the black fit are larger than the absolute misfit on the data point at log(fO_2) = 8 for the red and green fits. However, because the relative misfit is larger for the latter, the non-linear least squares minimization preferred a good fit on this data point over the others. This was observed consistently for elements where $[C]/[C]_0 \rightarrow 0$. By omitting these data points when fitting the model it resulted in n closer to expected values for all elements.

Regarding the second point there are multiple fits that have similar small sum of least squares misfits, but the magnitude of n and K* can vary significantly (Fig. **4.18**). This figure shows three fits with different n and K* where the one with the expected n_{Sn} = 2 actually has the largest misfit. This was, in part, correlated to the misfit on data points where $[C]/[C]_0 \rightarrow 0$. The Excel SOLVER will always fit for the lowest sum of least squares. To assess accuracy in this case the fits with variable and fixed n were

compared. One way in which this may be avoided would be to perform additional experiments to fill some of the gaps in data coverage as more data points would result in a more robust solution.

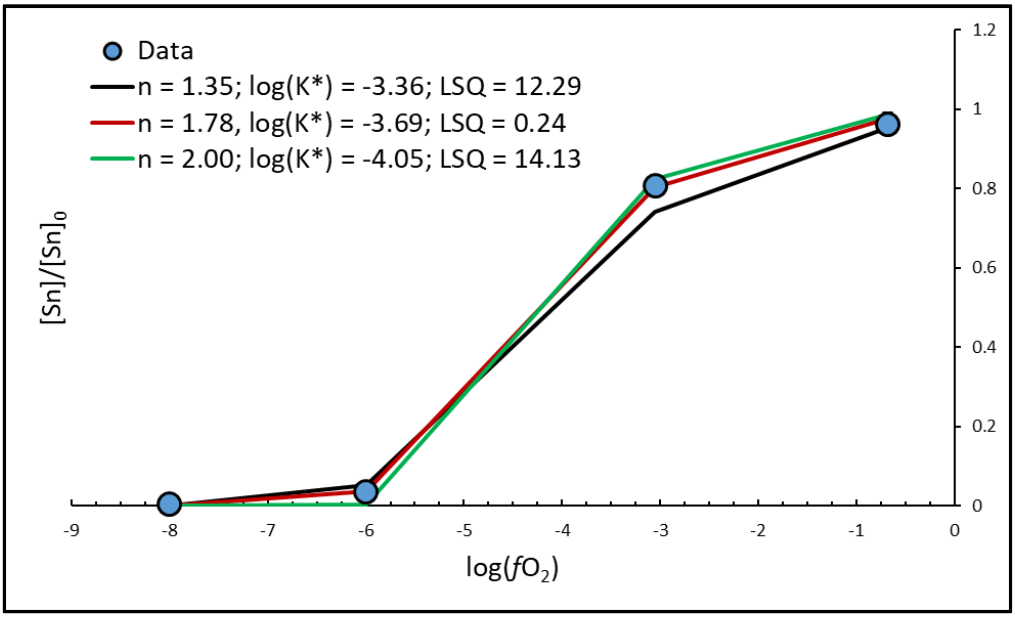


Figure 4.18: Three potential fits to the 60 minute fO_2 series of Sn in the SM composition. LSQ is the sum of the non-linear least squares misfit between the four data points and the model.

Chapter 5: Zinc Isotope Measurements

5.1 – Introduction

The Zn abundance of the bulk silicate Earth (BSE; 53.5 ± 5 ppm) is depleted relative to CI carbonaceous chondrites (361 ± 40 ppm; Palme and O'Neill, 2014; Paquet et al., 2023b). The average Zn isotopic composition of the BSE, obtained through the analysis of a range of peridotites, mid-ocean ridge basalts and ocean island basalts, is $\delta^{66}Zn_{Lyon}$ = 0.28 ± 0.05‰ (Chen et al., 2013a). This is identical within error compared to the Zn isotopic composition of enstatite and carbonaceous chondrite meteorites, the terrestrial building blocks and Mars. This suggested that isotope fractionation occurred in the solar nebula or during accretion and volatile loss on smaller precursor bodies and that the Zn isotopic composition of the bulk Earth remained constant throughout its subsequent evolutionary steps. The BSE Zn depletion is attributed to the volatility of Zn during terrestrial accretion and remained unaltered during late-stage accretionary events (Sossi et al., 2018b). Its lithophile behaviour suggests that terrestrial Zn will be concentrated in the mantle. In the absence of sulphide, halide and hydroxide species Zn will always be present as $Zn^{2+}O$ in the silicate melt and as Zn^0 in the gas phase which makes Zn a perfect element to study volatility as it has a simple evaporation chemistry that is insensitive to changes in redox conditions.

The Zn isotopic composition of (extra-)terrestrial materials exhibits a large range of values. Meteorites exhibit a range between $\delta^{66}Zn_{Lyon}$ = –7‰ in aubrites and $\delta^{66}Zn_{Lyon}$ = +7.5‰ in EL enstatite chondrites and lunar samples vary between $\delta^{66}Zn_{Lyon}$ = –4‰ in lunar pyroclastic glasses to $\delta^{66}Zn_{Lyon}$ = +6‰ in lunar regolith (Fig. **5.1**). Lunar basalts exhibit a heavy Zn isotope enrichment relative to the Earth, $\delta^{66}Zn_{Lyon}$ = +1.4 ± 0.2‰, which has been attributed to significant volatile loss following the Moon-forming Giant Impact (Day et al., 2020a). On the other hand, the Zn isotopic composition of terrestrial igneous rocks and Martian meteorites is generally homogeneous and indistinguishable from CI chondrites ($\delta^{66}Zn_{Lyon}$ = 0.25 ± 0.03‰; Day and Moynier, 2014).

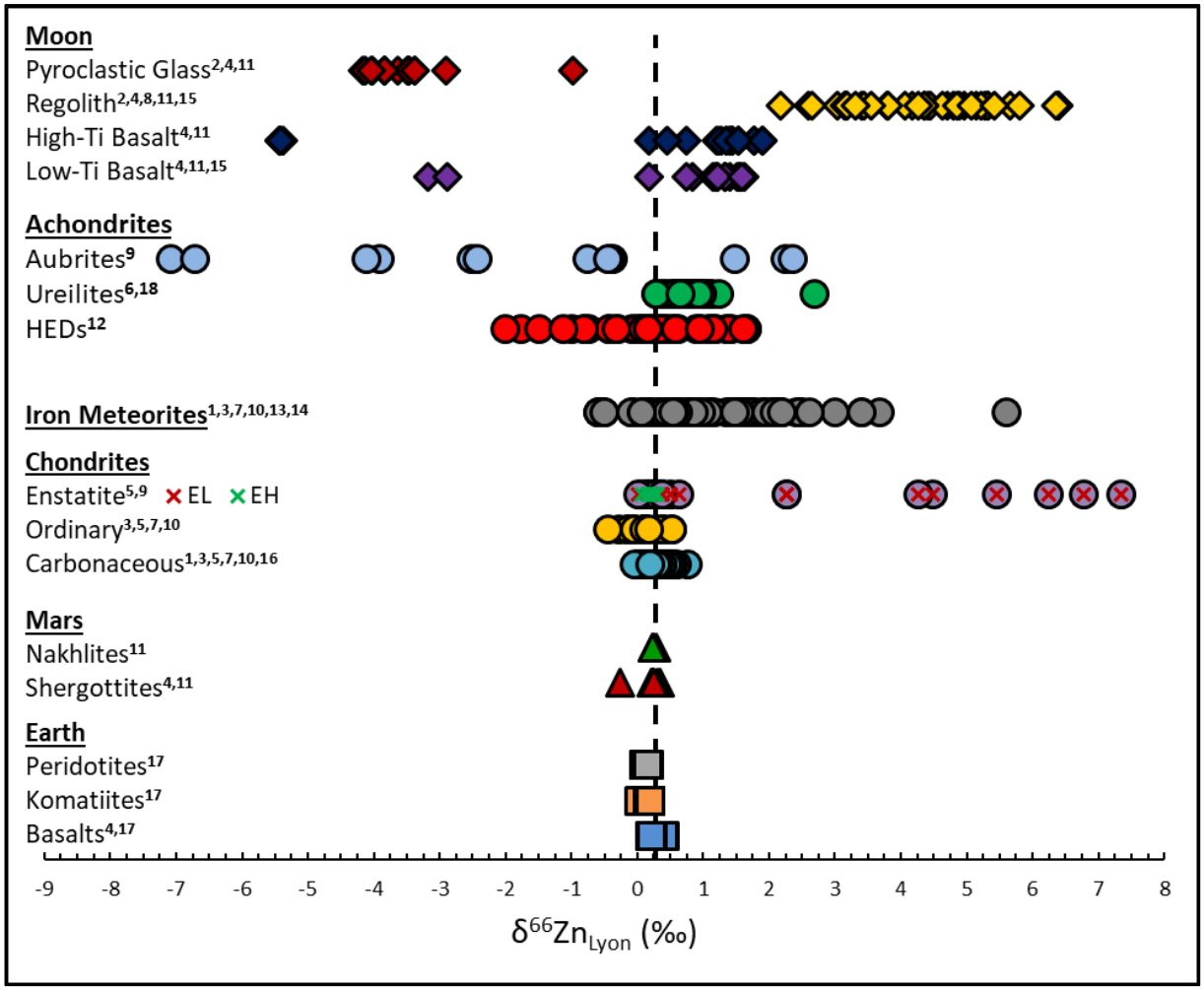


Figure 5.1: Overview of the Zn isotopic composition of various (extra-)terrestrial materials. The dashed line represents the average $\delta^{66}Zn_{Lyon}$ of the BSE (Chen et al., 2013a).
[1]Luck et al. (2005); [2]Moynier et al. (2006); [3]Moynier et al. (2007); [4]Herzog et al. (2009); [5]Moynier et al. (2009a); [6]Moynier et al. (2010); [7]Ghidan and Loss (2011); [8]Lindsay et al. (2011); [9]Moynier et al. (2011); [10]Barrat et al. (2012); [11]Paniello et al. (2012a); [12]Paniello et al. (2012b); [13]Chen et al. (2013b); [14]Bridgestock et al. (2014); [15]Kato et al. (2015); [16]Pringle et al. (2017); [17]Sossi et al. (2018b); [18]Brugier et al. (2019).

The first experimental data on Zn isotope fractionation in silicate melts was presented by Xue et al. (1996) who found that, in most conditions, evaporation of Zn from a silicate melt was limited by diffusion in the silicate melt. More recently Zn isotope fractionation during volatile loss at high temperature was studied by Wimpenny et al. (2019), who melted arkosic and rhyolitic soils as well as tektites at 1600 – 2200°C in air, and Sossi et al. (2020), who used a synthetic primitive basaltic composition at a range of T and fO_2 conditions. Sossi et al. (2020) covered a range of experimental conditions comparable to this study. They found significant Zn evaporation that was diffusion-limited and reported a heavy Zn isotope composition with fractionations upwards of $\delta^{66}Zn_{Lyon}$ = 12.48‰ for

the samples with the highest Zn depletion. This range of $\delta^{66}Zn$ covered the full range of positive $\delta^{66}Zn_{Lyon}$ values observed for natural (extra-)terrestrial samples.

This chapter discusses the results of the Zn isotope analyses of the SM and IB experiments described in Chapter **4**. It will examine how the $\delta^{66}Zn$ of these samples changed as a function of runtime, oxygen fugacity and the Zn abundance of the residual silicate melt and what this revealed about the evaporative environment. Three-isotope plots are used to distinguish between equilibrium and kinetic isotope fractionation. Liquid – vapour fractionation factors were determined and compared with theoretical values that can be determined for different evaporation environments based on previous work. These liquid – vapour fractionation factors were then used to compare with the isotope fractionation observed in various terrestrial and extra-terrestrial environments to assess the impact of volatile loss on the Zn abundance and isotopic composition in these environments and to assess the applicability of the experiments to natural environments.

5.2 – Results

5.2.1 – Processing of Samples and Starting Materials

5.2.1.1 – Zn Abundances and Double Spiking

It was important to accurately know the Zn abundance of the samples to accurately double spike them. Samples were double spiked using the Zn abundances obtained from LA-ICP-MS analyses (see Chapter **4**, Table **4.3**). The isotope dilution equations described in Chapter **3** were used to calculate the double spike:sample ratios of samples. This approach also enables the calculation of the Zn abundance of the purified Zn solutions if the initial sample masses are known. These calculations showed that there was variability in double spike:sample ratios (Fig. **5.4**). This figure showed that there was a variability in double spike:sample ratio between samples, but that it did not have a major impact on the errors of Zn double spike deconvolution for all but one sample. This variability was attributed to inaccurate LA-ICP-MS measurements as isotope dilution is considered to be among the most accurate methods of determining trace element abundances (Bulska and Ruszczyńska, 2017).

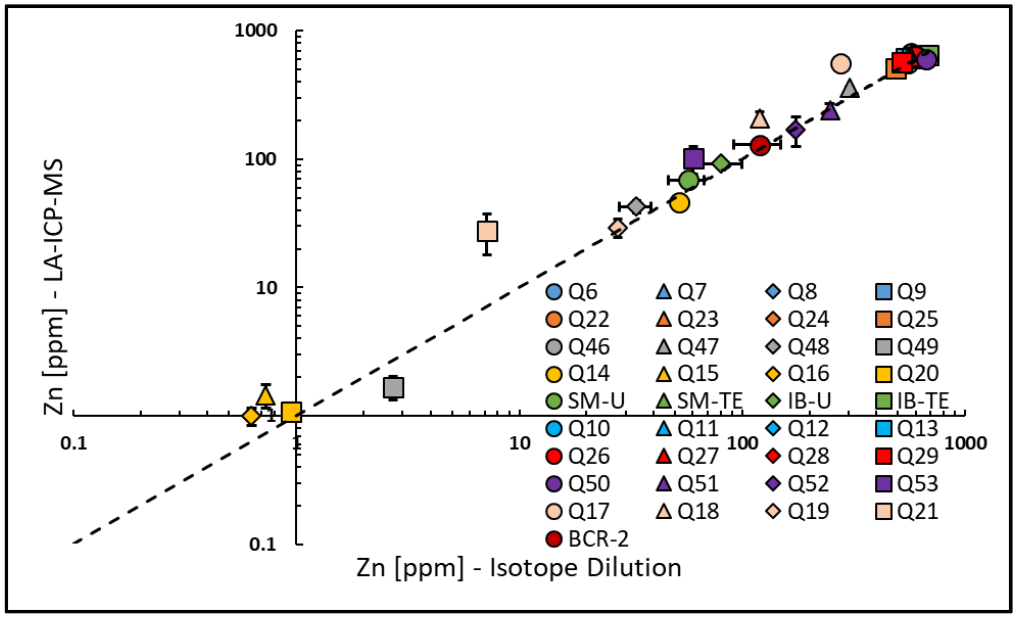


Figure 5.2: Comparison of Zn abundances obtained via isotope dilution and LA-ICP-MS measurements. The dashed line shows the one-to-one line. Error bars are 1 s.d. on the average.

A comparison of the LA-ICP-MS and isotope dilution Zn abundances showed that the LA-ICP-MS Zn concentrations were almost always higher than those obtained through isotope dilution (Fig. **5.2**). For most samples the misfit between the two approaches was ≤15% and Zn abundances matched the one-

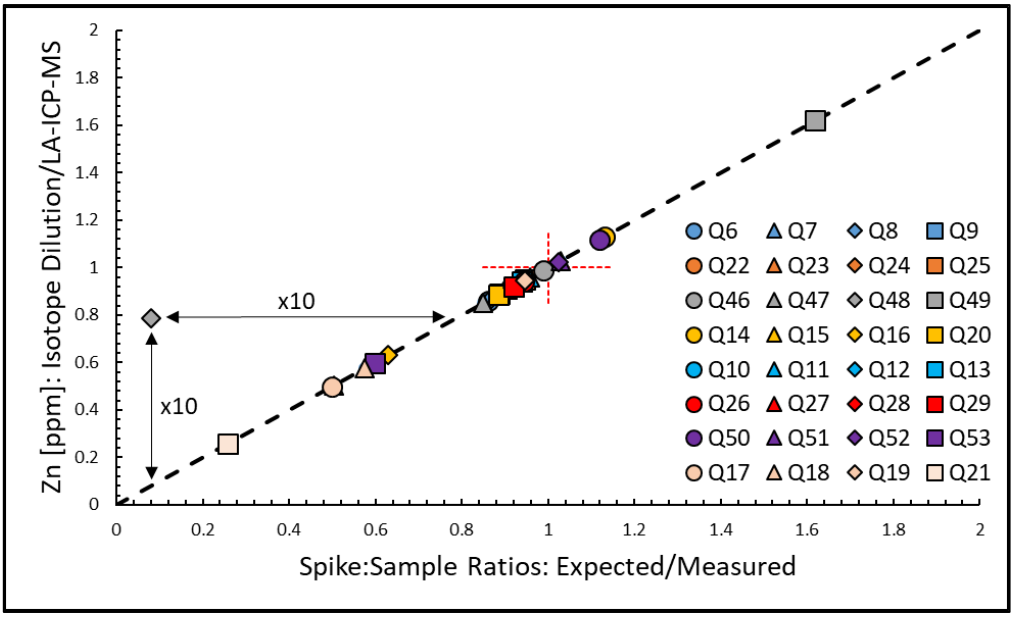


Figure 5.3: The effect of the Zn abundance on the accuracy of sample spiking. The dashed line indicates a one-to-one line. The dashed line is the one-to-one line and the red cross shows the expected spike:sample ratio of 1.4:1 ± 15% and compositional match of 1:1 ± 15%.

to-one line within error. There were seven samples that exhibited a larger misfit with six of those samples having $[Zn]_{LA\text{-}ICP\text{-}MS} > [Zn]_{Is.Dil}$ (Q15, Q16, Q17, Q18, Q21 and Q53) and one (Q49) where $[Zn]_{LA\text{-}ICP\text{-}MS} < [Zn]_{Is.Dil}$.

The difference between the LA-ICP-MS and isotope dilution Zn concentrations was the reason for the variability of the double spike:sample ratio between samples. This is illustrated using Figure **5.3** which shows the ratio of the expected (1.4:1) and measured double spike:sample ratio against the ratio of the two measured abundances. All but one sample fell on the one-to-one line, as would be expected if the LA-ICP-MS Zn concentrations was the cause of the misfit. The samples that deviated most from unity in Figure **5.3** were those with the biggest misfit between the two Zn abundances. There was one outlier, Q48, which was a factor ten from the one-to-one line because of a miscalculation during sample preparation. This resulted in a sample with an anomalously high double spike:sample ratio. However, due to limited sample material it was not possible to prepare a second aliquot with the correct double spike:sample ratio. An assessment of the errors introduced by this range in double spike:sample ratios using the Double Spike Toolbox (Rudge et al., 2009) showed that the range in double spike:sample ratios did not have a big impact on the error propagation during double spike

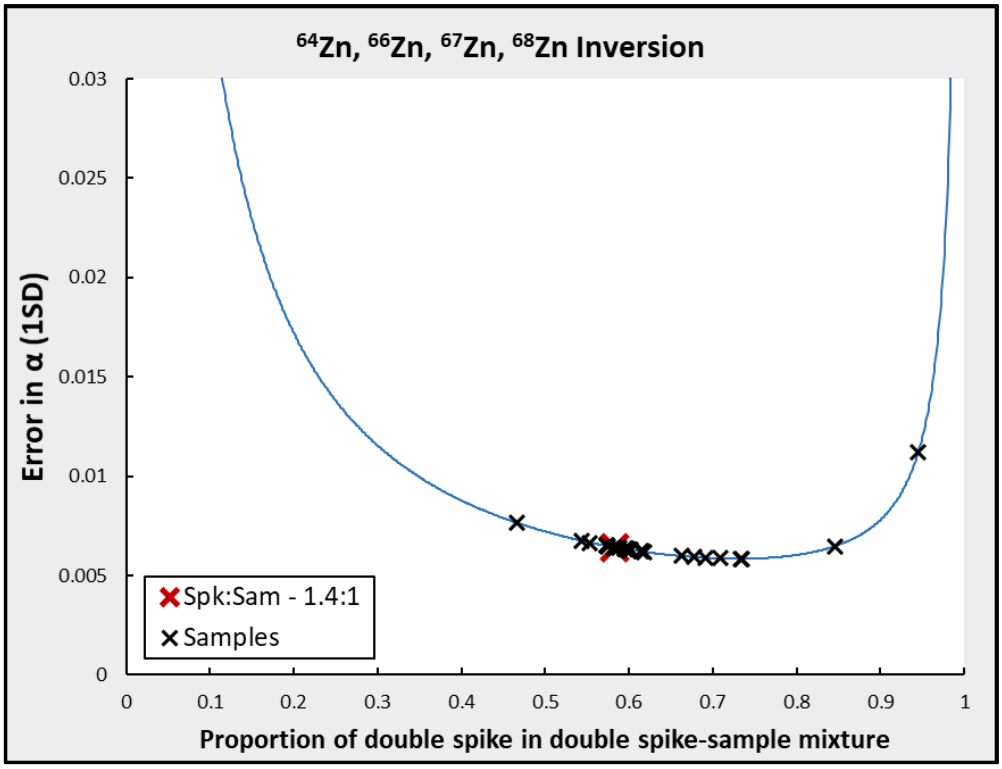


Figure 5.4: The effect of the double spike:sample ratio on the error of the double spike inversion. The red cross is the target double spike:sample ratio and the black crosses are the double spike:sample ratio of the samples.

inversion and actually slightly improved the error for the majority of samples as they had a slightly higher double spike:sample ratio (Fig. **5.4**; Table **5.1**). For Q48 the introduced error was approximately twice that of the other samples due to its anomalous double spike:sample ratio.

5.2.1.2 – Isotopic Composition of the Starting Materials

The Zn isotopic composition of the starting materials serves as a starting point in quantifying the isotope fractionation of the samples. The reagent-grade synthetic materials used to prepare the SM composition and the natural undoped IB starting material were not completely Zn-free. Therefore the $\delta^{66}Zn_{Lyon}$ of the doped starting material should fall on a mixing line between the $\delta^{66}Zn_{Lyon}$ of the undoped starting composition and the dopant, reagent-grade ZnO, where its position is controlled by the contribution of both end-members to the total Zn abundance in the doped starting material. This is shown on Figure **5.5** where the isotopic composition of the (un)doped starting materials and the ZnO were plotted against the fraction of Zn added via ZnO and it shows that the doped starting materials both fit on their respective mixing line.

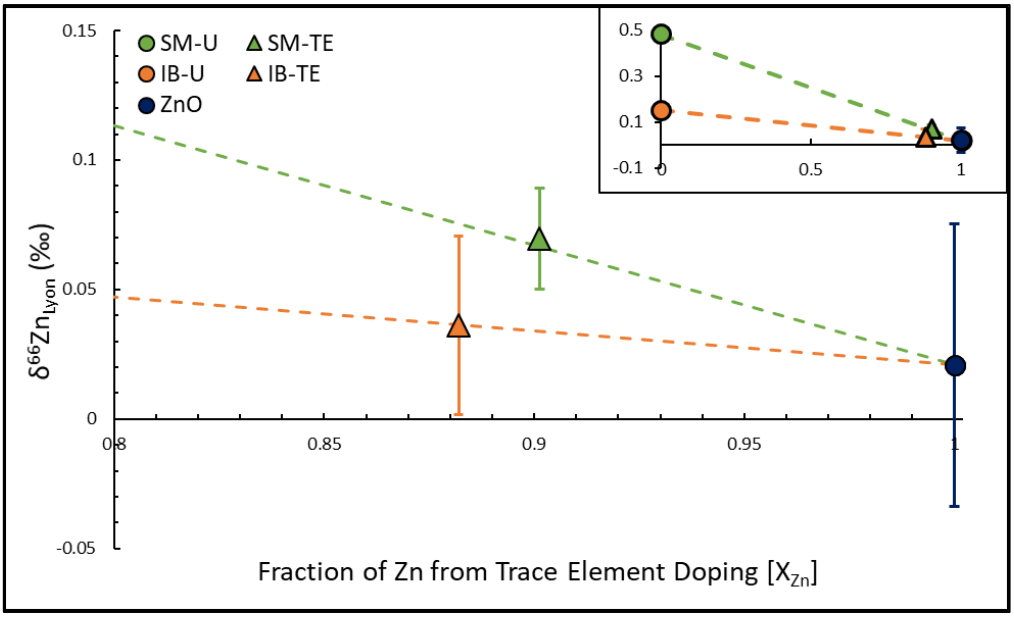


Figure 5.5: The fraction of Zn in the doped starting material [X_{Zn}] added as reagent-grade ZnO plotted against $\delta^{66}Zn_{Lyon}$ (‰) of the (un)doped starting materials and ZnO. Dashed lines represent the mixing lines between undoped starting material and ZnO. Main plot shows $X_{Zn} > 0.8$ with $0 < X_{Zn} < 1$ shown in the top right.

5.2.2 – Isotopic Composition of Samples

5.2.2.1 – Measured $\delta^{66}Zn$ Values

The obtained Zn concentration and isotope data for all samples is summarized in Table **5.1** which also contains the relevant experimental conditions; composition, oxygen fugacity (fO_2) and runtime.

Sample	Comp	log(fO_2)	t (s)	DSpk:Sam	Zn [ppm]	$\delta^{66}Zn_{Lyon}$ (‰)	*n*
Q6	SM	-0.68	180	1.596	572 ± 0.32	0.118 ± 0.019	3
Q7	SM	-0.68	900	1.509	571 ± 0.20	0.128 ± 0.049	3
Q8	SM	-0.68	1800	1.589	549 ± 2.61	0.202 ± 0.044	4
Q9	SM	-0.68	3600	1.345	542 ± 1.04	0.293 ± 0.103	4
Q22	SM	-3.05	180	1.509	564 ± 1.36	0.076 ± 0.097	4
Q23	SM	-3.05	900	1.495	547 ± 0.20	0.221 ± 0.062	4
Q24	SM	-3.05	1800	1.478	576 ± 0.59	0.393 ± 0.089	4
Q25	SM	-3.05	3600	1.348	486 ± 2.14	0.741 ± 0.115	5
Q46	SM	-5.98	180	1.392	553 ± 0.35	0.181 ± 0.154	4
Q47	SM	-5.98	900	1.621	303 ± 0.22	2.488 ± 0.031	4
Q48[1]	SM	-5.98	1800	17.11	33.6 ± 5.50	6.960 ± 0.554	4
Q49[1]	SM	-5.98	3600	0.874	2.72 ± 0.00	6.111 ± 0.247	2
Q14	SM	-8.01	180	1.189	52.3 ± 0.01	3.731 ± 0.037	4
Q15[2]	SM	-8.01	900	2.772	0.73 ± 0.00	8.245 ± 0.449	2
Q16[2]	SM	-8.02	1800	2.237	0.63 ± 0.00	6.013 ± 0.024	2
Q20[2]	SM	-8.02	3600	1.966	0.95 ± 0.00	12.124 ± 0.246	2
Q10	IB	-0.68	180	1.494	597 ± 1.89	0.047 ± 0.100	6
Q11	IB	-0.68	900	1.407	584 ± 0.38	0.124 ± 0.129	5
Q12	IB	-0.68	1800	1.472	600 ± 0.23	0.156 ± 0.167	6
Q13	IB	-0.68	3600	1.469	577 ± 0.42	0.215 ± 0.088	6
Q26	IB	-3.05	180	1.428	597 ± 0.40	0.055 ± 0.138	6
Q27	IB	-3.05	900	1.486	573 ± 0.26	0.259 ± 0.101	6
Q28	IB	-3.05	1800	1.506	552 ± 0.29	0.422 ± 0.119	6
Q29	IB	-3.05	3600	1.479	521 ± 0.21	0.682 ± 0.066	6
Q50	IB	-6.01	180	1.237	672 ± 0.52	0.447 ± 0.121	7
Q51	IB	-5.94	900	1.342	247 ± 0.10	2.645 ± 0.120	6
Q52	IB	-5.94	1800	1.344	174 ± 0.12	3.447 ± 0.050	5
Q53	IB	-6.01	3600	2.102	60.4 ± 0.10	5.199 ± 0.046	4
Q17	IB	-8.02	180	2.752	277 ± 0.22	1.005 ± 0.208	6
Q18	IB	-8.02	900	2.426	120 ± 0.24	2.000 ± 0.123	4
Q19[1]	IB	-8.02	1800	1.505	27.6 ± 0.04	3.934 ± 0.032	4
Q21[1]	IB	-7.98	3600	5.505	7.16 ± 0.01	3.904 ± 0.139	4
SM-U	SM	-	-	1.607	57.1 ± 10.3	0.483 ± 0.057	10
SM-TE	SM	-	-	1.490	578 ± 43.8	0.070 ± 0.068	11
IB-U	IB	-	-	1.525	80.2 ± 19.2	0.152 ± 0.093	12
IB-TE	IB	-	-	1.482	679 ± 65.9	0.036 ± 0.136	14
ZnO	-	-	-	1.289	-	0.021 ± 0.115	4
BCR-2	-	-	-	1.35 – 1.77	120 ± 28.2	0.231 ± 0.101	31
IRMM3702	-	-	-	1.2 – 1.7	1.08 ± 0.02	0.243 ± 0.116	63

Table 5.1: The Zn concentration [ppm; Isotope Dilution] and $\delta^{66}Zn_{Lyon}$ (‰) of samples, starting materials and secondary standards. Errors on the Zn abundance and $\delta^{66}Zn_{Lyon}$ are 2 standard deviations on the average.
[1]Ba correction was applied using $^{137}Ba^{2+}$ intensity instead of $^{138}Ba^{2+}$ intensity.
[2]Ba correction was applied using the modelled approach and $^{137}Ba^{2+}$ intensities.
The starting major and trace element composition of "SM" and "IB" can be found in Chapter **2** Table **2.2**.

For most samples the $I^{138}Ba^{2+}$ correction derived in Chapter **3** was applied. However, for some of the low Zn abundance samples, Q15, Q16, Q19, Q20, Q21, Q48 and Q49 this was not possible following either an interference on mass 69 and/or $I^{138}Ba^{2+}/I^{64}Zn$ ratios outside the limits of the correction, mostly attributed to low Zn abundances. For Q19, Q21, Q48 and Q49 the Ba correction was applied using $I^{137}Ba^{2+}/I^{64}Zn$ ratios and Q49 also had a significant Ni correction. For Q15, Q16 and Q20 Zn abundances were too low to apply any correction, therefore the Ba correction was modelled following the method outlined in Chapter **3**. Despite attempts at correcting for Ba interferences the isotopic composition of the most Zn depleted samples, Q15, Q16, Q20 and Q49 in the SM composition and Q21 in the IB composition, did not follow time and oxygen fugacity dependence observed for other samples and time series at other fO_2. This suggested that either Zn abundances were too low or Ni or Ba interferences too high to accurately determine $\delta^{66}Zn$ for these samples. In subsequent sections any trend involving at least one of these samples will be represented with a dashed line.

5.2.2.2 – Zn Abundance Dependence of $\delta^{66}Zn$

The $\delta^{66}Zn$ of the residual silicate melt increased with an increasing amount of volatile loss of Zn, here represented by the ln of the volatility factor (Fig. **5.6**). This matched expectations as the light ^{64}Zn isotope preferentially evaporates, leaving the residual melt enriched in the heavier ^{66}Zn isotope. Moreover, while the experimental set-up likely transports evaporating species away from the evaporation interface, ^{64}Zn would also diffuse through the gas phase faster than ^{66}Zn. For both the SM and IB compositions $\delta^{66}Zn$ increased with increasing volatile loss. However, the slope of this trend decreased with decreasing fO_2, matching the observations of Sossi et al. (2020). This suggested that the isotopic composition of the silicate melt at the evaporation interface varied between fO_2 series. If the melt was of identical composition and homogeneous at all fO_2 it is expected that isotope fractionation was solely dependent on the magnitude of the volatile loss. The most likely explanation for this would be the presence of a Zn depleted, chemically and isotopically distinct, boundary layer close to the evaporation interface as the evaporation rate of Zn exceeded its diffusion rate. In such

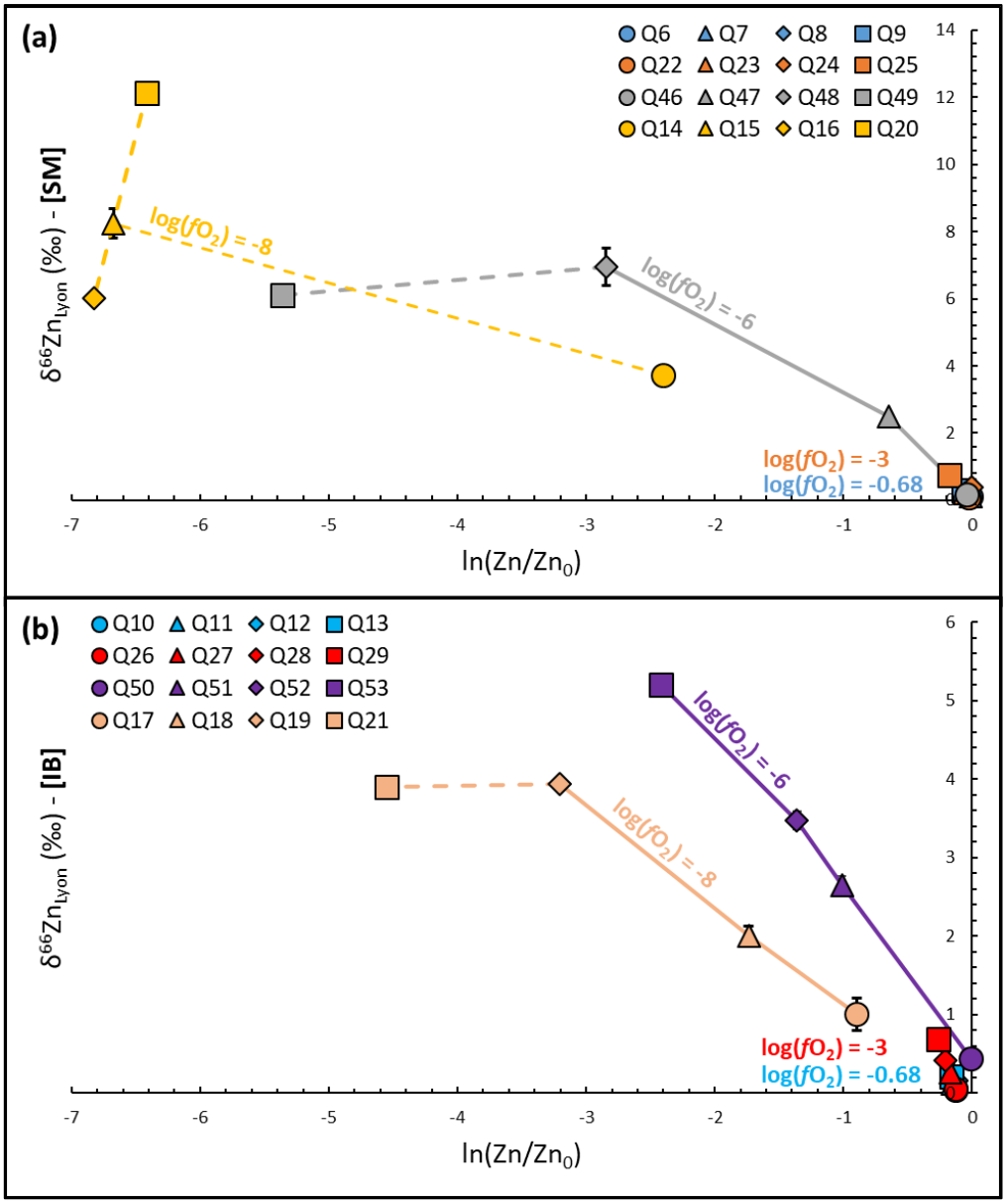


Figure 5.6: Plot of $\delta^{66}Zn_{Lyon}$ (‰) and the ln of the volatility factor for the **(a)** SM and **(b)** IB composition.

diffusion-limited evaporation environments, where the evaporating species is not replenished at a sufficient rate to maintain homogeneity in the silicate melt, the magnitude of isotope fractionation is smaller than for well-mixed phases (Richter, 2004). Since the evaporation rate of Zn increased with decreasing fO_2 whereas its diffusion rate was independent of fO_2 the residual silicate melt boundary layer became larger and isotopically heavier in more reducing conditions as diffusion was increasingly unable to keep up with evaporative loss. Therefore, the magnitude of $\delta^{66}Zn$ at a given degree of depletion is lower at lower fO_2, because the source melt is already depleted in ^{64}Zn. At present the effects of diffusion in evaporation experiments are not yet fully understood, but recent attempts have

been made at modelling diffusion-limited disequilibrium processes, such as evaporation (Guan and Liu, 2023).

That the evaporation rate exceeds the diffusion rate can be illustrated by comparing the timescales of evaporation (τ_{Evap}) and diffusion (τ_{Diff}) which are given by Equations **5.1** and **5.2** (Crank, 1975; Sossi et al., 2020).

$$(Eq. 5.1): \ \tau_{Evap} = \frac{t}{(1 - f_{Zn,surf})}$$

$$(Eq. 5.2): \ \tau_{Diff} = L^2/D_{Zn}$$

In these equations t is the runtime of the experiment, $f_{Zn,surf}$ is the volatility factor at the evaporating surface, L is the thickness of the sample, L_{Avg} = 1.5 mm, and D_{Zn} is the diffusivity of Zn in either melt composition. In the absence of surface concentrations these were assumed to equal the bulk concentration, probably incorrectly as they are likely lower following the presence of the Zn depleted boundary layer at the evaporative surface. Therefore τ_{Evap} is likely an overestimate. The evaporation timescale is seen to decrease with decreasing fO_2 at constant runtime. The τ_{Diff} only varied with composition and was determined using D_{Zn} obtained using Mungall (2002) which gave $D_{Zn,SM} = 1.29 \cdot 10^{-10}$ m^2s^{-1} and $D_{Zn,IB} = 6.88 \cdot 10^{-11}$ m^2s^{-1}. Considering the 60 minute experiments this yielded τ_{Diff}/τ_{Evap} = 0.40, 1.11, 4.85 and 4.85 for the SM composition at log(fO_2) = -0.68; -3.05; -6 and -8 respectively and τ_{Diff}/τ_{Evap} = 0.40, 1.08, 7.66 and 8.69 for the IB composition at log(fO_2) = -0.68; -3.05; -6 and -8 respectively. This showed that the experiments at log(fO_2) = -0.68 were the only ones where the timescale of evaporation exceeded the timescale of diffusion and evaporation was therefore not diffusion limited whereas the experiments at lower fO_2 were increasingly diffusion-limited as the gap between τ_{Diff} and τ_{Evap} grew. This is dependent on the chosen diffusivity of Zn as Sossi et al. (2020) consistently found $\tau_{Diff}/\tau_{Evap} < 1$ in their experiments with the SM composition, using their experimentally determined Zn diffusivity of $1.56 \cdot 10^{-9}$ m^2s^{-1}, but found a similar trend of τ_{Diff}/τ_{Evap} increasing with decreasing fO_2 and noted that their values were an order of magnitude below expected values.

5.2.2.3 – Time Dependence of $\delta^{66}Zn$

The observed $\delta^{66}Zn$ of the residual silicate melt was seen to increase linearly with increasing runtime, matching expectations that increased Zn loss would increase isotope fractionation (Fig. **5.7**). The slope of the time dependence increased with decreasing fO_2, reflecting the fO_2 dependence of the $ZnO\ (l) = Zn\ (g) + 0.5\ O_2\ (g)$ evaporation reaction where the equilibrium shifts more towards the gas phase with decreasing fO_2 at constant runtime. For both compositions it is observed that the temporal evolution trends at log(fO_2) = -0.68 and -3 and those at log(fO_2) = -6 and -8 have comparable slopes with a big change in slope between log(fO_2) = -3 and log(fO_2) = -6 which appears to match well with the observed evolution of τ_{Diff}/τ_{Evap} as a function of fO_2.

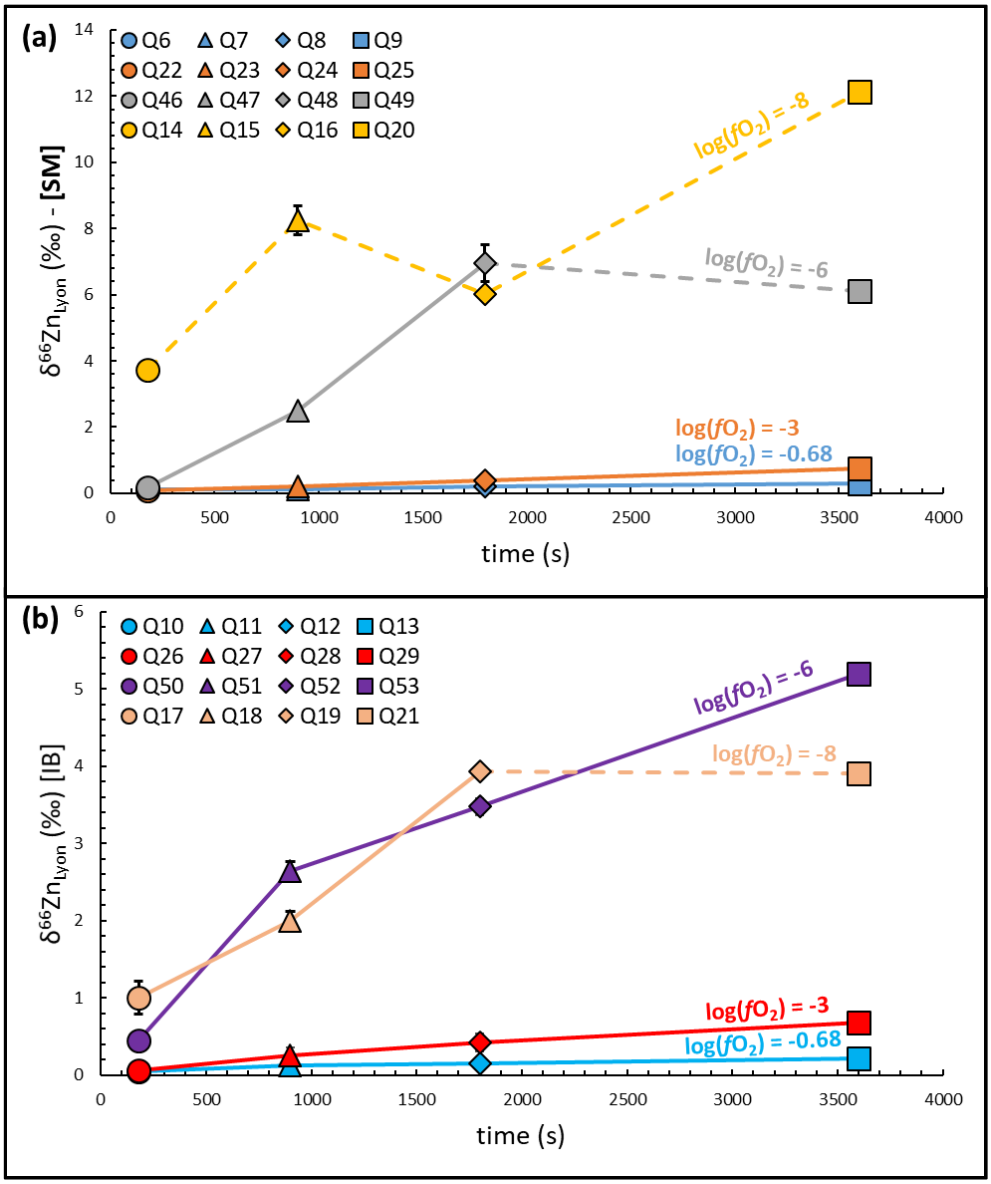


Figure 5.7: Plot of the time dependence of $\delta^{66}Zn_{Lyon}$ (‰) at fixed fO_2 for the **(a)** SM and **(b)** IB composition.

5.2.2.4 – Oxygen Fugacity Dependence of $\delta^{66}Zn$

The observed $\delta^{66}Zn$ of the residual silicate melt was seen to increase with decreasing fO_2, reflecting the fO_2 dependence of the $ZnO\ (l) = Zn\ (g) + 0.5\ O_2\ (g)$ evaporation reaction where the equilibrium shifts more towards the gas phase with decreasing fO_2 at constant runtime at a rate of $\log(K) \propto \frac{1}{2}\log(f O_2)$. This was not observed in the experiments as $\delta^{66}Zn$ increases exponentially with decreasing fO_2 with some of the experiments at $\log(fO_2)$ = -8 not adhering to the trend observed for the experiments in more oxidizing conditions (Fig. **5.8**).

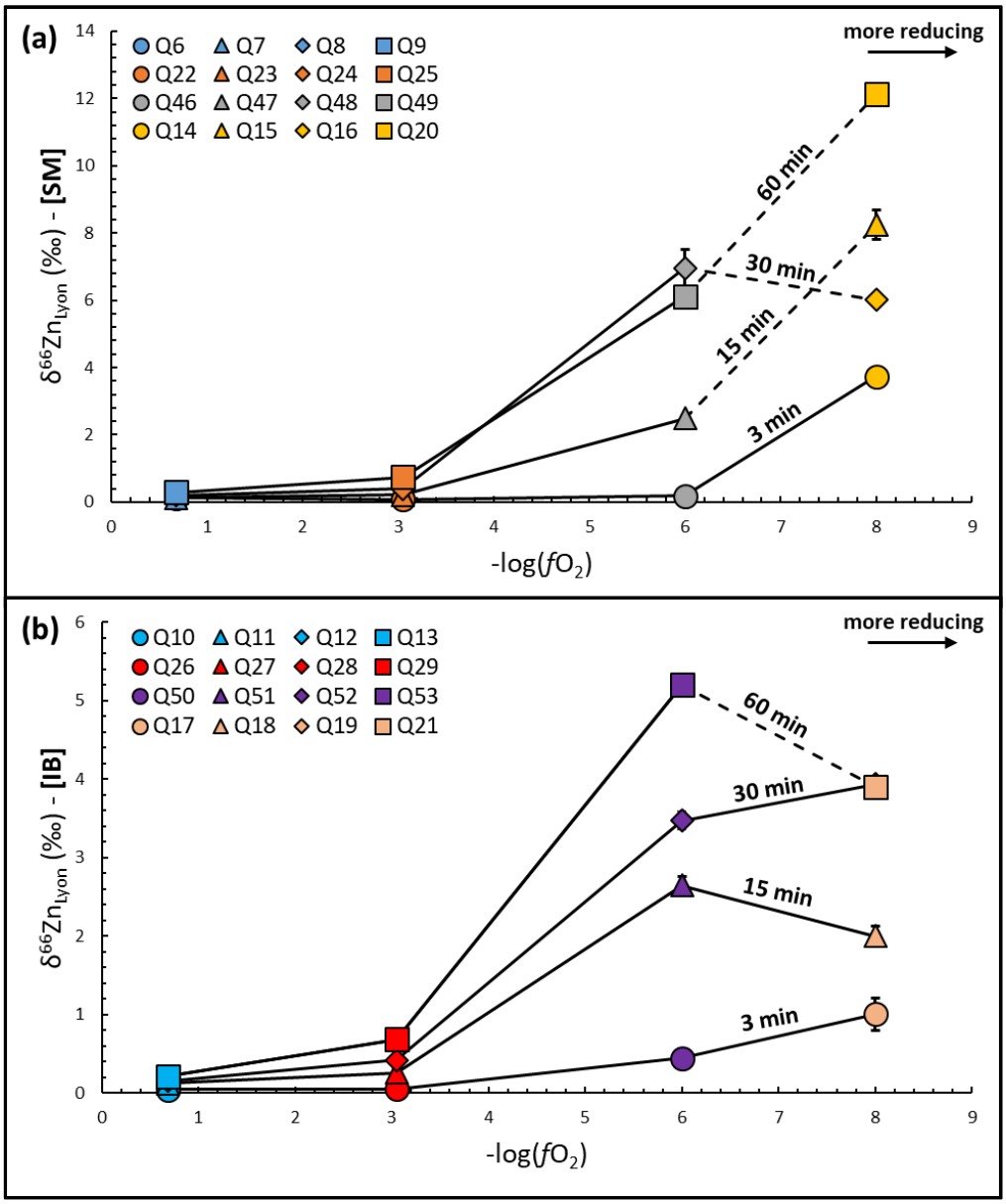


Figure 5.8: Plot of the oxygen fugacity dependence of $\delta^{66}Zn_{Lyon}$ (‰) at fixed runtimes for the **(a)** SM and **(b)** IB composition.

5.2.3 – Fractionation Factors

5.2.3.1 – Rayleigh Equation

The evolution of the isotopic composition of a finite reservoir can be described through the Rayleigh equation (Rayleigh, 1896; Eq. **5.3**).

$$(Eq.5.3):\ {}^{66/64}R_{Zn} = {}^{66/64}R_{Zn,0} f_{Zn}^{\ \alpha_{66/64}-1}$$

In Equation **5.3** ${}^{66/64}R_{Zn,0}$ and ${}^{66/64}R_{Zn}$ are the ^{66}Zn/^{64}Zn isotope ratios of the melt before and after the experiment – in this study that of the doped starting material and the sample respectively, f_{Zn} is the fraction of Zn remaining in the sample – the volatility factor, and $\alpha_{66/64}$ is the fractionation factor for ^{66}Zn and ^{64}Zn. To find the fractionation factor using delta values the Rayleigh equation can be approximated by Equation **5.4**.

$$(Eq.5.4):\ 10^{-3}(\delta^{66}Zn - \delta^{66}Zn_0) \cong \left(\alpha_{66/64} - 1\right)\ln(f_{Zn})$$

Equation **5.4** shows that a plot of $\ln(f_{Zn})$ against the difference in isotopic composition of sample and starting material should result in a straight line where the slope yields $\alpha_{66/64}$. The value of $\alpha_{66/64}$ changes depending on the process that generated the fractionation, in this study either diffusion in the silicate melt and/or gas phase or liquid – vapour fractionation.

5.2.3.2 – Calculating Fractionation Factors

Recent studies have enabled the prediction of the fractionation factor for various isotope fractionation processes (Richter et al., 2003, 2009; Dominguez et al., 2010; Young et al., 2019; Sossi et al., 2020; Watkins and Antonelli, 2021). For evaporation in an open system where evaporating species are immediately transferred away from the reaction interface and the equilibrium partial pressure (P_{eq}) far exceeds the actual partial pressure (P) of the gas phase the fractionation factor is described in terms of the difference in diffusivities of the different isotopes in the system (Eq. **5.5**; Richter et al., 2003).

$$(Eq.5.5):\ \alpha_{i/j} = \frac{D_i}{D_j} = \left(\frac{m_j}{m_i}\right)^{\beta}$$

In this equation $\alpha_{i/j}$ is the fractionation factor, D is the diffusivity of either isotope, m is the molar mass and β is an empirically determined exponent where 0 ≤ β ≤ 0.5. For ideal gases β = 0.5 and for silicate melts ≤ 0.3 (Watkins and Antonelli, 2021). For $^{66}Zn/^{64}Zn$, assuming ideal gas behaviour, this yielded an expected fractionation factor for diffusion in the gas phase of $\alpha_{66/64}$ = 0.9847. On the other hand, it was more challenging to determine $\alpha_{66/64}$ for diffusion in the silicate melt.

Diffusion in the silicate melt was observed to be a limiting factor for Zn in the SM and IB compositions. In the presence of a compositional gradient diffusion preferentially transports the lighter isotopes through the melt, leaving the remaining material enriched in the heavier isotope. The magnitude of β for diffusion in a silicate melt increases with increasing trace element diffusivity (Watkins and Antonelli, 2021). Only a single published value of β = 0.06 ± 0.01 was found for Zn diffusion, in olivine which may not accurately represent its behaviour in a silicate melt (Yang and Liu, 2023). The best approximation of β for diffusion of divalent elements with comparable mass to Zn in a silicate melt was β = 0.015 ± 0.010, obtained for Fe^{2+} diffusion in a basaltic melt by Richter et al. (2009). Using β = 0.06 ± 0.01 this gives $\alpha_{66/64}$ = 0.9982 ± 0.0003 and using β = 0.015 ± 0.010 this gives $\alpha_{66/64}$ = 0.9995 ± 0.0003.

Recent studies suggest that evaporation experiments were more accurately represented by scenarios where $P/P_{eq} \rightarrow 1$. Two similar equations were derived for separate scenarios of diffusion in the gas phase with either a forced convection environment (Young et al., 2019) or a natural convection environment (Sossi et al., 2020). These approaches were mostly identical, but different assumptions of diffusive behaviour in the gas phase resulted in a different expression for the mass transfer coefficient (k_c; Chilton and Colburn, 1934) which resulted in slightly different final equations. For both methods the fractionation factor is determined using Equation **5.6**.

$$(Eq.5.6): \quad \alpha_{i/j} = \frac{\alpha_{c,i}}{\alpha_{c,j}} \left(\frac{\mu_{jk}}{\mu_{ik}}\right)^{\beta}$$

In this equation α_c is the condensation coefficient, a parameter similar to the evaporation coefficient discussed in Chapter **4** that is equally poorly constrained, and μ_{ik} is the reduced mass of the isotope (i or j) in the gas phase (k) given by $\mu_{ik} = \frac{m_i m_k}{m_i + m_k}$, where m is the molar mass of each component. The difference between the methods is only in the exponent where β = 0.5 in Young et al. (2019) and β = 1/3 in Sossi et al. (2020). Due to a lack of available data it was assumed that α_c was identical for both Zn isotopes and therefore the fractionation factor was solely dependent on the reduced masses. The reduced masses varied with fO_2 as the composition of the ambient gas changed between experiments to buffer fO_2. Overall, it was observed that the liquid – vapour fractionation factor for both methods was highest in air. In experimental conditions where the fO_2 was buffered using a CO-CO_2 gas mix $\alpha_{66/64}$ increased with an increasing abundance of CO (Table **5.2**). This followed expectation as kinetic isotope fractionation is not affected by oxygen fugacity because the mass transfer coefficient is essentially independent of fO_2, apart from changes in the molar mass of the ambient gas used to buffer fO_2 (Sossi et al., 2020). They showed that an increase of the relative abundance of lower mass gas species increased the mass transfer coefficient, resulting in an increased $\alpha_{66/64}$.

log(fO_2)	m_k [gmol^{-1}]	β = 1/3	β = 0.5
-0.68	29.0	0.9968	0.9953
-3	44.0	0.9959	0.9938
-6	43.2	0.9959	0.9939
-8	38.6	0.9962	0.9943

Table 5.2: The average molar mass of the ambient gas and the expected liquid–vapour fractionation factor for $^{66}Zn/^{64}Zn$ at different fO_2 calculated using Equation **5.6**. See Table **2.1** for CO-CO_2 ambient gas composition.

5.2.3.3 - Samples

Equation **5.4** was used to calculate the fractionation factors for each individual sample which resulted in $\alpha_{66/64}$ between 0.9953 and 0.9999 with two outliers that comparatively had anomalously low fractionation factors (Q24: $\alpha_{66/64}$ = 0.9116 and Q50: $\alpha_{66/64}$ = 0.9641; Fig. **5.9**). This was caused by higher Zn abundances than expected for the measured isotope fractionation when compared with other sample in their respective time series. Overall, the fractionation factors better matched the

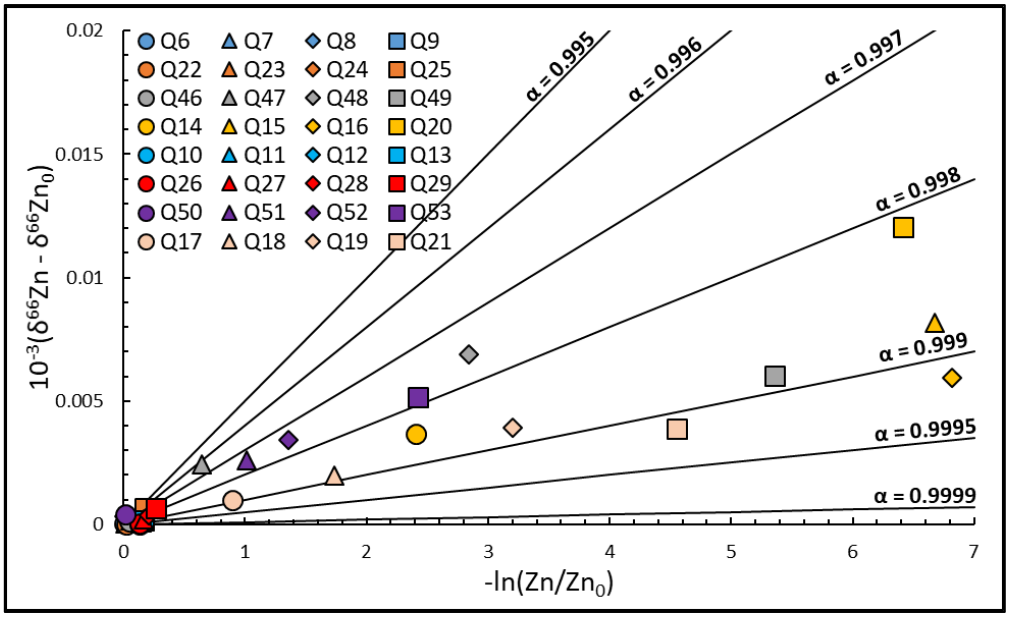


Figure 5.9: A plot of volatile loss plotted as a function of the difference in isotopic composition of sample and starting material. Solid lines represent different fractionation factors. Errors bars are smaller than symbol size and individual time series can be found in Figure **5.10** and **5.11**.

predicted values of Sossi et al. (2020) than those of Young et al. (2019). However, the magnitude of the measured $\alpha_{66/64}$ exceeds the predicted fractionation factors in Table **5.2**, particularly in more reducing conditions. The magnitude of $\alpha_{66/64}$ might be related to the assumed behaviour of the condensation coefficient, $\frac{\alpha_{c,i}}{\alpha_{c,j}} = 1$, as the misfit between the measured $\alpha_{66/64}$ and those predicted using Equation **5.4** with β = 1/3 was consistent at all experimental conditions, except SM in air. To reduce $\alpha_{66/64}$ and match the predicted values it would require that $\alpha_{c,66_{Zn}} < \alpha_{c,64_{Zn}}$. This is expected to be the case as the condensation coefficient is related to vibrational frequencies. This energetically favours the light isotope over the heavy (Ackermann et al., 1962). To match the expected values would require $\frac{\alpha_{c,66_{Zn}}}{\alpha_{c,64_{Zn}}}$ = 0.9978 ± 0.0004.

The measured $\alpha_{66/64}$ were independent of runtime in most time series, but broadly followed the fO_2 dependence observed in Table **5.2**. For the SM composition the time series average $\alpha_{66/64}$ at fixed fO_2 varied from 0.9962 ± 0.0009 in air to 0.9977 ± 0.0015 at log(fO_2) = -3 to 0.9976 ± 0.0009 at log(fO_2) = -6 to 0.9985 at log(fO_2) = -8. The poor quality of the data for SM samples at log(fO_2) = -8 meant that the fractionation factor was determined using a single sample, Q14. For the IB composition the time

series average $\alpha_{66/64}$ at fixed fO_2 varied from 0.9993 ± 0.0004 in air to 0.9986 ± 0.0008 at log(fO_2) = -3 to 0.9976 ± 0.0002 at log(fO_2) = -6 to 0.9989 ± 0.0001 at log(fO_2) = -8. These fractionation factors were closer to unity than the theoretically predicted values. This had been observed previously in experimental studies and was attributed to isotopic heterogeneity of the melt caused by a diffusion-limited evaporation environment (Richter et al., 2007; Sossi et al., 2020). The $\alpha_{66/64}$ obtained in this study compare well to those of Sossi et al. (2020) who got $\alpha_{66/64}$ = 0.9959 in air and $\alpha_{66/64}$ = 0.9967 – 0.9978 in various CO-CO_2 gas mixes with a starting composition that was comparable to the SM composition. Wimpenny et al. (2019) found $\alpha_{66/64}$ = 0.99879 for their experiments on arkosic soils in an Ar atmosphere, comparable to the $\alpha_{66/64}$ obtained in this study at log(fO_2) = -8.

5.2.3.4 – Comparing Samples and Modelled Fractionation

To compare the measured $\delta^{66}Zn$ to the different models described in the previous section a Rayleigh-based isotope fractionation model was used (Nielsen et al., 2021). This model considered a closed-

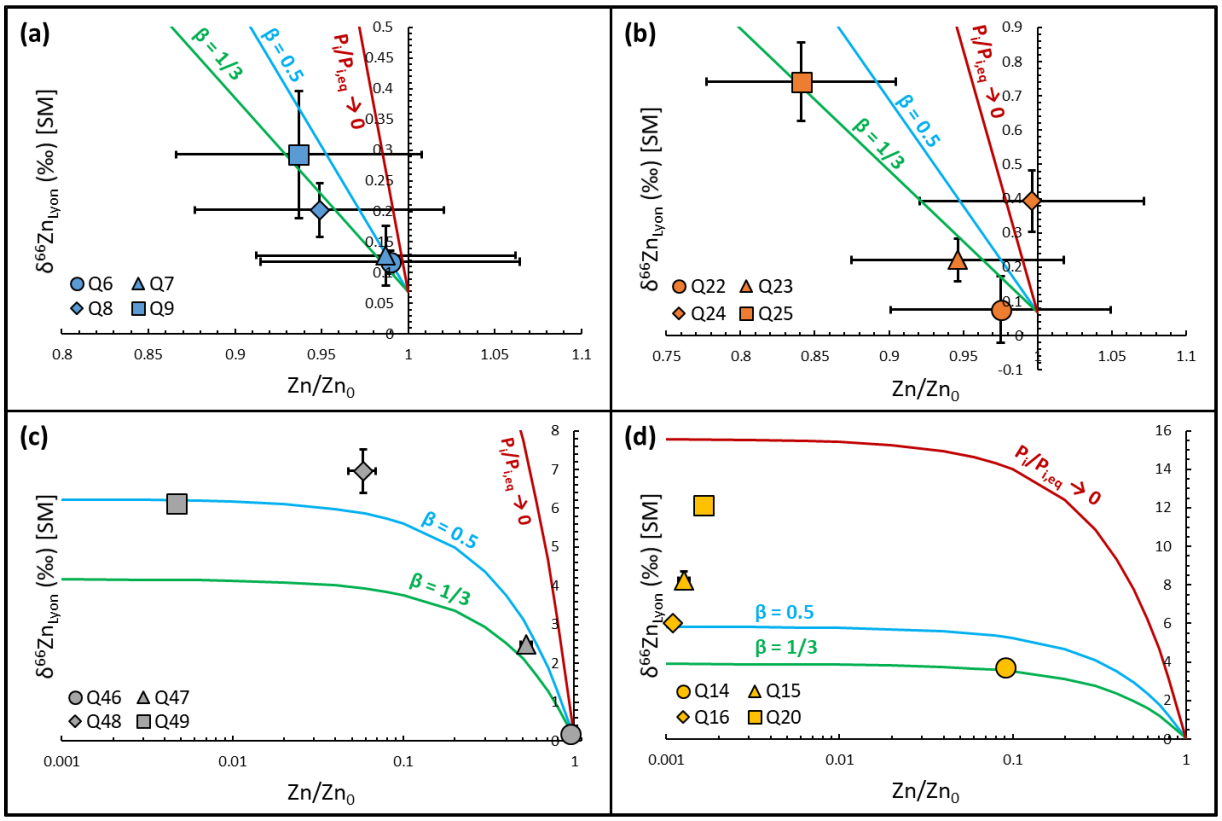


Figure 5.10: Comparison of the measured $\delta^{66}Zn_{Lyon}$ (‰) as a function of the volatility factor for the SM composition **(a)** in air, **(b)** at log(fO_2) = -3, **(c)** at log(fO_2) = -6 and **(d)** at log(fO_2) = -8. Coloured lines represent the different evaporation scenarios of Young et al. (2019) and Sossi et al. (2020) described in the main text.

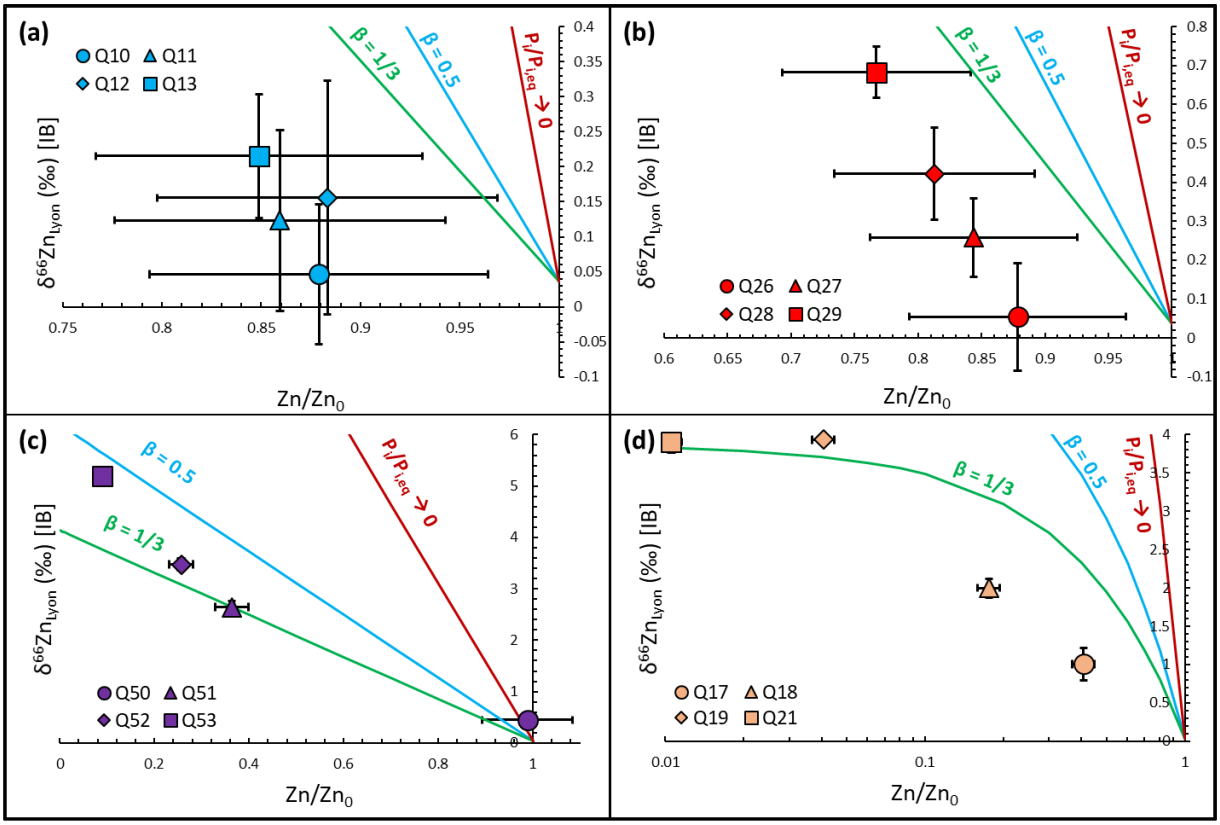


Figure 5.11: Comparison of the measured $\delta^{66}Zn_{Lyon}$ (‰) as a function of the volatility factor for the IB composition (**a)** in air, **(b)** at log(fO_2) = -3, **(c)** at log(fO_2) = -6 and **(d)** at log(fO_2) = -8. Coloured lines represent the different evaporation scenarios of Young et al. (2019) and Sossi et al. (2020) described in the main text.

system batch model where the evaporating species were equilibrated with the melt before being transported away from the evaporation interface (Eq. **5.7**).

$$(Eq.5.7): \quad {}^{66/64}R_{Zn} = {}^{66/64}R_{Zn,0}\frac{1}{f_{Zn} + \alpha_{66/64}(1 - f_{Zn})}$$

This model was likely not fully representative of the experimental environment as the gas flow through the furnace would have transported evaporating species away from the interface before equilibrium was established. The model determines how the initial $^{66}Zn/^{64}Zn$ isotope ratio changes due to evaporative loss as a function of the Zn abundance in the residual silicate melt and the liquid – vapour isotope fractionation factor. The three different evaporation scenarios described using Equation **5.5** and **5.6** were used to model expected isotope fractionation using Equation **5.7** and compared to the measured $\delta^{66}Zn$ of the samples (Fig **5.10** – **5.11**). These figures showed that the assumption that $P/P_{eq} \rightarrow 0$ does not match the observed isotope fractionation. Instead, the observed evaporative loss matches better with studies that found that evaporation was a diffusion-limited near-equilibrium

process with $P/P_{eq} \rightarrow 1$ (Sossi et al., 2020) which is also thought to have been the evaporative environment for evaporative loss from planetesimals (Young et al., 2019). Figures **5.10 – 5.11** show that the assumption of $P/P_{eq} \rightarrow 0$ did not match the assumptions used in the derivation of the modified HKL equation (Sossi et al., 2019). This was not a requirement for the application of the HKL as recent work by Liu et al. (2022) used a version of the modified HKL for cases where $P/P_{eq} \rightarrow 1$. However, this still requires a value for P which has thusfar not been determined experimentally. Instead, Liu et al. (2022) opted to assume that P/P_{eq} = 0.999 in their use of the modified HKL for near-equilibrium evaporation.

5.3 – Discussion

5.3.1 – Comparison with Previous Work

The difficulty in direct comparisons between results in this study and previous work following the effects of differences in sample geometry, experimental set-up and experimental conditions between studies on trace element volatility was discussed in detail in Chapter **4**. Therefore it was not possible to directly compare the $\delta^{66}Zn$ obtained in this study with those found in other experimental studies into Zn isotope fractionation by Xue et al. (1996), Wimpenny et al. (2019) and Sossi et al. (2020). However, the overall trends of increasing Zn isotope fractionation with decreasing fO_2 and increased runtime and decreasing Zn abundance in the silicate melt in a diffusion-limited evaporation environment are consistent observations in all studies. Moreover, liquid-vapour fractionation factors obtained in this study, Wimpenny et al. (2019) and Sossi et al. (2020) were comparable within error at comparable experimental conditions.

Experimental studies into evaporative loss and isotope fractionation of moderately volatile elements have covered elements other than Zn including K, Cr, Cu, Rb, Te and Tl (Ni et al., 2021; Nielsen et al., 2021; Zhang et al., 2021; Klemme et al., 2022; Neuman et al., 2022; Renggli et al., 2022). These studies found that that the experimentally obtained liquid – vapour fractionation factors were consistently higher than predicted values for all of the elements studied, reflective of a diffusion-limited evaporation environment. Neuman et al. (2022) were the only ones that actively attempted to avoid diffusion-limited evaporation. This was done by extending their experimental runtimes to multiple days to achieve $\tau_{Diff}/\tau_{Evap} << 1$, conditions were otherwise comparable to the experimental conditions in this study; T = 1300 – 1400°C, $-0.68 \leq \log(fO_2) \leq -10.7$ and a basaltic starting composition. They did not discuss their Zn isotope data as Zn was lost via evaporation and by incorporation into mineral phases. Their liquid – vapour fractionation factors for K and Cu were comparable to those in other studies and larger than the theoretically predicted values.

5.3.2 – The Zn Isotopic Composition of Solar System Bodies

5.3.2.1 – Experimental Conditions vs. Magma Ocean Conditions

It must be stated, as was done in Chapter **4**, that the experiments in this study are unlikely to accurately reflect the materials and/or conditions during the early evolution of the different rocky bodies in the solar system as both the silicate melt and gas phase are not necessarily representative of the potential surface magma oceans and early atmospheres. Moreover, experimental conditions were controlled and constant whereas those in a magma ocean would have been changing as the body evolved compositionally, cooled and became more oxidizing with time.

In the silicate melt the major element composition was not reflective of the average terrestrial, lunar or Martian (mantle) composition or that of their various chondritic meteorite building blocks (Palme and O'Neill, 2014; Yoshizaki and McDonough, 2020; 2021). The IB composition has comparable SiO_2 and FeO contents to the BSE, but other major elements diverge significantly. The SM composition shows an overall poor comparison to the BSE. In the previous chapter it was shown that compositional differences can have a strong effect on trace element volatility and therefore isotope fractionation. Moreover, the evolution of $\delta^{66}Zn$ with Zn abundance showed that evaporation in the experiments was diffusion-limited whereas rocky bodies of sufficient size would be able to minimize compositional gradients through convection. Overall, $\alpha_{66/64}$ is expected to be closer to unity for diffusion-limited evaporation than for evaporative loss unlimited by diffusion. Furthermore, it is likely the oxidation state of the magma oceans was more reducing than the conditions in the experiments (Wade and Wood, 2005; Barr, 2016), particularly in some of the meteorite parent bodies that accreted and differentiated in the early stages of solar system evolution (e.g. Keil, 2002; 2010). Moreover, while temperatures in the magma ocean are still heavily debated peak temperatures are expected to be higher than 1400°C particularly in the time shortly after the impact of large bodies (e.g. Canup et al., 2015; Lock et al., 2018).

The partial pressure and composition of the ambient gas in the experiments is also unlikely to reflect the early planetary atmospheres which consisted mainly of outgassed volcanic species, dominated by H_2O, CO_2 and N_2 with minor amounts of CO and H_2 and CH_4 and atmospheric pressures higher than observed on these bodies at the present-day as atmosphere partially or completely dissipated over time (Kulikov et al., 2007; Zahnle et al., 2010; Hirschmann, 2012). Moreover, stable atmospheres on the larger planetary bodies would have enabled equilibration between the atmosphere and evaporating species whereas smaller bodies were unable to retain an atmosphere and evaporation likely occurred into a thin or transient atmosphere or into vacuum. All of these factors affect liquid – vapour fractionation factors and therefore may be reasons for misfits between naturally observed $\alpha_{66/64}$ and those obtained experimentally in this study.

Considering these discrepancies between experimental data and natural samples it was considered to be most appropriate to use the liquid – vapour fractionation factors obtained for the most reducing experiments at log(fO_2) = -8 (ΔIW+1.7), $\alpha_{66/64,SM,-8}$ = 0.9985 and $\alpha_{66/64,IB,-8}$ 0.9989 ± 0.0001, to model volatile loss on extra-terrestrial bodies. These conditions most closely approached the expected conditions in a magma ocean. For terrestrial materials the experimental $\alpha_{66/64}$ used for comparison were discussed separately. Theoretical $\alpha_{66/64}$ were calculated using Equations **5.5** and **5.6** assuming the average mass of the atmosphere was that of the CO-CO_2 mix used to buffer fO_2 at log(fO_2) = -8.

5.3.2.2 – The Earth – Moon System

The Moon-forming Giant Impact, where a proto-Earth collided with a Mars-sized planetesimal, Theia, is thought to be the final stage of the accretion in the Earth – Moon system (Quintana et al., 2016). The partial vaporisation and subsequent condensation of the terrestrial mantle following the Giant Impact resulted in a chemically and isotopically similar terrestrial mantle and Moon for refractory lithophile elements. Lunar basalt samples exhibit trace element depletions and heavy isotope enrichments compared to the terrestrial mantle for a variety of moderately volatile elements which has been attributed to volatile loss (e.g. Herzog et al., 2009; Paniello et al., 2012a; Boyce et al., 2015;

Wang and Jacobsen, 2016; Kato and Moynier, 2017; Pringle and Moynier, 2017; Fehr et al., 2018; Wang et al., 2019). The Zn abundance (53.5 ± 5 ppm) and isotopic composition ($\delta^{66}Zn$ = 0.28 ± 0.05‰) of the BSE is mostly homogeneous in the terrestrial mantle and remains unfractionated during partial melting (Chen et al., 2013a), metal-silicate partitioning (Bridgestock et al., 2014; Mahan et al., 2017; Seegers et al., 2020) or sulphide sequestration (Xia et al., 2019). Therefore, the lower average Zn abundance (1.5 ± 0.4 ppm) and heavier isotopic composition ($\delta^{66}Zn$ = 1.4 ± 0.2‰) of lunar basalts has been attributed to volatile loss (Day et al., 2020a).

The paucity of data on the composition of the lunar interior means that the Zn abundance and isotopic composition of the lunar basalts has been assumed to be representative of a homogeneous lunar mantle. Other lunar samples include the Mg-suite cumulates, which are more Zn depleted ($[Zn]_{AVG}$ = 0.67 ppm) and have a heavier Zn isotopic composition ($\delta^{66}Zn$ = 2.4 – 9.6‰) which has been attributed to volatile loss from a lunar magma ocean (Day et al., 2020a). The isotopic composition of lunar pyroclastic glasses and regolith were not considered to be due to evaporative loss of Zn as their

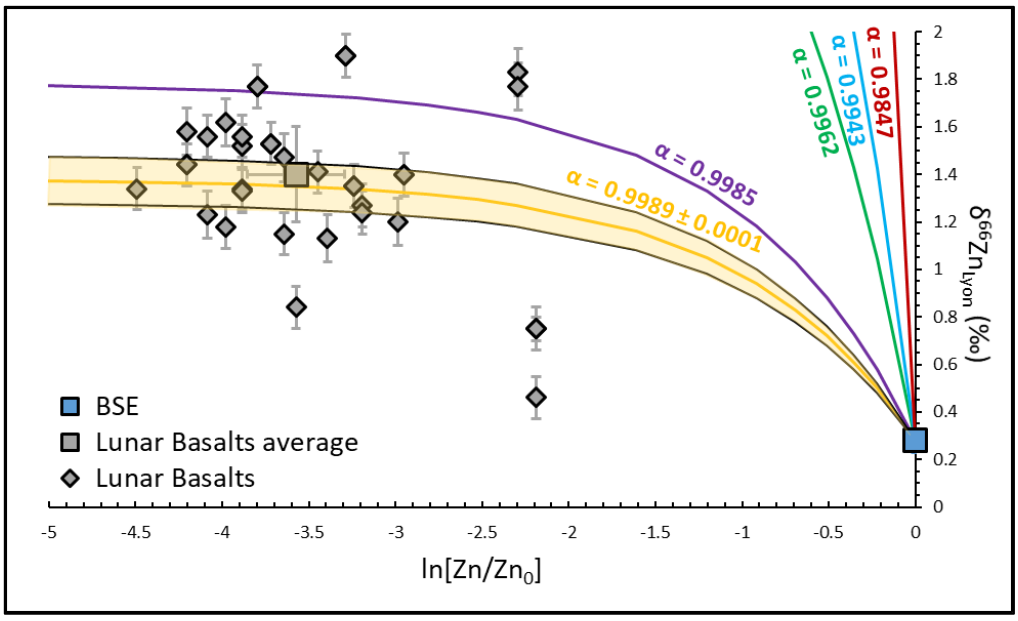


Figure 5.12: The Zn isotopic composition of the Earth – Moon system compared to different model fits. Trace element and isotopic data for terrestrial and lunar mantles and individual lunar basalts from Moynier et al. (2006), Herzog et al. (2009), Paniello et al. (2012a), Chen et al. (2013a), Palme and O'Neill (2014), Kato et al. (2015) and Day et al. (2020a). Coloured lines represent different model fits using $\alpha_{66/64}$ for **SM**, IB and the three theoretical approaches discussed in Section **5.2.3.2**.

primary isotopic signatures were likely overprinted by secondary processes and therefore not representative (Herzog et al., 2009; Paniello et al., 2012a).

The isotope fractionation model in Equation **5.7** was used to model the evolution of the isotopic composition of the Earth-Moon system using the experimentally obtained $\alpha_{66/64}$, taking the BSE $\delta^{66}Zn_{Lyon}$ as starting composition. Figure **5.12** shows that the $\alpha_{66/64}$ obtained for the IB composition ($\alpha_{66/64}$ = 0.9989 ± 0.0001) could reproduce the observed isotope fractionation behaviour in the Earth – Moon system within error. The modelled fractionation for the SM composition predicts that the average Zn isotopic composition of the Moon would be $\delta^{66}Zn \approx 1.75‰$. Using lunar basalts Sossi et al. (2020) found $\alpha_{66/64}$ = 0.9996 ± 0.0001 using a different $\delta^{66}Zn_{BSE}$ (0.16 ± 0.06‰) and lunar Zn abundance (2.1 ± 1 ppm). Day et al. (2020a) reported that Mg suite cumulates had a liquid – vapour fractionation factor of $\alpha_{66/64} \approx 0.9993$.

The theoretical $\alpha_{66/64}$ obtained using Equations **5.5** and **5.6** would predict significantly more isotopic fractionation. To reach fractionation factors that would fit the observed isotopic fractionation would require a H_2-rich atmosphere with minor amounts of heavier species, e.g. H_2O, CO or CO_2, with average molar mass $\sim$5 $gmol^{-1}$ for β = 0.5 and $\sim$8 $gmol^{-1}$ for β = 1/3. This matched the results of Sossi et al. (2020) who also required a low molar mass for the ambient gas to explain their liquid – vapour fractionation factors for Cu and Rb. They argued that this was likely not reflective of reality, but instead was a result of diffusion-limited evaporation in their experiments. Due to its size and its proximity to the Earth, the Moon was unlikely to have maintained anything beyond a transient atmosphere following major degassing events (van Kooten et al., 2020) and higher temperatures in the lunar mantle would have promoted convection which would have minimized compositional gradients in the silicate melt.

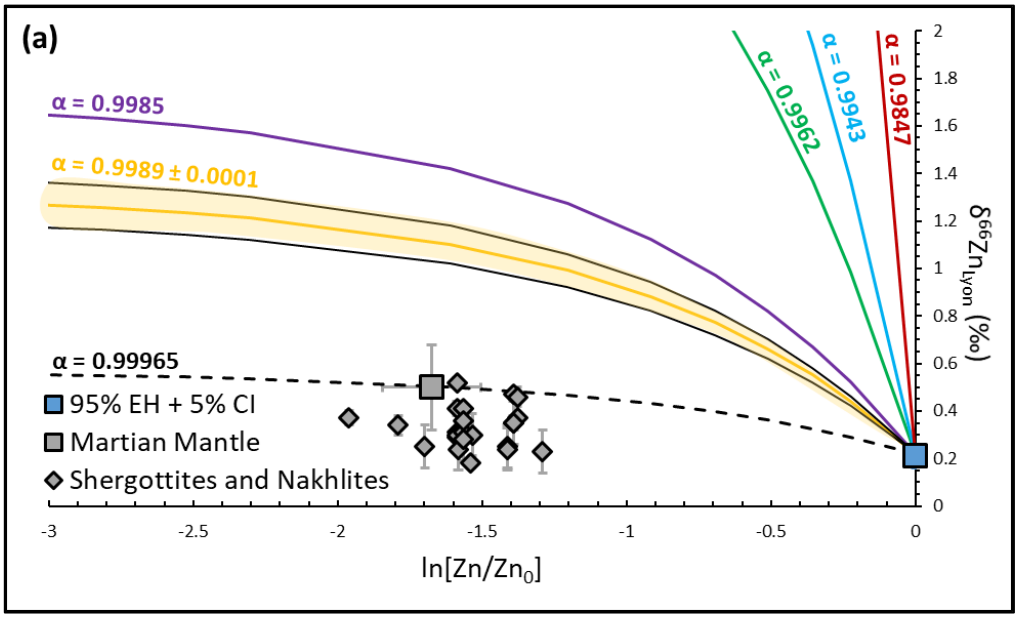
5.3.2.3 - Mars

The Zn abundance estimates of the Martian mantle (45 – 65.9 ppm) are comparable to those of the BSE, but the total Martian Zn abundance (89 – 99.8 ppm) is thought to be higher as the higher sulphur content of Mars would have sequestered significant amounts of Zn to the Martian core (Yoshizaki and McDonough, 2020; Kleine et al., 2023; Paquet et al., 2023a). Sulphide sequestration is not expected to have affected the Zn isotopic composition (Xia et al., 2019) of Mars which, based on Martian meteorites, is thought to be identical within error to the terrestrial mantle and indistinguishable from most chondrites ($\delta^{66}Zn$ = 0.25 ± 0.03‰; Herzog et al., 2009; Paniello et al. 2012a). This suggests that all major isotope fractionation processes for Martian materials occurred on its precursor bodies and that no later stage major isotope fractionation events occurred on Mars (Yoshizaki and McDonough, 2021). However, a recent study by Paquet et al. (2023a) argued that the Martian mantle has a heavier isotopic composition than the Earth of $\delta^{66}Zn$ = 0.50 ± 0.18‰, attributed to evaporative loss of Zn.

To reconcile that Mars might have a heavier Zn isotopic composition and has a higher Zn abundance than Earth, it would require Mars to have formed from different proportions of and/or different subgroups of chondritic meteorites than the Earth. Martian meteorites and the terrestrial mantle have clearly distinct nucleosynthetic Zn anomalies which suggested that Martian building blocks were ∼95% non-carbonaceous chondrites derived from the inner solar system with 4 – 6% carbonaceous chondrites, outer solar system material, whereas terrestrial Zn requires that Earth accreted from ∼70% inner solar system material and ∼30% carbonaceous chondrites (Savage et al., 2022; Kleine et al., 2023; Paquet et al., 2023a). This discrepancy could be related to difference in accretion time for Mars (∼2 Myr; Kruijer et al., 2017a) and Earth (≤ 30 Myr; Yin et al., 2002). The longer accretion time for the Earth compared to Mars meant that it could have accreted more diverse material from the outer solar system as it travelled inwards. The difference in building blocks and accretion time between Mars and the Earth could explain both the Zn isotopic composition suggested by Paquet et

al. (2023a) as well as the overall elevated volatile abundances on Mars compared to Earth without requiring a late stage evolutionary isotopic fractionation event (Yoshizaki and McDonough, 2021).

To assess potential evaporative loss through a late stage evolutionary event the expected Zn isotope fractionation was modelled using two potential end-member starting compositions, following the results of Paquet et al. (2023a), by mixing 95% EH enstatite chondrite ([Zn] = 290 ppm: δ^{66}Zn = 0.21 ± 0.04‰; Moynier et al., 2011; Pringle et al., 2017) or 95% ordinary chondrite (OC; [Zn] = 53 ppm: δ^{66}Zn = -0.01 ± 0.14‰; Creech and Moynier, 2019) with 5% CI carbonaceous chondrite (CI: [Zn] = 361 ± 40 ppm; δ^{66}Zn = 0.43 ± 0.05‰; Paquet et al., 2023b). These data were then compared to the different fractionation curves using Equation **5.7** (Fig **5.13**). This showed that there was no overlap between the experimental fractionation factors and the fractionation factor required to generate an isotopically heavier mantle on Mars. For the 95% EH + 5% CI starting composition the best fit $\alpha_{66/64}$ = 0.99965 approaches unity and exceeds all experimental and theoretical values, but matches the $\alpha_{66/64}$ range for Zn isotope fractionation due to diffusion in the silicate melt for β = 0.015 ± 0.01 within error. For the 95% OC + 5% CI starting composition the best fit $\alpha_{66/64}$ = 0.9974 falls between the experimental and theoretical values. Neither value matches that of Paquet et al. (2023a) for a 95% OC + 5% CI Mars, $\alpha_{66/64}$ ≈ 0.9989. This value is identical within error to the experimentally acquired $\alpha_{66/64}$ = 0.9989 ± 0.001 for the IB composition at log(fO$_2$) = -8. However, to match their model to the $\alpha_{66/64}$ = 0.9974



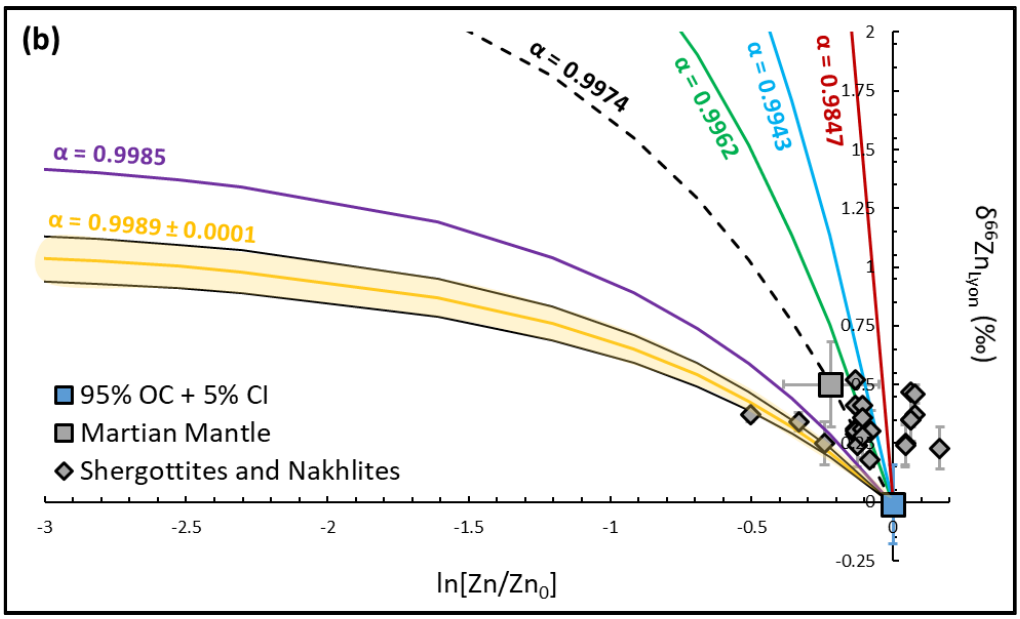


Figure 5.13: The Zn isotopic composition of the Martian mantle and meteorites (Paniello et al., 2012a; Paquet et al., 2023a), modelled using two separate chondrite starting compositions; **(a)** 95% EH enstatite chondrite + 5% carbonaceous chondrite and **(b)** 95% ordinary chondrite + 5% carbonaceous chondrite. Dashed lines represent best fit between average compositions. Coloured lines represent different model fits using $\alpha_{66/64}$ for SM, IB and the three theoretical approaches discussed in Section **5.2.3.2**.

obtained in this study would require the Zn/Mg ratio in their model to increase, e.g. by using a 95% EH + 5% CI starting composition, or to decrease the temperature in their modelling of $\alpha_{66/64}$. To have the theoretically determined $\alpha_{66/64}$ match the best fit $\alpha_{66/64}$ would require a near-vacuum atmosphere (m_k < 1 gmol^{-1}) for the 95% EH + 5% CI starting composition and an average molar mass of 13 gmol^{-1} with β = 0.5 or 22 gmol^{-1} with β = 1/3 for the 95% OC + 5% CI starting composition. It is also possible that the end-member models do not accurately reflect the Martian building blocks as there was no data available in literature discerning the relative contributions of EH and OC to the total budget of inner solar system material.

5.3.2.4 - Meteorites

5.3.2.4.1 – Chondrites

Chondritic meteorites are among the most primitive materials in the solar system and formed during the earliest stages in the solar nebula. They can be divided into three main groups, carbonaceous, enstatite and ordinary chondrites, with each having multiple subgroups. The different chondrites exhibit a range of Zn abundances and isotopic composition between the different sub-groups of

unaltered enstatite, carbonaceous and ordinary chondrites. Enstatite and ordinary chondrites are thought to have formed in the inner solar system and are depleted in highly volatile elements whereas the volatile-rich carbonaceous chondrites formed in the outer solar system and were transported inwards (Tsiganis et al., 2005). This difference in formation environment is reflected in the nucleosynthetic Zn isotope anomalies which differ between inner and outer solar system materials (e.g. Savage et al., 2022). On average Zn abundances are high in the CI carbonaceous and enstatite chondrites and are low in the ordinary chondrites. The other subgroups of carbonaceous chondrites cover a range of Zn abundances between CI carbonaceous and ordinary chondrites (Creech and Moynier, 2019; Paquet et al., 2023b).

The bulk $\delta^{66}Zn$ of unaltered enstatite and carbonaceous chondrites are comparable to or slightly heavier than the terrestrial mantle whereas ordinary chondrites exhibit more variability with -1.37‰ ≤ $\delta^{66}Zn$ ≤ 1.75‰ and average $\delta^{66}Zn$ = -0.01 ± 0.14‰ (Ghidan and Loss, 2011; Barrat et al., 2012; Pringle et al., 2017; Creech and Moynier, 2019; Paquet et al., 2023b). It was observed early on that the variability in [Zn] and $\delta^{66}Zn$ between carbonaceous chondrite subgroups was not caused by evaporative loss as $\delta^{66}Zn$ was proportional to 1/[Zn], indicating a single original Zn reservoir for all carbonaceous chondrites that was not fractionated via evaporation (Luck et al., 2005; Pringle et al., 2017; Bermingham et al., 2020). Enstatite and ordinary chondrite subgroups follow similar trends, but the slopes vary from carbonaceous chondrites, likely reflective of their location in the solar system during their accretion.

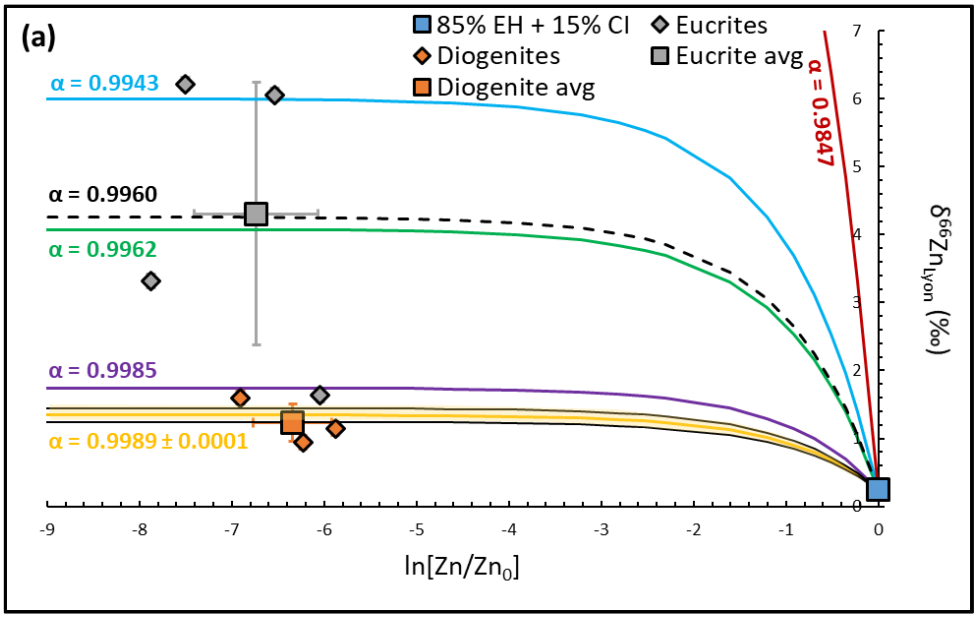
5.3.2.4.2 – Achondrites

Achondrites are stony meteorites that consist of igneous rocks that originated from solar system bodies that were of sufficient size to have experienced partial or whole chemical differentiation. These meteorites are among the oldest igneous rocks in the solar system, forming immediately after accretion and differentiation of asteroid bodies in the earliest stages of the solar system (Kleine et al., 2009; Touboul et al., 2015; Roszjar et al., 2016; Schiller et al., 2018). Among the achondrites are lunar

and Martian meteorites as well as meteorites thought to have originated from asteroidal bodies. The latter have been divided into several subcategories including howardite, eucrite and diogenite (HED) meteorites, thought to have originated from the asteroid 4 Vesta (McCord et al., 1970), angrites, aubrites and ureilites – which are all thought to have their own distinct, presently unidentified or no longer existent, partially or fully differentiated parent bodies (Bischoff et al., 2014; Zhu et al., 2020, 2021; Tissot et al., 2022). The Zn isotopic composition of achondrites is heavy compared to their chondritic building blocks which has been attributed wholly or partially to volatile loss (Moynier et al., 2010, 2011; Brugier et al., 2019; Kumler and Day, 2021). The isotopic composition of achondrites can be modelled to assess their Zn abundance and Zn isotopic composition in terms of volatile loss from a parent body of known composition. It should be noted that Zn abundance and isotope data on achondrites and their parent bodies are scarce, e.g. angrites were not included in the following discussion due to an absence of Zn isotope data in the literature.

5.3.2.4.2.1 – HEDs and Asteroid 4 Vesta

Among the HEDs unbrecciated eucrites and diogenites are thought to best represent the primary isotopic signature of the parent body as these are least likely to have been altered. On the other hand, the brecciated eucrites and diogenites and howardites, brecciated mixtures of eucrites and diogenites, are more complex polymicts and cumulates (Keil, 2002). Zinc abundances in HEDs are low (≤ 10 ppm)



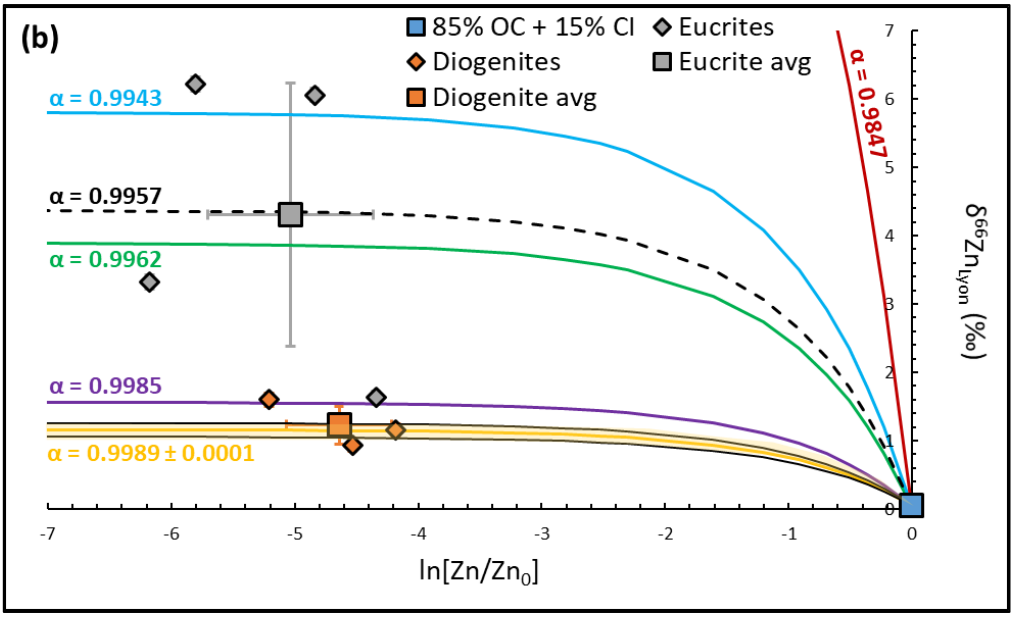


Figure 5.14: The Zn isotopic composition of unbrecciated eucrite and diogenite meteorites and asteroid 4 Vesta (Paniello et al., 2012b), modelled using two separate chondrite starting compositions; **(a)** 85% EH enstatite chondrite + 15% CI carbonaceous chondrite and **(b)** 85% ordinary chondrite + 15% CI carbonaceous chondrite. Dashed lines represent best fit between average compositions. Coloured lines represent different model fits using $\alpha_{66/64}$ for **SM**, IB and the three theoretical approaches discussed in Section **5.2.3.2**.

and rarely exceed 5 ppm (Paniello et al., 2012b). Zinc isotope data for HEDs is very scarce, but Paniello et al. (2012b) analysed 20 HEDs and found that they cover a range between $\delta^{66}Zn$ = -7.75‰ to $\delta^{66}Zn$ = +6.29‰. The average Zn isotopic composition of unbrecciated eucrites ($\delta^{66}Zn$ = 4.32 ± 1.93‰) and diogenites ($\delta^{66}Zn$ = 1.23 ± 0.28‰) are heavy Zn isotope enriched compared to chondritic meteorites which was attributed to isotope fractionation during volatile loss (Paniello et al., 2012b). Howardites ($\delta^{66}Zn$ = 0.26 ± 0.74‰) and brecciated diogenites ($\delta^{66}Zn$ = -0.31 ± 1.60‰) exhibited both heavy and light isotope enrichments, attributed to impact gardening and recondensation of isotopically light material (Paniello et al., 2012b; Zhang et al., 2019). Nucleosynthetic Ti and Cr isotope anomalies of HEDs suggest that Vesta accreted from a mixture of ~85% enstatite or ordinary chondrite inner solar system material and approximately 15% CI carbonaceous chondrite material (Schiller et al., 2018; Kruijer et al., 2020 and references therein). The relative contribution of enstatite and ordinary chondrites to the inner solar system material that formed Vesta is currently unknown. Therefore two end-member scenarios were investigated with Vesta consisting of 85% EH enstatite chondrite or ordinary chondrite and 15% CI carbonaceous chondrite. Figure **5.14** shows that the Zn isotopic

composition of the unbrecciated eucrites covered a range of values whereas the diogenites appear more homogeneous. Considering the average δ^{66}Zn of these samples the starting composition of Vesta had minimal effect on the best fit fractionation factor as $\alpha_{66/64} = 0.9960^{+0.0028}_{-0.0020}$ for an 85 % EH + 15% CI and $\alpha_{66/64} = 0.9957^{+0.0028}_{-0.0020}$ for an 85 % OC + 15% CI for the eucrites and $\alpha_{66/64}$ = 0.9990 ± 0.0003 for an 85 % EH + 15% CI and $\alpha_{66/64}$ = 0.9988 ± 0.0003 for an 85 % OC + 15% CI for the diogenites. The $\alpha_{66/64}$ of the diogenites matched the experimentally obtained $\alpha_{66/64}$ within error whereas $\alpha_{66/64}$ for the eucrites had a large scatter, but were on average smaller than experimental values and larger than the theoretical $\alpha_{66/64}$. The errors on $\alpha_{66/64}$ were determined by fitting the fractionation model through the most extreme data points.

To have the theoretically determined $\alpha_{66/64}$ match the best fit $\alpha_{66/64}$ obtained for the eucrites yielded a wide range for m_k following the limited data available and large scatter with $m_k = 23^{+19}_{-17}$ gmol^{-1} for β = 0.5 or $m_k = 41^{+50}_{-32}$ gmol^{-1} for β = 1/3 for the 85% EH + 15% CI starting composition and $m_k = 25^{+20}_{-18}$ gmol^{-1} for β = 0.5 or $m_k = 47^{+56}_{-36}$ gmol^{-1} for β = 1/3 for the 85% OC + 15% CI starting composition. For the diogenites the more homogeneous data yielded a smaller range with m_k = 5 ± 2 gmol^{-1} for β = 0.5 or m_k = 7 ± 2 gmol^{-1} for β = 1/3 for the 85% EH + 15% CI starting composition and m_k = 6 ± 2 gmol^{-1} for β = 0.5 or m_k = 9 ± 2 gmol^{-1} for β = 1/3 for the 85% OC + 15% CI starting composition. While it is apparent that volatile loss is the most likely explanation for the heavy Zn isotope enrichment observed in eucrites and diogenites, further study is required to better constrain the isotopic composition of the eucrites and to gain a better understanding of the nature of volatile loss from Vesta.

5.3.2.4.2.2 – Ureilites and the Ureilite Parent Body

Ureilites are carbon-bearing ultramafic meteorites, representative of a protoplanetary mantle, that originated from the ureilite parent body (UPB), one of the earliest accreted and differentiated bodies in the solar system that is thought to no longer exist (Bischoff et al., 2014; Schiller et al., 2018). Ureilites are compositionally heterogeneous, which has been attributed to incomplete chemical differentiation

before the breakup of the UPB (Downes et al., 2008). They are volatile depleted, but have unexpectedly high Zn abundances that can reach >300 ppm with $[Zn]_{avg}$ = 188 ± 58 ppm (Moynier et al., 2010; Brugier et al., 2019). The Zn isotopic composition of ureilites is heavy compared to chondritic material with 0.38 ‰ ≤ $\delta^{66}Zn$ ≤ 1.26 ‰, average $\delta^{66}Zn$ = 0.77 ± 0.19 ‰, with one outlier at $\delta^{66}Zn$ = 2.71. The Zn isotopic composition of ureilites became increasingly heavy with increasing shock levels, indicative of impact-induced Zn loss, likely following volatilization of Zn (Brugier et al., 2019). Moynier et al. (2010) argued that the observed isotope fractionation correlated well with volatile loss from an initially CI carbonaceous chondrite-like source material. However, this has been disputed as it cannot explain the compositional heterogeneity of the ureilites (Brugier et al., 2019; Collinet and Grove, 2020; Zhu et al., 2020) and nucleosynthetic Zn anomalies (Steller et al., 2022) which suggested that the UPB accreted from inner solar system chondritic material. Since ordinary chondrite Zn abundances are significantly lower they are unlikely to represent the building blocks of ureilites. Therefore, to reconcile the nucleosynthetic Zn anomalies and higher Zn abundances it was chosen to model the evolution of the Zn isotopic composition of ureilites by assuming an enstatite chondrite composition of the UPB (Fig. **5.15**).

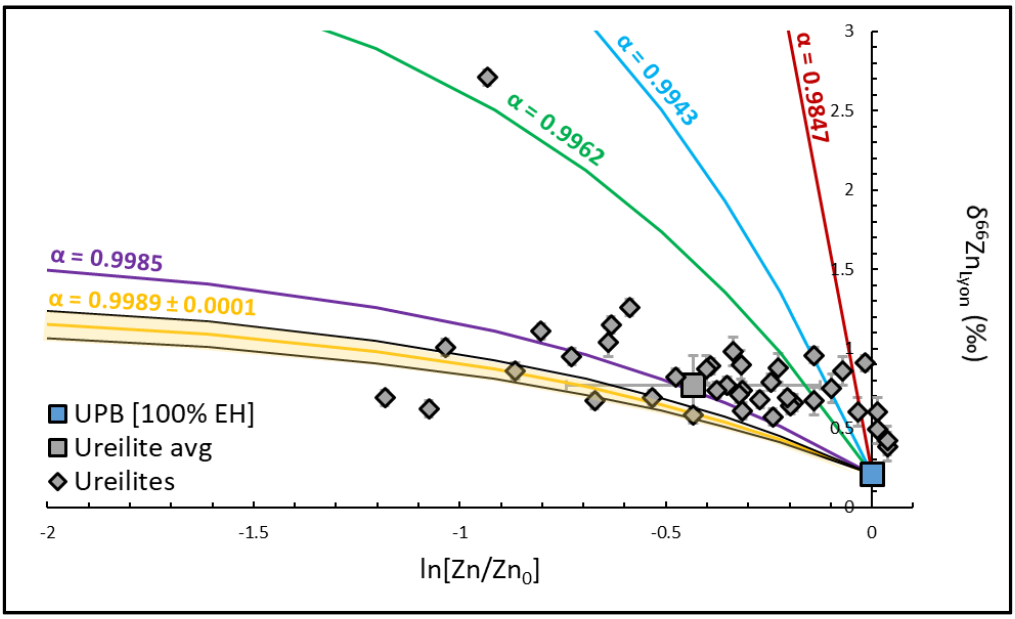


Figure 5.15: The Zn isotopic composition of ureilites (Moynier et al., 2010; Brugier et al., 2019) modelled using a UPB with an enstatite chondrite starting composition. Coloured lines represent different model fits using $\alpha_{66/64}$ for **SM**, IB and the three theoretical approaches discussed in Section **5.2.3.2**.

If the average ureilite composition is used as reference value and all Zn loss is assumed to be due to evaporation the data are best fit by $\alpha_{66/64}$= 0.9985. To have the theoretically determined $\alpha_{66/64}$ match this best fit value would require m_k = 7 gmol^{-1} for β = 0.5 or m_k = 11 gmol^{-1} for β = 1/3. However Figure **5.15** shows that, apart from one outlier at δ^{66}Zn = 2.71, the δ^{66}Zn of individual ureilites is seemingly independent of the degree of Zn depletion. Brugier et al. (2019) argue that volatile loss would still be able to produce this range of isotopic compositions, but it would rely on a heterogeneous UPB of presently unknown composition or multiple separate UPBs of distinct compositions, which has been argued for based on multiple different isotope systems such as C (Barrat et al., 2017), O (Bischoff et al., 2014) and Cr (Zhu et al., 2020). Brugier et al. (2019) also noted that the present ureilite meteorite collection was too limited to accurately assess the Zn isotopic composition of the UPB and therefore the starting composition in this model is still uncertain.

5.3.2.4.2.3 – Aubrites and the Aubrite Parent Body

Aubrites are the most reduced achondritic meteorites, ΔIW-2 – ΔIW-6, and originated from at least two separate differentiated protoplanetary bodies that accreted and differentiated in the first 1 Myr after solar system formation (Keil, 2010; Wilbur et al., 2022). They are thought to have originated in the innermost regions of the solar system and therefore serve as a compositional analogue for Mercury, although at present no aubrite has been identified as of Mercurian origin (Udry et al., 2019). Most aubrites are Zn depleted with [Zn] ≤ 3 ppm and exhibit light Zn isotope enrichments with -8.04 ‰ ≤ δ^{66}Zn ≤ -0.26 ‰, attributed to the recondensation of isotopically light vapour phases (Wolf et al., 1983; Mullane et al., 2005; Moynier et al., 2011). The Shallowater aubrite is considered to have originated from a separate parent body than other aubrite meteorites. Three separate aliquots of the Shallowater aubrite showed that it was less Zn depleted, [Zn] = 32 ppm, and heavy Zn isotope enriched, δ^{66}Zn = 2.03 ± 0.39 ‰, compared to other aubrites (Moynier et al., 2011). Its heavier Zn isotopic composition compared to chondritic meteorites has been attributed to volatile loss. The evolution of the Shallowater aubrite is modelled assuming an enstatite chondrite starting composition

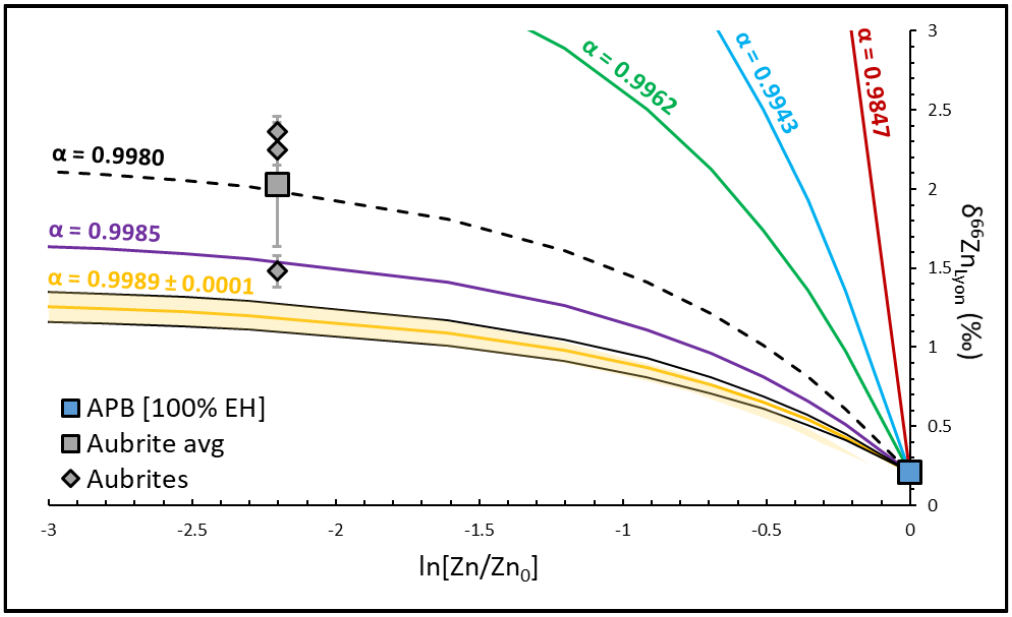


Figure 5.16: The Zn isotopic composition of the Shallowater aubrite (Moynier et al., 2011) modelled using an APB with an enstatite chondrite starting composition. The [Zn] of individual samples was not reported, so average [Zn] of Shallowater aubrite was used. Coloured lines represent different model fits using $\alpha_{66/64}$ for **SM**, IB and the three theoretical approaches discussed in Section **5.2.3.2**.

(Fig. **5.16**), as suggested by nucleosynthetic O and Cr isotope anomalies (Zhu et al., 2021). The Zn abundance of the individual aliquots of Moynier et al. (2011) were not reported and therefore the average bulk [Zn] was used for all aliquots. If it is assumed that this isotopic signature is generated via volatile loss it would yield a best-fit $\alpha_{66/64} = 0.9980^{+0.0006}_{-0.0003}$. To have the theoretically determined $\alpha_{66/64}$ match this best fit value would require $m_k = 10^{+2}_{-4}$ gmol^{-1} for β = 0.5 or $m_k = 16^{+3}_{-6}$ gmol^{-1} for β = 1/3.

5.3.3 – The Zn Isotopic Composition of Terrestrial Environments

5.3.3.1 – Volcanism

Volcanic activity is an important pathway for the evaporation of volatile elements, including Zn, from the terrestrial interior to the surface and atmosphere with evaporative Zn fluxes of individual volcanoes being in excess of 10^3 kg per day (Edmonds et al., 2022). Zinc speciation in volcanic gases has been studied in nature (e.g. Mason et al., 2018; Liotta et al., 2021) as well as experimentally (Renggli and Klemme, 2020) and, depending on the overall composition of the silicate melt and gas, Zn forms $ZnCl_2$, $Zn(OH)_2$, ZnS and elemental Zn gas species. Data on Zn isotope fractionation during evaporative loss in a volcanic setting is scarce as previous studies have focused mainly on identifying subducted material in the source (Liu et al., 2016; Yao et al., 2022), the interactions between the magma and water and the precipitation of minerals in a hydrothermal setting (Chen et al., 2014; Chiaradia et al., 2018; Zelenski et al., 2021). All of these processes have been shown to be capable of generating heavy Zn isotope compositions, similar to evaporative loss. Two studies measured the Zn isotopic composition of the fumarolic gas and gas condensates of individual volcanoes; Toutain et al. (2008) at Merapi in Indonesia and Chen et al. (2014) at La Soufrière on Guadeloupe. Chen et al. (2014) found that their Zn isotope data could be explained by degassing, but argued that it was instead derived from water-rock interactions whereas Toutain et al. (2008) attribute theirs to an interplay of evaporative loss and recondensation of Zn. Therefore the focus will be on assessing the degassing of Zn from the Merapi volcano.

Conditions in the gases emitted from Merapi were estimated to be at conditions slightly above the fayalite-magnetite-quartz oxygen buffer reaction, ΔFMQ+0.56 – ΔFMQ+0.83 at an emission temperature of 803°C (Moussallam et al., 2019), ~600°C below the experimental conditions used in this study. To compare results at a similar fO_2 it was most accurate to attempt to model the measured Zn isotope fractionation using the $\alpha_{66/64}$ obtained for the experiments at $\log(fO_2)$ = -6 (ΔFMQ+0.54). Toutain et al. (2008) found that $\alpha_{66/64}$ = 0.99983 was required to fractionate the Merapi host rock

($\delta^{66}Zn$ = 0.24‰) sufficiently to reach the Zn isotopic composition of the heaviest gas condensates, $\delta^{66}Zn$ = 0.85‰. This value was closer to unity than the experimentally obtained values, $\alpha_{66/64}$ = 0.9976 ± 0.0009 for SM and $\alpha_{66/64}$ = 0.9976 ± 0.0002 for IB. This can potentially be explained by considering the more complex evaporation environment where Zn may have evaporated as sulphide, chloride or hydroxide species and accounting for the inverse temperature dependence of $\alpha_{66/64}$ which moves towards unity with decreasing temperature (Criss, 1999). Moreover, Toutain et al. (2008) noted that the isotopic composition of the gas evolved from an initially isotopically light composition ($\delta^{66}Zn_{Lyon}$ = -0.10‰) near the magma interface to increasingly heavy values away from the magma. This suggested that the recondensation of isotopically light gaseous Zn causes the residual gaseous Zn to get an increasingly heavy Zn isotopic composition. As such, no available study focusing on Zn isotopes has managed to assess the effect of evaporative loss of Zn in the volcanic environment. Future studies could focus on this to gain a better understanding of the behaviour and isotopic fractionation of Zn in a volcanic environment.

5.3.3.2 – Tektites and Trinitites

Tektites and trinitites are silica-rich glasses that formed following the rapid melting and quenching of terrestrial rocks following high-energy impacts of meteorites on Earth's surface and nuclear explosions respectively. They were formed by the melting of upper continental crust (UCC) material, which can be considered homogenous and unaffected by partial melting with $\delta^{66}Zn$ = 0.28 ± 0.05‰ (Chen et al., 2013a) and [Zn] = 75 ppm (Hu and Gao, 2008) Tektites have been identified in at least four areas, two of which have available Zn isotope data; Ries crater, Germany (Engelhardt et al., 1987) and an undiscovered crater associated with tektites found in south-east Asia and Australia (Mizera et al., 2016). Tektites in these areas exhibit heavy Zn isotope compositions and Zn depletions compared to the UCC with the tektites associated with Ries crater having [Zn] = 1.9 – 34.5 ppm and 1.66 ‰ ≤ $\delta^{66}Zn$ ≤ 3.30 ‰ (Moynier et al., 2009b; Rodovská et al., 2017) whereas those associated with the

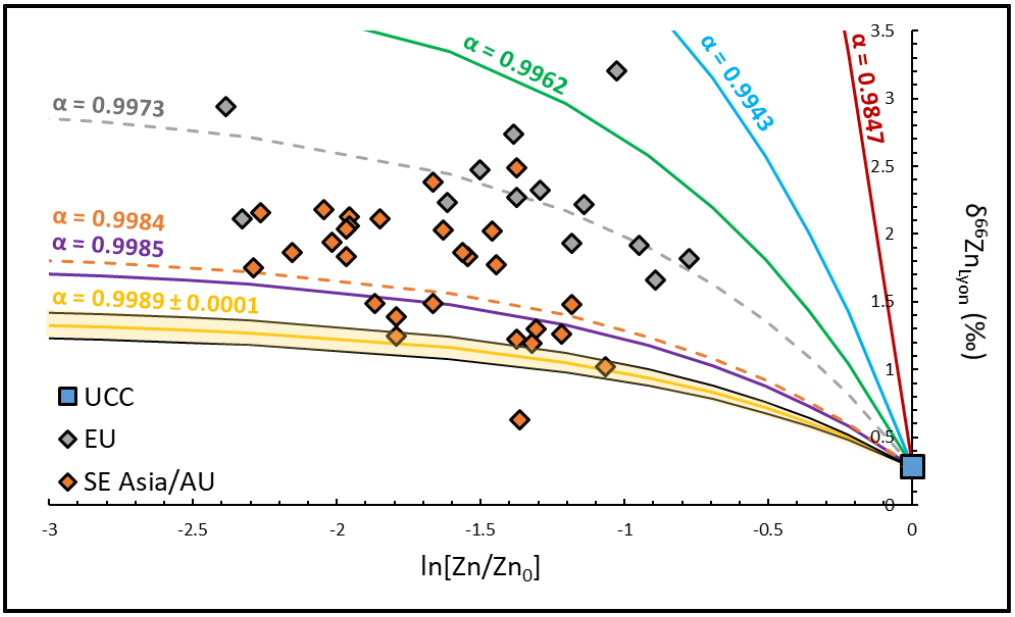


Figure 5.17: The Zn isotopic composition of tektites (Moynier et al., 2009b; Rodovská et al., 2017; Jiang et al., 2019; Wimpenny et al., 2019) modelled using an average upper crust (Hu and Gao, 2008; Chen et al., 2013a) as the starting composition. Dashed lines represent best fits for each data set. Solid lines represent different model fits using $\alpha_{66/64}$ for SM, IB and the three theoretical approaches discussed in Section **5.2.3.2**.

undiscovered SE Asian/Australian crater have [Zn] = 7.6 – 32.1 ppm and 0.63 ‰ ≤ δ^{66}Zn ≤ 2.49 ‰ (Moynier et al., 2009b; Jiang et al., 2019; Wimpenny et al., 2019).

Differences in the magnitude of observed volatile losses of K, Cu and Zn suggest that evaporative loss in tektites is a diffusion limited process (Moynier et al., 2009b). The conditions during tektite formation were highly reducing as Fe was predominantly present as Fe^{2+} (Skála et al., 2009) and gas species in melt inclusions were reduced (Žák et al., 2012). Therefore Zn evaporation from tektites is modelled and compared to the Zn isotope fractionation factors obtained for the most reducing experiments at log(fO_2) = -8 (Fig. **5.17**). This showed that the two sets of tektites follow different fractionation trends. The Ries crater tektites show minimal variability and follow a trend consistent with an $\alpha_{66/64}$ = 0.9973. The SE Asian/Australian tektites show a wider range of isotopic compositions with a best fit $\alpha_{66/64} = 0.9984^{+0.0005}_{-0.0006}$ covering most individual samples. This was within error of the range of $\alpha_{66/64}$ = 0.9988 – 0.9997 obtained by Wimpenny et al. (2019) for the south-east Asian tektites. Based on a subset of the SE Asian tektites with Zn abundances that exceeded estimates of the UCC it was suggested that the average initial Zn abundance of the volatilized material was higher than UCC abundances (Moynier

et al., 2009b). To match the isotopic composition of these tektites with an UCC δ^{66}Zn, using $\alpha_{66/64}$ = 0.999, would require $[Zn]_0 \approx 100$ ppm. Increasing $[Zn]_0$ to 100 ppm in the model would increase $\alpha_{66/64}$ by 0.0003, yielding values on the lower end of the $\alpha_{66/64}$ obtained by Wimpenny et al. (2019). Another explanation could be that the experimental conditions poorly reflect those of tektite formation as peak temperatures during meteorites impacts exceed 2000°C and localized pressures can exceed 100 GPa (French and Koeberl, 2010).

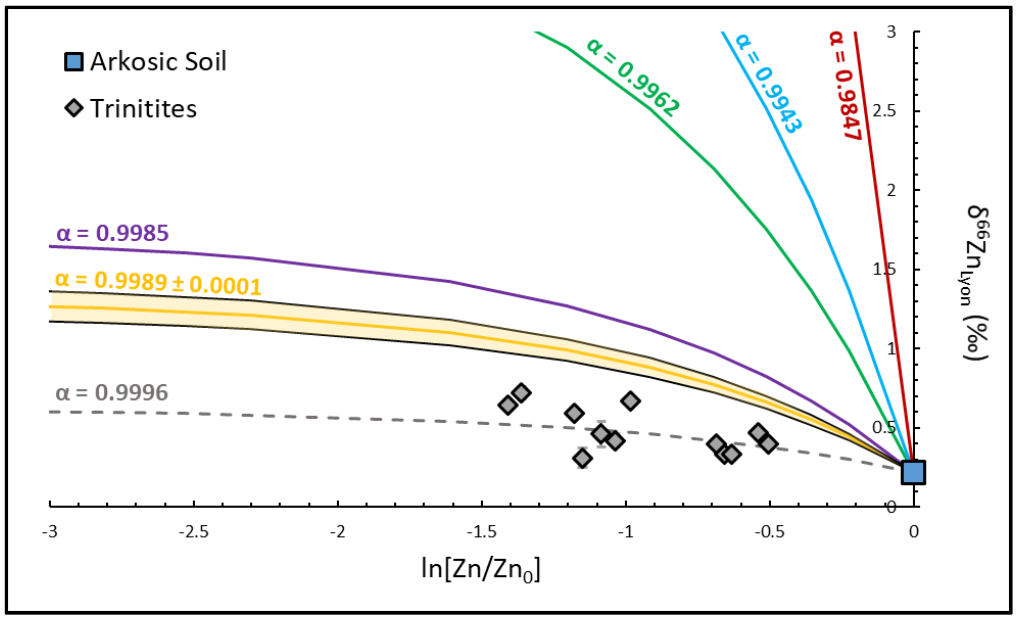


Figure 5.18: The Zn isotopic composition of trinitites (Day et al., 2017; Wimpenny et al., 2019) modelled using an arkosic soil starting composition (Wimpenny et al., 2019). Dashed line represents best fit for the data set. Solid lines represent different model fits using $\alpha_{66/64}$ for **SM**, IB and the three theoretical approaches discussed in Section **5.2.3.2**.

Trinitites are Zn depleted ($[Zn]_{Rhy}$ = 45.8 – 90 ppm; $[Zn]_{Ark}$ = 12.6 – 18.3 ppm) and have a heavy Zn isotopic composition (0.31 ‰ ≤ δ^{66}Zn ≤ 0.72 ‰) compared to their unaltered source materials; rhyolites ($[Zn]_{Rhy}$ = 149 ± 6 ppm; δ^{66}Zn = 0.28 ± 0.03 ‰) and arkosic soil ($[Zn]_{Ark}$ = 51.5 ± 0.8 ppm; δ^{66}Zn = 0.22 ± 0.02 ‰) depending on the sampling region (Day et al., 2017, 2020b; Wimpenny et al., 2019). The $\alpha_{66/64}$ = 0.9996 required to produce the measured fractionation is closer to unity than the experimental $\alpha_{66/64}$ (Fig. **5.18**). Wimpenny et al. (2019) also observed a similar difference between their evaporation experiments on rhyolites and arkosic soils and the trinitite samples. They attributed it to differences in the pressure of the ambient gas in experiments (1 atm (~10^{-4} GPa)) compared to trinitite formation (≤8 GPa; Day et al., 2017 and references therein), higher temperatures decreasing

$\alpha_{66/64}$ and the experimental set-up not accurately reflecting the natural environment during trinitite formation.

Chapter 6: Summary and Future Recommendations

6.1 – Summary

The solar system formed following the collapse of an interstellar molecular cloud. Planetary bodies accreted to form increasingly larger bodies in a protoplanetary disk. The gravitational interactions between planetesimals cleared the orbits of the larger bodies and resulted in a rearrangement of the solar system to the present-day configuration. During accretion planetary bodies were partially or wholly molten due to the heat generated by impactors and the decay of short-lived radionuclides. Inside these magma oceans the planetary interiors differentiated to form a Fe-metallic core and a silicate mantle and crust. This resulted in chemical differentiation with siderophile and chalcophile elements preferentially partitioning in the core and lithophile elements remaining in the mantle and crust. Simultaneously degassing at the surface resulted in the loss of moderately and highly volatile elements. The elemental and isotopic composition of the Earth suggests that it formed from predominantly inner solar system materials with contributions of volatile-rich outer solar system material. This study aimed to increase the understanding of how evaporative loss affected the trace element abundances and the Zn isotopic composition of the residual silicate melt as a function of time, fO_2 and melt composition. Secondly, it aimed to assess the effect of trace element volatility on the budget of moderately volatile elements on rocky bodies.

Chapter **2** discussed the experimental and analytical set-up of the evaporation experiments and explored the methods used to quantify volatility. Three major element compositions, a synthetic ferro-basalt (SM) and andesite (AN) and a natural mid-ocean ridge basalt (IB) were prepared and doped with a trace element mix containing a total of 22 elements. Experiments were performed in a one atmosphere gas mixing furnace with runtimes between 3 and 60 minutes at 1300°C and 1400°C and oxygen fugacities between air ($\log(fO_2) = -0.68$) and the iron-wüstite oxygen buffer reaction ($\log(fO_2) = -11$ at 1300°C). Major element and chlorine abundances were measured using electron probe

microanalysis and trace element were measured with laser ablation inductively coupled plasma mass spectrometry (LA-ICP-MS).

The volatility factor (Norris, 2016), the ratio of the trace element abundance after and before the experiment, and the modified Hertz-Knudsen-Langmuir (HKL) equation (Sossi et al., 2019), linking volatile loss to experimental conditions, the thermodynamic properties of the evaporation reaction(s) and trace element activity in the silicate melt, were described as methods of quantifying trace element volatility. The thermodynamic equations required to resolve the melt- and gas phase speciation of trace elements in the silicate melt were derived to aid in quantifying various parameters in the modified HKL equation.

Chapter **3** discussed the sample preparation and processing for Zn purification via ion exchange chromatography and established the analytical methodology and interference corrections required to obtain precise and accurate delta values from Zn isotope analysis. The isotopic composition of Zn was determined using a double spike method, where a sample of unknown composition and a double spike solution of known composition are mixed during sample preparation and deconvolved after analysis. This method corrected for any fractionation the sample experienced during processing, ion exchange chromatography and analysis.

Purified Zn samples were analysed using multi collector ICP-MS which revealed that there were significant Zn blanks and highlighted interferences on various Zn isotopes. The main interference was identified as Ba and for one sample a Ni interference was observed. A blank exercise of the relevant lab areas and consumables was performed to identify the source of interfering elements and to reduce the size of the Zn blank. This showed that consumable lab plastics, particularly gloves, and the Kimwipes could act as a source of both Zn and Ba. Based on these findings a more rigorous cleaning regimen and cleaner analytical approach was established to suppress Zn blanks to <10 ng and minimize Ni and Ba interferences.

A method was devised to correct for the Ni and Ba interferences using the measured intensities on various (half-)masses. This approach showed that the magnitude of the delta shift (Δ^{66}Zn) introduced by an interference could be predicted from the intensity of the relevant Zn and interfering isotopes. Therefore, by plotting Δ^{66}Zn as a function of the intensity and comparing the samples to the modelled correction it could be assessed whether the appropriate interference correction was applied. In this study the applied Ni and Ba corrections were sufficient to correct for observed interferences on measured Zn isotope intensities.

Chapter **4** discussed the results of the evaporation experiments described in Chapter **2**. The thermodynamic equations derived in Chapter **2** were used to determine the evaporation reactions for all trace elements which showed that Cs and Pb were the only volatile elements for which more than one evaporation reaction had to be considered. The presence of halogens and potential evaporation of trace elements as halide gas species was assessed by considering the Cl budget of the IB composition experiments. These abundances were used to compete the equilibrium partial pressure of the chloride gas species relative to the oxide gas species. This showed that some elements had potential chloride evaporation pathways. However, a comparison of volatile loss for these elements in a major element composition doped with a halogen-bearing and halogen-free trace element mix showed that the log(K*) obtained via the modified HKL equation suggested that evaporation through halide species was negligible.

Three trace elements exhibited no volatile loss – Li, P and V – and 3 elements – Ag, Cd and Tl – were too volatile to accurately assess their behaviour. For 11 other elements volatile loss increased with increasing runtime, decreasing fO_2 and decreasing melt viscosity. The observed compositional dependence suggested that diffusion acted as a strong control on trace element volatility. This was confirmed by transects of trace element abundances, measured perpendicular from the evaporation surface into the sample. This effect was minimal for the monovalent elements, but for the polyvalent

elements in the IB composition and particularly the AN composition experiments had ubiquitous compositional gradients resulting from diffusion-limited evaporative loss showing that the magnitude of volatile loss was a function of both the rate of evaporation and the rate of diffusion.

The volatility factors were compared to the CI chondrite normalized trace element abundance of the terrestrial mantle (BSE) and showed an overall good correlation with more volatile elements in the experiments being more depleted in the BSE. A similarly strong correlation was not observed for the 50% condensation temperature (T^{50}), a parameter often used to quantify volatility. This was attributed to the lack of applicability of T^{50} outside of solar nebula conditions. A reasonable correlation was observed between the equilibrium partial pressure of the gas species and the volatility factor with As and Sb as notable outliers. Correcting for non-ideal behaviour of the trace elements in the silicate melt also caused Sn to deviate from the trend. The 1% evaporation temperature, a novel parameter, defined by Sossi et al. (2019), applicable describing trace element volatility in any conditions, was calculated over a range of fO_2 and shown to match reasonably well for most elements. However, As, Rb and Sb plotted off the trend observed for the other elements, but formed a parallel line. The parameters describing volatility correlated reasonably well with the obtained data. However, a paucity of data on trace element activity in the silicate melt and evaporation coefficients for trace elements across a range of experimental conditions and compositions hampered correcting for the non-ideality of trace element behaviour in the silicate melt and the evaporation process. This, in combination with a paucity of knowledge regarding the evaporation coefficients left potentially large uncertainties on the accuracy of the results of the modified HKL.

The modified HKL was applied to all moderately volatile elements in two ways – variable and fixed change in valence of the trace element in the evaporation reaction (n) – with varying degrees of success. Care was taken to select only representative data points after it was identified that the non-linear least squares fitting skewed the model for data points where the volatility factor approached zero. For most elements fits with variable n were close to the expected values and the obtained

apparent equilibrium constant of the evaporation reaction (K*) was comparable to the value obtained with fixed n. Moreover, for most elements log(K*) compared well with values obtained in literature with Ga and In being the exception. A comparison of log(K*) and log(K) calculated from pure species data resulted in a poor correlation that was not improved by correction for non-ideal behaviour in the silicate melt. Finally, log(K*) was taken at both temperatures for the IB composition to infer the apparent enthalpy and entropy of the evaporation reactions. For some elements – Zn, Ge, In, Sb and one Pb evaporation reaction – it matched well with data for pure species and from literature whereas for Cu, As, Sn, Cs and one Pb evaporation reaction the match was poor.

Chapter **5** discussed the results of the zinc isotope analysis of the SM and IB composition experiments described in Chapter **4**. Here it was shown that there was a variability in double spike:sample ratios, despite care being taken to ensure a consistent double spike:sample ratio for all samples. This could be attributed to differences in the Zn abundance of the samples as measured with LA-ICP-MS compared to concentrations obtained by isotope dilution calculations. Next, the isotopic composition of the starting materials was shown to fall on the mixing line of the undoped starting material and the ZnO trace element dopant as expected. The Ni and Ba corrected δ^{66}Zn of the samples were reported and it was shown that the Ba interference correction method was not able to correct the δ^{66}Zn for some of the lowest Zn abundance samples.

It was shown that δ^{66}Zn increased with decreasing Zn abundance in the residual melt, however the slope of this trend decreased with decreasing fO_2. This was attributed to a Zn depleted and isotopically heavy boundary layer at the evaporative surface that formed as a result of the evaporation rate exceeding the diffusion rate. The decreasing slope of was caused by increased evaporation rates with decreasing fO_2 as Zn evaporated, via the $ZnO\ (g) = Zn\ (g) + 0.5\ O_2\ (g)$ reaction, while diffusion rates were independent of fO_2. The temporal evolution of δ^{66}Zn was shown to be linear with time where δ^{66}Zn was comparable between compositions in oxidizing conditions, but varied significantly in

reducing conditions, reflective of the growing differences between evaporation and diffusion rates with decreasing fO_2.

The slope of three isotope plots matched end-member kinetic isotope fractionation within error, confirming expectations for high-temperature isotope fractionation. Next, liquid – vapour fractionation factors for fractionation of ^{66}Zn and ^{64}Zn ($\alpha_{66/64}$) were determined for individual experiments using the Rayleigh equation and compared to previously established formalisms of predicting $\alpha_{66/64}$ using the (reduced) masses of the two isotopes and the ambient gas for various evaporation regimes. For the experiments in air the measured $\alpha_{66/64}$ in this study were within error of theoretically predicted values, but in more reducing conditions experimental $\alpha_{66/64}$ were always closer to unity with a growing discrepancy with decreasing fO_2 which was attributed to the diffusion-limited evaporation regime. Direct comparisons with previous work were hampered by different experimental conditions and/or set-ups, but generally the experimentally acquired $\alpha_{66/64}$ matched those of Wimpenny et al. (2019) and Sossi et al. (2020) at comparable conditions within error.

The $\alpha_{66/64}$ showed that it was unlikely that the assumption of $P_i/P_{i,eq} \rightarrow 0$, used in the derivation of the modified HKL in Chapter **2**, was likely incorrect and that the observed evaporative loss more likely reflected a near-equilibrium evaporative environment limited by diffusion in the silicate melt where P_i is a significant parameter that cannot be assumed negligible (Young et al., 2019; Sossi et al., 2020). This is because the theoretically predicted $\alpha_{66/64}$ for such evaporative environment would predict significantly more isotope fractionation than is observed and out of the theoretical approaches it matched the worst with the experiments. This signified the necessity of a re-evaluation of the modified HKL in future work to accurately reflect its evaporative environment.

Next, the experimental $\alpha_{66/64}$ were compared to best-fit $\alpha_{66/64}$ to match the observed Zn isotopic composition of various terrestrial materials and extra-terrestrial bodies if all Zn isotope fractionation could be attributed to evaporative loss. This was done using a closed-system batch model of Nielsen

et al. (2021) where it was assumed evaporating species were equilibrated with the melt before being transported away from the evaporation interface. For these comparisons only the $\alpha_{66/64}$ obtained for the most reducing time series were used as these most closely matched the expected conditions during the formation or early evolution of the different materials used for comparison.

The best matches between experimental data and natural samples was observed for the diogenite meteorites and the Earth-Moon system where the lunar basalts fell within error of the isotope fractionation trend predicted using experimental $\alpha_{66/64}$. For other extra-terrestrial materials, Mars and various (a)chondritic meteorite reservoirs, the experimental fractionation factors did not match fractionation factor required to attain the assumed or measured isotopic composition of these bodies. Alternatively, volatility was only assumed to have been part contributor to the overall Zn isotopic composition of the body and therefore a volatile loss model could not adequately explain all observed heterogeneities or the assumed evaporation environment did not match the natural environment at the time of evaporative loss of Zn. For terrestrial materials volcanic gases, tektites and trinitites were considered and comparative fits were overall poor with the natural fractionation factors being substantially closer to unity than the experimentally derived $\alpha_{66/64}$.

6.2 – Future Recommendations

6.2.1 – Preparation of the Starting Materials

The synthetic major element compositions were prepared to accurately reflect speciation in the silicate melt by decarbonation of $CaCO_3$ to CaO and reduction of Fe_2O_3 to FeO. Trace element doping did not incorporate similar steps to adjust trace element speciation to reflect their speciation in the silicate melt. The majority of trace elements were introduced as oxides and reflect their speciation in the silicate melt, however those introduced as carbonate, halide or phosphate species did not. The properties of the non-oxide species differed from the element speciation in the silicate melt. This may have resulted in volatile loss not representative of the trace element volatility in the silicate melt during decomposition to an oxide. In this study the problem was alleviated by normalizing concentration to the shortest experiment instead of the calculated starting abundance. However, it is suggested that future trace element doped starting materials are always melted, quenched to a glass and reground to a powder prior to experiments to ensure trace elements are dissolved in the silicate melt before the experiment (Pangritz et al., 2022). This should be done at a temperature above the liquidus in oxidizing conditions, preferably in a closed container, to minimize the loss of the most volatile elements during sample preparation while ensuring complete melting of the material.

In this study the starting trace element composition was determined by calculating the expected trace element abundances based on the amount of trace element mix added and combining it with the measured trace element abundance of the undoped starting materials. It is suggested that future studies directly measure the trace element abundance of the doped starting material. For starting materials prepared using the method suggested in the previous paragraph a chip of glass may be analysed directly. For unmelted starting material it is proposed that a small amount of sample is melted in a closed capsule at high pressure, e.g. using a piston cylinder apparatus, to suppress volatility and dissolve trace elements in the melt for analysis.

6.2.2 – Experimental Set-up

Trace element volatility was shown to decrease with increasing melt polymerization, resulting in ubiquitous compositional gradients in more viscous compositions compared to the inviscid compositions. Moreover, the Zn isotope data showed that Zn depleted boundary layers were present in all experiments. With the current experiments it was not possible to accurately quantify trace element volatility as evaporative loss was limited by diffusion in the silicate melt. To accurately assess trace element volatility diffusion must be avoided in future experiments. To minimize the diffusion in the silicate melt, experiments could be performed in a stirring furnace (Norris, 2016) where a metal rod stirs the melt to maintain compositional homogeneity. This would require further consideration of the experimental conditions and the metal used for the stirring rod to minimize interactions between the rod and the silicate melt. An alternative approach would be to significantly increase the experimental runtime (e.g. Neuman et al., 2022) such that the evaporation time exceeds the diffusion time. However, for the more volatile elements this would likely result in complete depletion in the silicate melt.

For some elements interactions with the sample holder may have affected their calculated volatility. To remove these effects future experiments could be performed in a high temperature conical nozzle levitation apparatus (Pack et al., 2010) where the sample is suspended using a pressurized gas flow and heated with a CO_2 laser. This method does not require noble metal sample holders and therefore removes potential interactions between sample and sample holder.

6.2.3 – Starting Compositions and Experimental Conditions

The starting materials in this study were chosen to cover a range of materials. The SM and IB starting compositions in this study were used to allow for direct comparison with previous work by Norris (2016) and Sossi et al. (2019). The results showed that there was a compositional dependence on volatility and therefore choosing alternative starting composition more reflective of the topic of

interest, i.e. the Bulk Silicate Earth, various meteorite (sub-)groups or parent-body compositions may remove a complicating factor when applying experimental data to the evolution of the volatile budgets of these bodies. Moreover, expanding the range of major element compositions involved should allow for the determination of the effects of individual major element species on trace element volatility as the three compositions used in this study were insufficient for a multivariate linear regressions for all major elements.

Expanding the range of temperature and fO_2 to fill gaps in the current dataset and including additional trace elements in future studies will provide additional insight into trace element evaporation. For example, other studies by Sossi et al. (2019), Heck (2022) and Liu et al. (2022) covered a larger temperature range which enabled them to quantify the enthalpy and entropy of the evaporation reactions from the temperature dependence of K* more accurately.

6.2.4 – Analysis of Gas Species

At present, most studies considering trace element volatility use thermodynamic properties of pure species to make predictions regarding the evaporation pathways (e.g. Sossi et al., 2019; Heck, 2022; Liu et al., 2022). Where trace element speciation in the silicate melt is relatively well-understood, gas speciation relies on thermodynamic calculations. It may be more appropriate for future studies to consider analysing the gas species. This could be achieved either in situ by linking the directly transporting the evaporating species into a mass spectrometer or ex situ by deposition of the gas species on a surface and subsequently analysing these species. In the latter scenario the temperature gradient within the tube of the one atmosphere furnace would result in the gas species being separated based on their condensation temperatures. Recent studies by Scholtysik and Canil (2018; 2021), Nekvasil et al. (2019) and Renggli and Klemme (2020) have investigated the deposition of gas species on silica glass tubes in conditions appropriate to the terrestrial volcanic environment. In these studies they were able to identify individual species as they has condensed on the tubes, separated

across the temperature gradient. Further understanding of gas speciation in experimentally relevant conditions would aid in the understanding of trace element volatility.

Analysis of the gas speciation in situ would be more challenging as condensation of the metallic gas species at lower temperatures would require direct sampling from the furnace. Norris (2016) discussed that this would be theoretically possible using a Knudsen cell mass spectrometer set-up where the furnace acted as a Knudsen cell. However, practical issues in buffering fO_2, preventing leakage and minimizing compositional gradients in the silicate melt would make this difficult to achieve. Instead, Norris (2016) argued that it would be more practical, but still incredibly complex, to directly sample inside the furnace with spectroscopic analysis of the gases.

Condensing the gas species would also enable assessment of the isotopic composition of the condensed species and identify potential differences in isotope fractionation for different evaporation reactions. However, this will require complete condensation as otherwise isotope fractionation during deposition on the silica glass tube will affect the results. This may aid in the understanding of the genesis of isotopically light natural rock samples, e.g. the light Zn isotope enriched lunar basalt samples that are thought to have formed by interactions between the gas and melt phases (Herzog et al., 2009; Paniello et al., 2012a; Ma and Liu, 2019).

6.2.5 – Thermodynamic Properties

The thermodynamic database used in this study (Barin et al., 1989) did not always contain data on the pure species. For example, Liu et al. (2022) consider InO (g), a species which was not present in Barin et al. (1989). For P, As, Ag, Cs and Tl thermodynamic data for some species was only available at lower temperatures. For these the data was extrapolated, sometimes in excess of 1000 K beyond the available temperature range. It may be that these pure species are unstable at these conditions, but an increased coverage of the thermodynamic properties across a broader temperature range would improve the accuracy of these values.

6.2.6 – Trace Element Activity and Evaporation Coefficient Data

In this study it was mostly assumed that trace element behave ideally in the silicate melt which is not necessarily reflective of their natural behaviour. However, the paucity of trace element activity data and the limited range of experimental and compositional values that current trace element activity models cover (e.g. O'Neill and Eggins, 2002; Wood and Wade, 2013; Norris, 2016) inhibit accurate determination of trace element activities at conditions relevant to this study. This became abundantly clear when corrections were made for non-ideality in the silicate melt by considering compositionally relevant activity coefficients of Norris (2016) for IB and Sossi et al. (2019) for SM which worsened the fits.

The evaporation coefficient is a generally poorly understood parameter which can only be determined empirically at present despite efforts to develop methods to determine its value from experimental data (Alexander, 2001; Fedkin et al., 2006) or by deriving equations from thermodynamic and quantum mechanical principles (Bourdon and Fitoussi, 2020). The majority of data available in literature at present is focused on major element evaporation coefficients in Ca-Al rich inclusions and the formation of chondrules (e.g. Shornikov, 2015; Dullemond et al., 2016; Ivanova et al., 2021).

A further understanding of trace element activity and evaporation coefficients and how these parameters change as a function of silicate melt composition, temperature and oxygen fugacity would increase the accuracy of the thermodynamic predictions of gas speciation as well as aid in solving the modified Hertz-Knudsen-Langmuir equation and increase the overall understanding of trace element evaporation from silicate melts.

6.2.7 – Application to Volcanic Environment

Volcanic gas emissions are another environment in which evaporative loss of trace elements is an important process. The experiments conducted in this study are mostly insufficient to study terrestrial volcanism as the conditions are different from the volcanic environment; temperatures are lower and

the oxygen fugacity is more oxidizing than those in the majority of the experiments (Delmelle et al., 2018). Moreover, evaporation pathways in the volcanic environment include those of halide, sulphide and hydroxide complexation (Mason et al., 2018) which were not the focus of this study (e.g. Renggli and Klemme, 2020). Future experiments could focus on more T-fO_2 conditions appropriate for volcanism and/or consider recent developments in the understanding of the properties of chlorine (Thomas and Wood, 2021) and sulphur (Boulliung and Wood, 2022) in the silicate melt and include these evaporation pathways to expand the understanding of volatile loss in the volcanic environment.

6.2.8 – Integration into Planetary Formation and Evolution Models

This study focused on experimentally quantifying trace element volatility from silicate melts. The results of these experiments provided additional insight and constraints on trace element volatility that may prove important to improve model of the formation and/or chemical evolution of the rocky bodies in the solar system or exoplanets (e.g. Lichtenberg, 2021). Experimental conditions did not match those of the early solar nebula, as reflected in the poor correlation of volatile loss with T^{50}. Instead, they correlated relatively well with CI chondrite normalized abundance of the terrestrial mantle, suggesting that the present-day BSE trace element abundances were affected by significant volatile loss in addition to core-mantle segregation. However, the Zn isotopic composition of the terrestrial mantle and chondritic and Martian meteorites were identical within error which suggested that isotope fractionation is more likely to have occurred on smaller precursor bodies instead of in large planetary scale magma oceans. An increased understanding of evaporative loss from silicate melt in conditions relevant to a planetary magma ocean could improve models of planetary formation and evolution.

6.2.9 – Expansion of Isotope Systems

In this study Zn was used to measure the isotope fractionation during evaporative loss. Initially the aim of this project was to also consider Cd isotopes, but its high volatility and low abundances inhibited

this. Next, an attempt was made to process samples for Cu isotope fractionation measurements. However, due to time constraints this was abandoned. Experimental evaporation induced isotope fractionation studies have considered other isotope systems including Mg, Ca, K, Ti, Cr, Fe, Cu, Zn, Ge, Te and Tl (Xue et al., 1996; Zhang et al., 2014; Luais et al., 2018; Wimpenny et al., 2019; Sossi et al., 2020; Ni et al. 2021; Nielsen et al., 2021; Zhang et al., 2021; Klemme et al, 2022; Neuman et al., 2022; Renggli et al., 2022; Young et al., 2022). Further expansion of the array of elements covered may aid in reconciling observed isotope fractionation in natural samples with experimental results.

References

Ackermann, R.J., Thorn, R.J., Winslow, G.H. (1962). Some fundamental aspects of vaporization, AEC Research and Development Report. No. ANL-6663. Argonne National Laboratory, Illinois

Albarède, F., Beard, B. (2004). Analytical Methods for Non-Traditional Isotopes. Reviews in Mineralogy and Geochemistry, vol. 55, p. 113-152

Alexander, C.M.O'D. (2001). Exploration of quantitative kinetic models for the evaporation of silicate melts in vacuum and in hydrogen. Meteoritics and Planetary Science, vol. 36, p. 255-283

Amet, Q., Fitoussi, C. (2020). Chemical procedure for Zn purification and double spike method for high precision measurement of Zn isotopes by MC-ICPMS. International Journal of Mass Spectrometry, vol. 457, 116413

Archer, C., Vance, D. (2004). Mass discrimination correction in multiple-collector plasma source mass spectrometry: an example using Cu and Zn isotopes. Journal of Analytical Atomic Spectroscopy, vol. 19, p. 656-665

Archer, C., Andersen, M.B., Cloquet, C., Conway, T.M., Dong, S., Ellwood, M., Moore, R., Nelson, J., Rehkämper, M., Rouxel, O., Samanta, M., Shin, K-C., Sohrin, Y., Takano, S., Wasylenki, L. (2017) Inter-calibration of a proposed new primary reference standard AA-ETH Zn for zinc isotopic analysis. Journal of Analytical Atomic Spectrometry, vol. 32, p. 415-419

Armitage, P.J. (2011). Dynamics of Protoplanetary Disks. Annual Review of Astronomy and Astrophysics, vol. 49, p. 195-236

Armstrong, K., Frost, D.J., McCammon, C.A., Rubie, D.C., Ballaran, T.B. (2019). Deep magma ocean formation set the oxidation state of Earth's mantle. Science, vol. 365, p. 903-906

Barin, I., Sauert, F., Schultze-Rhonhof, E., Sheng, W.S. (1989). Thermochemical Data of Pure Substances. Cambridge, United Kingdom, VCH Publishers Ltd.

Barr, A.C. (2016). On the origin of Earth's Moon. Journal of Geophysical Research: Planets, vol. 121, p. 1573-1601

Barrat, J.A., Zanda, B., Moynier, F., Bollinger, C., Liorzou, C., Bayon, G. (2012). Geochemistry of CI chondrites: Major and trace elements, and Cu and Zn isotopes. Geochimica et Cosmochimica Acta, vol. 83, p. 79-92

Barrat, J.A., Sansjofre, P., Yamaguchi, A., Greenwood, R.C., Gillet, P. (2017). Carbon isotopic variation in ureilites: Evidence for an early, volatile-rich Inner Solar System. Earth and Planetary Science Letters, vol. 478, p. 143-149

Bermingham, K.R., Füri, E., Lodders, K., Marty, B. (2020). The NC-CC Isotope Dichotomy: Implications for the Chemical Isotopic Evolution of the Early Solar System. Space Science Reviews, vol. 216, 133

Bigalke, M., Weyer, S., Kobza, J., Wilcke, W. (2010). Stable Cu and Zn isotope ratios as tracers of sources and transport of Cu and Zn in contaminated soil. Geochimica et Cosmochimica Acta, vol. 74, p. 6801-6813

Bigeleisen, J., Mayer, M.G. (1947). Calculation of Equilibrium Constants for Isotopic Exchange Reactions. Journal of Chemical Physics, vol. 15, p. 261-267

Bischoff, A., Horstmann, M., Barrat, J.A., Chaussidon, M., Pack, A., Herwartz, D., Ward, D., Vollmer, C., Decker, S. (2014). Trachyandesitic volcanism in the early Solar System. Proceedings of the Natural Academy of Sciences, vol. 111, p. 12689-12692

Blanchard, I., Badro, J., Siebert, J., Ryerson, F.J. (2015). Composition of the core from gallium metal-silicate partitioning experiments. Earth and Planetary Science Letters, vol. 427, p. 191-201

Boelrijk, N.A.I.M. (1968). A general formula for "double" isotope dilution analysis. Chemical geology, vol. 3, p. 323-325

Borisov, A., Jones, J.H. (1999). An evaluation of Re, as an alternative to Pt, for the 1 bar loop technique: An experimental study at 1400°C. American Mineralogist, vol. 84, p. 1528-1534

Borisov, A.A. (2009). Influence of SiO2 and Al2O3 on the Activity Coefficients of Alkalis in Melts: An Experimental Study. Petrologiya, vol. 17, p. 623-635

Borrok, D.M., Gieré, R., Ren, M., Landa, E.R. (2010). Zinc Isotopic Composition of Particulate Matter Generated during the Combustion of Coal and Coal + Tire-Derived Fuels. Environmental Science & Technology, vol. 44, p. 9219-9224

Boulliung, J., Wood, B.J. (2022). SO2 solubility and degassing behaviour in silicate melts. Geochimica et Cosmochimica Acta, vol. 336, p. 150-164

Bourdon, B., Roskosz, M., Hin, R.C. (2018). Isotope tracers of core formation. Earth-Science Reviews, vol. 181, p. 61-81

Bourdon, B., Fitoussi, C. (2020). Isotope Fractionation during Condensation and Evaporation during Planet Formation Processes. ACS Earth and Space Chemistry, vol. 4, p. 1408-1423

Boyce, J.W., Treiman, A.H., Guan, Y., Ma, C., Eiler, J.M., Gross, J., Greenwood, J.P., Stolper, E.M. (2015). The chlorine isotope fingerprint of the lunar magma ocean. Science Advances, vol. 1, doi: 10.1126/sciadv.1500380

Brand, W.A., Coplen, T.B., Vogl, J., Rosner, M., Prohaska, T. (2014). Assessment of international reference materials for isotope ratio analysis (IUPAC Technical Report). Pure and Applied Chemistry, vol. 86, p. 425-467

Braukmüller, N., Wombacher, F., Hezel, D.C., Escoube, R., Münker, C. (2018). The chemical composition of carbonaceous chondrites: Implications for volatile element depletion, complementarity and alteration. Geochimica et Cosmochimica Acta, vol. 239, p. 17-48

Braukmüller, N., Wombacher, F., Funk, C., Münker, C. (2019). Earth's volatile element depletion pattern inherited from a carbonaceous chondrite-like source. Nature Geoscience, vol. 12, p. 564-568

Bridgestock, L.J., Williams, H., Rehkämper, M., Larner, F., Giscard, M.D., Hammond, S., Coles, B., Andreasen, R., Wood, B.J., Theis, K.J., Smith, C.L., Benedix, G.K., Schönbächler, M. (2014). Unlocking the zinc isotope systematics of iron meteorites. Earth and Planetary Science Letters, vol. 400, p. 153-164

Brown, S.M., Elkins-Tanton, L.T. (2009). Compositions of Mercury's earliest crust from magma ocean models. Earth and Planetary Science Letters, vol. 286, p. 446-455

Brugier, Y.A., Barrat, J.A., Gueguen, B., Agranier, A., Yamaguchi, A., Bischoff, A. (2019). Zinc isotopic variations in ureilites. Geochimica et Cosmochimica Acta, vol. 246, p. 450-460

Bulska, E., Ruszczyńska, A. (2017). Analytical Techniques for Trace Element Determination. Physical Sciences Reviews, vol. 2, 20178002

Burkhardt, C., Kleine, T., Oberli, F., Pack, A., Bourdon, B., Wieler, R. (2011). Molybdenum isotope anomalies in meteorites: Constraints on solar nebula evolution and origin of the Earth. Earth and Planetary Science Letters, vol. 312, p. 390-400

Campbell, I.H., O'Neill, H.St.C. (2012). Evidence against a chondritic Earth. Nature, vol. 483, p. 553-558

Canup, R.M., Visscher, C., Salmon, J., Fegley Jr., B. (2015). Lunar volatile depletion due to incomplete accretion within an impact-generated disk. Nature Geoscience, vol. 8, p. 918-921

Capobianco, C.J., Drake, M.J., De'Aro, J. (1999). Siderophile geochemistry of Ga, Ge and Sn: Cationic oxidation states in silicate melts and the effect of composition in iron-nickel alloys. Geochimica et Cosmochimica Acta, vol. 63, p. 2667-2677

Carmichael, I.S.E., Turner, F.J., Verhoogen, J. (1974). Igneous Petrology, McGraw-Hill, New York.

Chambers, J.E. (2016). Pebble accretion and the diversity of planetary systems. The Astrophysical Journal, vol. 825, p. 63

Chapman, J.B., Mason, T.F.D., Weiss, D.J., Coles, B.J., Wilkinson, J.J. (2006). Chemical Separation and Isotopic Variations of Cu and Zn for Five Geological Reference Materials. Geostandards and Geoanalytical Research, vol. 30, p. 5-16

Chen, H., Savage, P.S., Teng, F.Z., Helz, R.T., Moynier, F. (2013a). Zinc isotope fractionation during magmatic differentiation and the isotopic composition of the bulk Earth. Earth and Planetary Science Letters, vol. 369-370, p. 34-42

Chen, H., Nguyen, B.M., Moynier, F. (2013b). Zinc isotopic composition of iron meteorites: Absence of isotopic anomalies and origin of the volatile element depletion. Meteoritics and Planetary Sciences, vol. 48, p. 2441-2450

Chen, J.B., Gaillardet, J., Dessert, C., Villemant, B., Louvat, P., Crispi, O., Birck, J.L., Wang, Y.N. (2014). Zn isotope compositions of the thermal spring waters of La Soufrière volcano, Guadeloupe Island. Geochimica et Cosmochimica Acta, vol. 127, p. 67-82

Chen, S., Liu, Y., Hu, J., Zhang, Z., Hou, Z., Huang, F., Yu, H. (2016). Zinc Isotopic Compositions of NIST SRM 683 and Whole-Rock Reference Materials. Geostandards and Geoanalytical Research, vol. 40, p. 417-432

Chiaradia, M., Pujol-Solà, N., Farré-de-Pablo, J., Aiuppa, A., Paonita, A., Rizzo, A.L., Brusca, L. (2018). Geochemistry and isotope composition (Sr, Pb, δ66Zn) of Vulcano fumaroles (Aeolian Islands, Italy). Chemical Geology, vol. 493, p. 153-171

Chilton, T.H., Colburn A.P. (1934). Mass Transfer (Absorption) Coefficients: Prediction from Data on Heat Transfer and Fluid Friction. Industrial and Engineering Chemistry, vol. 26, p. 1183-1187

Cloquet, C., Carignan, J., Libourel, G. (2006). Isotopic Composition of Zn and Pb Atmospheric Depositions in an Urban/Periurban Area of Northeastern France. Environmental Science & Technology, vol. 40, p. 6594-6600

Coath, C.D., Elliott, T., Hin, R.C. (2017). Double-spike inversion for three-isotope systems. Chemical Geology, vol. 451, p. 78-89

Collinet, M., Grove, T.L. (2020). Incremental melting in the ureilite parent body: Initial composition, melting temperatures, and melt compositions. Meteoritics and Planetary Science, vol. 55, p. 832-856

Connelly, J.N., Bollard, J., Bizzarro, M. (2017). Pb-Pb chronometry and the early Solar System. Geochimica et Cosmochimica Acta, vol. 201, p. 345-363

Costas-Rodriguez, M., van Heghe, L., Vanhaecke, F. (2014). Evidence for a possible dietary effect on the isotopic composition of Zn in blood via isotopic analysis of food products by multi-collector ICP-mass spectrometry. Metallomics, vol. 6, p. 139-146

Crank, J. (1975). The Mathematics of Diffusion. Second Edition. Clarendon Press, Oxford, United Kingdom

Creech, J.B., Moynier, F. (2019). Tin and Zinc stable isotope characterisation of chondrites and implications for early Solar System evolution. Chemical Geology, vol. 511, p. 81-90

Criss, R.H. (1999). Principles of Stable Isotope Distribution. Oxford University Press, Oxford, United Kingdom

Dauphas, N. (2017). The isotopic nature of the Earth's accreting material through time. Nature, vol. 541, p. 521-524

Day, J.M.D., Moynier, F. (2014). Evaporative fractionation of volatile stable isotopes and their bearing on the origin of the Moon. Philosophical Transactions of the Royal Society, vol. 372, 20130259

Day, J.M.D., Qiu, L., Ash, R.D., McDonough, W.D., Teng, F.-Z., Rudnick, R.L., Taylor, L.A. (2016). Evidence for high-temperature fractionation of lithium isotopes during differentiation of the Moon. Meteoritics & Planetary Science, vol. 51, p. 1046-1062

Day, J.M.D., Moynier, F., Meshik, A.P., Pradivtseva, O.V., Petit, D.R. (2017). Evaporative fractionation of zinc during the first nuclear detonation. Science Advances, vol. 3, e1602668

Day, J.M.D., van Kooten, E.M.M.E., Hofmann, B.A., Moynier, F. (2020a). Mare basalt meteorites, magnesian-suite rocks and KREEP reveal loss of zinc during and after lunar formation. Earth and Planetary Science Letters, vol. 531, 115998

Day, J.M.D., Moynier, F., Sossi, P.A., Wang,, K., Meshik, A.P., Pravdivtseva, O.V., Pettit, D.R. (2020b). Moderately volatile element behaviour at high temperature determined from nuclear detonation. Geochemical Perspectives Letters, vol. 35, p. 54-60

Debaille, V., Brandon, A.D., Yin, Q.Z., Jacobsen, B. (2007). Coupled 142Nd-143Nd evidence for a protracted magma ocean in Mars. Nature, vol. 450, p. 525-528

Deines, P., Nafziger, R.H., Ulmer, G.C., Woermann, E. (1974). Temperature-oxygen fugacity tables for selected gas mixtures in the system C-H-O at 1 atm total pressure. Bulletin of Earth and Mineral Sciences Experiment Station number 88. Pennsylvania State University, College of Earth and Mineral Sciences

Delmelle, P., Wadsworth, F.B., Maters, E.C., Ayris, P.M. (2018). High Temperature Reactions Between Gas and Ash Particles in Volcanic Eruption Plumes. Reviews in Mineralogy and Geochemistry, vol. 84, p. 285-308

Dhaliwal, J.K., Day, J.M.D., Moynier, F. (2018). Volatile element loss during planetary magma ocean phases. Icarus, vol. 300, p. 249-260

Dodson, M.H. (1963). A theoretical study of the use of internal standards for precise isotopic analysis by the surface ionization technique: Part I – General first-order algebraic solutions. Journal of Scientific Instruments, vol. 40, p. 289-295

Dominguez, G., Wilkins, G., Thiemens, M.H. (2010). The Soret effect and isotopic fractionation in high-temperature silicate melts. Nature, vol. 473, p. 70-73

Doucet, L.S., Mattielli, N., Ionov, D.A., Debouge, W., Golovin, A.V. (2016). Zn isotopic heterogeneity in the mantle: A melting control? Earth and Planetary Sciences, vol. 451, p. 232-240

Downes, H., Mittlefehldt, D.W., Kita, N.T., Valley, J.W. (2008). Evidence from polymict ureilite meteorites for a disrupted and re-accreted single ureilite parent asteroid gardened by several distinct impactors. Geochimica et Cosmochimica Acta, vol. 72, p. 4825-4844

Dullemond, C.P., Monnier, J.D. (2010). The Inner Regions of Protoplanetary Disks. Annual Review of Astronomy and Astrophysics, vol. 48, p. 205-239

Dullemond, C.P., Harsono, D., Stammler, S.M., Johansen, A. (2016). Forming chondrules in impact splashes. II. Volatile Retention. The Astrophysical Journal, vol. 832, p. 91-109

Edmonds, M. (2015). Partitioning of light lithophile elements during basalt eruptions on Earth and application to Martian shergottites. Earth and Planetary Science Letters, vol. 411, p. 142-150

Edmonds, M., Mason, E., Hogg, O. (2022). Volcanic Outgassing of Volatile Trace Metals. Annual Review of Earth and Planetary Sciences, vol. 50, p. 79-98

Elkins-Tanton, L.T., Burgess, S., Yin, Q.-Z. (2011). The lunar magma ocean: Reconciling the solidification process with lunar petrology and geochronology. Earth and Planetary Science Letters, vol. 304, p. 326-336

Engelhardt, W.V., Luft, E., Arndt, J., Schock, H., Weiskirchner, W. (1987). Origin of moldavites. Geochimica et Cosmochimica Acta, vol. 51, p. 1425-1443

Epov, V.N., Malinovskiy, D., Vanhaecke, F., Bégué, D., Donard, O.F.X. (2011). Modern mass spectrometry for studying mass-independent fractionation of heavy stable isotopes in environmental and biological sciences. Journal of Analytical Atomic Spectrometry, vol. 26, p. 1142-1156

Fedkin, A.V., Grossman, L., Ghiorso, M.S. (2006). Vapor pressures and evaporation coefficients for melts of ferromagnesian chondrule-like compositions. Geochimica et Cosmochimica Acta, vol. 70, p. 206-223

Fehr, M.A., Hammond, S.J., Parkinson, I.J. (2018). Tellurium stable isotope fractionation in chondritic meteorites and some terrestrial samples. Geochimica et Cosmochimica Acta, vol. 222, p. 17-33

Filby, R.H. (1964). Determination of the Zinc-68-Zinc-64 Ratio in Rocks and Minerals by Neutron Activation Analysis. Analytical Chemistry, vol. 36, p. 1597-1600

Fischer, R.A., Campbell, A.J., Ciesla, F.J. (2017). Sensitivities of Earth's core and mantle compositions to accretion and differentiation processes. Earth and Planetary Science Letters, vol. 458, p. 252-262

French, B.M., Koeberl, C. (2010). The convincing identification of terrestrial meteorite impact structures: What works, what doesn't and why. Earth-Science Reviews, vol. 98, p. 123-170

Fujii, T., Moynier, F., Albarède, F. (2006). Nuclear field vs. nucleosynthetic effects as cause of isotopic anomalies in the early Solar System. Earth and Planetary Science Letters, vol. 247, p. 1-9

Fujii, T., Moynier, F., Uehara, A., Abe, M., Yin, Q.Z., Nagai, T., Yamana, H. (2009). Mass-Dependent and Mass-Independent Isotope Effects of Zinc in a Redox Reaction. Journal of Physical Chemistry A, vol. 113, p. 12225-12232

Galer, S.J.G. (1999). Optimal double and triple spiking for high precision lead isotopic measurement. Chemical Geology, vol. 157, p. 255-274

Garçon, M., Sauzéat, L., Carlson, R.W., Shirey, S.B., Simon, M., Balter, V., Boyet, M. (2017). Nitrile, Latex, Neoprene and Vinyl Gloves: A Primary Source of Contamination for Trace Element and Zn Isotopic Analyses in Geological and Biological Samples. Geostandards and Geoanalytical Research, vol. 41, p. 367-380

Gargano, A., Dottin, J., Hopkins, S.S., Sharp, Z., Shearer, C., Halliday, A.N., Larner, F., Farquar, J., Simon, J.I. (2022). The Zn, S and Cl isotopic compositions of mare basalts: Implications for the effects of eruption style and pressure on volatile element stable isotope fractionation on the Moon. American Mineralogist, vol. 107, p. 1985-1994

Gellissen, M., Holzheid, A., Kegler, Ph., Palme, H. (2019). Heating experiments relevant to the depletion of Na, K and Mn in the Earth and other planetary bodies. Geochemistry, vol. 79, 125540

Ghidan, O.Y., Loss, R.D. (2011). Isotope fractionation and concentration measurements of Zn in meteorites determined by the double spike, IDMS-TIMS techniques. Meteoritics and Planetary Science, vol. 46, p. 830-842

Ghidan, O.Y., Loss, R.D. (2012). Zinc isotope fractionation analyses by thermal ionization mass spectrometry and a double spiking technique. International Journal of Mass Spectrometry, vol. 309, p. 79-87

Goldschmidt, V.M. (1930). Geochemische Verteilungsgesetze und kosmische Häufigkeit der Elemente. Naturwissenschaften, vol. 18, p. 999-1013

Greber, N.D., Dauphas, N., Puchtel, I.S., Hofmann, B.A., Arndt, N.T. (2017). Titanium stable isotopic variations in chondrites, achondrites and lunar rocks. Geochimica et Cosmochimica Acta, vol. 213, p. 534-552

Gualda G.A.R., Ghiorso M.S. (2015) MELTS_Excel: A Microsoft Excel-based MELTS interface for research and teaching of magma properties and evolution. Geochemistry, Geophysics, Geosystems vol. 16, p. 315-324

Guan, Z.X., Liu, Y. (2023). How to estimate isotope fractionations of a Rayleigh-like but diffusion-limited disequilibrium process. Acta Geochimica, vol. 42, p. 24-37

Guignard, J., Quitte, G., Meheut, M., Toplis, M.J., Poitrasson, F., Connetable, D., Koskosz, M. (2020). Nickel isotope fractionation during metal-silicate differentiation of planetesimals: Experimental petrology and ab initio calculations. Geochimica et Cosmochimica Acta, vol. 269, p. 238-256

Haisch Jr., K.E., Lada, E.A., Lada, C.J. (2001). Disk Frequencies and Lifetimes in Young Clusters. The Astrophysical Journal, vol. 553, p. L153-L156

Halliday, A.N., Lee, D.C., Christensen, J.N., Walder, A.J., Freedman, P.A., Jones, C.E., Hall, C.M., Yi, W., Teagle, D. (1995). Recent developments in inductively coupled plasma magnetic sector multiple collector mass spectrometry. International Journal of Mass Spectrometry and Ion Processes, vol. 146-147, p. 21-33

Halliday, A.N. (2008). A young Moon-forming giant impact at 70-110 million years accompanied by late-stage mixing, core formation and degassing of the Earth. Philosophical Transactions of the Royal Society, vol. 366, p. 4163-4181

Halliday, A.N., Canup, R.M. (2023). The accretion of planet Earth. Nature Reviews: Earth and Environment, vol. 4, p. 19-35

Hauri, E.H., Saal, A.E., Rutherford, M.J., Van Orman, J.A. (2015). Water in the Moon's interior: Truth and consequences. Earth and Planetary Sciences Letters, vol. 409, p. 252-264

Heck, W. (2022) Experimental Degassing of Moderately Volatile Chalcophile Elements from Silicate Melt. PhD Thesis

Herzog, G.F., Moynier, F., Albarede, F., Berezhnoy, A.A. (2009). Isotopic and elemental abundances of copper and zinc in lunar samples, Zagami, Pele's hairs, and a terrestrial basalt. Geochimica et Cosmochimica Acta, vol. 73, p. 5884-5904

Hin, R.C., Coath, C.D., Carter, P.J., Nimmo, F., Lai, Y.-J., Pogge van Strandmann, P.A.E., Willbold, M., Leinhardt, Z.M., Walter, M.J., Elliott, T. (2017). Magnesium isotope evidence that accretional vapour loss shapes planetary compositions. Nature, vol. 549, p. 511-515

Hirschmann, M.M. (2012). Magma ocean influence on early atmosphere mass and composition. Earth and Planetary Science Letters, vol. 341, p. 48-57

Hirschmann, M.M. (2022). Magma ocean, iron and chromium redox, and the origin of comparatively oxidized planetary mantles. Geochimica et Cosmochimica Acta, vol. 328, p. 221-241

Hirth, J.P., Pound, G.M. (1963). Condensation and Evaporation: Nucleation and growth kinetics. Pergamon Press, Oxford, United Kingdom

Hoefs, J. (2021). Stable Isotope Geochemistry, 9th edition, Springer Nature, Cham, Switzerland.

Hołyst, R., Litniewski, M., Jakubczyk, D. (2015). A molecular dynamics test of the Hertz-Knudsen equation for evaporating liquids. Soft Matter, vol. 11, p. 7201-7206

Holzheid, A., Lodders, K. (2001). Solubility of copper in silicate melts as function of oxygen and sulphur fugacities, temperature and silicate composition. Geochimica et Cosmochimica Acta, vol. 65, p. 1933-1951

Hopkins, S.S. (2019). Vanadium and Zinc Isotope Ratios in Lunar Basalts. PhD Thesis

Hopp, T., Fischer-Gödde, M., Kleine, T. (2018). Ruthenium isotope fractionation in protoplanetary cores. Geochimica et Cosmochimica Acta, vol. 223, p. 75-89

Hu, Z., Gao, S. (2008). Upper crustal abundances of trace elements: A revision and update. Chemical Geology, vol. 253, p. 205-221

Huang, J., Zhang, X.C., Chen, S., Tang, L., Wörner, G., Yu, H., Huang, F. (2018). Zinc isotopic systematics of Kamchatka-Aleutian arc magmas controlled by mantle melting. Geochimica et Cosmochimica Acta, vol. 238, p. 85-101

Ivanov, M.V., Babikov, D. (2013). On molecular origin of mass-independent fractionation of oxygen isotopes in ozone forming recombination reaction. Proceedings of the Natural Academy of Sciences, vol. 110, p. 17708-17713

Ivanova, M.A., Mendybaev, R.A., Shornikov,S.I., Lorenz, C.A., McPherson, G.J. (2021). Modeling the evaporation of CAI-like melts, and constraining the origin of CH-CB CAIs. Geochimica et Cosmochimica Acta, vol. 296, p. 97-116

Jacobson, S.A., Rubie, D.C., Hernlund, J., Morbidelli, A., Nakajima, M. (2017). Formation, stratification, and mixing of the cores of Earth and Venus. Earth and Planetary Science Letters, vol. 474, p. 375-386

Javoy, M., Kaminski, E., Guyot, F., Andrault, D., Sanloup, C., Moreira, M., Labrosse, S., Jambon, A., Agrinier, P., Davaille, A., Jaupart, C. (2010). The chemical composition of the Earth: Estatite chondrite models. Earth and Planetary Science Letters, vol. 293, p. 259-268

Jiang, Y., Chen, H., Fegley Jr., B., Lodders, K., Hsu, W., Jacobsen, S.B., Wang, K. (2019). Implications of K, Cu and Zn isotopes for the formation of tektites. Geochimica et Cosmochimica Acta, vol. 259, p. 170-187

Jochum, K.P., Willbold, M., Raczek, I., Stoll, B., Herwig, K. (2005a). Chemical Characterisation of the USGS Reference Glasses GSA-1G, GSC-1G, GSD-1G, GSE-1G, BCR-2G, BHVO-2G and BIR-1G Using EPMA, ID-TIMS, ID-ICP-MS and LA-ICP-MS. Geostandards and Geoanalytical Research, vol. 29, p. 285-302

Jochum, K.P., Nohl, U., Herwig, K., Lammel, E., Stoll, B., Hofmann, A.W. (2005b). GeoReM: A New Geochemical Database for Reference Materials and Isotopic Standards. Geostandards and Geoanalytical Research, vol. 29, p. 333-338

Jochum, K.P., Wies, U., Stoll, B., Kuzmin, D., Yang, Q., Raczek, I., Jacob, D.E., Stracke, A., Birbaum, K., Frick, D.A., Günther, D., Enzweiler, J. (2011). Determination of Reference Values for NIST SRM 610-617 Following ISO Guidelines. Geostandards and Geoanalytical Research, vol. 35, p. 397-429

Johansen, A., Mac Low, M.M., Lacerda, P., Bizzarro, M. (2015). Growth of asteroids, planetary embryos, and Kuiper belt objects by chondrule accretion. Science Advances, vol. 1, DOI: 10.1126/sciadv.1500109

Johnson, C.M., Beard, B.L. (1999). Correction of instrumentally produced mass fractionation during isotopic analysis of Fe by thermal ionization mass spectrometry. International Journal of Mass Spectrometry, vol. 193, p. 87-99

Kamber, B.S., Schoenberg, R. (2020). Evaporative loss of moderately volatile metals from the superheated 1849 Ma Sudbury impact melt sheet inferred from stable Zn isotopes. Earth and Planetary Science Letters, vol. 544, 116356

Kato, C., Moynier, F., Valdes, M.C., Dhaliwal, J.K., Day, J.M.D. (2015). Extensive volatile loss during formation and differentiation of the Moon. Nature Communications, vol. 6, p. 7617-7620

Kato, C., Moynier, F. (2017). Gallium isotopic evidence for the fate of moderately volatile elements in planetary bodies and refractory inclusions. Earth and Planetary Science Letters, vol. 479, p. 330-339

Keil, K. (2002). Geological history of asteroid 4 Vesta: The “smallest terrestrial planet”. Asteroids, vol. 3, p. 573

Keil, K. (2010). Enstatite achondrite meteorites (aubrites) and the histories of their asteroidal parent bodies. Chemie der Erde, vol. 70, p. 295-317

Klaver, M., Coath, C.D. (2019). Obtaining Accurate Isotopic Compositions with the Double Spike Technique: Practical Considerations. Geostandards and Geoanalytical Research, vol. 43, p. 5-22

Kleine, T., Touboul, M., Bourdon, B., Nimmo, F., Mezger, K., Palme, H., Jacobsen, S.B., Yin, Q.Z., Halliday, A.N. (2009). Hf-W chronology of the accretion and early evolution of asteroids and terrestrial planets. Geochimica et Cosmochimica Acta, vol. 73, p. 5150-5188

Kleine, T., Steller, T., Burkhardt, C., Nimmo, F. (2023). An inner solar system origin of volatile elements in Mars. Icarus, vol. 397, p. 115519

Klemme, S., Genske, F., Sossi, P.A., Berndt, J., Renggli, C.J., Stracke, A. (2022). Cr stable isotope fractionation by evaporation from silicate melts. Chemical Geology, vol. 610, p. 121096

Knudsen, M. (1909). Die Gesetze der Molekularströmung und der inneren Reibungsströmung der Gase durch Röhren. Annalen der Physik, vol. 333, p. 75-130

Kokubo, E., Ida, S. (1998). Oligarchic Growth of Protoplanets. Icarus, vol. 131, p. 171-178

Kruijer, T.S., Touboul, M., Fischer-Gödde, M., Bermingham, K.R., Walker, R.J., Kleine, T. (2014). Protracted core formation and rapid accretion of protoplanets. Science, vol. 344, p. 1150-1154

Kruijer, T.S., Kleine, T., Borg, L.E., Brennecka, G.A., Irving, A.J., Bischoff, A., Agee, C.B. (2017a). The early differentiation of Mars inferred from Hf-W chronometry. Earth and Planetary Science Letters, vol. 474, p. 345-354

Kruijer, T.S., Burkhardt, C., Budde, G., Kleine, T. (2017b). Age of Jupiter inferred from distinct genetics and formation times of meteorites. Proceedings of the National Academy of Science, vol. 114, p. 6712-6716

Kruijer, T.S., Kleine, T., Borg, L.E. (2020). The great isotopic dichotomy of the early Solar System. Nature Astronomy, vol. 4, p. 32-40

Kulikov, Y.N., Lammer, H., Lichtenegger, H.I.M., Penz, T., Breuer, D., Spohn, T., Lundin, R., Biernat, H.K. (2007). A Comparative Study of the Influence of the Active Young Sun on the Early Atmospheres of Earth, Venus and Mars. Space Science Reviews, vol. 129, p. 207-249

Kumler, B., Day, J.D. (2021). Trace element variations generated by magmatic and post-crystallization processes in eucrite meteorites. Geochimica et Cosmochimica Acta, vol. 301, p. 211-229

Kushida, A., Tanaka, K., Numakura, H. (2003). Chemical Diffusion in L10-Ordered FePt. Material Transactions, vol. 44, p. 59-62

Langmuir, I. (1916). The Evaporation, Condensation and Reflection of Molecules and the Mechanism of Adsorption. Physical Review, vol. 8, p. 149

Lanzirotti, A., Lee, L., Head, E., Sutton, S.R., Newville, M., McCanta, M., Lerner, A.H., Wallace, P.J. (2019). Direct measurements of copper speciation in basalt glasses: understanding the relative roles of sulphur and oxygen in copper complexation melts. Geochimica et Cosmochimica Acta, vol. 267, p. 164-178.

Lee, C-T.A., Luffi, P., Le Roux, V., Dasgupta, R., Albarede, F., Leeman, W.P. (2010). The redox state of arc mantle using Zn/Fe systematics. Nature, vol., 468, p. 681-685.

Lichtenberg, T. (2021). Redox Hysteresis of Super-Earth Exoplanets from Magma Ocean Circulation. The Astrophysical Journal Letters, vol. 914, p. L4

Lindsay, F.N., Herzog, G.F., Albarède, F., Korotev, R.L. (2011). Elemental and Isotopic Abundances of Fe, Cu and Zn in Low-Ti Lunar Basalts. 42nd Lunar and Planetary Science Conference, Abstract 1907

Liotta, M., Martínez Cruz, M., Ferrufino, A., Rüdiger, J., Gutmann, A., Rojas Cerda, K.V., Bobrowski, N., de Moor, J.M. (2021). Magmatic signature in acid rain at Masaya volcano, Nicaragua: Inferences on element volatility during lava lake degassing. Chemical Geology, vol. 585, 120562

Liu, Y., Zhang, L., Yu, D. (2009). Diffusion Mobilities in fcc Cu-Au and fcc Cu-Pt Alloys. Journal of Phase Equilibria and Diffusion, vol. 30, p. 136-145

Liu, S.A., Wang, Z.Z., Li, S.G., Huang, J., Yang, W. (2016). Zinc isotope evidence for a large-scale carbonated mantle beneath eastern China. Earth and Planetary Science Letters, vol. 444, p. 169-178

Liu, D., Moynier, F., Siebert, J., Sossi, P.A., Hu, Y., Kubik, E. (2022). Origin of moderately volatile element depletion on differentiated bodies: Insights from the evaporation of indium from silicate melts. Geochimica et Cosmochimica Acta, vol. 339, p. 46-57

Lock, S.J., Stewart, S.T., Petaev, M.I., Leinhardt, Z., Mace, M.T., Jacobsen, S.B., Ćuk, M. (2018). The origin of the Moon within a Terrestrial Synestia. Journal of Geophysical Research: Planets, vol. 123, p. 910-951

Lodders, K. (2003). Solar System abundances and condensation temperatures of the elements. The Astrophysical Journal, vol. 591, p. 1220-1247

Loss, R.D., Lugmair, G.W. (1990). Zinc isotope anomalies in Allende meteorite inclusions. The Astrophysical Journal, vol. 360, p. L59-L62

Luais, B., Wood, B.J., Norris, C.A. (2018). Experimental investigation of Germanium isotopic fractionation during Evaporation Processes. 16th Experimental Mineralogy, Petrology and Geochemistry Conference Abstract, p. 90

Luck J.M., Ben Othman, D., Albarède, F. (2005). Zn and Cu isotopic variations in chondrites and iron meteorites: Early solar nebula reservoirs and parent-body processes. Geochimica et Cosmochimica Acta, vol. 69, p. 5351-5363

Ma, C., Liu, Y. (2019). Discovery of a zinc-rich mineral on the surface of lunar orange pyroclastic beads. American Mineralogist, vol. 104, p. 447-452

Maciag, B.J., Brenan, J.M. (2020). Speciation of arsenic and antimony in basaltic magmas. Geochimica et Cosmochimica Acta, vol. 276, p. 198-218

Mahan, B., Siebert, J., Blanchard, I., Borensztajn, S., Badro, J., Moynier, F. (2017). Constraining compositional proxies for Earth's accretion and core formation through high pressure and high temperature Zn and S metal-silicate partitioning. Geochimica et Cosmochimica Acta, vol. 235, p. 21-40

Maréchal, C.N., Télouk, P., Albarède, F. (1999). Precise analysis of copper and zinc isotopic compositions by plasma-source mass spectrometry. Chemical Geology, vol. 156, p. 251-273

Martins, R., Kuthning, S., Coles, B.J., Kreissig, K., Rehkämper, M. (2023). Nucleosynthetic isotope anomalies of Zn in meteorites constrain the origin of Earth's volatiles. Science, vol. 379, p. 369-372

Mason, E., Wieser, P.E., Liu, E.J., Edmonds, M., Ilyinskaya, E., Whitty, R.C.W., Mather, T.A., Elias, T., Nadeau, P.A., Wilkes, T.C., McGonigle, A.J.S., Pering, T.D., Mims, F.M., Kern, C., Schneider, D.J., Oppenheimer, C. (2018). Volatile metal emissions from volcanic degassing and lava-seawater interactions at Kīlauea Volcano, Hawai'i. Communications Earth & Environment, vol. 2, p. 79-94

Mather, T.A., Witt, M.L.I., Pyle, D.M., Quayle, B.M., Aiuppa, A., Bagnato, E., Martin, R.S., Sims, K.W.W., Edmonds, M., Sutton, A.J., Ilyinskaya, E. (2012). Halogens and trace metal emissions from the ongoing 2008 summit eruption of Kilauea volcano, Hawaii. Geochimica et Cosmochimica Acta, vol. 83, p. 292-323

May, T.W., Wiedmeyer, R.H. (1998). A Table of Polyatomic Interferences in ICP-MS. Atomic Spectroscopy, vol. 19, p. 150-155

McCord, T.B., Adams, J.B., Johnson, T.V. (1970). Asteroid Vesta: Spectral Reflectivity and Compositional Implications. Science, vol. 168, p. 1445-1447

McSween Jr., H.Y., Raymond, C.A., Stolper, E.M., Mittlefehldt, D.W., Baker, M.B., Lunning, N.G., Beck, A.W., Hahn, T.M. (2019). Differentiation and magmatic history of Vesta: Constraints from HED meteorites and Dawn spacecraft data. Geochemistry, vol. 79, 125526

Melja, J., Coplen, T.B., Berglund, M., Brand, W.A., De Bièvre, P., Gröning, M., Holden, N.E., Irrgeher, J., Loss, R.D., Walczyk, T., Prohaska, T. (2016). Isotpic composition of the elements 2013 (IUPAC Technical Report). Pure and Applied Chemistry, vol. 88, p. 293-306

Mezger, K., Schönbächler, M., Bouvier, A. (2020). Accretion of the Earth – Missing Components? Space Science Reviews, vol. 216, p. 27-51

Mills, K.C. (1993). The influence of Structure on the Physico-chemical properties of Slags. ISIJ International, vol 33, p. 148-156

Mizera, J., Řanda, Z., Kameník, J. (2016). On a possible parent crater for Australasian tektites: Geochemical, isotopic, geographical and other constraints. Earth-Science reviews, vol. 154, p. 123-137

Moeller, K., Schoenberg, R., Pedersen, R.B., Weiss, D., Dong, S. (2012). Calibration of the New Certified Reference Materials ERM-AE633 and ERM-AE647 for Copper and IRMM-3702 for Zinc Isotope Amount Ratio Determinations. Geostandards and Geoanalytical Research, vol. 36, p. 177-199

Monteux, J., Andrault, D., Samuel, H. (2016). On the cooling of a deep terrestrial magma ocean. Earth and Planetary Science Letters, vol. 448, p. 140-149

Moore, R.E.T. (2017). The Biomedical Potential of High Precision Zinc Isotope Analysis. PhD Thesis.

Moussallam, Y., Oppenheimer, C., Scaillet, B. (2019). On the relationship between oxidation state and temperature of volcanic gas emissions. Earth and Planetary Science Letters, vol. 520, p. 260-267

Moynier, F., Albarède, F., Herzog, G.F. (2006). Isotopic composition of zinc, copper, and iron in lunar samples. Geochimica et Cosmochimica Acta, vol. 70, p. 6103-6117

Moynier, F., Blichtert-Toft, J., Telouk, P., Luck, J.M., Albarède, F. (2007). Comparative stable isotope geochemistry of Ni, Cu, Zn and Fe in chondrites and iron meteorites. Geochimica et Cosmochimica Acta, vol. 71, p. 4365-4379

Moynier, F., Dauphas, N., Podosek, F.A. (2009a). A Search for 70Zn Anomalies in Meteorites. The Astrophysical Journal, vol. 700, p. L92-L95

Moynier, F., Beck, P., Jourdan, F., Yin, Q.Z., Reimold, U., Koeberl, C. (2009b). Isotopic fractionation of zinc in tektites. Earth and Planetary Science Letters, vol. 277, p. 482-489

Moynier, F., Beck, P., Yin, Q.Z., Ferroir, T., Barrat, J.A., Paniello, R., Telouk, P., Gillet, P. (2010). Volatilization induced by impact recorded in Zn isotope composition of urelites. Chemical Geology, vol. 276, p. 374-379

Moynier, F., Paniello, R.C., Gounelle, M., Albarède, F., Beck, P., Podosek, F., Zanda, B. (2011). Nature of volatile depletion and genetic relationships in enstatite chondrites and aubrites inferred from Zn isotopes. Geochimica et Cosmochimica Acta, vol. 75, p. 297-307

Moynier, F., Vance, D., Fujii, T., Savage, P. (2017). The Isotope Geochemistry of Zinc and Copper. Reviews in Mineralogy and Geochemistry, vol. 82, p. 543-600

Mullane, E., Russell, S.S., Gounelle, M. (2005). Aubrites: an iron and zinc isotope study. Lunar and Planetary Science 36 abstract, p. 1251

Mungall, J.E. (2002). Empirical models relating viscosity and tracer diffusion in magmatic silicate melts. Geochimica et Cosmochimica Acta, vol. 66, p. 125-143

Nekvasil, H., Di Francesco, N.J., Rogers, A.D., Coraor, A.E., King, P.L. (2019). Vapor-Deposited Minerals Contributed to the Martian Surface During Magmatic Degassing. Journal of Geophysical Research: Planets, vol. 124, p. 1471-1632

Neuman, M., Holzheid, A., Lodders, K., Fegley Jr., B., Jolliff, B.L., Koefoed, P., Chen, H., Wang, K. (2022). High temperature evaporation and isotope fractionation of K and Cu. Geochimica et Cosmochimica Acta, vol. 316, p. 1-20

Ni, P., Macris, C.A., Darling, E.A., Shahar, A. (2021). Evaporation-induced copper isotope fractionation: Insights from laser levitation experiments. Geochimica et Cosmochimica Acta, vol. 298, p. 131-148

Nielsen, S.G., Shu, Y., Wood, B.J., Blusztajn, J., Auro, M., Norris, C.A., Wörner, G. (2021). Thallium Isotope Fractionation During Magma Degassing: Evidence From Experiments and Kamchatka Arc Lavas. Geochemistry, Geophysics, Geosystems, DOI: 10.1029/2020GC009608

Norris, C.A. (2016). Volatilities of Trace Elements in Silicate Melts, PhD Thesis

Norris, C.A., Wood, B.J. (2017). Earth's volatile contents established by melting and vaporization. Nature, vol. 549, p. 507-510

O'Neill, H.St.C., Pownceby, M.I. (1993). Thermodynamic data from redox reactions at high temperatures I. An experimental and theoretical assessment of the electrochemical method using stabilized zirconia electrolytes with revised values for the Fe – "FeO", Co – CoO, Ni – NiO and Cu – Cu2O oxygen buffers, and new data for the W – WO2 buffer. Contributions to Mineralogy and Petrology, vol. 114, p. 296-314

O'Neill, H.St.C., Eggins, S.M. (2002). The effect of melt composition on trace element partitioning: an experimental investigation of the activity coefficients of FeO, NiO, CoO, MoO2 and MoO3 in silicate melts. Chemical Geology, vol. 186, p. 151-181

Pack, A., Kremer, K., Albrecht, N., Simon, K., Kronz, A. (2010). Description of an aerodynamic levitation apparatus with applications in Earth Sciences. Geochemical Transactions, vol. 11, 4

Palme, H., O'Neill, H.St.C. (2014). Cosmochemical Estimates of Mantle Composition, Treatise on Geochemistry, vol. 3, 2nd ed. Elsevier, p. 1-39

Palme, H., Lodders, K., Jones, A. (2014). Solar System Abundances of the Elements. In: Planets, Asteroids, Comets and The Solar System, volume 2 of Treatise on Geochemistry. Ed: A.M. Davis, Elsevier, p. 15-36

Pangritz, P., Renggli, C.J., Berndt, J., Rohrbach, A., Klemme, S. (2022). Synthesis of Large Amounts of Volatile Element-Bearing Silicate Glasses Using a Two-Stage Melting Process. ACS Earth and Space Chemistry, vol. 6, p. 1108-1114

Paniello, R.C., Day, J.M.D., Moynier, F. (2012a). Zinc isotopic evidence for the origin of the Moon. Nature, vol. 490, p. 376-379

Paniello, R.C., Moynier, F., Beck, P., Barrat, J.A., Podosek, F.A., Pichat, S. (2012b). Zinc isotopes in HEDs: Clues to the formation of 4-Vesta, and the unique composition of Pecora Escarpment 82502. Geochimica et Cosmochimica Acta, vol. 86, p. 76-87

Paquet, M., Sossi, P.A., Moynier, F. (2023a). Origin and abundances of volatiles on Mars from the zinc isotopic composition of Martian meteorites. Earth and Planetary Science Letters, vol. 611, p. 118126

Paquet, M., Moynier, F., Yokoyama, T., Dai, W., Hu, Y., Abe, Y., Aléon, J., Alexander, C.M.O'D., Amari, S., Amelin, Y., Bajo, K., Bizzarro, M., Bouvier, A., Carlson, R.W., Chaussidon, M., Choi, B.G., Dauphas, N., Davis, A.M., Di Rocco, T., Fujiya, W., Fukai, R., Gautum, I., Haba, M.K., Hibiya, Y., Hidaka, H., Homma, H., Hoppe, P., Huss, G.R., Ichida, K., Iizuka, T., Ireland, T.R., Ishikawa, A., Ito, M., Itoh, S., Kawasaki, N., Kita, N.T., Kitajima, K., Kleine, T., Komatani, S., Krot, A.N., Liu, M.C., Masuda, Y., McKeegan, K.D., Morita, M., Motomura, K., Nakai, I., Nagashima, K., Nesvorný, D., Nguyen, A.N., Nittler, L., Onose, M., Pack, A., Park, C., Piani, L., Qin, L., Russell, S.S., Sakamoto, N., Schönbächler, M., Tafla, L., Tang, H., Terada, K., Terada, Y., Usui, T., Wada, S., Wadhwa, M., Walker, R.J., Yamashita, K., Yin, Q.Z., Yoneda, S., Young, E.D., Yui, H., Zhang, A.C., Nakamura, T., Naraoka, H., Noguchi, T., Okazaki, R., Sakamoto, K., Yabuta, H., Abe, M., Miyazaki, A., Nakato, A., Nishimura, M., Okada, T., Yada, T., Yogata, K., Nakazawa, S., Saiki, T., Tanaka, S., Terui, F., Tsuda, Y., Watanabe, S., Yoshikawa, M., Tachibana, S., Yurimoto, H. (2023b). Contribution of Ryugu-like material to Earth's volatile inventory by Cu and Zn isotopic analysis. Nature Astronomy, vol. 7, p. 182-189

Pavlov, A.A., Kasting, J.F. (2002). Mass-Independent Fractionation of Sulfur Isotopes in Archean Sediments: Strong Evidence for an Anoxic Archean Atmosphere. Astrobiology, vol. 2, p. 27-41

Pedley, J.B., Marshall, E.M. (1983). Thermochemical Data for Gaseous Monoxides. Journal of Physical and Chemical Reference Data, vol. 12, p. 963-1031, doi:10.1063/1.555698

Petit, J.C.J., de Jong, J., Chou, L., Mattielli, N. (2008). Development of Cu and Zn Isotope MC-ICP-MS Measurements: Application to Suspended Particulate Matter and Sediments from the Scheldt Estuary. Geostandards and Geoanalytical Research, vol. 32, p. 149-166

Pickard, H., Palk, E., Schönbächler, M., Moore, R.E.T., Coles, B.J., Kreissig, K., Nilsson-Kerr, K., Hammond, S.J., Takazawa, E., Hémond, C., Tropper, P., Barfod, D.N., Rehkämper, M. (2022). The cadmium and zinc isotope compositions of the silicate Earth – Implications for terrestrial volatile accretion. Geochimica et Cosmochimica Acta, vol. 338, p. 165-180

Pons, M.L., Debret, B., Bouilhol, P., Delacour, A., Williams, H. (2016). Zinc isotope evidence for sulfate-rich fluid transfer across subduction zones. Nature Communications, vol. 7, 13794

Ponzevera, E., Quétel, C.R., Berglund, M., Taylor, P.D.P., Evans, P., Loss, R.D., Fortunato, G. (2006). Mass Discrimination During MC-ICPMS Isotopic Ratio Measurements: Investigation by Means of Synthetic Isotopic Mixtures (IRMM-007 Series) and Application to the Calibration of Natural-Like Zinc Materials (Including IRMM-3702 and IRMM-651). Journal of the American Society for Mass Spectrometry, vol. 17, p. 1412-1427

Pringle, E.A., Moynier, F., Savage, P.S., Badro, J., Barrat, J.A. (2014). Silicon isotopes in angrites and volatile loss in planetesimals. Proceedings of the National Academy of Science, vol. 111, p. 17029-17032

Pringle, E.A., Moynier, F. (2017). Rubidium isotopic composition of the Earth, meteorites and the Moon: Evidence for the origin of volatile loss during planetary accretion. Earth and Planetary Science Letters, vol. 473, p. 62-70

Pringle, E.A., Moynier, F., Beck, P., Paniello, R., Hezel, D.C. (2017). The origin of volatile element depletion in early solar system material: Clues from Zn isotopes in chondrules. Earth and Planetary Science Letters, vol. 468, p. 62-71

Quintana, E.V., Barclay, T., Borucki, W.J., Rowe, J.F., Chambers, J.E. (2016). The frequency of giant impacts on Earth-like worlds. The Astrophysical Journal, vol. 821, p. 126 – 138

Rayleigh, L. (1896). L. Theoretical considerations respecting the separation of gases by diffusion and similar processes. The London, Edinburgh and Dublin Philosophical Magazine and Journal of Science, vol. 42, p. 493-498

Render, J., Fischer-Gödde, M., Burkhardt, C., Kleine, T. (2017). The cosmic molybdenum-neodymium isotope correlation and the building material of the Earth. Geochemical Perspectives Letters, vol. 3, p. 170-178

Renggli, C.J., Klemme, S. (2020). Experimental constraints on metal transport in fumarolic gases. Journal of Volcanology and Geothermal Research, vol. 400, p. 106929

Renggli, C.J., Hellmann, J.L., Burkhardt, C., Klemme, S., Berndt, J., Pangritz, P., Kleine, T. (2022). Tellurium isotope fractionation during evaporation from silicate melts. Geochimica et Cosmochimica Acta, vol. 339, p. 35-45

Reyes, R.A., Gaskell, D.R. (1983). The thermodynamic activity of ZnO in silicate melts. Metallurgical Transactions B, vol. 14, p. 725-731

Rosca, C., Schoenberg, R., Tomlinson, E.L., Kamber, B.S. (2019). Combined zinc-lead isotope and trace-metal assessment of recent atmospheric pollution recorded in Irish peatlands. Science of the Total Environment, vol. 658, p. 234-249

Rosman, K.J.R. (1972). A survey of the isotopic and elemental abundance of zinc. Geochimica et Cosmochimica Acta, vol. 36, p. 801-819

Richter, F.M., Davis, A.M., DePaolo, D.J., Watson, E.B. (2003). Isotope fractionation by chemical diffusion between molten basalt and rhyolite. Geochimica et Cosmochimica Acta, vol. 67, p. 3905-3923

Richter, F.M. (2004). Timescales determining the degree of kinetic isotope fractionation by evaporation and condensation. Geochimica et Cosmochimica Acta, vol. 68, p. 4971-4992

Richter, F.M., Janney, P.E., Mendybaev, R.A., Davis, A.M., Wadha, M. (2007). Elemental and isotopic fractionation of Type B CAI-like liquids by evaporation. Geochimica et Cosmochimica Acta, vol. 71, p. 5544-5564

Richter, F.M., Dauphas, N., Teng, F.Z. (2009). Non-traditional fraction of non-traditional isotopes: Evaporation, chemical diffusion and Soret diffusion. Chemical Geology, vol. 258, p. 92-103

Richter, F.M., Mendybaev, R.A., Christensen, J.N., Ebel, D., Gaffney, A. (2011). Laboratory experiments bearing on the origin and evolution of olivine-rich chondrules. Meteoritics and Planetary Science, vol. 46, p. 1152-1178

Righter, K. (2002). Metal-Silicate Partitioning of Siderophile Elements and Core Formation in the Early Earth. Annual Reviews in Earth and Planetary Sciences, vol. 31, p. 135-174

Righter, K., Sutton, S.R., Newville, M., Le, L., Schwandt, C.S., Uchida, H., Lavina, B., Downs, R.T. (2006). An experimental study of the oxidation state of vanadium in spinel and basaltic melt with implications for the origin of planetary basalt. American Mineralogist, vol. 91, p. 1643-1656

Righter, K. (2016). Metal-silicate partitioning of siderophile elements and core-mantle segregation. In: Deep Earth: Physics and Chemistry of the Lower Mantle and Core, Geophysical Monograph 217. Ed: H. Terasaki and R.A. Fischer, John Wiley & Sons, Inc.

Righter, K., Drake, M.J. (1997). A magma ocean on Vesta: Core formation and petrogenesis of eucrites and diogenites. Meteoritics & Planetary Science, vol. 32, p. 929-944

Riner, M.A., Lucey, P.G., Desch, S.J., McCubbin, F.M. (2009). Nature of opaque components on Mercury: Insights into a Mercurian magma ocean. Geophysical Research Letters, vol. 36, L02201, doi: 10.1029/2008GL036128

Rodovská, Z., Magna, T., Žák, K., Kato, C., Savage, P.S., Moynier, F., Skála, R., Ježek, J. (2017). Implications for behaviour of volatile elements during impacts – Zinc and copper systematics in sediments from the Ries impact structure and central European tektites. Meteoritics & Planetary Science, vol. 52, p. 2178-2192

Rogaski, A., Ustunisik, G.K., Yang, S., Humayun, M. (2018). Germanium, Zinc and Lithium in Martian Basalts and the Role of Degassing in Alteration of Surface Lithologies, American Geophysical Union, Fall Meeting 2018 abstract, nr. MR23B-0094

Rosman, K.J.R. (1972). A survey of the isotopic and elemental abundance of zinc. Geochimica et Cosmochimica Acta, vol. 36, p. 801-819

Roszjar, J., Whitehouse, M.J., Srinivasan, G., Mezger, K., Scherer, E.E., Van Orman, J.A., Bischoff, A. (2016). Prolonged magmatism on 4 Vesta inferred from Hf-W analyses of eucrite zircon. Earth and Planetary Science Letters, vol. 452, p. 216-226

Rubie, D.C., Laurenz, V., Jacobson, S.A., Morbidelli, A., Palme, H., Vogel, A.K., Frost, D.J. (2016). Highly siderophile elements were stripped from Earth's mantle by iron sulphide segregation. Science, vol. 353, p. 1141-1144

Rudge, J.F., Reynolds, B.C., Bourdon, B. (2009). The double spike toolbox. Chemical Geology, vol. 265, p. 420-431

Savage, P.S., Moynier, F., Chen, H., Shofner, G., Siebert, J., Badro, J., Puchtel, I.S. (2015). Copper isotope evidence for large-scale sulphide fractionation during Earth's differentiation. Geochemical Perspectives Letters, vol. 1, p. 53-64

Savage, P.S., Moynier, F., Boyet, M. (2022). Zinc isotope anomalies in primitive meteorites identify the outer solar system as an important source of Earth's volatile inventory. Icarus, vol. 386, 115172

Schauble, E.A. (2004). Applying Stable Isotope Fractionation Theory to New Systems. Reviews in Mineralogy and Geochemistry, vol. 55, p. 65-111

Schiller, M., Bizzarro, M., Fernandes, V.A. (2018). Isotopic evolution of the protoplanetary disk and the building blocks of Earth and the Moon. Nature, vol. 555, p. 507-510

Scholtysik, R., Canil, D. (2018). Condensation behaviour of volatile trace metals in laboratory benchtop fumarole experiments. Chemical Geology, vol. 492, p. 49-58

Scholtysik, R., Canil, D. (2021). The effects of S, Cl and oxygen fugacity on the sublimation of volatile trace melts degassed from silicate melts with implications for volcanic emissions. Geochimica et Cosmochimica Acta, vol. 301, p. 141-157

Schönbächler, M., Carlson, R.W., Horan, M.F., Mock, R.D., Hauri, E.H. (2010). Heterogeneous accretion and the moderately volatile budget of Earth. Science, vol. 328, p. 884-887

Seegers, A., van Zuilen, K., Stelwagen, R.G., van Westrenen, W., Vroon, P.R. (2020). Equilibration time of Fe & Zn concentrations and isotopes in metal-silicate partitioning experiments. Goldschmidt Conference Abstract, p. 2331

Sharp, Z.D., Shearer, C.K., McKeegan, K.D., Barnes, J.D., Wang, Y.Q. (2010). The chlorine isotope composition of the Moon and implications for an anhydrous mantle. Science, vol. 329, p. 1050-1053

Shaw, H.R. (1972). Viscosities of magmatic silicate liquids: an empirical method of prediction. American Journal of Science, vol. 272, p. 870-893

Shiel, A.E., Weis, D., Orians, K.J. (2010). Evaluation of zinc, cadmium and lead isotope fractionation during smelting and refining. Science of the Total Environment, vol. 408, p. 2357-2368

Shornikov, S.I. (2015). Vaporization Coefficients of Oxides Contained in the Melts of Ca-Al-Inclusions in Chondrites. Geochemistry International, vol. 53, p. 1080-1089

Skála, R., Strnad, L., McCammon, C., Čada, M. (2009). Moldavites from the Cheb Basin, Czech Republic. Geochimica et Cosmochimica Acta, vol. 73, p. 1145-1179

Siebert, J., Corgne, A., Ryerson, F.J. (2011). Systematics of metal-silicate partitioning for many siderophile elements applied to Earth's core formation. Geochimica et Cosmochimica Acta, vol. 75, p. 1451-1489

Sonke, J.E., Sivry, Y., Viers, J., Freydier, R., Dejonghe, L., André, L., Aggarwal, J.K., Fontan, F., Dupré, B. (2008). Historical variations in the isotopic composition of atmospheric zinc deposition from a zinc smelter. Chemical Geology, vol. 252, p. 145-157

Sossi, P.A., Halverson, G.P., Nebel, O., Eggins, S.M. (2015). Combined Separation of Cu, Fe and Zn from rock Matrices and Improced Analytical Protocols for Stable Isotope Determination. Geostandards and Geoanalytical Research, vol. 39, p. 129-149

Sossi, P.A., Nebel, O., Anand, M., Poitrasson, F. (2016). On the iron isotope composition of Mars and volatile depletion in the terrestrial planets. Earth and Planetary Science Letters, vol. 449, p. 360-371

Sossi, P.A., Fegley Jr., B. (2018). Thermodynamics of Element Volatility and its Application to Planetary Processes. Reviews in Mineralogy and Geochemistry, vol. 84, p. 393-459

Sossi, P.A., Nebel, O., O'Neill, H.St.C, Moynier, F. (2018a). Zinc isotope composition of the Earth and its behaviour during planetary accretion. Chemical Geology, vol. 477, p. 73-84

Sossi, P.A., Moynier, F., van Zuilen, K. (2018b). Volatile loss following cooling and accretion of the Moon revealed by chromium isotopes. Proceedings of the National Academy of Sciences, vol. 115, p. 10920-10925

Sossi, P.A., Klemme, S., O'Neill, H.St.C., Berndt, J., Moynier, F. (2019). Evaporation of moderately volatile elements from silicate melts: experiments and theory. Geochimica et Cosmochimica Acta, vol. 260, p. 204-231

Sossi, P.A., Moynier, F., Treilles, R., Mokhtari, M., Wang, X., Siebert, J. (2020). An experimentally-determined general formalism for evaporation and isotope fractionation of Cu and Zn from silicate melts between 1300 and 1500°C and 1 bar. Geochimica et Cosmochimica Acta, vol. 288, p. 316-340

Spitzer, F., Burkhardt, C., Nimmo, F., Kleine, T. (2022). Nucleosynthetic Pt isotope anomalies and the Hf-W chronology of core formation in inner and outer solar system planetesimals. Earth and Planetary Science Letters, vol. 576, p. 117211

Steenstra, E.S., Knibbe, J.S., Rai, N., van Westrenen, W. (2016). Constraints on core formation in Vesta from metal-silicate partitioning of siderophile elements. Geochimica et Cosmochimica Acta, vol. 177, p. 48-61

Steenstra, E.S., Seegers, A.X., Putter, R., Berndt, J., Klemme, S., Matveev, S., Bullock, E.S., van Westrenen, W. (2020). Metal-silicate partitioning systematics of siderophile elements at reducing conditions: A new experimental database. Icarus, vol. 335, p. 113391

Steller, T., Burkhardt, C., Yang, C., Kleine, T. (2022). Nucleosynthetic zinc isotope anomalies reveal a dual origin of terrestrial volatiles. Icatur, vol. 386, 115171

Suhr, N., Schoenberg, R., Chew, D., Rosca, C., Widdowson, M., Kamber, B.S. (2018). Elemental and isotopic behaviour of Zn in Deccan basalt weathering profiles: Chemical weathering from bedrock to laterite and links to Zn deficiency in tropical soils. Science of the Total Environment, vol. 619-620, p. 1451-1463

Sun, P., Niu, Y., Duan, M., Chen, S., Guo, P., Gong, H., Xiao, Y., Wang, X. (2023). Zinc isotope fractionation during mid-ocean ridge basalt differentiation: Evidence from lavas on the East Pacific Rise at 10°30'N. Geochimica et Cosmochimica Acta, vol. 346, p. 180-191

Sweere, T. (2018). Zn and Cd isotopes as proxies for geochemical change in Mesozoic oceans. PhD Thesis.

Sweere, T., Dickson, A.J., Jenkyns, H.C., Porcelli, D., Elrick, M., van den Boorn, S.H.J.M., Henderson, G.M. (2018). Isotopic evidence for changes in the zinc cycle during Oceanic Anoxic Event 2 (Late Cretaceous). Geology, vol. 46, p. 463-466

Tachibana, S., Nagahara, H., Ozawa, K., Ikeda, Y., Nomura, R., Tatsumi, K., Joh, Y. (2011). Kinetic condensation and evaporation of metallic iron and implications for metallic iron dust formation. The Astrophysical Journal, vol. 736, doi:10.1088/0004-637X/736/1/16

Thomas, R.W., Wood, B.J. (2021). The chemical behaviour of chlorine in silicate melts. Geochimica and Cosmochimica Acta, vol. 294, p. 28-42

Tissot, F.L.H., Collinet, M., Namur, O., Grove, T.L. (2022). The case for the angrite parent body as the archetypal first-generation planetesimal: Large, reduced and Mg-enriched. Geochimica et Cosmochimica Acta, vol. 338, p. 278-301

Touboul, M., Sprung, P., Aciego, S.M., Bourdon, B., Kleine, T. (2015). Hf-W chronology of the eucrite parent body. Geochimica et Cosmochimica Acta, vol. 156, p. 106-121

Toutain, J.P., Sonke, J., Munoz, M., Nonell, A., Polvé, M., Viers, J., Freydier, R., Sortino, F., Joron, J.L., Sumarti, S. (2008). Evidence for Zn isotopic fractionation at Merapi volcano. Chemical Geology, vol. 253, p. 74-82

Tsiganis, K., Gomes, R., Morbidelli, A., Levison, H.F. (2005). Origin of the orbital architecture of the giant planets of the Solar System. Nature, vol. 435, p. 459-461

Udry, A., Wilbur, Z.E., Rahib, R.R., McCubbin, F.M., vander Kaaden, K.E., McCoy, T.J., Ziegler, K., Gross, J., Defelice, C., Combs, L., Turrin, B.D. (2019). Reclassification of four aubrites as enstatite chondrite impact melts: Potential geochemical analogs for Mercury. Meteoritics and Planetary Science, vol. 54, p. 785-810

Urey, H.C. (1947). The Thermodynamic Properties of Isotopic Substances. Journal of the Chemical Society, 1947, p. 562-581

Van Heghe, L., Engström, E., Rodushkin, I., Cloquet, C., Vanhaecke, F. (2012). Isotopic analysis of the metabolically relevant transition metals Cu, Fe and Zn in human blood from vegetarians and omnivores using multi-collector ICP-mass spectrometry. Journal of Analytical Atomic Spectrometry, vol. 27, p. 1327-1334

Van Kooten, E.M.M.E., Moynier, F., Day, J.M.D. (2020). Evidence for Transient Atmospheres during Eruptive Outgassing on the Moon. The Planetary Science Journal, vol. 1, p. 67-78

Viers, J., Oliva, P., Nonell, A., Gélabert, A., Sonke, J.E., Freydier, R., Gainville, R., Dupré, B. (2007). Evidence of Zn isotopic fractionation in a soil-plant system of a pristine tropical watershed (Nsimi, Cameroon). Chemical Geology, vol. 239, p. 124-137

Visscher, C., Fegley Jr., B. (2013). Chemistry of Impact-Generated Silicate Melt-Vapor Debris Disks. The Astrophysical Journal Letters, vol. 767, p. L12-L17

Völkening, J., Papanastassiou, D.A. (1990). Zinc Isotope Anomalies. The Astrophysical Journal, vol. 358, p. L29-L32

Vollstaedt, H., Mezger, K., Alibert, Y. (2020). Carbonaceous Chondrites and the Condensation of Elements from the Solar Nebula. The Astrophysical Journal, vol. 897, p. 82-95

Wade, J., Wood, B.J. (2005). Core formation and the oxidation state of the Earth. Earth and Planetary Science Letters, vol. 236, p. 78-95

Wang, K., Jacobsen, S.B. (2016). Potassium isotopic evidence for a high-energy giant impact origin of the Moon. Nature, vol. 358, p. 487-490

Wang, Z., Laurenz, V., Petitgirard, S., Becker, H. (2016). Earth's moderately volatile element composition may not be chondritic: Evidence from In, Cd and Zn. Earth and Planetary Science Letters, vol. 435, p. 136-146

Wang, Z.Z., Liu, S.A., Liu, J., Huang, J., Xiao, Y., Chu, Z.Y., Zhao, X.M., Tang, L. (2017). Zinc isotope fractionation during mantle melting and constraints on the Zn isotope composition of Earth's upper mantle. Geochimica et Cosmochimica Acta, vol. 198, p. 151-167

Wang, X., Fitoussi, C., Bourdon, B., Fegley Jr, B., Charnoz, S. (2019). Tin isotopes indicative of liquid-vapour equilibration and separation in the Moon-forming disk. Nature Geoscience, vol. 12, p. 707-711

Watkins, J.M., Antonelli, M.A. (2021). Beyond Equilibrium: Kinetic Isotope Fractionation in High-Temperature Environments. Elements, vol. 17, p. 383-388

Weidenschilling, S.J., Spaute, D., Davis, D.R., Marzari, F., Ohtsuki, K. (1997). Accretional Evolution of a Planetesimal Swarm. Icarus, vol. 128, p. 429-455

Wilbur, Z.E., Udry, A., McCubbin, F.M., vander Kaaden, K.E., Defelice, C., Ziegler, K., Ross, D.K., McCoy, T.J., Gross, J., Barnes, J.J., Dygert, N., Zeigler, R.A., Turrin, B.D., McCoy, C. (2022). The effects of highly reduced magmatism revealed through aubrites. Meteoritics and Planetary Science, vol. 57, p. 1387-1420

Williams, H.M., Wood, B.J., Wade, J., Frost, D.J., Tuff, J. (2012). Isotopic evidence for internal oxidation of the Earth's mantle during accretion. Earth and Planetary Science Letters, vol. 321, p. 54-63

Wimpenny, J., Marks, N., Knight, K., Rolison, J.M., Borg, L., Eppich, G., Badro, J., Ryerson, F.J., Sanborn, M., Huyskens, M.H., Yin, Q.Z. (2019). Experimental determination of Zn isotope fractionation during evaporative loss at extreme temperatures. Geochimica et Cosmochimica Acta, vol. 259, p. 391-411

Witt-Eickschen, G., Palme, H., O'Neill, H.St.C., Allen, C.M. (2009). The geochemistry of the volatile trace elements As, Cd, Ga, In and Sn in the Earth's mantle: New evidence from in situ analyses of mantle xenoliths. Geochimica et Cosmochimica Acta, vol. 73, p. 1755-1778

Wolf, R., Ebhiara, M., Richter, G.R., Anders, E. (1983). Aubrites and diogenites: Trace element clues to their origin. Geochimica et Cosmochimica Acta, vol. 47, p. 2257-2270

Wood, B.J., Walter, M.J., Wade, J. (2006). Accretion of the Earth and segregation of its core. Nature Reviews, vol. 441, p. 825-833

Wood, B.J., Wade, J., Kilburn, M.R. (2009). Core formation and the oxidation state of the Earth: Additional constraints from Nb, V and Cr partitioning. Geochimica et Cosmochimica Acta, vol. 72, p. 1415-1426

Wood, B.J., Wade, J. (2013). Activities and volatilities of trace components in silicate melts: a novel use of metal-silicate partitioning data. Contributions to Mineralogy and Petrology, vol. 166, p. 911-921

Wood, B.J., Kiseeva, E.S., Mirolo, F.J. (2014). Accretion and core formation: The effects of sulphur on metal-silicate partition coefficients. Geochimica et Cosmochimica Acta, vol. 145, p. 248-267

Wood, B.J., Smythe, D.J., Harrison, T. (2019). The condensation temperature of the elements: A reappraisal. American Mineralogist, vol. 104, p. 844-856

Xia, Y., Kiseeva, E.S., Wade, J., Huang, F. (2019). The effect of core segregation on the Cu and Zn isotope composition of the silicate Moon. Geochemical Perspectives Letters, vol. 12, p. I2-I7

Xue, S., Yu, Y., Hewins, R.H., Hall, G.S., Herzog, G.F. (1996). Zinc losses from and Zinc isotopic abundances in residues formed by heating of Zn, ZnO, ZnS and Zn-doped silicate glass. Lunar and Planetary Science Conference, vol. 27

Yang, C., Liu, S.A. (2023). Kinetic zinc isotope fractionation in olivine phenocrysts records magma evolution history of intra-plate basalts. Geochimica et Cosmochimica Acta, vol. 346, p. 149-164

Yao, J., Huang, J., Zhang, G. (2022). Zinc isotope constraints on carbonated mantle sources for rejuvenated-stage lavas from Kaua'i, Hawai'i. Chemical Geology, vol. 605, p. 120967

Yin, Q., Jacobsen, S.B., Yamashita, K., Blichtert-Toft, J., Télouk, P., Albarède, F. (2002). A short timescale for terrestrial planet formation from Hf-W chronometry of meteorites. Nature, vol. 418, p. 949-952

Yoshizaki, T., McDonough, W.F. (2020). The composition of Mars. Geochimica et Cosmochimica Acta, vol. 273, p. 137-162

Yoshizaki, T., McDonough, W.F. (2021). Earth and Mars – Distinct inner solar system products. Geochemistry, vol. 81, p. 125746

Young, E.D., Galy, A., Nagahara, H. (2002). Kinetic and equilibrium mass-dependent isotope fractionation laws in nature and their geochemical and cosmochemical significance. Geochimica et Cosmochimica Acta, vol. 66, p. 1095-1104

Young, E.D., Manning, C.E., Schauble, E.A., Shahar, A., Macris, C.A., Lazar. C., Jordan, M. (2015). High-temperature equilibrium isotope fractionation of non-traditional stable isotopes: Experiments, theory and applications. Chemical Geology, vol. 395, p. 176-195

Young, E.D., Shahar, A., Nimmo, F., Schlichting, H.E., Schauble, E.A., Tang H., Labidi, J. (2019). Near-equilibrium isotope fractionation during planetesimal evaporation. Icarus, vol. 323, p. 1-15

Young, E.D., Macris, C.A., Tang, H., Hogan, A.A., Schollenberger, Q.R. (2022). Isotope velocimetry: Experimental and theoretical demonstration of the potential importance of gas flow for isotope fractionation during evaporation of protoplanetary material. Earth and Planetary Science Letters, vol. 589, p. 117575

Zahnle, K., Schaefer, L., Fegley, B. (2010). Earth's Earliest Atmospheres. Cold Spring Harbor Perspectives in Biology, vol. 2, a004895

Žák, K., Skála, R., Řanda, Z., Mizera, J. (2012). A review of volatile compounds in tektites, and carbon content and isotopic composition of moldavite glass. Meteoritics and Planetary Science, vol. 47, p. 1010-1028

Zelenski, M., Malik, N., Taran, Y. (2014). Emissions of trace elements during the 2012-2013 effusive eruption of Tolbachik volcano, Kamchatka: enrichment factors, partition coefficients and aerosol contribution. Journal of Volcanology and Geothermal Research, vol. 285, p. 136-149

Zelenski, M., Simakin, A., Taran, Y., Kamenetsky, V.S., Malik, N. (2021). Partitioning of elements between high-temperature, low-density aqueous fluid and silicate melt as derived from volcanic gas geochemistry. Geochimica et Cosmochimica Acta, vol. 295, p. 112-134

Zerkle, A.L., Claire, M.W., Di Rocco, T., Grassineau, N.V., Nisbet, E.G., Sun, R., Yin, R. (2021). Sulfur and Mercury MIF suggest volcanic contributions to Earth's atmosphere at 2.7 Ga. Geochemical Perspectives Letters, vol. l8, p. 48-52

Zhang, J., Huang, S., Davis, A.M., Dauphas, N., Hashimoto, A., Jacobsen, S.B. (2014). Calcium and titanium isotopic fractionation during evaporation. Geochimica et Cosmochimica Acta, vol. 140, p. 365-380

Zhang, C., Miao, B., He, H. (2019). Oxygen isotopes in HED meteorites and their constraints on parent asteroids. Planetary and Space Science, vol. 168, p. 83-94

Zhang, Z.J., Nie, N.X., Mendybaev, R.A., Liu, M.C., Hu, J.J., Hopp, T., Alp, E.E., Lavina, B., Bullock, E.S., McKeegan, K.D., Dauphas, N. (2021). Loss and Isotopic Fractionation of Alkali Elements during Diffusion-Limited Evaporation form Molten Silicate: Theory and Experiments. ACS Earth and Space Chemistry, vol. 5, p. 755-784

Zhu, K., Moynier, F., Schiller, M., Wielandt, D., Larsen, K.K., van Kooten, E.M.M.E., Barrat, J.A., Bizzarro, M. (2020). Chromium Isotopic Constraints on the Origin of the Ureilite Parent Body. The Astrophysical Journal, vol. 888, p. 126-135

Zhu, K., Moynier, F., Schiller, M., Becker, H., Barrat, J.A., Bizzarro, M. (2021). Tracing the origin and core formation of the enstatite achondrite parent bodies using Cr isotopes. Geochimica et Cosmochimica Acta, vol. 308, p. 256-272

Appendix 1 – Description of Cleaning and Preparation of Lab Plastics

Cleaning Procedures for Plastics
Savillex® Beaker, Teflon vial and auto-sampler vial cleaning
Remove any writing using ethanol and Kimwipes
Submerge in 18 MΩ H_2O with detergent and leave overnight on hotplate at 120°C
Remove from hotplate and rinse 3x with 18 MΩ H_2O
Submerge in a 50% reagent grade conc. HCl/50% 18 MΩ H_2O solution and leave on hotplate at 120°C for 48 hours
Remove from hotplate and rinse 3x with 18 MΩ H_2O
Submerge in a 50% reagent grade conc. HNO_3/50% 18 MΩ H_2O solution and leave on hotplate at 120°C for 48 hours
Remove from hotplate and rinse 3x with 18 MΩ H_2O
Submerge in 18 MΩ H_2O and leave on hotplate at 120°C overnight
Pour out the hot water, collect the plastics on Kimwipes and leave to dry in laminar flow hood.
Dry plastics are closed with lids or Parafilm™ and stored in zip-locked plastic bags
Before use: reflux with sub-boiled conc. HNO_3 at 120°C overnight

Shrink Teflon Columns: First Cleaning
Rinse multiple times with 18 MΩ H_2O and dry on Kimwipe
Fill up and rinse with ethanol
Rinse multiple times with 18 MΩ H_2O and place in Savillex pot
Submerge in 50% reagent grade conc. HNO_3/50% 18 MΩ H_2O and leave on hotplate at 90°C for 48 hours
Remove from hotplate and rinse 3x with 18 MΩ H_2O
Submerge in 6M HCl and leave on hotplate at 90°C for 48 hours
Remove from hotplate and rinse 3x with 18 MΩ H_2O
Submerge in 18 MΩ H_2O and leave on hotplate at 90°C for 48 hours

Frits: First Cleaning
Submerge in 4M HNO_3 and leave for a week at room temperature
Rinse 3x with 18 MΩ H_2O
Let them dry on Kimwipes in the laminar flow hood
Submerge in 6M HCl and leave for a week at room temperature
Rinse 3x with 18 MΩ H_2O
Let them dry on Kimwipes in the laminar flow hood
Submerge in 18 MΩ H_2O and leave for a week at room temperature
Rinse 3x with 18 MΩ H_2O
Dried in a clean Savillex beaker
Stored in Savillex beaker in 18 MΩ H_2O

Assembled Columns: Regular Cleaning
Submerge the column, with frit, in 30% (~3M) HCl on hotplate at 90°C for 48 hours
Rinse 3x with 18 MΩ H_2O
Transfer columns directly to 10% (~1M) HCl and leave until use
Rinse 3x with 18 MΩ H_2O

Pipette Tips
Submerge the pipette tips in a 50% reagent grade conc. HCl/50% 18 MΩ H_2O solution
Rinse 3x with 18 MΩ H_2O
Submerge the pipette tips in a 50% reagent grade conc. HNO_3/50% 18 MΩ H_2O solution
Rinse 3x with 18 MΩ H_2O
Collect the pipette tips on Kimwipes and leave to dry in laminar flow hood
Clean pipette tips are stored in racks, ready for use.

Table A1.1: The cleaning procedures for the different lab plastics.

Resin Cleaning and Preparation
Add resin to a cleaned 1 L bottle and fill with 18 MΩ H_2O
Shake bottle and allow resin to settle
Pour out water, refill and repeat this process 15-20 times
Pour out 90% of water and top up with 6M HCl
Shake bottle and allow resin to settle 5-7 times
Pour HCl into waste beaker and top-up with 18 MΩ H_2O
Store resin in dilute HCl

Table A1.2: The cleaning and preparation of the AG1-X8 200-400 mesh resin.

Appendix 2 – Thermodynamic Predictions: Gas Speciation during Evaporation

A2.1 – Monometallic Gas Species

There were twelve moderately volatile trace elements in the trace element mix for which there were multiple gas species to consider. This appendix discusses how the number of evaporation reactions was limited to those discussed in Chapter **4** by calculating the relative partial pressure of each gas

	Potential Evaporation Reactions	n	A	B
Li	Li_2O (l) = 2 Li (g) + 0.5 O_2 (g)	1	-47630	17.13
	Li_2O (l) + 0.5 O_2 (g) = 2 LiO (g)	-1	-39828	13.91
	Li_2O (l) + 1.5 O_2 (g) = 2 LiO_2 (g)	-3	-12770	10.72
P*	P_2O_5 (l) = 2 P (g) + 2.5 O_2 (g)	5	-110736	36.06
	P_2O_5 (l) = 2 PO (g) + 1.5 O_2 (g)	3	-75125	31.28
	P_2O_5 (l) = 2 PO_2 + 0.5 O_2 (g)	1	-44713	23.73
V	V_2O_5 (l) = 2 V (g) + 2.5 O_2 (g)	5	-133474	35.80
	V_2O_5 (l) = 2 VO (g) + 1.5 O_2 (g)	3	-92830	29.44
	V_2O_5 (l) = 2 VO_2 + 0.5 O_2 (g)	1	-55234	22.41
	V_2O_4 (l) = 2 V (g) + 2 O_2 (g)	4	-127245	32.11
	V_2O_4 (l) = 2 VO (g) + O_2 (g)	2	-86601	25.75
	V_2O_4 (l) = 2 VO_2 (g)	0	-49005	18.72
	V_2O_3 (l) = 2 V (g) + 1.5 O_2 (g)	3	-116863	28.59
	V_2O_3 (l) = 2 VO (g) + 0.5 O_2 (g)	1	-76218	22.22
	V_2O_3 (l) + 0.5 O_2 (g) = 2 VO_2 (g)	-1	-38622	15.19
	VO (l) = V (g) + 0.5 O (g)	1	-49175	12.20
	VO (l) = VO (g)	0	-28853	9.017
	VO (l) + 0.5 O_2 (g) = VO_2 (g)	-1	-10055	5.502
Cu	Cu_2O (l) = 2 Cu (g) + 0.5 O_2 (g)	1	-43045	17.78
	Cu_2O (l) + 0.5 O_2 (g) = 2 CuO (g)	-1	-40542	13.37
Ga	Ga_2O_3 (l) = 2 Ga (g) + 1.5 O_2 (g)	3	-85059	28.67
	Ga_2O_3 (l) = 2 GaO (g) + 0.5 O_2 (g)	1	-71348	19.66
Ge	GeO_2 (l) = Ge (g) + O_2 (g)	4	-49655	16.95
	GeO_2 (l) = GeO (g) + 0.5 O_2 (g)	2	-27496	14.00
As*	As_2O_3 (l) = 2 As (g) + 1.5 O_2 (g)	3	-65473	27.38
	As_2O_3 (l) = 2 AsO (g) + 0.5 O_2 (g)	1	-27946	22.46
Cd	CdO (l) = Cd (g) + 0.5 O_2 (g)	2	-19191	10.75
	CdO (l) = CdO (g)	0	-17586	8.806
Sn	SnO_2 (l) = Sn (g) + O_2 (g)	4	-45889	16.28
	SnO_2 (l) = SnO (g) + 0.5 O_2 (g)	2	-31122	13.95
Sb	Sb_2O_3 (l) = 2 Sb (g) + 1.5 O_2 (g)	3	-64145	26.14
	Sb_2O_3 (l) = 2 SbO (g) + 0.5 O_2 (g)	1	-26453	23.21
Cs*	Cs_2O (l) = 2 Cs (g) + 0.5 O_2 (g)	1	-22095	11.41
	Cs_2O (l) + 0.5 O_2 (g) = 2 CsO (g)	-1	-10407	8.995
Pb	PbO (l) = Pb (g) + 0.5 O_2 (g)	2	-21175	9.849
	PbO (l) = PbO (g)	0	-14622	7.788

Table A2.1: Summary of the potential evaporation reactions for the trace elements with multiple evaporation reactions, considering only monometallic gas species. Thermodynamic data taken from Barin et al. (1989). *Indicates thermodynamic data was extrapolated to cover the experimental temperature range.

species using the thermodynamic properties of the pure species. Table **A2.1** lists the elements that have multiple monometallic gas species, the evaporation reactions, change in oxidation state of the trace element during evaporation (n) and the constants (A and B) that were used to calculate the equilibrium constant of the evaporation reaction (K) at the target temperature as the equilibrium constant is temperature dependent as $\log(K) = A/T\ (in\ K) + B$. All calculations in this appendix assume ideal gas behaviour and the activity of the melt phases to equal one. A more detailed discussion regarding these thermodynamic calculations is provided in Chapter **2**.

A2.1.1 – Lithium

For Li there were three potential evaporation reactions to consider (Table **A2.1**). The relative partial pressure of these species was determined across a range of fO_2 at fixed temperature. This showed that there were two gas species that should be considered (Fig. **A2.1**). At oxygen fugacities down to log(fO_2) = -6 the most abundant gas species is LiO_2 (g). Between log(fO_2) = -6 and log(fO_2) = -9 the gas phase is a mixture of Li (g) and LiO_2 (g). In more reducing conditions Li (g) will be the abundant gas species. Two reactions would have to be considered for the modified Hertz-Knudsen-Langmuir equation for lithium.

$$Li_2O\ (l) + 0.5\ O_2\ (g) = 2\ LiO\ (g)$$

$$Li_2O\ (l) + 0.5\ O_2\ (g) = 2\ LiO\ (g)$$

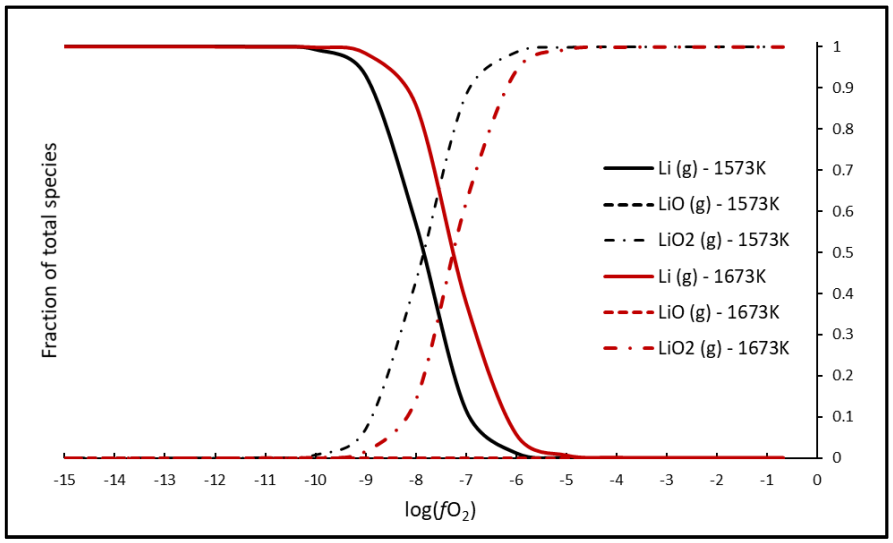


Figure A2.1: The relative partial pressures of Li (g), LiO (g) and LiO_2 (g) plotted as a function of fO_2.

A2.1.2 – Phosphorus

For P there were three potential evaporation reactions to consider (Table **A2.1**). The relative partial pressure of these species was determined across a range of fO_2 at fixed temperature. This showed that there were two gas species that should be considered (Fig. **A2.2**). At oxygen fugacities down to log(fO_2) = -5 the most abundant gas species is PO_2 (g). Between log(fO_2) = -5 and log(fO_2) = -9.5 the gas phase is a mixture of PO (g) and PO_2 (g). In more reducing conditions PO (g) will be the abundant gas species. Two reactions would have to be considered for the modified Hertz-Knudsen-Langmuir equation for phosphorus.

$$P_2O_5\ (l) = 2\ PO_2\ (g) + 0.5\ O_2\ (g)$$

$$P_2O_5\ (l) = 2\ PO\ (g) + 1.5\ O_2\ (g)$$

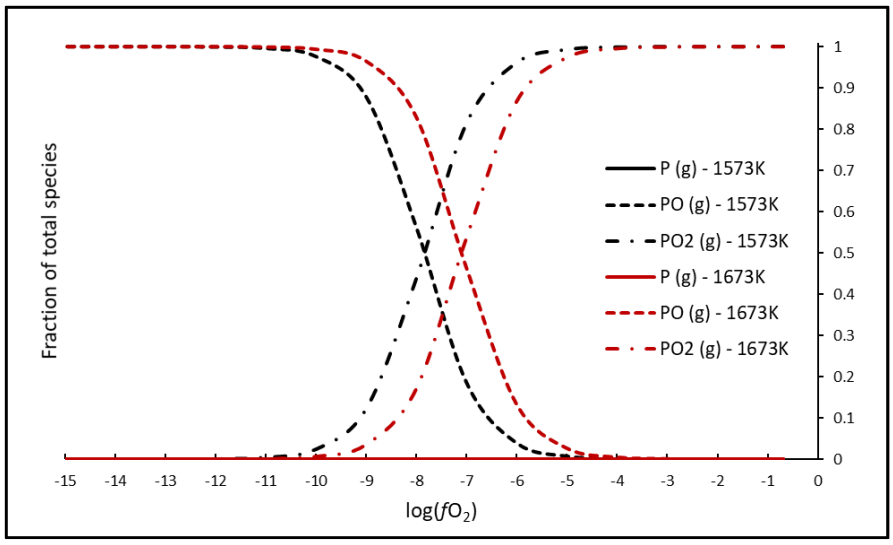


Figure A2.2: The relative partial pressures of P (g), PO (g) and PO_2 (g) plotted as a function of fO_2.

A2.1.3 – Vanadium

For V there were twelve potential evaporation reactions to consider (Table **A2.1**). The relative partial pressure of these species was determined across a range of fO_2 at fixed temperature. This showed that there was only one gas species that should be considered, VO_2 (g) is the abundant gas species in all experiments (Fig. **A2.3**). Because V is the only element in this study for which multiple melt species are expected across the range of experimental conditions, it requires a specific version of the modified Hertz-Knudsen-Langmuir equation that was not discussed in this study. The interested reader is

referred to Sossi et al. (2019) for a discussion of this evaporation environment. Four evaporation reactions would have to be considered for the modified Hertz-Knudsen-Langmuir Equation.

$$V_2O_5\ (l) = 2\,VO_2\ (g) + 0.5\,O_2\ (g)$$

$$V_2O_4\ (l) = 2\,VO_2\ (g)$$

$$V_2O_3\ (l) + 0.5\,O_2\ (g) = 2\,VO_2\ (g)$$

$$VO\ (l)\ +\ 0.5\,O_2\ (g) = VO_2\ (g)$$

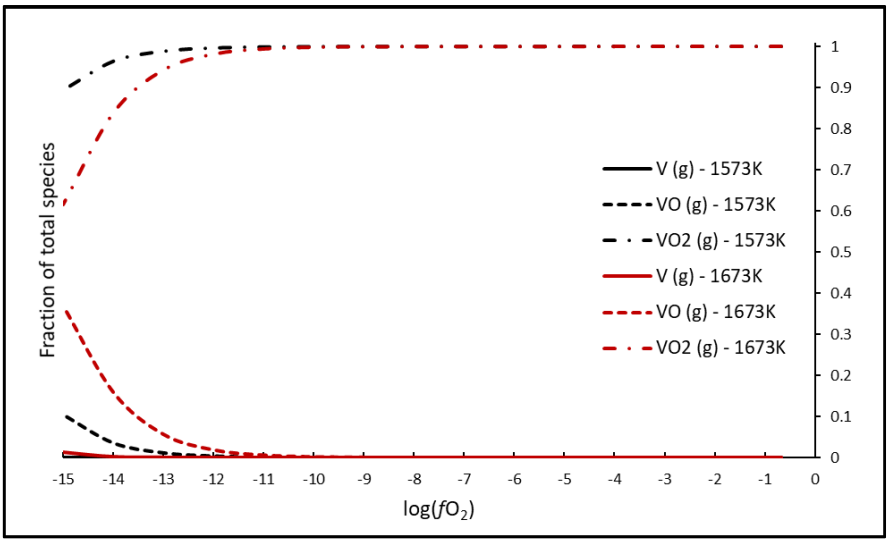


Figure A2.3: The relative partial pressures of V (g), VO (g) and VO_2 (g) plotted as a function of fO_2.

A2.1.4 – Copper

For Cu there were two potential evaporation reactions to consider (Table **A2.1**). The relative partial pressure of these species was determined across a range of fO_2 at fixed temperature. This showed that there was only one gas species that should be considered, Cu (g) is the abundant gas species in

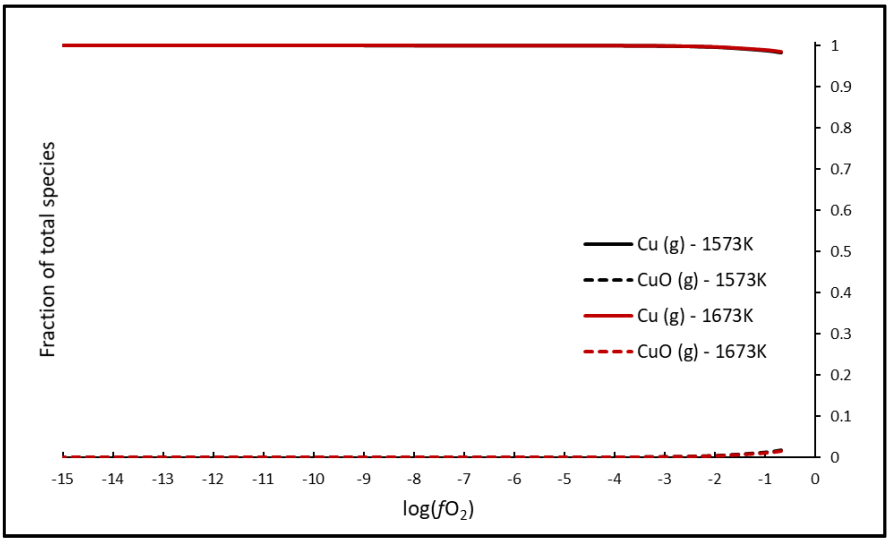


Figure A2.4: The relative partial pressures of Cu (g) and CuO (g) plotted as a function of fO_2.

all experiments (Fig. **A2.4**). The only evaporation reaction that had to be considered for the modified Hertz-Knudsen-Langmuir equation for copper was

$$Cu_2O\ (l) = 2\ Cu\ (g) + 0.5\ O_2\ (g)$$

A2.1.5 – Gallium

For Ga there were two potential evaporation reactions to consider (Table **A2.1**). The relative partial pressure of these species was determined across a range of fO_2 at fixed temperature. This showed that there were two gas species that should be considered (Fig. **A2.5**). Between log(fO_2) = -0.68 and log(fO_2) = -2.5 the gas phase is a mixture of GaO (g) and Ga (g). In more reducing conditions Ga (g) will be the abundant gas species. Two reactions would have to be considered for the modified Hertz-Knudsen-Langmuir equation. However, Ga exhibited no volatile loss in oxidizing conditions and therefore only one evaporation reaction was considered for gallium.

$$Ga_2O_3\ (l) = 2\ Ga\ (g) + 1.5\ O_2\ (g)$$

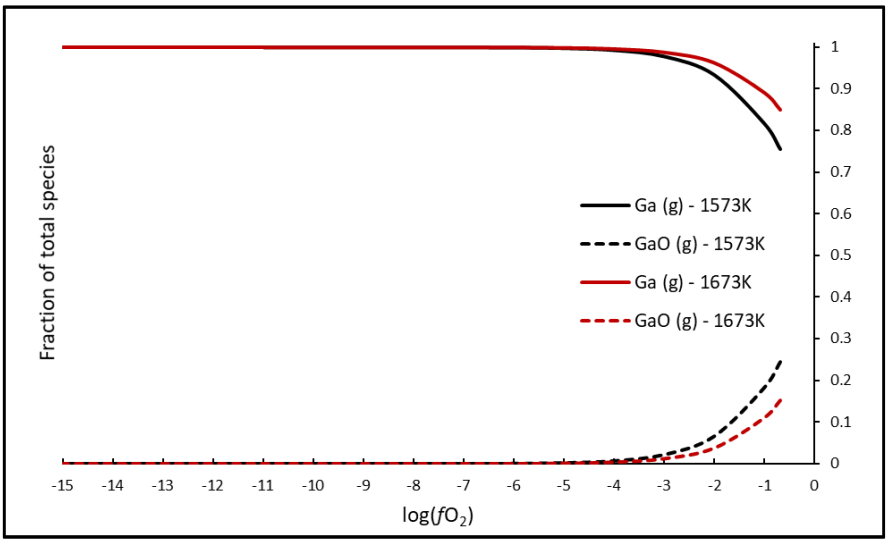


Figure A2.5: The relative partial pressures of Ga (g) and GaO (g) plotted as a function of fO_2.

A2.1.6 - Germanium

For Ge there were two potential evaporation reactions to consider (Table **A2.1**). The relative partial pressure of these species was determined across a range of fO_2 at fixed temperature. This showed that there was only one gas species that should be considered, GeO (g) is the abundant gas species in

all experiments (Fig. **A2.6**). The only evaporation reaction that had to be considered for the modified Hertz-Knudsen-Langmuir equation for germanium was

$$GeO_2\ (l) = GeO\ (g) + 0.5\ O_2\ (g)$$

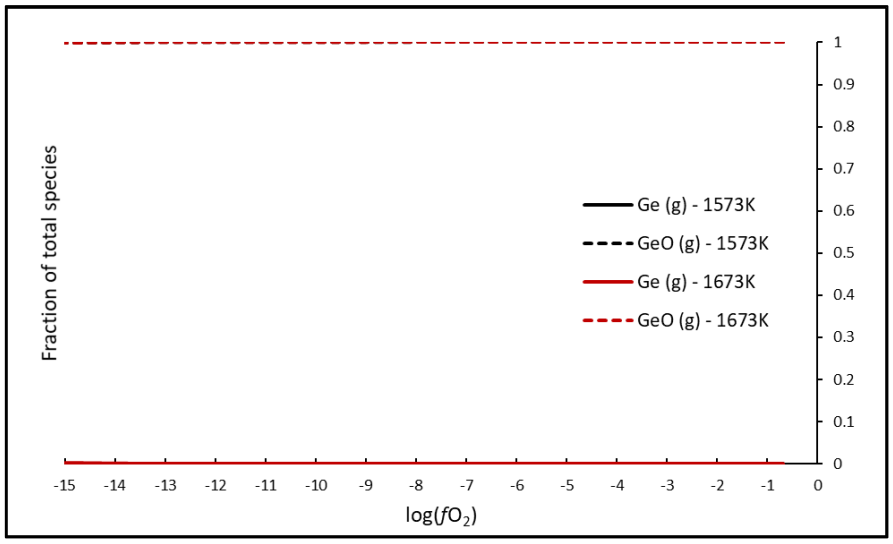


Figure A2.6: The relative partial pressures of Ge (g) and GeO (g) plotted as a function of fO_2.

A2.1.7 - Arsenic

For As there were two potential evaporation reactions to consider (Table **A2.1**). The relative partial pressure of these species was determined across a range of fO_2 at fixed temperature. This showed that there was only one gas species that should be considered, AsO (g) is the abundant gas species in

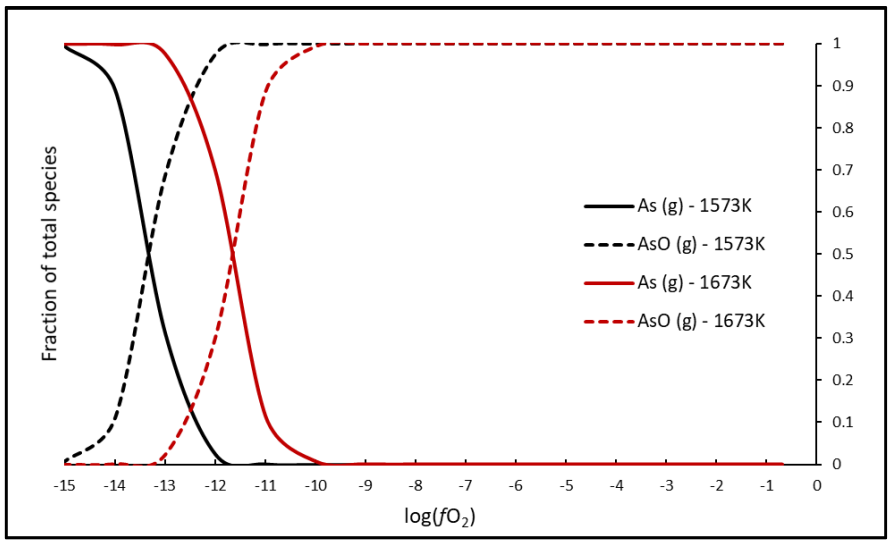


Figure A2.7: The relative partial pressures of As (g) and AsO (g) plotted as a function of fO_2.

all experiments (Fig. **A2.7**). The only evaporation reaction that had to be considered for the modified Hertz-Knudsen-Langmuir equation for arsenic was

$$As_2O_3\ (l) = 2\ AsO\ (g) + 0.5\ O_2\ (g)$$

A2.1.8 - Cadmium

For Cd there were two potential evaporation reactions to consider (Table **A2.1**). The relative partial pressure of these species was determined across a range of fO_2 at fixed temperature. This showed that there was only one gas species that should be considered, Cd (g) is the abundant gas species in all experiments (Fig. **A2.8**). The only evaporation reaction that had to be considered for the modified Hertz-Knudsen-Langmuir equation for cadmium was

$$CdO\ (l) = Cd\ (g) + 0.5\ O_2\ (g)$$

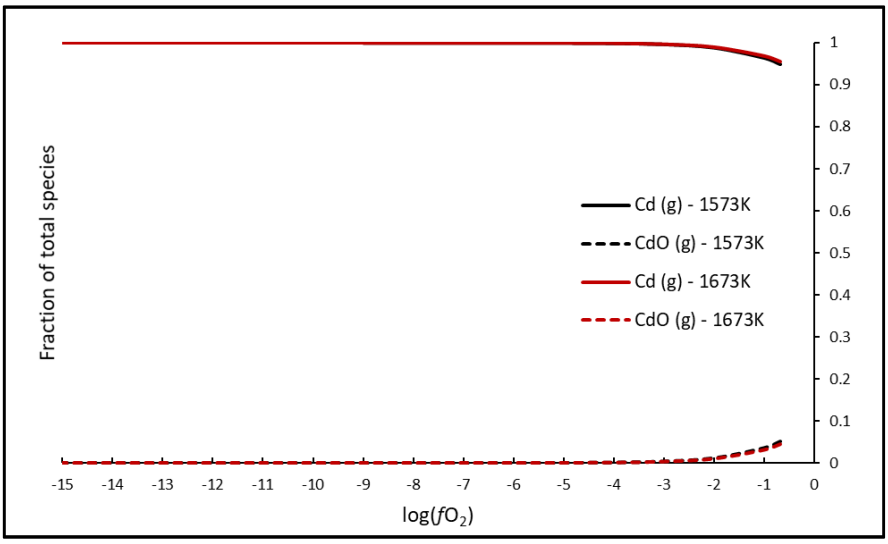


Figure A2.8: The relative partial pressures of Cd (g) and CdO (g) plotted as a function of fO_2.

A2.1.9 – Tin

For Sn there were two potential evaporation reactions to consider (Table **A2.1**). The relative partial pressure of these species was determined across a range of fO_2 at fixed temperature. This showed that there was only one gas species that should be considered, SnO (g) is the abundant gas species in all experiments (Fig. **A2.7**). The only evaporation reaction that had to be considered for the modified Hertz-Knudsen-Langmuir equation for tin was

$$SnO_2\ (l) = SnO\ (g) + 0.5\ O_2\ (g)$$

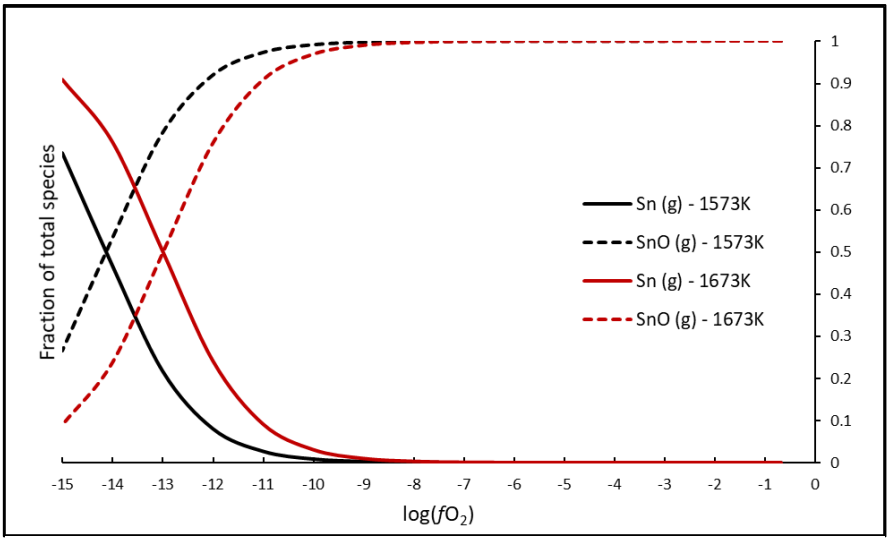


Figure A2.9: The relative partial pressures of Sn (g) and SnO (g) plotted as a function of fO_2.

A2.1.10 – Antimony

For Sb there were two potential evaporation reactions to consider (Table **A2.1**). The relative partial pressure of these species was determined across a range of fO_2 at fixed temperature. This showed that there was only one gas species that should be considered, SbO (g) is the abundant gas species in all experiments (Fig. **A2.10**). The only evaporation reaction that had to be considered for the modified Hertz-Knudsen-Langmuir equation for antimony was

$$Sb_2O_3\ (l) = 2\ SbO\ (g) + 0.5\ O_2\ (g)$$

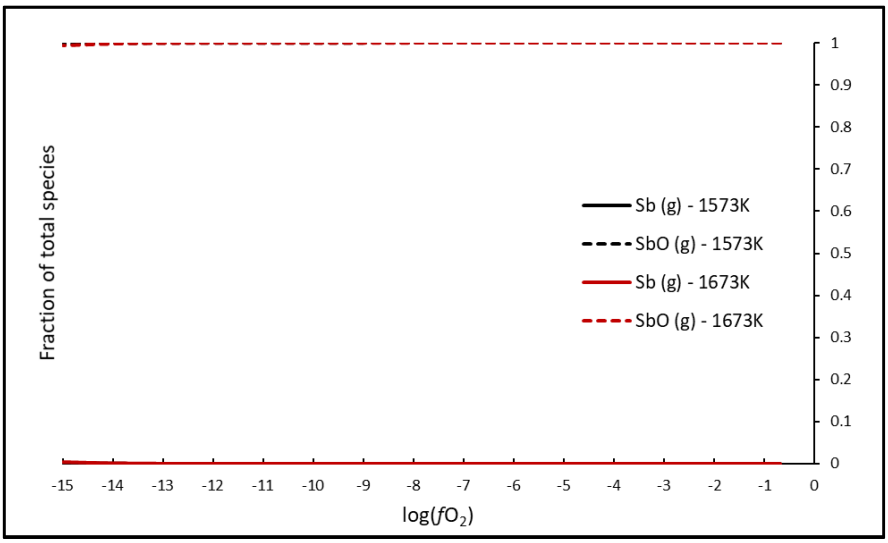


Figure A2.10: The relative partial pressures of Sb (g) and SbO (g) plotted as a function of fO_2.

A2.1.11 – Caesium

For Cs there were two potential evaporation reactions to consider (Table **A2.1**). The relative partial pressure of these species was determined across a range of fO_2 at fixed temperature. This showed that there were two gas species that should be considered (Fig. **A2.2**). At oxygen fugacities down to log(fO_2) = -2.5 the most abundant gas species is CsO (g). Between log(fO_2) = -2.5 and log(fO_2) = -7.5 the gas phase is a mixture of CsO (g) and Cs (g). In more reducing conditions Cs (g) will be the abundant gas species. Two reactions would have to be considered for the modified Hertz-Knudsen-Langmuir equation for caesium.

$$Cs_2O\ (l) + 0.5\ O_2\ (g) = 2\ CsO\ (g)$$

$$Cs_2O\ (l) = 2\ Cs\ (g) + 0.5\ O_2\ (g)$$

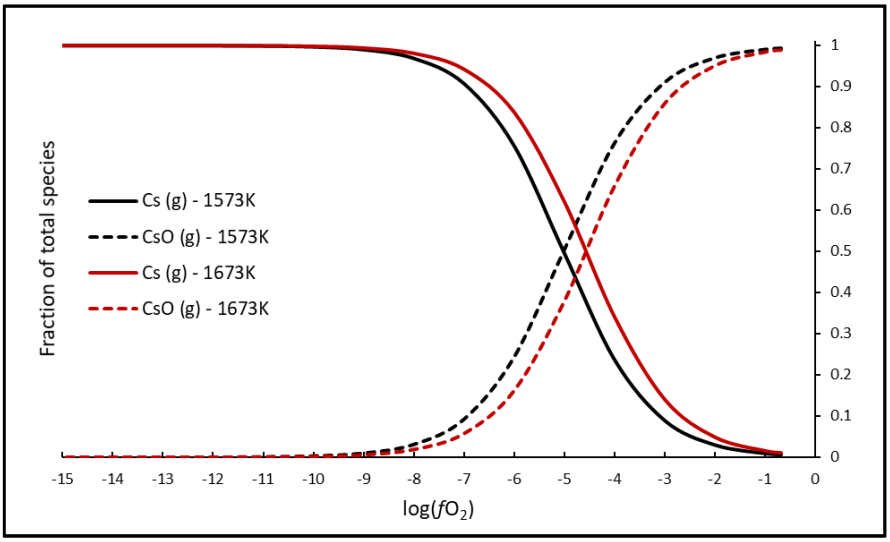


Figure A2.11: The relative partial pressures of Cs (g) and CsO (g) plotted as a function of fO_2.

A2.1.12 – Lead

For Pb there were two potential evaporation reactions to consider (Table **A2.1**). The relative partial pressure of these species was determined across a range of fO_2 at fixed temperature. This showed that there were two gas species that should be considered (Fig. **A2.2**). At oxygen fugacities down to log(fO_2) = -1.5 the most abundant gas species is PbO (g). Between log(fO_2) = -1.5 and log(fO_2) = -6.5 the gas phase is a mixture of PbO (g) and Pb (g). In more reducing conditions Pb (g) will be the abundant gas species. Two reactions would have to be considered for the modified Hertz-Knudsen-Langmuir equation for lead.

$$PbO\ (l) = PbO\ (g)$$

$$PbO\ (l) = Pb\ (g) + 0.5\ O_2\ (g)$$

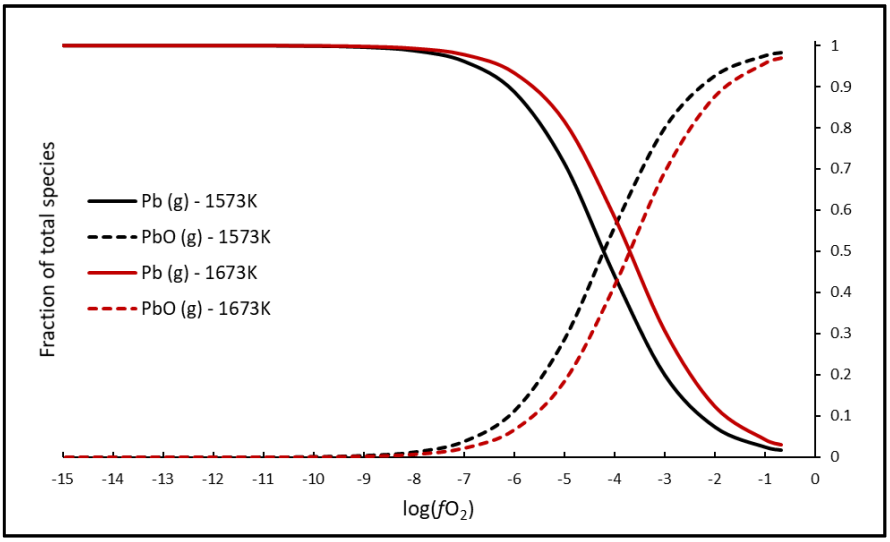


Figure A2.12: The relative partial pressures of Pb (g) and PbO (g) plotted as a function of fO_2.

A2.2 – Mono- and Polymetallic Gas Species

The previous section and the main text only consider evaporation reactions involving monometallic gas species (See Chapter **2** for reasoning). However, there are multiple elements for which polymetallic gas species exist (Li, Ga, As, Rb, In, Sb, Cs, Tl and Pb). This section will discuss these elements in more detail and examine the effect of polymetallic gas species on the relative partial pressure of different gas species. Table **A2.2** shows all evaporation reactions that are considered for these elements in this case.

	Potential Evaporation Reactions	n	A	B
Li	Li_2O (l) = 2 Li (g) + 0.5 O_2 (g)	1	-47630	17.13
	Li_2O (l) = Li_2 (g) + 0.5 O_2 (g)	1	-41928	12.71
	Li_2O (l) + 0.5 O_2 (g) = 2 LiO (g)	-1	-39828	13.91
	Li_2O (l) + 1.5 O_2 (g) = 2 LiO_2 (g)	-3	-12770	10.72
	Li_2O (l) + 0.5 O_2 (g) = Li_2O_2 (g)	-1	-18414	6.489
Ga	Ga_2O_3 (l) = 2 Ga (g) + 1.5 O_2 (g)	3	-85059	28.67
	Ga_2O_3 (l) = Ga_2O (g) + O_2 (g)	2	-51224	19.72
	Ga_2O_3 (l) = 2 GaO (g) + O_2 (g)	1	-71348	19.66
As*	As_2O_3 (l) = 2 As (g) + 1.5 O_2 (g)	3	-65473	27.38
	As_2O_3 (l) = As_2 (g) + 1.5 O_2 (g)	3	-45454	21.64
	3 As_2O_3 (l) = 2 As_3 (g) + 4.5 O_2 (g)	3	-129128	59.85
	2 As_2O_3 (l) = As_4 (g) + 3 O_2 (g)	3	-75880	35.38
	As_2O_3 (l) = 2 AsO (g) + 0.5 O_2 (g)	1	-27946	22.46
	2 As_2O_3 (l) = As_4O_6 (g)	0	-5541	7.991
Rb	Rb_2O (l) = 2 Rb (g) + 0.5 O_2 (g)	1	-25795	15.50
	Rb_2O (l) = Rb_2 (g) + 0.5 O_2 (g)	1	-23228	11.78
In	In_2O_3 (l) = 2 In (g) + 1.5 O_2 (g)	3	-73331	27.70
	In_2O_3 (l) = In_2O (g) + O_2 (g)	2	-44440	19.47
Sb	Sb_2O_3 (l) = 2 Sb (g) + 1.5 O_2 (g)	3	-64145	26.14
	Sb_2O_3 (l) = Sb_2 (g) + 1.5 O_2 (g)	3	-48509	20.40
	2 Sb_2O_3 (l) = Sb_4 (g) + 3 O_2 (g)	3	-83786	32.85
	Sb_2O_3 (l) = 2 SbO (g) + 0.5 O_2 (g)	1	-26453	23.21
Cs	Cs_2O (l) = 2 Cs (g) + 0.5 O_2 (g)	1	-22095	11.41
	Cs_2O (l) = Cs_2 (g) + 0.5 O_2 (g	1	-24299	13.49
	Cs_2O (l) = Cs_2O (g)	0	-21385	10.25
	Cs_2O (l) + 0.5 O_2 (g) = 2 CsO (g)	-1	-10407	8.995
Tl	Tl_2O (l) = 2 Tl (g) + 0.5 O_2 (g)	1	-27410	15.71
	Tl_2O (l) = Tl_2O (g)	0	-8810	7.957
Pb	PbO (l) = PbO (g)	0	-21175	9.849
	PbO (l) = Pb (g) + 0.5 O_2 (g)	2	-39264	15.88
	2 PbO (l) = Pb_2 (g) + O_2 (g)	2	-14622	7.788

Table A2.2: Summary of all evaporation reactions for the trace elements considering all potential gas species. Thermodynamic data taken from Barin et al. (1989). *Indicates thermodynamic data was extrapolated to cover the experimental temperature range.

A2.2.1 – Lithium

For Li there were five evaporation reactions to consider (Table **A2.2**). The relative partial pressure of these species was determined across a range of fO_2 at fixed temperature. This showed that the polymetallic gas species, Li_2 (g) and Li_2O_2 (g) did not significantly impact the speciation of lithium in the gas phase (Fig. **A2.13**).

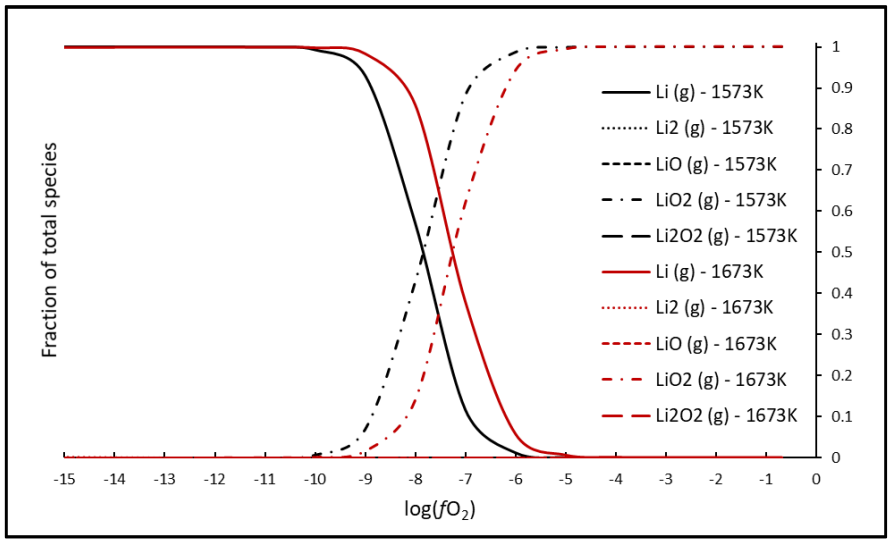


Figure A2.13: The partial pressure of potential Li gas species as a function of oxygen fugacity.

A2.2.2 – Gallium

For Ga there were three evaporation reactions to consider (Table **A2.2**). The relative partial pressure of these species was determined across a range of fO_2 at fixed temperature. This showed that the inclusion of Ga_2O (g) had a major impact on the predicted speciation of Ga in the gas phase (Fig. **A2.14**). Between log(fO_2) = -0.68 and log(fO_2) = -1.5 the gas phase is a mixture of GaO (g), Ga_2O (g) and Ga (g).

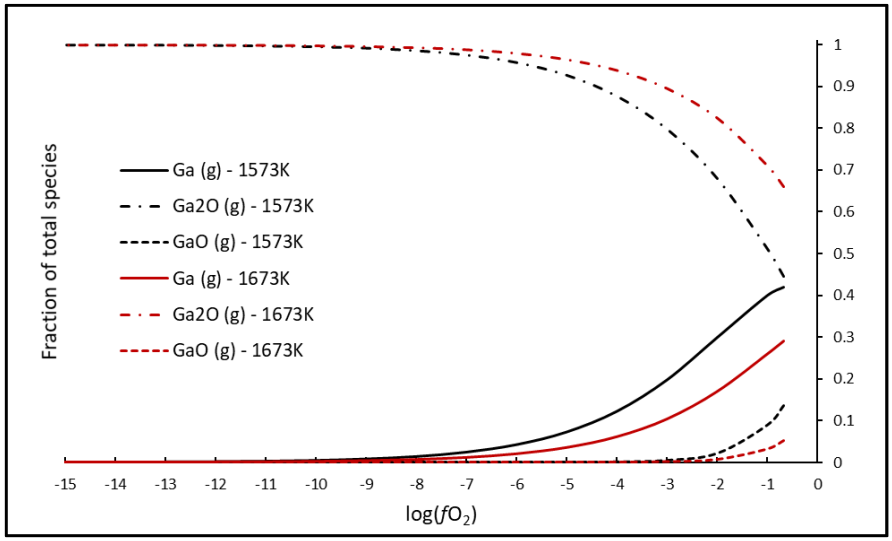


Figure A2.14: The partial pressure of potential Ga gas species as a function of oxygen fugacity.

Between log(fO_2) = -1.5 and log(fO_2) = -6.5 the gas phase is a mixture of Ga_2O (g) and Ga (g). In more reducing conditions Ga_2O (g) will be the abundant gas species.

A2.2.3 – Arsenic

For As there were six evaporation reactions to consider (Table **A2.2**). The relative partial pressure of these species was determined across a range of fO_2 at fixed temperature. This showed that the inclusion of polymetallic gas species had a major impact on the predicted speciation of As in the gas phase (Fig. **A2.15**). Between log(fO_2) = -0.68 and log(fO_2) = -4 the gas phase is a mixture of As_4O_6 (g) and AsO (g). Between log(fO_2) = -4 and log(fO_2) = -6.5 the gas phase is a mixture of As_4O_6 (g), AsO (g) and As_4 (g). In more reducing conditions As_4 (g) will be the abundant gas species.

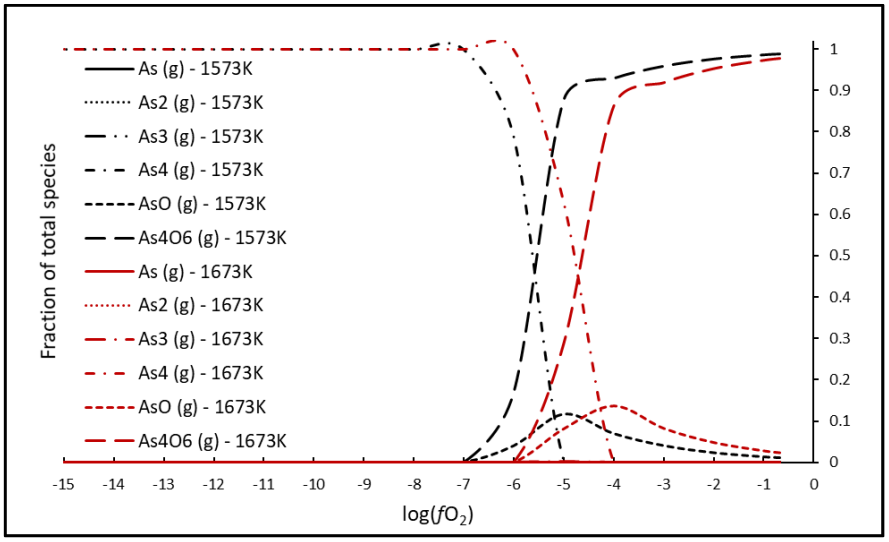


Figure A2.15: The partial pressure of potential As gas species as a function of oxygen fugacity.

A2.2.4 – Rubidium

For Rb there were two evaporation reactions to consider (Table **A2.2**). The relative partial pressure of these species was determined across a range of fO_2 at fixed temperature. This showed that the inclusion of Rb_2 (g) had a major impact on the predicted speciation of Rb in the gas phase (Fig. **A2.16**). Between log(fO_2) = -0.68 and log(fO_2) = -3 Rb (g) is the only abundant gas species. In more reducing conditions the speciation in the gas phase is a mixture of Rb (g) and Rb_2 (g).

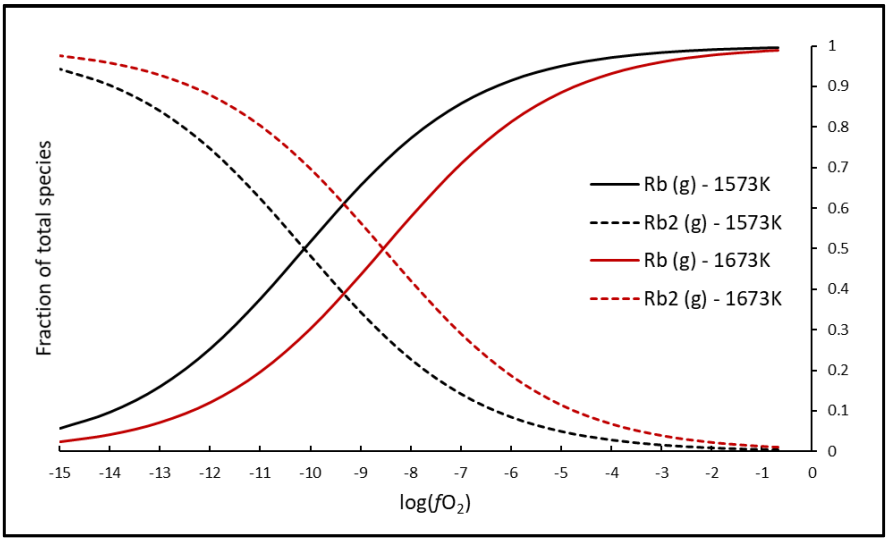


Figure A2.16: The partial pressure of potential Rb gas species as a function of oxygen fugacity.

A2.2.5 – Indium

For In there were two evaporation reactions to consider (Table **A2.2**). The relative partial pressure of these species was determined across a range of fO_2 at fixed temperature. This showed that the inclusion of In_2O (g) had a major impact on the predicted speciation of indium in the gas phase (Fig. **A2.17**). Between log(fO_2) = -0.68 and log(fO_2) = -2.5 the gas phase is a mixture of In_2O (g) and Ga (g). In more reducing conditions In_2O (g) will be the abundant gas species.

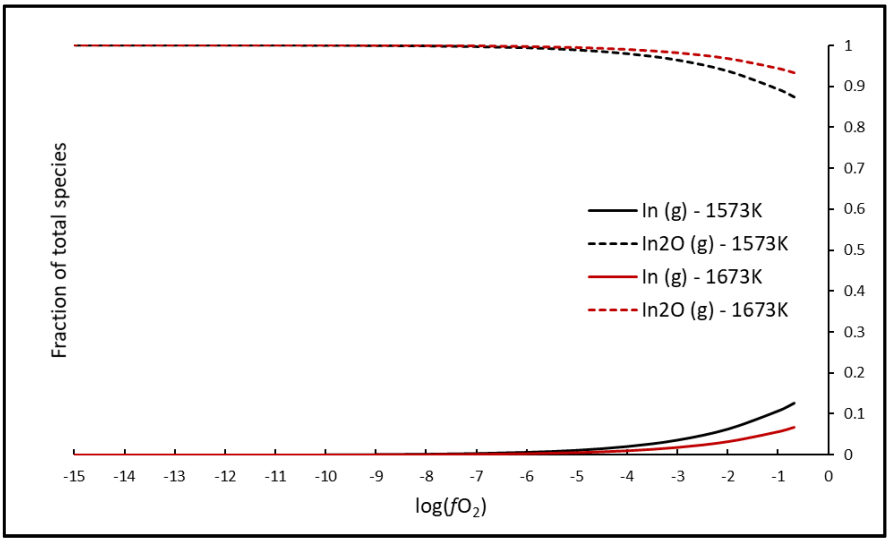


Figure A2.17: The partial pressure of potential In gas species as a function of oxygen fugacity.

A2.2.6 - Antimony

For Sb there were four evaporation reactions to consider (Table **A2.2**). The relative partial pressure of these species was determined across a range of fO_2 at fixed temperature. This showed that the inclusion of polymetallic species had a major impact on the predicted speciation of Sb in the gas phase

(Fig. **A2.18**). In oxidizing conditions the abundant gas species is SbO (g). Between log(fO_2) = -7.5 and log(fO_2) = -9 the gas phase is a mixture of SbO (g) and Sb_4 (g). In more reducing conditions Sb_4 (g) is the abundant gas species.

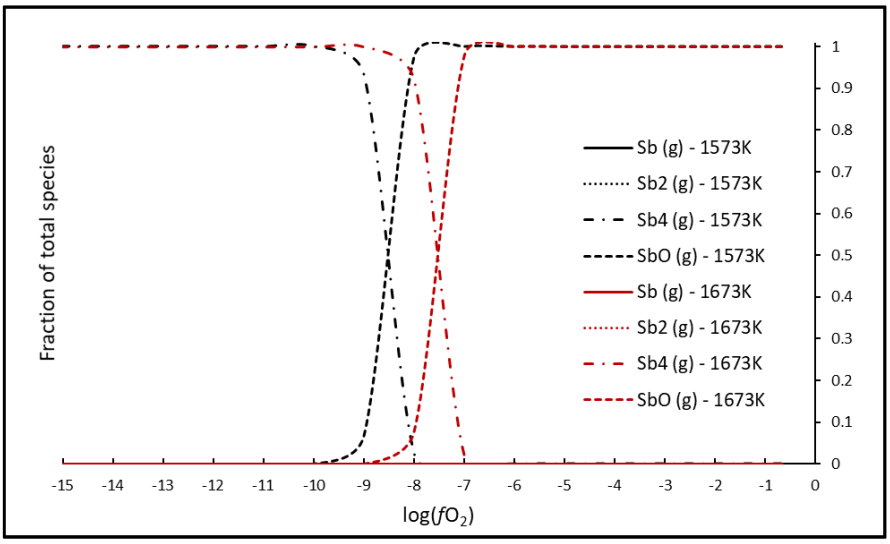


Figure A2.18: The partial pressure of potential Sb gas species as a function of oxygen fugacity.

A2.2.7 – Caesium

For Cs there were four evaporation reactions to consider (Table **A2.2**). The relative partial pressure of these species was determined across a range of fO_2 at fixed temperature. This showed that the inclusion of polymetallic species had a major impact on the predicted speciation of Cs in the gas phase (Fig. **A2.19**). Between log(fO_2) = -0.68 and log(fO_2) = -8 the gas phase is a mixture of CsO (g), Cs (g) and Cs_2 (g). In more reducing conditions Cs_2 (g) is the abundant gas species.

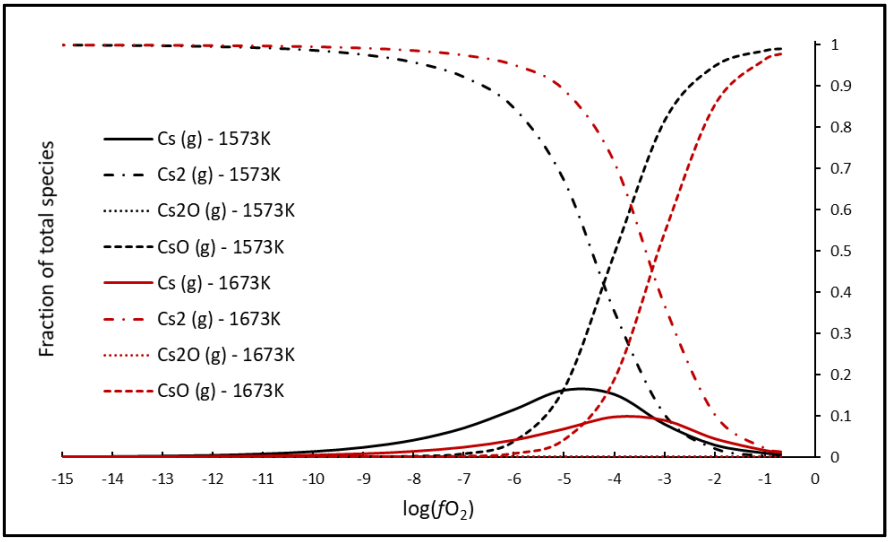


Figure A2.19: The partial pressure of potential Cs gas species as a function of oxygen fugacity.

A2.2.8 – Thallium

For Tl there were two evaporation reactions to consider (Table **A2.2**). The relative partial pressure of these species was determined across a range of fO_2 at fixed temperature. This showed that the inclusion of Tl_2O (g) had a major impact on the predicted speciation of Tl in the gas phase (Fig. **A2.20**). In oxidizing conditions the abundant gas species is Tl_2O (g). Between log(fO_2) = -2.5 and log(fO_2) = -6 the gas phase is a mixture of Tl_2O (g) and Tl (g). In more reducing conditions Tl (g) is the abundant species.

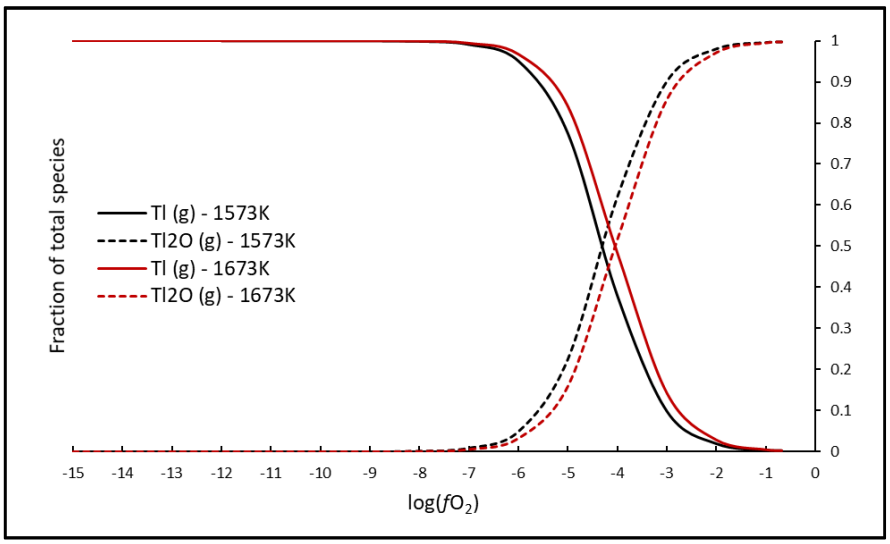


Figure A2.20: The partial pressure of potential Tl gas species as a function of oxygen fugacity.

A2.2.9 – Lead

For Pb there were three evaporation reactions to consider (Table **A2.2**). The relative partial pressure of these species was determined across a range of fO_2 at fixed temperature. This showed that the

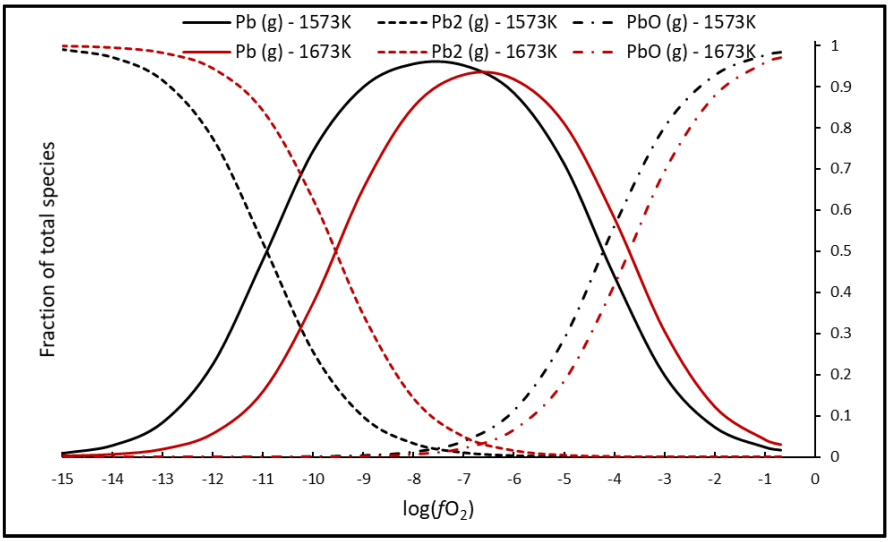


Figure A2.21: The partial pressure of potential Pb gas species as a function of oxygen fugacity.

inclusion of Pb_2 (g) had a major impact on the predicted speciation of Pb in the gas phase (Fig. **A2.21**). Between log(fO_2) = -0.68 and log(fO_2) = -7 the gas phase is a mixture of PbO (g) and Pb (g). In more reducing conditions the gas phase is a mixture of Pb (g) and Pb_2 (g).

A2.3 – Total Partial Pressures

In Chapter **4** the total partial pressure of each trace element was calculated using only the evaporation reactions of monometallic gas species (Table **4.1**). Figure **A2.22** shows the partial pressures when all potential evaporation reactions in Table **A2.2** are considered. Substantial increases in partial pressure are observed for all elements considered above, but particularly for As and Sb as As_3, As_4 and Sb_3, Sb_4 partial pressures increase substantially quicker than those of As and Sb due to the stoichiometry of those evaporation reactions.

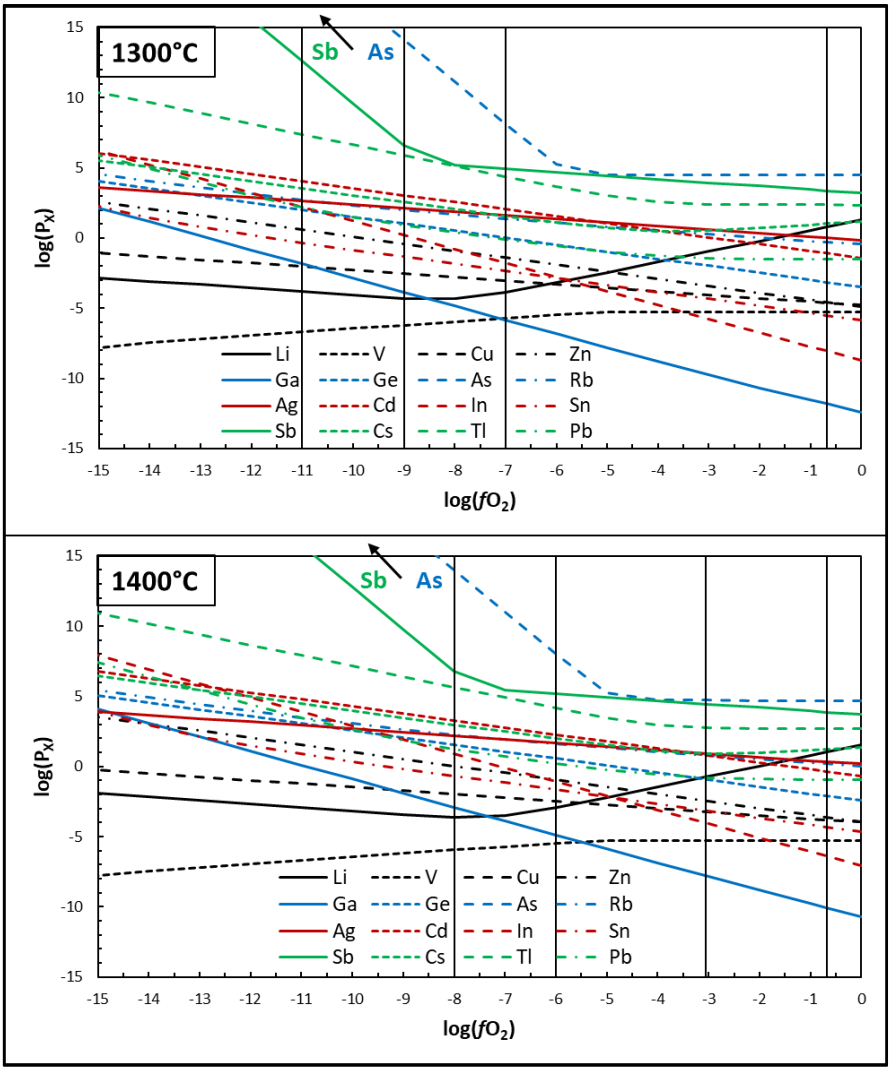


Figure A2.22: The total partial pressure of trace elements considering all potential gas species.

A2.3.1 - Volatility Factor Plots – Ideal Trace Element Behaviour

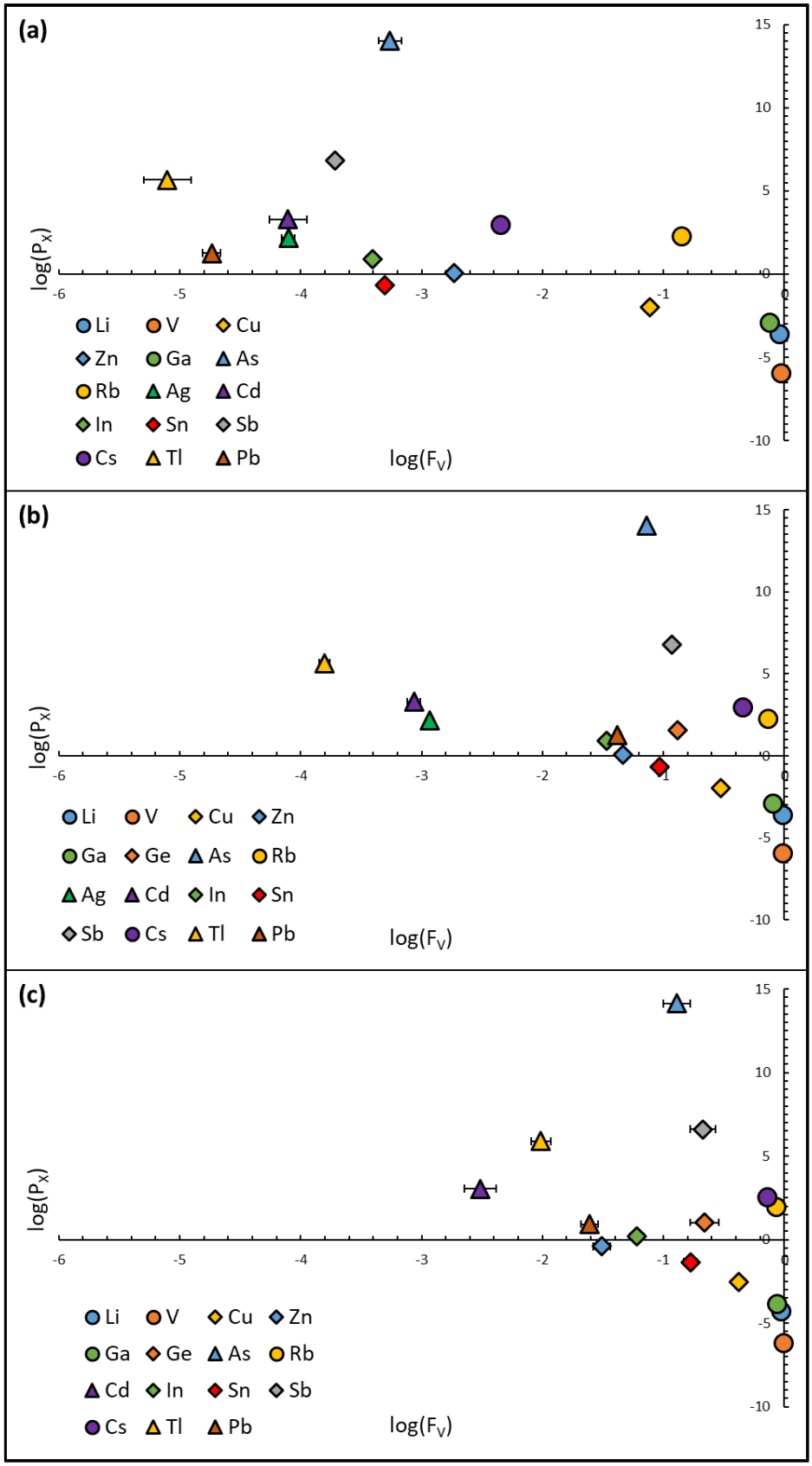


Figure A2.23: The volatility factor plotted against the total equilibrium partial pressure of the oxide gas species for the **(a)** SM and **(b)** IB experiments at log(fO_2) = -8 and **(c)** IB-G at log(fO_2) = -9 assuming ideal trace element behaviour in the silicate melt.

A2.3.2 - Volatility Factor Plots – Non-Ideal Trace Element Behaviour

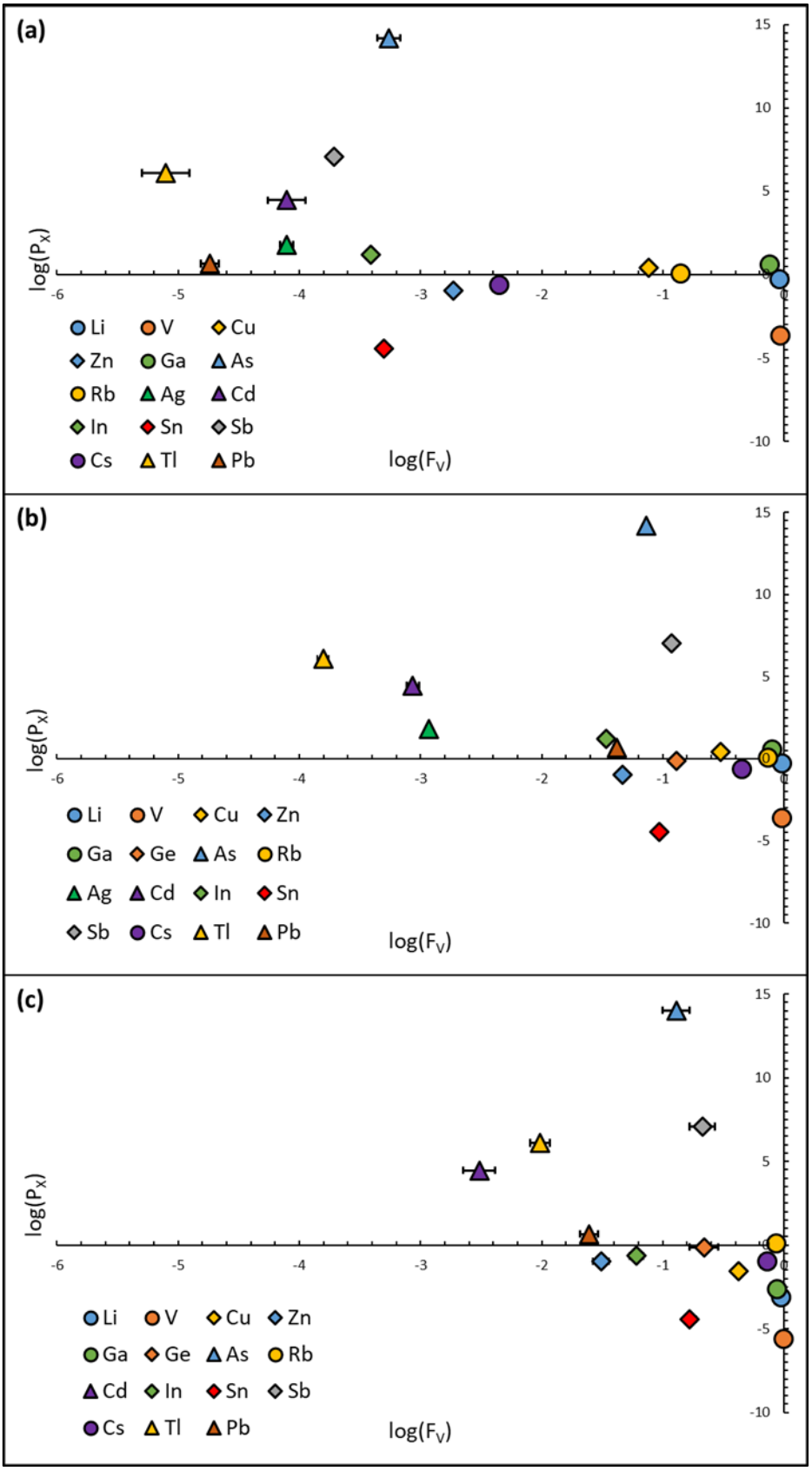


Figure A2.24: The volatility factor plotted against the total equilibrium partial pressure of the oxide gas species for the **(a)** SM and **(b)** IB experiments at log(fO_2) = -8 and **(c)** IB-G at log(fO_2) = -9 considering non-ideal trace element behaviour in the silicate melt.

A2.4 – References

Barin, I., Sauert, F., Schultze-Rhonhof, E., Sheng, W.S. (1989). Thermochemical Data of Pure Substances. Cambridge, United Kingdom, VCH Publishers Ltd.

Sossi, P.A., Klemme, S., O'Neill, H.St.C., Berndt, J., Moynier, F. (2019). Evaporation of moderately volatile elements from silicate melts: experiments and theory. Geochimica et Cosmochimica Acta, vol. 260, p. 204-231

Appendix 3 – Thermodynamic Predictions: Formation of Chloride Gas Species

A3.1 – Chloride Gas Speciation

This appendix explores the partitioning of a trace element between chloride and elemental or oxide gas species as a function of fO_2 and fCl_2 by calculating the partial pressures of the monometallic chloride gas species and comparing them to the partial pressures of the monometallic elemental and oxide gas species listed in Chapter **4**. This was done to identify for which elements evaporation as halide species would have been a potential evaporation pathway following the presence of halogens in the trace element mix. In these calculations only the elements that exhibited volatile loss were considered. The potential evaporation reactions are listed in Table **A3.1**. The equations used to explore the importance of chloride gas species formation are discussed in Chapter **2**.

	Gas Interspecies Reactions	n_{Cl}	El/Ox	n_{Ox}
Cu	Cu_2O (l) + Cl_2 (g) = 2 CuCl (g) + 0.5 O_2 (g)	0	Cu	1
Zn	ZnO (l) + Cl_2 (g) = $ZnCl_2$ (g) + 0.5 O_2 (g)	0	Zn	2
Ga	Ga_2O_3 (l) + Cl_2 (g) = 2 GaCl (g) + 1.5 O_2 (g)	2	Ga	3
	Ga_2O_3 (l) + 2 Cl_2 (g) = 2 $GaCl_2$ (g) + 1.5 O_2 (g)	1		
	Ga_2O_3 (l) + 3 Cl_2 (g) = 2 $GaCl_3$ (g) + 1.5 O_2 (g)	0		
Ge	GeO_2 (l) + 0.5 Cl_2 (g) = GeCl (g) + O_2 (g)	3	GeO	2
	GeO_2 (l) + Cl_2 (g) = $GeCl_2$ (g) + O_2 (g)	2		
	GeO_2 (l) + 1.5 Cl_2 (g) = $GeCl_3$ (g) + O_2 (g)	1		
	GeO_2 (l) + 2 Cl_2 (g) = $GeCl_4$ (g) + O_2 (g)	0		
As	As_2O_3 (l) + 3 Cl_2 (g) = 2 $AsCl_3$ (g) + 1.5 O_2 (g)	0	AsO	1
Rb	Rb_2O (l) + Cl_2 (g) = 2 RbCl (g) + 0.5 O_2 (g)	0	Rb	1
Ag	Ag_2O (l) + Cl_2 (g) = 2 AgCl (g) + 0.5 O_2 (g)	0	Ag	1
Cd	CdO (l) + Cl_2 (g) = $CdCl_2$ (g) + 0.5 O_2 (g)	0	Cd	2
In	In_2O_3 (l) + Cl_2 (g) = 2 InCl (g) + 1.5 O_2 (g)	2	In	3
	In_2O_3 (l) + 2 Cl_2 (g) = 2 $InCl_2$ (g) + 1.5 O_2 (g)	1		
	In_2O_3 (l) + 3 Cl_2 (g) = 2 $InCl_3$ (g) + 1.5 O_2 (g)	0		
Sn	SnO_2 (l) + 0.5 Cl_2 (g) = SnCl (g) + O_2 (g)	3	SnO	2
	SnO_2 (l) + Cl_2 (g) = $SnCl_2$ (g) + O_2 (g)	2		
	SnO_2 (l) + 2 Cl_2 (g) = $SnCl_4$ (g) + O_2 (g)	0		
Sb	Sb_2O_3 (l) + Cl_2 (g) = 2 SbCl (g) + 1.5 O_2 (g)	2	SbO	1
	Sb_2O_3 (l) + 3 Cl_2 (g) = 2 $SbCl_3$ (g) + 1.5 O_2 (g)	0		
Cs	Cs_2O (l) + Cl_2 (g) = 2 CsCl (g) + 0.5 O_2 (g)	0	Cs	1
			CsO	-1
Tl	Tl_2O (l) + Cl_2 (g) = 2 TlCl (g) + 0.5 O_2 (g)	0	Tl	1
Pb	PbO (l) + 0.5 Cl_2 (g) = PbCl (g) + 0.5 O_2 (g)	1	Pb	0
	PbO (l) + Cl_2 (g) = $PbCl_2$ (g) + 0.5 O_2 (g)	0	PbO	2

Table A3.1: The evaporation potential evaporation reactions involving monometallic chloride gas species, n_{Cl} is the change in oxidation state for chloride evaporation. El/Ox are the stable and abundant monometallic elemental and oxide gas species, n_{Ox} is the change in oxidation state for these gas species.

Figures **A3.1 – A3.14** show how the total partial pressure of the monometallic chloride species changes compared to that of the monometallic elemental and oxide gas species as a function of fO_2 and fCl_2. These partial pressure ratios were calculated using the thermodynamic data of Barin et al. (1989). In Figures **A3.1 – A3.14** the Cl melt abundance contours are a proxy for fCl_2, because $[Cl]_{melt}$ can be converted to fCl_2 at known fO_2 using the equation of Thomas and Wood (2021). These calculations assume that trace element activity in the melt is ideal and that gas species follow ideal gas behaviour. If $\log\left(\Sigma P_{MCl(g)}/\Sigma P_{MO(g)}\right) < 0$ the total partial pressure of the elemental and oxide gas species exceeds that of the chloride gas species. If $\log\left(\Sigma P_{MCl(g)}/\Sigma P_{MO(g)}\right) > 0$ the partial pressure of the chloride species exceed that of the elemental and oxide gas species.

A3.2 – Element-Specific Plots

A3.2.1 – Copper

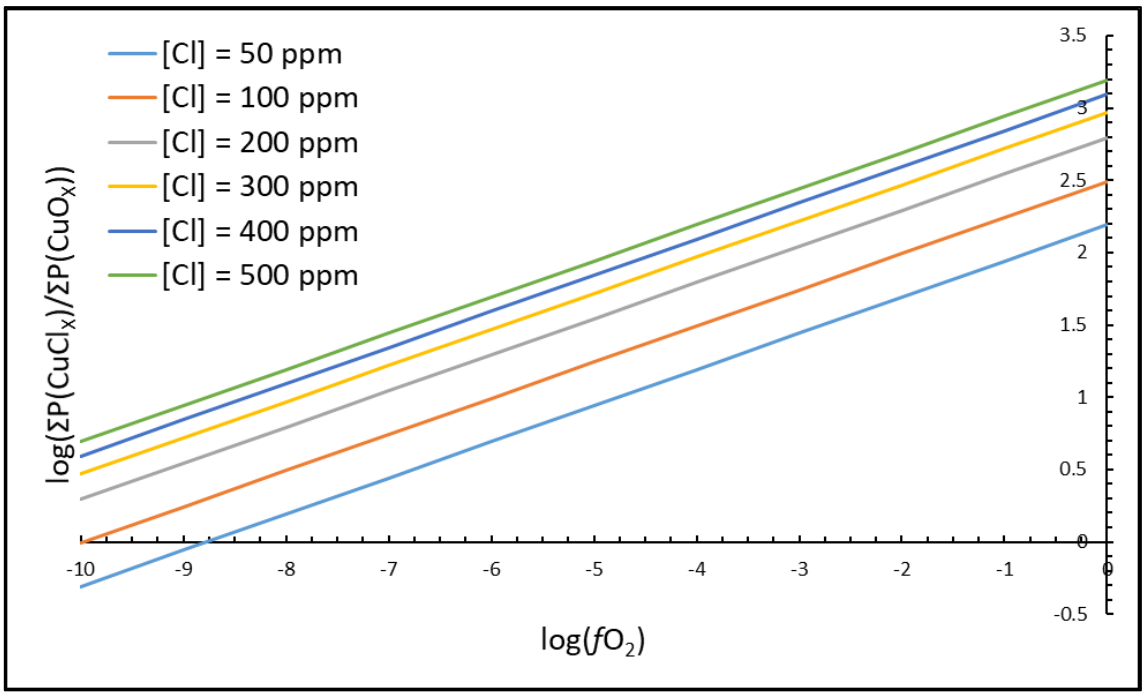


Figure A3.1: The ratio of the total partial pressure of the Cu chloride and oxide gas species as a function of fCl_2 and fO_2.

A3.2.2 – Zinc

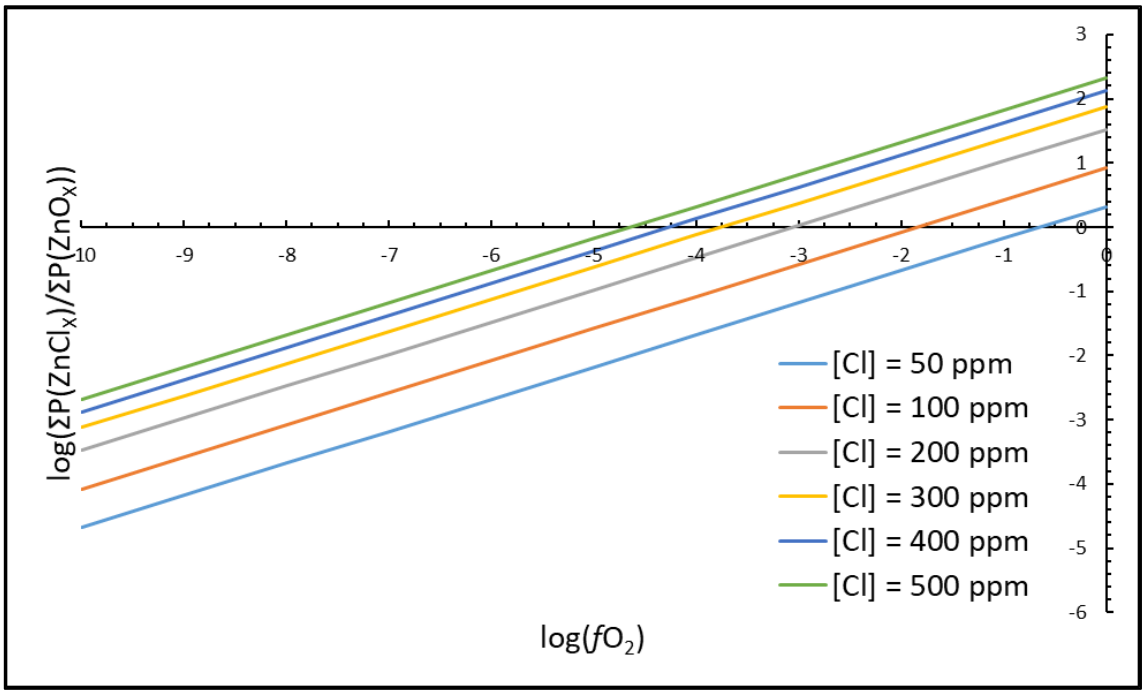


Figure A3.2: The ratio of the total partial pressure of the Zn chloride and oxide gas species as a function of fCl_2 and fO_2.

A3.2.3 – Gallium

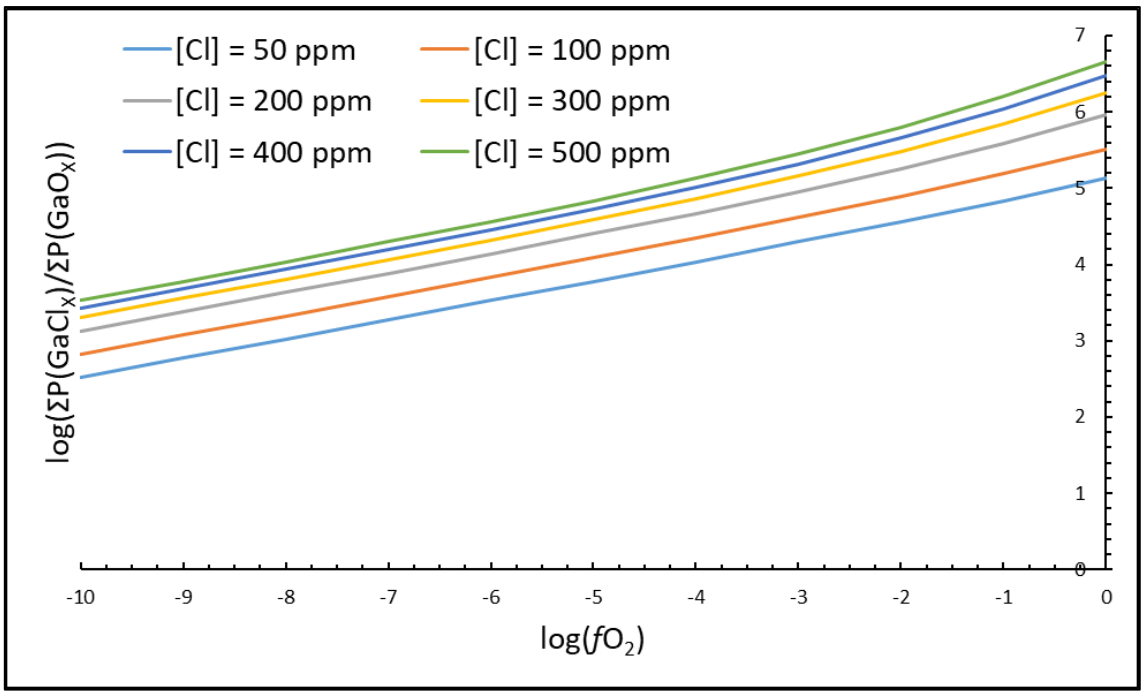


Figure A3.3: The ratio of the total partial pressure of the Ga chloride and oxide gas species as a function of $f\mathrm{Cl}_2$ and $f\mathrm{O}_2$.

A3.2.4 – Germanium

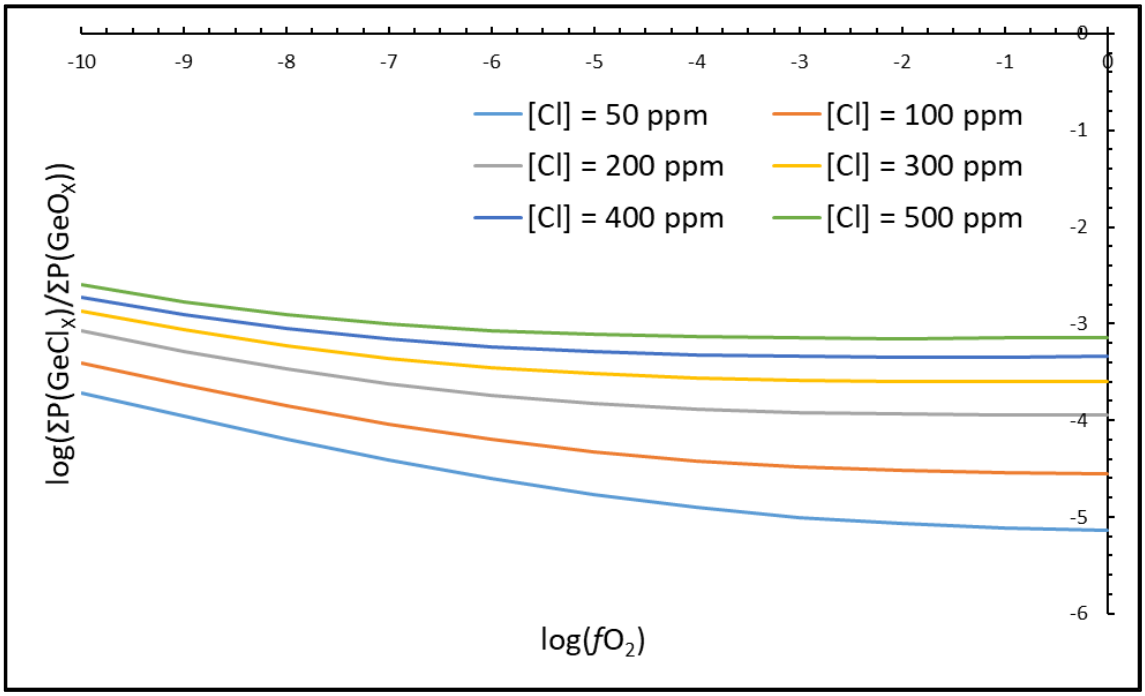


Figure A3.4: The ratio of the total partial pressure of the Ge chloride and oxide gas species as a function of $f\mathrm{Cl}_2$ and $f\mathrm{O}_2$.

A3.2.5 – Arsenic

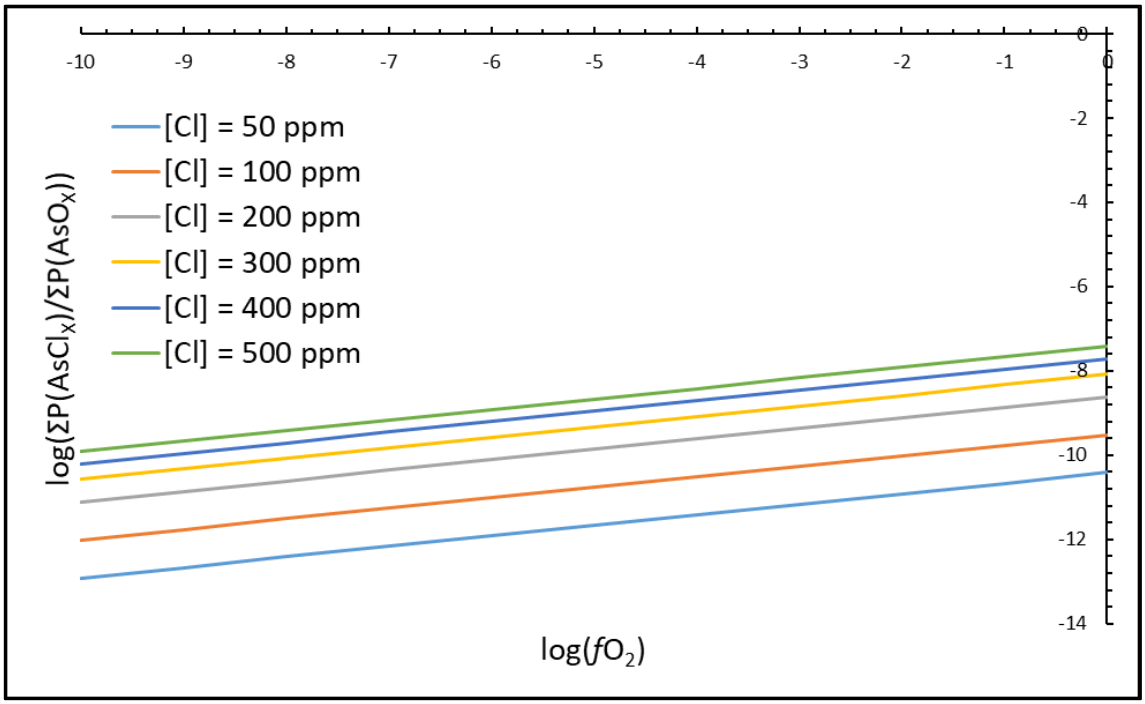


Figure A3.5: The ratio of the total partial pressure of the As chloride and oxide gas species as a function of fCl_2 and fO_2.

A3.2.6 – Rubidium

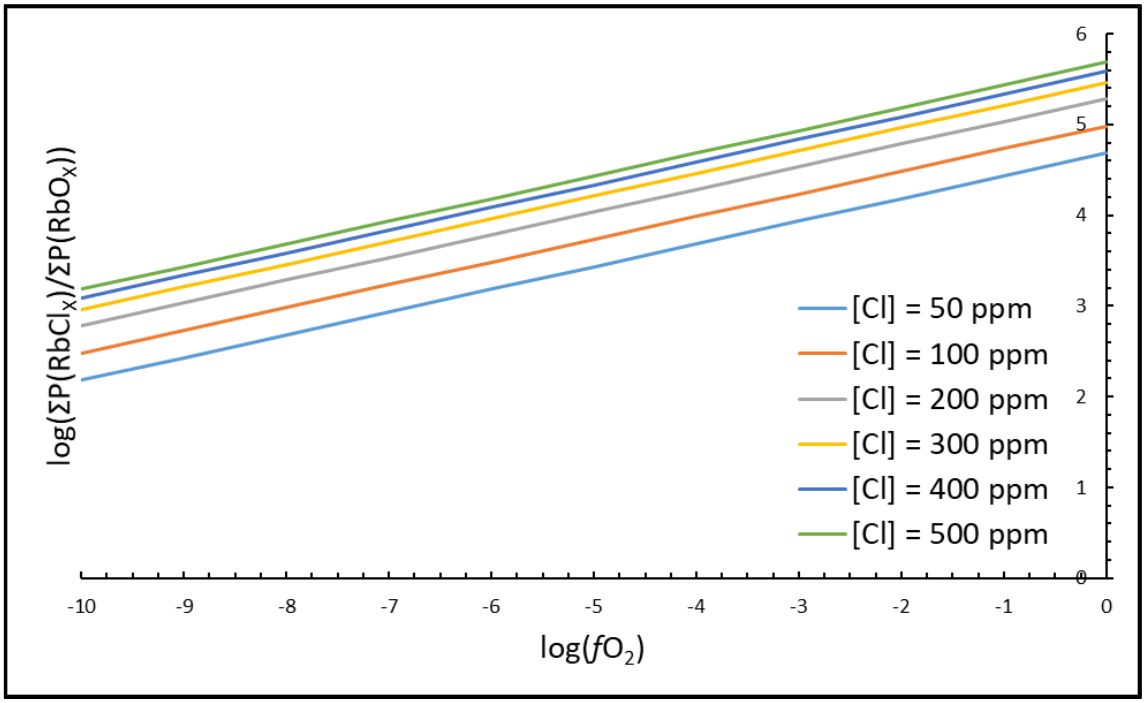


Figure A3.6: The ratio of the total partial pressure of the Rb chloride and oxide gas species as a function of fCl_2 and fO_2.

A3.2.7 – Silver

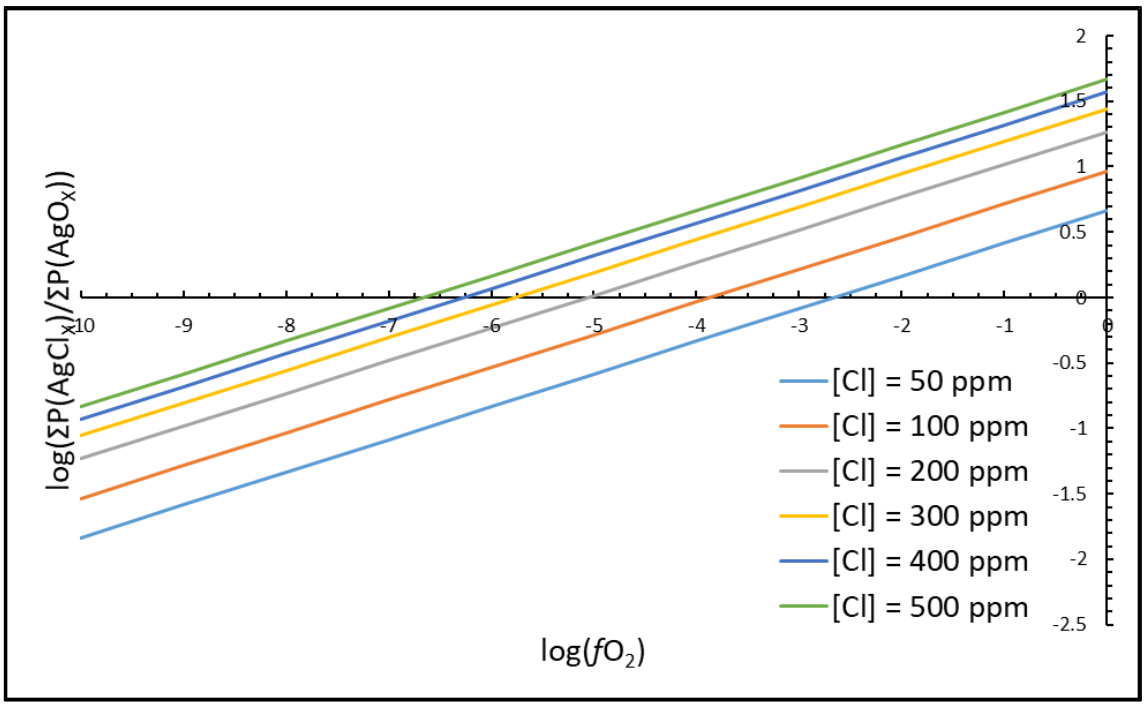


Figure A3.7: The ratio of the total partial pressure of the Ag chloride and oxide gas species as a function of fCl_2 and fO_2.

A3.2.8 – Cadmium

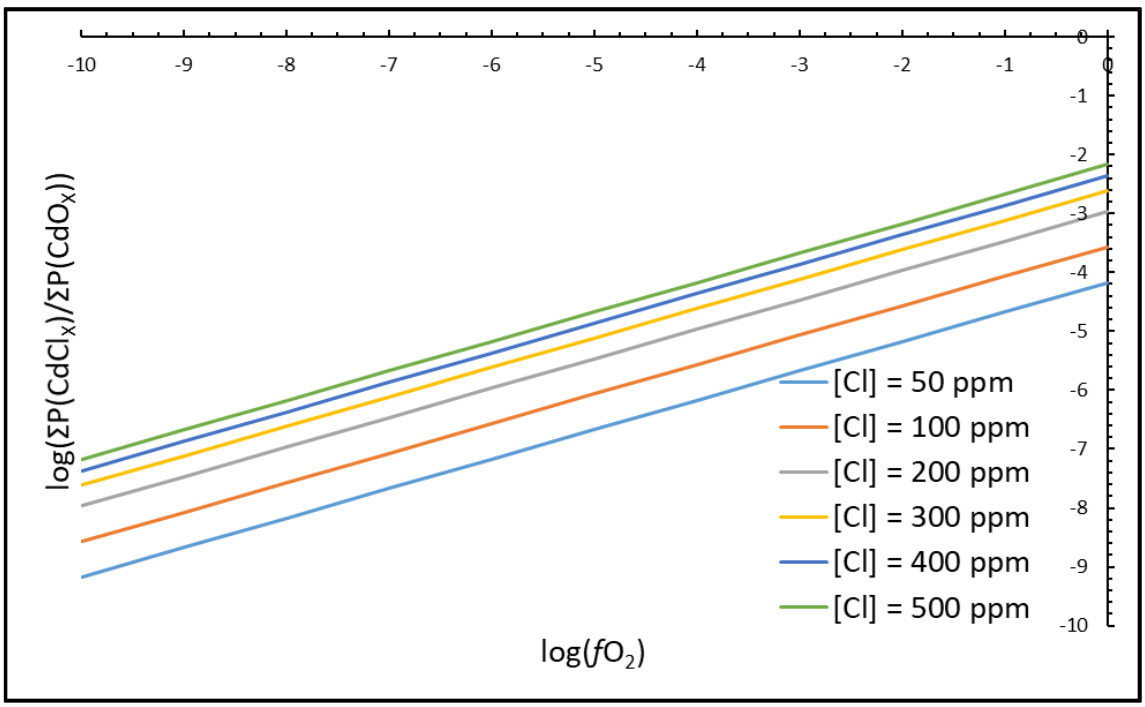


Figure A3.8: The ratio of the total partial pressure of the Cd chloride and oxide gas species as a function of fCl_2 and fO_2.

A3.2.9 – Indium

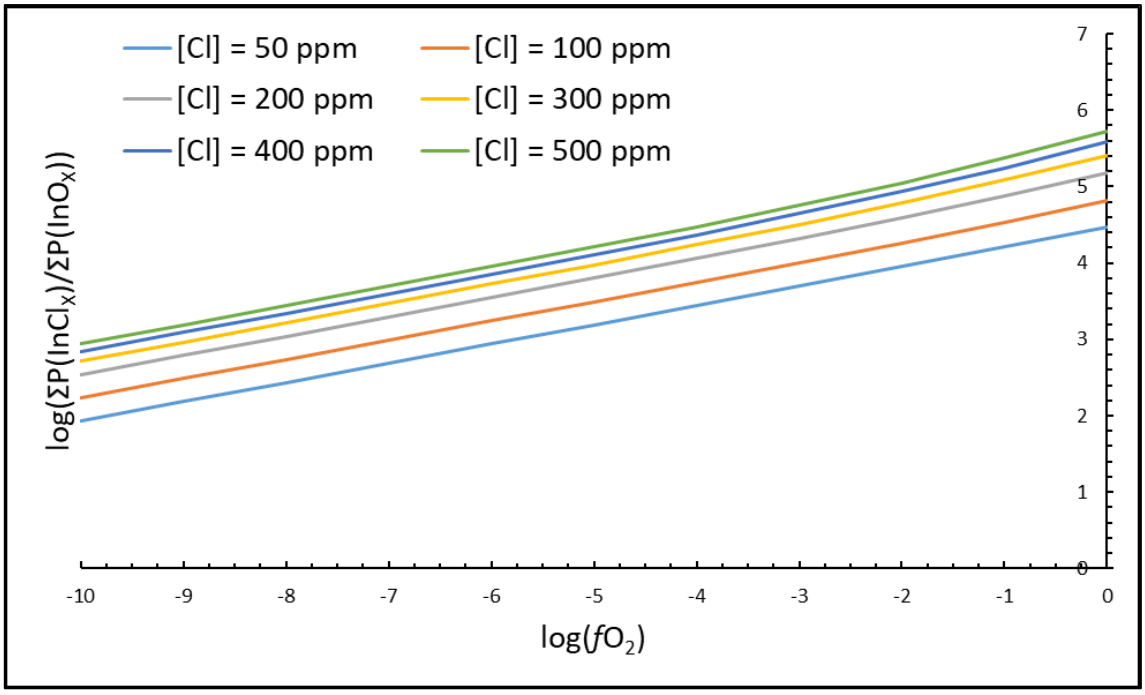


Figure A3.9: The ratio of the total partial pressure of the In chloride and oxide gas species as a function of fCl_2 and fO_2.

A3.2.10 – Tin

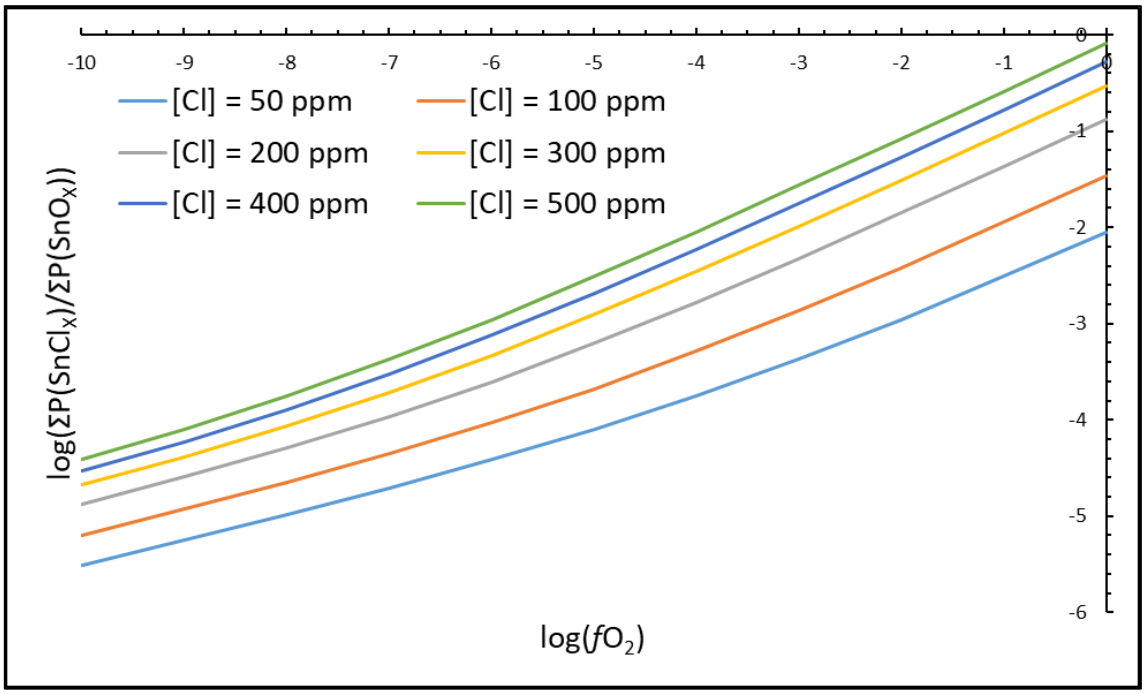


Figure A3.10: The ratio of the total partial pressure of the Sn chloride and oxide gas species as a function of fCl_2 and fO_2.

A3.2.11 – Antimony

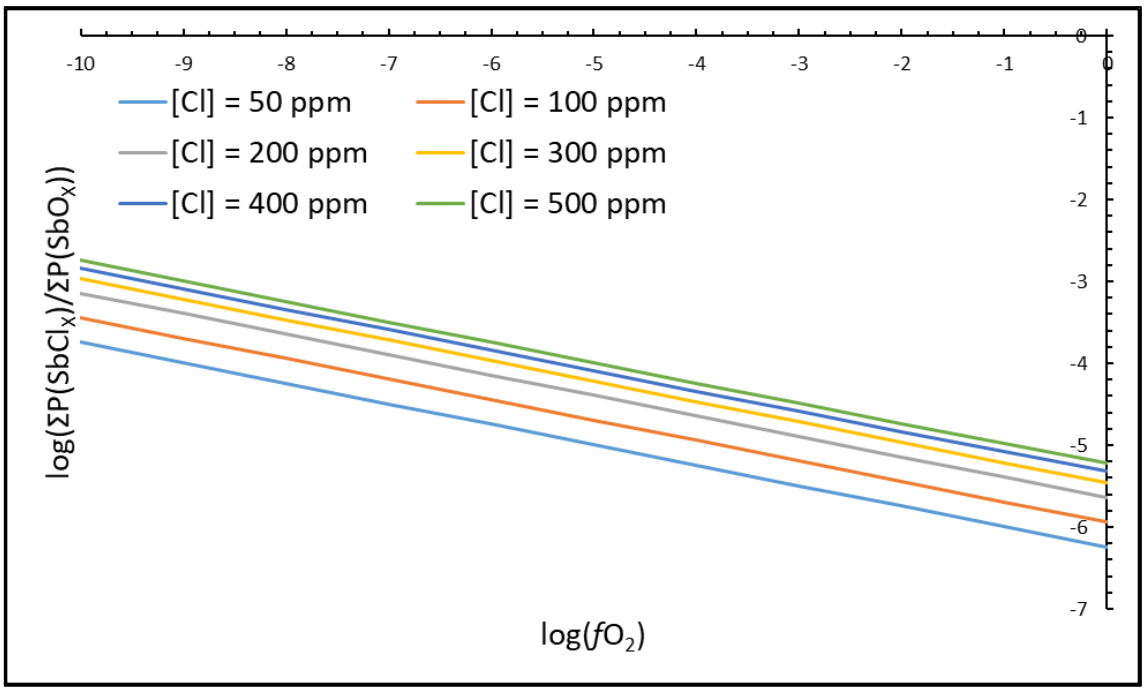


Figure A3.11: The ratio of the total partial pressure of the Sb chloride and oxide gas species as a function of fCl_2 and fO_2.

A3.2.12 – Caesium

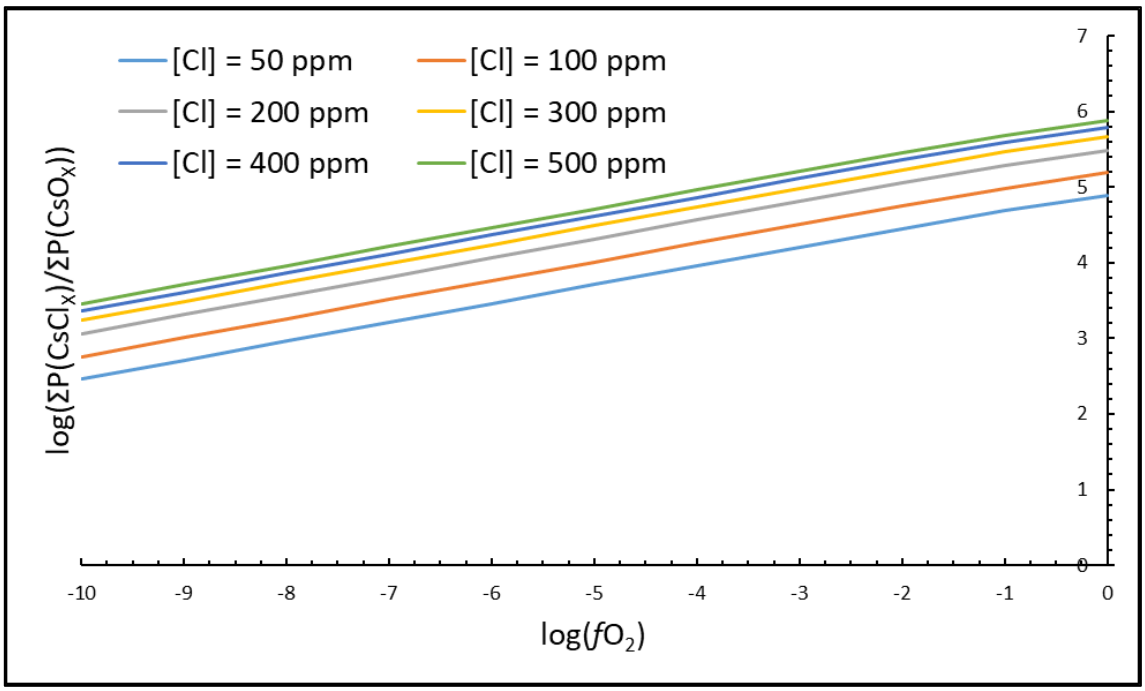


Figure A3.12: The ratio of the total partial pressure of the Cs chloride and oxide gas species as a function of fCl_2 and fO_2.

A3.2.13 – Thallium

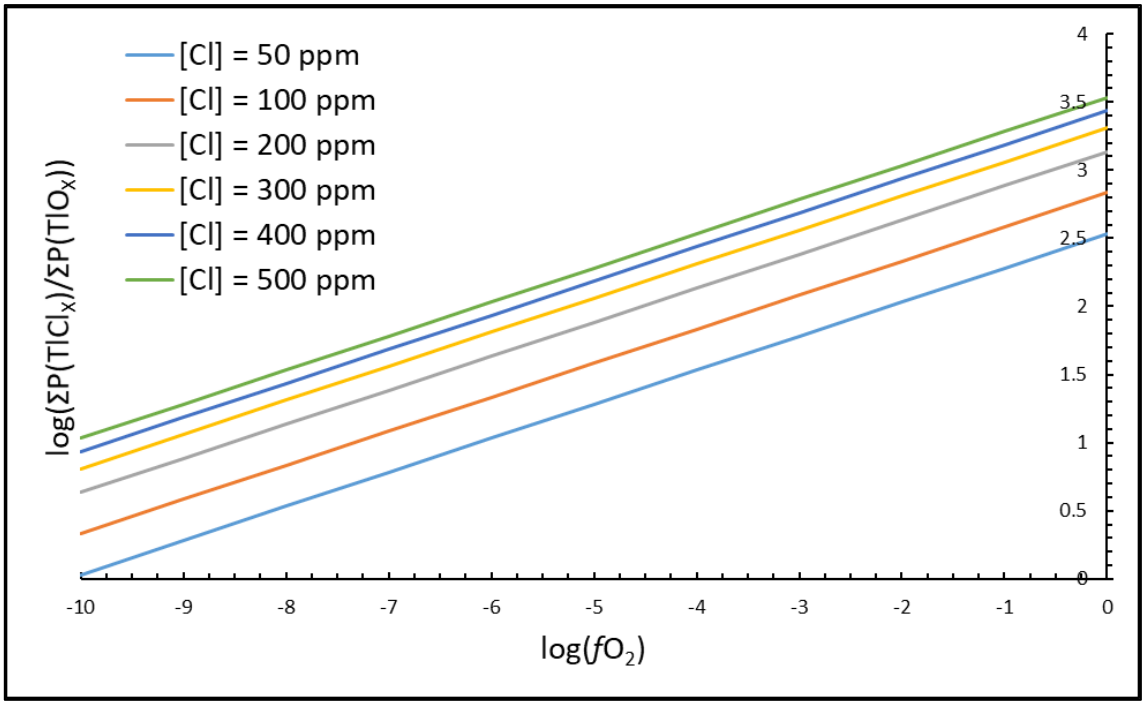


Figure A3.13: The ratio of the total partial pressure of the Tl chloride and oxide gas species as a function of fCl_2 and fO_2.

A3.2.14 – Lead

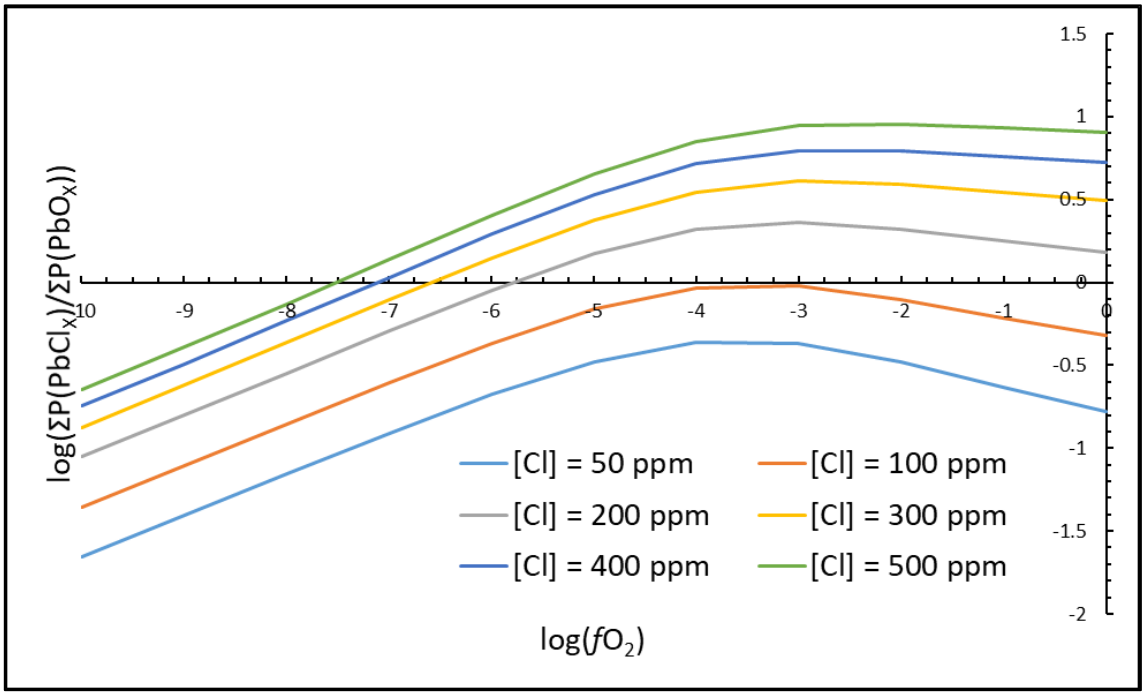


Figure A3.14: The ratio of the total partial pressure of the Tl chloride and oxide gas species as a function of fCl_2 and fO_2.

A3.3 – References

Barin, I., Sauert, F., Schultze-Rhonhof, E., Sheng, W.S. (1989). Thermochemical Data of Pure Substances. Cambridge, United Kingdom, VCH Publishers Ltd.

Thomas, R.W., Wood, B.J. (2021). The chemical behaviour of chlorine in silicate melts. Geochimica and Cosmochimica Acta, vol. 294, p. 28-42

Appendix 4 – Standard Deviations on Trace Element Abundances and Volatility Factors

This appendix contains the volatility factors normalized to the shortest experiment in each time series (Table **A4.2**) and those normalized to the Table **2.2** trace element abundances (Table **A4.4**). It also contains the errors on Table **4.3** trace element abundances (Table **A4.1**), Table **A4.2** volatility factors (Table **A4.3**) and Table **4.4** volatility factors (Table **A4.5**).

	Li	P	V	Cu	Zn	Ga	Ge	As	Rb	Ag	Cd	In	Sn	Sb	Cs	Tl	Pb
Q6	9.05	5.21	5.28	14.2	15.1	5.88	6.95	9.64	1.86	3.80	5.03	2.69	9.26	5.88	4.24	0.20	2.26
Q7	3.54	7.34	7.94	13.6	12.4	9.25	3.45	5.21	5.94	1.33	1.16	5.21	5.33	4.12	2.41	0.05	4.92
Q8	12.6	3.41	4.08	15.6	24.0	8.79	4.86	2.05	4.70	0.39	0.18	11.8	9.23	6.31	0.84	0.03	1.71
Q9	9.38	13.7	10.9	24.3	12.0	17.5	14.0	1.23	10.0	0.60	0.17	12.7	13.0	8.45	5.53	0.02	1.14
Q22	9.61	8.74	5.65	45.7	5.53	20.9	19.2	11.1	6.52	24.8	20.6	14.0	11.4	10.6	8.81	0.03	10.8
Q23	5.36	9.83	5.23	10.8	4.14	6.86	7.43	27.1	3.42	5.23	7.90	8.64	12.1	8.39	9.27	0.02	23.4
Q24	10.2	15.0	7.54	12.7	14.4	10.2	14.2	15.9	6.21	1.63	0.14	14.1	16.3	13.4	8.93	0.01	14.6
Q25	13.7	16.4	6.26	5.93	7.94	7.21	6.88	1.99	2.65	0.18	0.03	5.41	10.4	10.8	4.60	0.01	2.73
Q46	17.4	25.0	9.77	30.9	18.6	14.6	11.4	36.8	14.1	34.4	38.7	16.3	22.9	22.7	16.0	0.34	14.1
Q47	8.96	29.4	1.49	20.8	12.2	4.27	33.9	24.6	8.90	2.72	7.11	20.5	14.1	10.8	9.03	0.19	22.2
Q48	6.17	27.1	8.00	20.2	5.16	10.0	6.75	1.62	8.12	0.79	0.27	3.01	1.70	6.94	4.82	0.02	6.15
Q49	11.9	27.3	8.01	2.59	0.36	15.5	0.87	0.07	15.6	0.10	0.01	11.1	4.52	5.07	10.5	-	0.26
Q14	10.4	19.5	5.36	20.3	6.03	11.7	3.13	3.52	7.19	0.68	0.29	2.87	5.79	5.57	17.5	0.04	1.87
Q15	13.4	16.2	5.33	14.5	0.29	7.48	1.25	0.37	3.46	0.45	0.05	0.18	0.14	0.42	3.60	0.004	0.01
Q16	10.2	10.6	6.03	9.60	0.16	10.9	0.31	0.08	6.43	0.09	0.11	0.06	0.11	0.09	2.26	0.002	0.10
Q20	5.04	16.7	8.53	3.29	0.12	8.68	-	0.02	2.36	0.04	0.02	0.02	0.02	0.02	0.09	0.001	0.003
Q10	10.5	28.1	13.3	20.4	14.5	20.6	22.6	26.1	19.0	5.42	12.8	10.4	12.1	14.1	8.94	0.30	18.5
Q11	4.48	9.09	13.1	9.78	8.12	11.9	20.5	55.5	9.94	3.62	23.6	15.9	13.8	13.2	4.03	0.13	30.8
Q12	4.89	7.23	8.63	20.4	19.2	7.64	11.4	11.2	8.23	1.02	1.80	7.16	13.4	17.3	5.26	0.04	15.5
Q13	5.30	5.43	3.02	16.5	4.81	5.73	14.6	15.3	11.5	0.50	1.09	7.39	13.0	11.8	4.99	0.05	9.63
Q26	8.12	28.2	7.71	18.7	9.75	16.8	16.6	14.9	6.76	5.23	10.8	11.5	4.57	3.15	9.99	0.03	9.22
Q27	10.8	7.47	4.87	14.1	14.4	8.30	9.60	17.5	7.95	5.29	11.3	17.9	14.6	10.8	2.04	0.04	13.1
Q28	16.0	29.8	9.08	9.44	15.7	12.5	16.0	26.5	12.6	2.06	2.68	18.9	5.36	16.2	10.4	0.05	5.33
Q29	11.4	22.1	6.90	4.76	11.0	9.51	32.0	10.6	14.0	0.40	1.10	15.3	18.8	8.59	11.0	0.08	23.2
Q50	11.2	11.1	5.93	39.0	53.3	47.6	62.0	38.3	13.0	35.5	5.76	58.6	79.0	43.4	11.3	0.18	41.4
Q51	16.7	30.1	9.72	21.8	31.3	7.76	23.6	14.4	4.87	1.19	0.17	20.6	11.7	18.8	6.06	0.08	14.9

	Li	P	V	Cu	Zn	Ga	Ge	As	Rb	Ag	Cd	In	Sn	Sb	Cs	Tl	Pb
Q52	23.5	30.6	15.0	24.6	44.2	17.4	24.5	8.00	3.10	0.88	0.60	10.0	2.96	14.5	13.6	0.09	20.2
Q53	21.9	42.0	17.3	20.4	24.9	23.9	5.91	2.08	22.4	0.11	0.26	14.4	2.32	24.4	16.5	0.04	17.2
Q17	8.51	51.3	12.4	26.0	30.5	14.2	63.5	13.6	1.28	27.4	3.12	14.4	16.8	18.3	6.29	0.25	28.7
Q18	11.0	50.4	8.11	27.2	23.5	16.0	25.9	17.4	6.31	5.19	0.64	11.9	20.6	17.5	3.66	0.05	18.0
Q19	11.5	32.3	13.8	28.9	4.84	12.8	12.7	11.1	10.8	0.07	0.07	4.65	9.51	35.1	24.8	0.02	5.33
Q21	13.6	28.7	14.5	20.6	9.77	15.1	17.5	9.16	11.3	0.19	0.15	5.48	13.9	15.5	21.8	0.02	7.87
Q30	22.9	79.8	16.4	20.3	21.0	18.0	86.8	14.3	38.8	14.8	41.1	17.1	25.7	29.7	50.8	0.78	20.5
Q31	18.7	84.0	12.2	33.5	4.70	27.8	32.5	11.8	27.8	24.8	10.3	46.6	26.8	24.6	25.1	1.08	13.5
Q32	9.18	29.4	6.48	18.5	11.5	28.4	20.5	19.9	9.25	12.6	14.2	26.4	21.2	11.3	9.66	0.54	16.2
Q33	7.98	20.4	4.66	15.4	26.5	15.2	43.4	4.47	10.7	3.11	28.8	4.98	6.15	8.53	9.19	0.24	10.4
Q34	24.1	96.9	14.8	55.4	28.9	41.2	83.0	12.7	43.8	22.1	31.9	70.8	46.7	30.6	50.6	8.07	34.2
Q35	9.67	54.6	34.0	30.4	9.37	28.5	33.5	22.5	27.5	12.3	17.4	26.2	16.3	23.5	27.8	1.72	21.0
Q36	16.9	26.9	6.22	26.7	17.1	33.7	77.4	20.7	20.8	6.67	15.8	28.5	22.5	23.2	22.3	0.53	29.5
Q37	12.2	21.7	4.23	9.02	13.2	34.9	45.4	10.2	18.6	2.10	9.84	27.5	7.30	12.1	15.8	0.22	16.2
Q38	12.3	54.6	10.4	72.1	18.4	35.9	110	47.9	41.6	25.3	36.0	47.1	36.3	42.5	56.2	5.17	39.0
Q39	12.2	72.2	9.72	9.43	12.1	51.9	78.2	15.2	23.7	2.32	9.44	24.1	17.4	8.67	35.4	3.52	9.28
Q40	12.1	44.0	10.5	37.7	12.3	19.5	20.9	14.0	10.1	4.13	33.4	19.5	17.9	7.19	11.4	3.77	17.9
Q41	16.2	20.9	17.2	14.4	6.46	17.6	37.6	20.5	10.6	2.00	21.9	19.0	39.6	16.5	8.27	4.72	22.5
Q42	15.9	82.8	19.9	21.0	26.7	55.9	32.0	16.4	45.6	9.72	25.4	48.2	17.4	10.3	46.4	1.82	16.7
Q43	17.4	56.9	16.2	45.1	19.6	38.2	83.1	11.3	28.0	7.50	17.9	33.2	31.6	27.2	28.5	1.13	23.9
Q44	29.1	51.5	18.2	23.2	16.3	27.4	23.8	16.6	6.50	1.37	28.6	38.6	13.6	9.68	3.44	2.17	17.0
Q45	16.9	42.4	13.9	27.5	24.3	23.2	46.0	15.0	26.9	0.54	28.1	84.6	38.5	9.82	29.0	0.44	22.0
Q54	13.0	11.4	7.86	35.2	13.2	15.7	14.9	55.7	16.0	26.9	62.9	37.4	21.5	15.1	18.7	7.60	50.1
Q55	6.76	15.5	8.16	9.56	28.9	8.70	10.9	37.5	12.4	4.17	7.61	7.16	11.4	13.5	7.72	0.41	18.3
Q56	7.12	15.5	7.49	21.7	9.39	14.9	15.5	18.6	20.8	6.50	7.48	17.2	21.7	16.1	13.7	0.39	23.5
Q63	11.2	10.8	7.88	36.9	29.8	6.40	78.0	67.0	11.9	1.88	3.27	25.6	66.2	31.9	13.4	0.51	37.4
Q64	9.53	16.0	5.92	14.4	42.0	6.86	56.3	52.0	14.2	0.40	2.32	22.6	41.3	26.6	14.1	0.49	31.6
Q65	9.74	18.7	8.19	9.70	14.2	5.77	26.5	3.68	3.72	0.01	0.04	14.2	4.48	18.8	9.77	0.01	4.27
Q57	5.71	9.88	7.38	15.7	33.1	5.99	30.9	31.5	1.60	0.95	2.51	30.9	30.6	33.6	7.57	0.57	20.4
Q58	8.71	12.6	5.39	15.2	19.9	8.62	23.3	16.9	5.85	0.12	0.90	16.1	24.4	23.5	7.66	0.35	12.4
Q59	7.58	12.5	10.6	11.2	3.00	5.72	29.9	17.8	7.82	-	0.40	3.59	9.53	24.7	12.3	0.10	2.25
Q60	14.7	13.4	17.1	80.1	42.5	27.2	60.3	58.4	29.9	8.90	20.6	44.5	36.8	51.4	27.6	2.28	33.2
Q61	14.0	26.0	9.19	33.3	25.1	24.2	20.0	20.3	16.9	1.91	4.94	20.5	28.6	21.3	12.3	1.46	28.1

	Li	P	V	Cu	Zn	Ga	Ge	As	Rb	Ag	Cd	In	Sn	Sb	Cs	Tl	Pb
Q62	10.4	35.5	9.28	10.6	17.3	42.0	58.6	7.79	22.6	0.03	4.42	12.3	30.7	25.9	15.7	0.99	18.1
Q66	-	-	-	50.0	80.1	-	27.2	-	-	102	262	-	35.3	-	-	253	-
Q67	-	-	-	51.2	100	-	53.0	-	-	184	289	-	71.4	-	-	148	-
Q68	-	-	-	49.2	55.7	-	53.7	-	-	49.9	83.8	-	65.6	-	-	68.7	-
Q69	-	-	-	31.5	104	-	48.2	-	-	29.6	18.1	-	57.9	-	-	6.88	-
Q70	-	-	-	227	35.0	-	34.8	-	-	137	327	-	30.2	-	-	173	-
Q71	-	-	-	23.7	49.3	-	50.4	-	-	60.7	34.3	-	45.5	-	-	61.0	-
Q72	-	-	-	62.4	120	-	95.2	-	-	11.6	0.99	-	109	-	-	2.88	-
Q73	-	-	-	17.8	76.6	-	69.6	-	-	2.79	0.6	-	62.1	-	-	3.45	-
Q74	-	-	-	17.8	224	-	239	-	-	55.4	24.7	-	190	-	-	34.5	-
Q75	-	-	-	133	40.7	-	18.1	-	-	0.003	0.02	-	34.9	-	-	0.01	-
Q76	-	-	-	57.4	7.10	-	7.19	-	-	0.02	0.003	-	18.1	-	-	0.002	-
Q77	-	-	-	33.2	0.18	-	0.04	-	-	0.002	0.004	-	0.32	-	-	0.005	-
Q78	-	-	-	44.5	44.1	-	168	-	-	39.3	0.02	-	94.9	-	-	31.5	-
Q79	-	-	-	46.3	0.31	-	4.38	-	-	1.65	0.01	-	38.3	-	-	0.04	-
Q80	-	-	-	52.5	0.22	-	2.18	-	-	0.03	0.01	-	15.4	-	-	0.07	-
Q81	-	-	-	33.8	0.07	-	-	-	-	-	0.01	-	0.35	-	-	0.003	-

Table A4.1: The standard deviations (1 s.d.; ppm) for the trace element abundances in Table **4.3**. Calculated as the standard deviation on the average of individual points. The error on individual LA-ICP-MS measurements was discussed in Chapter **2**.

	t (min)	comp	log(fO_2)	T (°C)	Li	P	V	Cu	Zn	Ga	Ge	As	Rb	Ag	Cd	In	Sn	Sb	Cs	Tl	Pb
Q6	3	SM	-0.68	1400	1	1	1	1	1	1	1	1	1	1	1	1	1	1	1	1	1
Q7	15	SM	-0.68	1400	0.993	0.989	0.999	0.970	0.965	1.027	1.002	0.441	0.954	0.270	0.103	1.015	1.006	0.927	0.800	0.123	0.463
Q8	30	SM	-0.68	1400	0.963	0.964	0.986	0.952	0.950	0.996	0.963	0.120	0.918	0.052	0.005	0.969	0.942	0.800	0.676	0.017	0.136
Q9	60	SM	-0.68	1400	0.946	0.976	0.981	0.903	0.919	0.992	0.975	0.065	0.872	0.050	0.008	0.953	0.963	0.754	0.542	0.021	0.088
Q22	3	SM	-3.05	1400	1	1	1	1	1	1	1	1	1	1	1	1	1	1	1	1	1
Q23	15	SM	-3.05	1400	0.985	1.025	0.988	0.674	0.979	0.995	1.003	0.443	0.959	0.204	0.078	0.967	0.933	0.921	0.851	0.418	0.585
Q24	30	SM	-3.05	1400	0.963	1.019	0.986	0.476	1.016	0.977	0.908	0.138	0.917	0.038	0.001	0.928	0.833	0.833	0.734	0.132	0.236
Q25	60	SM	-3.05	1400	0.972	1.040	0.999	0.445	0.830	1.028	0.850	0.024	0.815	0.005	0.0002	0.995	0.806	0.819	0.473	0.098	0.056
Q46	3	SM	-5.98	1400	1	1	1	1	1	1	1	1	1	1	1	1	1	1	1	1	1
Q47	15	SM	-5.98	1400	0.995	1.011	1.016	0.602	0.637	1.028	0.699	0.406	0.994	0.109	0.202	0.789	0.343	0.628	0.900	0.571	0.441
Q48	30	SM	-5.98	1400	0.996	1.010	0.997	0.257	0.076	1.002	0.144	0.028	0.893	0.015	0.005	0.297	0.070	0.182	0.674	0.103	0.029
Q49	60	SM	-5.98	1400	1.001	1.006	1.020	0.227	0.003	0.992	0.100	0.002	0.810	0.002	0.001	0.123	0.036	0.086	0.533	-	0.001
Q14	3	SM	-8.01	1400	1	1	1	1	1	1	1	1	1	1	1	1	1	1	1	1	1
Q15	15	SM	-8.01	1400	1.004	0.966	1.004	0.611	0.031	0.986	0.073	0.044	0.755	0.044	0.048	0.044	0.021	0.050	0.395	0.115	0.007
Q16	30	SM	-8.02	1400	0.991	0.970	0.995	0.341	0.022	0.952	0.008	0.009	0.495	0.020	0.105	0.006	0.005	0.004	0.138	0.070	0.012
Q20	60	SM	-7.99	1400	0.983	0.961	1.007	0.100	0.023	0.883	-	0.005	0.202	0.006	0.036	0.003	0.004	0.001	0.011	0.045	0.001
Q10	3	IB	-0.68	1400	1	1	1	1	1	1	1	1	1	1	1	1	1	1	1	1	1
Q11	15	IB	-0.68	1400	0.975	0.981	1.000	0.924	0.949	1.016	0.964	0.837	0.921	0.464	0.627	0.919	0.942	0.937	0.758	0.153	0.799
Q12	30	IB	-0.68	1400	0.993	0.930	1.016	0.885	0.991	1.063	0.923	0.295	0.975	0.197	0.097	0.971	0.927	0.886	0.952	0.082	0.526
Q13	60	IB	-0.68	1400	0.999	0.929	1.010	0.859	0.957	1.045	0.909	0.202	0.958	0.107	0.033	0.978	0.893	0.819	0.863	0.060	0.313
Q26	3	IB	-3.05	1400	1	1	1	1	1	1	1	1	1	1	1	1	1	1	1	1	1
Q27	15	IB	-3.05	1400	1.055	1.013	0.979	0.746	0.984	1.060	0.999	1.149	1.028	0.350	0.686	1.165	0.974	0.969	1.019	0.886	1.031
Q28	30	IB	-3.05	1400	1.037	1.030	0.995	0.535	0.951	1.004	0.917	0.620	1.024	0.138	0.198	1.148	0.810	0.872	1.034	0.671	0.775
Q29	60	IB	-3.05	1400	1.017	1.020	0.982	0.405	0.894	1.021	0.745	0.304	1.011	0.030	0.044	1.141	0.629	0.807	1.006	0.378	0.468
Q50	3	IB	-6.01	1400	1	1	1	1	1	1	1	1	1	1	1	1	1	1	1	1	1
Q51	15	IB	-5.94	1400	0.990	0.993	1.016	0.558	0.400	0.988	0.512	0.349	0.984	0.029	0.023	0.603	0.265	0.654	0.974	0.185	0.285
Q52	30	IB	-5.94	1400	0.985	1.038	1.004	0.335	0.283	0.959	0.456	0.236	0.986	0.028	0.050	0.418	0.121	0.388	0.994	0.130	0.166
Q53	60	IB	-6.01	1400	0.975	1.009	0.986	0.262	0.168	0.913	0.313	0.133	0.961	0.007	0.021	0.316	0.087	0.278	0.920	0.075	0.139
Q17	3	IB	-8.02	1400	1	1	1	1	1	1	1	1	1	1	1	1	1	1	1	1	1
Q18	15	IB	-8.02	1400	0.954	1.132	1.018	0.722	0.376	0.988	0.574	0.520	0.877	0.149	0.310	0.424	0.495	0.567	0.763	0.420	0.381
Q19	30	IB	-8.02	1400	1.003	1.148	1.044	0.516	0.053	1.050	0.347	0.287	0.946	0.003	0.025	0.111	0.215	0.282	0.864	0.064	0.056
Q21	60	IB	-7.98	1400	0.987	1.094	1.029	0.317	0.050	0.928	0.144	0.096	0.846	0.002	0.025	0.066	0.127	0.144	0.690	0.071	0.053

	t (min)	comp	log(fO_2)	T (°C)	Li	P	V	Cu	Zn	Ga	Ge	As	Rb	Ag	Cd	In	Sn	Sb	Cs	Tl	Pb
Q30	3	AN	-0.68	1400	1	1	1	1	1	1	1	1	1	1	1	1	1	1	1	1	1
Q31	15	AN	-0.68	1400	0.995	0.963	0.936	0.905	0.964	1.109	0.961	0.970	1.011	0.817	0.909	1.086	0.996	0.994	1.058	1.582	1.027
Q32	30	AN	-0.68	1400	0.963	0.997	0.951	0.825	0.976	1.075	0.900	0.976	0.968	0.481	0.883	1.038	0.967	0.976	1.025	0.992	1.000
Q33	60	AN	-0.68	1400	0.950	0.938	0.942	0.656	0.974	1.090	0.938	0.964	0.948	0.235	0.851	1.079	0.979	0.946	0.979	0.878	1.010
Q34	3	AN	-3.05	1400	1	1	1	1	1	1	1	1	1	1	1	1	1	1	1	1	1
Q35	15	AN	-3.05	1400	0.980	0.976	1.058	0.889	0.999	0.965	0.932	1.025	0.956	0.633	0.973	0.906	0.963	0.945	0.928	0.474	0.996
Q36	30	AN	-3.05	1400	1.014	0.972	1.026	0.792	1.005	1.048	0.767	1.061	0.967	0.338	0.974	0.625	0.966	0.963	0.906	0.135	0.995
Q37	60	AN	-3.05	1400	0.994	0.969	1.046	0.713	1.007	1.070	0.868	1.048	0.981	0.146	0.966	0.976	0.960	0.972	0.939	0.048	1.012
Q38	3	AN	-6.05	1400	1	1	1	1	1	1	1	1	1	1	1	1	1	1	1	1	1
Q39	15	AN	-6.05	1400	0.994	0.984	1.010	0.656	1.011	1.036	0.966	0.959	1.022	0.333	1.074	0.843	1.124	1.034	1.041	1.493	1.012
Q40	30	AN	-5.98	1400	1.012	1.053	1.057	0.406	0.995	1.045	1.031	1.024	1.046	0.052	0.886	0.820	0.992	0.992	1.043	0.892	0.940
Q41	60	AN	-5.98	1400	1.038	1.123	1.051	0.314	0.985	1.035	1.007	0.971	1.066	0.020	0.850	0.810	0.992	0.968	1.046	0.961	0.924
Q42	3	AN	-8.02	1400	1	1	1	1	1	1	1	1	1	1	1	1	1	1	1	1	1
Q43	15	AN	-8.02	1400	0.983	0.830	0.958	0.848	1.020	1.144	1.405	1.031	1.009	0.230	0.997	0.995	1.036	1.040	1.008	0.985	1.016
Q44	30	AN	-8.02	1400	0.940	0.866	0.935	0.605	0.921	0.990	1.157	0.909	0.902	0.059	0.731	0.949	0.897	0.909	0.882	2.280	0.853
Q45	60	AN	-8.02	1400	0.981	0.826	0.989	0.366	0.878	1.120	1.356	0.905	0.964	0.009	0.703	0.901	0.909	0.977	0.903	0.297	0.823
Q54	15	IB-G	-0.68	1300	1.006	1.003	0.990	1.047	0.980	1.015	0.990	0.864	0.977	0.764	0.691	0.981	1.030	0.981	0.938	0.317	0.890
Q55	30	IB-G	-0.68	1300	0.989	0.992	0.978	0.974	0.921	0.990	0.970	0.634	0.955	0.319	0.143	0.964	1.002	0.944	0.890	0.049	0.562
Q56	60	IB-G	-0.68	1300	1.006	0.987	0.987	0.974	0.950	0.978	0.938	0.503	0.925	0.164	0.077	0.941	0.982	0.907	0.834	0.032	0.431
Q63	15	IB-G	-6.99	1300	1.006	1.014	0.988	0.865	0.768	0.960	0.696	0.367	0.942	0.049	0.021	0.819	0.597	0.821	0.878	0.035	0.563
Q64	30	IB-G	-6.99	1300	0.987	0.988	0.983	0.845	0.604	0.983	0.638	0.295	0.957	0.006	0.013	0.760	0.464	0.778	0.882	0.025	0.407
Q65	60	IB-G	-6.99	1300	0.994	1.047	0.986	0.637	0.107	1.030	0.239	0.048	0.969	$2{\cdot}10^{-4}$	$3{\cdot}10^{-4}$	0.338	0.093	0.419	0.874	0.001	0.041
Q57	15	IB-G	-8.94	1300	0.972	1.003	0.982	0.941	0.219	1.003	0.551	0.365	0.900	0.005	0.023	0.344	0.537	0.644	0.787	0.040	0.182
Q58	30	IB-G	-8.94	1300	0.978	1.014	0.958	0.710	0.131	0.952	0.449	0.300	0.925	0.001	0.009	0.170	0.366	0.496	0.837	0.025	0.111
Q59	60	IB-G	-8.94	1300	0.983	0.969	0.968	0.473	0.029	0.876	0.223	0.158	0.883	-	0.004	0.060	0.178	0.224	0.751	0.012	0.030
Q60	15	IB-G	-11.00	1300	1.011	1.021	1.013	0.692	0.476	0.976	0.821	0.788	0.970	0.066	0.380	0.507	0.703	0.788	0.924	0.369	0.537
Q61	30	IB-G	-11.00	1300	1.035	1.032	1.014	0.349	0.256	0.889	0.525	0.225	1.007	0.014	0.209	0.289	0.473	0.417	0.947	0.196	0.327
Q62	60	IB-G	-11.00	1300	1.016	0.966	1.005	0.146	0.060	0.691	0.287	0.040	0.958	$5{\cdot}10^{-4}$	0.035	0.066	0.190	0.154	0.854	0.046	0.091
Q66	3	SM-2	-0.68	1400	-	-	-	1	1	-	1	-	-	1	1	-	1	-	-	1	-
Q67	15	SM-2	-0.68	1400	-	-	-	0.896	0.980	-	0.991	-	-	0.556	0.422	-	0.981	-	-	0.303	-
Q68	30	SM-2	-0.68	1400	-	-	-	0.776	0.973	-	0.978	-	-	0.302	0.188	-	0.975	-	-	0.115	-
Q69	60	SM-2	-0.68	1400	-	-	-	0.616	0.890	-	0.933	-	-	0.060	0.014	-	0.888	-	-	0.006	-
Q70	3	SM-2	-3.05	1400	-	-	-	1	1	-	1	-	-	1	1	-	1	-	-	1	-

	t (min)	comp	log(fO_2)	T (°C)	Li	P	V	Cu	Zn	Ga	Ge	As	Rb	Ag	Cd	In	Sn	Sb	Cs	Tl	Pb
Q71	15	SM-2	-3.05	1400	-	-	-	0.564	0.893	-	0.937	-	-	0.175	0.063	-	0.809	-	-	0.248	-
Q72	30	SM-2	-3.05	1400	-	-	-	0.461	0.843	-	0.853	-	-	0.058	0.007	-	0.736	-	-	0.050	-
Q73	60	SM-2	-3.05	1400	-	-	-	0.295	0.760	-	0.671	-	-	0.013	0.001	-	0.488	-	-	0.016	-
Q74	3	SM-2	-6.10	1400	-	-	-	1	1	-	1	-	-	1	1	-	1	-	-	1	-
Q75	15	SM-2	-6.10	1400	-	-	-	0.899	0.165	-	0.110	-	-	0.001	0.001	-	0.255	-	-	$2\cdot10^{-4}$	-
Q76	30	SM-2	-6.10	1400	-	-	-	0.723	0.018	-	0.014	-	-	$5\cdot10^{-4}$	0.001	-	0.067	-	-	$1\cdot10^{-4}$	-
Q77	60	SM-2	-6.10	1400	-	-	-	0.416	$4\cdot10^{-4}$	-	$4\cdot10^{-4}$	-	-	0.001	0.006	-	0.002	-	-	$2\cdot10^{-4}$	-
Q78	3	SM-2	-8.01	1400	-	-	-	1	1	-	1	-	-	1	1	-	1	-	-	1	-
Q79	15	SM-2	-8.01	1400	-	-	-	0.627	0.005	-	0.022	-	-	0.038	0.580	-	0.125	-	-	0.001	-
Q80	30	SM-2	-8.01	1400	-	-	-	0.440	0.003	-	0.012	-	-	0.001	0.394	-	0.051	-	-	0.001	-
Q81	60	SM-2	-8.01	1400	-	-	-	0.171	0.002	-	-	-	-	-	0.628	-	0.001	-	-	$1\cdot10^{-4}$	-

Table A4.2: The volatility factors normalized to the shortest experiment in each time series for SM, SM-2, IB and AN. For IB-G it was normalized against the trace element abundance of the starting material. These volatility factors were used to quantify volatility using the modified Hertz-Knudsen-Langmuir equation.
For "comp" SM, IB and AN were doped with the halogen-bearing trace element mix, IB-G is the glassed starting material and SM-2 was doped with a halogen-free trace element mix. For oxygen fugacity a log(fO_2) of -0.68 represents air at 1400°C: log(fO_2) values of -3, -6 and -8 correspond to ΔIW+6.7, ΔIW+3.7 and ΔIW+1.7 respectively. At 1300°C: log(fO_2) values of -7, -9 and -11 correspond to ΔIW+3.8, ΔIW+1.8 and ΔIW-0.2.
The standard deviation on the volatility factors can be found in Table **A4.3**.

	Li	P	V	Cu	Zn	Ga	Ge	As	Rb	Ag	Cd	In	Sn	Sb	Cs	Tl	Pb
Q6	0.048	0.250	0.024	0.023	0.033	0.024	0.027	0.042	0.034	0.031	0.057	0.066	0.045	0.051	0.072	0.080	0.085
Q7	0.049	0.250	0.024	0.023	0.034	0.025	0.028	0.019	0.034	0.009	0.006	0.071	0.048	0.050	0.061	0.011	0.042
Q8	0.049	0.245	0.024	0.023	0.034	0.025	0.027	0.005	0.034	0.002	0.0004	0.071	0.046	0.045	0.054	0.002	0.013
Q9	0.050	0.251	0.025	0.023	0.035	0.026	0.029	0.003	0.034	0.002	0.001	0.075	0.051	0.046	0.046	0.003	0.009
Q22	0.055	0.273	0.028	0.029	0.041	0.031	0.040	0.048	0.039	0.037	0.061	0.055	0.045	0.052	0.057	0.089	0.084
Q23	0.056	0.282	0.029	0.020	0.043	0.033	0.043	0.022	0.039	0.008	0.006	0.057	0.044	0.050	0.052	0.042	0.053
Q24	0.056	0.281	0.029	0.015	0.046	0.033	0.040	0.007	0.039	0.002	0.0004	0.056	0.041	0.047	0.046	0.019	0.022
Q25	0.059	0.289	0.031	0.014	0.040	0.037	0.040	0.001	0.037	0.0002	$4 \cdot 10^{-5}$	0.065	0.042	0.049	0.032	0.017	0.006
Q46	0.071	0.226	0.052	0.075	0.089	0.072	0.078	0.087	0.086	0.105	0.122	0.126	0.131	0.115	0.134	0.253	0.204
Q47	0.062	0.261	0.042	0.035	0.042	0.057	0.041	0.027	0.065	0.007	0.015	0.071	0.033	0.052	0.090	0.106	0.061
Q48	0.062	0.252	0.042	0.015	0.006	0.057	0.011	0.003	0.060	0.001	0.001	0.027	0.007	0.016	0.068	0.024	0.005
Q49	0.063	0.245	0.044	0.014	0.001	0.058	0.001	0.001	0.056	0.0004	0.0003	0.012	0.004	0.008	0.056	-	0.0002
Q14	0.052	0.266	0.035	0.037	0.104	0.039	0.070	0.103	0.050	0.115	0.221	0.110	0.096	0.103	0.082	0.191	0.284
Q15	0.053	0.257	0.036	0.023	0.002	0.040	0.003	0.003	0.039	0.002	0.007	0.003	0.001	0.003	0.034	0.037	0.001
Q16	0.054	0.260	0.038	0.014	0.001	0.041	0.001	0.001	0.027	0.001	0.015	0.0005	0.0003	0.0003	0.013	0.037	0.001
Q20	0.050	0.257	0.031	0.003	0.001	0.030	-	0.001	0.009	0.0004	0.006	0.0002	0.0003	0.0001	0.001	0.023	0.0001
Q10	0.060	0.267	0.028	0.028	0.043	0.029	0.034	0.048	0.047	0.043	0.082	0.095	0.064	0.073	0.103	0.113	0.121
Q11	0.061	0.264	0.029	0.026	0.043	0.031	0.035	0.042	0.045	0.021	0.055	0.093	0.064	0.073	0.083	0.018	0.102
Q12	0.054	0.244	0.030	0.026	0.041	0.033	0.035	0.015	0.043	0.008	0.007	0.079	0.052	0.059	0.083	0.009	0.056
Q13	0.055	0.245	0.030	0.026	0.041	0.034	0.036	0.011	0.044	0.004	0.002	0.081	0.052	0.056	0.077	0.006	0.034
Q26	0.053	0.278	0.023	0.026	0.032	0.026	0.029	0.038	0.025	0.031	0.037	0.032	0.030	0.031	0.025	0.065	0.035
Q27	0.056	0.281	0.023	0.020	0.032	0.029	0.030	0.045	0.026	0.011	0.027	0.038	0.030	0.031	0.026	0.062	0.037
Q28	0.055	0.286	0.023	0.015	0.032	0.028	0.027	0.022	0.026	0.005	0.008	0.040	0.025	0.029	0.027	0.051	0.028
Q29	0.054	0.284	0.023	0.011	0.031	0.029	0.022	0.013	0.027	0.001	0.003	0.041	0.021	0.028	0.027	0.039	0.019
Q50	0.049	0.295	0.023	0.025	0.045	0.039	0.048	0.061	0.041	0.032	0.066	0.058	0.056	0.054	0.059	0.078	0.066
Q51	0.052	0.274	0.029	0.021	0.020	0.042	0.021	0.014	0.046	0.002	0.004	0.037	0.015	0.034	0.064	0.024	0.025
Q52	0.052	0.283	0.031	0.015	0.016	0.045	0.020	0.011	0.053	0.002	0.007	0.030	0.009	0.025	0.075	0.022	0.022
Q53	0.049	0.295	0.024	0.008	0.009	0.039	0.019	0.006	0.045	0.001	0.003	0.021	0.006	0.017	0.062	0.014	0.012
Q17	0.059	0.274	0.043	0.045	0.057	0.049	0.062	0.071	0.063	0.046	0.075	0.098	0.073	0.088	0.104	0.137	0.128
Q18	0.059	0.312	0.046	0.035	0.023	0.051	0.038	0.041	0.058	0.008	0.025	0.044	0.038	0.053	0.084	0.061	0.055
Q19	0.055	0.310	0.037	0.019	0.002	0.041	0.014	0.013	0.047	0.0001	0.002	0.008	0.012	0.020	0.070	0.008	0.006
Q21	0.056	0.298	0.037	0.012	0.003	0.038	0.010	0.008	0.044	0.0001	0.003	0.005	0.008	0.013	0.058	0.010	0.006

	Li	P	V	Cu	Zn	Ga	Ge	As	Rb	Ag	Cd	In	Sn	Sb	Cs	Tl	Pb
Q30	0.056	0.280	0.026	0.032	0.042	0.034	0.039	0.047	0.031	0.041	0.050	0.047	0.041	0.043	0.031	0.057	0.048
Q31	0.057	0.270	0.025	0.030	0.041	0.038	0.038	0.047	0.032	0.035	0.046	0.047	0.042	0.043	0.032	0.093	0.051
Q32	0.056	0.280	0.027	0.029	0.044	0.039	0.038	0.049	0.032	0.022	0.048	0.048	0.043	0.045	0.035	0.063	0.053
Q33	0.051	0.265	0.024	0.019	0.040	0.034	0.033	0.042	0.027	0.009	0.045	0.039	0.034	0.034	0.029	0.044	0.044
Q34	0.051	0.281	0.023	0.020	0.045	0.027	0.032	0.040	0.025	0.026	0.066	0.027	0.028	0.028	0.025	0.007	0.043
Q35	0.051	0.280	0.027	0.023	0.045	0.029	0.040	0.042	0.027	0.022	0.060	0.028	0.029	0.028	0.028	0.022	0.043
Q36	0.053	0.279	0.026	0.021	0.046	0.032	0.029	0.044	0.028	0.012	0.062	0.030	0.030	0.029	0.028	0.006	0.044
Q37	0.053	0.279	0.027	0.019	0.049	0.034	0.037	0.045	0.029	0.006	0.065	0.033	0.032	0.031	0.030	0.003	0.048
Q38	0.056	0.272	0.031	0.039	0.052	0.037	0.039	0.053	0.042	0.050	0.057	0.052	0.058	0.056	0.059	0.087	0.086
Q39	0.056	0.290	0.029	0.056	0.049	0.034	0.037	0.053	0.038	0.140	0.050	0.056	0.048	0.050	0.052	0.054	0.077
Q40	0.059	0.282	0.035	0.027	0.056	0.041	0.048	0.061	0.046	0.009	0.052	0.058	0.057	0.060	0.066	0.059	0.092
Q41	0.061	0.297	0.036	0.022	0.058	0.043	0.050	0.060	0.050	0.004	0.053	0.062	0.061	0.062	0.071	0.068	0.097
Q42	0.057	0.315	0.028	0.029	0.051	0.037	0.041	0.048	0.034	0.044	0.072	0.035	0.037	0.038	0.037	0.061	0.056
Q43	0.057	0.234	0.028	0.025	0.066	0.053	0.065	0.051	0.036	0.011	0.097	0.040	0.040	0.038	0.039	0.062	0.059
Q44	0.058	0.224	0.035	0.029	0.069	0.049	0.061	0.057	0.048	0.005	0.071	0.070	0.067	0.061	0.066	0.263	0.098
Q45	0.062	0.234	0.040	0.019	0.069	0.059	0.093	0.060	0.056	0.001	0.072	0.074	0.075	0.071	0.075	0.040	0.104
Q54	0.031	0.036	0.016	0.037	0.030	0.040	0.033	0.104	0.040	0.058	0.146	0.041	0.056	0.039	0.043	0.130	0.095
Q55	0.025	0.038	0.017	0.023	0.050	0.029	0.026	0.070	0.034	0.011	0.018	0.026	0.040	0.035	0.024	0.007	0.038
Q56	0.026	0.038	0.016	0.028	0.026	0.038	0.034	0.035	0.048	0.014	0.017	0.049	0.055	0.039	0.033	0.007	0.045
Q63	0.029	0.036	0.016	0.036	0.051	0.025	0.154	0.124	0.033	0.004	0.008	0.057	0.140	0.069	0.033	0.009	0.070
Q64	0.027	0.038	0.015	0.022	0.069	0.026	0.112	0.096	0.037	0.001	0.005	0.050	0.088	0.058	0.034	0.008	0.058
Q65	0.028	0.042	0.017	0.016	0.023	0.026	0.052	0.007	0.024	$6{\cdot}10^{-6}$	0.0001	0.031	0.010	0.041	0.027	0.0002	0.008
Q57	0.024	0.035	0.016	0.025	0.053	0.026	0.062	0.059	0.022	0.002	0.006	0.068	0.066	0.072	0.022	0.010	0.037
Q58	0.026	0.037	0.014	0.020	0.032	0.028	0.047	0.031	0.025	0.0002	0.002	0.035	0.052	0.051	0.023	0.006	0.023
Q59	0.026	0.036	0.019	0.014	0.005	0.023	0.059	0.033	0.027	-	0.001	0.008	0.021	0.052	0.030	0.002	0.004
Q60	0.034	0.038	0.026	0.067	0.069	0.060	0.120	0.109	0.066	0.018	0.048	0.097	0.080	0.109	0.061	0.042	0.062
Q61	0.033	0.047	0.018	0.028	0.041	0.054	0.040	0.038	0.042	0.004	0.012	0.045	0.062	0.046	0.032	0.026	0.052
Q62	0.029	0.055	0.018	0.009	0.028	0.088	0.116	0.014	0.052	0.0001	0.010	0.027	0.065	0.055	0.037	0.017	0.033
Q66	-	-	-	0.015	0.024	-	0.010	-	-	0.026	0.073	-	0.011	-	-	0.068	-
Q67	-	-	-	0.015	0.030	-	0.020	-	-	0.047	0.080	-	0.023	-	-	0.040	-
Q68	-	-	-	0.014	0.017	-	0.020	-	-	0.013	0.023	-	0.021	-	-	0.018	-
Q69	-	-	-	0.009	0.032	-	0.018	-	-	0.008	0.005	-	0.019	-	-	0.002	-
Q70	-	-	-	0.066	0.011	-	0.013	-	-	0.035	0.091	-	0.010	-	-	0.046	-

	Li	P	V	Cu	Zn	Ga	Ge	As	Rb	Ag	Cd	In	Sn	Sb	Cs	Tl	Pb
Q71	-	-	-	0.007	0.015	-	0.019	-	-	0.016	0.009	-	0.015	-	-	0.016	-
Q72	-	-	-	0.018	0.037	-	0.035	-	-	0.003	0.0003	-	0.035	-	-	0.001	-
Q73	-	-	-	0.005	0.023	-	0.026	-	-	0.001	0.0002	-	0.020	-	-	0.001	-
Q74	-	-	-	0.005	0.068	-	0.088	-	-	0.014	0.007	-	0.062	-	-	0.009	-
Q75	-	-	-	0.039	0.012	-	0.007	-	-	$7{\cdot}10^{-7}$	$5{\cdot}10^{-6}$	-	0.011	-	-	$2{\cdot}10^{-6}$	-
Q76	-	-	-	0.017	0.002	-	0.003	-	-	$4{\cdot}10^{-6}$	$7{\cdot}10^{-7}$	-	0.006	-	-	$6{\cdot}10^{-7}$	-
Q77	-	-	-	0.010	$5{\cdot}10^{-5}$	-	$2{\cdot}10^{-5}$	-	-	$1{\cdot}10^{-6}$	$3{\cdot}10^{-6}$	-	0.0001	-	-	$1{\cdot}10^{-6}$	-
Q78	-	-	-	0.013	0.013	-	0.062	-	-	0.010	$5{\cdot}10^{-6}$	-	0.031	-	-	0.008	-
Q79	-	-	-	0.013	0.0001	-	0.002	-	-	0.0004	$4{\cdot}10^{-6}$	-	0.012	-	-	$1{\cdot}10^{-5}$	-
Q80	-	-	-	0.015	$7{\cdot}10^{-5}$	-	0.001	-	-	$8{\cdot}10^{-6}$	$2{\cdot}10^{-6}$	-	0.005	-	-	$2{\cdot}10^{-5}$	-
Q81	-	-	-	0.010	$2{\cdot}10^{-5}$	-	-	-	-	-	$3{\cdot}10^{-6}$	-	0.0001	-	-	$9{\cdot}10^{-6}$	-

Table A4.3: The standard deviations (1 s.d.; ppm) for the volatility factors in Table **A4.2**.

	Li	P	V	Cu	Zn	Ga	Ge	As	Rb	Ag	Cd	In	Sn	Sb	Cs	Tl	Pb
Q6	0.963	0.967	0.952	0.912	1.157	0.967	1.006	0.728	0.833	0.449	0.360	1.037	0.938	0.977	0.608	0.008	0.779
Q7	0.956	0.956	0.950	0.885	1.117	0.992	1.008	0.321	0.796	0.121	0.037	1.053	0.946	0.905	0.486	0.001	0.360
Q8	0.925	0.932	0.938	0.868	1.099	0.961	0.969	0.087	0.764	0.023	0.002	1.006	0.885	0.781	0.411	0.0001	0.106
Q9	0.910	0.945	0.934	0.824	1.063	0.959	0.980	0.047	0.727	0.023	0.003	0.988	0.904	0.736	0.328	0.0002	0.069
Q22	0.957	0.917	0.925	0.710	1.075	0.948	0.949	0.957	0.884	0.512	0.008	0.980	0.913	0.942	0.741	0.001	0.987
Q23	0.944	0.940	0.913	0.478	1.052	0.942	0.953	0.425	0.847	0.105	0.059	0.947	0.852	0.868	0.630	0.0003	0.579
Q24	0.923	0.935	0.911	0.338	1.092	0.924	0.863	0.132	0.811	0.005	0.001	0.910	0.760	0.785	0.542	0.0001	0.233
Q25	0.932	0.954	0.923	0.316	0.892	0.973	0.808	0.023	0.721	0.002	0.0001	0.975	0.737	0.771	0.349	0.0001	0.055
Q46	0.963	0.899	0.919	0.748	0.974	0.936	0.939	0.706	0.847	0.502	0.528	0.894	0.850	0.857	0.687	0.002	0.816
Q47	0.959	0.909	0.932	0.450	0.620	0.961	0.657	0.288	0.843	0.055	0.106	0.706	0.290	0.539	0.617	0.001	0.360
Q48	0.959	0.909	0.915	0.192	0.074	0.938	0.135	0.020	0.756	0.008	0.003	0.266	0.059	0.156	0.463	0.0002	0.024
Q49	0.964	0.904	0.936	0.169	0.003	0.928	0.009	0.002	0.686	0.001	0.0004	0.110	0.031	0.074	0.366	-	0.001
Q14	0.935	0.936	0.928	0.772	0.080	0.859	0.222	0.103	0.697	0.014	0.002	0.122	0.110	0.139	0.407	0.0002	0.018
Q15	0.939	0.904	0.932	0.472	0.003	0.845	0.016	0.005	0.527	0.001	0.0001	0.005	0.002	0.007	0.160	$2{\cdot}10^{-5}$	0.0001
Q16	0.927	0.909	0.925	0.263	0.002	0.816	0.002	0.001	0.346	0.0003	0.0002	0.001	0.001	0.001	0.056	$2{\cdot}10^{-5}$	0.0002
Q20	0.920	0.899	0.936	0.077	0.002	0.758	-	0.001	0.141	0.0001	0.0001	0.0004	0.001	0.0002	0.004	$8{\cdot}10^{-6}$	$2{\cdot}10^{-5}$
Q10	0.973	0.956	0.969	0.969	1.074	0.928	0.952	0.540	0.932	0.505	0.406	0.994	0.821	0.864	0.746	0.018	0.818
Q11	0.949	0.938	0.969	0.896	1.018	0.943	0.918	0.452	0.857	0.235	0.254	0.916	0.774	0.810	0.565	0.003	0.654
Q12	0.966	0.890	0.985	0.857	1.064	0.987	0.878	0.159	0.908	0.100	0.039	0.967	0.762	0.766	0.709	0.001	0.431
Q13	0.973	0.889	0.979	0.833	1.027	0.970	0.865	0.109	0.891	0.054	0.013	0.972	0.735	0.708	0.644	0.001	0.256
Q26	0.970	0.908	0.981	0.716	1.059	0.949	0.921	0.576	0.852	0.446	0.270	0.727	0.759	0.861	0.676	0.002	0.921
Q27	1.022	0.920	0.960	0.534	1.042	1.006	0.921	0.663	0.877	0.156	0.185	0.848	0.738	0.835	0.689	0.001	0.950
Q28	1.003	0.935	0.976	0.383	1.007	0.952	0.845	0.357	0.873	0.062	0.053	0.835	0.614	0.750	0.700	0.001	0.715
Q29	0.985	0.927	0.963	0.290	0.946	0.970	0.687	0.175	0.861	0.013	0.012	0.829	0.478	0.969	0.680	0.001	0.431
Q50	0.992	0.910	0.952	0.763	1.005	0.952	0.801	0.295	0.877	0.243	0.059	0.903	0.595	0.810	0.707	0.003	0.810
Q51	0.981	0.903	0.967	0.426	0.401	0.941	0.410	0.103	0.863	0.007	0.001	0.543	0.158	0.529	0.689	0.001	0.232
Q52	0.976	0.945	0.955	0.256	0.284	0.912	0.366	0.070	0.865	0.007	0.003	0.378	0.072	0.313	0.704	0.0004	0.134
Q53	0.966	0.919	0.938	0.200	0.169	0.869	0.250	0.039	0.844	0.002	0.001	0.284	0.052	0.225	0.651	0.0002	0.113
Q17	0.978	0.773	0.939	0.943	0.926	0.865	0.903	0.759	0.871	0.535	0.035	0.514	0.738	0.822	0.656	0.002	0.779
Q18	0.934	0.875	0.957	0.681	0.348	0.853	0.519	0.394	0.764	0.080	0.011	0.218	0.366	0.466	0.501	0.001	0.297
Q19	0.981	0.888	0.980	0.487	0.049	0.909	0.313	0.219	0.824	0.001	0.001	0.057	0.159	0.232	0.567	0.0001	0.043
Q21	0.966	0.846	0.967	0.299	0.046	0.802	0.131	0.073	0.736	0.001	0.001	0.034	0.094	0.118	0.452	0.0002	0.042

	Li	P	V	Cu	Zn	Ga	Ge	As	Rb	Ag	Cd	In	Sn	Sb	Cs	Tl	Pb
Q30	1.019	0.997	1.023	0.815	1.076	0.848	1.035	1.041	0.934	0.863	1.211	0.890	0.984	0.988	0.826	0.019	1.031
Q31	1.012	0.960	0.957	0.737	1.037	0.942	0.994	1.010	0.943	0.705	1.098	0.967	0.980	0.982	0.874	0.030	1.059
Q32	0.980	0.994	0.973	0.672	1.050	0.912	0.931	1.016	0.904	0.416	1.069	0.923	0.951	0.965	0.848	0.019	1.029
Q33	0.968	0.936	0.965	0.535	1.048	0.925	0.971	1.004	0.885	0.203	1.030	0.961	0.963	0.935	0.809	0.017	1.040
Q34	0.993	0.977	0.936	0.776	1.039	0.912	1.128	0.994	0.910	0.762	1.130	1.008	0.957	0.976	0.850	0.155	1.033
Q35	0.975	0.953	0.990	0.690	1.039	0.879	1.051	1.020	0.869	0.471	1.098	0.913	0.922	0.921	0.790	0.073	1.029
Q36	1.007	0.950	0.959	0.614	1.045	0.956	0.866	1.055	0.879	0.258	1.100	0.933	0.926	0.939	0.771	0.021	1.027
Q37	0.988	0.947	0.979	0.553	1.046	0.975	0.978	1.043	0.893	0.111	1.091	0.984	0.947	0.949	0.799	0.007	1.046
Q38	0.975	0.889	0.901	0.640	0.972	0.835	0.933	0.977	0.823	0.621	1.061	1.069	0.834	0.862	0.750	0.091	0.998
Q39	0.970	0.874	0.911	0.420	0.983	0.864	0.902	0.937	0.842	0.207	1.140	0.902	0.937	0.892	0.782	0.136	1.011
Q40	0.987	0.936	0.953	0.260	0.968	0.871	0.963	1.000	0.862	0.032	0.941	0.876	0.828	0.857	0.782	0.081	0.940
Q41	1.012	0.999	0.948	0.201	0.959	0.864	0.941	0.949	0.877	0.012	0.902	0.866	0.828	0.835	0.786	0.087	0.921
Q42	1.005	1.064	0.977	0.884	0.993	0.821	0.792	0.977	0.893	0.365	1.053	0.969	0.943	0.906	0.811	0.023	0.982
Q43	0.988	0.883	0.936	0.750	1.013	0.940	1.112	1.006	0.901	0.084	1.049	0.963	0.977	0.941	0.818	0.023	0.996
Q44	0.946	0.921	0.913	0.535	0.914	0.814	0.916	0.888	0.811	0.022	0.770	0.919	0.845	0.823	0.715	0.053	0.837
Q45	0.987	0.878	0.965	0.323	0.872	0.921	1.073	0.885	0.862	0.003	0.740	0.872	0.857	0.884	0.732	0.007	0.808
Q54	0.962	0.974	1.011	0.937	1.034	1.010	0.970	0.706	0.944	0.621	0.492	0.980	0.964	0.931	0.906	0.250	0.737
Q55	0.946	0.964	0.997	0.872	0.971	0.986	0.951	0.519	0.924	0.259	0.102	0.963	0.939	0.895	0.860	0.039	0.467
Q56	0.963	0.959	1.007	0.873	1.002	0.975	0.919	0.411	0.895	0.134	0.055	0.941	0.920	0.860	0.805	0.025	0.357
Q63	0.963	0.985	1.008	0.775	0.810	0.957	0.682	0.300	0.911	0.040	0.015	0.819	0.560	0.778	0.849	0.028	0.467
Q64	0.943	0.960	1.003	0.757	0.637	0.979	0.625	0.241	0.926	0.005	0.009	0.760	0.434	0.738	0.851	0.020	0.337
Q65	0.952	1.018	1.005	0.571	0.112	1.025	0.235	0.039	0.936	0.0002	0.0002	0.338	0.087	0.398	0.845	0.001	0.034
Q57	0.930	0.975	1.001	0.843	0.230	0.998	0.540	0.298	0.870	0.004	0.016	0.345	0.503	0.610	0.761	0.032	0.151
Q58	0.936	0.985	0.977	0.636	0.138	0.948	0.440	0.244	0.895	0.001	0.006	0.170	0.344	0.470	0.809	0.020	0.092
Q59	0.940	0.941	0.987	0.423	0.031	0.872	0.219	0.129	0.860	-	0.003	0.060	0.167	0.212	0.725	0.010	0.025
Q60	0.968	0.993	1.033	0.620	0.502	0.971	0.805	0.644	0.938	0.054	0.270	0.507	0.658	0.746	0.893	0.291	0.445
Q61	0.990	1.003	1.035	0.312	0.270	0.887	0.515	0.184	0.973	0.011	0.149	0.288	0.442	0.396	0.916	0.155	0.272
Q62	0.972	0.939	1.024	0.131	0.064	0.689	0.280	0.033	0.926	0.0004	0.025	0.066	0.178	0.145	0.826	0.036	0.075
Q66	-	-	-	0.685	1.074	-	0.803	-	-	0.589	0.709	-	0.782	-	-	0.357	-
Q67	-	-	-	0.614	1.053	-	0.796	-	-	0.328	0.299	-	0.767	-	-	0.108	-
Q68	-	-	-	0.531	1.045	-	0.786	-	-	0.177	0.133	-	0.762	-	-	0.041	-
Q69	-	-	-	0.422	0.957	-	0.750	-	-	0.035	0.010	-	0.694	-	-	0.002	-
Q70	-	-	-	0.614	1.036	-	0.780	-	-	0.509	0.404	-	0.751	-	-	0.274	-

	Li	P	V	Cu	Zn	Ga	Ge	As	Rb	Ag	Cd	In	Sn	Sb	Cs	Tl	Pb
Q71	-	-	-	0.346	0.925	-	0.731	-	-	0.089	0.026	-	0.608	-	-	0.068	-
Q72	-	-	-	0.283	0.874	-	0.666	-	-	0.029	0.003	-	0.553	-	-	0.014	-
Q73	-	-	-	0.181	0.788	-	0.523	-	-	0.006	0.0005	-	0.367	-	-	0.004	-
Q74	-	-	-	0.668	0.696	-	0.493	-	-	0.029	0.005	-	0.498	-	-	0.009	-
Q75	-	-	-	0.601	0.115	-	0.054	-	-	$2{\cdot}10^{-5}$	$8{\cdot}10^{-6}$	-	0.127	-	-	$3{\cdot}10^{-6}$	-
Q76	-	-	-	0.483	0.013	-	0.007	-	-	$1{\cdot}10^{-5}$	$6{\cdot}10^{-6}$	-	0.033	-	-	$1{\cdot}10^{-6}$	-
Q77	-	-	-	0.278	0.0003	-	0.0002	-	-	$2{\cdot}10^{-5}$	$4{\cdot}10^{-5}$	-	0.001	-	-	$3{\cdot}10^{-6}$	-
Q78	-	-	-	0.656	0.085	-	0.158	-	-	0.020	$1{\cdot}10^{-5}$	-	0.357	-	-	0.023	-
Q79	-	-	-	0.411	0.0004	-	0.004	-	-	0.001	$8{\cdot}10^{-6}$	-	0.044	-	-	$3{\cdot}10^{-5}$	-
Q80	-	-	-	0.289	0.0002	-	0.002	-	-	$2{\cdot}10^{-5}$	$6{\cdot}10^{-6}$	-	0.018	-	-	$2{\cdot}10^{-5}$	-
Q81	-	-	-	0.112	0.0002	-	-	-	-	-	$8{\cdot}10^{-6}$	-	0.001	-	-	$3{\cdot}10^{-6}$	-

Table A4.4: The volatility factors as normalized to the starting trace element abundances in Table **2.2**. These volatility factors were used to construct the time, fO_2 and compositional dependence figures in Sections **4.2.2** – **4.2.4**.

	Li	P	V	Cu	Zn	Ga	Ge	As	Rb	Ag	Cd	In	Sn	Sb	Cs	Tl	Pb
Q6	0.034	0.175	0.019	0.018	0.029	0.019	0.022	0.023	0.022	0.011	0.015	0.050	0.031	0.036	0.031	0.0005	0.047
Q7	0.036	0.176	0.019	0.018	0.030	0.020	0.023	0.010	0.022	0.003	0.002	0.056	0.035	0.038	0.028	0.0001	0.025
Q8	0.036	0.174	0.019	0.018	0.031	0.020	0.023	0.003	0.023	0.001	0.0001	0.057	0.034	0.035	0.025	$1\cdot10^{-5}$	0.008
Q9	0.038	0.180	0.020	0.018	0.033	0.021	0.025	0.002	0.024	0.001	0.0002	0.064	0.039	0.037	0.023	$2\cdot10^{-5}$	0.006
Q22	0.038	0.181	0.020	0.016	0.033	0.023	0.029	0.034	0.026	0.014	0.032	0.040	0.030	0.036	0.031	$4\cdot10^{-5}$	0.060
Q23	0.041	0.183	0.022	0.017	0.036	0.025	0.032	0.037	0.028	0.016	0.039	0.044	0.034	0.040	0.035	$5\cdot10^{-5}$	0.067
Q24	0.041	0.188	0.022	0.008	0.038	0.025	0.030	0.005	0.027	0.001	0.0003	0.043	0.029	0.035	0.027	$1\cdot10^{-5}$	0.017
Q25	0.044	0.194	0.024	0.008	0.035	0.029	0.031	0.001	0.027	0.0001	$3\cdot10^{-5}$	0.052	0.032	0.038	0.019	$1\cdot10^{-5}$	0.004
Q46	0.050	0.148	0.035	0.041	0.062	0.048	0.053	0.044	0.052	0.037	0.050	0.083	0.079	0.070	0.065	0.0004	0.118
Q47	0.036	0.187	0.019	0.011	0.016	0.023	0.015	0.008	0.022	0.001	0.003	0.021	0.009	0.014	0.020	0.0001	0.013
Q48	0.037	0.178	0.020	0.005	0.003	0.025	0.005	0.001	0.022	0.0003	0.001	0.009	0.002	0.005	0.017	$3\cdot10^{-5}$	0.001
Q49	0.038	0.170	0.022	0.005	0.001	0.028	0.001	0.0004	0.024	0.0002	0.0002	0.005	0.001	0.003	0.017	-	0.0001
Q14	0.035	0.180	0.025	0.021	0.011	0.025	0.015	0.012	0.025	0.003	0.001	0.013	0.012	0.014	0.024	$2\cdot10^{-5}$	0.008
Q15	0.037	0.175	0.026	0.014	0.0002	0.026	0.001	0.0003	0.020	$4\cdot10^{-5}$	$3\cdot10^{-5}$	0.0003	0.0001	0.0004	0.010	$5\cdot10^{-6}$	$1\cdot10^{-5}$
Q16	0.039	0.178	0.028	0.008	0.0002	0.028	0.0002	0.0002	0.015	$2\cdot10^{-5}$	0.0001	0.0001	$4\cdot10^{-5}$	$5\cdot10^{-5}$	0.004	$6\cdot10^{-6}$	$3\cdot10^{-5}$
Q20	0.034	0.174	0.019	0.002	0.0001	0.017	-	0.0001	0.004	$1\cdot10^{-5}$	$3\cdot10^{-5}$	$2\cdot10^{-5}$	$3\cdot10^{-5}$	$2\cdot10^{-5}$	0.0002	$4\cdot10^{-6}$	$3\cdot10^{-6}$
Q10	0.043	0.297	0.034	0.023	0.041	0.022	0.027	0.020	0.032	0.016	0.024	0.073	0.044	0.050	0.056	0.001	0.071
Q11	0.045	0.298	0.036	0.023	0.042	0.024	0.028	0.018	0.033	0.008	0.017	0.075	0.046	0.052	0.048	0.0003	0.063
Q12	0.034	0.268	0.037	0.023	0.037	0.026	0.029	0.007	0.029	0.003	0.001	0.048	0.031	0.035	0.036	0.0001	0.027
Q13	0.035	0.271	0.038	0.023	0.038	0.027	0.030	0.005	0.030	0.001	0.001	0.051	0.032	0.035	0.035	0.0001	0.017
Q26	0.038	0.295	0.030	0.016	0.031	0.021	0.023	0.017	0.017	0.011	0.008	0.019	0.021	0.023	0.014	0.0001	0.025
Q27	0.040	0.298	0.029	0.013	0.032	0.023	0.024	0.020	0.018	0.004	0.006	0.024	0.021	0.023	0.015	0.0001	0.027
Q28	0.040	0.304	0.031	0.009	0.033	0.023	0.021	0.010	0.019	0.002	0.002	0.025	0.018	0.022	0.016	0.0001	0.021
Q29	0.040	0.301	0.031	0.007	0.032	0.024	0.018	0.006	0.019	0.0004	0.001	0.026	0.015	0.022	0.016	0.0001	0.014
Q50	0.036	0.313	0.029	0.017	0.039	0.029	0.031	0.016	0.027	0.005	0.003	0.041	0.028	0.035	0.031	0.0002	0.036
Q51	0.040	0.268	0.039	0.016	0.019	0.033	0.012	0.003	0.033	0.0004	0.0003	0.028	0.008	0.022	0.036	0.0001	0.015
Q52	0.041	0.273	0.043	0.011	0.015	0.037	0.012	0.003	0.040	0.0004	0.0004	0.024	0.005	0.018	0.046	0.001	0.015
Q53	0.036	0.310	0.031	0.005	0.009	0.031	0.014	0.002	0.032	0.0001	0.0002	0.016	0.003	0.012	0.036	$4\cdot10^{-5}$	0.008
Q17	0.043	0.247	0.048	0.035	0.045	0.032	0.044	0.038	0.040	0.017	0.002	0.039	0.045	0.057	0.050	0.0002	0.068
Q18	0.044	0.283	0.053	0.028	0.019	0.035	0.028	0.024	0.039	0.003	0.001	0.018	0.025	0.036	0.043	0.0001	0.031
Q19	0.036	0.275	0.032	0.011	0.001	0.020	0.006	0.005	0.021	$4\cdot10^{-5}$	0.0001	0.002	0.005	0.008	0.020	$1\cdot10^{-5}$	0.002
Q21	0.038	0.268	0.033	0.007	0.002	0.020	0.006	0.004	0.021	$5\cdot10^{-5}$	0.0001	0.001	0.004	0.007	0.019	$2\cdot10^{-5}$	0.003

	Li	P	V	Cu	Zn	Ga	Ge	As	Rb	Ag	Cd	In	Sn	Sb	Cs	Tl	Pb
Q30	0.042	0.203	0.022	0.020	0.033	0.022	0.030	0.036	0.022	0.027	0.044	0.033	0.030	0.031	0.020	0.001	0.037
Q31	0.042	0.196	0.021	0.019	0.033	0.025	0.030	0.037	0.023	0.023	0.042	0.033	0.031	0.033	0.021	0.001	0.040
Q32	0.043	0.202	0.022	0.019	0.037	0.027	0.031	0.040	0.024	0.015	0.045	0.035	0.034	0.036	0.023	0.001	0.043
Q33	0.036	0.193	0.019	0.010	0.031	0.020	0.023	0.029	0.018	0.005	0.042	0.021	0.021	0.020	0.018	0.001	0.030
Q34	0.037	0..204	0.019	0.016	0.033	0.021	0.025	0.030	0.020	0.020	0.048	0.022	0.022	0.022	0.019	0.005	0.032
Q35	0.037	0.198	0.020	0.014	0.035	0.021	0.034	0.032	0.020	0.013	0.051	0.022	0.022	0.022	0.019	0.003	0.034
Q36	0.039	0.197	0.020	0.013	0.037	0.024	0.024	0.034	0.021	0.007	0.054	0.023	0.023	0.023	0.019	0.001	0.036
Q37	0.040	0.197	0.021	0.012	0.040	0.026	0.033	0.035	0.022	0.004	0.059	0.026	0.025	0.025	0.021	0.0003	0.040
Q38	0.040	0.173	0.022	0.012	0.038	0.024	0.026	0.037	0.027	0.008	0.048	0.034	0.039	0.036	0.033	0.008	0.062
Q39	0.039	0.191	0.020	0.017	0.033	0.021	0.023	0.035	0.023	0.020	0.039	0.035	0.030	0.030	0.028	0.005	0.052
Q40	0.042	0.173	0.026	0.009	0.043	0.029	0.034	0.044	0.032	0.002	0.047	0.042	0.043	0.042	0.041	0.006	0.074
Q41	0.045	0.180	0.027	0.008	0.046	0.031	0.037	0.045	0.036	0.001	0.049	0.046	0.047	0.045	0.046	0.008	0.081
Q42	0.041	0.260	0.022	0.020	0.032	0.023	0.023	0.034	0.023	0.012	0.045	0.025	0.026	0.027	0.023	0.001	0.040
Q43	0.042	0.186	0.022	0.018	0.045	0.035	0.039	0.038	0.025	0.003	0.066	0.029	0.029	0.027	0.024	0.001	0.044
Q44	0.045	0.160	0.030	0.024	0.050	0.035	0.039	0.048	0.039	0.002	0.049	0.060	0.059	0.054	0.051	0.006	0.091
Q45	0.049	0.172	0.035	0.016	0.051	0.043	0.063	0.051	0.046	0.0004	0.051	0.065	0.067	0.063	0.059	0.001	0.097
Q54	0.031	0.036	0.016	0.037	0.030	0.040	0.033	0.104	0.040	0.058	0.146	0.041	0.056	0.039	0.043	0.130	0.095
Q55	0.025	0.038	0.017	0.023	0.050	0.029	0.026	0.070	0.034	0.011	0.018	0.026	0.040	0.035	0.024	0.007	0.038
Q56	0.026	0.038	0.016	0.028	0.026	0.038	0.034	0.035	0.048	0.014	0.017	0.049	0.055	0.039	0.033	0.007	0.045
Q63	0.029	0.036	0.016	0.036	0.051	0.025	0.154	0.124	0.033	0.004	0.008	0.057	0.140	0.069	0.033	0.009	0.070
Q64	0.027	0.038	0.015	0.022	0.069	0.026	0.112	0.096	0.037	0.001	0.005	0.050	0.088	0.058	0.034	0.008	0.058
Q65	0.028	0.042	0.017	0.016	0.023	0.026	0.052	0.007	0.024	$6{\cdot}10^{-6}$	0.0001	0.031	0.010	0.041	0.027	0.0002	0.008
Q57	0.024	0.035	0.016	0.025	0.053	0.026	0.062	0.059	0.022	0.002	0.006	0.068	0.066	0.072	0.022	0.010	0.037
Q58	0.026	0.037	0.014	0.020	0.032	0.028	0.047	0.031	0.025	0.0002	0.002	0.035	0.052	0.051	0.023	0.006	0.023
Q59	0.026	0.036	0.019	0.014	0.005	0.023	0.059	0.033	0.027	-	0.001	0.008	0.021	0.052	0.030	0.002	0.004
Q60	0.034	0.038	0.026	0.067	0.069	0.060	0.120	0.109	0.066	0.018	0.048	0.097	0.080	0.109	0.061	0.042	0.062
Q61	0.033	0.047	0.018	0.028	0.041	0.054	0.040	0.038	0.042	0.004	0.012	0.045	0.062	0.046	0.032	0.026	0.052
Q62	0.029	0.055	0.018	0.009	0.028	0.088	0.116	0.014	0.052	0.0001	0.010	0.027	0.065	0.055	0.037	0.017	0.033
Q66	-	-	-	0.015	0.024	-	0.010	-	-	0.026	0.073	-	0.011	-	-	0.068	-
Q67	-	-	-	0.015	0.030	-	0.020	-	-	0.047	0.080	-	0.023	-	-	0.040	-
Q68	-	-	-	0.014	0.017	-	0.020	-	-	0.013	0.023	-	0.021	-	-	0.018	-
Q69	-	-	-	0.009	0.032	-	0.018	-	-	0.008	0.005	-	0.019	-	-	0.002	-
Q70	-	-	-	0.066	0.011	-	0.013	-	-	0.035	0.091	-	0.010	-	-	0.046	-

	Li	P	V	Cu	Zn	Ga	Ge	As	Rb	Ag	Cd	In	Sn	Sb	Cs	Tl	Pb
Q71	-	-	-	0.007	0.015	-	0.019	-	-	0.016	0.009	-	0.015	-	-	0.016	-
Q72	-	-	-	0.018	0.037	-	0.035	-	-	0.003	0.0003	-	0.035	-	-	0.001	-
Q73	-	-	-	0.005	0.023	-	0.026	-	-	0.001	0.0002	-	0.020	-	-	0.001	-
Q74	-	-	-	0.005	0.068	-	0.088	-	-	0.014	0.007	-	0.062	-	-	0.009	-
Q75	-	-	-	0.039	0.012	-	0.007	-	-	$7{\cdot}10^{-7}$	$5{\cdot}10^{-6}$	-	0.011	-	-	$2{\cdot}10^{-6}$	-
Q76	-	-	-	0.017	0.002	-	0.003	-	-	$4{\cdot}10^{-6}$	$7{\cdot}10^{-7}$	-	0.006	-	-	$6{\cdot}10^{-7}$	-
Q77	-	-	-	0.010	0.0001	-	$2{\cdot}10^{-5}$	-	-	$1{\cdot}10^{-6}$	$3{\cdot}10^{-6}$	-	0.0001	-	-	$1{\cdot}10^{-6}$	-
Q78	-	-	-	0.013	0.013	-	0.062	-	-	0.010	$5{\cdot}10^{-6}$	-	0.031	-	-	0.008	-
Q79	-	-	-	0.013	0.0001	-	0.002	-	-	0.0004	$4{\cdot}10^{-6}$	-	0.012	-	-	$1{\cdot}10^{-5}$	-
Q80	-	-	-	0.015	0.0001	-	0.001	-	-	$8{\cdot}10^{-6}$	$2{\cdot}10^{-6}$	-	0.005	-	-	$2{\cdot}10^{-5}$	-
Q81	-	-	-	0.010	$2{\cdot}10^{-5}$	-	-	-	-	-	$3{\cdot}10^{-6}$	-	0.0001	-	-	$9{\cdot}10^{-6}$	-

Table A4.5: The standard deviations (1 s.d.; ppm) for the volatility factors in Table **A4.4**.

Appendix 5 – Element-Specific Time Series Plots of Volatility

A5.1 – Lithium

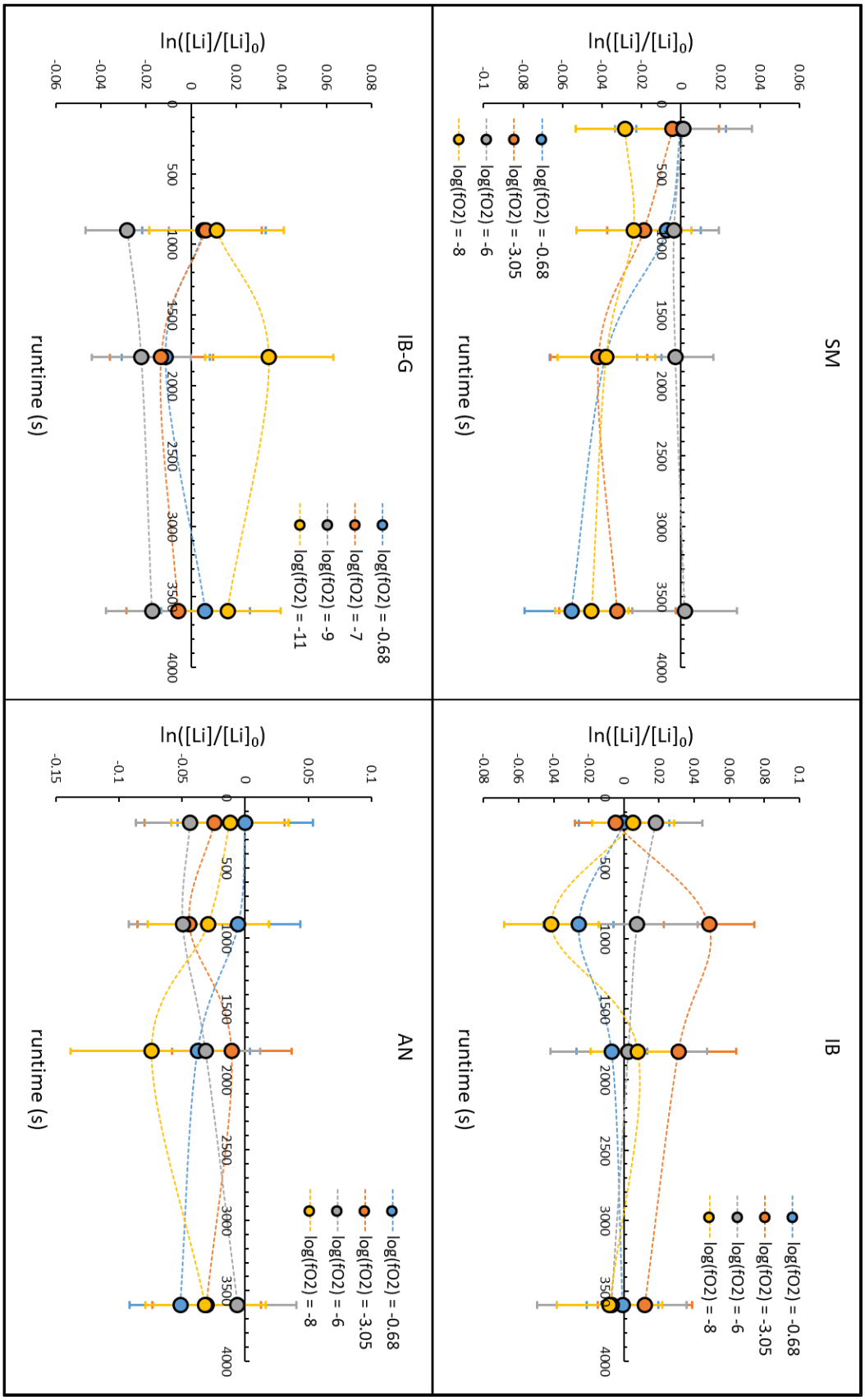


Figure A5.1: Temporal evolution of the volatility factor for Li in all compositions.

A5.2 – Phosphorus

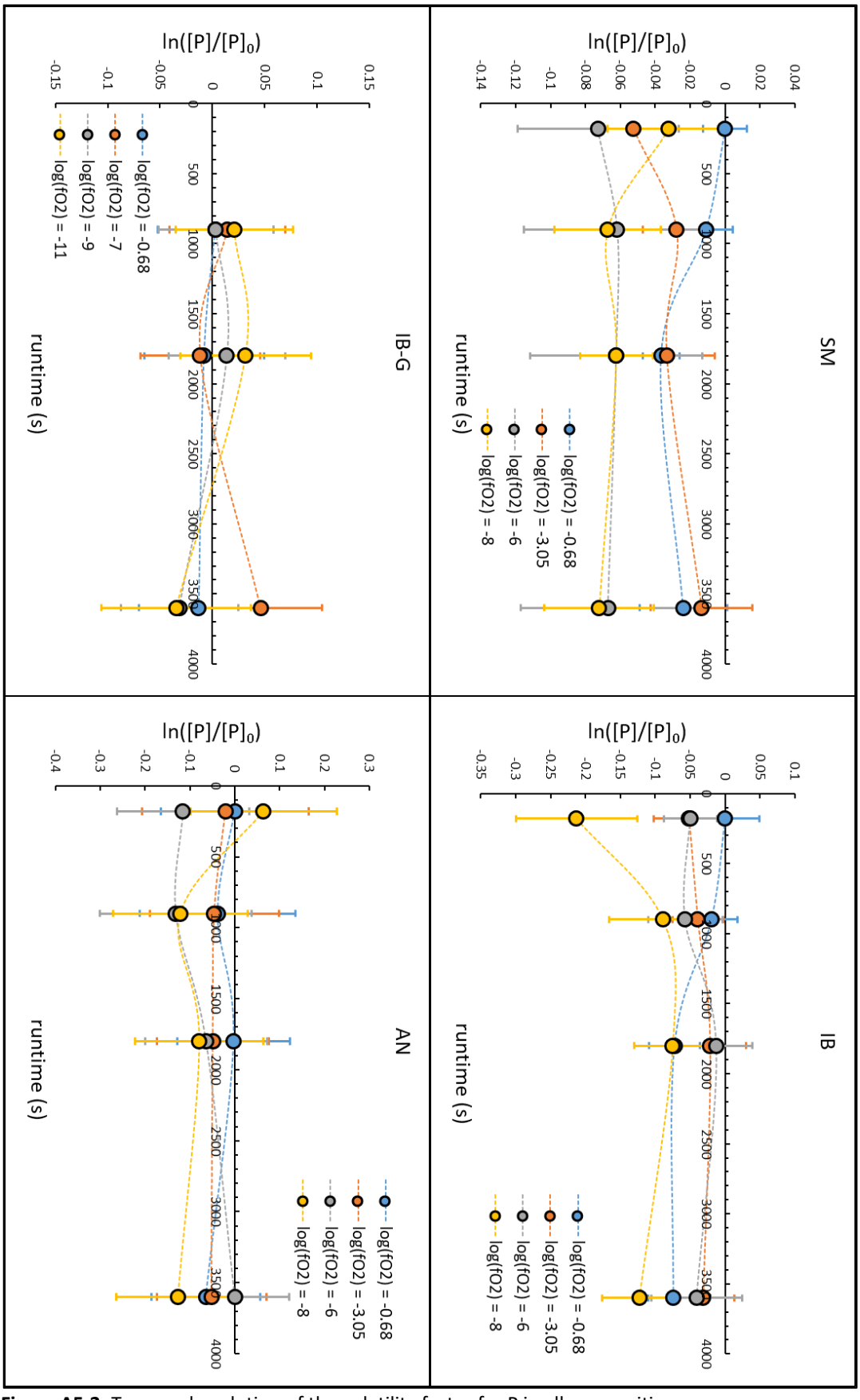


Figure A5.2: Temporal evolution of the volatility factor for P in all compositions.

A5.3 – Vanadium

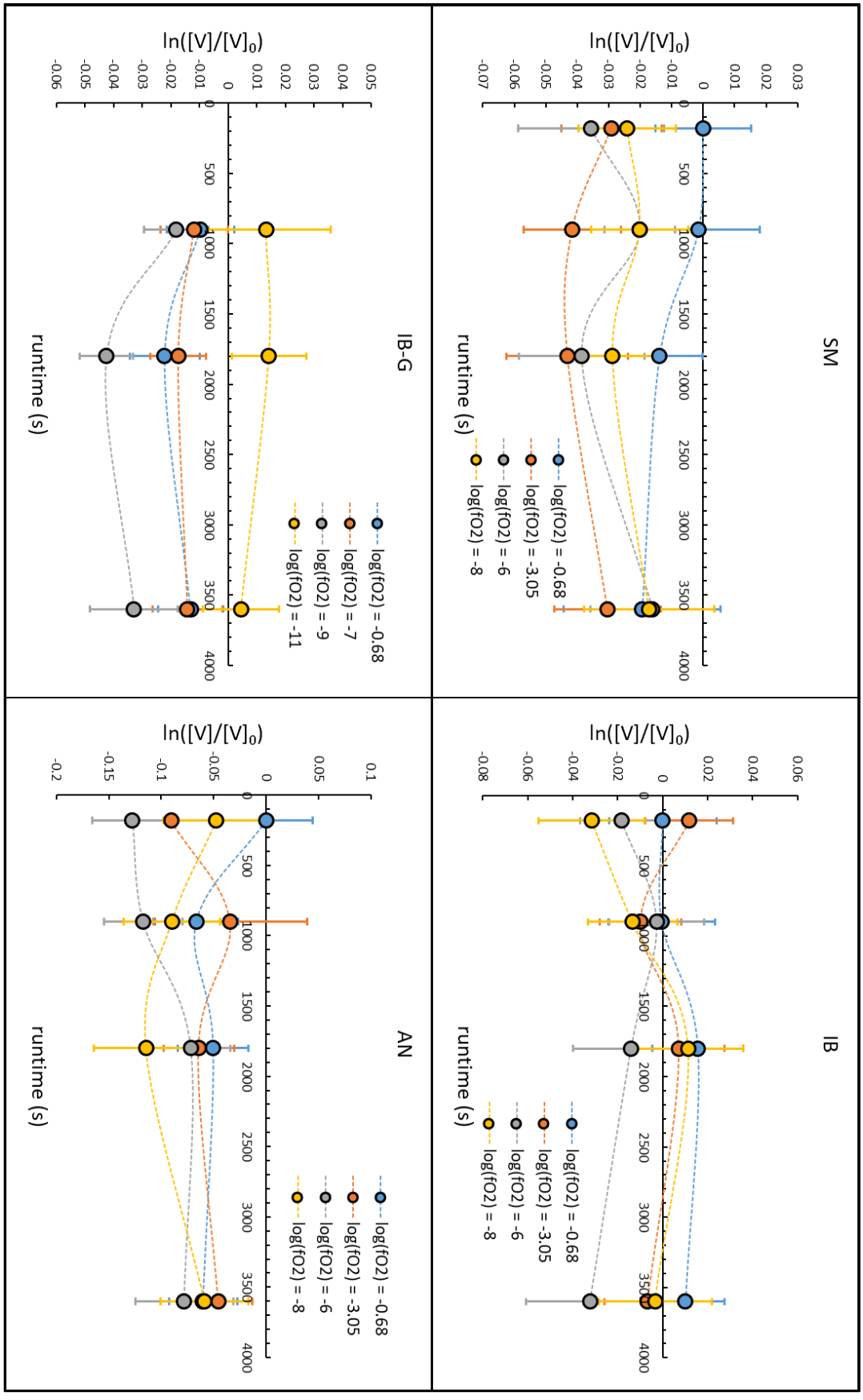
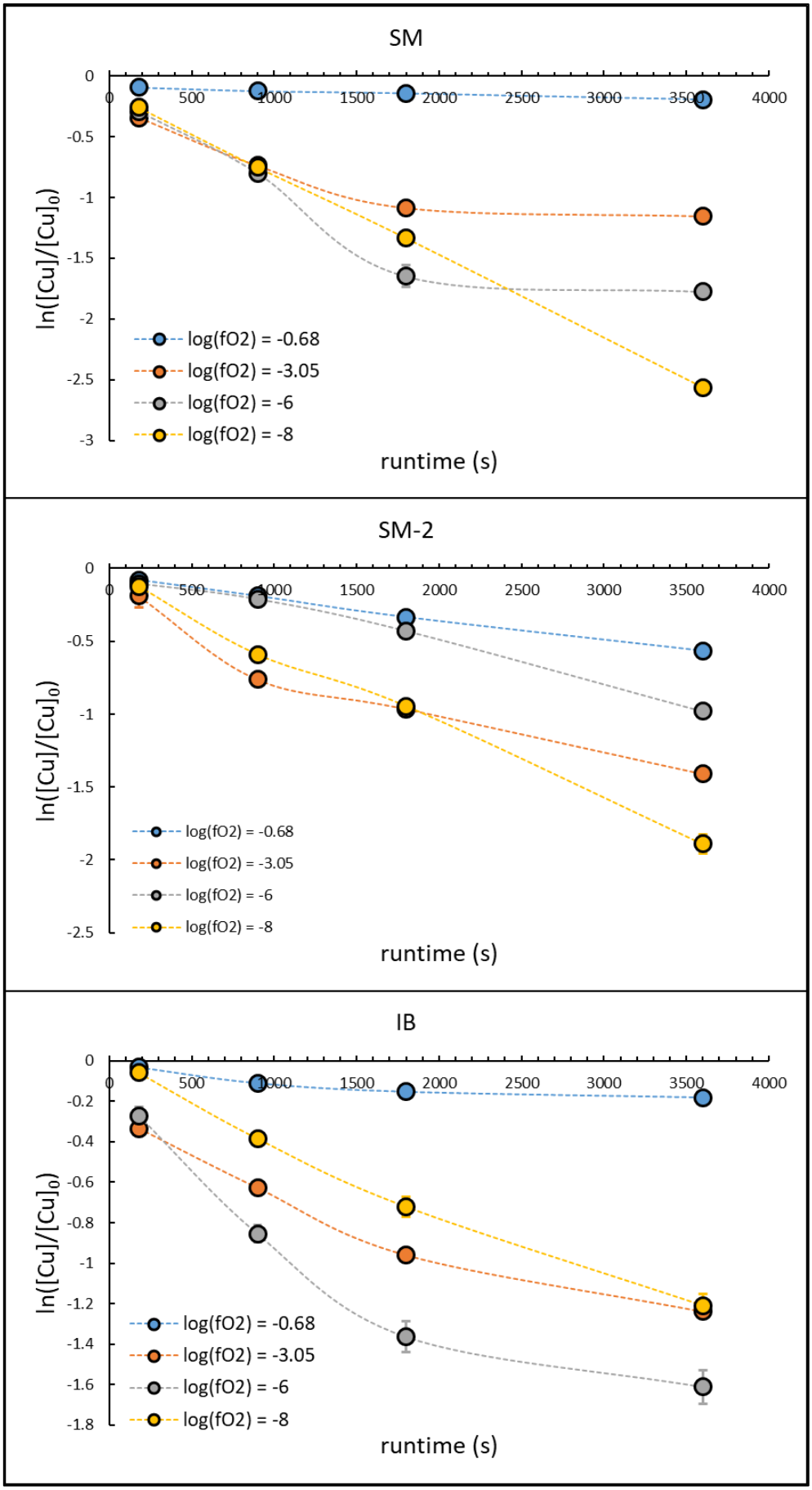


Figure A5.3: Temporal evolution of the volatility factor for V in all compositions.

A5.4 – Copper


SM
ln([Cu]/[Cu]0)
runtime (s)
log(fO2) = -0.68
log(fO2) = -3.05
log(fO2) = -6
log(fO2) = -8
SM-2
ln([Cu]/[Cu]0)
runtime (s)
log(fO2) = -0.68
log(fO2) = -3.05
log(fO2) = -6
log(fO2) = -8
IB
ln([Cu]/[Cu]0)
runtime (s)
log(fO2) = -0.68
log(fO2) = -3.05
log(fO2) = -6
log(fO2) = -8

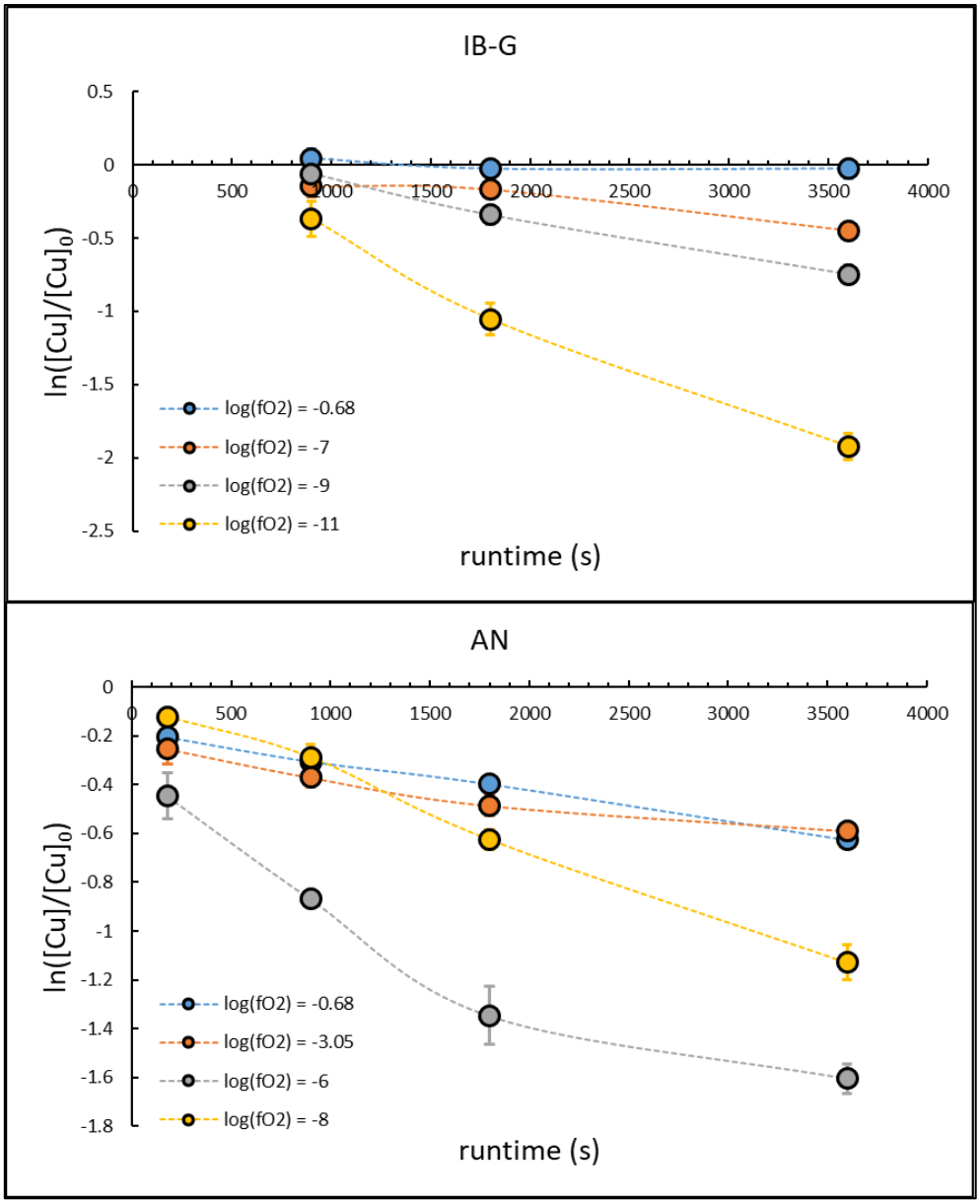
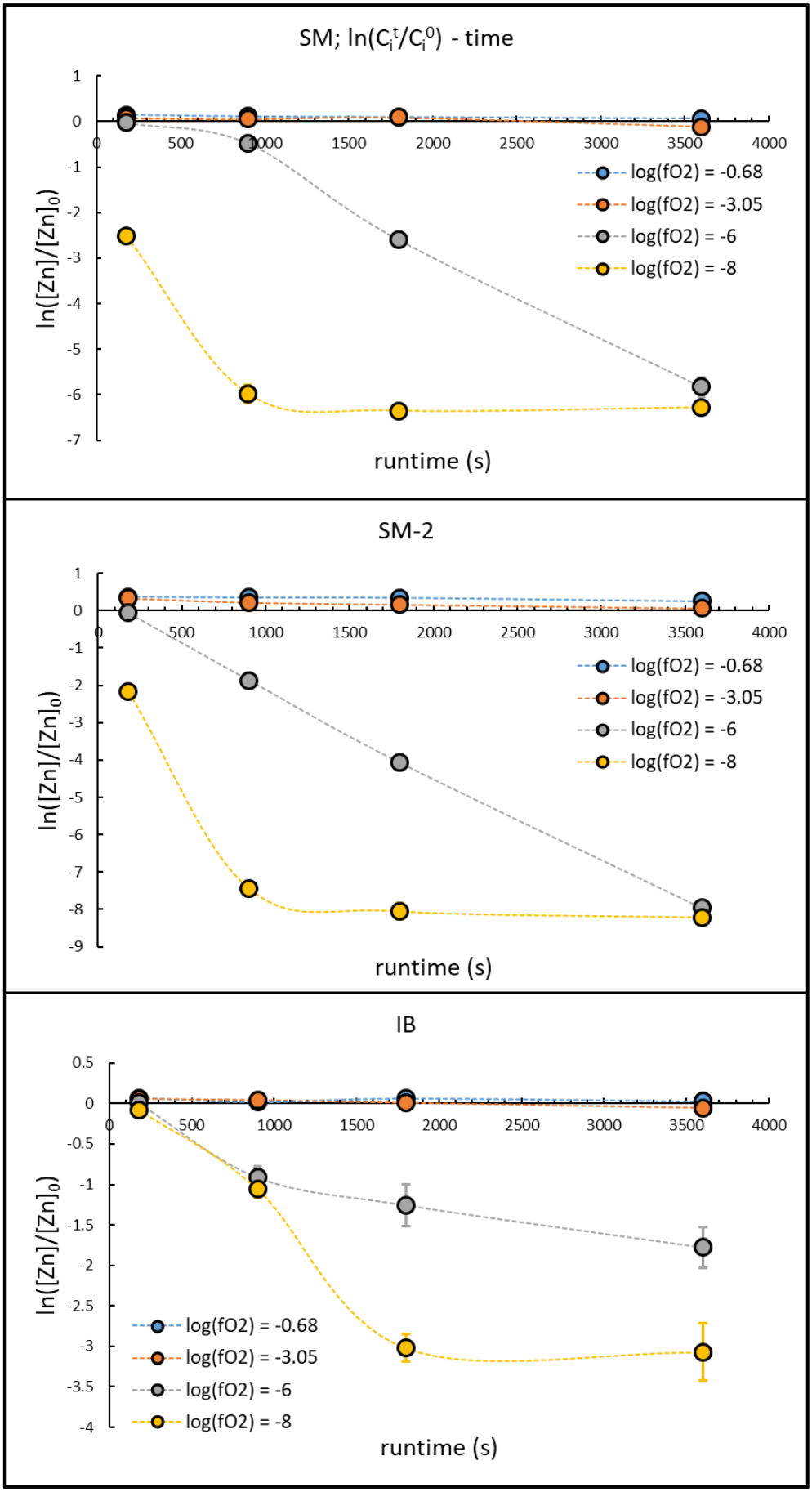


Figure A5.4: Temporal evolution of the volatility factor for Cu in all compositions.

A5.5 – Zinc


SM; ln(C_i^t/C_i^0) - time
ln([Zn]/[Zn]_0)
runtime (s)
log(fO2) = -0.68
log(fO2) = -3.05
log(fO2) = -6
log(fO2) = -8
SM-2
ln([Zn]/[Zn]_0)
runtime (s)
log(fO2) = -0.68
log(fO2) = -3.05
log(fO2) = -6
log(fO2) = -8
IB
ln([Zn]/[Zn]_0)
runtime (s)
log(fO2) = -0.68
log(fO2) = -3.05
log(fO2) = -6
log(fO2) = -8

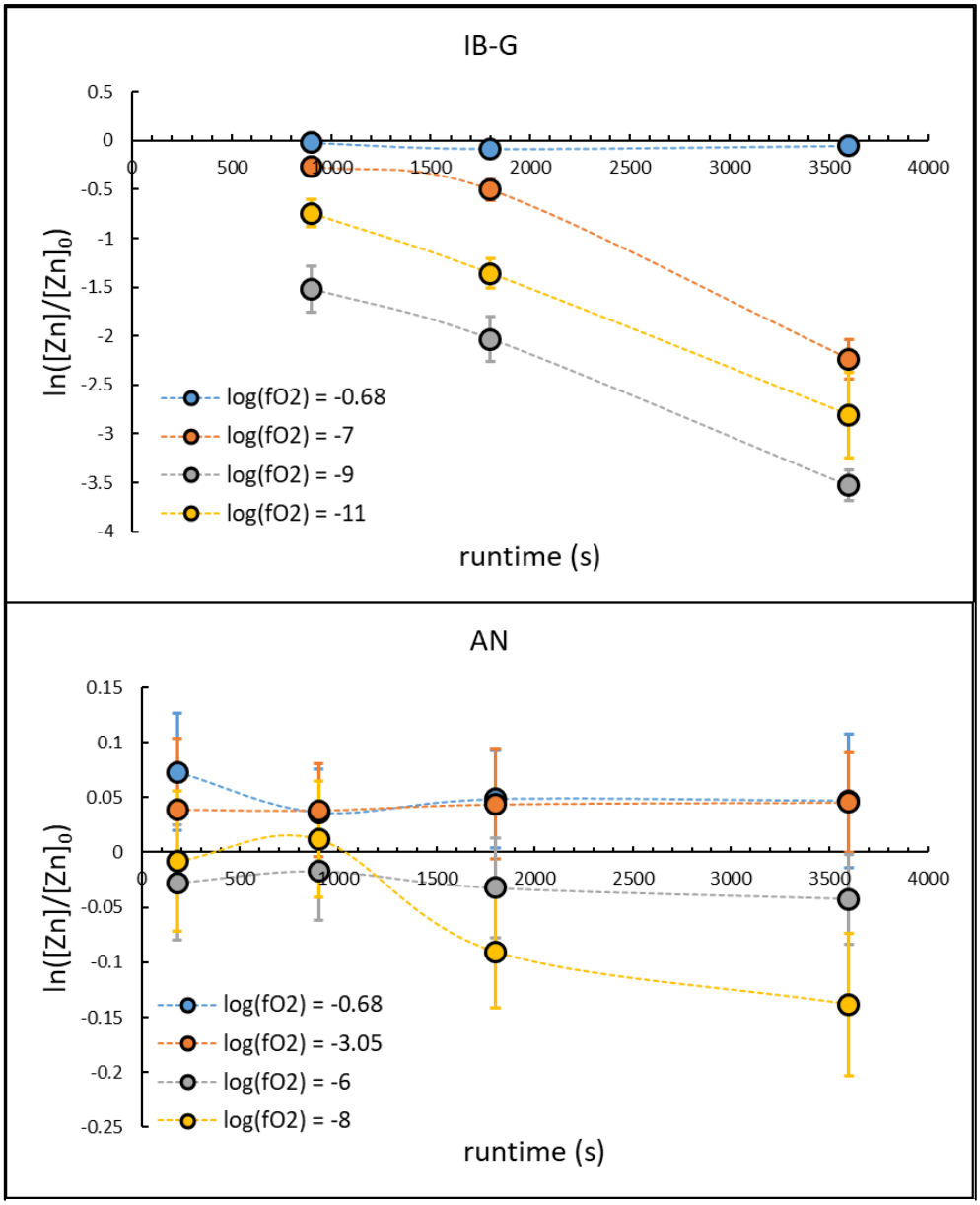


Figure A5.5: Temporal evolution of the volatility factor for Zn in all compositions.

A5.6 – Gallium

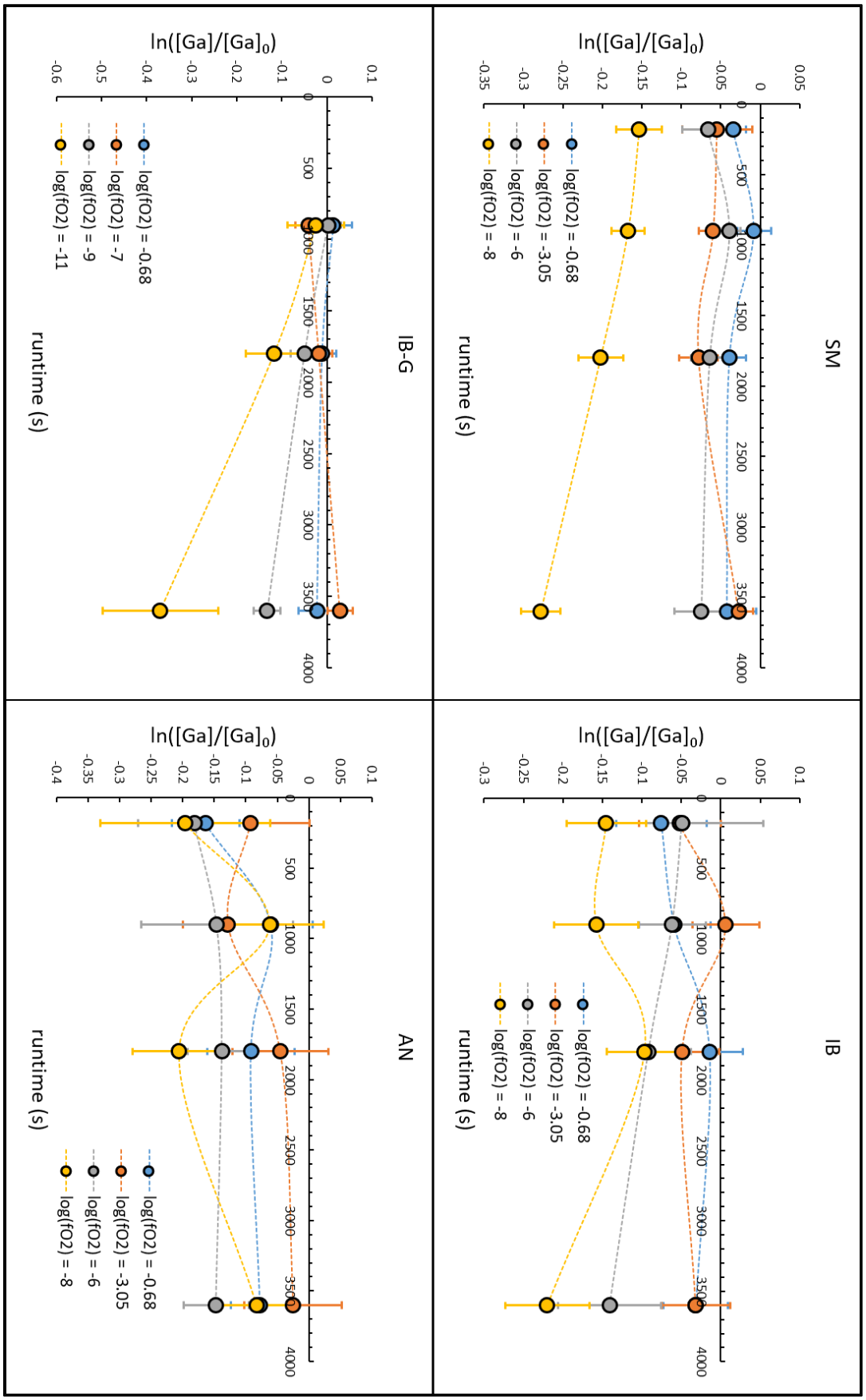
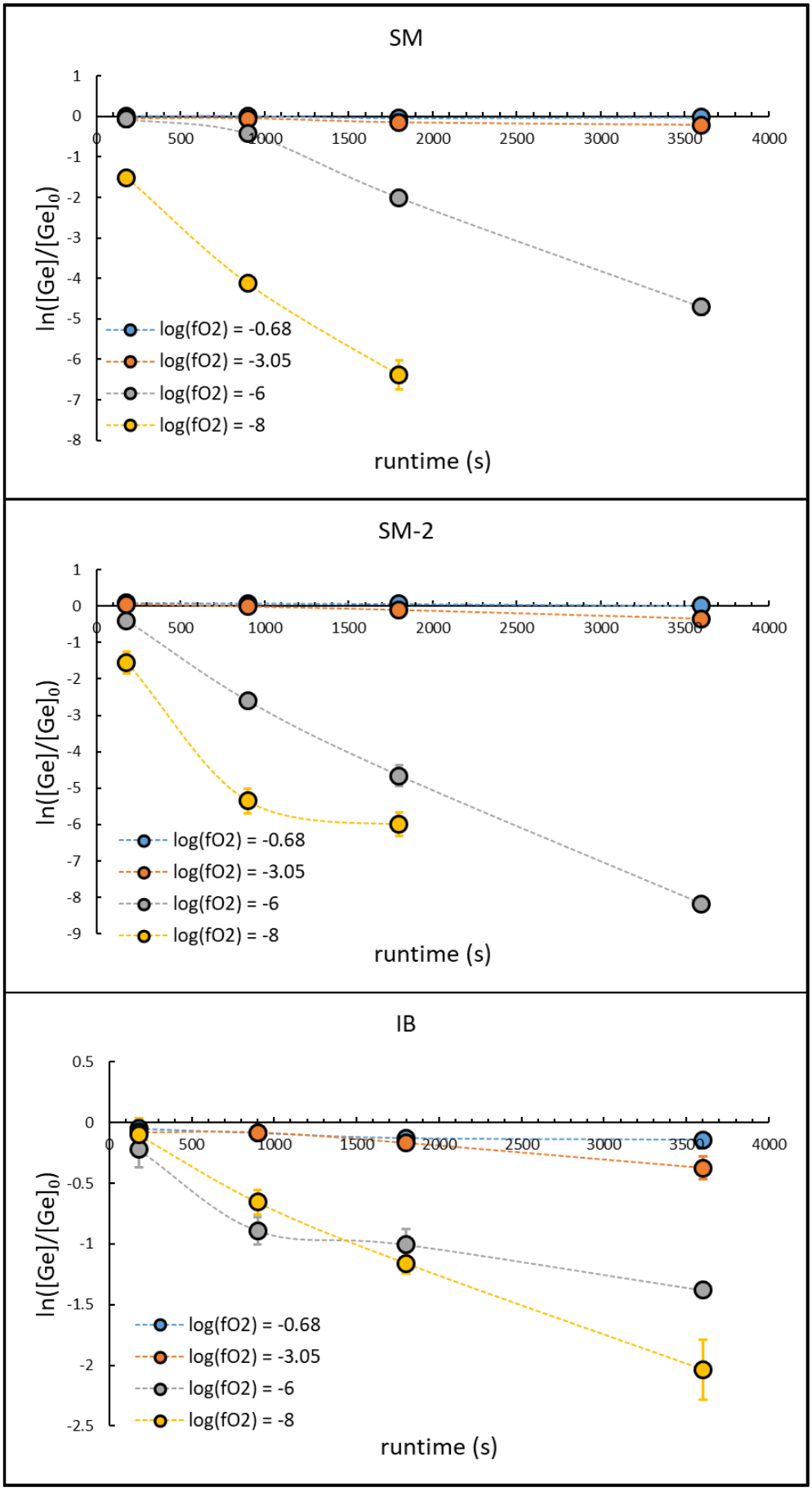


Figure A5.6: Temporal evolution of the volatility factor for Ga in all compositions.

A5.7 – Germanium



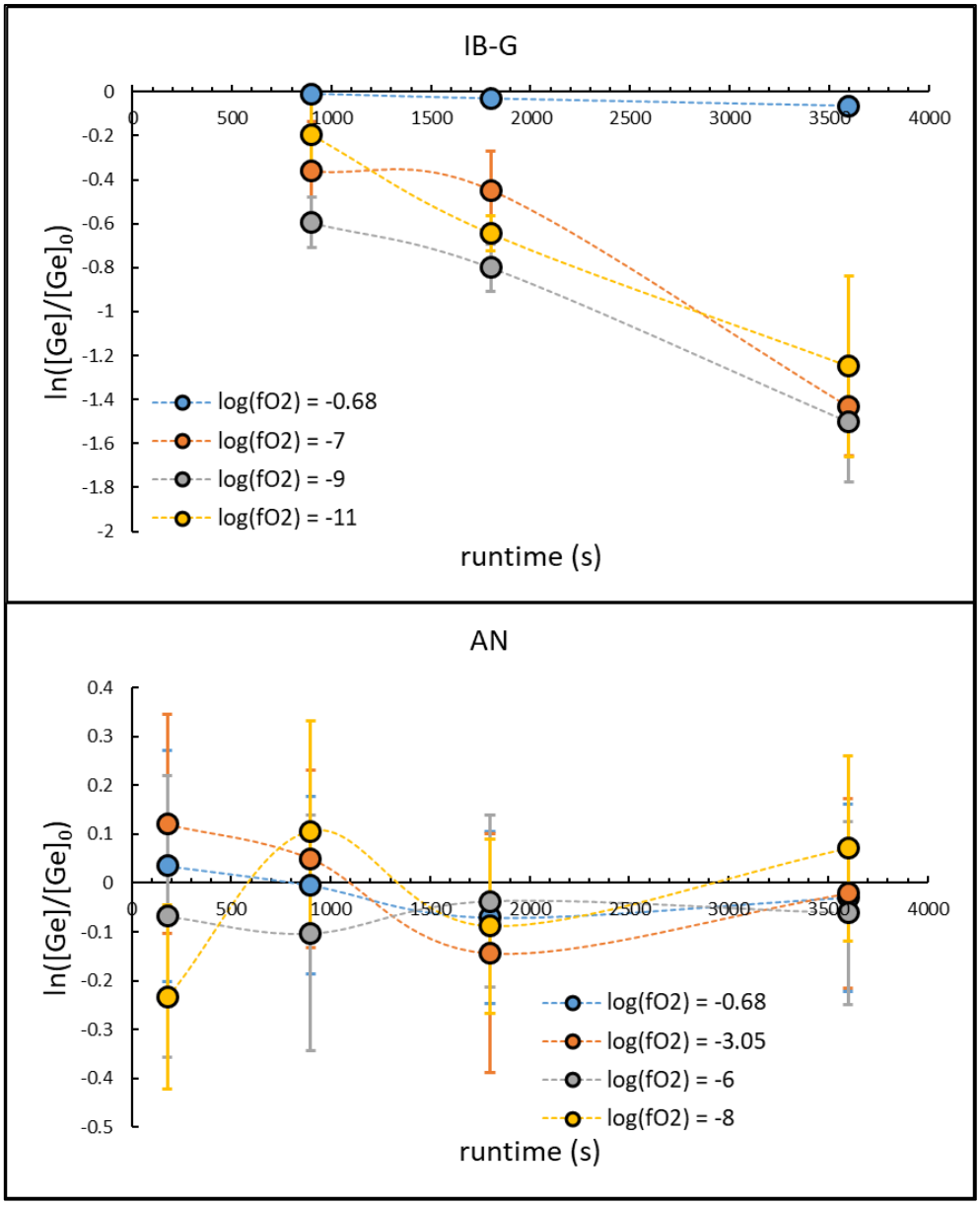


Figure A5.7: Temporal evolution of the volatility factor for Ge in all compositions.

A5.8 – Arsenic

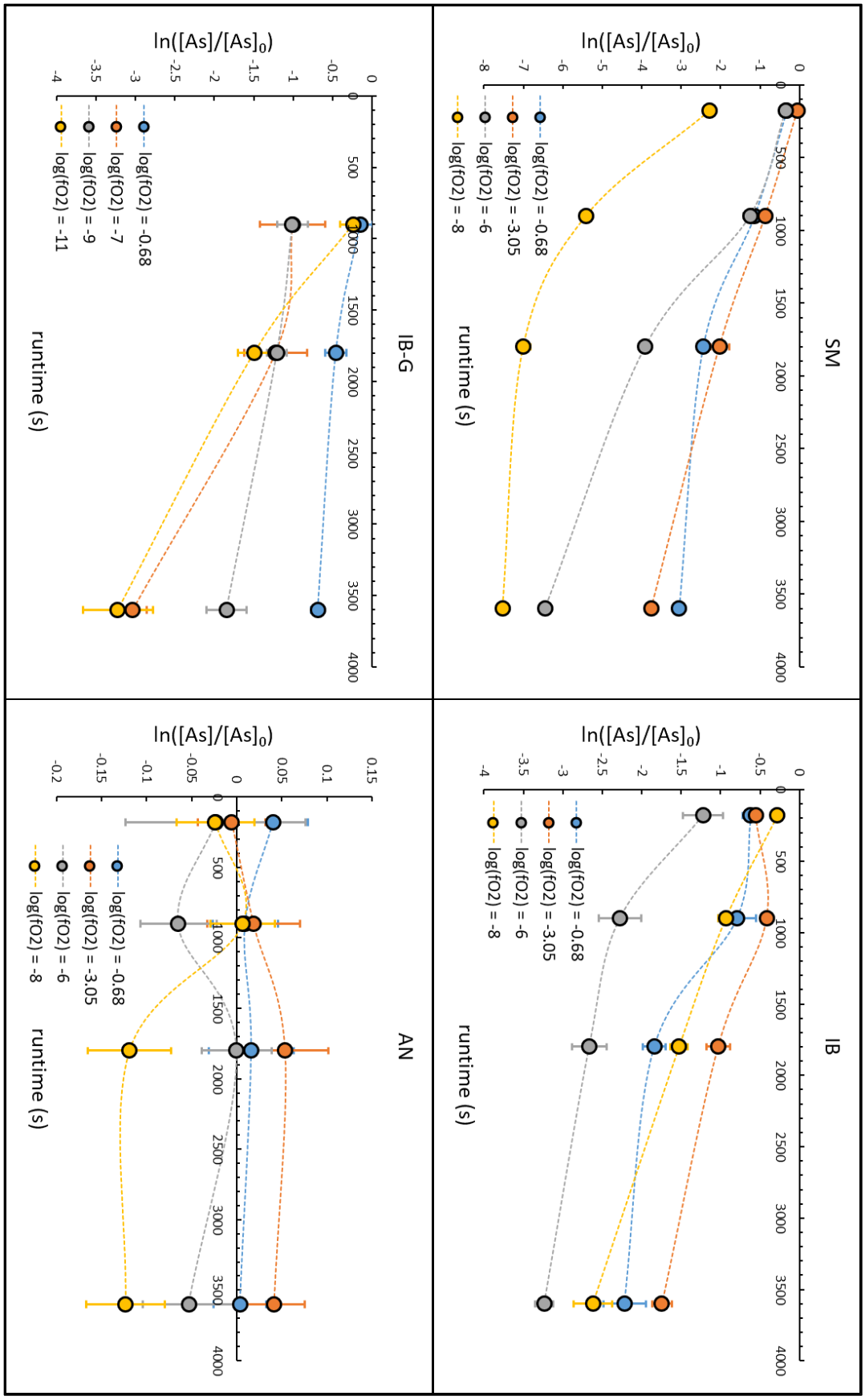


Figure A5.8: Temporal evolution of the volatility factor for As in all compositions.

A5.9 – Rubidium

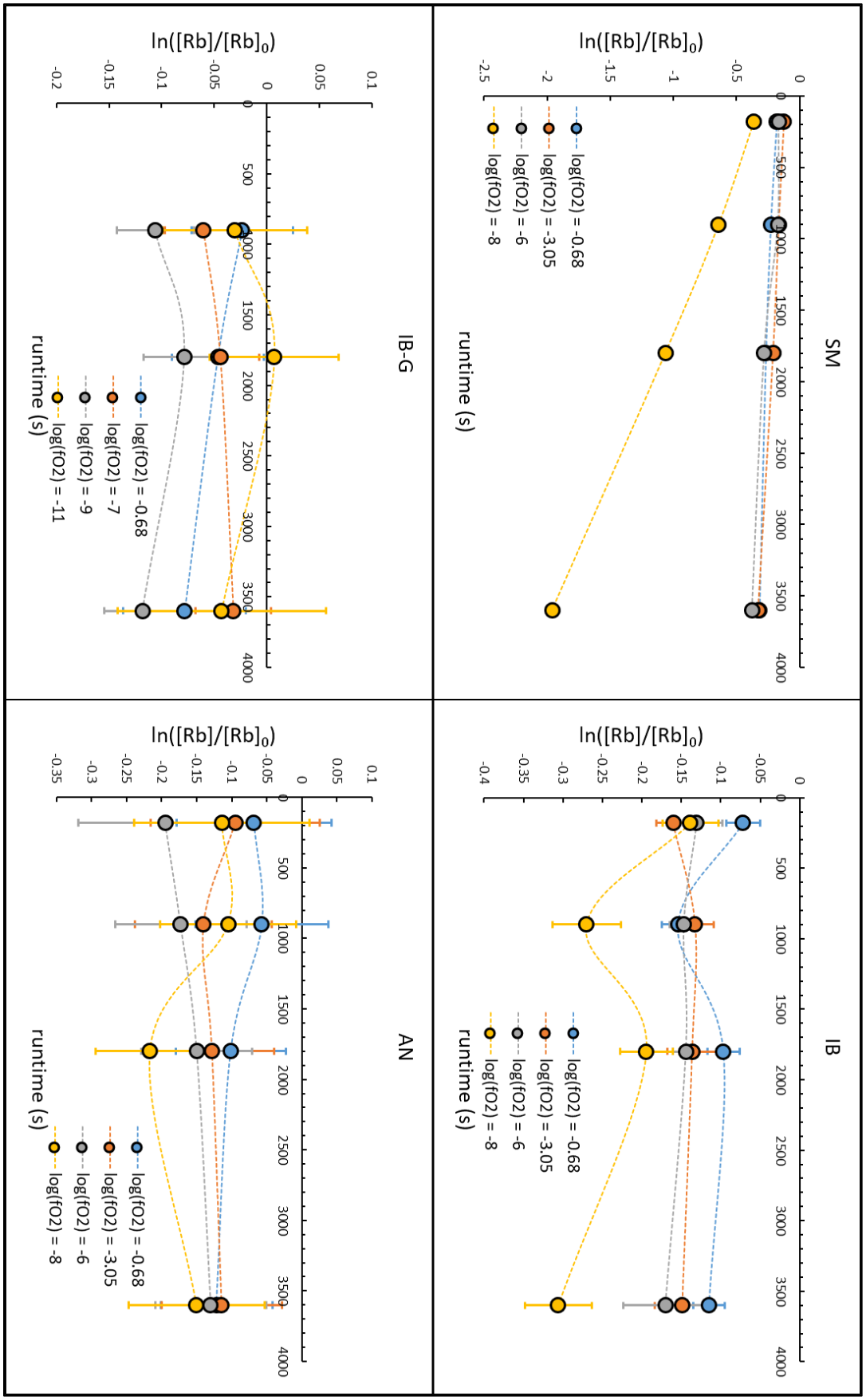
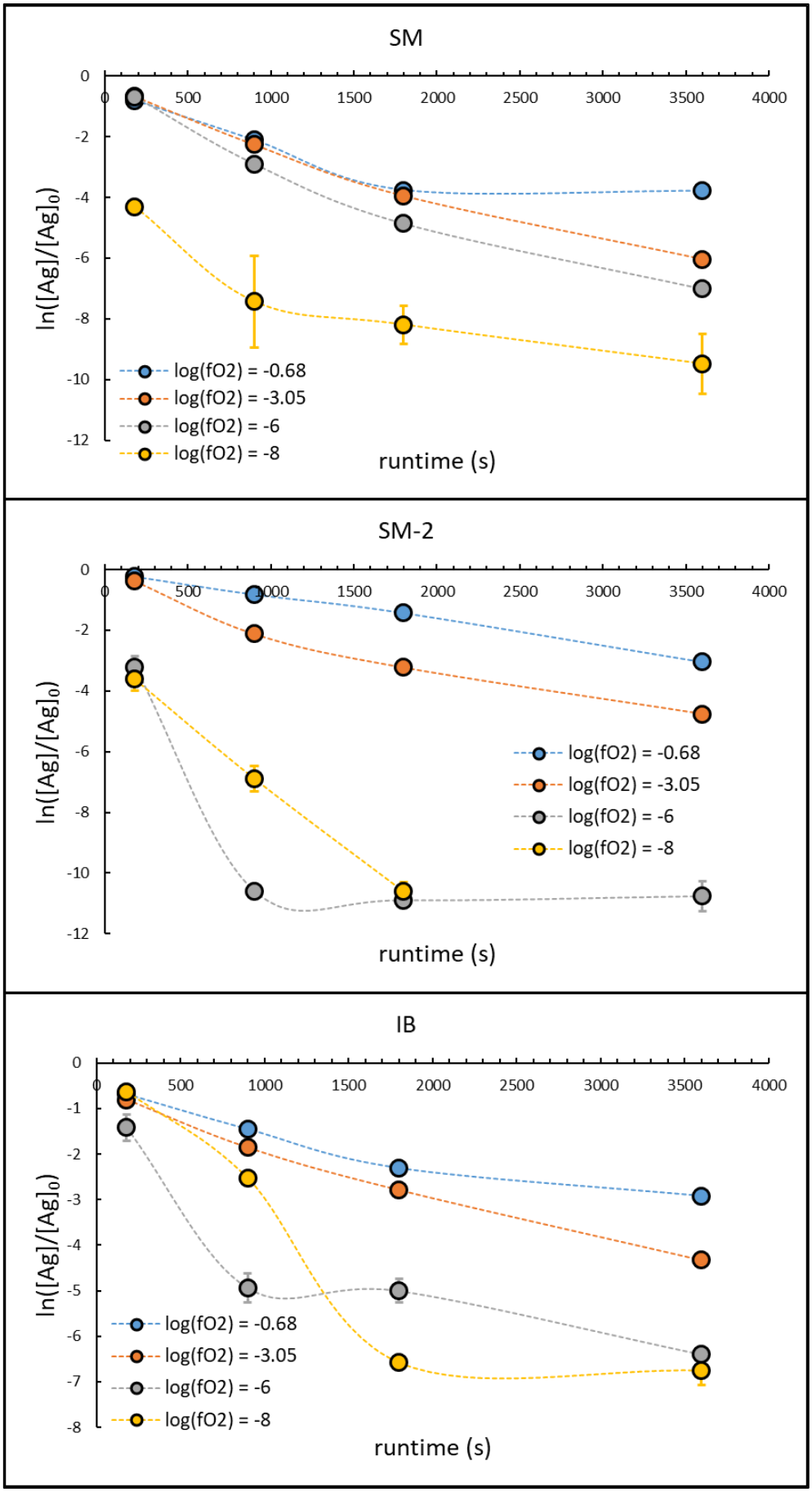


Figure A5.9: Temporal evolution of the volatility factor for Rb in all compositions.

A5.10 – Silver


SM
ln([Ag]/[Ag]0)
runtime (s)
log(fO2) = -0.68
log(fO2) = -3.05
log(fO2) = -6
log(fO2) = -8
SM-2
ln([Ag]/[Ag]0)
runtime (s)
log(fO2) = -0.68
log(fO2) = -3.05
log(fO2) = -6
log(fO2) = -8
IB
ln([Ag]/[Ag]0)
runtime (s)
log(fO2) = -0.68
log(fO2) = -3.05
log(fO2) = -6
log(fO2) = -8

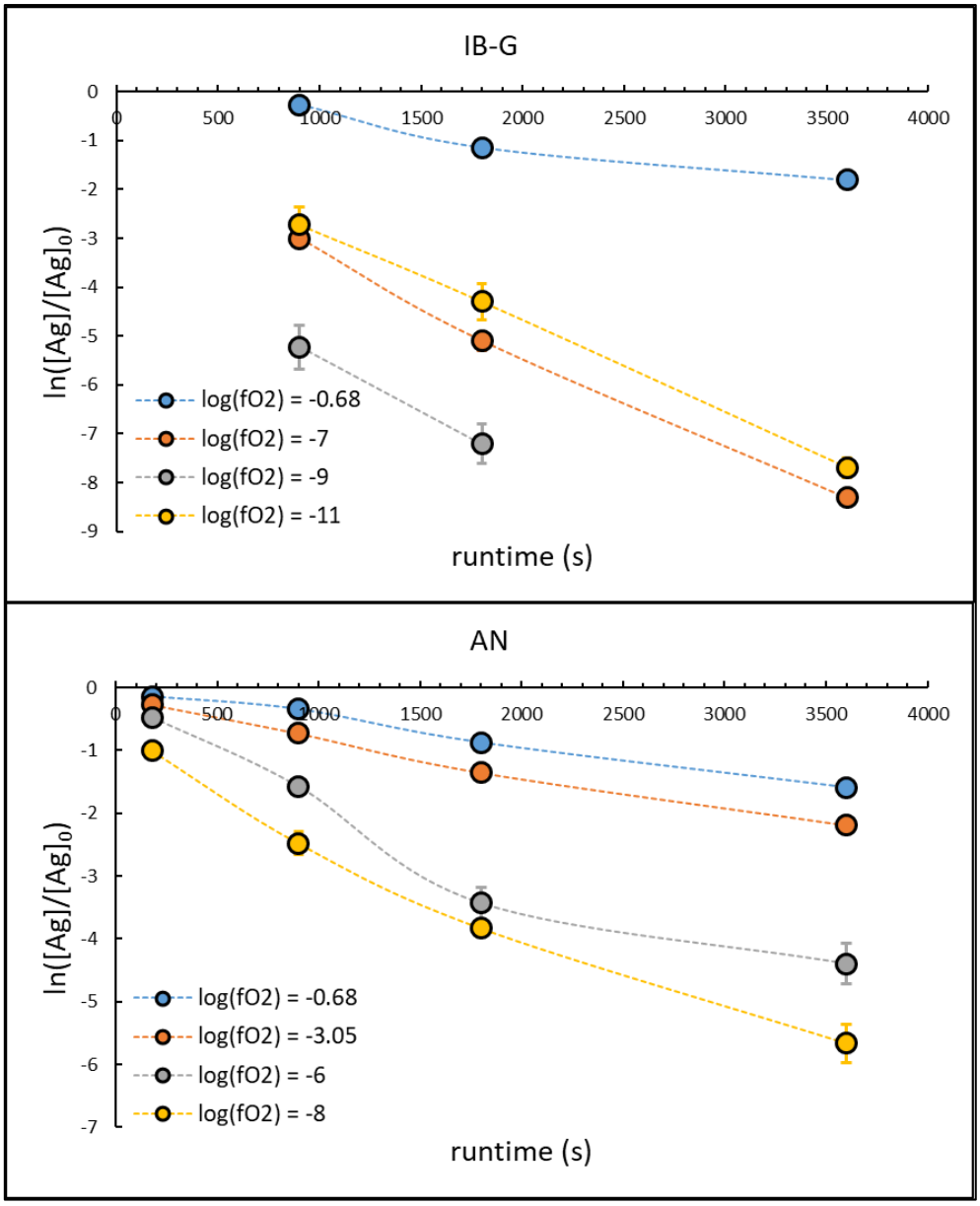
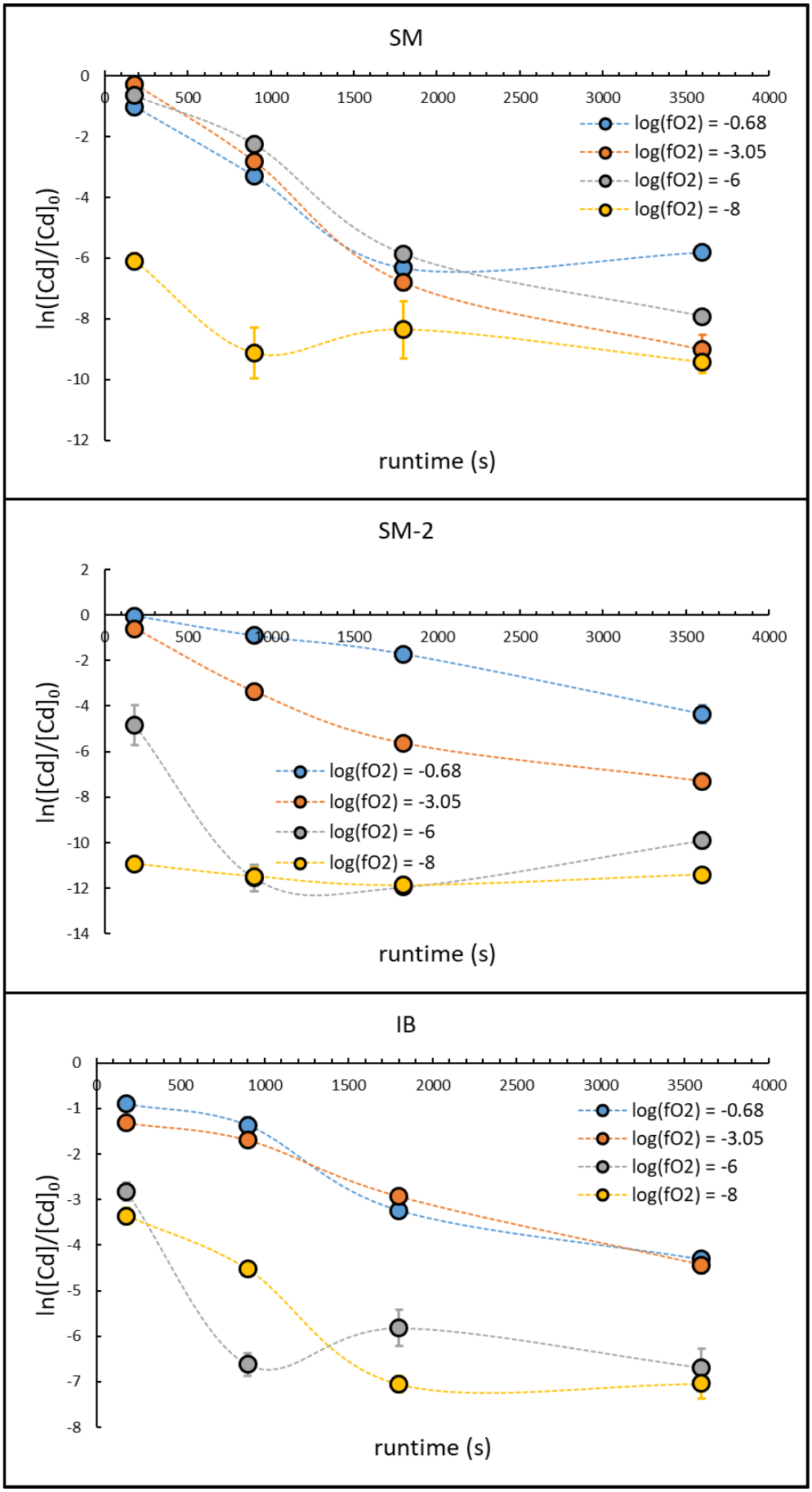


Figure A5.10: Temporal evolution of the volatility factor for Ag in all compositions.

A5.11 – Cadmium



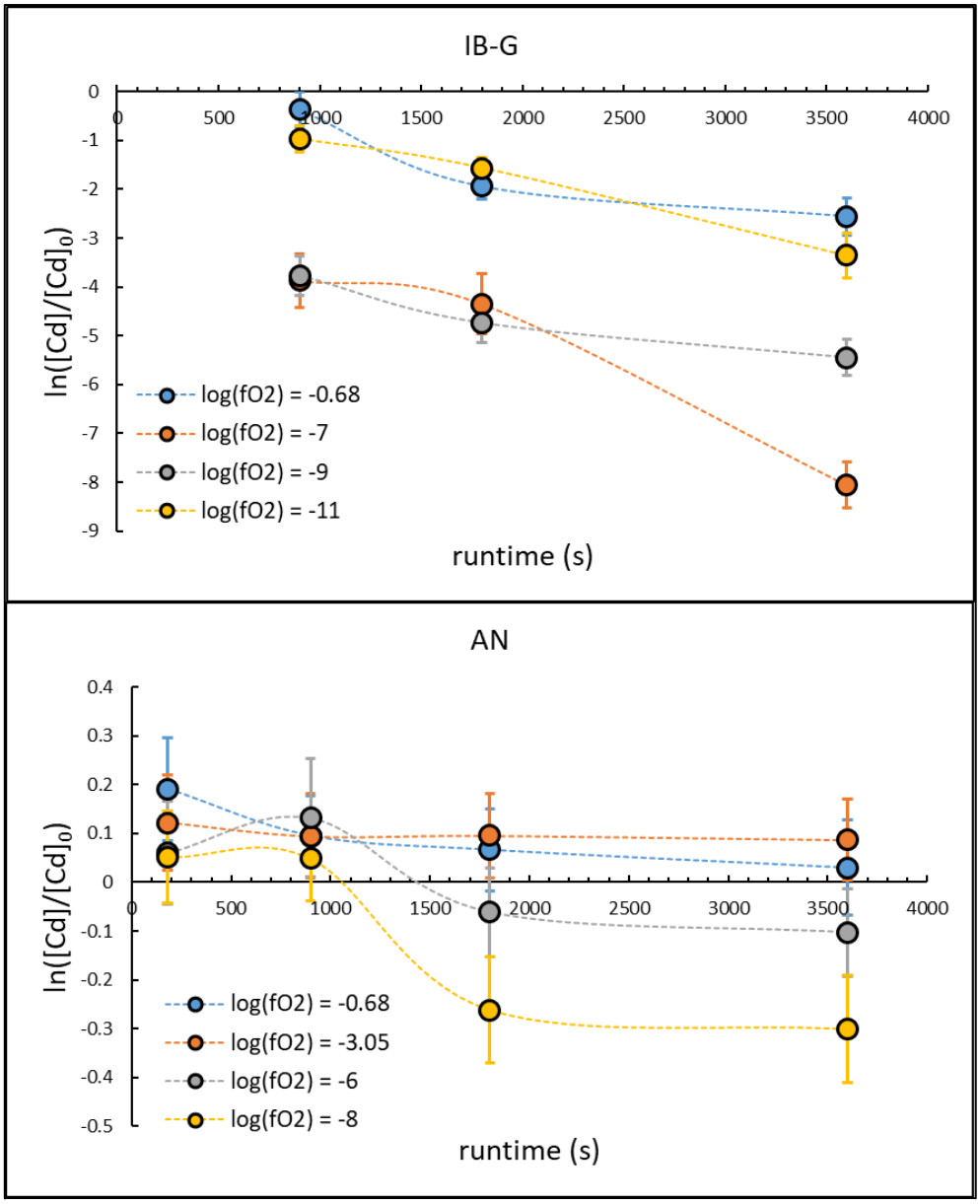


Figure A5.11: Temporal evolution of the volatility factor for Cd in all compositions.

A5.12 – Indium

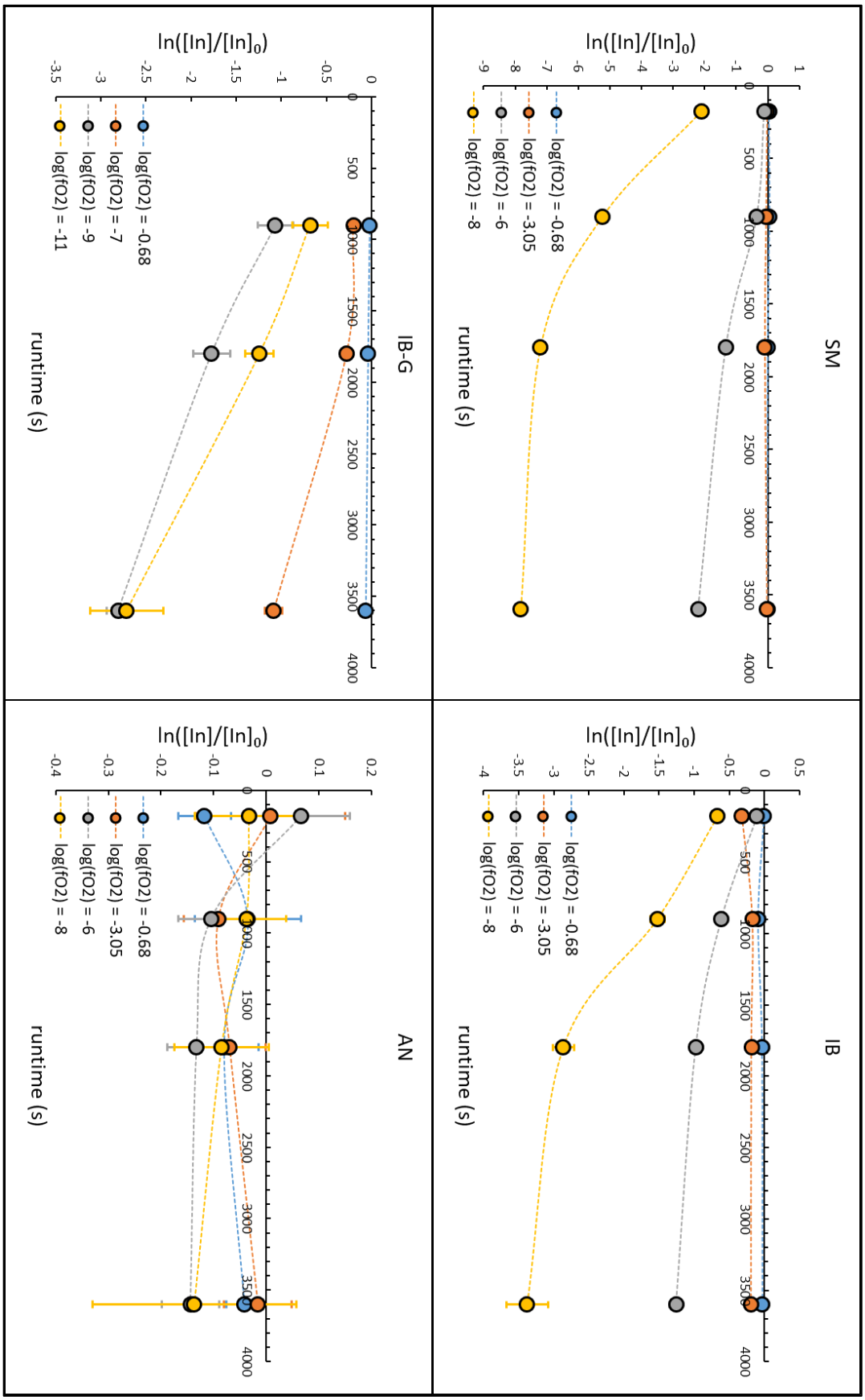
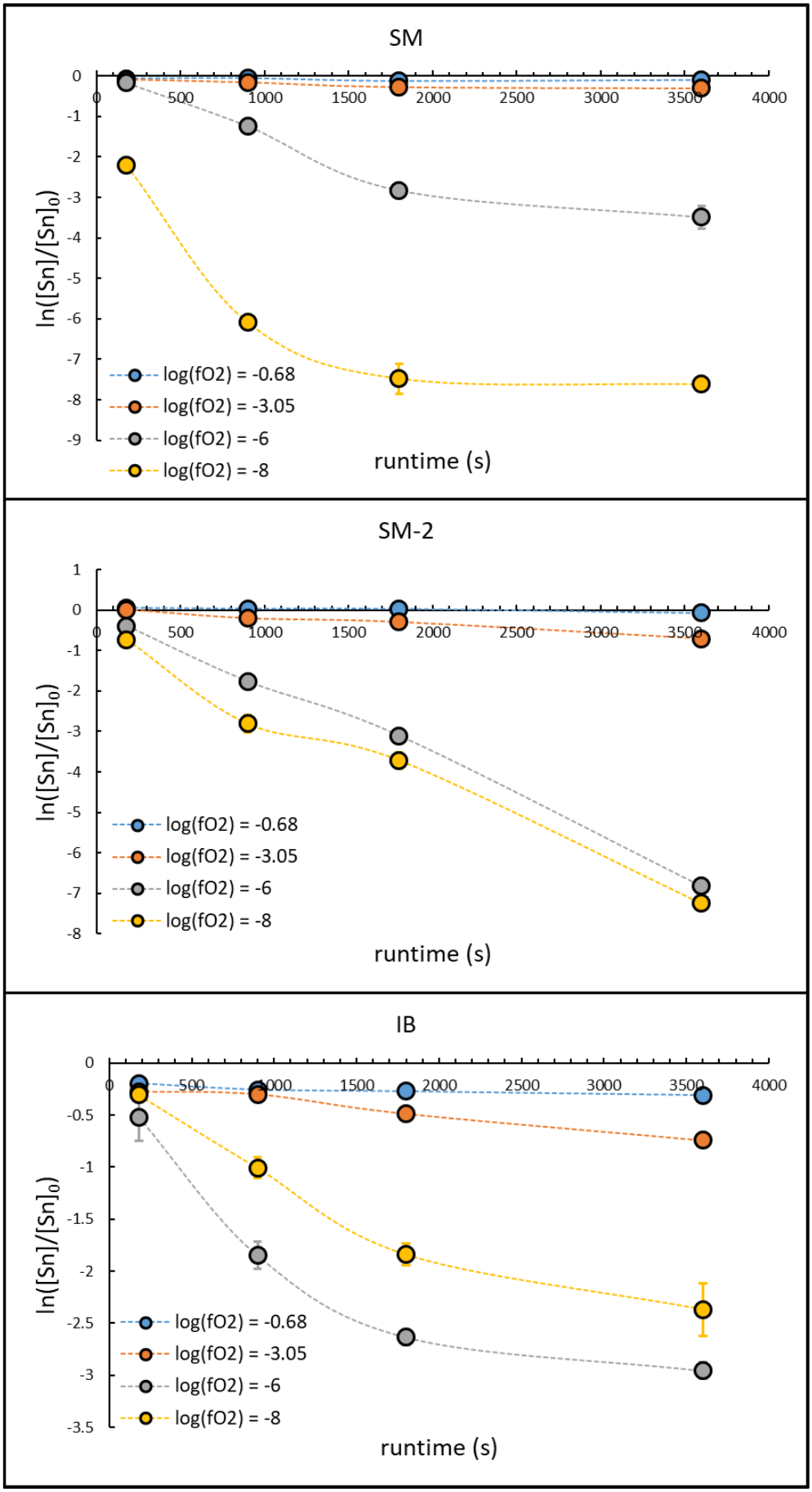


Figure A5.12: Temporal evolution of the volatility factor for In in all compositions.

A5.13 – Tin


SM
ln([Sn]/[Sn]0)
runtime (s)
log(fO2) = -0.68
log(fO2) = -3.05
log(fO2) = -6
log(fO2) = -8
SM-2
ln([Sn]/[Sn]0)
runtime (s)
log(fO2) = -0.68
log(fO2) = -3.05
log(fO2) = -6
log(fO2) = -8
IB
ln([Sn]/[Sn]0)
runtime (s)
log(fO2) = -0.68
log(fO2) = -3.05
log(fO2) = -6
log(fO2) = -8

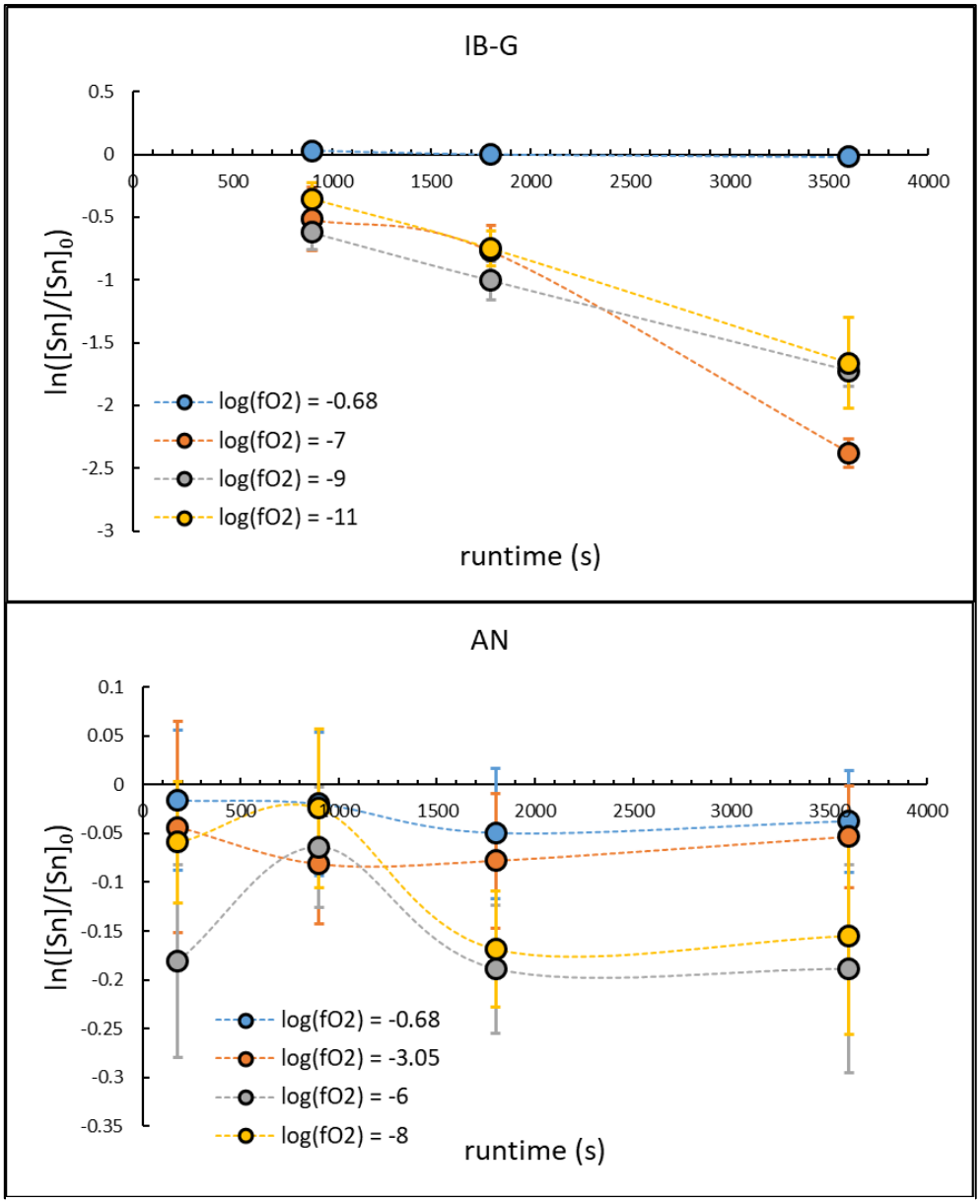


Figure A5.13: Temporal evolution of the volatility factor for Sn in all compositions.

A5.14 – Antimony

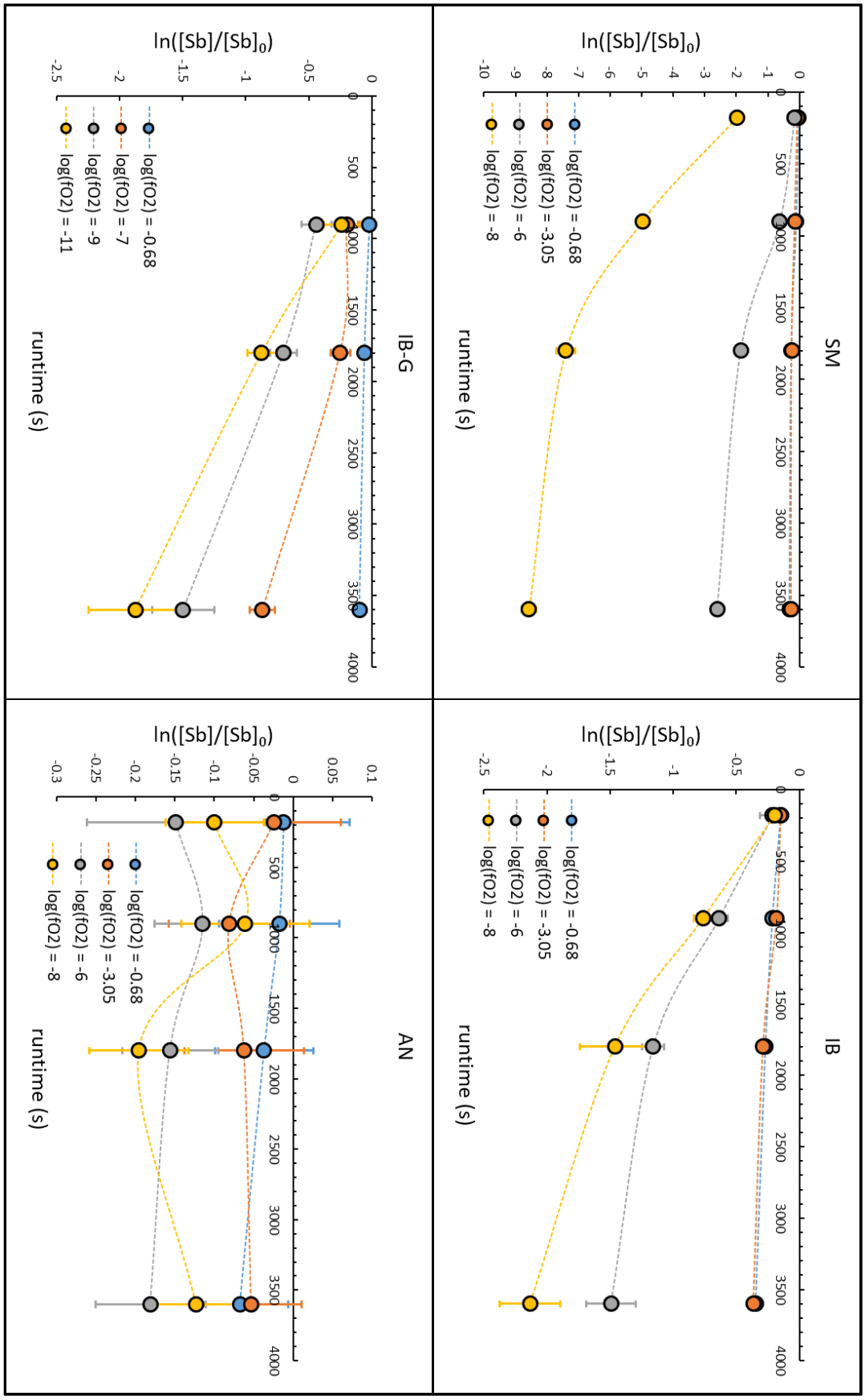


Figure A5.14: Temporal evolution of the volatility factor for Sb in all compositions.

A5.15 – Caesium

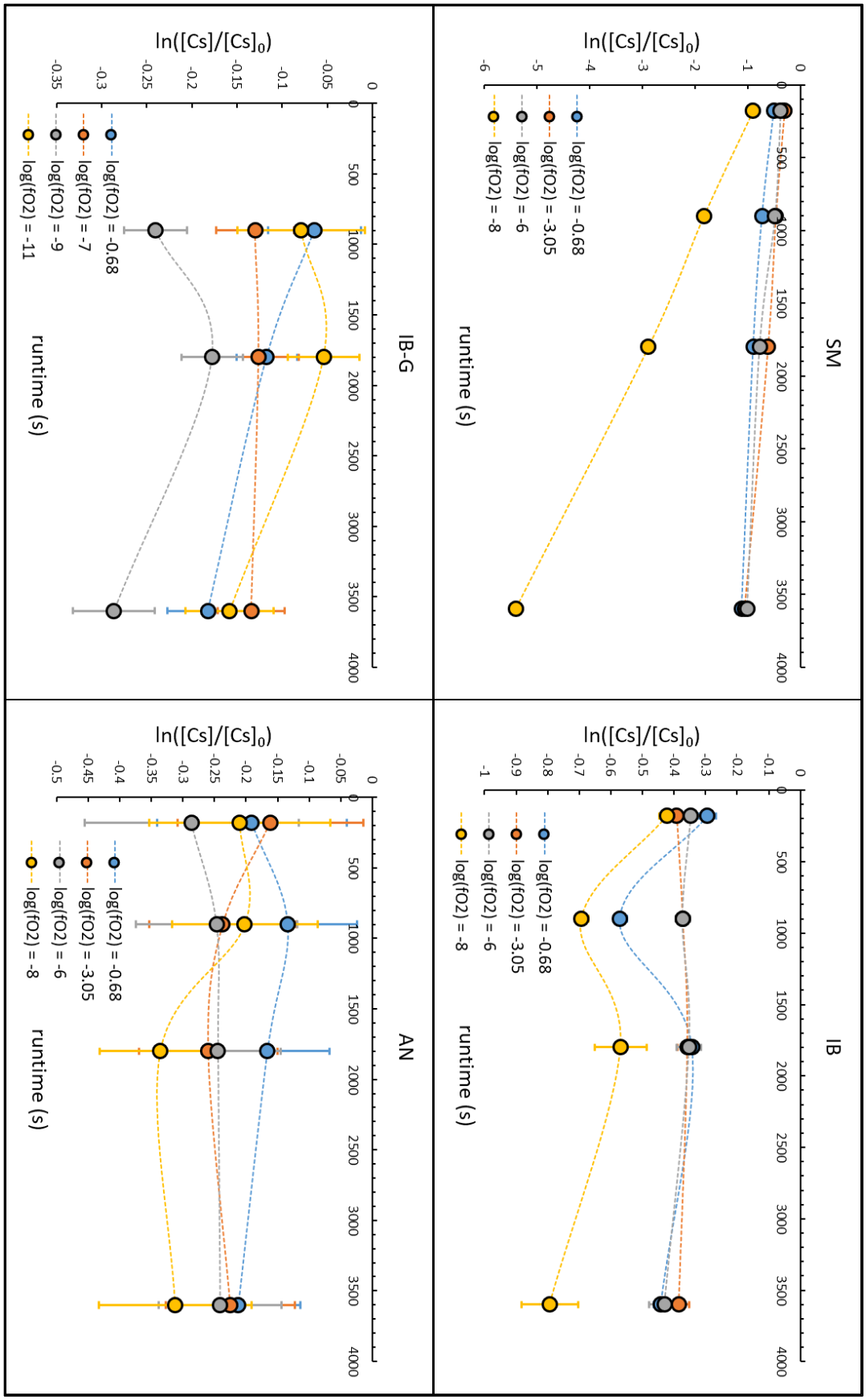
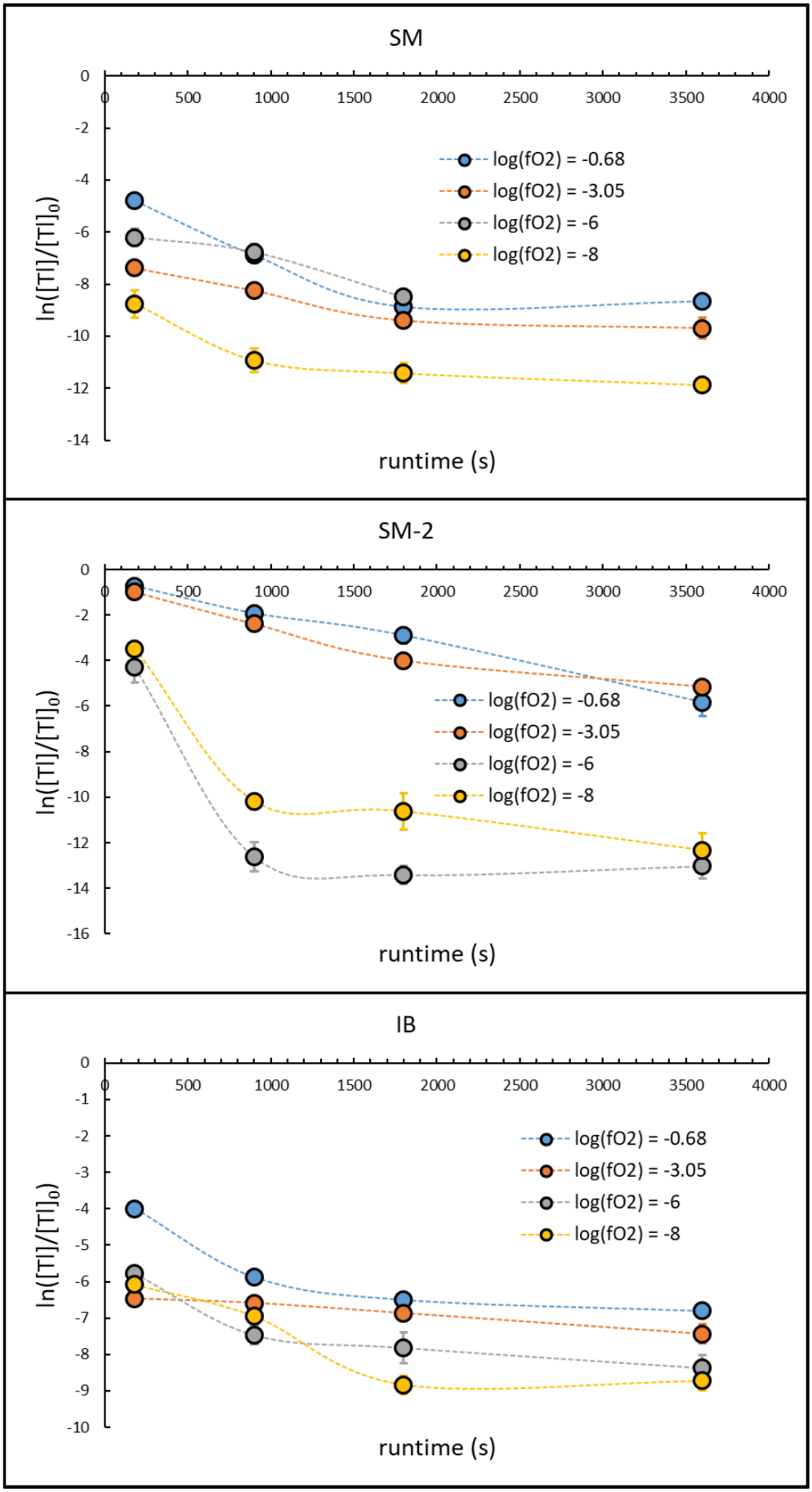


Figure A5.15: Temporal evolution of the volatility factor for Cs in all compositions.

A5.16 – Thallium



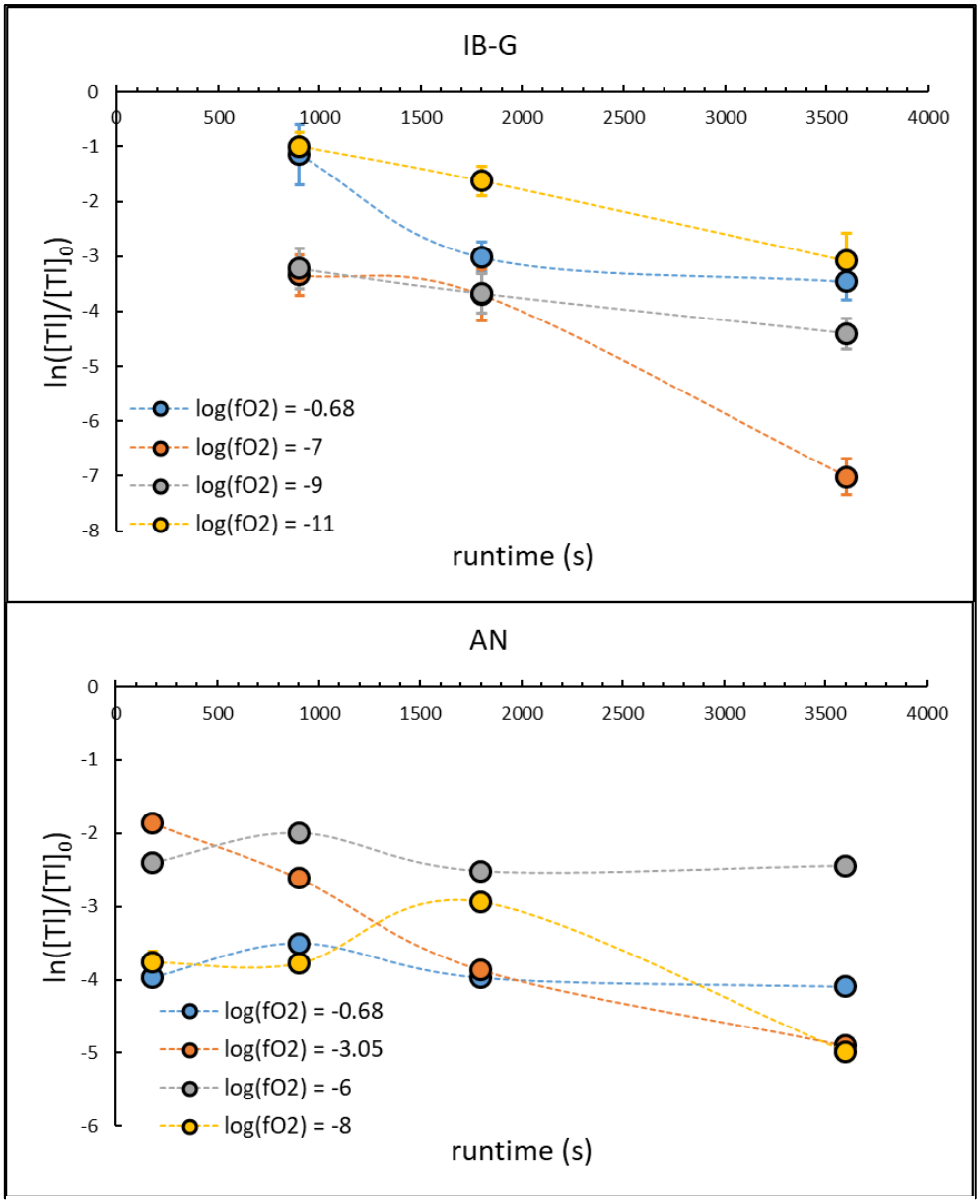


Figure A5.16: Temporal evolution of the volatility factor for Tl in all compositions.

A5.17 – Lead

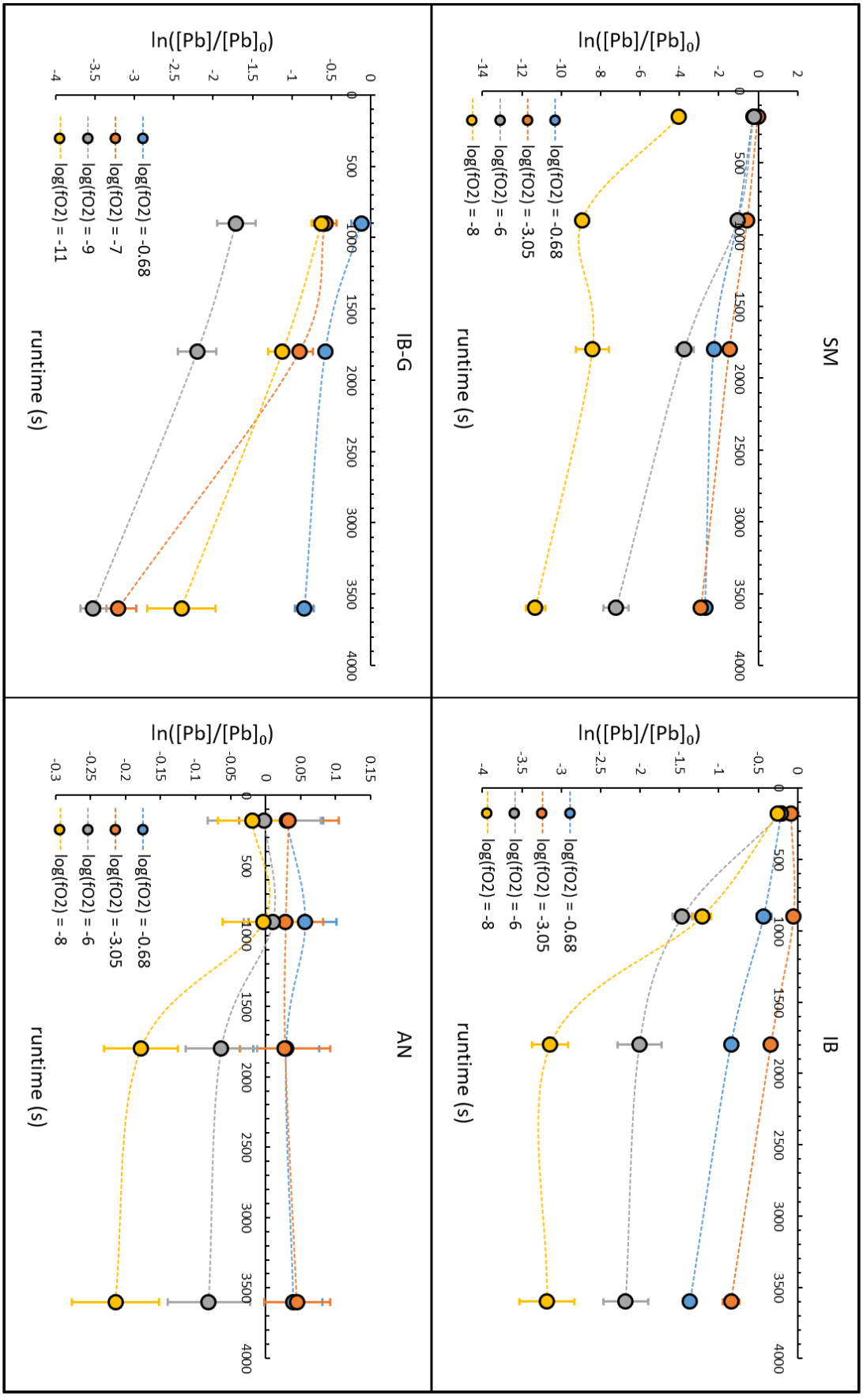


Figure A5.17: Temporal evolution of the volatility factor for Pb in all compositions.

Appendix 6 – The Effect of Sample Geometry

A6.1 – General Equations

In this appendix an equation is derived that describes the difference in exposed surface area between spherical and slab-shaped samples. This derivation was based solely on sample geometry (Eq. **A6.1 – A6.5**).

$$(A6.1):\ V_{Sphere} = \frac{4}{3}\pi r^3$$

$$(A6.2):\ A_{Sphere} = 4\pi r^2$$

$$(A6.3):\ r = \sqrt[3]{\frac{3V}{4\pi}}$$

$$(A6.4):\ V_{Beam} = lwh$$

$$(A6.5):\ A_{Beam,\ all\ faces} = 2(hl + hw + lw)$$

In these equations V is the volume and A the surface area of both geometries, r is the radius of the sphere and h, l and w are the height, length and width of the slab.

A6.2 – Evaporative Surface Area

The ratio of the surface areas of the sphere and slab was found by dividing Equations **A6.2** and **A6.5** (Eq. **A6.6**).

$$(A6.6):\ \frac{A_{Sphere}}{A_{Beam}} = \frac{4\pi r^2}{2(hl + hw + lw)}$$

In this study most samples were slabs, so their dimensions could be measured. However, to assess the volume of a sphere for an otherwise identical experiment some assumptions had to be made. All experiments used ~70 mg of a given starting material, so mass and density should be the same. Therefore, the sphere and slab should have an identical volume despite the change of shape ($V_{Sphere} = V_{Beam} = lwh$). Slight differences in melt density as a result of different rates of trace element evaporation are assumed to be negligible. Combining Equations **A6.1-2, A6.4** and **A6.6** gives

an equation that describes the ratio of the surface area of the sphere and slab solely in terms of slab geometry (Eq. **A6.7**).

$$(A6.7): \quad \frac{A_{Sphere}}{A_{Beam}} = \frac{4\pi\left(\sqrt[3]{\frac{3V_{Sp}}{4\pi}}\right)^2}{2(hl+hw+lw)} = \frac{4\pi\left(\frac{3lwh}{4\pi}\right)^{\frac{2}{3}}}{2(hl+hw+lw)}$$

This was rewritten to arrive at Equation **A6.8**.

$$(A6.8): \quad \frac{A_{Sphere}}{A_{Beam}} = \frac{\sqrt[3]{36\pi(lwh)^2}}{2(hl+hw+lw)}$$

Equation **A6.8** considers all six faces of the beam to be exposed. In the experiments only the top surface was exposed and others were assumed to always be in direct contact with the sample holder. In this scenario only a single surface, with dimensions lw, was exposed which yields Equation **A6.9**.

$$(A6.9): \quad \frac{A_{Sphere}}{A_{Beam}} = \left(\frac{\sqrt[3]{36\pi(lwh)^2}}{lw}\right)$$

This equation was rewritten to obtain the final equation describing the ratio of exposed surface area for a sphere and beam with a single exposed surface (Eq. **A6.10**).

$$(A6.10): \quad \frac{A_{Sphere}}{A_{Beam}} = \sqrt[3]{\frac{36\pi h^2}{lw}}$$

Equation **A6.10** shows that for beam-shaped samples of average dimensions 4.5x4.5x1.5 mm the $\frac{A_{Sphere}}{A_{Beam}}$ = 2.325.